OCS Study
MMS 2008-031

Survey of Deepwater Currents in the Northwestern Gulf of Mexico

Volume II: Technical Report

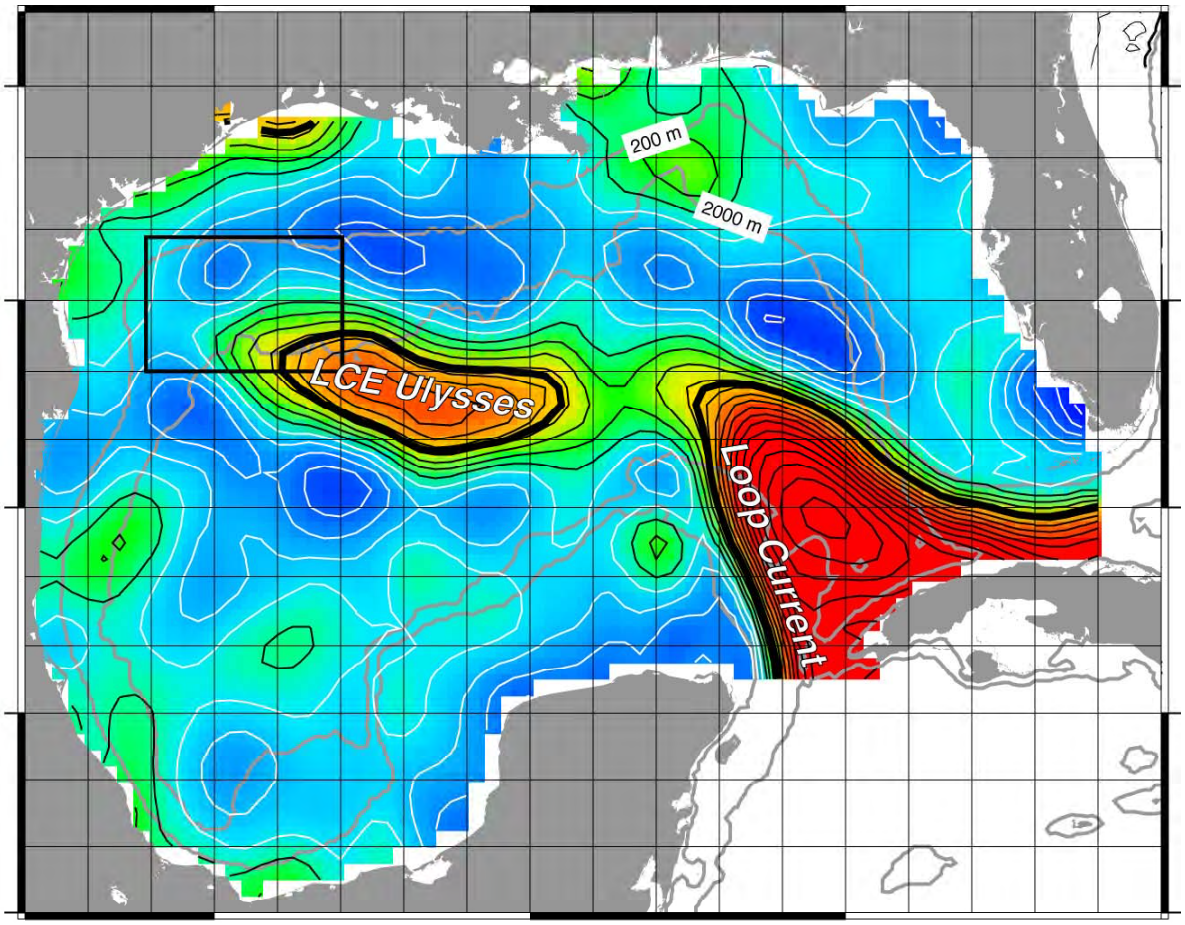

MMS U.S. Department of the Interior
Minerals Management Service
Gulf of Mexico OCS Region

OCS Study
MMS 2008-031

Survey of Deepwater Currents in the Northwestern Gulf of Mexico

Volume II: Technical Report

Authors

Kathleen Donohue
Peter Hamilton
Robert Leben
Randolph Watts
Evans Waddell

Prepared under MMS Contract
1435-01-03-CT-71562
by
Science Applications International Corporation
615 Oberlin Road, Suite 100
Raleigh, North Carolina 27605

Published by

U.S. Department of the Interior
Minerals Management Service
Gulf of Mexico OCS Region

New Orleans
June 2008

DISCLAIMER

This report was prepared under contract between the Minerals Management Service (MMS) and Science Applications International Corporation. This report has been technically reviewed by the MMS, and it has been approved for publication. Approval does not signify that the contents necessarily reflect the views and policies of the MMS, nor does mention of trade names or commercial products constitute endorsement or recommendation for use. It is, however, exempt from review and compliance with the MMS editorial standards.

REPORT AVAILABILITY

Extra copies of this report may be obtained from the Public Information Office (Mail Stop 5034) at the following address:

U.S. Department of the Interior
Minerals Management Service
Gulf of Mexico OCS Region
Public Information Office (MS 5034)
1201 Elmwood Park Blvd.
New Orleans, LA 70123-2394

Telephone: (504) 736-2519 or
1-800-200-GULF

CITATION

Donohue, K., P. Hamilton, R. Leben, R.Watts, and E. Waddell. 2008. Survey of deepwater currents in the northwestern Gulf of Mexico. Volume II: Technical report. U.S. Dept. of the Interior, Minerals Management Service, Gulf of Mexico OCS Region, New Orleans, LA. OCS Study MMS 2008-031. 375 pp.

ABOUT THE COVER

Shows an image of satellite altimetry that includes the large Loop Current Eddy (LCE) Ulysses just after it had merged with another anticyclone as it entered the southeastern portion of the study area. Although this eddy was never completely within the study area, it and eddies into which it was cleaved had a significant influence on the upper-layer circulation patterns and processes within the northwestern Gulf of Mexico.

ACKNOWLEDGMENT

The support, encouragement and patience of Dr. Alexis Lugo-Fernandez, the MMS COTR, from project inception through completion has been fundamental to the program success and resulting oceanographic insights. Valuable suggestions and support from the Science Review Group (Dr. J. Bane, Dr. William Schmitz and Dr. Wilton Sturges), during the course of the study, were positive, constructive and greatly appreciated. SAIC program personnel, Paul Blankinship (Data Management) and James Singer (Field Operations and Logistics), were crucial to the smooth data support and the outstanding data return and field activities. Mr. G. Chaplin (URI) very successfully conducted all aspects of the PIES instrumentation and field operations. Many additional people, too numerous to identify individually, were important to the program success, e.g., the captains and crews of the *R/V Longhorn* and the *R/V Pelican.* The patience, diligence, and expertise of Mrs. Carol Harris in the production of these reports are greatly appreciated by the Program Manager.

TABLE OF CONTENTS

Page

TABLE OF CONTENTS (continued)

Page

TABLE OF CONTENTS (continued)

Page

LIST OF FIGURES

LIST OF FIGURES (continued)

LIST OF FIGURES (continued)

LIST OF FIGURES (continued)

LIST OF FIGURES (continued)

LIST OF FIGURES (continued)

LIST OF FIGURES (continued)

LIST OF FIGURES (continued)

LIST OF FIGURES (continued)

LIST OF FIGURES (continued)

LIST OF FIGURES (continued)

LIST OF FIGURES (continued)

LIST OF FIGURES (continued)

LIST OF FIGURES (continued)

LIST OF FIGURES (continued)

LIST OF FIGURES (continued)

LIST OF FIGURES (continued)

LIST OF TABLES

LIST OF TABLES (continued)

ABBREVIATIONS AND ACRONYMS

ADCP	Acoustic Doppler Current Profiler
APL	Applied Physics Laboratory
AVHRR	Advanced Very High Resolution Radiometer
CCAR	Colorado Center for Astrodynamics Research
CE	Cyclonic Eddy
CEOF	Complex EOF
CERSAT	Centre ERS d'Archivage et de Traitement
CICESE	Centro de Investigacion Cientifica y de Educacion Superior de Ensenada
CNES	Centre National d'Etudes Spatiales, France
CPD	Cycles per Day
CTD (or C/T/D)	Conductivity/Temperature/Depth
CUPOM	University of Colorado – Princeton Ocean Model
DGPS	Digital Global Positioning System
DLP	Day Low Pass
DOF	Degrees of Freedom
EEZ	Exclusive Economic Zone
EKE	Eddy Kinetic Energy
EOF	Empirical Orthogonal Function
ERS-2	Earth Resources Satellite – 2
GDR	Geophysical Data Record
GEM	Gravest Empirical Mode
GEOSAT	Geodetic Satellite
GFO	Geosat Follow-On
GMT	Greenwich Mean Time or UTC
GOM	Gulf of Mexico
GSFC	Goddard Space Flight Center
IES	Inverted Echo Sounder
HBP	Hour Band Pass
HLP	Hour Low Pass
JHU/APL	Johns Hopkins University/Applied Physics Laboratory
KE	Kinetic Energy
LATEX	Louisiana-Texas
LC	Loop Current
LCE	Loop Current Eddy
LCFE	Loop Current Frontal Eddy
LHS	Left Hand Side
LUMCON	Louisiana Universities Marine Consortium
MAB	Meters Above Bottom
MMS	Minerals Management Service
MODIS	Moderate Resolution Imaging Spectroradiometer
NAD	North American Datum
NASA	National Aeronautics and Space Administration
NDBC	National Data Buoy Center
NESDIS	National Environmental Satellite, Data, and Information Service

NOAA	National Oceanic and Atmospheric Administration
OA	Objective Analysis
PDR	Precision Depth Recorder
PI	Principal Investigator
PIES	Inverted Echo Sounder with Pressure
PNG	Portable Network Graphics
PO.DAAC	Physical Oceanography Distributed Active Archive Center
PSU	Practical Salinity Unit
PV	Potential Vorticity
RAFOS	Ranging and Fixing of Sound (SOFAR spelled backwards)
RFP	Request for Proposal
RHS	Right Hand Side
RMS	Route Mean Square
SAIC	Science Applications International Corporation
SCULP	Surface Current and Lagrangian-drift Program
SeaWiFS	Sea-viewing Wide Field-of-view Sensor
SNR	Signal-to-Noise Ratio
SSH	Sea Surface Height
SSHA	Sea Surface Height Anomaly
SST	Sea Surface Temperature
SUW	Subtropical Underwater
T	Temperature
TABS	Texas Automated Buoy System
TAMU	Texas A&M University
T/C/P	Temperature/Conductivity/Pressure
TOPEX/Poseidon	Ocean Topography Experiment
TOP/POS	TOPEX/Poseidon
T/P	Temperature/Pressure
TRW	Topographic Rossby Wave
T/S	Temperature/Salinity
T/P/S	Temperature/Pressure/Salinity
T/S/P	Temperature/Salinity/Pressure
UNOLS	University-National Oceanographic Laboratory System
UTC	Coordinated Universal Time or GMT
UTMSI	University of Texas Marine Science Institute
WGS	World Geodetic System

CHAPTER 1 INTRODUCTION AND OBJECTIVES

1.1 Background

The Minerals Management Service (MMS) awarded a contract to Science Applications International Corporation (SAIC) to conduct a study titled: *Survey of Deepwater Currents in the Northwestern Gulf of Mexico* (often referred to as the NW Gulf Study). The timing and general area of investigation extends the focus of a series of preliminary studies that as a group will provide a basis for effective design and implementation of comprehensive ocean investigations having a goal of in-depth understanding and characterization of Gulf of Mexico (GOM) circulation and dynamics. These prior MMS-funded studies include the Deepwater Physical Oceanography Reanalysis and Synthesis of Historical Data (Nowlin et al., 2001), the DeSoto Canyon Eddy Intrusion Study (Hamilton et al., 2000), the Study of Deepwater Observations in the Northern Gulf of Mexico from In-Situ Current Meters and PIES (Hamilton et al., 2003), and the recently completed Exploratory Study of Deepwater Currents in the GOM (Donohue et al., 2006). Additionally, the MMS is presently funding a field measurement/data synthesis program titled: *A Study of Deepwater Currents in the Eastern Gulf of Mexico*. Clearly, the NW Gulf Study should be viewed in the context of an expanding multi-program database that is providing insights to initial characterization of dynamical aspects of the GOM circulation patterns that vary significantly in both time and space.

For the MMS, the NW Gulf Study is one component of concurrent MMS-funded measurement efforts in the western GOM. Support was provided by the MMS for measurements in an American Sector and a Mexican Sector. The program in the Mexican Sector was separately funded by the MMS through an agreement with Centro de Investigacion Cientifica-y de Educaion Superior de Ensenada (CICESE.) The dividing line between the sectors was the Exclusive Economic Zone (EEZ) boundary between the United States and Republic of Mexico (Figure 1.1-1). The MMS coordinated the timing and placement of instrumentation so observations would be mutually compatible, and hence, support a combined or integrated data analysis and process synthesis.

Boundaries of the NW Gulf Study area are shown in Figure 1.1-1 that also identifies selected major and relevant bathymetric and cultural features. Within the American Sector, the Sigsbee Escarpment is a major bathymetric feature that can have a substantial influence on various dynamic ocean processes (Donohue et al., 2006). It is apparent in this figure that within the American Sector, the area of deeper water (depths greater than ~ 2500 m) at the base of the Sigsbee Escarpment is relatively limited. However, within the contiguous Mexican Sector, there are extensive areas of deepwater below the base of the Sigsbee Escarpment and its extension on the western margin of the GOM, the Perdido Escarpment. In the American Sector, the western and northern study area boundaries were defined by the 200-m isobath. Hence, the focus of measurements and processes of interest are those that occur on and over the continental slope and upper rise in the northwestern corner of the GOM.

The MMS-specified objectives for this study are:

A. To collect current data to increase our deepwater database and knowledge of the deep circulation in the northwestern GOM;

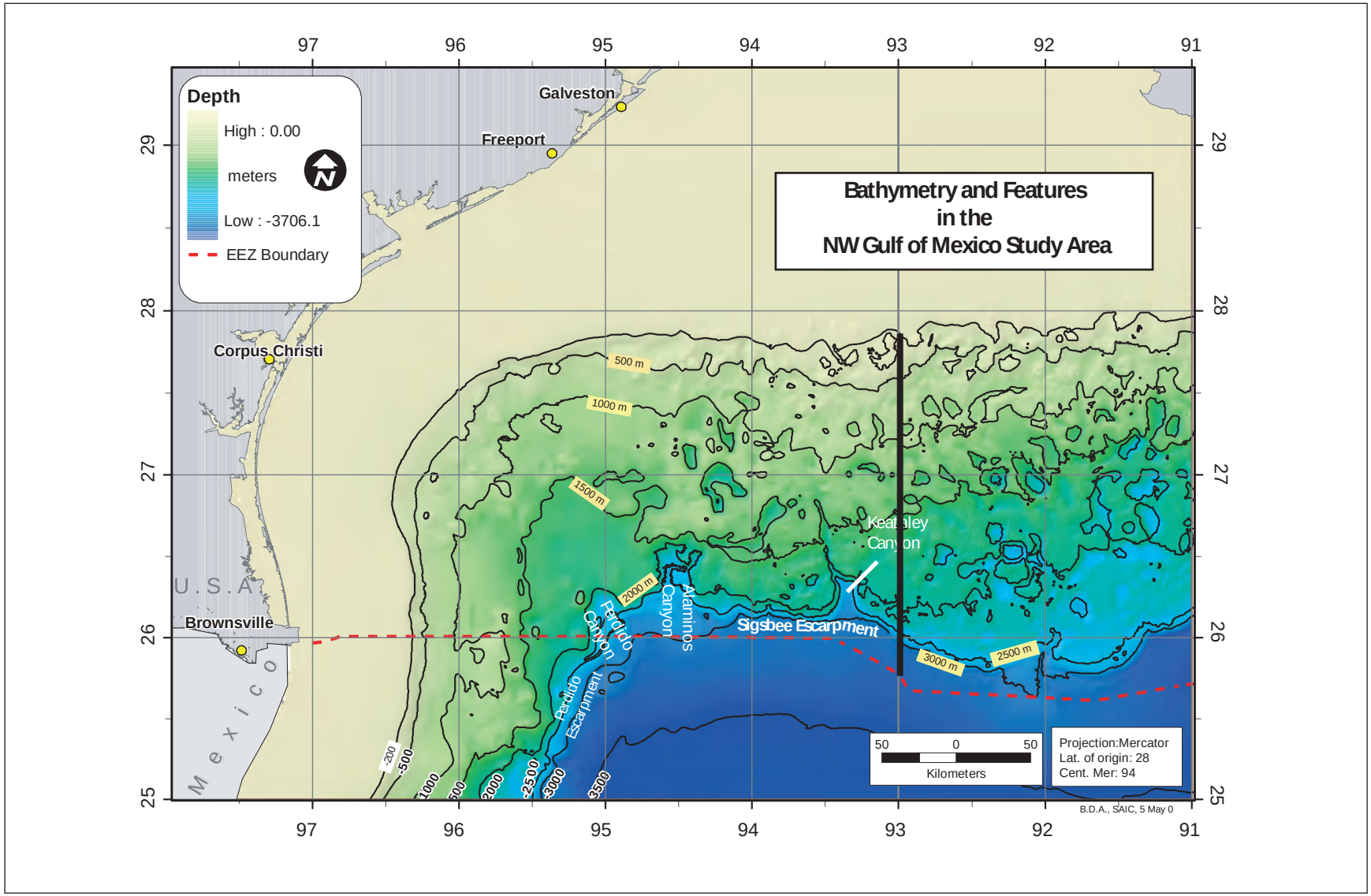

Figure 1.1-1. Complex bathymetry and key bottom features within the NW Gulf study area. The study area eastern boundary is 93°W. The western and northern boundaries are the 200-m isobath. The southern boundary is the EEZ. Note, in this map area the Sigsbee Escarpment extends to the east of the study area along the 2500-m and 3000-m isobaths.

B. To gather information to estimate oceanographic parameters needed to make experimental designs of full-scale physical oceanography studies in deepwater; and

C. To provide information to use in oil spill analyses including the emerging deep spill analysis, other ongoing studies, to help evaluate exploration plans, and contribute to the preparation of NEPA documents.

1.2 General Program Description

As identified in the Request for Proposal (RFP), a possible design for the study involved 13 full-depth moorings instrumented with various and appropriate sensors to resolve and estimate key parameters and conditions within the study area. Additionally, a combination of remotely sensed (satellite) data types (e.g., altimetry, Sea-Surface Temperature (SST), and color) were to be acquired and used to aid in the interpretation of mesoscale features and physical data in the study area. Within the scope of work for this study, there was a specification for coordination of all activities with oceanographers from Mexico who were responsible for Mexican Sector activities and data.

Using direct and acoustic current sensors, various temperature and salinity sensors, and remote sensing, the SAIC team of scientists and engineers designed an innovative, data rich, and observationally integrated field measurement program that supported all of the program objectives (Figure 1.2-1). As an Option in its original proposal, SAIC recommended that MMS support use of Inverted Echo Sounders with Pressure (PIES) as part of an integrated field measurement program. PIES had proven to provide valuable and cost-effective information for resolving both upper and lower-layer baroclinic and barotropic processes when used as part of the Exploratory Study (Donohue et al., 2006). When MMS exercised the PIES option, the initial observations on the moored arrays were supplemented with PIES placed at locations that used the PIES and existing moorings to create an observational program that resolved key ocean parameters and patterns at finer spatial scales than could be resolved with moorings alone. In addition, selected hydrocasts were made to support calibration of the PIES observations.

As proposed, PIES in conjunction with conventional current meter moorings provided the following key cost-effective design enhancements:

- Full-depth profiles at 10 sites over the study area (See PIES locations relative to mooring locations in Figure 1.2-1).

- Substantially broader and better resolved time varying, 3-D coverage of the temperature and salinity structure than was possible with 13 conventional moorings.

- Bottom-pressure measurements at 10 PIES sites to help map deep eddies and help try and distinguish between deep eddies and topographic Rossby waves (TRWs).

- An analytical method for determining the baroclinic and barotropic bottom pressure contributions to altimeter measurements of sea-surface-height (SSH).

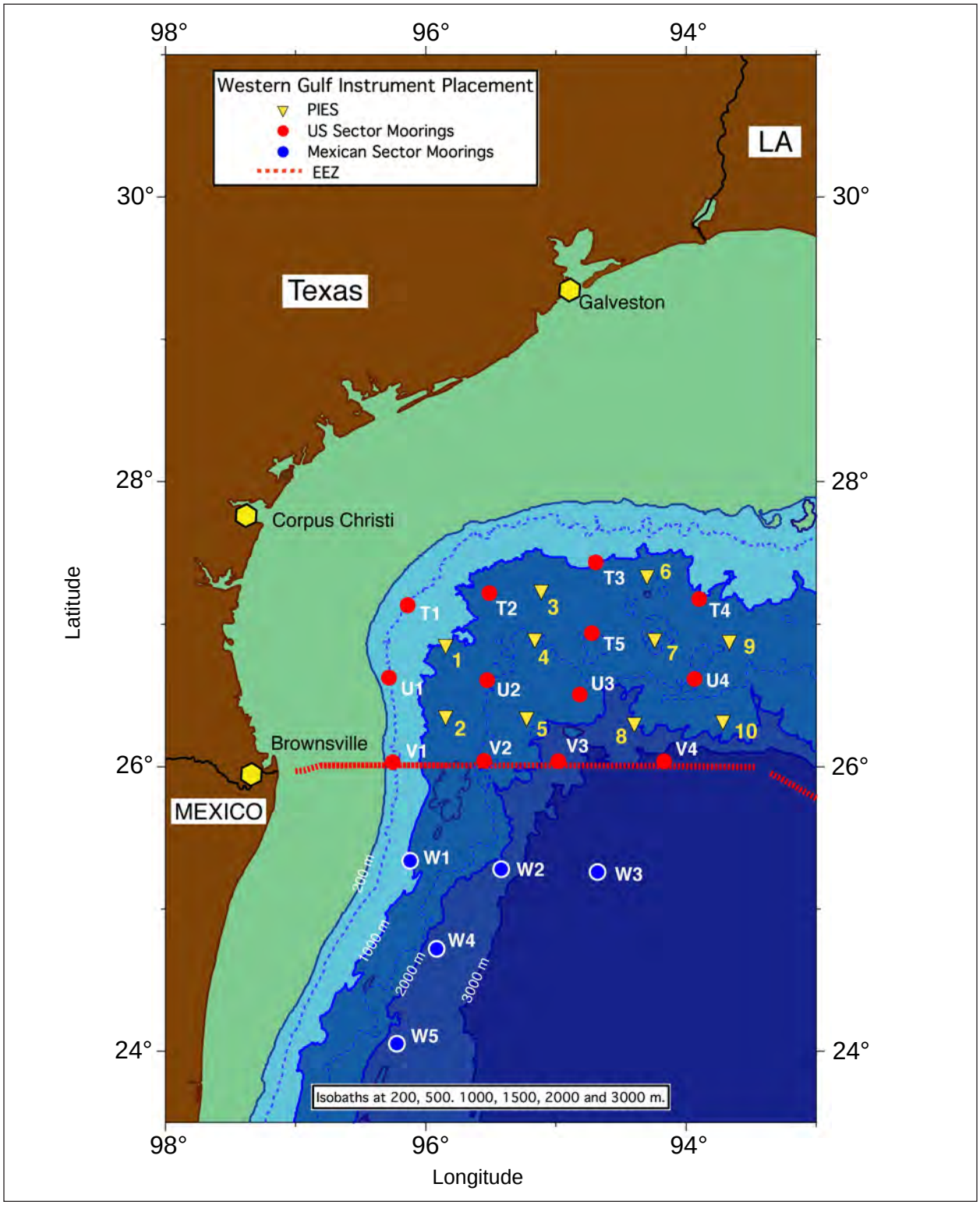

Figure 1.2-1. Locations of moorings and PIES in the American and Mexican Sectors. The red line indicates the American or international EEZ boundary.

1.3 General Program Schedule

The general schedule of field measurements and data gathering activities is shown in Figure 1.3-1. The contract was awarded in October 2003 with mobilization occurring over the first six months. As originally designed, one-year mooring deployments occurred in late March 2004 with rotation to have occurred in September 2004 and recovery in March 2005. With a goal of having the most overlap with PIES and observations in the Mexican Sector, the mooring rotation cruise was conducted in early October and the recovery in August 2005 for a total mooring deployment interval of 15 months. Approval of the PIES option and associated implementation resulted in the PIES being deployed in October 2004 and recovered in early August 2005. Moorings in the Mexican Sector were deployed in September 2004 and recovered in October 2005. The overlap of American Sector moorings and Mexican Sector moorings was approximately nine months. Satellite imagery was obtained and processed to document conditions and support observations in both the American and Mexican Sectors – approximately from February 2004 through August 2005.

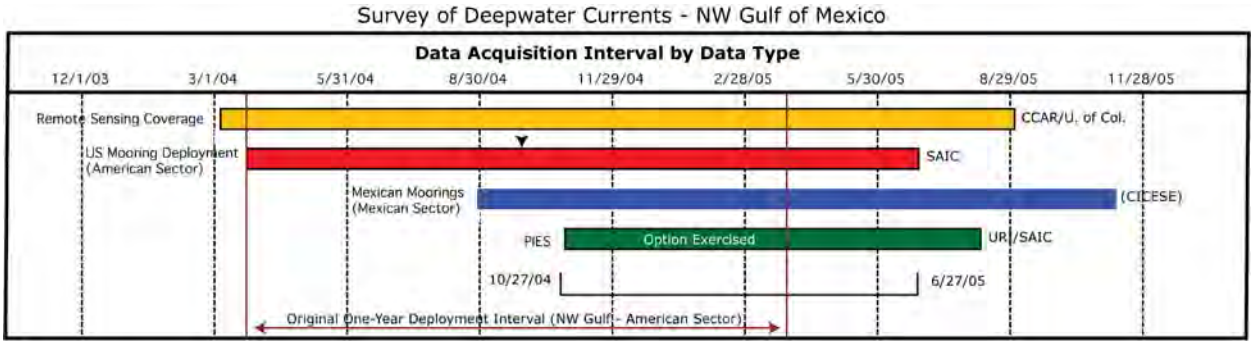

Figure 1.3-1. Schedule and relationship of various data types collected and used in this study.

1.4 Study Participants

Presented below are Science Team/Principal Investigators (PIs) who contributed to the analyses and subsequent writing of this report. Also shown are the primary SAIC personnel who supported the project. Note that the PIs were supported in their various activities by scientists and engineers at their home institutions. These additional support personnel were essential to the success of all aspects of the study from observations to analyses to graphics production.

Science Team and associated primary, but not sole, measurement responsibility:

PIES

Dr. Kathleen Donohue, University of Rhode Island

Dr. Randolph Watts, University of Rhode Island

Remote Sensing

Dr. Robert Leben, University of Colorado

In-situ Current Measurements

Dr. Peter Hamilton, SAIC

It is important to note that the complete and comprehensive data set from the American and Mexican Sectors was available to each of the members of the Science Team, thus, a multivariate approach was used by US and Mexican scientists. In conjunction with this approach, there was considerable collegial interaction so that combined expertise was brought to bear on the complex processes occurring in the upper and lower layers of the water column in the study areas.

The Science Team was supported by Management and Logistics personnel as follows:

Dr. Evans Waddell - Program Manager

Mr. James Singer - Logistics Manager and Cruise Chief Scientist

Mr. Paul Blankinship - Data Manager

All moored current-meter arrays were the responsibility of SAIC. University of Rhode Island was responsible for PIES instrumentation, including building, preparation, deployment and recovery. Satellite remote sensing was handled by the University of Colorado.

1.5 Report Organization

This report provides a dynamic characterization of processes occurring during the study interval in the upper and lower layers of the northwestern GOM over the interval of April 2004 through July 2005. In support of this goal, report chapters include:

Chapter 1: Introduction that describes the general context and content of the study.

Chapter 2: Experimental Design and Methodology that briefly describes measurements made and observations used in the study.

Chapter 3: Description of Upper-Layer Circulation.

Chapter 4: Description of Lower-Layer, Deep Circulation.

Chapter 5: High-frequency Oscillations describes the measured current variations that occurred at or above the tidal or inertial frequency with a tentative explanation for some of the episodes documented.

Chapter 6: Summary and Conclusions.

CHAPTER 2 EXPERIMENTAL DESIGN/METHODOLOGY

2.1 Moored Arrays

2.1.1 Array Design

The moored array consisted of 13 full-depth moorings in the U.S. part of the northwestern GOM, and five full-depth moorings over the western margin of the Mexican continental slope. The locations are shown in Figure 1.2-1, and though experimental operations of mooring deployments, rotation, and recovery were undertaken by separate entities (SAIC and CICESE for the U.S. and Mexican sectors, respectively), the experimental design was jointly conceived to map circulation processes over the northwestern slope and abyssal regions. The initial deployments of the Mexican sector moorings occurred five months later than for the U.S. sector, therefore, the second deployment of the 13 U.S. sector moorings delayed final recovery by three months to maximize the overlap.

The horizontal spacing of the moorings in the U.S. sector was chosen to resolve the larger scale eddy structures that had been observed in previous studies. The principal data sources were high-resolution hydrographic surveys of the NW slope taken from the LATEX-C program (Berger et al., 1996), and a comprehensive survey of the northwestern margin by B/O Altair in 1986 (SAIC, 1988). Horizontal maps of the thermal fields (e.g., the depth of the 15°C isotherm) derived from the surveys were sub-sampled at the locations of the proposed moored array. The locations were optimized so that the major eddies in the surveys were most accurately mapped when compared to the high-resolution data. It was also an important part of the design that an adequate region of the slope be covered by the array so that typical eddy features could be mapped fairly completely. The resulting coverage area was checked against the CCAR altimetric maps of the region. The inevitable compromise between area covered and spatial resolution of the array resulted in the roughly rectangular array in the U.S. sector (Figure 1.2-1) with approximately equal north and east spacing of about 60 km. The regular spacing of the array also makes the calculations of dynamical quantities involving horizontal gradients (e.g., relative vorticity) less error prone. The addition of PIES to the array (see Section 2.2) was designed in part to increase the horizontal resolution, because for geostrophic dynamics, full-depth moorings and PIES can be considered as providing equivalent information.

The American sector moorings range in water depth from 500 to 3100 m. Previous observations in this region had indicated that the vertical structure of the currents is similar to the rest of the deep GOM, with baroclinic eddies in the upper layer, reaching from the surface to about 800 to 1200 m depth, and nearly barotropic fluctuations in the lower layer. Strong vertical shears, along with large vertical temperature gradients, often characterize the upper-layer eddy currents. The upper layer also has the largest magnitude inertial oscillations, which are the dominant high-frequency fluctuations, since tides in deep water have essentially negligible current magnitudes. There was also the possibility that sub-surface jets (DiMarco et al., 2004) could occur in the upper part of the water column. Therefore, current profiles were measured by upward-looking 75-kHz Long Ranger ADCPs placed 450 m below the water surface on all the moorings except those on the 500-m isobath. 75-kHz ADCPs resolve the current profile with 8-m bins. Below this, current meters were placed at 250-m intervals to 1000 m, and 500-m intervals from 1000 m

to the bottom. There was always a current meter 100 m above the bottom. All the current meters measured temperature, and additional temperature sensors were placed between 75 m and 450 m below the water surface to measure the upper-layer temperature fields. The 500-m depth moorings used 300-kHz ADCPs at 90 m, which allows measurements at higher resolution (4 m versus 8 m) and closer to the surface (10 m versus 40 m) than the 75-kHz instruments, with current meters at 250 m and 450 m, and additional temperature sensors at 75, 150 and 350 m. All the U.S. sector moorings had temperature and salinity measurements, using MicroCats, at 150 m. This was used primarily as a detection array for the occurrence of Subtropical Underwater (SUW), which has salinities > 36.5 psu, and is transported to the western Gulf in the centers of Loop Current Eddies (LCEs). Thus, water masses of LC origin, which have a maximum salinity at ~ 150 to 200-m depth, can be tagged within the study region.

2.2 Equipment and Instruments

2.2.1 Introduction

Moored data collection consisted primarily of in-situ moored current, temperature, conductivity and pressure measurements at thirteen mooring sites. In addition, twenty Conductivity / Temperature / Depth (CTD) casts (two at each station) were made to support calibration of Inverted Echo Sounder with pressure (PIES) measurements made at ten locations during the last nine months of the field effort.

2.2.2 Moored and PIES Instruments

Moored current, temperature, conductivity and pressure measurements were made from thirteen tall current meter moorings deployed in the NW Gulf of Mexico, north of 26°N (to ~27º30'N) and west of 93º40'W (to ~96º20'W), in waters ranging in depth from 500 meters to 3100 meters. Mooring tops were at 60 to 70 meters depth. Measurements at these sites were made continuously for more than 15 months beginning in late March 2004 and ending in early July 2005. The moorings were rotated after 6.5 months. During the last nine months of measurements, ten PIES were also deployed in the study area. The locations and deployment periods for all thirteen moorings and the ten PIES are listed in Tables 2.2-1 through 2.2-3. These locations are shown in Figure 1.2-1.

Table 2.2-1

Triangulated Mooring Locations and Depths by Deployment for the NW Gulf of Mexico Program

Mooring (DD)	Deployment 1	Depth (m)	Deployment 2	Depth (m)	Distance Between (km)
T1 (500 m)	27°07.823'N 96°08.133'W	506 [502]	27°07.836'N 96°08.115'W	505 [503]	0.038
T2 (1200 m)	27°13.144'N 95°30.935'W	1214 [1205]	27°13.146'N 95°30.921'W	1217 [1204]	0.023
T3 (1000 m)	27°24.669'N 94°40.184'W	999 [999]	27°24.685'N 94°40.195'W	1007 [999]	0.035
T4 (1000 m)	27°09.867'N 93°54.157'W	1012 [1003]	27°09.896'N 93°54.146'W	1011 [998]	0.057
T5 (1500 m)	26°55.425'N 94°43.387'W	1486 [1498]	26°55.321'N 94°43.411'W	1511 [1497]	0.197
U1 (500 m)	26°37.408'N 96°16.958'W	500 [500]	26°37.414'N 96°16.967'W	499 [500]	0.019
U2 (1500 m)	26°37.511'N 95°32.818'W	1506 [1490]	26°37.502'N 95°32.850'W	1493 [1491]	0.056
U3 (1700 m)	26°30.413'N 94°48.684'W	1716 [1703]	26°30.366'N 94°48.687'W	1716 [1703]	0.087
U4 (1500 m)	26°37.077'N 93°55.692'W	1517 [1508]	26°37.111'N 93°55.652'W	1518 [1503]	0.092
V1 (500 m)	26°02.023'N 96°15.153'W	495 [498]	26°01.974'N 96°15.172'W	501 [498]	0.096
V2 (1500 m)	26°02.849'N 95°35.024'W	1510 [1501]	26°02.827'N 95°35.060'W	1510 [1503]	0.073
V3 (2500 m)	26°02.868'N 94°57.019'W	2507 [2494]	26°02.901'N 94°57.229'W	2502 [2491]	0.355
V4 (3100 m)	26°02.182'N 94°05.614'W	3098 [3098]	26°02.260'N 94°05.492'W	3101 [3099]	0.250

Deployment 1: 19 March 2004 – 14 October 2004.
Deployment 2: 3 October 2004 – 3 July 2005.
(DD) = Mooring Design Depth.

[ ] = Mooring Depth calculated from MicroCat/SeaCat or ADCP pressure sensor data, whichever produced smaller variation from planned instrument depth.

Table 2.2-2

Mooring Deployment Periods for the NW Gulf of Mexico Program

Mooring	Deployment Number	Deployment Periods (UTC)
T1	1	03/23/04 - 10/10/04
	2	10/11/04 - 06/30/05
T2	1	03/24/04 - 10/12/04
	2	10/13/04 - 07/01/05
T3	1	03/28/04 - 10/14/04
	2	10/15/04 - 07/02/05
T4	1	03/30/04 - 10/03/04
	2	10/04/04 - 07/03/05
T5	1	03/25/04 - 10/13/04
	2	10/14/04 - 07/02/05
U1	1	03/26/04 - 10/11/04
	2	10/12/04 - 06/29/05
U2	1	03/26/04 - 10/10/04
	2	10/12/04 - 07/01/05
U3	1	03/28/04 - 10/06/04
	2	10/07/04 - 07/02/05
U4	1	03/29/04 - 10/03/04
	2	10/04/04 - 06/27/05
V1	1	03/22/04 - 10/08/04
	2	10/09/04 - 06/29/05
V2	1	03/21/04 - 10/08/04
	2	10/09/04 - 06/28/05
V3	1	03/20/04 - 10/06/04
	2	10/08/04 - 06/28/05
V4	1	03/19/04 - 10/04/04
	2	10/05/04 - 06/27/05

Table 2.2-3

PIES Locations and Deployment Periods for the NW Gulf of Mexico Program

PIES (Serial Number)	Location	Depth (m)*	Deployment Periods (UTC)
P1 (081)	26°50.04'N 95°54.40'W	960	10/26/04 - 08/09/05
P2 (084)	26°22.68'N 95°47.17'W	1298	10/26/04 - 08/09/05
P3 (079)	27°14.24'N 95°07.39'W	1252	10/27/04 - 08/09/05
P4 (106)	26°52.37'N 95°12.20'W	1590	10/27/04 - 08/09/05
P5 (085)	26°20.92'N 95°12.91'W	1677	10/26/04 - 08/09/05
P6 (087)	27°20.50'N 94°18.41'W	1048	10/27/04 - 08/07/05
P7 (089)	26°53.92'N 94°12.99'W	1387	10/27/04 - 08/08/05
P8 (080)	26°22.39'N 94°21.08'W	1757	10/28/04 - 08/08/05
P9 (090)	26°53.00'N 93°46.15'W	1332	10/27/04 - 08/08/05
P10 (088)	26°19.83'N 93°48.29'W	1709	10/28/04 - 08/08/05

*Depths are from PDR on R/V LONGHORN.

The navigation datum used for mooring placement was WGS 84, which is the same as NAD 83. After deployment, mooring locations were triangulated and depth determined based on DGPS fixes, PDR readings, and minimum ranges. Later, instrument pressure data were evaluated as another check on mooring depth. Fallback of each mooring from the anchor drop site to the final resting place on the bottom was also determined. This ranged from a minimum of approximately 100 meters for the 500-meter isobath moorings up to 400 meters for the 3100-meter isobath mooring.

Each mooring was equipped to measure near-surface currents with an upward looking 75-kHz ADCP deployed at 450-meters depth or an upward looking 300-kHz ADCP deployed at 90-meters depth. Currents were also measured at 750-meters and 1000-meters depth, as appropriate, and at 500-meter increments below that to the bottom, except that each mooring also measured currents at approximately 50 or 100 meters above the bottom (mab). Temperature data were

collected at each current-meter level as well as at 75, 150, 250, and 350 meters depth. Salinity data were collected at only the 150-meter level on each mooring.

2.2.3 Instrumentation

The moorings were instrumented with a number of different types of current meters. These included Aanderaa RCM-7s and 8s (rotor type), and RCM-11s (Doppler type) at depths of and greater than 750 meters. In addition, InterOcean S4 current meters were deployed at shallower depths on the 500-meter isobath moorings (at 250 meters and 450 meters) and at the 750-meter level on some 1000-meter isobath and deeper moorings. RDI Sentinel and LongRanger ADCPs were deployed at the following depths:

- 300-kHz Sentinel ADCP (at 90 meters depth on the three 500-meter isobath moorings, Moorings T1, U1, and V1)
- 300-kHz Sentinel ADCP (at 194 meters depth during one deployment each of Moorings T2 and T4)
- 75-kHz LongRanger ADCP (at 450 meters depth on all ten moorings where bottom depths were greater than 500 meters)

The moorings also included Hugrún Seamon Mini Temperature Recorders, Sea-Bird Conductivity / Temperature Recorders, Star-Oddi Starmon Mini Temperature Recorders, and Star-Oddi DST Milli TP Recorders deployed at the following depths:

- Hugrún Seamon Mini Temperature Recorder (at 75 meters on all moorings)
- Sea-Bird MicroCat or SeaCat (at 150 meters on all moorings)
- Star-Oddi Starmon Mini Temperature Recorder (at 250 meters on all ten moorings where bottom depths were greater than 500 meters)
- Star-Oddi Starmon Mini Temperature Recorder (at 350 meters on all moorings)
- Star Oddi DST Milli TP Recorder (at 90 meters and 194 meters w/300-kHz ADCPs and at 750 meters w/S4 Current Meters)

Table 2.2-4a-c summarizes the measurement levels for each of the instruments deployed on the moorings during the program. The PIES instruments (manufactured by the Univ. of Rhode Island) were deployed on low profile stands and were actually mounted about one meter above the bottom.

Table 2.2-4a

Mooring Locations and Moored Instrument Levels for the American Sector of the NW Gulf of Mexico Program with Nominal Mooring and Instrument Depths (Moorings T1-T5)

NW GULF OF MEXICO (03/19/04 - 07/03/05)				
Mooring	**Location**	**Water Depth (M)**	**Instrument Depth (M) (MAB)**	**Instrument Type (Serial No.)**
T1	27°07.823'N 96°08.133'W 27.130°N 96.136°N	500	75 90/UP 90 150 250 350 450 (50)	TEMP (D591) 300 KHz ADCP (197) (209) T/P (M6159) T/S/P (1719) (2696) S4 (08111780) (07801678) TEMP (T1153) S4 (04020660) (08111779)
T2	27°13.144'N 95°30.935'W 27.219°N 95.516°W	1200	75 150 194 [2]/UP 194 [2] 250 350 450/UP 458 [2] 750 750 1100 (100)	TEMP (D585) T/S/P (1342) 300 KHz ADCP (1200) T/P (M4670) TEMP (T1267) TEMP (T1154) 75 KHz ADCP (4887) (4888) RCM-11 (359) S4 (08111746) (08582010) T/P (M6160) (M4663) RCM-11 (349) (355)
T3	27°24.669'N 94°40.184'W 27.411°N 94.670°W	1000	75 150 250 350 450/UP 750 750 900 (100)	TEMP (D593) T/S/P (2693) (2695) TEMP (T1270) TEMP (T1155) 75 KHz ADCP (4913) S4 (08291851) (08111750) T/P (M6164) RCM-11 (348) (350)
T4	27°09.867'N 93°54.157'W 27.164°N 93.903°W	1000	75 150 194 [1]/UP 194 [1] 250 350 450/UP 458 [1] 750 750 [2] 900 (100)	TEMP (D614) T/S/P (3387) (3391) 300 KHz ADCP (214) T/P (M6166) TEMP (T1271) TEMP (T1156) 75 KHz ADCP (4888) (924) RCM-7 (11389) S4 (08161758) (08161755) T/P (M6166) RCM-11 (356) RCM-7 (11791)
T5	26°55.425'N 94°43.387'W 26.924°N 94.723°W	1500	75 150 194 [2] 250 350 450/UP 750 750 1000 1400 (100)	TEMP (D597) T/S/P (3388) RCM-11 (354) TEMP (T1275) TEMP (T1157) 75 KHz ADCP (4855) S4 (08111750) (08111746) T/P (M6161) RCM-7/8 (6922) (10533) RCM-11 (350) (349)

MAB = Meters Above Bottom.
[ ] = Deployed during indicated deployment only.

Table 2.2-4b

Mooring Locations and Moored Instrument Levels for the American Sector of the NW Gulf of Mexico Program with Nominal Mooring and Instrument Depths (Moorings U1-U4, V1-V2)

NW GULF OF MEXICO (03/19/04 - 07/03/05)				
Mooring	**Location**	**Water Depth (M)**	**Instrument Depth (M) (MAB)**	**Instrument Type (Serial No.)**
U1	26°37.408'N 96°16.958'W 26.623°N 96.283°W	500	75 90/UP 90 150 250 350 450 (50)	TEMP (D583) 300 kHz ADCP (1200) (197) T/P (M6163) T/S/P (1720) (2694) S4 (08582010) (07961709) TEMP (T1158) S4 (07961708) (04020660)
U2	26°37.511'N 95°32.818'W 26.625°N 95.547°W	1500	75 150 250 350 450/UP 750 750 1000 1400 (100)	TEMP (D595) T/S/P (3389) TEMP (T1276) TEMP (T1159) 75 kHz ADCP (4918) S4 (07961709) (07961708) T/P (M6162) RCM-7/8 (9950) (12788) RCM-11 (352)
U3	26°30.413'N 94°48.684'W 26.507°N 94.811°W	1700	75 150 250 350 450/UP 750 1000 1600 (100)	TEMP (D617) T/S/P (3390) TEMP (T1277) TEMP (T439) 75 kHz ADCP (4914) (4856) RCM-11 (360) (364) RCM-8 (10533) (12789) RCM-7 (9949) (10350)
U4	26°37.077'N 93°55.692'W 26.618°N 93.928°W	1500	75 150 250 350 450/UP 750 1000 1400 (100)	TEMP (D620) T/S/P (3391) (3387) TEMP (T1278) TEMP (T1160) 75 kHz ADCP (4866) RCM-11 (361) RCM-7 (9524) RCM-7 (10350) (10881) RCM-11 (353) RCM-8 (12804)
V1	26°02.023'N 96°15.153'W 26.034°N 96.253°W	500	75 90/UP 90 150 250 350 450 (50)	TEMP (D581) 300 kHz ADCP (209) (214) T/P (M6158) T/S/P (1341) S4 (07801678) (08161757) TEMP (T1162) S4 (08111779) (08161758)
V2	26°02.849'N 95°35.024'W 26.047°N 95.584°W	1500	75 150 250 350 450/UP 750 1000 1400 (100)	TEMP (D621) T/S/P (3392) TEMP (T1279) (C943) TEMP (T442) 75 kHz ADCP (4865) RCM-11 (362) (360) RCM-7/8 (9948) (7582) RCM-11 (354) (351)

MAB = Meters Above Bottom.
[ ] = Deployed during indicated deployment only.

Table 2.2-4c

Mooring Locations and Moored Instrument Levels for the NW Gulf of Mexico Program with Nominal Mooring and Instrument Depths (Moorings V3-V4)

NW GULF OF MEXICO (03/19/04 - 07/03/05)				
Mooring	**Location**	**Water Depth (M)**	**Instrument Depth (M) (MAB)**	**Instrument Type (Serial No.)**
V3	26°02.868'N 94°57.019'W 26.048°N 94.950°W	2500	75 150 250 350 450/UP 750 1000 1500 2000 2400 (100)	TEMP (D633) T/S/P (3393) TEMP (T1280) TEMP (T440) 75 kHz ADCP (4856) (4914) RCM-11 (363) RCM-7 (9985) (11450) RCM-7 (6892) RCM-11 (351) (357) RCM-11 (355) (358)
V4	26°02.182'N 94°05.614'W 26.036°N 94.094°W	3100	75 150 250 350 450/UP 750 1000 1500 2000 2500 3000 (100)	TEMP (D634) T/S/P (3394) TEMP (T1187) TEMP (T441) 75 kHz ADCP (4817) RCM-11(364) (361) RCM-7 (9636) (11432) RCM-8 (7582) (7528) RCM-11 (357) RCM-8 (12806) RCM-11 (358) (356) RCM-11 (359) (353)

MAB = Meters Above Bottom.
[ ] = Deployed during indicated deployment only.

2.2.4 Instrument Performance and Data Return

A total of 222 instrument deployments were made over the course of the 15+ month field effort, and the total data return from the moorings was approximately 97%. This return was calculated based on the maximum number of "good" data points expected for the various type instruments at their respective settings. However, since an ADCP generally works or does not work, the data return for these instruments reflects only that "good data" were obtained for at least one level, though anywhere from 20 depth cells on the Sentinel to 51 depth cells on the LongRanger may have provided useful data. Figure 2.2-1a-e presents a timeline of the data return by instrument level and Table 2.2-5 summarizes the moored instrument data return by instrument type. Note that not all levels were instrumented on each mooring during each deployment period and that periods where some data were lost are identified as having occurred for a variety of reasons including instrument malfunctions, battery failures and instrument leaks. A number of instrument types did provide 100% data return. These included the Aanderaa RCM-11 Doppler current meter, the Hugrún Seamon Mini temperature recorder and the RD Instruments 75-kHz LongRanger and 300-kHz Sentinel ADCPs. It is noted that even though one of the LongRangers had a clock problem, no data were lost. Statistics and 40-HLP vector plots of these velocity data are presented in Appendices A and B, respectively.

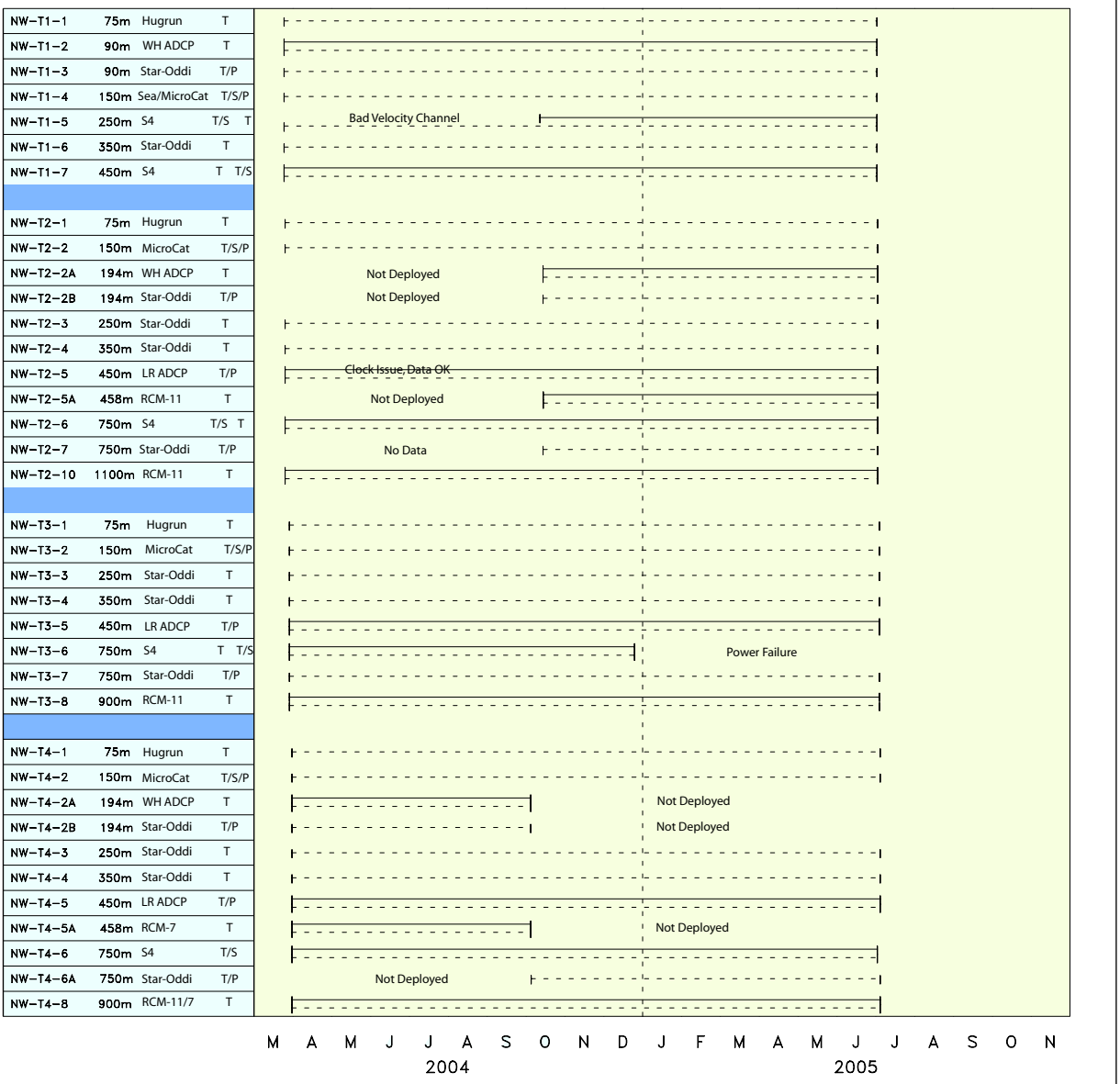

Figure 2.2-1a. Timeline of data return for instruments on Moorings T1, T2, T3 and T4. Shown in addition to the instrument/measurment ID is the instrument type, placement depth, variables measured and when deployed. Instruments are numbered down from the upper instrument on a mooring line. "Not Deployed" indications are for instruments deployed for shorter intervals to provide data comparisons (hopefully redundant) relative to longer term instrument deployments. Dashed lines represent vector quantities, e.g., velocity and solid lines represent scalar quantities, e.g., temperature.

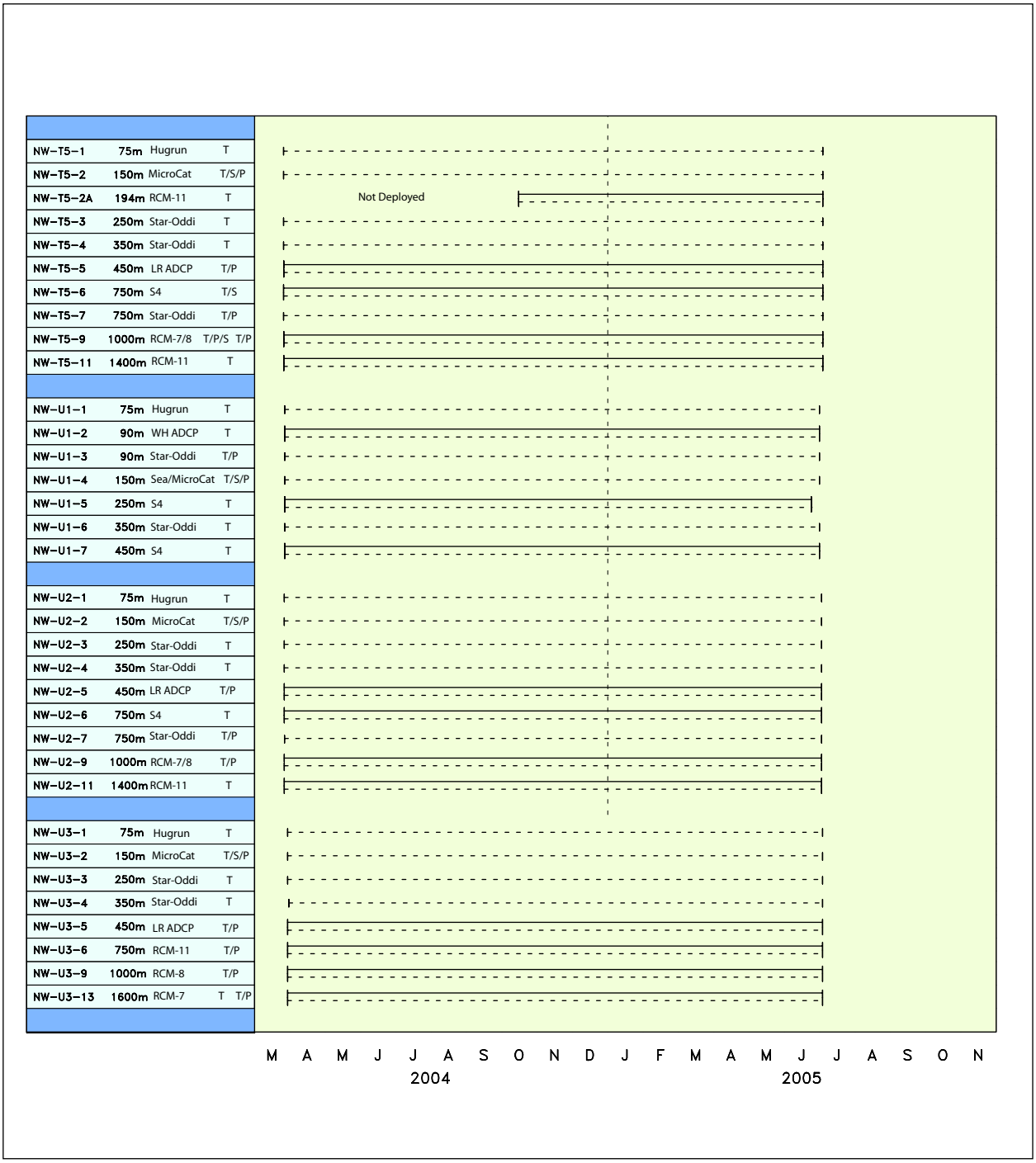

Figure 2.2-1b. Timeline of data return for instruments on Moorings T5, U1, U2 and U3. Shown in addition to the instrument/measurment ID is the instrument type, placement depth, variables measured and when deployed. Instruments are numbered down from the upper instrument on a mooring line. "Not Deployed" indications are for instruments deployed for shorter intervals to provide calibration comparisons (hopefully redundant) relative to longer term instrument deployments. Dashed lines represent vector quantities, e.g., velocity and solid lines represent scalar quantities, e.g., temperature.

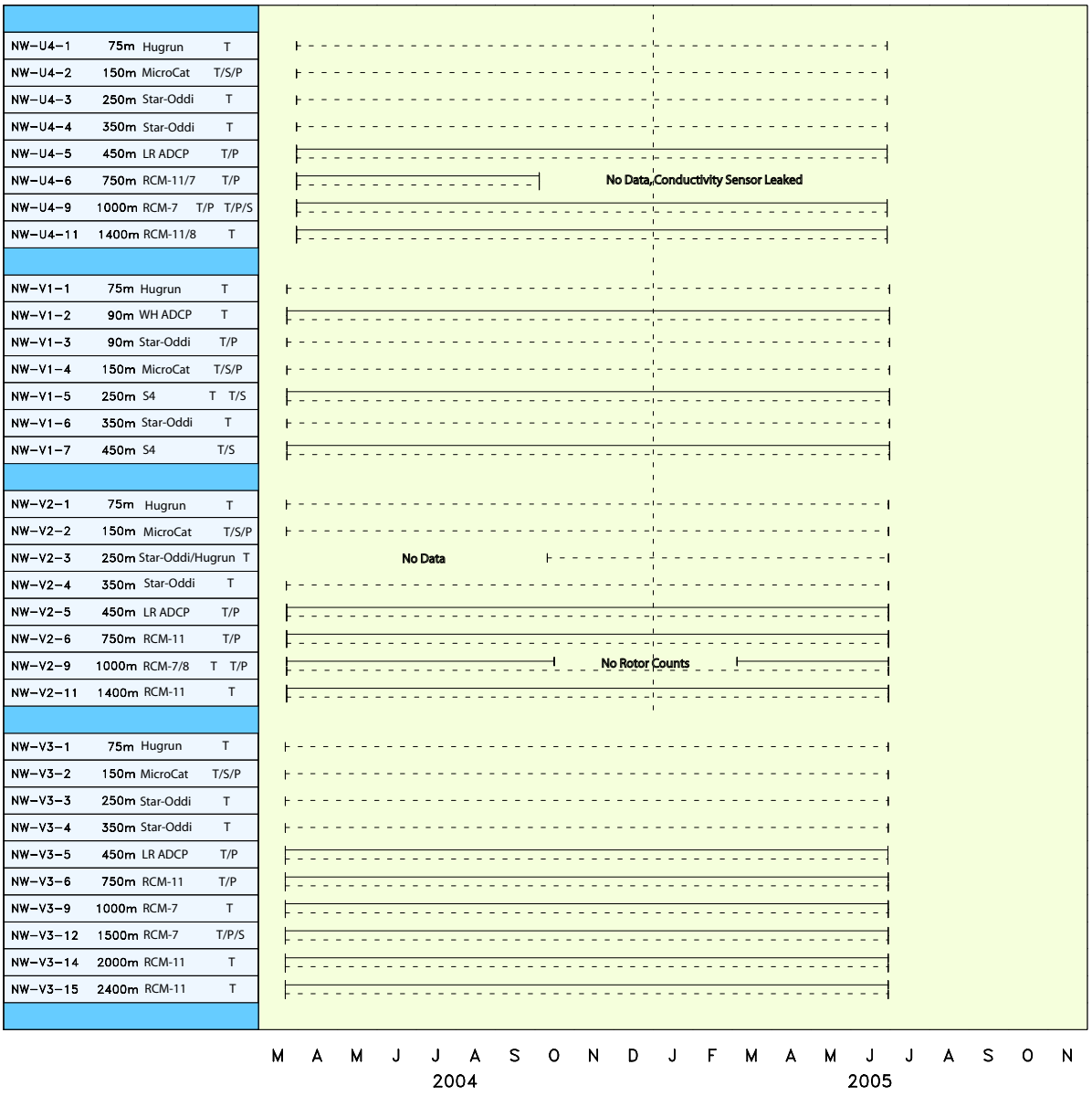

Figure 2.2-1c. Timeline of data return for instruments on Moorings U4, V1, V2 and V3. Shown in addition to the instrument/measurment ID is the instrument type, placement depth, variables measured and when deployed. Instruments are numbered down from the upper instrument on a mooring line. Dashed lines represent vector quantities, e.g., velocity and solid lines represent scalar quantities, e.g., temperature.

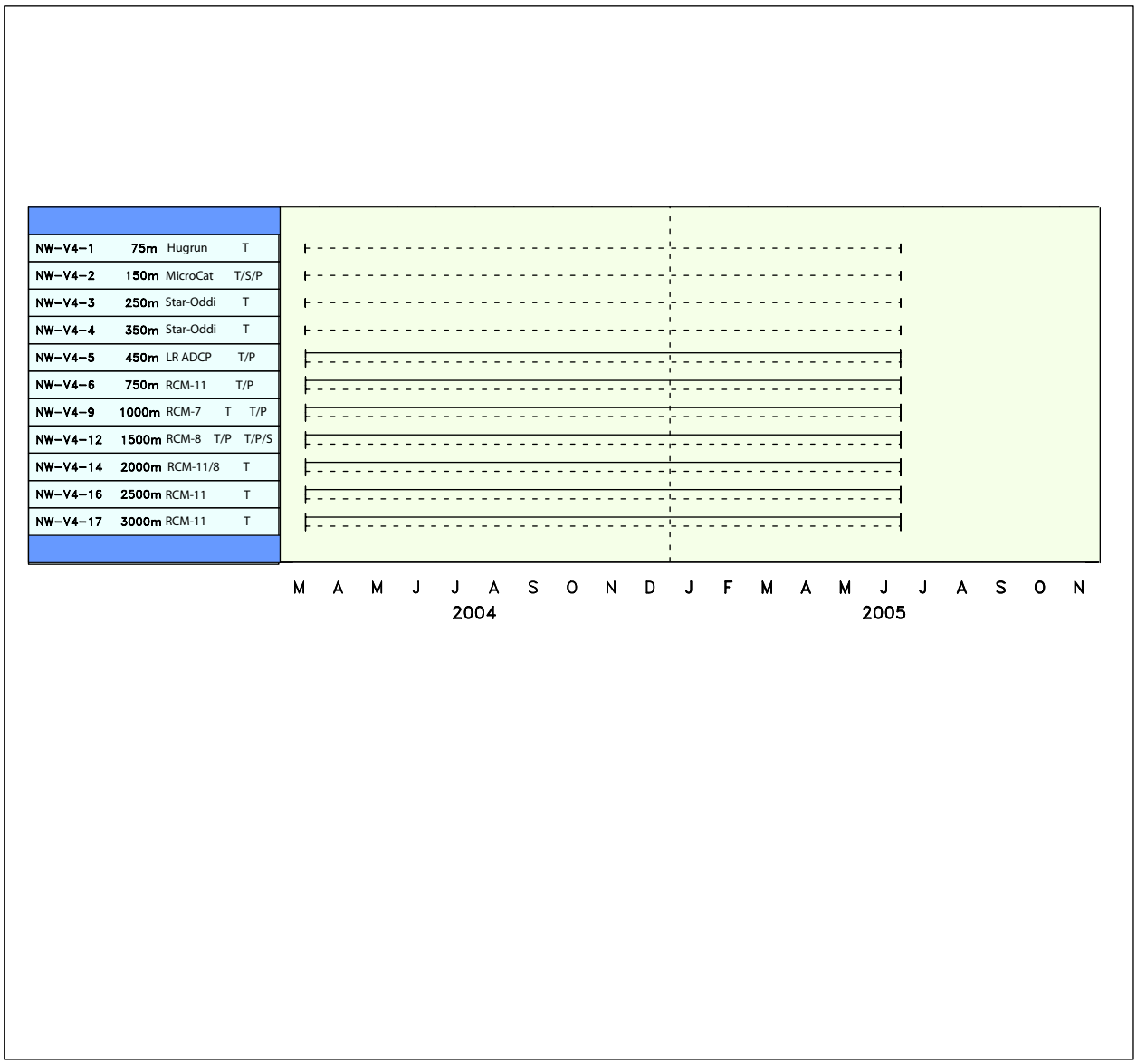

Figure 2.2-1d. Timeline of data return for instruments on Mooring V4. Shown in addition to the instrument/ measurment ID is the instrument type, placement depth, variables measured and when deployed. Instruments are numbered down from the upper instrument on a mooring line. Dashed lines represent vector quantities, e.g., velocity and solid lines represent scalar quantities, e.g., temperature.

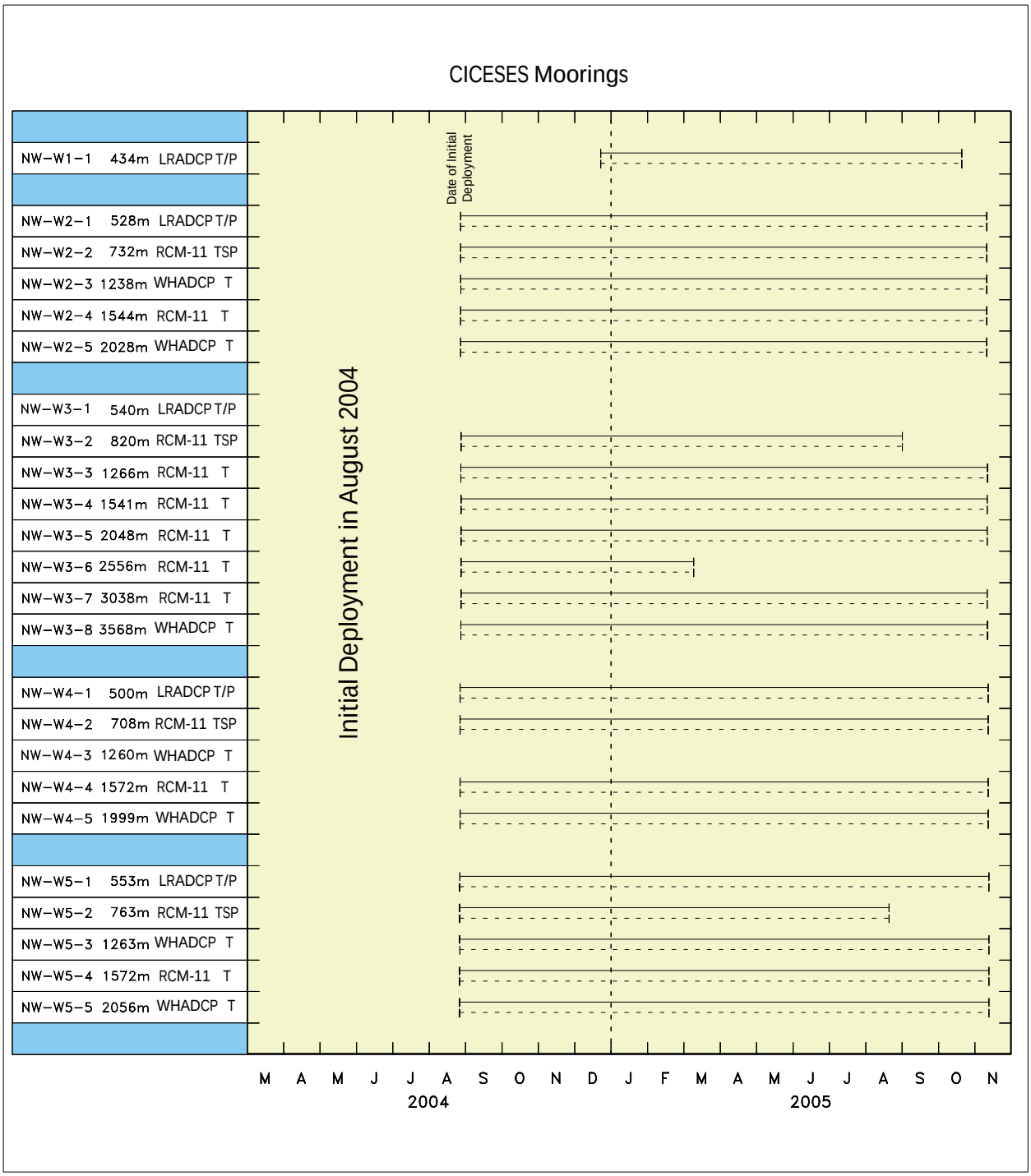

Figure 2.2-1e. Timeline of instrument on Moorings W1-W5 that were deployed by CICESE in the Mexican sector of the MMS-funded field measurement program. Shown in addition to the instrument/measurment ID is the instrument type, placement depth, variables measured and when deployed. Instruments are numbered down from the upper instrument on a mooring line. The mooring and instrument numbering scheme used by CICESE may differ from that used above. Dashed lines represent vector quantities, e.g., velocity and solid lines represent scalar quantities, e.g., temperature.

Table 2.2-5

Moored Instrument Data Return (by Good Record Count) during the NW Gulf of Mexico Program

Deployment	Aanderaa RCM-7/8 (CUR+T)	Aanderaa RCM-11 (CUR+T)	Hugrun Seamon Mini (T)
1	103,546/103,546 (11)	160,988/160,988 (17)	123,397/123,397 (13)
2	159,231/178,158 (14)	189,198/189,198 (15)	177,094/177,094 (14)
TOTALS	262,777/281,704 (25)	350,186/350,186 (32)	300,491/300,491 (27)
Percent Good	93.3%	100%	100%
Deployment	**InterOcean S4 (CUR+T)**	**RD Instruments ADCP* (CUR+T)**	**Sea-Bird MicroCat/SeaCat (T+S)**
1	99,719/104,542 (11)	170,218/170,218 (14)	208,222/227,596 (13)
2	129,160/138,300 (11)	227,296/227,296 (14)	319,145/329,040 (13)
TOTALS	228,879/242,842 (22)	397,514/397,514 (28)	527,367/556,636 (26)
Percent Good	94.3%	100%	94.7%
Deployment	**Star-Oddi Starmon Mini (T)**	**Star-Oddi DST Milli (T+P)**	**GRAND TOTAL**
1	208,283/217,911 (23)	66,716/ 76,416 (8)	1,141,089/1,184,614 (110)
2	278,704/278,704 (22)	113,480/113,480 (9)	1,593,308/1,631,270 (112)
TOTALS	486,987/496,615 (45)	180,196/189,896 (17)	2,734,397/2,815,884 (222)
Percent Good	98.1%	94.9%	97.1%

* All ADCP bin levels for each instrument counted as one (1) time series record.
(#) = Number of Instrument Deployments.

2.3 CTD Data

Twenty CTD casts were made to full ocean depth at the ten PIES deployment sites. Their purpose was to help in creating an appropriate Gravest Empirical Mode (GEM) to be used to calibrate the PIES data. These casts are documented in Table 2.3-1.

2.3.1 CTD Data Acquisition Systems

The CTD data acquisition systems consisted of two Sea-Bird 911 Plus systems provided and operated by the technical staff onboard two different research vessels. These were the R/V PELICAN, a UNOLS vessel operated by Louisiana Universities Marine Consortium (LUMCON) at Cocodrie, Louisiana, and the R/V LONGHORN, a UNOLS vessel operated by the University of Texas Marine Science Institute (UTMSI) at Port Aransas, Texas. Each CTD was equipped with redundant Sea-Bird CT sensors, a Datasonics altimeter and a Sea-Bird Carousel or General Oceanics Rosette Water Sampler with Niskin water sample bottles. The lowering speed of the CTD was varied from 15 meters per minute for the first 90 meters of descent to 30 meters per minute from 90 to 200 meters depth, and then increased to 60 meters per minute once below the 200 meter level. This was to eliminate or significantly reduce the possibility of CT sensor mismatch which can cause salinity spiking when passing through a sharp thermocline.

Table 2.3-1

Listing of CTD Casts Made at PIES Sites during the NW Gulf of Mexico Program

Station	Date (UTC)	Time (UTC)	Cruise
P30	10/28/04 06/30/05	2329 - 0015 2137 - 2221	LH-873 PE05-45
P31	10/28/04 06/28/05	1850 - 1954 2255 - 0004	LH-873 PE05-45
P32	07/01/05* 08/06/05	0608 - 0722 1210 - 1328	PE05-45 LH-886
P33	10/29/04 07/01/05	0751 - 0854 0230 - 0349	LH-873 PE05-45
P34	10/28/04 07/01/05	1159 - 1304 2238 - 0004	LH-873 PE05-45
P35	07/03/05 08/06/05	0314 - 0415 1838 - 1947	PE05-45 LH-886
P36	07/03/05 08/07/05	0726 - 0831 1616 - 1717	PE05-45 LH-886
P37	06/28/05 08/07/05	0535 - 0709 1046 - 1206	PE05-45 LH-886
P38	06/27/05 08/07/05	2359 - 0104 0020 - 0147	PE05-45 LH-886
P39	06/27/05 08/07/05	0721 - 0844 0550 - 0710	PE05-45 LH-886

* Salinity data bad; temperature data OK.

2.3.2 CTD Performance and Data Return

All twenty casts were completed, but the salinity data for one station (Station P32 in July 2005) were discarded. Distilled water used to clean the conductivity cell between stations had been left trapped in the cell during the subsequent cast. The temperature data were unaffected.

2.4 Moored Measurements in the Mexican Sector

In addition to the above moorings, current meter data are available from five MMS-funded moorings (W1 – W5 in Figure 1.2-1) deployed by CICESE within the Mexican EEZ in water depths ranging from 438 m to 3524 m. The locations and deployment periods are presented in Table 2.4-1

Table 2.4-1

Mexican Mooring Locations and Deployment Periods during the NW Gulf of Mexico Program

NW GULF OF MEXICO (Mexican Moorings)			
Mooring	**Location**	**Water Depth (m)**	**Deployment Period**
W1*	25°26.150'N 96°18.827'W	438	12/22/04 - 11/09/05
W2	25°23.368'N 95°26.324'W	2000	08/26/04 - 11/09/05
W3	25°16.324'N 94°53.392'W	3524	08/26/04 - 11/10/05
W4	24°39.088'N 96°04.962'W	1996	08/26/04 - 11/10/05
W5	24°02.686'N 96°18.066'W	2003	08/25/04 - 11/11/05
Canekito	25°05.150'N 90°30.000'W	3590	05/11/03 - 08/27/04

*W1 Mooring reported recovered by a U.S. shrimper approx. 09/24/2004 after deployment in August 2004. Redeployed in December 2004.

These moorings were deployed approximately five months after the thirteen NW Gulf of Mexico moorings were initially deployed, and recovered approximately four months after the NW Gulf of Mexico moorings were finally removed. The common deployment period for the two sets of moorings was approximately ten months. A sixth Mexican mooring, Canekito (Donohue et al., 2006), was deployed in support of the Exploratory study east of the present study area near 25°00'N, 90°30'W in a water depth of 3590 meters. It overlapped with the NW GOM moorings by approximately five months.

2.5 PIES

At locations described in the preceding section, an array of ten inverted echo sounders with pressure gauges (PIES) were deployed to increase spatial resolution of the moored array (Figure 1.2-1). The PIES is a bottom-mounted instrument that emits 12-kHz sound pulses and measures the round trip travel times or τ (tau) of these acoustic pulses from sea floor to sea surface and back. The PIES were also equipped with a pressure gauge to measure bottom pressure. A detailed description of instrument and initial data processing may be found in Hamilton et al. (2003) and Donohue et al. (2006). Key steps in initial data processing are discussed in the present report section. Data return from the PIES was excellent (Figures 2.5-1 and 2.5-2); full deployment records are available from all PIES with one exception. PIES 3 did not have valid pressure records for the first four months.

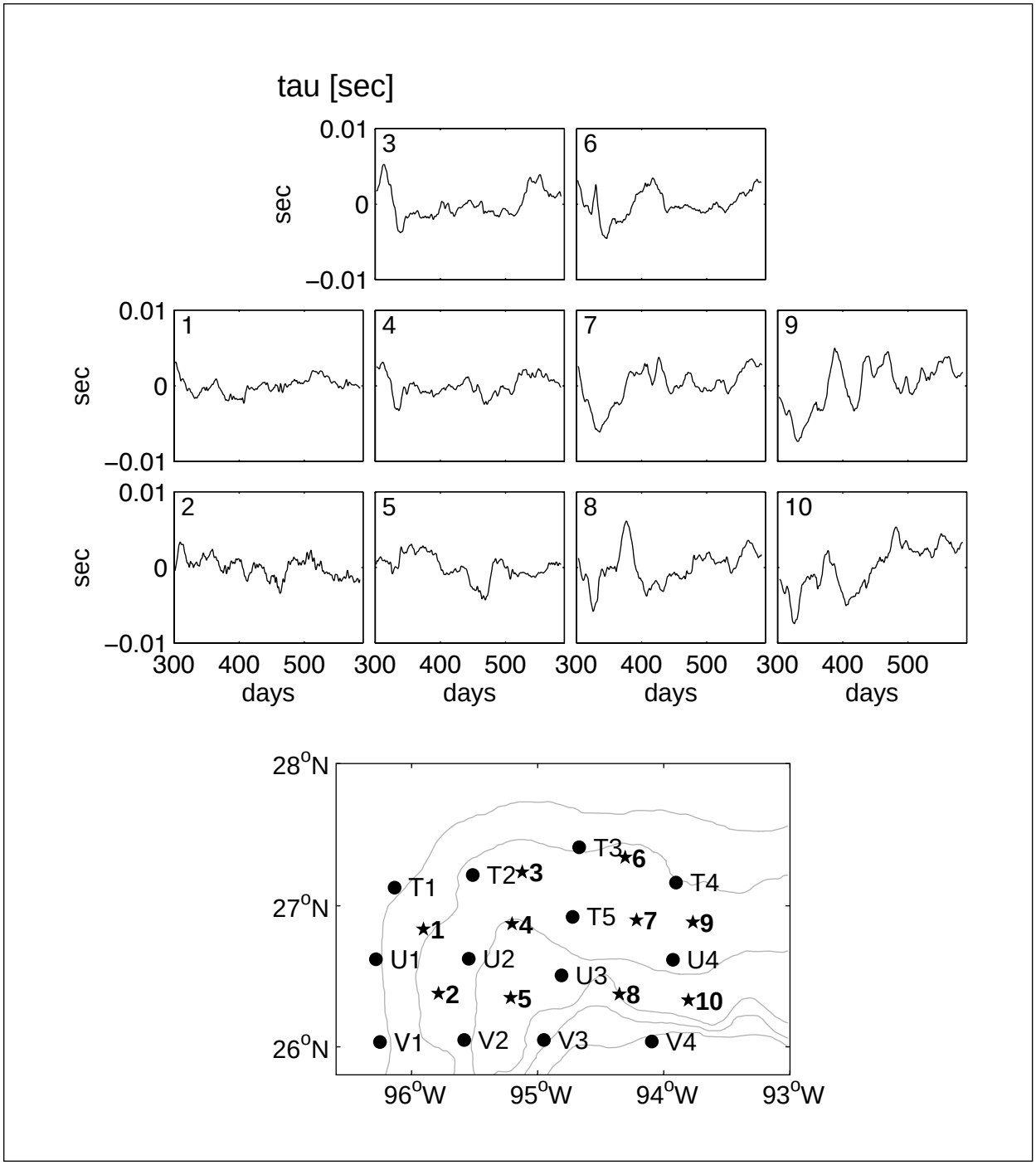

Figure 2.5-1. Time series of τ anomaly in seconds plotted according to approximate geographic location. Instrument number noted in the upper left corner of each subplot. Bathymetry contoured every 500 m depth. PIES are denoted as stars; tall moorings as circles.

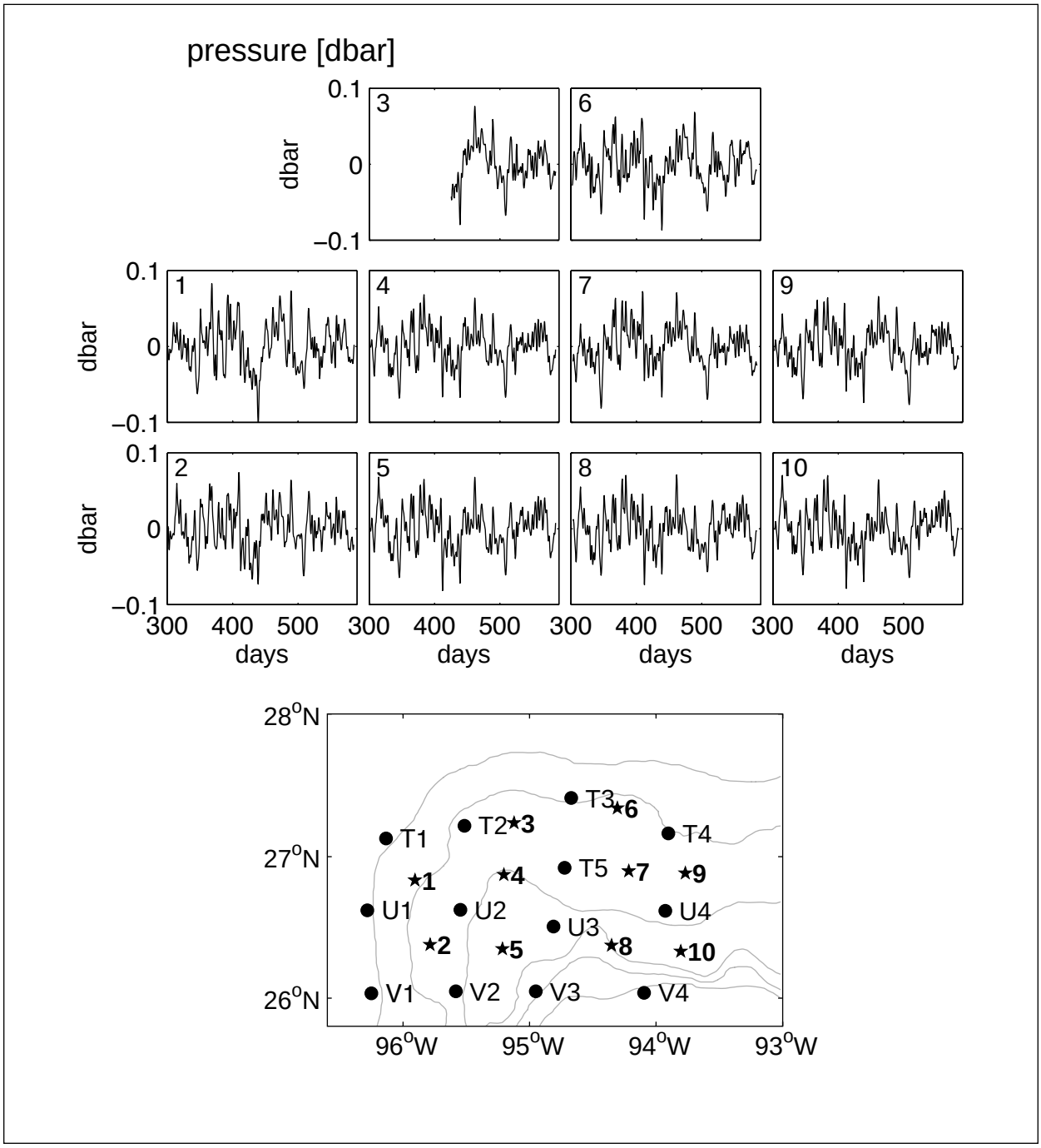

Figure 2.5-2. Time series of bottom pressure anomaly in dbar plotted according to approximate geographic location. Instrument number noted in the upper left corner of each subplot. Bathymetry contoured every 500 m depth. PIES are denoted by stars, moorings by circles.

The array of PIES combined with measurements from the tall moorings enabled a quantitative mapping of the regional circulation. Round-trip acoustic travel time measured by the inverted echo sounder, allowed estimates of vertical profiles of temperature, salinity, and density, utilizing empirical relationships established with historical hydrography. We also used these relationships to convert the tall moorings into pseudo inverted echo sounders (IESs). Pressure was leveled via geostrophy using mean current measurements. Deep pressure records combined with estimated horizontal density gradients yielded referenced geostrophic velocities. With this array, 4-D maps of temperature, salinity, density, and velocity were produced. The tall moorings were recovered in late June 2005; therefore, circulation maps were created for nearly eight months. Figure 2.5-3 illustrates the various views of current and temperature structure provided by the PIES and deep current meter mooring array for April 17, 2005.

2.5.1 Gravest Empirical Mode Method

For this experiment PIES τ measurements were converted into profiles of temperature, salinity, and specific volume anomaly through the use of a look-up table. A relationship has been established between a τ index and vertical profiles of temperature, salinity, and specific volume anomaly using historical hydrography. This is the so-called Gravest Empirical Mode (GEM) representation (e.g., Meinen and Watts, 2000). The procedure consists of two branches. First the empirical relationship was created. Second, the PIES measured τ was converted to the τ index of the look-up table.

2.5.1.1 Determine τ Index

Round-trip travel time between the 150 and 1000-dbar surface, τ(150-1000), was used as the τ index. The 150-dbar upper limit of the τ integration avoided the influence of the seasonal cycle most evident in this upper layer. Further refinements discussed below detail a seasonal correction. The 1000-dbar lower limit of the τ integration balanced two needs: extend the integration below the thermocline and retain as many of the acquired historical hydrocasts as possible.

2.5.1.2 Assemble Regional Hydrographic Data Set

The hydrographic data set derived from historical hydrography supplemented by CTD hydrocasts taken during the field operations and hydrocasts from profiling floats (Figure 2.5-4). Due to the integral nature of τ, only high vertical resolution CTD hydrocasts were used. The historical database contains 498 hydrographic stations from the GOM HYDRO Database compiled by TAMU as part of the MMS-funded Deepwater Reanalysis (Nowlin et al., 2001) as well as additional stations provided by SAIC. The northwestern GOM is well sampled; hydrocasts represent about 20 years of sampling; hydrocasts sampled most of the annual cycle except in June and December; the bulk of casts extend between 1000 to 2000 dbar with relatively few casts below 2000 dbar. We also included 242 hydrocasts taken by the profiling floats from the MMS sponsored Exploratory Study of Deepwater Currents in the Gulf of Mexico (Donohue et al., 2006). They substantially increase the spatial and temporal sampling. These casts reached maximum depths of 1000 m.

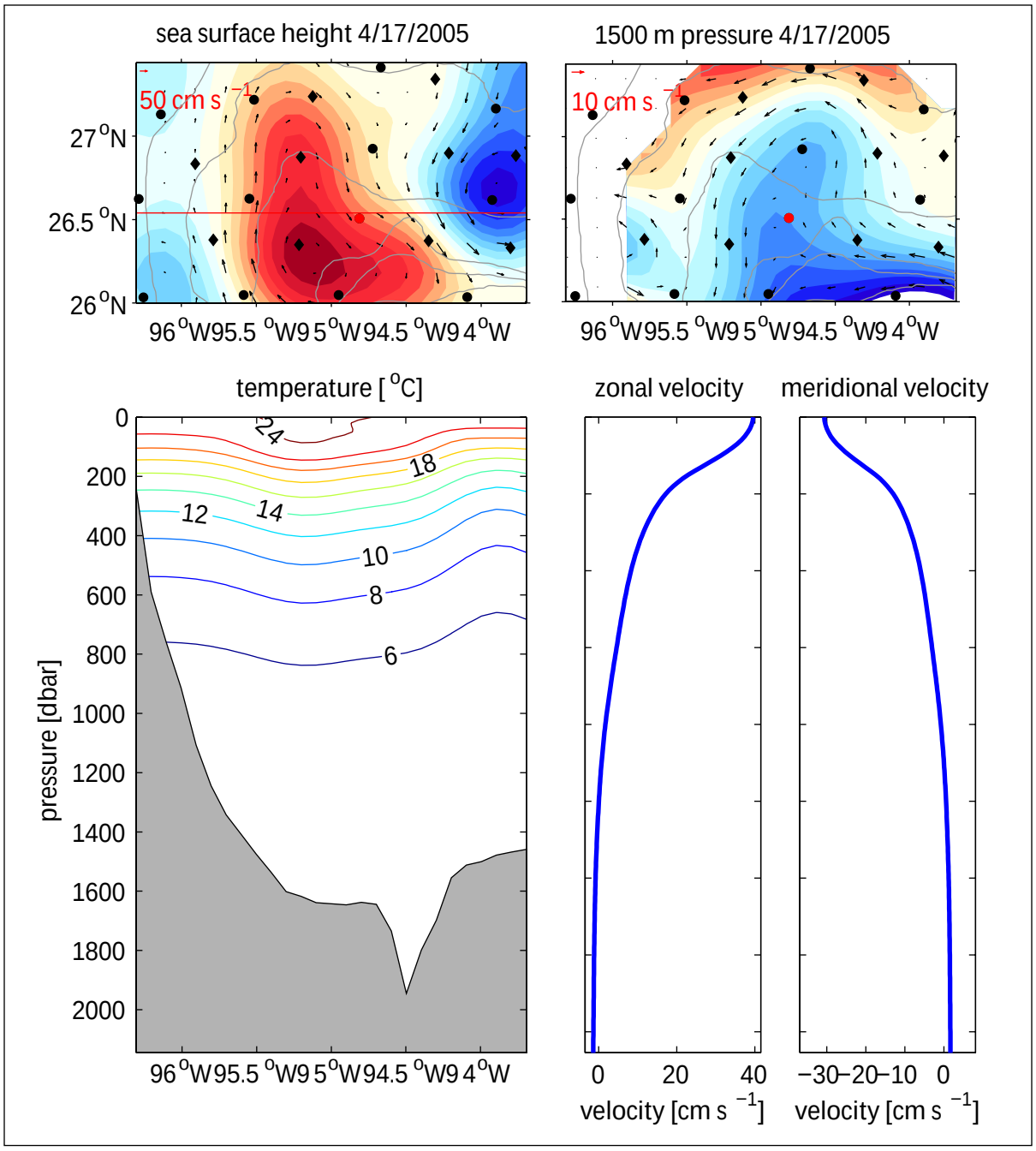

Figure 2.5-3. Views of current and temperature structure for April 17, 2005, based on PIES and current-meter measurements. Top panels: Sea-surface height (left) and pressure at 1500 m (right) in plan view. Contour intervals are 2.5 cm and 0.004 dbar, respectively. Anticyclonic circulations are shown by reddish hues; cyclonic by bluish hues. Current vectors plotted at 20 km spacing. PIES sites denoted by the diamonds; current-meter moorings indicated by circles. Bottom left panel: Cross-section of temperature in °C along the red line in the top left panel. Bottom two right panels: Zonal and meridional velocity at the red dot in the upper panels.

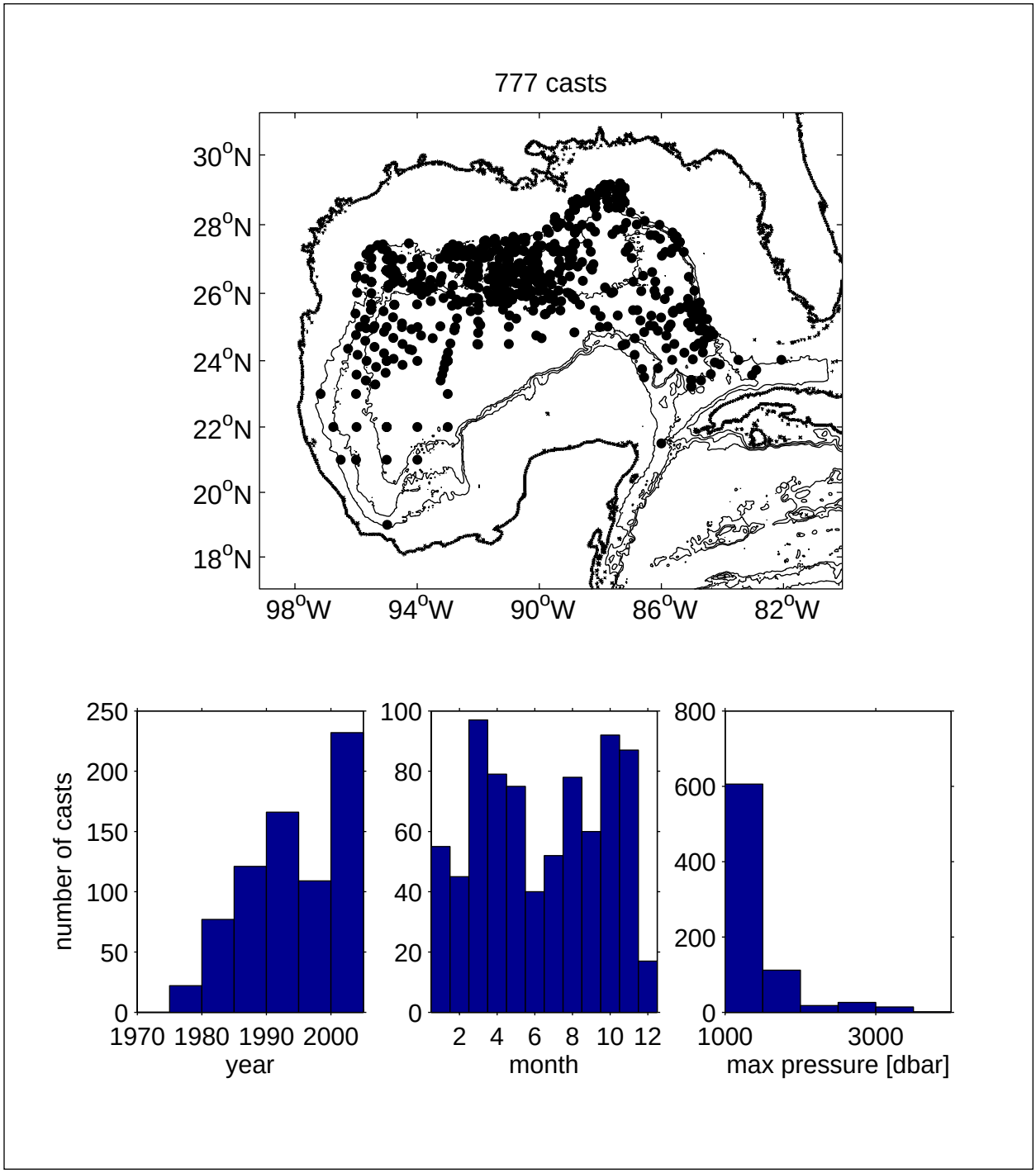

Figure 2.5-4. Spatial and temporal distribution of hydrocasts used to construct the Gravest Empirical Mode. Data provided by the Gulf of Mexico HYDRO Database compiled by TAMU as part of the MMS-funded Deepwater Reanalysis and additional stations provided by SAIC, and profiling float hydrocasts. Top panel: Spatial distribution of the hydrocasts with bathymetry contoured every 1000 m. Bottom panels: Histograms of the maximum hydrocast pressure (bottom right), year of hydrocast (left), and month of hydrocast (middle).

2.5.1.3 Sort Hydrographic Data by τ Index

Hydrocasts were linearly interpolated to a uniform 10-dbar grid and sorted by τ(150-1000) (Figure 2.5-5). This figure shows the results for temperature. The same methodology was applied to salinity and specific volume. Every 10 dbar, a cubic smoothing spline was fitted to temperature as a function of τ(150-1000) (Figure 2.5-6). Root-mean-square residual, rms, for each curve provides an indication of the departure any individual profile might have from the GEM curve. The rms values for temperature are small, 0.25°C within the thermocline, and decreased with increasing pressure. The curves show that a functional relationship exists between the integrated variable, τ(150-1000), and vertical profiles of temperature. The two-dimensional GEM field are shown in Figure 2.5-7. Note that there is little structure in the field below 1000 dbar and this reflects the relatively uniform deepwater temperatures in the Gulf of Mexico.

An example of how the GEM look-up table works is illustrated in Figure 2.5-8. Station 10 was a hydrocast taken during the PIES recovery cruise in August 2005 near PIES10 prior to the instruments recovery. τ(150-1000), calculated from the profile, is plotted as the vertical line in the GEM field. We 'look up' the temperature and salinity profiles (blue lines) given the calculated τ(150-1000). GEM-determined profiles agree well with the measured profiles. Note that for this illustration the GEM fields did not include this hydrocast.

2.5.1.4 Seasonal Correction

Finally, a seasonal correction was made to the upper 150 dbar of the temperature GEM field (Figures 2.5-9 and 2.5-10). The procedure utilized all available data and was as follows. (1) Fit a cubic spline under tension every 10 dbar from the surface to 150 dbar. (2) Determine the residual from the cubic spline curve. (3) Sort residual by time of year and create a smoothed empirical relationship for the residual as a function of time of year. This became the 'correction' to the profile determined by the GEM field. The amplitude of the temperature seasonal correction is about 3°C at the surface and decays to less than 0.5°C by 90 dbar. No seasonal correction has been applied to salinity because while there was variability in the surface layer it did not appear to be seasonal.

2.5.2 Conversion of Measured τ to τ(150-1000)

In order to use the GEM fields with the PIES τ measurements, measured τ was converted to τ(150-1000). Advantage was taken of the fact that τ at any deep pressure is linearly related to τ at any other deep pressure, $\tau(150\text{-}1000) = A \times \tau_{p1} + B$. Historical hydrography established the slope of this relationship and hydrocasts taken during the PIES deployment and PIES and mooring recovery cruises determined B for each time series. Each PIES had two calibration casts except for PIES 3 which had a single cast available for calibration. Calibrations at each PIES with two hydrocasts agreed with each other within a half millisecond. The mean pressure of each instrument was determined from the record average pressure adjusted for the vertical offset between the pressure sensor and the transducer (0.6 dbar) and mean atmospheric pressure (10.16 dbar). The final τ(150-1000) records are shown in Figure 2.5-11.

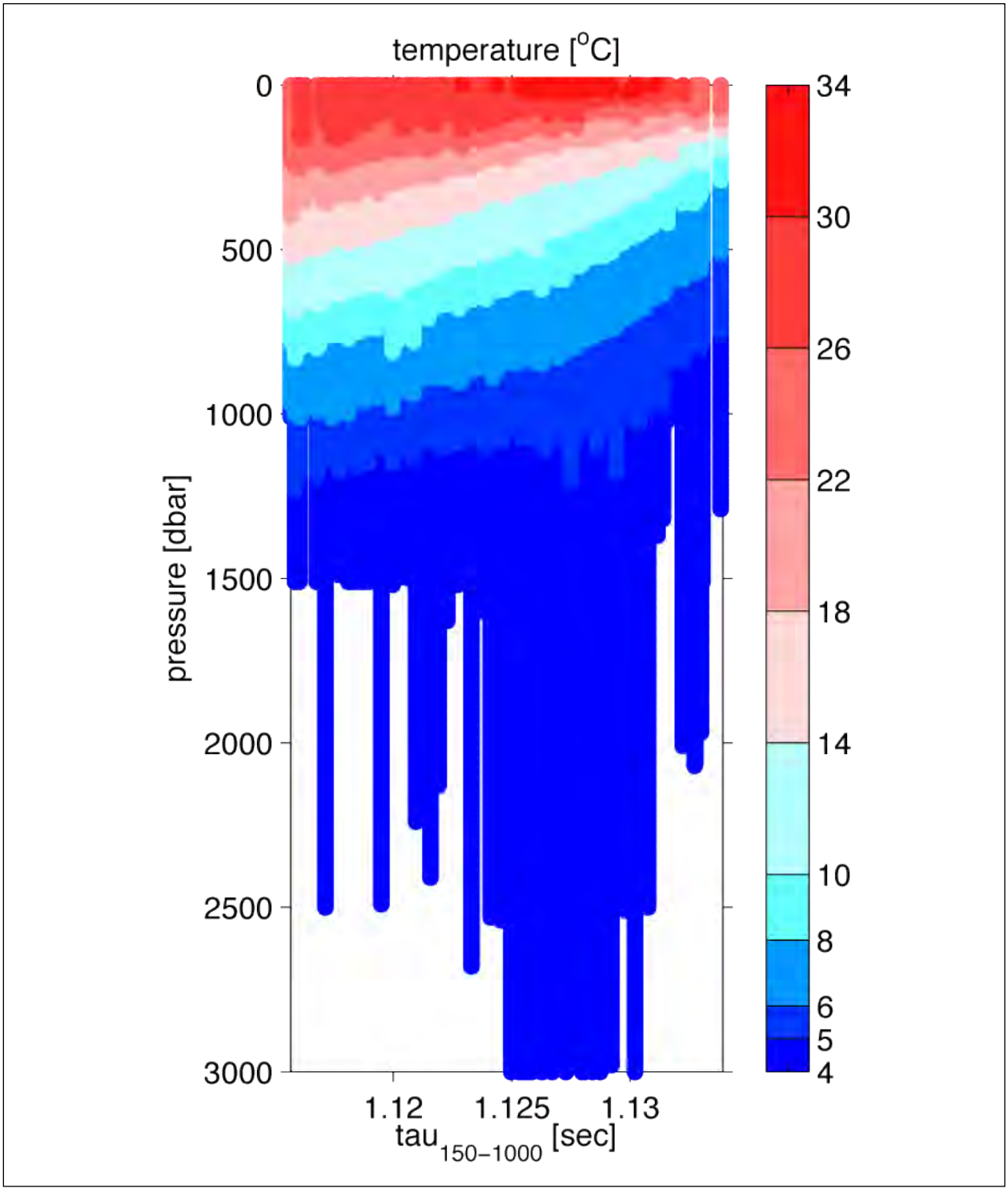

Figure 2.5-5. Temperature profiles interpolated every 10 dbar and sorted by τ(150-1000).

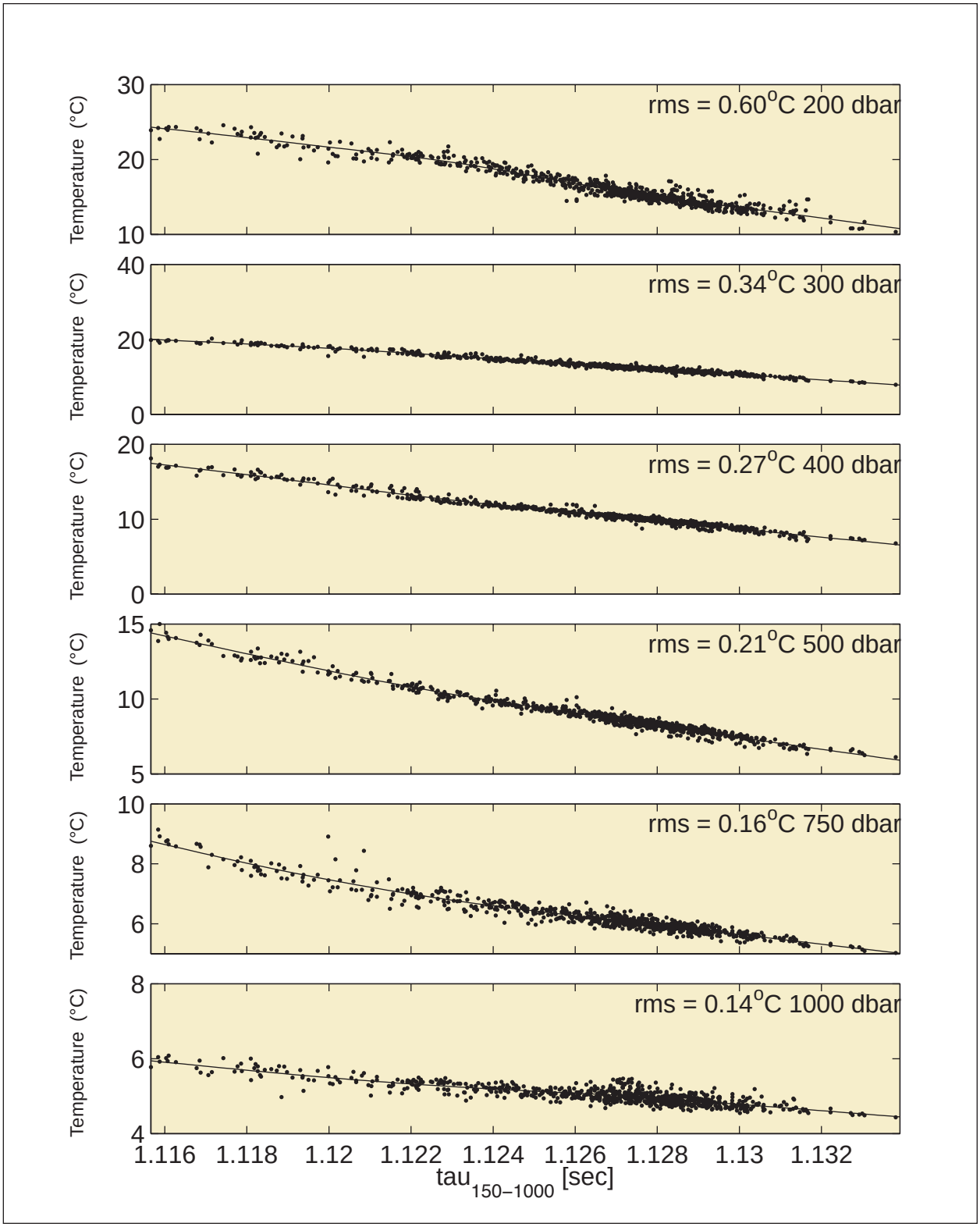

Figure 2.5-6. Scatter plots of temperature versus τ(150-1000) for six representative pressure levels. At each pressure, the temperature versus τ(150-1000) data were fit by a cubic smoothing spline (solid curve).

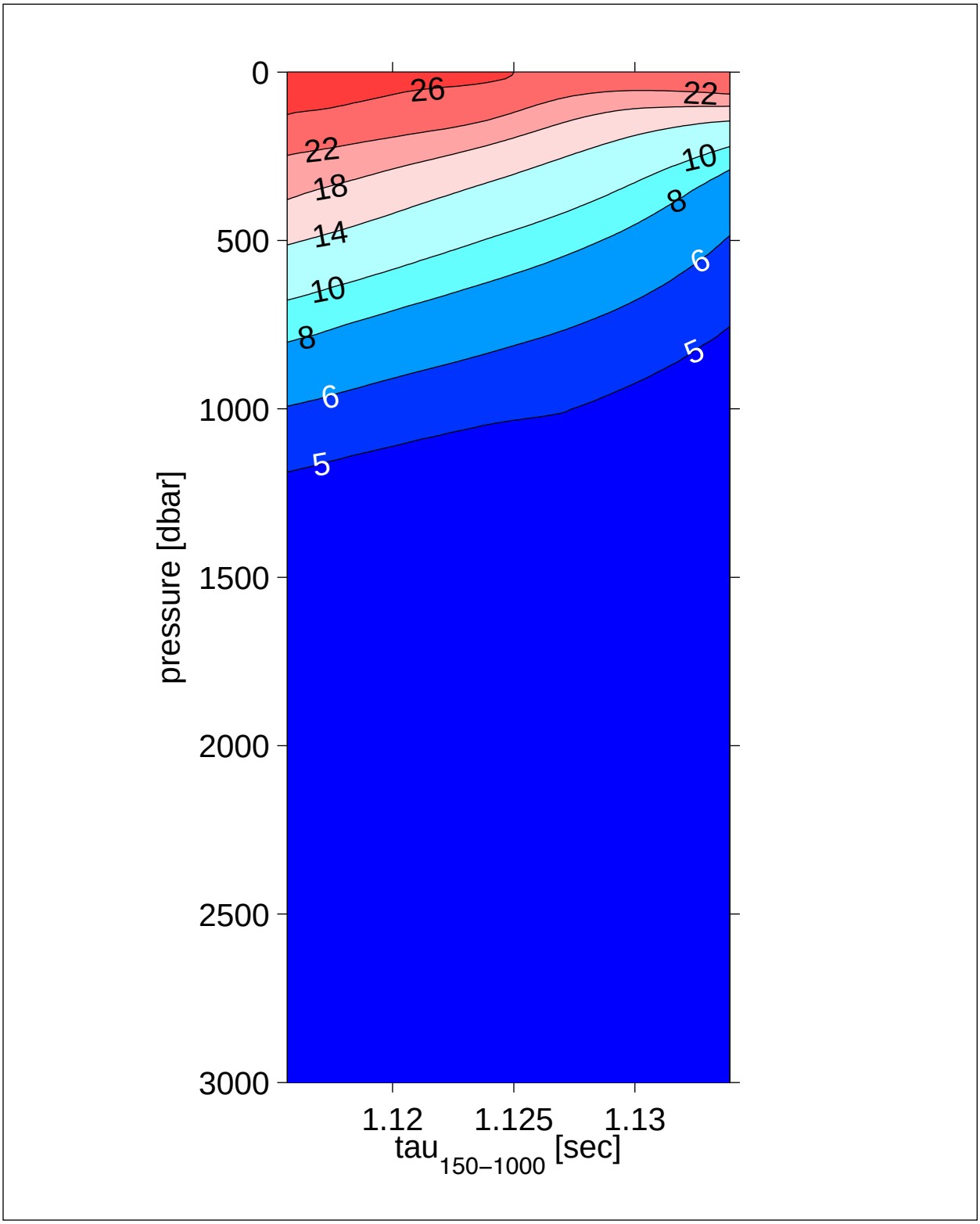

Figure 2.5-7. Contour plot of the cubic smoothing spline fits for the temperature GEM field.

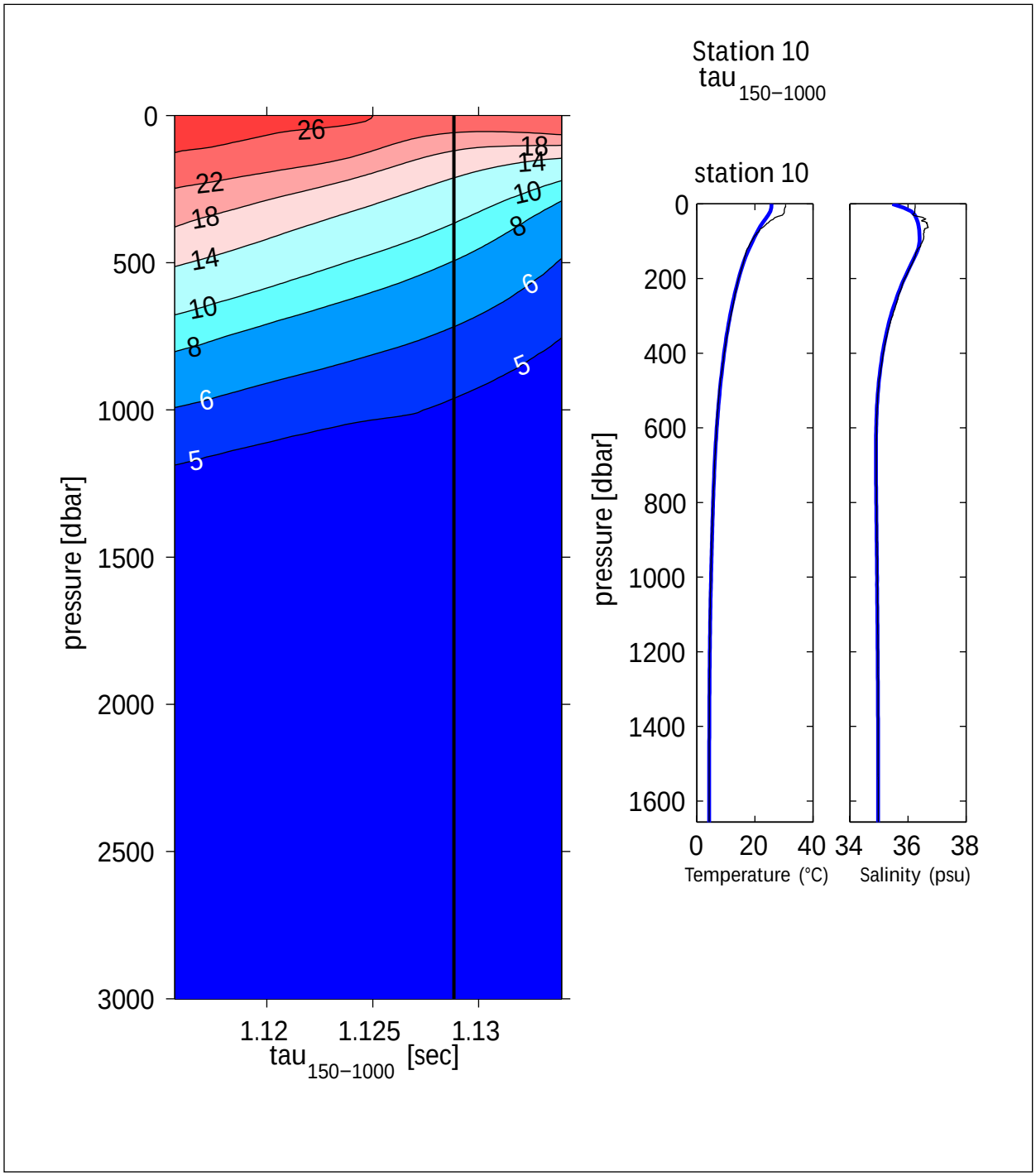

Figure 2.5-8. GEM-determined temperature and salinity profiles agree well with measured profiles. Left panel: t(150-1000) from a hydrocast taken near PIES 10 during the PIES recovery cruise is plotted as a vertical line in the temperature GEM field. Middle and right panels: Temperature and salinity profiles from the hydrocast (black). Temperature and salinity profiles are "looked up" given the calculated t(150-1000) and produced estimates shown with the blue line.

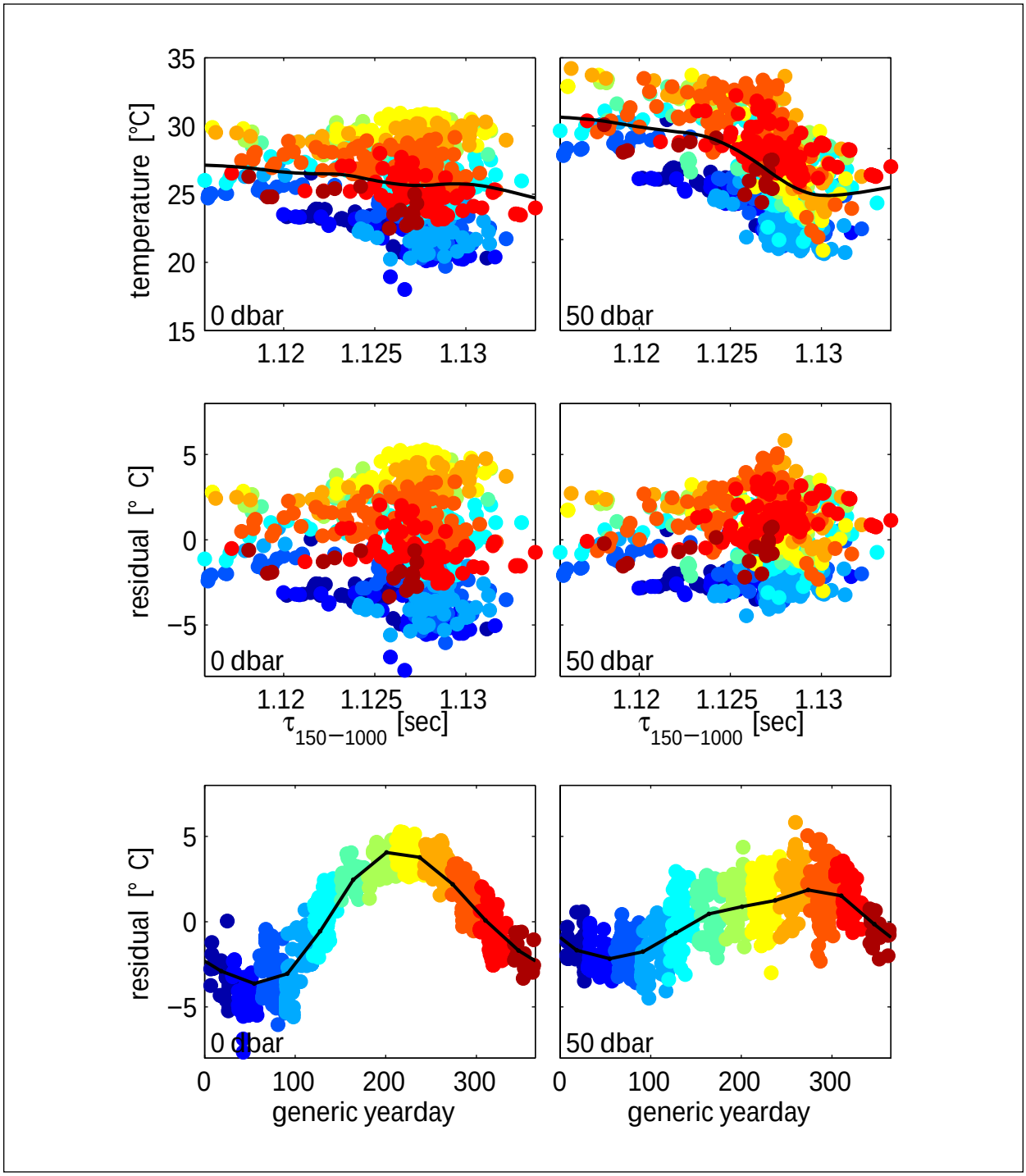

Figure 2.5-9. Upper panels: Scatter plots of temperature versus (150-1000) for surface (left) and 50 dbar with the cubic spline fit shown as a solid dark line. All samples in all panels are color coded by generic yearday transitioning from blue in January to red in December. Middle panels: Residual from the cubic spline fit. Lower panels: A clear seasonal signal in temperature emerges when the residual is sorted by time of year.

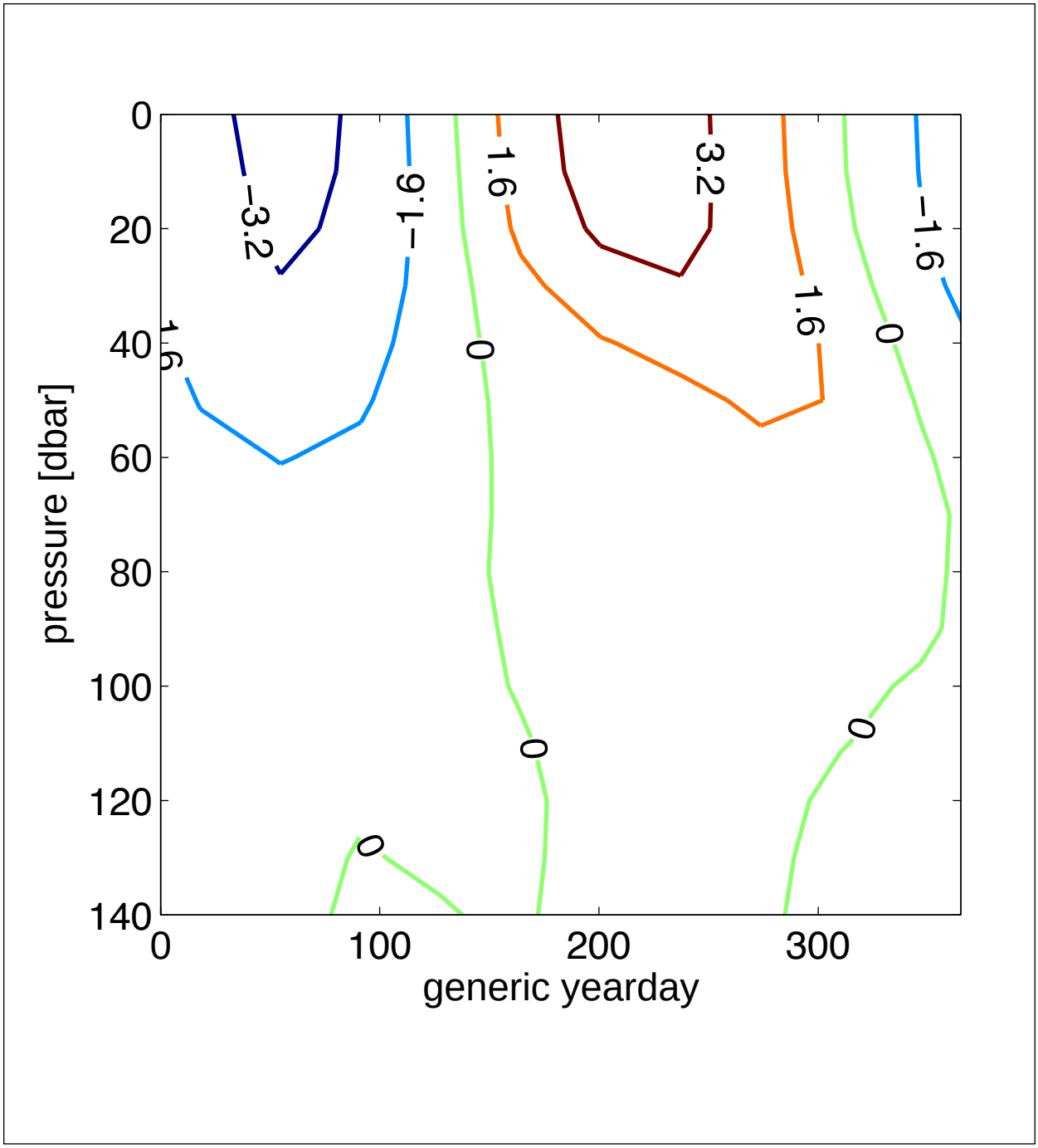

Figure 2.5-10. Seasonal temperature correction/amplitude contoured as function of yearday and pressure. The amplitude of the temperature seasonal correction is about 3°C at the surface and decays to less than 0.5°C by 90 dbar.

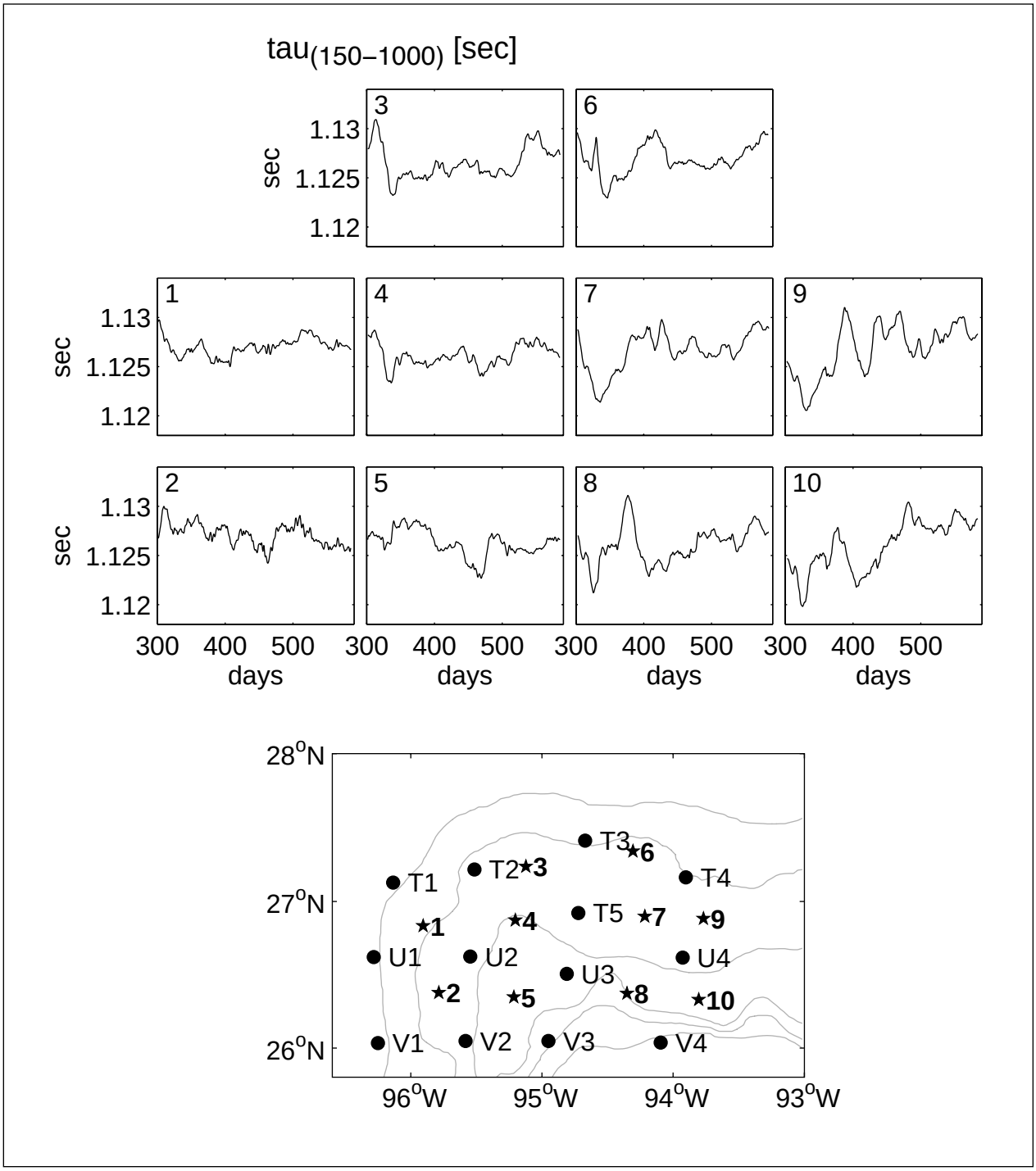

Figure 2.5-11. τ(150-1000) for each time series. The time series are shown in approximate geographic location. Instrument number in the upper left corner of each subplot. Bathymetry contoured every 500 m.

Before measured τ records were converted to τ(150-1000), a seasonal τ signal was subtracted from the τ records. This seasonal signal was determined from the historical hydrography in a manner similar to the seasonal temperature adjustment. Here we considered the influence of the seasonal cycle in τ between the surface and 150 dbar because the hydrography showed that there is little seasonal signal below 150 dbar. The scatter plot of τ(0-150) versus τ(150-1000) was largely due to the seasonal cycle and we determined the amplitude of the residual to be 0.3320 milliseconds (Figure 2.5-12). The correction was small, about 2% of the total range in τ(150-1000).

We estimated the error in τ(150-1000) to be near 0.0005 sec. This error derives from the measured hourly τ error, 0.0004 sec, and calibration error, 0.0004 sec. The hourly error was estimated as follows: individual τ records have an error of 0.002 sec and divided by the square root of twenty four, the number of samples, yielded 0.0004 sec. Note that we calibrated the CTD τ to the hourly measured τ. A potential spatial offset between PIES and calibration CTD was the largest contribution to the calibration error (see Meinen and Watts, 1998) and was estimated as 0.0002 sec, the maximum spatial gradient of τ in the western Gulf, $7.8e^{-5}$ sec per km, multiplied by a spatial offset of the CTD from the PIES that could be as large as 2.5 kilometers. The hourly scatter and the spatial offset errors add independently of each other.

τ(150-1000) values in Figure 2.5-11 occupy a mid-range position in the GEM look-up table with minimum and maximum τ(150-1000) values of 1.1157 and 1.1339, respectively. We investigated whether it was better to restrict input-stations to the GEM to come from near the NW Gulf array by constructing several GEM look-up tables based upon the proximity of the hydrocasts to the western Gulf array region. Comparison showed insignificant differences between the regional GEM and Gulf-wide look-up tables, except, of course, that the Gulf-wide tables were based upon substantially more data. This allows us to utilize a Gulf-wide database rather than a regionally restricted database.

2.5.3 Conversion of Tall Moorings to Pseudo Inverted Echo Sounders

Horizontal eddy correlation scales are near 50 km, therefore an array with ~70 km resolution is not eddy-resolving; the PIES and mooring measurements must be combined to provide maps whose extrema and gradients can be accurately estimated. One option would be to map temperature or current at the discrete depths of mooring sensors; the other option is to convert the moorings to pseudo IES records so that SSH and temperature and specific volume anomaly can be mapped to any pressure. With the goal to map eddy-scales and properties at any pressure and avoid the need for a mooring motion correction, we converted tall moorings to pseudo IES by conducting a reverse look-up of τ(150-1000) from mooring temperature and pressure records from a nominal depth of 450 m for sites T2, T3, T4, T5, U2, U3, U4, V2, V3, V4 and from 90 m for the shallow moorings at sites T1, U1, and V1. The 90-m temperature records were first "deseasoned" before the reverse look-up. Inclusion of the pseudo IES improved array resolution from 70 km to 45 km; adjacent records are visually coherent (Figure 2.5-13). The pseudo IES τ(150-1000) errors have been estimated to be approximately 0.001 sec, double that of the IES records. This error derives mainly from uncertainty in the absolute pressure of the mooring temperature sensor, with additional uncertainty in the reverse lookup procedure. We assumed that the absolute sensor depths are known within 10 m.

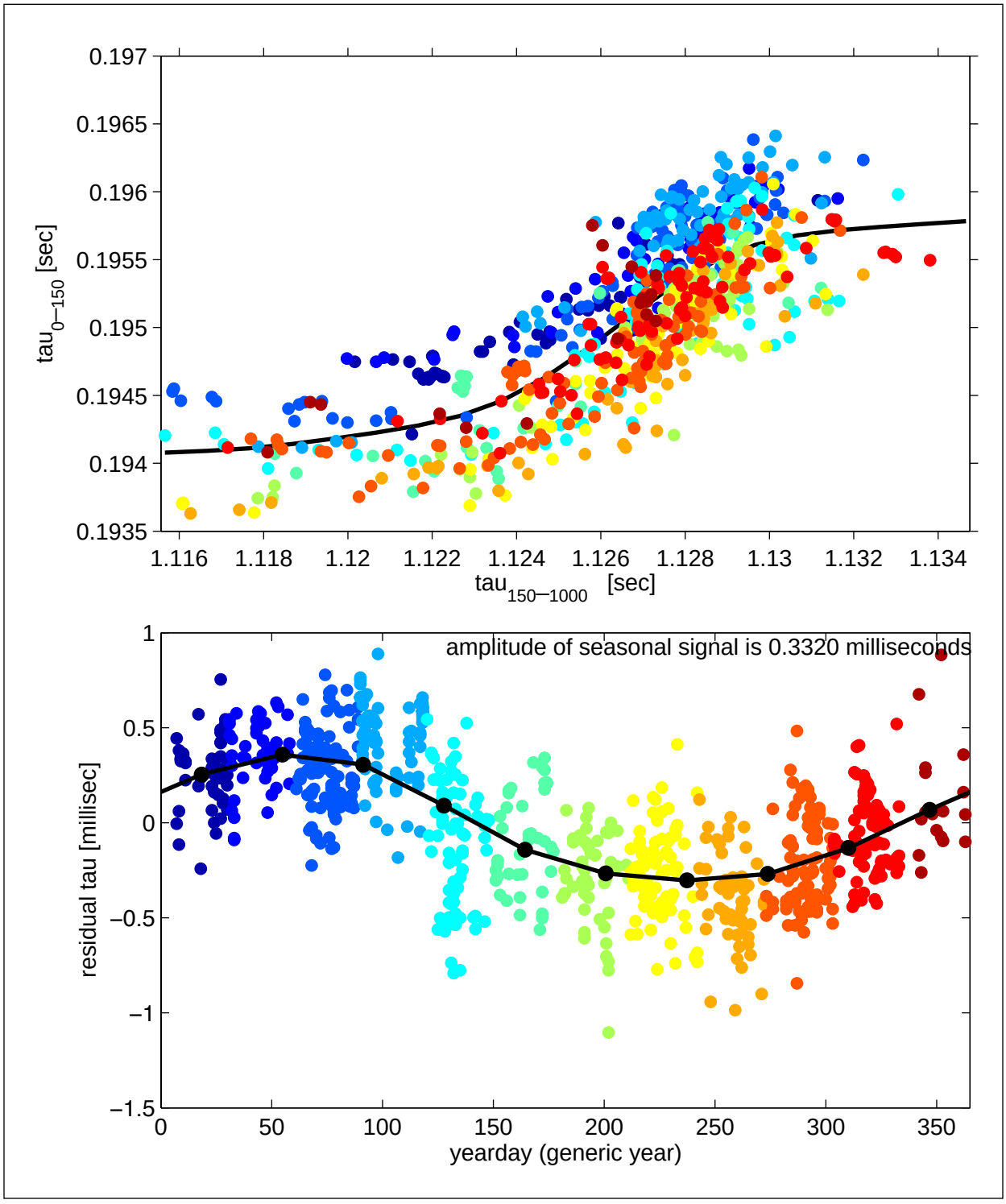

Figure 2.5-12. Upper panel: Scatter plots of τ(0-150) versus τ(150-1000). Each point is color coded by generic yearday transitioning from blue in January to red in December. The scatter about the spline fit (solid dark line) is largely due to the seasonal cycle. Lower panel: The residual from the cubic spline fit shown in the upper panel sorted by generic yearday showed a clear annual signal.

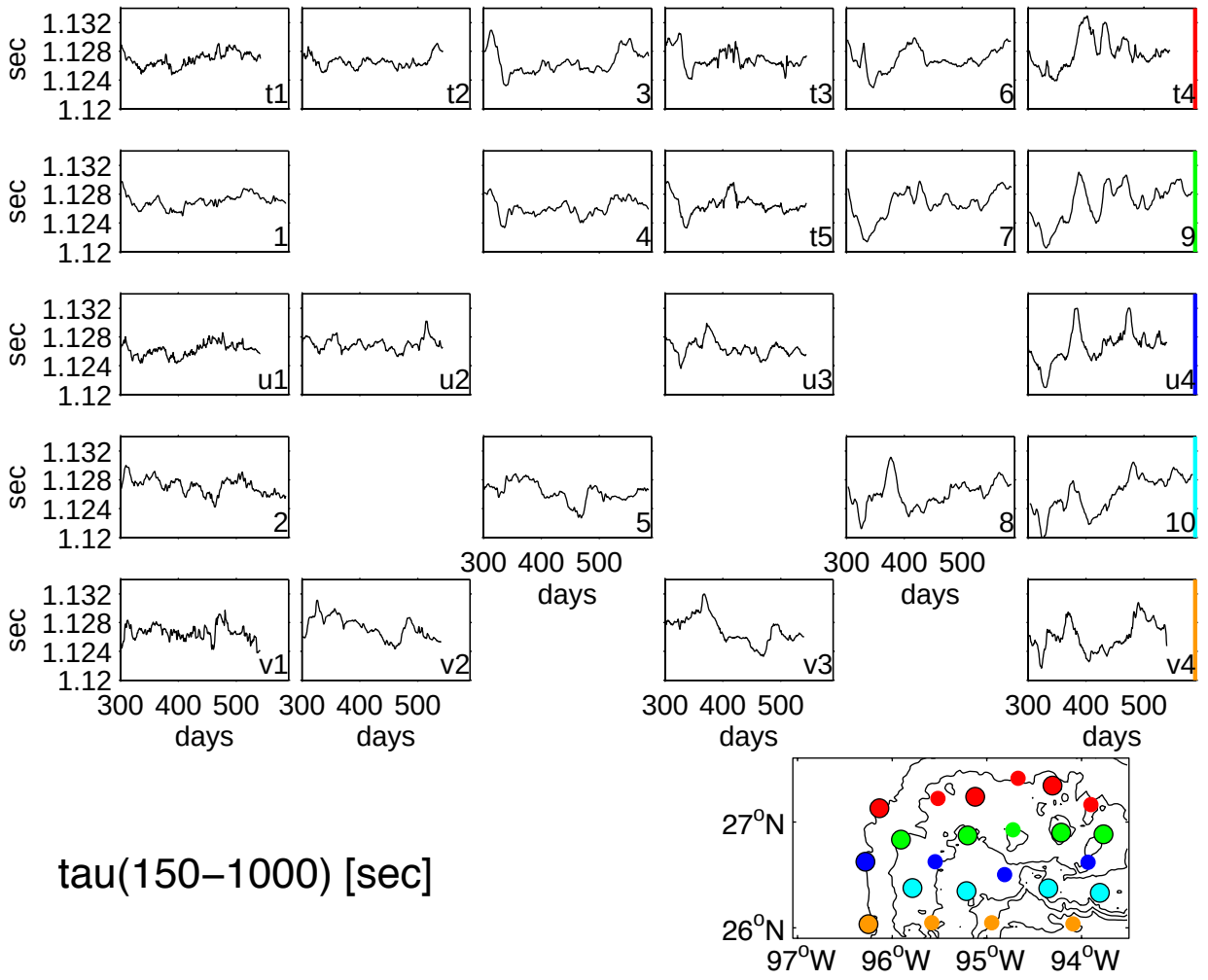

Figure 2.5-13. τ(150-1000) for each time series. The time series are shown in approximate geographic location. Instrument number noted in the lower right corner of each subplot. Bathymetry contoured every 500 m.

2.5.4 Upper-Ocean Maps

Maps were produced with optimal interpolation techniques adapted from Bretherton et al. (1976) and outlined in Watts et al. (1989, 2001). Optimal interpolation requires that the input fields have zero mean and uniform variance. To meet this requirement a mean field must be subtracted from the observed fields before mapping and then added back to produce maps of the total field. We removed the mean in such a way that the mapped fields behaved well outside the measurement sites. Additionally, the cross-correlations among the measurements determined the correlation function and length scales utilized in the optimal interpolation to map anomalies. We employed a Gaussian correlation function to construct maps. Multivariate optimal interpolation mapped geopotential and velocity, constrained to be geostrophic.

Maps of upper-ocean fields such as temperature and geostrophic shear were calculated by subtracting a 60-day low-passed field, mapped with a correlation length scale of 70 km. We then mapped an anomaly field with a shorter correlation length scale of 50 km. Correlation functions of the measurement anomalies determined the correlation length scales (Figure 2.5-14). The measurement correlation functions were nearly isotropic indicating that the use of an isotropic Gaussian correlation function for the objective analysis was appropriate.

The 10 PIES increased the resolution of the mooring array and improved mapping. The 50-km correlation scale indicates that the original array with nominal resolution of 70 km would have marginally resolved eddy-scale features. We can illustrate this by evaluating the optimal interpolation at a specific mooring site for three scenarios. First, we map τ(150-1000) using all pseudo IES records. Second, we repeated the mapping procedure but excluded the mooring as input. Third, we mapped τ(150-1000) using all PIES and pseudo IES records but excluded the mooring as input. In essence, we were testing robustness of the array due to instrument loss. Note that one must look closely to notice any differences between the black and the blue curve because the output from the first scenario is nearly identical to the input mooring time series (Figures 2.5-15 and 2.5-16). This illustrates that the mapping technique did not statistically modify the input. Results for both interior (U2) and exterior (U4) moorings show that the inclusion of the PIES records yielded estimates that agree better with the mooring record than the sparse array of only pseudo IESs.

2.5.5 Bottom Pressure

Several bottom-pressure processing details are noteworthy. First, experience indicates that preconditioning greatly reduces pressure drift. Sensors were subjected to pressures near 3000 dbar for 1-2 months in the lab prior to their first deployment. Second, pressure data were detided. Tidal response analysis (Munk and Cartwright, 1966) determined the eight major (largest amplitudes) tidal constituents for each instrument. Tidal amplitudes are generally small. The largest tidal amplitudes are near 15 cm for O1 and K1, near 5 cm for P1, and less than 5 cm for Q1 and for the remaining semidiurnal constituents. Estimated tides and phases vary smoothly across the array. Finally, pressure drift was removed using techniques found in Watts and Kontoyiannis (1990): an exponential-plus-linear drift curve determined by a least- squares fit was removed from the measurements. Instruments experienced small drifts. The maximum drift was 0.15 dbar and 6 instruments had drift less than 0.1 dbar.

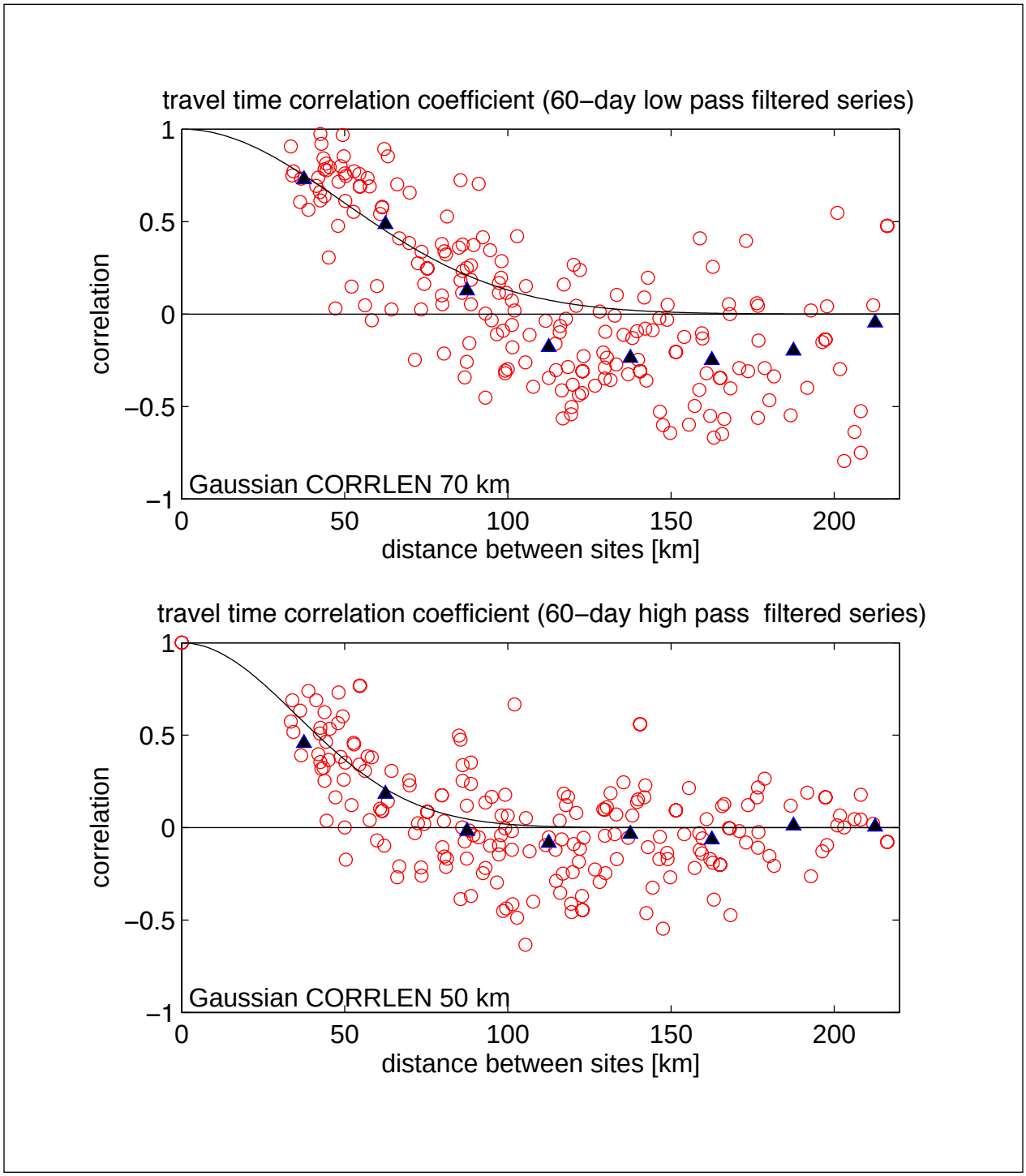

Figure 2.5-14. Correlation coefficient between pairs of PIES and pseudo IES τ(150-1000) records. Correlation coefficients plotted as a function of separation distance and binned every 25 km (black triangles). Upper panel: Time series have been 60-day low-pass filtered. A 70-km Gaussian function is plotted with a black line. Lower panel: Time series have been 60-day high-pass filtered. A-50 km Gaussian function is plotted with a black line.

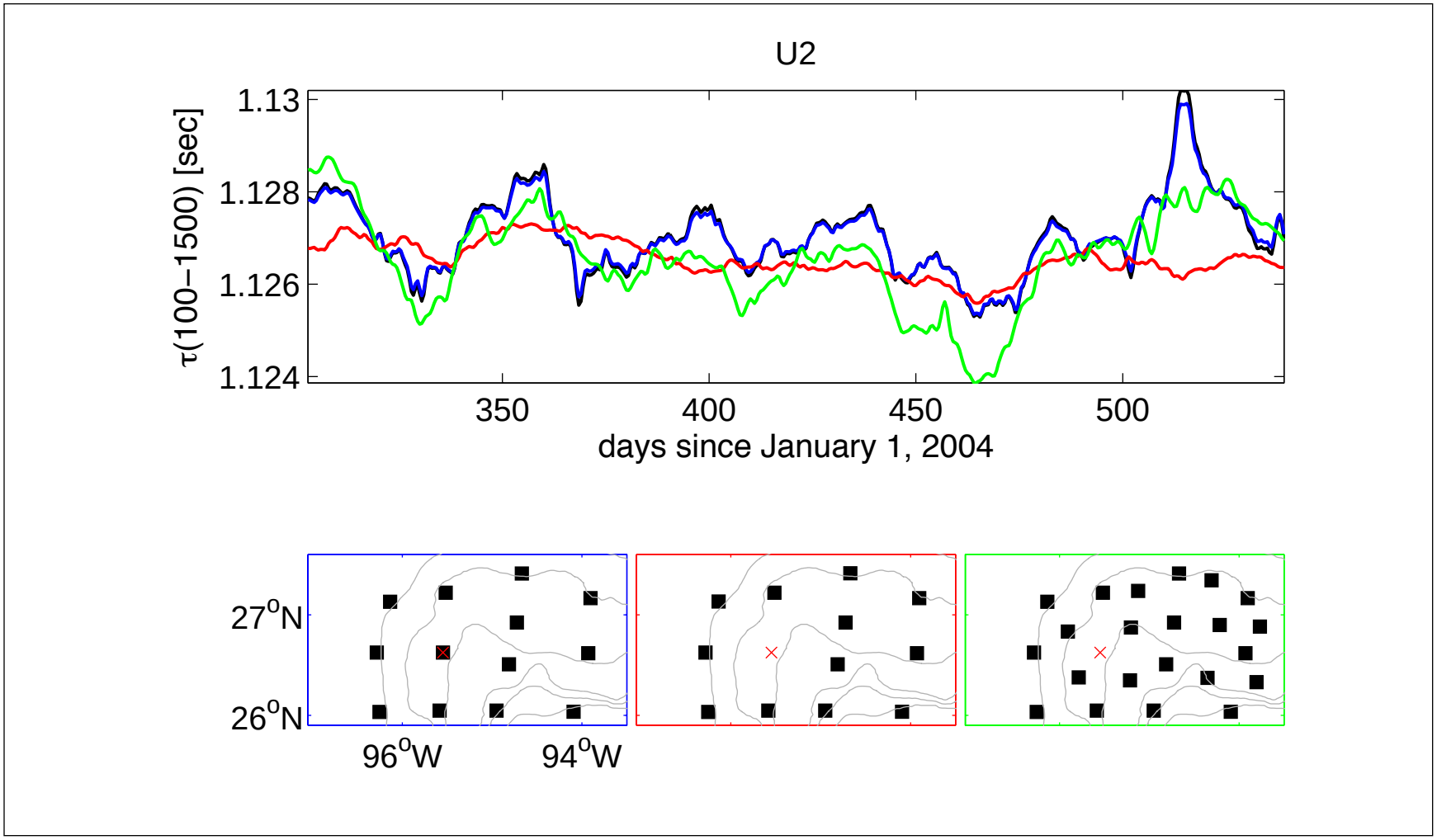

Figure 2.5-15. Upper panel shows time series of τ(150-1000) at U2 mooring (red x in lower panels) from the conversion of U2 temperature and pressure to τ(150-1000) via a GEM reverse look-up (black) and from optimal interpolation with input τ(150-1000) records from all pseudo-IESs (blue), all pseudo-IES except U2 (red), and all PIES and pseudo-IES except U2 (green). The color codes correspond between curve and box boundary in the lower panels.

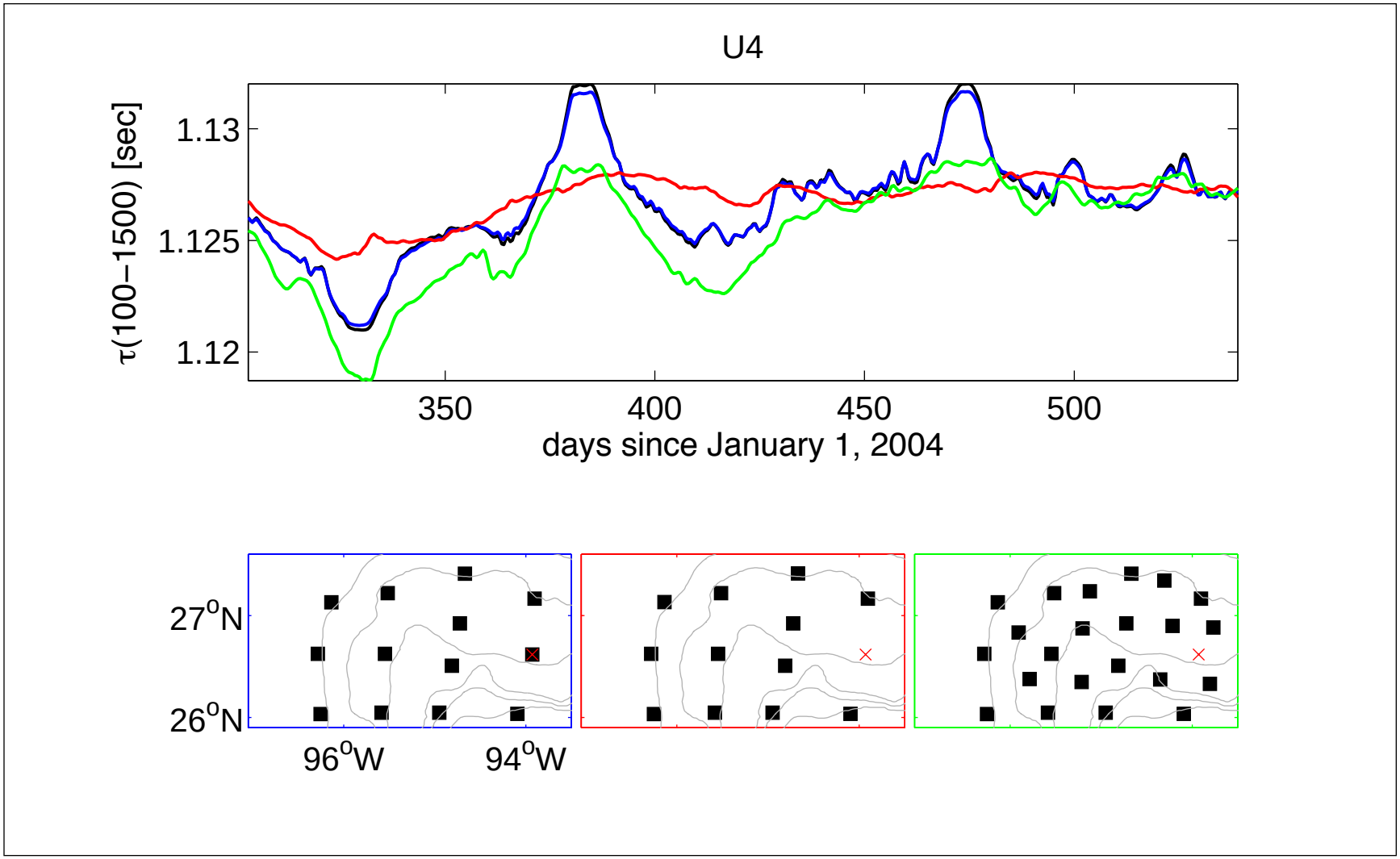

Figure 2.5-16. Upper panel shows time series of τ(150-1000) at U4 mooring (red x in lower panels) from the conversion of U4 temperature and pressure to τ(150-1000) via a GEM reverse look-up (black) and from optimal interpolation with input τ(150-1000) records from all pseudo-IESs (blue), all pseudo-IES except U4 (red), and all PIES and pseudo-IES except U4 (green). The color codes correspond between curve and box boundary in the lower panels.

Our ultimate goal was to map the near-bottom circulation. Bottom-pressure measurements must be leveled to produce spatially consistent maps, since each de-drifted pressure record has an undetermined additive constant offset relative to the other records. 'Leveled bottom pressures' refers to bottom pressures that have been adjusted to the same geopotential surface. Mean near-bottom currents and bottom pressures were dynamically constrained to be in geostrophic balance. Watts et al. (2001) provide a detailed description of the leveling procedure as applied to similar PIES arrays and here we highlight methods specific to this experiment. The reader is also referred to early work leveling pressure gauges in Drake Passage by Whitworth, 1983, with a recent revaluation by Cunningham et al. (2003). Niiler et al., (2003) also discuss a procedure for satellite SSH.

The choice of reference level requires discussion especially since in this experiment, PIES were moored at a variety of depths between 980 and 1800 m, and the shallower sites were significantly affected by the baroclinic and barotropic velocities. Our methodology yields absolute geostrophic current profiles composed of two vertical modes, a geostrophic shear referenced to zero at the reference level and a depth-independent component that is equivalent to the velocity at the reference level. Figure 2.5-17 illustrates our model. Any depth could serve as the reference level but a deep reference reduces error because the level is close to the velocity and pressure measurements, and furthermore, a deep reference velocity results in two modes that can be identified with physical modes, a baroclinic mode which contains the shear/steric signal and a barotropic mode which is depth independent. In this study a deep reference level, 1500 dbar was used, that mainly lies beneath the influence of baroclinic shear. This level is referred to as 1500 m, for convenience. We accounted for the steric contribution to pressure by converting each instrument's τ(150-1000) record via the GEM look-up to a geopotential height difference between the instrument's mean pressure and the reference level. Expressed in terms of variance, this adjustment ranged from 3.5 percent for PIES 6 (1060 m depth) to 0.2 percent at PIES 4 (1590 m depth). The deep reference-level currents derived from the measured 1500-m currents at T5, U2, U3, U4, V2, V3, and V4. Currents were interpolated to 1500-m depth if the nearest current meter was within 200 m.

For shallow moorings T1, T2, T3, T4, U1, and V1, the reference-level velocities were constructed by the following method shown schematically in Figure 2.5-17. Geostrophic shears relative to 1500 m at each mooring were calculated via optimal interpolation as discussed in the previous section. Note that the GEM look-up allowed determination of geostrophic shears beneath the deepest common level. Shears were referenced with the deepest available currents. The absolute velocity at 1500 m, determined as the difference between measured velocity and the shear referenced to 1500 m, served as the reference-level current for that mooring.

2.5.6 Reference-Level Maps

Lower-ocean mapping paralleled the upper-ocean procedure. Before mapping, a common mode or array-average pressure was subtracted from the 1500-dbar pressures (Figure 2.5-18). The common mode in the deep pressures simply adds a time-dependent array-wide constant which has no dynamical significance for the mesoscale circulation so it is better to subtract it from all records prior to mapping. Spectra of the common mode reveals dominant peaks near 14 and 6

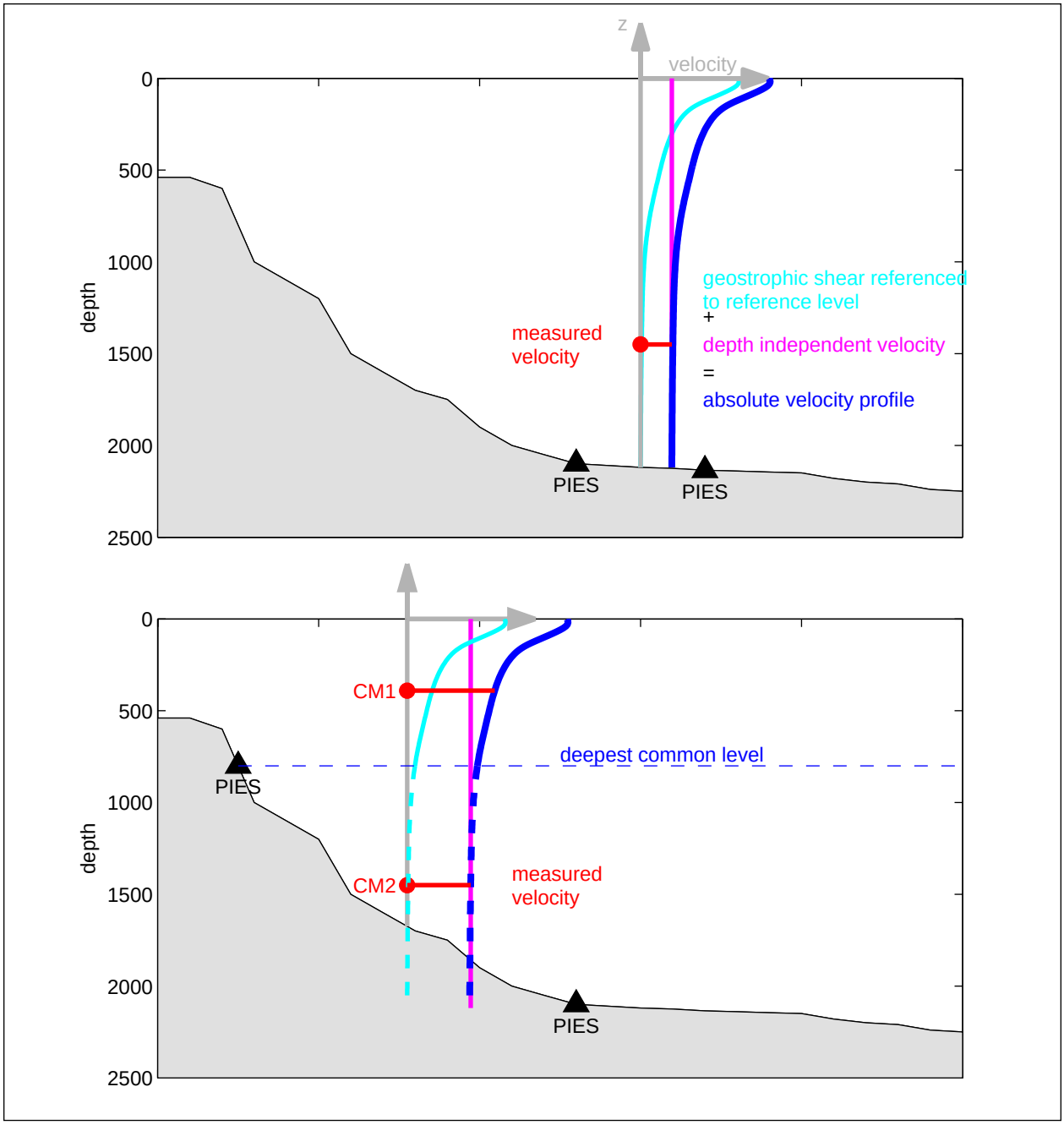

Figure 2.5-17. Upper panel: PIES methodology yields absolute current profiles (blue) composed of two vertical modes, a geostrophic shear referenced to zero at the reference level (cyan) and a depth-independent component (red) that is equivalent to the velocity at the reference level. Lower panel: Velocity at reference level can be determined by direct measurements (CM2) or by measurements at another level. For example, the GEM look-up determines geostrophic shears referenced to zero at the reference level (cyan). Shear can be referenced with available currents at CM1. Reference level currents are the difference between absolute (blue) and shear (cyan) velocities at the reference level.

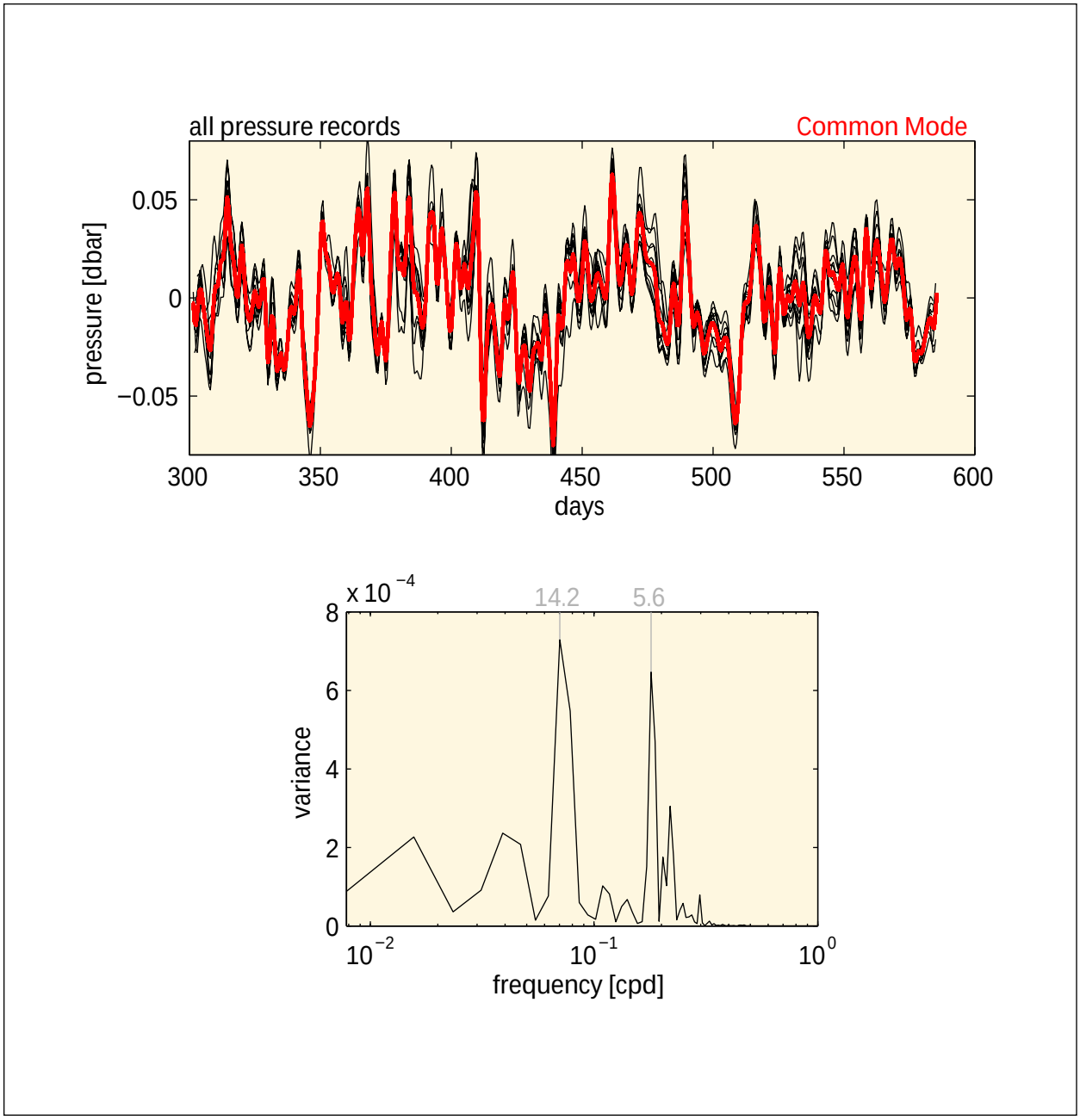

Figure 2.5-18. Top panel: Common mode subtracted from bottom pressure records before mapping deepwater dynamical properties. Bottom panel: Spectra of common mode reveals dominant peaks near 14 and 5 days.

days. The 6-day signal is likely the barotropic oceanic response to the atmospheric Rossby-Haurwitz wave (Park and Watts, 2006). The 14-day peak has a slightly lower period compared to the nearly 16-day period found in the exploratory bottom pressure data set (Donohue et al., 2006). The source of this signal remains unexplained, however, the signal is coherent and in-phase with coastal tide gauges west of Pensacola (west of the broad shallow Floridian continental shelf). Figure 2.5-19 shows the bottom pressure records with the common mode removed. The mean field was derived from fitting a plane to the mean 1500-dbar pressures. A 60-km correlation length scale determined from the near-bottom-pressure correlations was used to map anomaly fields (Figure 2.5-20). The correlations indicate that perhaps a smaller correlation length scale near 50 km could be used but due to the relative sparseness of the array 60 km length scale was used. This will better fill the gaps between measurement sites at the expense of slightly over-smoothing the mapped daily streamfunction and velocity fields. Similar to the τ time series, the near-bottom pressure autocorrelations are nearly isotropic (not shown). Streamfunction maps were created by inputs from both pressure and current-meter data. The inclusion of the current-meter data sharpens gradients.

2.5.7 Total Maps

The combination of upper and lower-circulation maps estimated absolute velocities throughout the water column. Upper-ocean relative velocities were created by mapping velocities referenced to zero at 1500 dbar. The 1500 dbar-level velocities created with the bottom pressure and current-meter records then referenced these to generate absolute upper-ocean relative velocities. Absolute sea-surface heights were also determined. First, 1500-dbar pressures were converted to their height equivalent (pressure divided by gravity and density). Second, surface geopotentials referenced to 1500 dbar were converted to their height equivalent (geopotential divided by gravity). The 1500-dbar referenced and 1500-dbar fields were combined to yield absolute SSH.

2.5.8 Mooring Comparisons

Here we compare mooring measurements of temperature and current to PIES-derived estimates. This comparison is not strictly a validation of the PIES methodology because the design of the array does not lend itself to strict verification: point measurements differ intrinsically from mapped geostrophic estimates; the conversion of the moorings to pseudo-PIES increased the errors in the technique; and the absolute pressure of the discrete mooring measurements was unknown and contributed discrepancies. However, after accounting for these differences, the comparisons below show that the measurements and PIES-derived estimates track each other and agree within the anticipated bounds.

Three tall moorings (T5, U2, and U3) embedded in the middle of the array provided measurements to evaluate our PIES-derived fields of temperature. We opted to exclude sites from these comparisons if they were located around the periphery of the mapping grid. Differences derive from instrument errors (both mooring and PIES) and the GEM parameterization (Figures 2.5-21 through 2.5-23). Table 2.5-1 documents the anticipated differences between mooring and PIES. For each nominal depth (column 1) the table provides the rms in the GEM table (GEM error, column 2), the error in the GEM table look-up due to τ

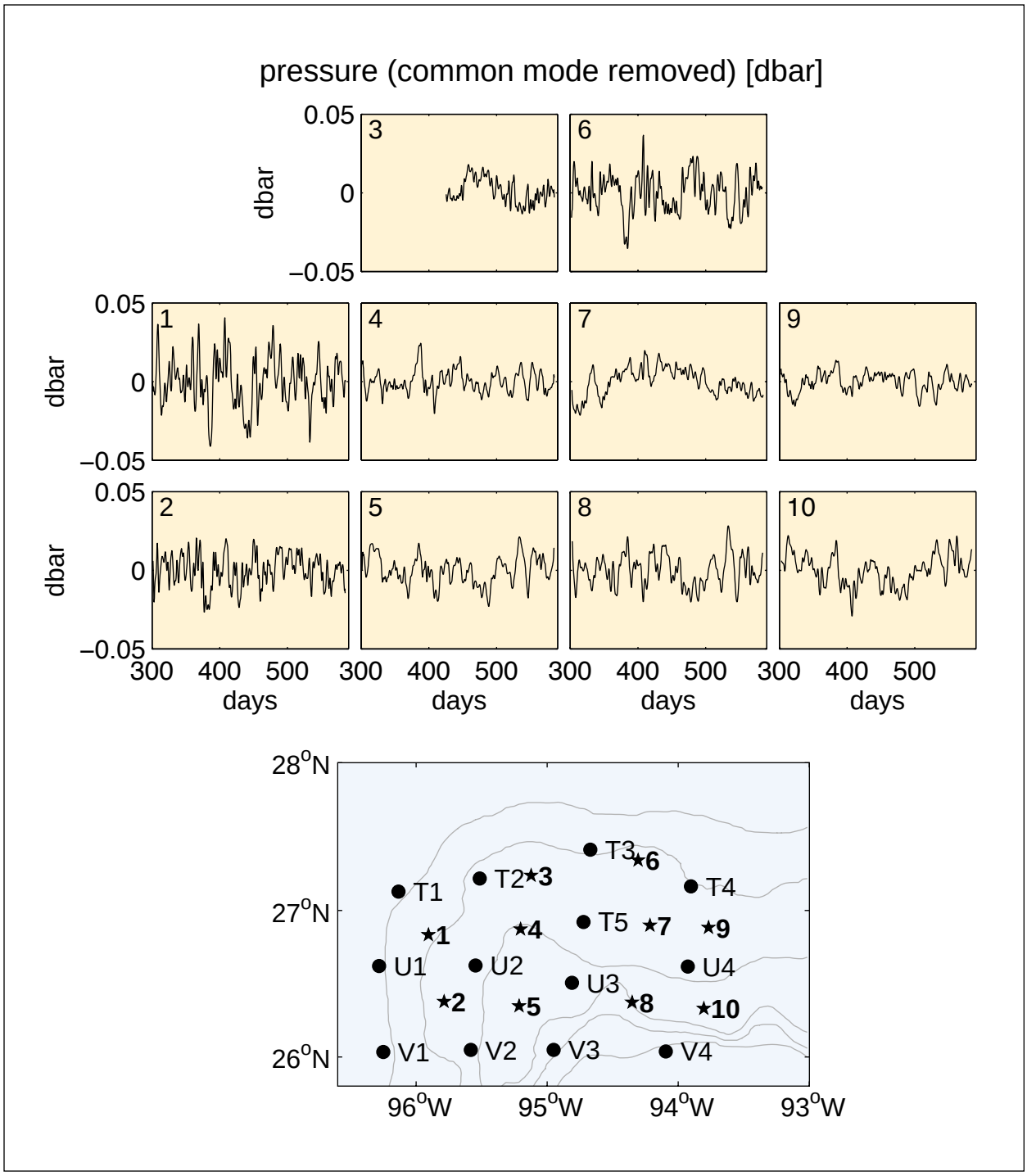

Figure 2.5-19. Time series of bottom pressure anomaly with the common mode removed in dbar plotted according to approximate geographic location. Instrument number noted in the upper left corner of each subplot. Bathymetry contoured every 500 m.

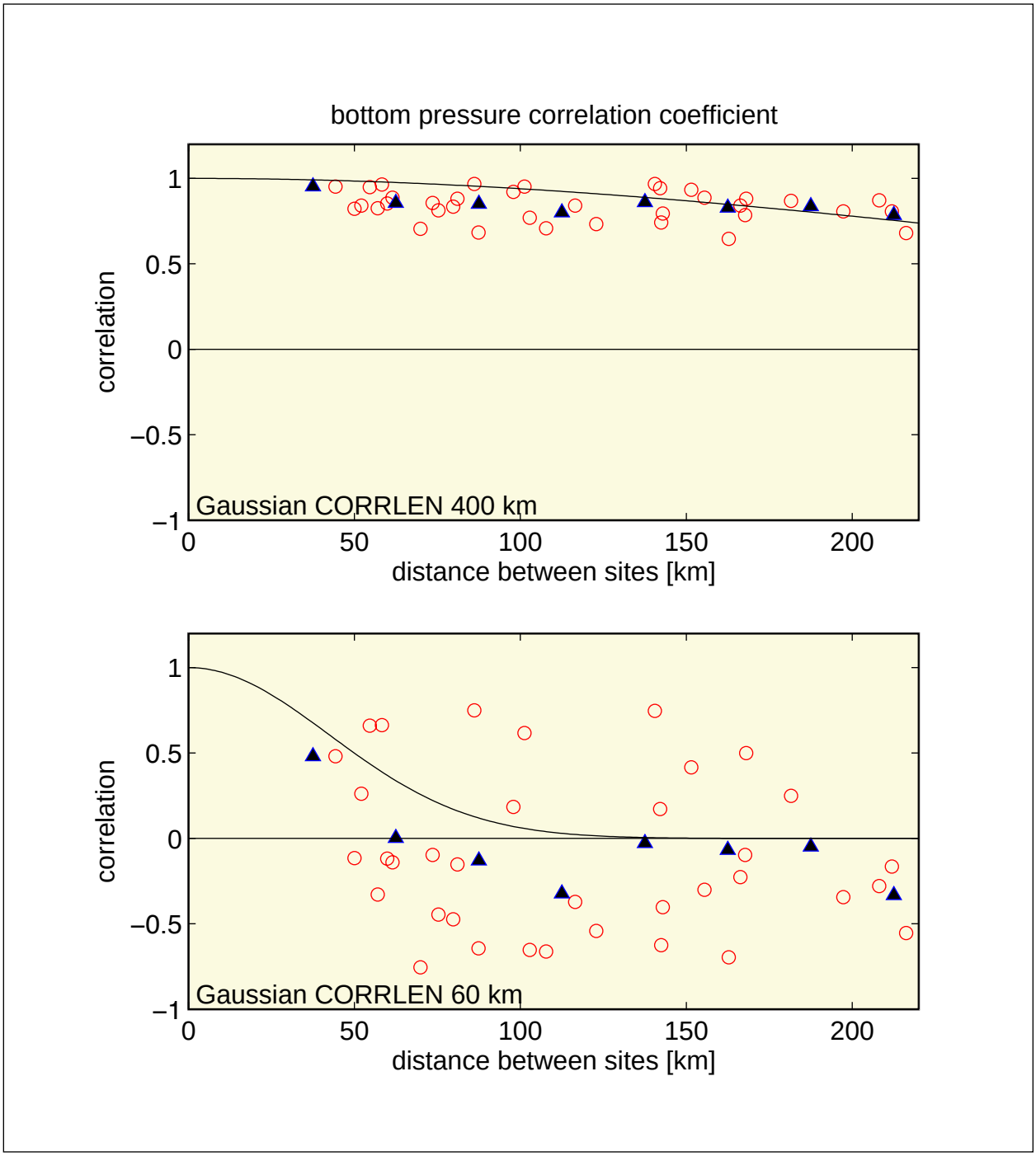

Figure 2.5-20. Correlation coefficient between pairs of pressure records. Upper panel: Correlations coefficient plotted as a function of separation distance (open red circles) and binned every 25 km (black triangles). The common mode produces long correlations. A 400 km Gaussian function is plotted with black line. Lower panel: Correlation coefficients contoured as a function of separation distance (open red circles) and binned every 25 km (black triangles) after the common mode has been removed. A 60 km Gaussian function is plotted in black.

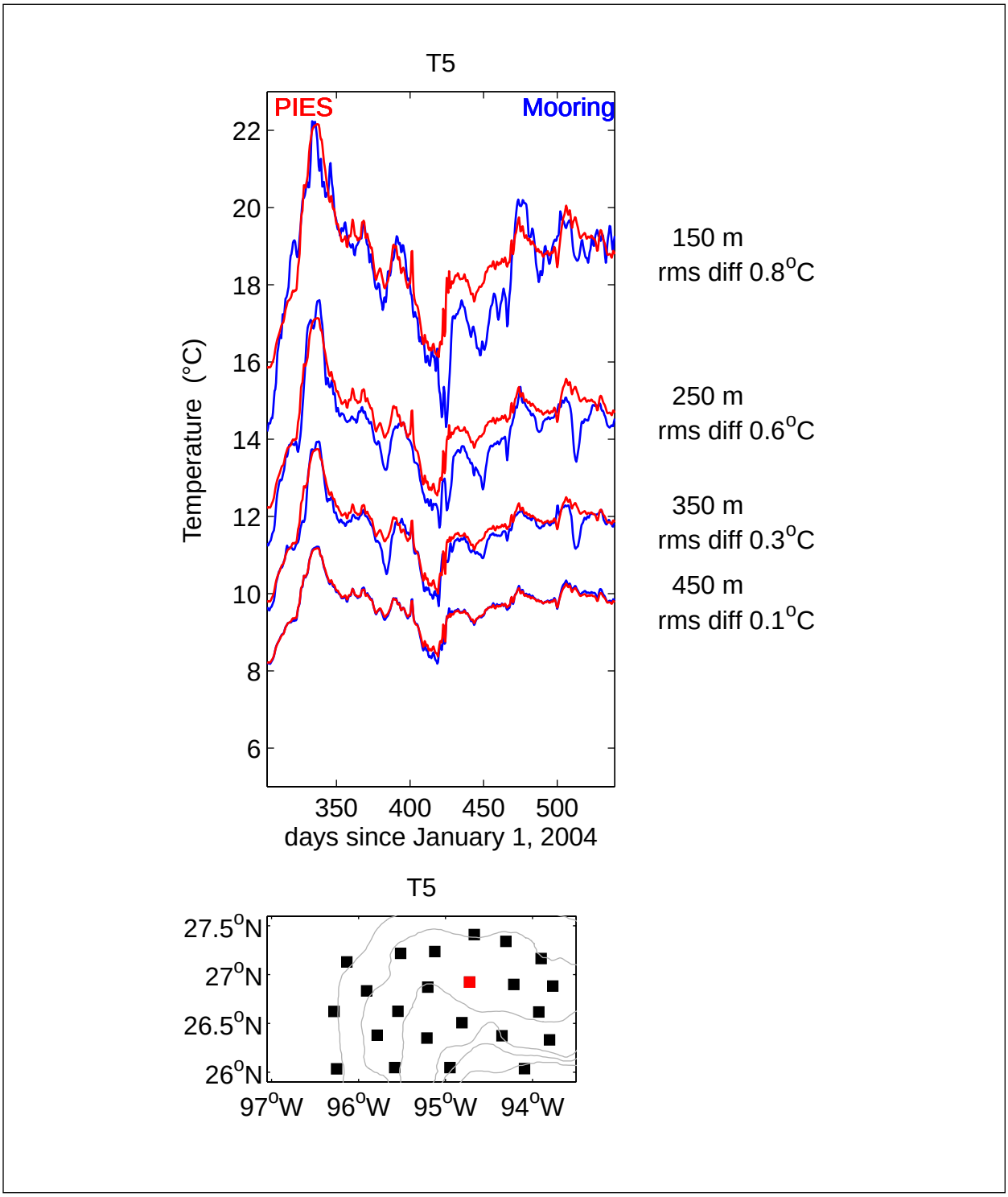

Figure 2.5-21. Comparison between the T5 mooring (blue) and PIES-derived (red) temperature. The nominal depth and rms difference between PIES and the T5 mooring are noted to the right of each series. The bottom panel shows the location of the PIES (black) and pseudo-IES (black) and the T5 mooring (red). Bathymetry contoured every 500 m depth.

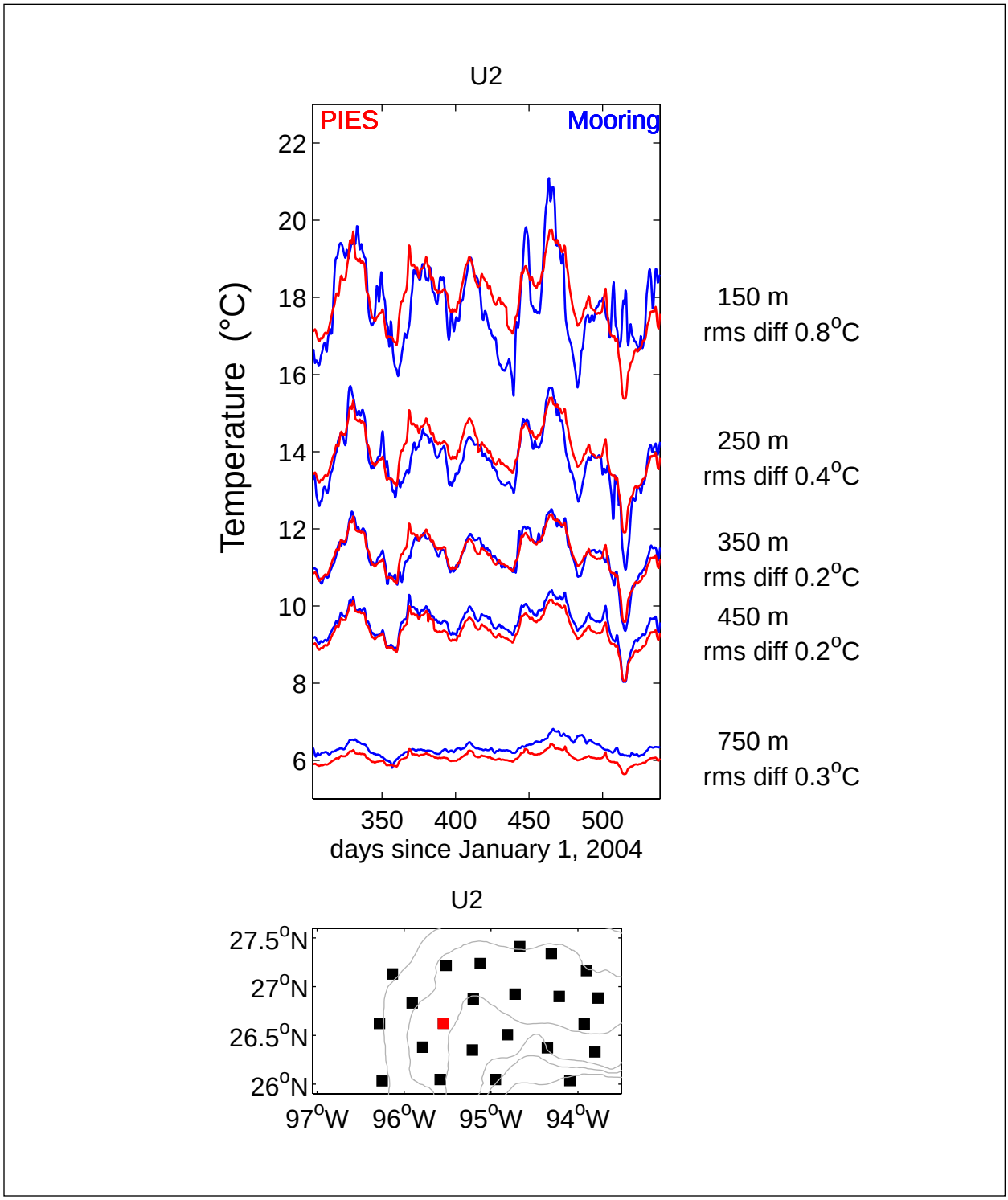

Figure 2.5-22. Comparison between the U2 mooring (blue) and PIES-derived (red) temperature. The nominal depth and rms difference between PIES and the U2 mooring are noted to the right of each series. The bottom panel shows the location of the PIES (black) and pseudo-IES (black) and the U2 mooring (red). Bathymetry contoured every 500 m.

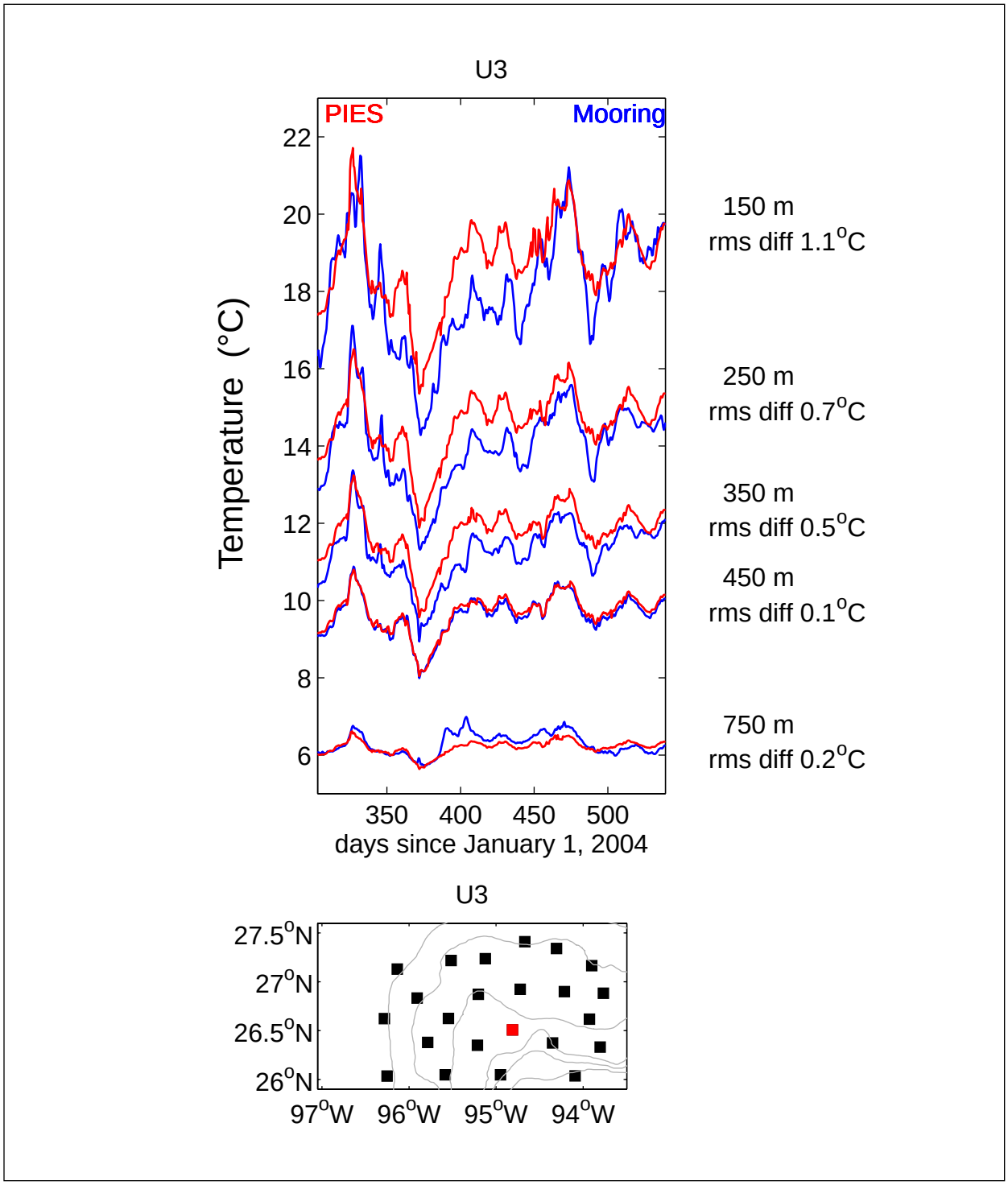

Figure 2.5-23. Comparison between the U3 mooring (blue) and PIES-derived (red) temperature. The nominal depth and rms difference between PIES and the U3 mooring are noted to the right of each series. The bottom panel shows the location of the PIES (black) and pseudo-IES (black) and the U3 mooring (red). Bathymetry contoured every 500 m.

uncertainty of 0.001 which we determined as τ_error*dT/dτ (IES instrument error, column 3), and the impact of a 10 m uncertainty in absolute mooring sensor pressure which we determined as P_error*dT/dp (uncertainty in mooring pressure, column 4). The total predicted difference is the square root of the sum of the squares of columns 2 through 4 and is listed in column 5. We do not consider the discrepancy between point and mapped measurement here because the 450-m mooring temperature records were used to convert moorings to pseudo IESs. Observed differences were somewhat smaller than predicted.

Table 2.5-1

Predicted Differences Between Measured and PIES-Estimated Temperatures for Four Nominal Depths

Nominal Depth [m]	GEM Error [°C]	IES Instr. Error [°C]	Mooring Pressure Uncertainty [°C]	Total Predicted Difference [°C]
150	0.84	0.68	0.47	1.17
250	0.43	0.70	0.32	0.89
350	0.30	0.70	0.23	0.80
450	0.23	0.54	0.17	0.61
750	0.16	0.20	0.06	0.27

The comparisons indicate how well the GEM look-up describes the temperature structure providing that we know the pressure of the temperature sensor as a function of time. Note that the tall moorings experienced some vertical motion when ocean currents caused the moorings to blow over or draw down. The proper comparison is between measured and estimated T(t,p(t)). We used the pressure record at the 450-m level from each mooring to estimate draw down at each sensor. In other words we assumed that the mooring motion at the 450-m level was the same at all other levels. We assumed that the absolute sensor depths are known within 10 m . The inability to determine the absolute pressure of the sensors can lead to discrepancies. For example, a themocline temperature gradient of 0.035°C $dbar^{-1}$ combined with a 10-dbar uncertainty leads to a 0.35°C difference between PIES estimated and measured temperature. In several cases, the visible offset between records likely results from uncertainty in p(t), see for example the comparisons for mooring T5 at 250 m and mooring U3 at 150, 250, and 350 m.

RMS differences listed on these three figures are within anticipated discrepancies at each depth (last column in Table 2.5-1). Recall that the pseudo IES records have twice the error of a PIES-only array. Features with relatively small vertical scales are not reproduced and given the vertical instrument spacing it was not anticipated that such fine scales would be reproduced. For example, the intrathermocline eddy measured by mooring T5 at 250-m and 350-m depths just after day 500 does not appear in the PIES-derived maps (Figure 2.5-21).

We compare PIES-mapped currents to mooring currents in Figure 2.5-24 through Figure 2.5-26. The series track each other well, especially within the thermocline. The rms differences reflect instrument errors (both mooring and PIES), errors associated with the GEM parameterization

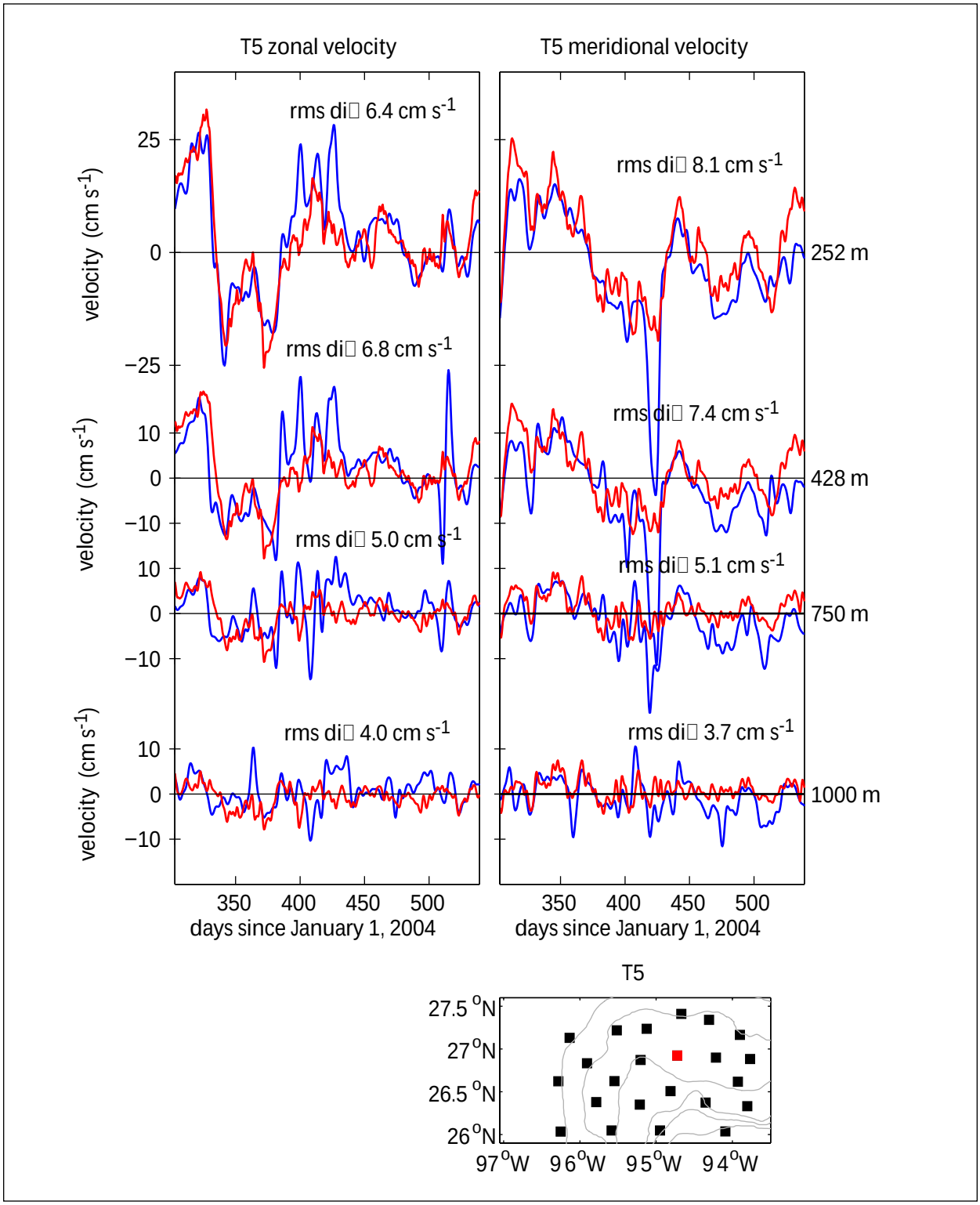

Figure 2.5-24. Comparison between the T5 mooring (blue) and PIES-derived (red) zonal (left) and meridional (right) velocities. The nominal depth and rms difference between PIES and the T5 mooring are noted to the right of each series. The bottom panel shows the location of the PIES (black) and pseudo-IES (black) and the T5 mooring (red). Bathymetry contoured every 500-m depth.

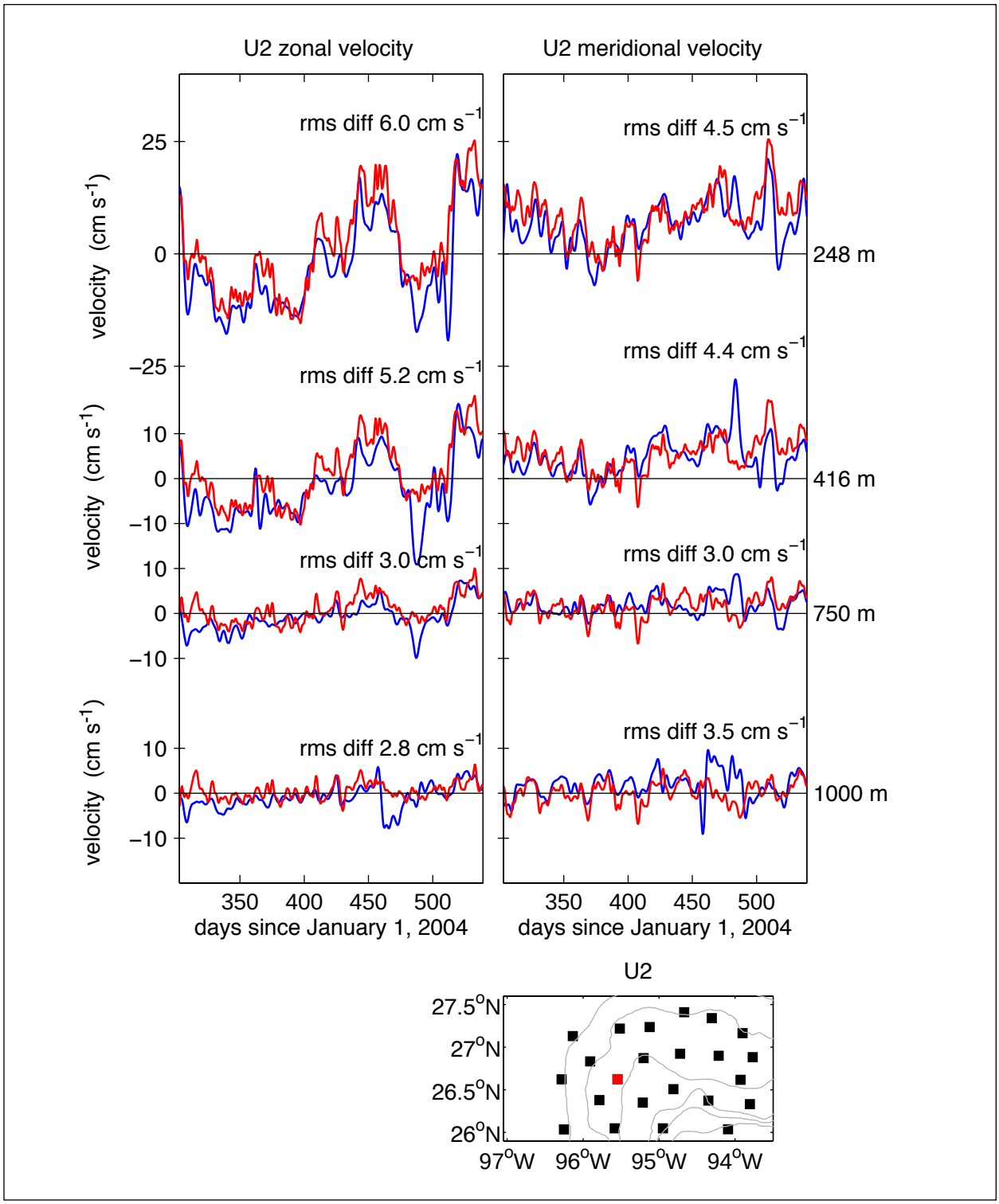

Figure 2.5-25. Comparison between the U2 mooring (blue) and PIES-derived (red) zonal (left) and meridional (right) velocities. The nominal depth and rms difference between PIES and the U2 mooring are noted to the right of each series. The bottom panel shows the location of the PIES (black) and pseudo-IES (black) and the U2 mooring (red). Bathymetry contoured every 500-m depth

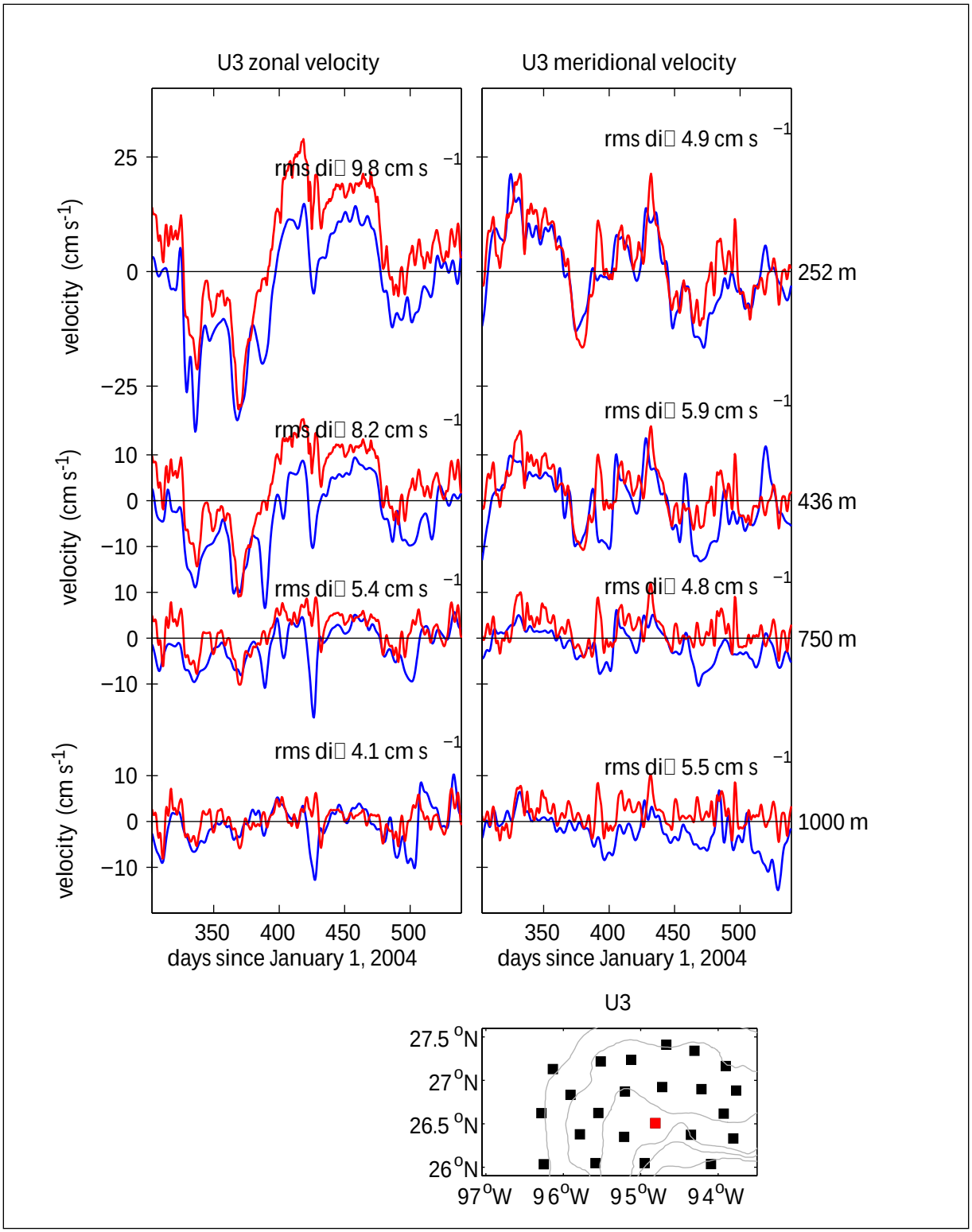

Figure 2.5-26. Comparison between the U3 mooring (blue) and PIES-derived (red) zonal (left) and meridional (right) velocities. The nominal depth and rms difference between PIES and the U3 mooring are noted to the right of each series. The bottom panel shows the location of the PIES (black) and pseudo-IES (black) and the U3 mooring (red). Bathymetry contoured every 500-m depth.

and the intrinsic difference between a point measurement and a mapped geostrophic estimate. The second column of Tables 2.5-2 indicates the rms in the GEM field. The third column gives the error in the GEM table look-up due to τ uncertainty of 0.001 which we determined as τ_error*dΦ/dτ (IES instrument error, column 3). The fourth column gives the total error which is the square root of the sum of the squares of columns two and three. Ageostrophic motion such as high vertical wavenumber inertial currents will not be reproduced in the maps of geostrophic velocity. Tables 2.5-2 and 2.5-3 explicitly account for these differences except for the contribution of ageostrophic motion which is hard to anticipate a priori and the error in mooring velocity due to uncertainty in sensor pressure because the relatively weak velocity shears. The observed rms differences are within the expected range and in fact are well below the predicted discrepancy. The predicted range is large, however, and merits further discussion.

Table 2.5-2

Predicted Error in Geopotential Anomaly, Φ, Referenced to1500 m at Four Nominal Depths

Nominal Depth [m]	**GEM rms [m^2sec^{-2}]**	**IES and pseudo-IES Instr. Error [m^2sec^{-2}]**	**Total Φ Error [m^2sec^{-2}]**
250	0.17	0.31	0.35
400	0.17	0.22	0.28
750	0.16	0.11	0.19
1000	0.12	0.05	0.12

Table 2.5-3

Predicted Differences Between Mooring and Mapped Geostrophic Velocities at Four Nominal Depths

Nominal Depth [m]	**Mapped Velocity Error [$m\ sec^{-1}$]**	**Map vs Point Difference [$m\ sec^{-1}$]**	**Predicted Difference [$m\ sec^{-1}$]**
250	13.5	6.0	14.8
400	10.9	4.0	11.6
750	7.4	2.2	7.7
1000	5.2	2.1	5.6

First, the errors in baroclinic shear estimates contributed the most to geostrophic velocity estimates. The error in geopotential anomaly referenced to 1500 dbar for four nominal depths are listed in Table 2.5-3. The table provides the predicted error in the geostrophic velocity at 26°N with nominal spacing of 50 km (column 2) and estimated difference between mapped geostrophic and point measurement with a 50 km Gaussian correlation length scale (column 3). The total predicted difference between the point measurement and the mapped geostrophic estimate is the square root of the sum of the squares of columns 2 and 3. Recall that the conversion of the moorings to pseudo inverted echo sounders doubled the τ_error in column 2.

The velocity error was determined by straightforward propagation of errors through the geostrophic equation assuming that the geopotential estimates at each instrument were independent of each other, (sqrt(2)*Φ_error)/(f*Δx), where Φ is geopotential anomaly and f is the Coriolis parameter. This error is not dependent on the magnitude of the horizontal density gradients but is dependent on the station spacing and latitude. Recall again that τ error from inverted echo sounders is half that arising from the conversion of the moorings to pseudo inverted echo sounders. An all-PIES array would have two-thirds the errors listed in column two of Table 2.5-3. Although not explicitly tabulated, current meter measurements are not without error either. The contemporary RCM-11, an acoustic current meter manufactured by Aanderaa, may have a bias of about 10 to 25 percent for speeds less than 15 cm s^{-1} and 2 cm s^{-1} for larger speeds (Hogg and Frye 2007).

The difference between point measurements and mapped estimates was determined by the optimal interpolation mapping error (Bretherton, 1976) assuming a 50-km correlation length scale and a signal to noise ratio of 0.0001 (no instrument error). Expressed as percent of the variance, this difference was 25%. This is not an indication of error in the geostrophic estimate but reflects the expected intrinsic difference between a point measurement and a mapped geostrophic estimate and depends solely upon the array resolution relative to the correlation scale.

In conclusion, the degree to which the point measurement (mooring) and the mapped estimate agree depends greatly upon the spacing between instruments in the array relative to the horizontal correlation-scales of the motion in addition to the instrument errors. The conversion of moored temperatures into pseudo-IES was a rational way to treat the data consistently throughout the array (and was quite essential given the large and fairly uncorrelated array spacing), but this array design did substantially increased uncertainties in mapped stream-functions and currents.

2.6 Remote Sensing

The remote sensing component of the NW Gulf Program acquired remotely sensed (satellite) data to aid in the interpretation of mesoscale features and physical data in the study area. A combination of satellite observing systems has been used.

To carry out this task, Colorado Center for Astrodynamics Research (CCAR) collected and processed a complementary suite of satellite observations from satellite altimeter and radiometer remote sensing data systems. This suite includes SSH data with high-resolution SST data and ocean-color imagery. Satellite altimetry provides the all-weather multi-satellite monitoring capability required to map mesoscale circulation variability in the GOM. During cloud-free conditions, multi-channel radiometry is used to supplement the altimetric sampling by providing high-resolution synoptic SST and ocean-color imagery to monitor the rapidly evolving eddy field in the western GOM and small-scale eddies in and around the study region.

2.6.1 Altimetry

Altimeter data used during the NW Gulf Program are the near real-time and archival data streams available from TOPEX/Poseidon (TOP/POS), ERS-2, Geosat Follow-on (GFO), Jason-1, and Envisat satellite missions. Processing of the SSH data is based on near real-time mesoscale analysis techniques designed to exploit the multi-satellite altimetric sampling (Leben et al., 2002). This method has been used to monitor operationally the GOM since November 1995. Altimeter data from a total of five satellites were available during the program interval. Basic information on each of the missions is given in Table 2.6-1. The groundtrack coverage provided by these satellites in the study region is shown in Figure 2.6-1.

Table 2.6-1

Satellite Altimeter Missions during NW Gulf Program

Satellite	Launch Date	Agency	Repeat Period (days)	Crosstrack Spacing	
				Degrees of Longitude	km*
TOPEX/Poseidon	10 Sep 1992	NASA/CNES	10	2.83	282
ERS-2	21 Apr 1995	ESA	35	0.72	71
Geosat Follow-On	10 Feb 1998	U. S. Navy	17	1.47	147
Jason-1	18 Dec 1999	NASA/CNES	10	2.83	285
Envisat	1 Mar 2002	ESA	35	0.72	71
					*at 26.5°N
Tandem/Interleaved Mission: 20 Sep 2000 to 6 Jan 2006.					
TOPEX/Poseidon/Jason-1 Interleaved			10	1.42	141

Note that during the NW Gulf Program, the TOP/POS and Jason-1 satellites were in tandem orbits with interleaved groundtracks. NASA/CNES scientists selected this configuration to improve the sampling of mesoscale ocean circulation by precision altimeters (Fu et al., 2003). The space/time sampling provided from the 10-day repeat orbit of the TOP/POS satellite, which was selected to map the ocean topography associated with large-scale variations in SSH, is not sufficient for monitoring mesoscale variability because of the large distance between neighboring ascending or descending tracks. In the GOM, this spacing is 2.83° of longitude or about 282 km at 26.5°N, which is also the distance between crossover points between ascending and descending tracks. Moving TOP/POS onto a parallel groundtrack that is midway between two adjacent groundtracks of the original TOP/POS orbit, which Jason-1 now occupies, reduced this distance by half to a crosstrack spacing of 141 km at 26.5°N. At latitudes midway between intra- and inter-satellite crossover points, the ascending/descending groundtrack sampling improves by another factor of two to a crosstrack spacing of just 72 km. Thus, the average crosstrack sampling from the tandem mission data alone is 70 to 140 km within the study region. The addition of GFO and ERS/Envisat data augments this spatial sampling but at irregular sampling times.

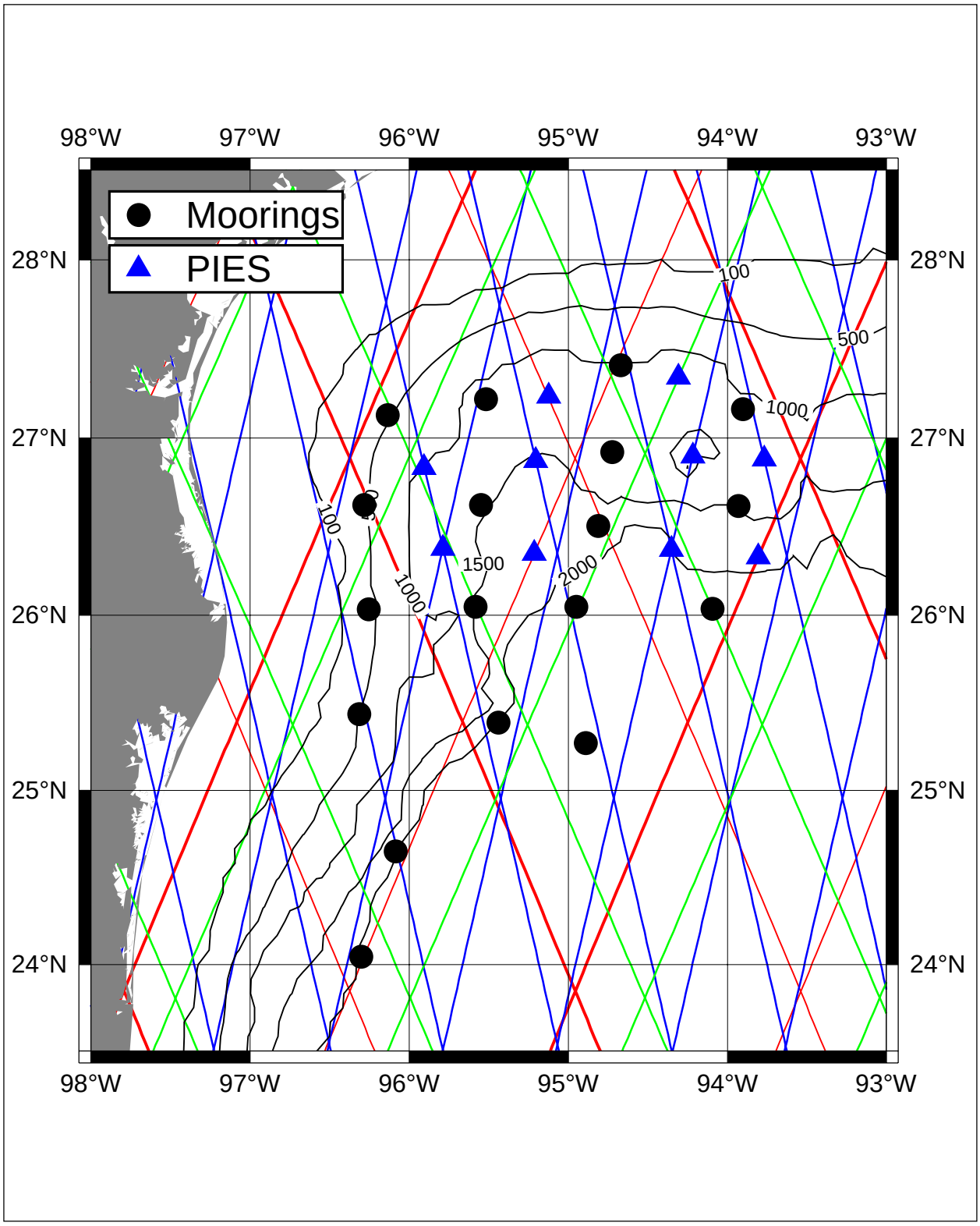

Figure 2.6-1. Satellite altimeter groundtrack coverage in study region. TOP/POS (thin red), Jason-1 (thick red), GFO (green), and ERS-2/Envisat (blue) are shown with a schematic of the instrument array.

Intuitively, sampling should improve by combining data from multiple altimeters. SSH fields produced by combining multi-mission altimetry, however, may not be better than those constructed from TOP/POS or Jason data alone if uniform errors and wavelength/frequency resolution satisfying the Nyquist criteria are required of the space/time gridded product as has been proposed by Greenslade et al. (1997). While these metrics may be reasonable for theoretical sampling studies or mission design, the constraints are too limiting for mesoscale mapping. Operational multiple satellite objective mapping of the mesoscale circulation must therefore rely on suboptimal smoothing to resolve eddy-scale wavelength albeit with the commensurate errors caused by non-uniform sampling and aliasing. This is true of both formal “optimal” interpolation and suboptimal objective analysis schemes. Nevertheless, the efficacy of the suboptimal interpolated fields can be evaluated by comparing the interpolated altimetry with coincident in situ data to quantitatively assess the processing and gridding strategies. PIES data are an ideal in-situ measurement type for these comparisons, and we selected instrument sites along altimeter groundtracks where it was possible to allow accurate assessment of not only the space/time gridded products, but the alongtrack data as well.

2.6.1.1 Alongtrack Altimeter Data

Alongtrack data were collected from the agencies providing archival altimeter geophysical data records (GDRs). The TOP/POS and Jason-1 data are from the Physical Oceanography Distributed Active Archive Center (PO.DAAC) at the Jet Propulsion Laboratory. ERS-2 and Envisat data are from the "Centre ERS d'Archivage et de Traitement" (CERSAT), the French Processing and Archiving Facility for ERS-1, ERS-2, and Envisat data. GFO data are from the NOAA/NESDIS Laboratory for Satellite Altimetry.

All of the altimeter data sets were processed in as consistent a fashion as possible to produce accurate analysis maps based on the blended altimetric observations. Standard corrections were applied to the alongtrack data including inverted barometer, electromagnetic bias, ionosphere, and wet/dry troposphere corrections. Ocean tides were removed using the tide model supplied on the GDRs for TOP/POS, Jason, and Envisat. GFO and ERS-2 ocean tides were removed using the tide solution derived from the CCAR tide model (Tierney et al., 1998). The alongtrack coverage provided by the altimeter satellites during the time period consistently covered the study area.

Each cycle of corrected 10-day repeat TOP/POS and Jason, 17-day repeat of GFO, and 35-day repeat of ERS-2 and Envisat data was linearly interpolated to reference groundtracks based on precision orbit determination ephemeredes for each satellite at one sample per second alongtrack spacing. The TOP/POS and Jason reference track used the computed groundtrack for TOP/POS cycle 18. The TOP/POS interleaved mission reference groundtrack was the same groundtrack with an offset in longitude corresponding to the nominal interleaved orbit. The ERS-2 and Envisat 35-day reference groundtracks are based on repeat cycle 6 of the ERS-1 Multidisciplinary 1 Mission. The GFO reference groundtrack is based on cycle 2 from the GEOSAT Exact Repeat Mission.

2.6.1.2 Mesoscale Analysis

The processing of the altimeter data is designed to retain mesoscale signals while filtering out longer wavelength altimetric errors. This filtering, however, also removes long wavelength oceanographic signals. A detailed description of this processing and its implementation and validation in the GOM can be found in Leben et al. (2002). The procedure incorporates data from all of the available satellites, treating each data set in a consistent fashion as follows:

1. All sub-satellite data are referenced to an independent gridded mean sea surface by subtracting the mean sea-surface value at the sub-satellite point from each observation.
2. Alongtrack loess filtering is used to remove residual orbit and environmental correction errors. The loess filter removes a running least squares fit of a tilt plus bias within a sliding window from the alongtrack data. The window width is approximately 15° of latitude (200, once-per-second alongtrack data points).
3. A multigrid preconditioned Cressman analysis with temporal weighing is used to objectively interpolate the alongtrack data to a 1/4° grid.
4. A model mean SSH field is added to the mapped SSH anomaly field to provide an estimate of the total SSH in the GOM.

2.6.1.3 Mean Reference Surface and Model Mean SSH

All alongtrack data are referenced to an existing altimetric mean sea surface. The data are treated as non-repeating groundtracks and are referenced directly to the mean sea surface by interpolating the mean sea-surface value to the sub-satellite point and subtracting it from the SSH. This applies an implicit crosstrack geoid gradient correction to the alongtrack data before interpolation to the reference groundtracks.

The GSFC00.1_MSS, which was computed by Y. M. Wang of Raytheon ITSS (Wang, 2001), was used as the reference surface. This mean sea surface is based on six years of TOP/POS data (Cycles 11 to 232), multiple years of ERS-1&2 35-day exact repeat data (ERS-1 Phase C: Cycles 1 to 18; Phase G: Cycles 1 to 13; ERS-2: Cycles 1 to 29), Geosat 17-day exact repeat data (Cycles 1 to 41), Geosat Geodetic Mission data, and both cycles of the ERS-1 168-day repeat data. All the altimeter data used to calculate the mean sea surface came from the GSFC's Altimeter Pathfinder products (Koblinsky et al., 1999).

To calculate the synthetic SSH estimates, we used the model mean SSH computed for the time period 1993 through 1999 from a data assimilation hindcast experiment performed by Drs. Lakshmi Kantha and Jei Choi for the MMS Deepwater Physical Oceanography Reanalysis and Synthesis Program (Nowlin et al., 2001). The data assimilation experiment used the University of Colorado-Princeton Ocean Model (CUPOM) and assimilated alongtrack TOPEX and ERS-1&2 SSH anomalies into CUPOM on a track-by-track basis as subsurface temperature anomalies (Kantha et al., 2005). Before adding the model mean to the gridded SSH anomaly fields, we averaged the 1993 through 1999 SSH anomaly fields and removed the residual anomalous altimetric mean over the time period. This references the SSH anomaly fields to a mean spanning the same time period as determined from the CUPOM hindcast data assimilation experiment. The anomalous altimetric mean reflects the difference between the mean circulation contained in

the GSFC mean sea surface and the 1993-1999 data assimilation mean. More discussion of these differences is found in Leben et al. (2002).

2.6.1.4 Objective Mapping

Daily analysis maps of height anomaly relative to the mean sea surface were estimated using an objective analysis (OA) procedure (Cressman, 1959) to interpolate the alongtrack data to a 1/4° spatial grid. The method uses an iterative difference-correction scheme to update an initial guess field and converge to a final gridded map. A multi-grid procedure provides the initial guess. Five iterations were used with radii of influences of 200, 175, 150, 125, and 100 km while employing a 100-km spatial decorrelation length scale in the isotropic Cressman weighting function. The data were weighted in time using a 12-day decorrelation time-scale relative to the analysis date using a ±10 day window for the TOP/POS and Jason data and a ±17 day window for the ERS-2, Envisat, and GFO data. Details of the space and time-weighted version of the multigrid preconditioned Cressman analysis is described next and is based on the space-weighting only technique described in Hendricks et al. (1996).

2.6.1.5 Objective Analysis Procedure

An OA procedure is used to interpolate the alongtrack SSH anomalies onto a regularly spaced 1/4° global grid. The OA algorithm is based on the iterative difference-correction scheme of Cressman (1959). The initial guess field for the Cressman algorithm is supplied by an efficient multigrid procedure.

A rough estimate of the 1/4° field is created by collecting the alongtrack SSH anomaly data into 1/4° grid cells. In grid cells where at least one SSH measurement is available, the average of all measurements within the cell is computed. Some of the grid cells may not contain data depending on the spacing of groundtracks. The OA procedure is designed to fill in these data gaps by creating a SSH anomaly field that is consistent with the alongtrack measurements.

The 1/4°-binned data can be used as an initial guess in the Cressman algorithm; however, having initial values in the empty grid cells can enhance the efficiency of the iteration procedure. A simple multigrid procedure is used to estimate values in cells where no altimeter measurements are available. Multigrid methods (Briggs, 1987) rapidly solve a set of equations by working at several grid resolutions. In this case, if the alongtrack data are binned into 1° or 2° grid cells, there would be fewer or even no empty ocean grid cells. Using a multigrid interpolation strategy to efficiently compute the means, a set of progressively coarser grids (1/2°, 1°, 2°, …) are created from the global 1/4° grid, and the average SSH is computed at all coarser grid resolutions in each cell containing data. The mean values are transferred back to the original 1/4° grid from the finest-scale grid containing a mean value coincident with that location. Finally, a fast red-black smoothing operator (e.g., see Press et al., 1992) is used on the 1/4° initial guess field to smooth high-frequency noise introduced by the multigrid interpolation.

Cressman objective analysis uses an iterative-difference-corrections scheme in which a new estimate of the SSH value for a given grid cell is equal to the sum of the previously estimated SSH at that location and a correction term. The correction term is forced by the difference

between the estimated heights and the original data values over all grid cells within a specified radius of influence. A weight based on the number of original measurements within a grid cell is included in the correction term, as is a weight based on the distance of a grid cell from the point being updated.

The *n*th iteration for the SSH at grid cell *i* is computed using:

$$h_i^n = h_i^{n-1} + \frac{\sum w_m n_m^* \left(h_m^* - h_m^{n-1}\right)}{\sum w_m n_m^*}, \qquad (1)$$

where the sums are taken over all *m* grid cells within the specified radius of influence *R* from the grid cell *i* being updated. The variables in (Eq. 1) are defined as:

h_i^n the *n*th iteration of SSH at grid cell *i*;

h_i^{n-1} the *(n-1)*th iteration of SSH at grid cell *i*;

h_m^* the average height at grid cell *m* based on the original data;

h_m^{n-1} the *(n-1)*th iteration of SSH at grid cell *m*.

n_m^* the number of original measurements within grid cell *m*.

The weights in the correction term are defined by:

$$w_m = \exp(-a r_m^2 / R^2) \text{ for } r \le R;$$
$$w_m = 0 \quad \text{for } r > R;$$

where r_m is the distance between grid cell *m* and the grid cell being updated and *R* is the maximum radius of influence. The parameter *a* is an adjustable weighting factor that scales the exponential spatial weighting of the data.

To incorporate weighting of the data in time, the data and the number of original measurements within a grid cell are each scaled by the weighting function:

$$w_t = \exp(-b \Delta t_m^2 / T^2) \text{ for } \Delta t \le T;$$
$$w_t = 0 \quad \text{for } \Delta t > T;$$

where Δt_m is the difference between the measurement time and the time corresponding to the analyzed field. The parameter *b* is the time weighting factor and *T* is the maximum time window of influence.

The empirical weighting parameters, *a* and *b*, are selected to map the mesoscale structure within the limitation of the scales resolvable by the crosstrack altimeter sampling. The mesoscale

analysis uses a = 4 and b = 2, which correspond to decorrelation space and time scales of 100 km and 12 days, respectively, for R = 200 km and T = 17 days. The maximum radius of influence, R, is decreased between the Cressman iterations to allow smaller scales to converge more quickly and to increase resolution when alongtrack sampling is available. For this study, R is decreased from 200 to 100 km over five iterations giving a decorrelation length scale of 50 km on the final Cressman iteration.

2.6.2 Ocean Color Imagery

Daily ocean color imagery was downloaded from the OceanColor group web and ftp sites (http://oceancolor.gsfc.nasa.gov/) at the NASA Goddard Space Flight Center (GSFC). These images are a 9-km resolution blended product incorporating data from the Sea-viewing Wide Field-of-view Sensor (SeaWiFS) satellite and the Moderate Resolution Imaging Spectroradiometer (MODIS) instrument onboard the Aqua satellite. The empirical chlorophyll algorithms OC4v4 and OC3M (O'Reilly et al., 1998) are used with measured radiances from SeaWiFS and MODIS, respectively, to calculate the individual chlorophyll fields from each satellite image. Both SeaWiFS and MODIS data are Level-3 processed before being merged. This processing involves the spatial and temporal binning of Level-2 data into 4 and 9-km equi-rectangular projections and is described in detail in Hooker et al. (1995). Combining the data from the two missions increases the coverage over a single mission product on average by over 50% for the daily product and by over 20% for the 8-day composite product. A variety of multi-day composites were made to help with the detection and tracking of oceanographic features in and around the study region. GSFC MODIS Level-2 ocean-color imagery at 2-km resolution was also downloaded and used for some of the higher resolution analyses in this report.

2.6.3 SST Imagery

SST products were acquired for remote sensing and data synthesis activities. We used Advanced Very High Resolution Radiometer (AVHRR) imagery from the Johns Hopkins University/Applied Physics Laboratory (JHU/APL) Ocean Remote Sensing Group. Three-day warmest pixel composite images in Portable Network Graphics (PNG) format were downloaded from the JHU/APL Ocean Remote Sensing Group website. These images have 1-km resolution with image values (0-255) corresponding to the rounded integer SST values. The full precision values before rounding were calculated by the multi-channel algorithm used in the TerraScan software that converts raw antenna brightness temperatures to SST values in the APL ground station. Although the rounding limits the accuracy to only 0.5°C, which is less than required for most scientific work, the capability to detect spatial features was not compromised, and the data were sufficiently accurate for data synthesis activities. The images collected for the NW Gulf Program were once-per-day 3-day composite images from 1 Jan 2004 through 31 Dec 2005.

2.7 PIES/Altimetry Evaluation and Comparison

PIES and satellite altimetry are complementary data types. Although the two measurement systems measure completely different physical quantities, they both yield an estimate of the height of the ocean surface relative to some datum, which is commonly referred to as SSH (SSH).

In this section, we evaluate the altimeter SSH measurement system using PIES data as a benchmark for theoretical analyses and for comparison of PIES SSH directly to the coincident altimeter-derived SSH collected during the NW Gulf study program. This is the second opportunity for these types of analyses and comparisons in the GOM. The first was reported for the central GOM in the Exploratory Study technical report (Donohue et al., 2006). Some of the statistics prepared for that report will be presented again here and discussed in light of the results obtained in NW Gulf. These types of analyses and comparisons have the potential to identify problems in current data sets and to develop and test improvements in the altimeter data processing techniques used to produce future data products. This will facilitate the synthesis of altimetry data and PIES data from current and future arrays deployed in the deepwater GOM, which will improve observing and understanding of deepwater circulation patterns and dynamics throughout the water column.

2.7.1 Altimetric Sampling and Aliasing

Satellite altimeters provide discrete SSH measurements at sub-satellite points spaced approximately 5–7 km along groundtracks that repeat every 10, 17, or 35 days for the satellites used during the study program (Table 2.7-1). Orbital dynamics determine the space/time sampling pattern achieved on orbit, and there is a trade-off between spatial and temporal resolution when selecting an orbit during the mission design phase of a satellite program. As an example, see the discussion of the TOP/POS mission in Parke et al. (1987). For single satellite sampling, high spatial resolution using a nadir pointing altimeter is achieved only at the expense of less frequent sampling of the sea surface in time, and vice versa.

Unlike ground-based instruments where the sampling rate can be selected to satisfy a specific Nyquist criterion, satellite-based measurement systems in non-geosynchronous orbits have a temporal sampling rate imposed by the period at which a point on the Earth's surface is sampled from orbit. To increase the temporal sampling rate for a nadir pointing altimeter, therefore, requires either the addition of more satellites in the same orbit or a shorter repeat period resulting in a loss of spatial sampling density. Neither option can usually be justified from an economic, scientific, or operational perspective. Anecdotally, when additional sampling became available from TOP/POS after the commissioning phase of the TOP/POS and Jason-1 tandem mission, the decision made was to increase the spatial sampling density (Fu et al., 2003) and, by default, accept the existing level of temporal aliasing of the 10-day repeat sampling. A number of studies have addressed spatial/temporal aliasing issues (Schlax and Chelton, 1994; Parke et al., 1998) including assessment of the aliasing of well known periodic signals such as tides; however, few studies have assessed the SSH variance associated with the aliased signal from under-sampled SSH ocean measurements.

The temporal aliasing of ocean signals by satellite altimeter sampling can be addressed using the high-rate in situ SSH data provided by PIES measurements. Hendry et al. (2002) performed the first study along these lines using PIES data collected within the North Atlantic Current in the Newfoundland Basin. They found that the time scales of motion observed in the region are such that 86-95% of the subinertial period SSH variability was not aliased by the approximately 10-day TOP/POS repeat period sampling. Gille and Hughes (2001) performed an earlier study of

sampling using only bottom-pressure records; however, that type of study would not be appropriate in the GOM where the time scales associated with the bottom-pressure variability are not representative of the time scales of the SSH variability.

Table 2.7-1

Satellite Altimeter Mission Exact-Repeat Periods and Periods Associated with the Nyquist Sampling Frequency

Satellite	Approximate Repeat	Repeat Period (days)	Nyquist Sampling Period (days)
TOPEX/Poseidon	10-day	9.9156	19.8313
ERS-2	35-day	35	70
Geosat Follow-On	17-day	17.0505	34.1010
Jason-1	10-day	9.9156	19.8313
Envisat	35-day	35	70

Following the methodology of Hendry et al. (2002), we made an assessment of the SSH signal in the Exploratory Study region in the central Gulf (Donohue et al., 2006) and now report here the results for the NW Gulf Study region. These results were determined for the approximately 10-day, 17-day, and 35-day repeat period sampling available from the ongoing satellite altimeter missions. We computed power spectra for each of the SSH time series, barotropic, baroclinic, and combined, and calculated the percentage of cumulative power in the spectra up to each of the Nyquist frequencies associated with the 10-day, 17-day, and 35-day repeat sampling periods. The periods corresponding to the Nyquist frequency for each of the altimeter satellites are tabulated in Table 2.7-1. Figures 2.7-1, 2.7-2, and 2.7-3 show maps of the unaliased variance associated with 10-day, 17-day, and 35-day repeat sampling periods in the study region for the current altimeter missions from the barotropic, baroclinic, and combined SSH signals, respectively. NW Gulf summary statistics are tabulated in Table 2.7-2 along with the statistics from the Exploratory Program PIES array. Tabulated values for each of the NW Gulf PIES stations are listed in Table 2.7-3**.**

The aliasing of the barotropic SSH signal is the most severe because of the shorter time scales associated with that signal in the GOM. The mean value over the NW Gulf array of 10-day sampling period unaliased variance was 62%, only slightly better than the 59% estimated for the Exploratory Program array. The individual station results ranged from a minimum of 56% at PIES 8 to a maximum of 72% at PIES 3, which was smaller than the 44% to 77% range found for the Exploratory program. With 35-day sampling, the mean value decreased to 37% and ranged from a minimum of 36% at PIES 2 to a maximum of 47% at PIES 7. The mean value, 37%, was the same in the Exploratory Program, and the Exploratory Program range, 29% to 45%, was once again larger than the range in the NW Gulf.

In the NW Gulf, the barotropic signal on the upper continental slope exhibited less aliasing than the signal on the lower slope. The spatial structure of the region of less aliased signal, shifts from

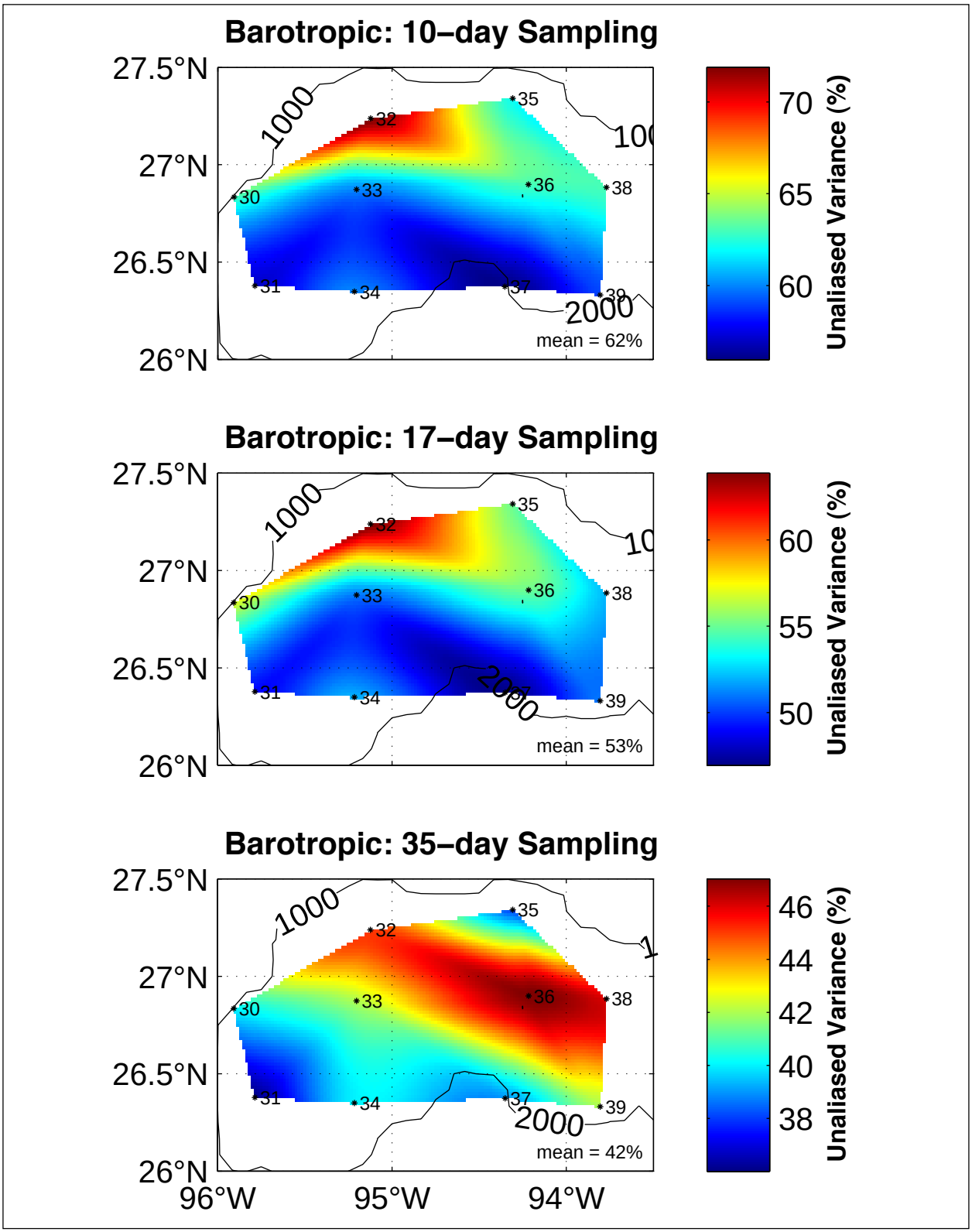

Figure 2.7-1. Maps of PIES barotropic unaliased variance for 10-day, 17-day, and 35-day sampling.

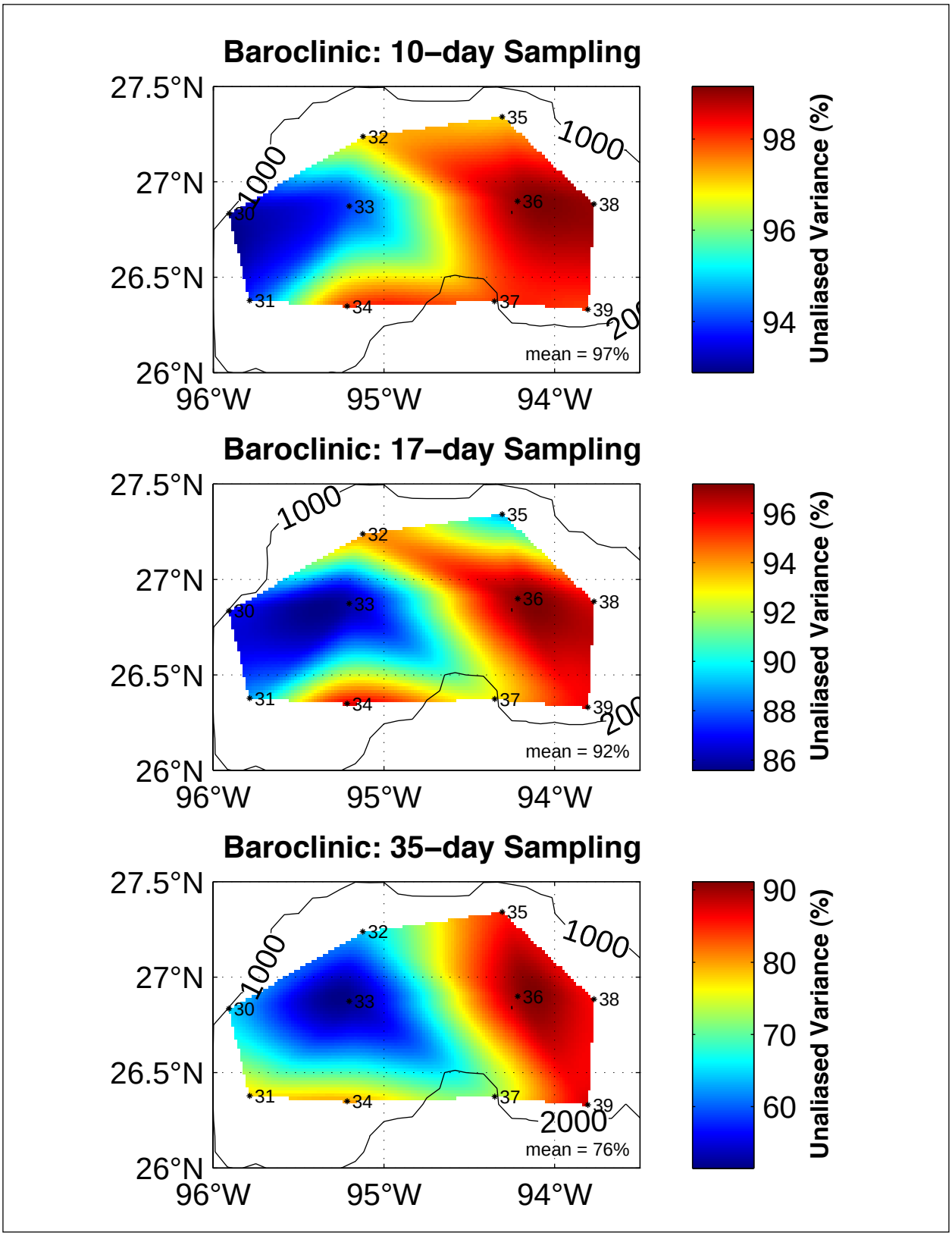

Figure 2.7-2. Maps of PIES baroclinic unaliased variance for 10-day, 17-day, and 35-day sampling.

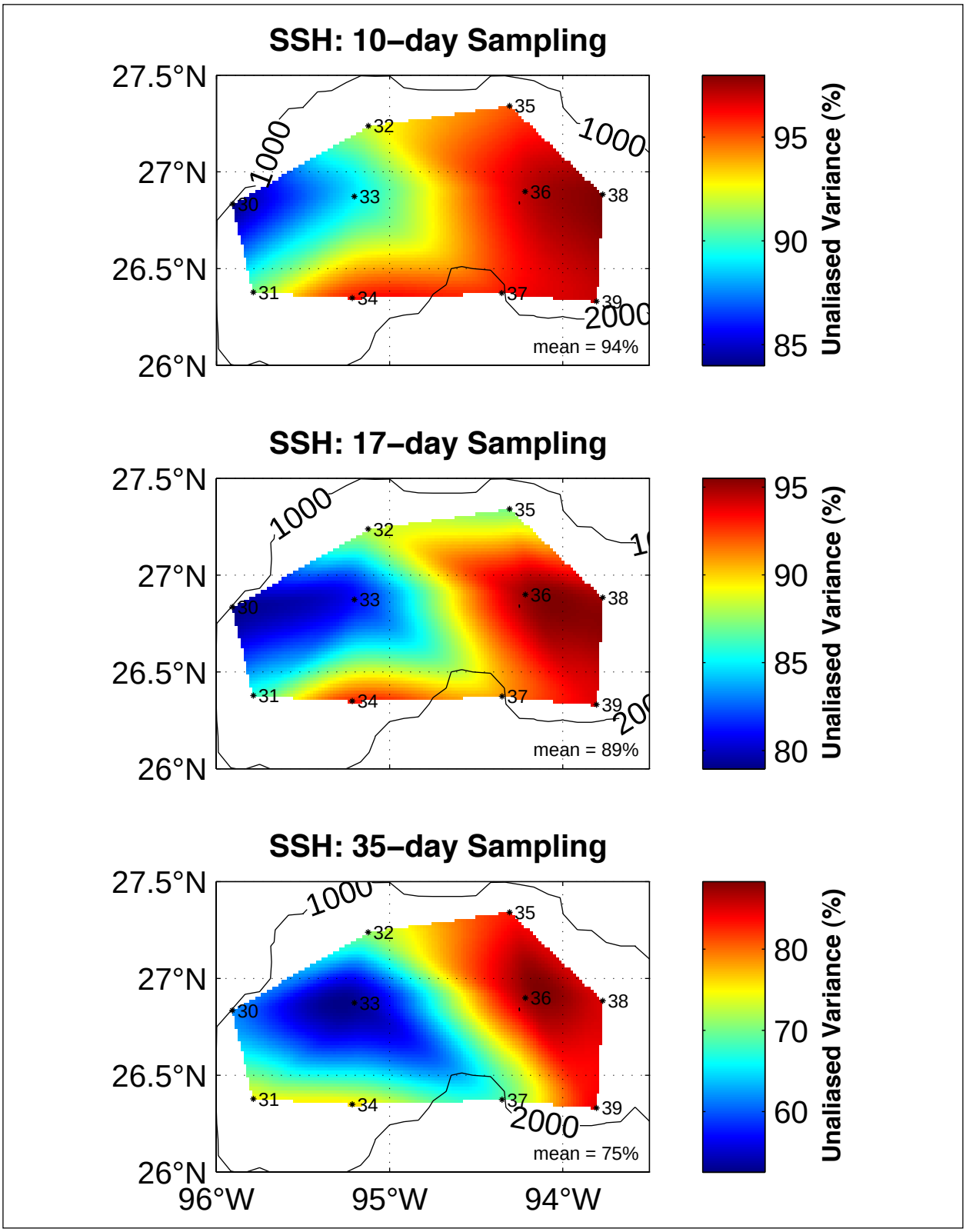

Figure 2.7-3. Maps of PIES SSH unaliased variance for 10-day, 17-day, and 35-day sampling.

Table 2.7-2

Unaliased Variance Statistics for 10-Day, 17-Day, and 35-Day Exact Repeat Sampling of the PIES Barotropic, Baroclinic, and Combined SSH Signals

Stations	Barotropic Signal Mean (%)			Baroclinic Signal Mean (%)			Total SSH Signal Mean (%)		
Repeat:	**10-day**	**17-day**	**35-day**	**10-day**	**17-day**	**35-day**	**10-day**	**17-day**	**35-day**
NW Gulf Program									
all stations	62	53	42	97	92	76	94	89	75
Exploratory Program									
all stations	59	47	37	97	93	78	95	92	78
above escarpment	56	45	39	96	93	75	94	91	75
below escarpment	61	49	36	97	93	80	96	93	79
Stations	**Barotropic Signal Maximum (%)**			**Baroclinic Signal Maximum (%)**			**Total SSH Signal Maximum (%)**		
Repeat:	**10-day**	**17-day**	**35-day**	**10-day**	**17-day**	**35-day**	**10-day**	**17-day**	**35-day**
NW Gulf Program									
all stations	72	64	47	99	97	90	98	95	87
Exploratory Program									
all stations	77	60	45	99	98	93	99	98	93
above escarpment	60	50	42	99	98	90	97	96	90
below escarpment	77	60	45	99	98	93	99	98	93
Stations	**Barotropic Signal Minimum (%)**			**Baroclinic Signal Minimum (%)**			**Total SSH Signal Minimum (%)**		
Repeat:	**10-day**	**17-day**	**35-day**	**10-day**	**17-day**	**35-day**	**10-day**	**17-day**	**35-day**
NW Gulf Program									
all stations	56	47	36	93	86	52	84	79	53
Exploratory Program									
all stations	44	38	29	92	86	54	87	82	54
above escarpment	51	42	36	92	86	54	87	82	54
below escarpment	44	38	29	93	87	56	92	85	56

Table 2.7-3

PIES SSH, Baroclinic, and Barotropic Statistics and Percent of Unaliased Variance Measured by Satellites In 10-Day, 17-Day, and 35-Day Exact Repeat Orbits (The time series' length, standard deviation (Std), and half-power period ($T_{0.5}$) are also shown.)

PIES	Signal	Length (days)	Std (cm)	$T_{0.5}$ (days)	Unaliased Variance (%) 10-day	17-day	35-day
1	SSH	285	5.9	79	84	79	62
	Baroclinic		4.7	85	93	87	65
	Barotropic		2.9	23	63	57	40
2	SSH	285	8.4	128	91	86	75
	Baroclinic		7.8	158	94	89	78
	Barotropic		2.6	14	57	49	36
3	SSH	285	6.6	108	92	88	71
	Baroclinic		7.9	85	97	94	64
	Barotropic		2.5	47	72	64	45
4	SSH	285	6.3	66	89	81	53
	Baroclinic		6.1	66	94	86	52
	Barotropic		2.4	17	60	51	42
5	SSH	285	9.7	146	96	93	76
	Baroclinic		9.1	228	98	96	80
	Barotropic		2.5	18	60	52	40
6	SSH	285	9.4	146	95	87	83
	Baroclinic		9.1	146	97	89	85
	Barotropic		2.6	20	62	55	38
7	SSH	285	12.2	186	97	95	87
	Baroclinic		12.6	186	99	97	90
	Barotropic		2.5	23	63	55	47
8	SSH	285	10.7	102	96	91	69
	Baroclinic		10.9	102	98	93	73
	Barotropic		2.5	14	56	47	39
9	SSH	285	15.5	228	98	95	85
	Baroclinic		16.0	205	99	96	86
	Barotropic		2.5	22	63	52	46
10	SSH	285	14.7	293	97	94	85
	Baroclinic		14.6	293	98	96	88
	Barotropic		2.5	15	59	51	42

the middle of the array to the east and further down the slope when going from a 10-day or 17-day sampling period to 35-day sampling. Significant changes in the aliased-signal spatial structure over the Exploratory program array were also observed as the sampling period was increased from 10 days or 17 days to 35 days. These changes were presumably associated with aliasing of the TRW signal in the 34 to 70 day period band that was observed in the central Gulf; that frequency band is only aliased by the 35-day sampling period. Energetic TRWs in the western Gulf are confined primarily to the base of the continental slope, suggesting that the greater aliasing observed at deeper stations, like PIES 8, may be associated with that signal. The generally low mean values for all of the altimetric sampling frequencies in both the NW and central Gulf are attributable to the aliasing of the frequencies associated with the 6-day barotropic oceanic response to an atmospheric Rossby-Haurwitz wave (Park and Watts, 2006) and the 14-day to 16-day Gulf-wide common mode.

The unaliased variance of the baroclinic and total SSH signal is much higher than the barotropic-only case because of the longer-period baroclinic signals and the dominance of the more energetic baroclinic component on the total SSH. Still, there are large differences between the 10-day and 35-day patterns, while the 10-day and 17-day patterns are more similar. For a 10-day sampling period of the baroclinic signal in the NW Gulf, the unaliased-variance mean value over the array was 97% and ranged from a minimum of 93% at PIES 1 to a maximum of 99% at PIES 7 and 9. The 35-day sampling mean value decreased to 76% and ranged from a minimum of 52% at PIES 4 to a maximum of 90% at PIES 7. The total combined baroclinic and barotropic SSH signal shows similar patterns. The SSH 10-day period unaliased-variance mean value over the array was 94% and ranged from a minimum of 84% at PIES 1 to a maximum of 98% at PIES 9. The 35-day sampling mean value decreased to 75% and ranged from a minimum of 53% at PIES 4 to a maximum of 87% at PIES 7. These results were remarkably similar to the analysis of the Exploratory PIES, further confirming how similar the baroclinic signals are in the two regions at least during these two observational intervals.

In summary, 84% to 98% and 87% to 99% of the subinertial-period SSH variability in the NW Gulf and Exploratory Study regions, respectively, are unaliased by the TOP/POS 10-day repeat period sampling. This is comparable to the 86% to 95% estimated from the Newfoundland Basin array by Hendry et al. (2002). The results for the 17-day and 35-day repeat sampling show, however, that there can be significant aliasing of GOM SSH signals in satellite altimetry even with the dominance of the longer period baroclinic signals associated with the LC and LCEs in the GOM deepwater. The degree to which this affects the space/time interpolated maps of altimetric SSH needs to be investigated in more detail. It is also unclear whether the weak surface signature of TRWs can be mapped effectively using satellite altimetry given the presence of the strong baroclinic SSH and the difficulties associated with aliasing of the barotropic signal. Also, the presence of the ubiquitous common mode needs to be considered when processing SSH. In most cases, this signal will be removed by standard altimetric processing techniques and the aliasing mitigated. However, the signal may be retained as more sophisticated processing and higher frequency corrections are applied to the data.

2.7.2 Signal-to-Noise

A useful metric for assessing the accuracy of altimeter-derived estimates of SSH is the ratio of the unaliased variance to the aliased variance of the SSH signal, which is an estimate of the signal-to-noise ratio (SNR) of a perfect on-orbit measurement system. This is also a function of the repeat sampling period of the satellite altimeter as can be seen in Figure 2.7-4. Note that we do not consider the barotropic and baroclinic components separately because they cannot be distinguished from on-orbit measurements alone. Also, the "noise" in the unaliased to aliased SNR is colored noise associated with undersampled geophysical signals that are very difficult to remove without excessive smoothing or filtering of the alongtrack data before interpolation. This is the primary reason that the requirement of uniform errors and wavelength/frequency resolution satisfying the Nyquist criteria as proposed by Greenslade et al. (1997) for gridded altimeter products is unrealistic in practice.

Table 2.7-4 shows a summary of the SNR statistics estimated from the NW Gulf and Exploratory PIES data. The SNR in both study regions is very good for 10-day and 17-day altimetric sampling. The 35-day sampling is more problematic. The 35-day sampling spatial map (Figure 2.7-4 lowest panel) shows SNR ratios in the low single digits over much of the NW Gulf array, which would make it difficult to distinguish between signal and aliased signals at that sampling frequency from a single point measurement. Similar low SNR regions were found in the central GOM. Quantifying the SNR for combined sampling by multiple altimeters will be reported in future work.

Table 2.7-4

Signal-to-Noise Ratio (SNR) Statistics for 10-Day, 17-Day, and 35-Day Exact Repeat Sampling of the PIES Barotropic, Baroclinic and Combined SSH Signals

Stations	**Mean SNR**			**Minimum SNR**			**Maximum SNR**		
Repeat:	**10-day**	**17-day**	**35-day**	**10-day**	**17-day**	**35-day**	**10-day**	**17-day**	**35-day**
NW Gulf Program									
all stations	22	11	4	5	4	1	49	19	7
Exploratory Program									
all stations	28	16	5	7	5	1	99	49	13
above escarpment	20	13	4	7	5	1	32	24	9
below escarpment	33	19	5	12	6	1	99	49	13

2.7.3 SSH Time Scales

Following the methodology of Hendry et al. (2002), the period corresponding to the frequency at which the cumulative power spectrum reaches 50% of the total variance – the half-power period, $T_{0.5}$ – was determined from the spectral analysis of each of the PIES SSH anomaly time series. $T_{0.5}$ is a more robust measure of time scale than the temporal autocorrelation zero crossing, T_0, and is the preferred scale to be used to define the effective degrees of freedom of a time series (Fofonoff and Hendry, 1985). This robustness is due, in large part, to the global and integral nature of the $T_{0.5}$ metric, which is less sensitive to competing time scales within the time series.

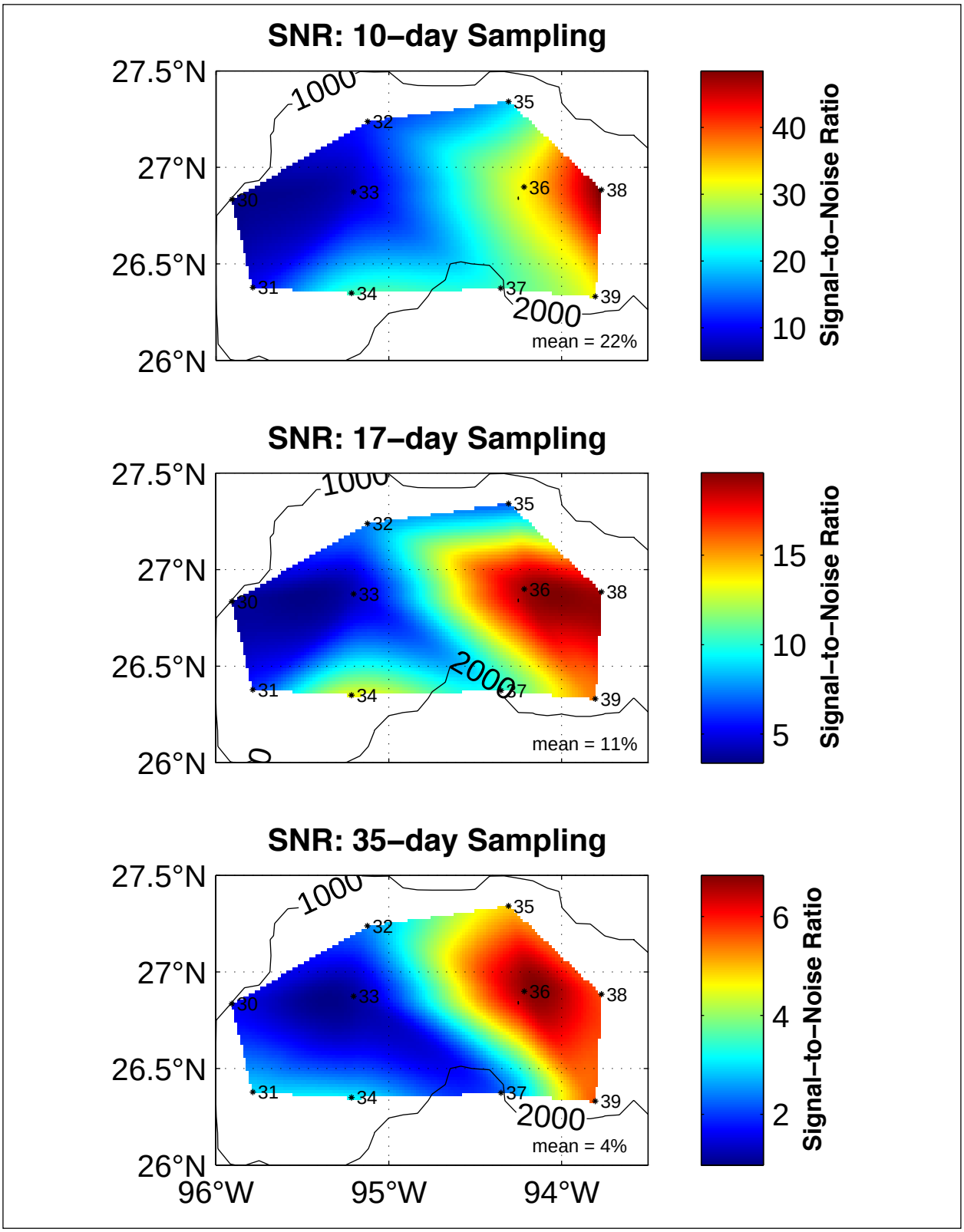

Figure 2.7-4. Maps of PIES SSH signal-to-noise ratio (SNR) for 10-day, 17-day, and 35-day sampling. SNR is estimated from the ratio of unaliased to aliased variance.

In contrast, the calculation of T_0 is a less robust measure because the first zero crossing of the temporal autocorrelation function is quite sensitive to the presence of multiple time scales and/or secular trends in the time series.

The half-power periods were computed from the 280-day NW Gulf and 1-year Exploratory PIES barotropic, baroclinic, and SSH anomaly time series. We did not detrend the time series before calculating the spectra because of the relatively short duration of the records. This allows estimation of the longer time scales of variability associated with the LC and LCEs that occur in most of the records. Spatial maps of $T_{0.5}$ for each of the three signals are shown in Figure 2.7-5. Mean $T_{0.5}$ values are listed in Table 2.7-5 for each program showing the average time scales for each of the signals at all PIES stations. The Exploratory Program averages for stations above and below the Sigsbee Escarpment are also shown.

The mean half-power periods of the barotropic signals are quite similar between the two regions and are dominated by the Gulf-wide common mode. The spatial distributions, however, are notably different. In the NW Gulf, the longer period barotropic signals are on the upper slope with a maximum at PIES 3. This is in contrast to the central Gulf where the longer period signals were in the south-central part of the array below the Sigsbee Escarpment.

The time scales of the baroclinic and combined barotropic and baroclinic SSH anomaly signals are similar because of the small contribution by the barotropic mode to the total signal. The long half-power periods associated with these signals show the dominance of the low-frequency LC and LCE variability observed in both regions during the observational records. In the NW Gulf, these longer periods, 150 days and greater, are confined to the eastern and southern boundaries of the array and associated with the passage of LCE Ulysses/U2. Regions with the shortest half-power periods, less than 150 days, are found over much of the NW Gulf array. The higher frequency signals associated with these shorter periods likely arise from the SSH variability generated by eddies over the continental slope and by frontal or companion eddies around the periphery of LCE Ulysses/U2.

Table 2.7-5

Half-Power Period of PIES Barotropic, Baroclinic, and Total SSH Signals

	Barotropic Signal Half-Power Period (days)			**Baroclinic Signal Half-Power Period (days)**			**Total SSH Signal Half-Power Period (days)**		
Stations	**mean**	**max**	**min**	**mean**	**max**	**min**	**mean**	**max**	**min**
NW Gulf Program									
all stations	21	47	14	155	293	66	148	293	66
Exploratory Program									
all stations	19	34	12	230	34	12	232	512	60
above escarpment	16	18	14	188	18	14	195	341	64
below escarpment	21	34	12	262	34	12	260	512	60

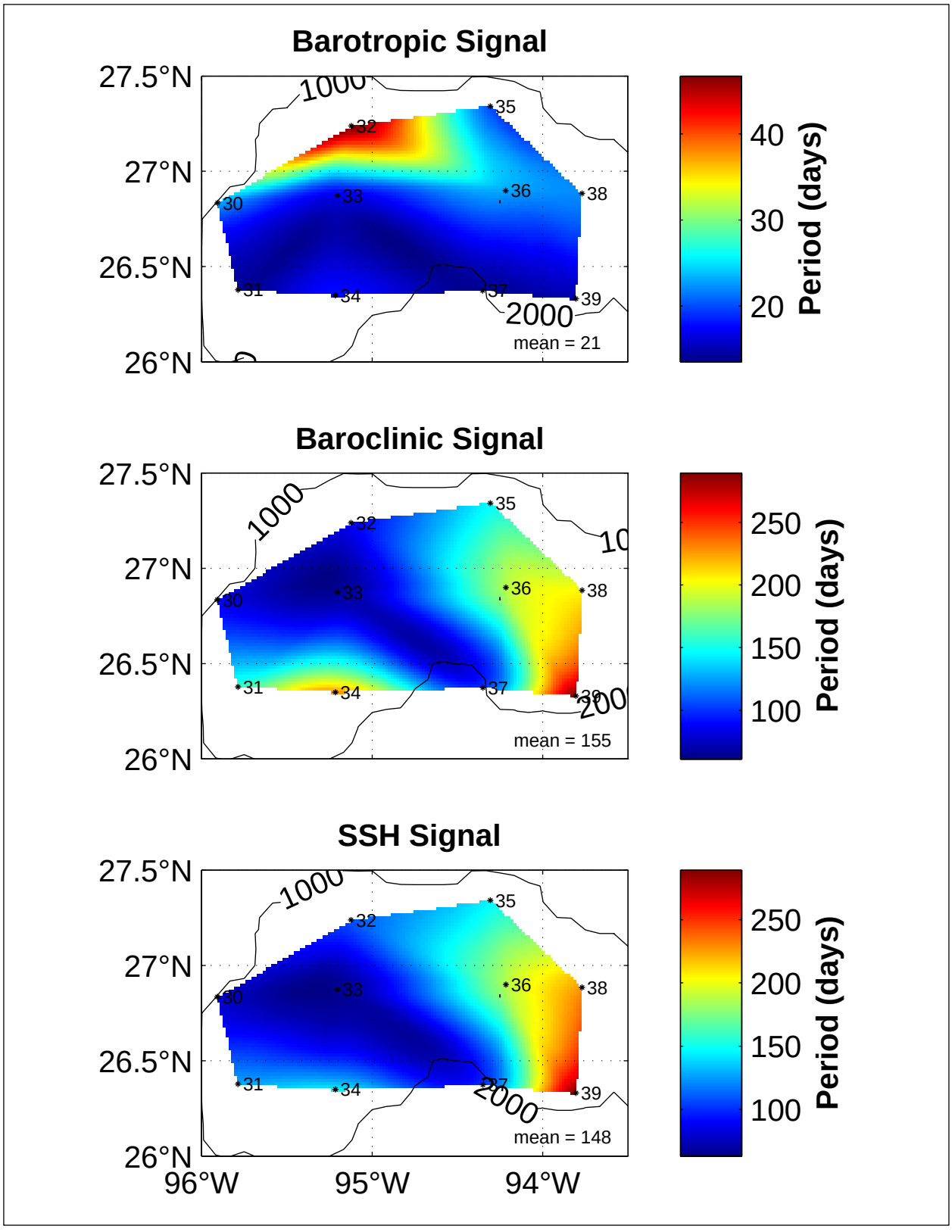

Figure 2.7-5. Spatial maps of the half-power period, $T_{0.5}$, computed from the PIES barotropic, baroclinic, and combined SSH anomaly time series with means over all stations.

2.7.4 Comparison of CCAR Mesoscale and PIES SSH

The CCAR mesoscale SSH gridded altimeter data product that was distributed and used for data synthesis activities in this report was evaluated by comparison with the coincident PIES SSH time series at each of the PIES stations in the NW Gulf array. A spatial map of the CCAR/PIES correlation is shown in Figure 2.7-6. The nearest 1/4° grid point from the CCAR product was used to calculate the temporal correlation coefficient. The overall mean correlation for the NW Gulf program data sets is 76%, which is slightly lower than the Exploratory program mean value of 82% in the central GOM. Lowest correlations are in the northwestern corner of the NW Gulf study array. The correlations are highest along the eastern and southern margins of the array where LCE influences were more pronounced during the measurement time period.

Taking advantage of the placement of PIES on satellite groundtracks (Figure 2.6-1), we compared the alongtrack detrended SSH anomaly data from each altimeter to the coincident PIES SSH data collected on collocated groundtrack points. Scatterplots and correlation coefficients for the altimeter and PIES measurements are shown in Figure 2.7-7 for each of the five satellites that were operational during the study program. The correlations are 81% (Envisat), 73% (ERS-2), 78% (GFO), 86% (Jason), and 63% (TOP/POS). With the exception of GFO, these correlations are slightly better than the values in central Gulf during the Exploratory program, which are 79% (Envisat), 72% (ERS-2), 81% (GFO), 77% (Jason), and 56% (TOP/POS). As were noted in the Exploratory report (Donohue et al., 2006), these values are very sensitive to the alongtrack smoothing/gridding employed to interpolate the raw sub-satellite measurement points to a reference groundtrack. The CCAR alongtrack gridding technique does not smooth the raw alongtrack data and uses linear interpolation between sub-satellite points. This method was consistently applied to produce all of the alongtrack data for each satellite. The Cressman objective analysis that was used to interpolate the alongtrack data to a regular space/time grid, however, does apply some filtering/smoothing to the data, which is why the gridded product correlations with the PIES SSH time series can, in some cases. be higher than the alongtrack correlations. The low correlation found between the TOP/POS alongtrack and PIES SSH data may be residual geoid error caused by referencing the alongtrack data to the GSFC mean sea surface. This mean surface predates the Tandem Mission so no SSH data along the TOP/POS interleaved groundtrack was used in the estimation of the mean. Updated mean sea surfaces that include TOP/POS Tandem Mission data in the estimation procedure are now becoming available. When one of these updated mean sea surfaces is incorporated into the CCAR data processing system an improvement in the TOP/POS correlation with the PIES should be observed. Thus, the Exploratory and NW Gulf program PIES data can help to improve satellite altimeter data processing and to evaluate the performance of the satellite-based observing systems.

Our ongoing work is directed toward improving the CCAR SSH product by using optimal interpolation techniques and space/time correlation functions tuned to the SSH variability in the GOM. The ultimate goal is to combine altimeter and PIES SSH in a single data product exploiting the full sampling capabilities of both systems.

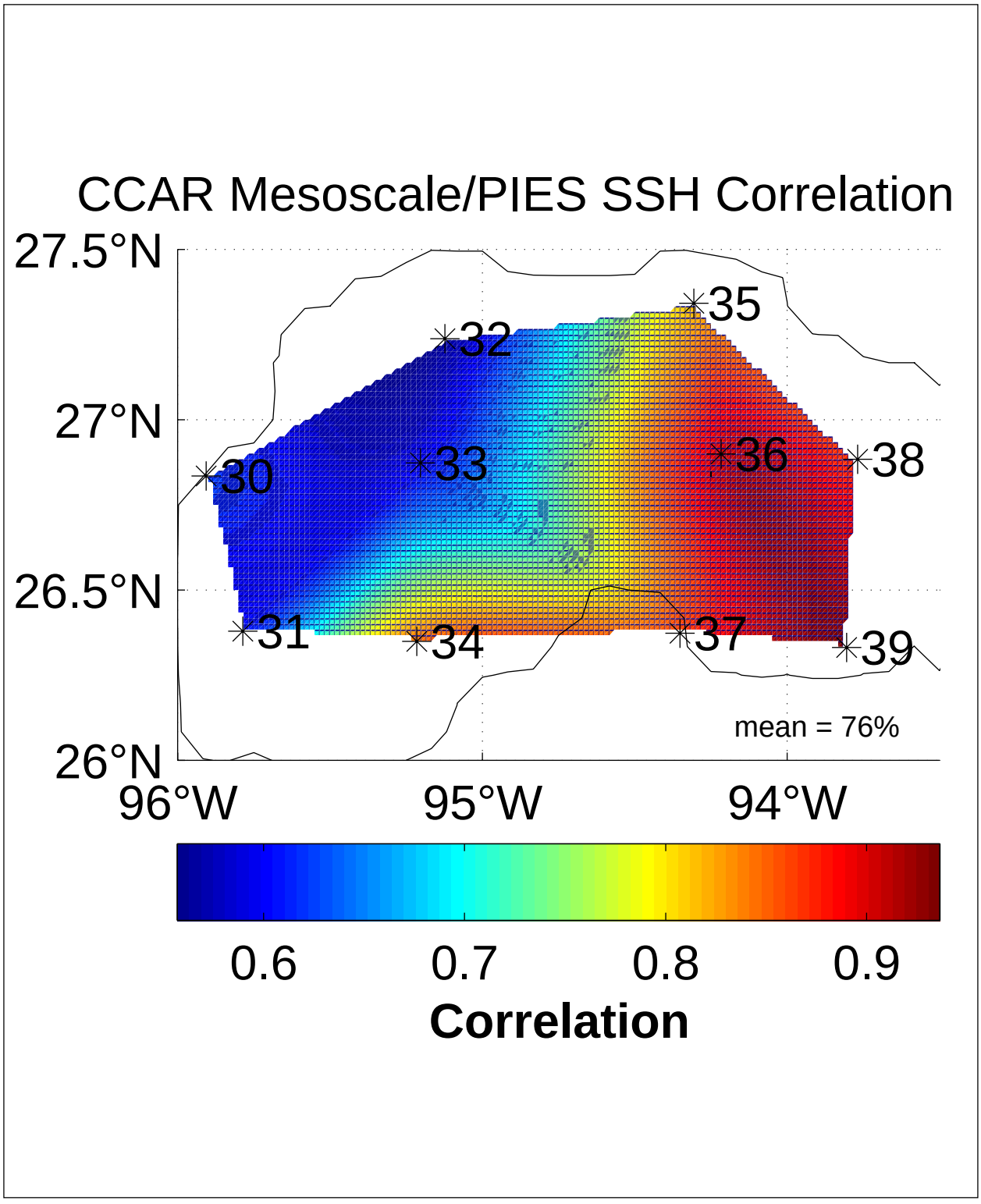

Figure 2.7-6. Spatial map of the CCAR/PIES SSH temporal correlation. Average over all stations of the correlation of the CCAR gridded mesoscale SSH data product to the collocated PIES time series is 76%. The 1000-m and 2000-m isobaths are shown.

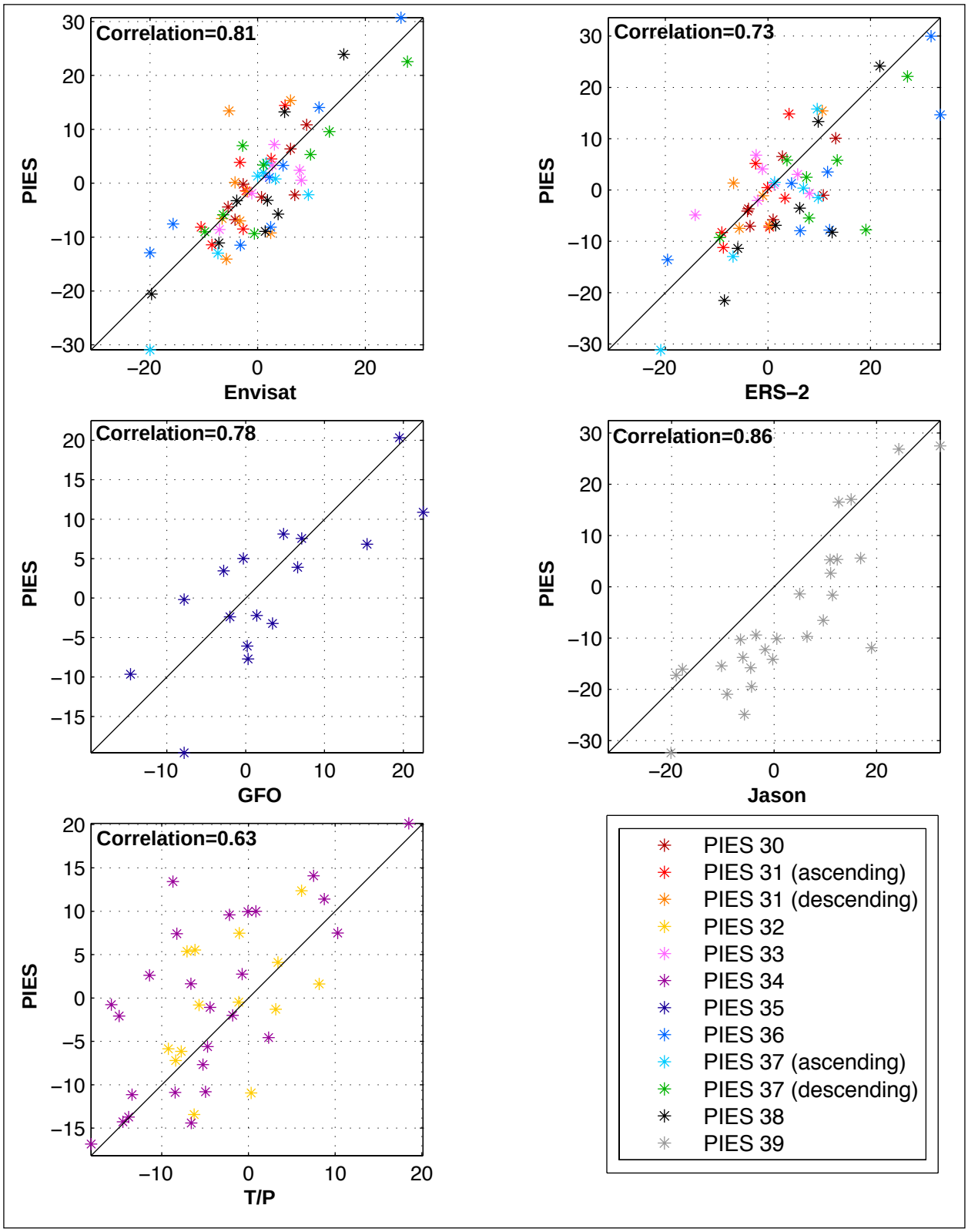

Figure 2.7-7. Scatterplot and correlation of the altimeter alongtrack detrended SSH and the coincident PIES SSH collected on the collocated groundtrack point. Results from all five satellites operational during the study program are shown.

CHAPTER 3 BASIC DESCRIPTION OF UPPER-LAYER CIRCULATION IN STUDY ARRAY

3.1 Historical Perspective of Upper-Ocean Circulation in the Western Gulf

The LC and its associated mesoscale eddy field dominate the upper-ocean circulation in much of the deepwater of the GOM because of the strength of the current and the limited area of the semi-enclosed GOM basin. Aperiodically, the LC intrudes northward and westward into the GOM to form a loop of clockwise-flowing current extending from the Yucatan Channel into the deep GOM basin and out through the Florida Straits. At irregular intervals, ranging from a few weeks to as long as 18 months (Sturges and Leben, 2000; Leben, 2000), the looping segment of the LC closes to form a ring of current that completely detaches and separates from the LC to propagate westward through the GOM as an anticyclonic oceanic vortex. This ring of current is commonly referred to as a Loop Current eddy (LCE). Like the majority of the deepwater GOM, the western GOM is strongly influenced by the LC. This influence, however, is not usually by direct intrusion of the current into the region. Rather it is more typically indirect, resulting primarily from the westward advection of LCEs (Elliot, 1982).

In addition to the LC and LCE influences, the upper-ocean circulation in the western GOM has a wind-driven component that contributes to the anticyclonic circulation observed in the upper layers of the central and northwestern GOM at seasonal and longer time scales (Sturges, 1993). Ohlmann et al., (2001) found that eddy forcing of the mean circulation dominates the direct wind forcing, especially along the western GOM continental slope base. This conclusion is based on the mean eddy momentum convergence estimated from altimeter-derived SSH anomaly; however, the efficacy of such calculations using altimetry has not been validated. Thus, the eddy variability may be remotely forced by the LC through the propagation and decay of LCEs or wind generated through the formation and interaction of boundary currents with the continental slope. The respective contribution of the two sources is difficult to quantify and remains an open research topic [see the review by Schmitz et al., (2005)].

For a historical perspective of the surface circulation in the western GOM, this discussion is limited to mesoscale variability associated with the LC, LCEs, and the energetic eddy field – the "synoptic" scale of the ocean circulation patterns that corresponds to the key circulation events in the upper ocean that occurred during the *in situ* observational record. The western GOM is an eddy-rich region exhibiting a broad range of energetic scales from the deepwater to the shelf break. Anticyclone-cyclone dipoles (Merrel and Vazquez, 1983) and tripoles (Vidal et al., 1994) are some of the largest scales of motion in the western GOM. Cyclones and anticyclones over the northwestern continental slope are smaller than those in the western GOM deepwater, which may be attributed to the smaller baroclinic radius of deformation over the slope (Hamilton, 2007). Slope eddies are a ubiquitous component of the upper-ocean mesoscale circulation along the western GOM continental slope margin (Hamilton et al., 2003) and are jostled around by the deepwater eddies (Hamilton, 1992). Deepwater eddies also interact with each other, splitting (Biggs et al., 1996) and merging (Lewis and Kirwan, 1985; Lewis et al., 1989; Berger et al., 1996) in energetic eddy-eddy interactions. Both deepwater and slope eddies have an effect on the offshore and onshore exchange of mass between the shelf and deepwater through the cross-slope flow generated in the confluence between cyclonic and anticyclonic eddies. Eddy

variability, thus, is a key (if not the dominant) upper-layer process in the western GOM. These eddy-eddy and eddy-slope interactions are also the scales of motion that are well observed using modern remote sensing techniques, and have been well recorded for over a decade in the multi-satellite altimeter record.

The use of only altimetry for a historical perspective, however, precludes direct observation of the "mean" circulation and LCEs in the western GOM. Synthetic techniques that combine climatological or model means with altimetry, which have been successfully used in the eastern GOM for monitoring the LC (Leben, 2005), would be very difficult to implement and validate in the western GOM. Seasonal and longer time scales, therefore, must be relegated to future observational studies spanning longer time periods, and indeed they will provide an important motivation for *in situ* observational programs of longer duration.

3.1.1 Remote Sensing Overview

Remote sensing of SSH, ocean color, and sea-surface temperature provide a unique perspective for identifying the historical and Gulf-wide context of the detailed *in situ* measurements made during the NW Gulf program. Briefly, these remote sensing data types are reviewed using examples from the measurement-program time period.

The altimeter record from 1 Jan 1993 through 30 June 2006 provides the most complete observational record for evaluating the historical perspective of mesoscale circulation in the GOM. This 13.5-year altimetric record provides continuous monitoring of LC intrusion, LCE propagation through the western GOM, and mesoscale activity in and around the study region. An example of altimetric mapping in the GOM is shown in Figure 3.1-1 from August 2, 2004. Altimeter-derived SSH anomaly plus a model mean are shown in the upper panel. A zoom of the study region overlaid with currents at 50 m and 250 m depths from the moorings is shown in the lower panel. Eddy Titanic and the Ulysses LC intrusion are labeled. Eddy Titanic separated from the LC on 31 Dec 2003 and propagated along a southwest path, taking eight months to travel the 660 km from its location at separation to the location shown. The average propagation speed is 3.1 $km \cdot day^{-1}$, a little slower than the 3.64 $km \cdot day^{-1}$ average reported for LCEs in the central GOM by Hamilton et al., (1999). Eddy Titanic remained well south of the study region throughout its lifetime; nevertheless, on the date of this map, three other large anticyclonic eddies are easily identified in the western GOM including one located within the study array. Large and small cyclonic eddies can also be easily detected by the negative (dashed) closed contours around SSH lows. This example highlights the unique capability of altimetry for mesoscale circulation monitoring in the GOM.

Ocean-color data are available from SeaWIFS and MODIS, since 1997 and 2002, respectively. Ocean-color imagery is a complementary data set to satellite altimetry because of the close relationship between biological productivity and mesoscale circulation. In the western GOM, cyclonic eddies exhibit enhanced biological productivity supported by nutrient-rich waters upwelling from depth into the euphotic (light) zone. This higher productivity distinguishes cyclonic eddies from anticyclonic eddies or LCEs that are regions of downwelling and low productivity consisting primarily of nutrient-poor Caribbean water. Along the GOM continental slope, both anticyclonic and cyclonic-eddy boundaries may be demarcated by high-chlorophyll

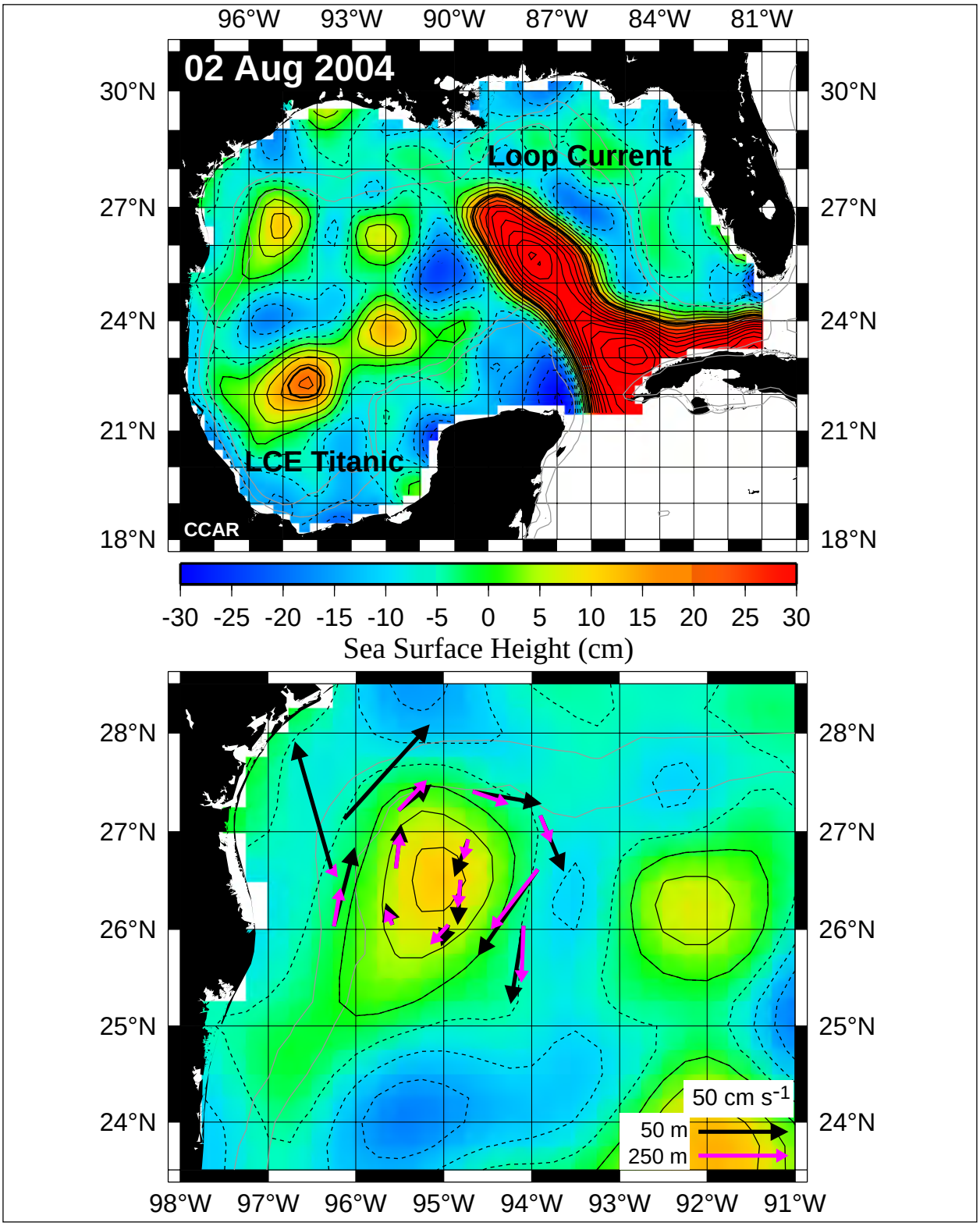

Figure 3.1-1. SSH map from 2 Aug 2004 showing Loop Current and LCE Titanic (upper panel) and a zoom of the study region overlaid with currents at 50 and 250 m depth (lower panel).

shelf waters that are pulled off of the continental shelf by the eddy field over the adjacent slope or deepwater (Biggs et al., 2005). Regardless of the actual coupling mechanisms or pathways, there is often a close relationship between biological and physical variability that makes the chlorophyll concentration from ocean-color imagery useful as a "false color" background for SSH contour maps in the GOM.

A good example is the 8-day composite color image showing chlorophyll concentration on 23 Sep 2004 (Figure 3.1-2). Altimeter-derived SSH are shown overlaid on the color image in the upper panel, and in the lower panel, a zoom color image in the study region is overlaid with both the altimetry and currents at 50 m and 250 m depths from the moorings. In the upper panel, Eddy Ulysses was located NW of the retreated LC and is visible in the color image as a region of low chlorophyll concentration. Eddy Ulysses separated from the LC on 23 Aug 2004 based on the 17-cm tracking contour shown by the thicker SSH contour line also overlaid on the image. Around the periphery of Ulysses were high chlorophyll concentrations associated with strong cyclonic eddies to the NE and SW of the eddy. Some of this chlorophyll signal was advected off of the northern continental shelf; however, a large portion of the enhanced chlorophyll, especially to the SW of Ulysses, was associated with hurricane-forced upwelling (Walker et al., 2005). Hurricane Ivan, a category 4 hurricane, passed directly over Eddy Ulysses on 15 Sep 2004 before making landfall as a strong category 3 hurricane near Gulf Shores, AL. As Ivan passed over Ulysses, the strong cyclonic hurricane-wind forcing intensified the upwelling in the cyclonic circulation around Ulysses producing the strong chlorophyll signals. Cyclonic eddies, however, are not only associated with the LC. An enlargement of the study region is shown in the lower panel for the same date. The strong chlorophyll signal associated with a pair of cyclonic eddies over the continental slope is clearly identified within the study region. This example shows that color imagery often provides a better, albeit qualitative view, of the synoptic circulation in comparison to altimetry. Care must be exercised, however, because ocean-color signals can change rapidly due to changes in the nutrient supply. In some cases, very strong biological signals decay rapidly because of nutrient depletion, whereas the underlying physical circulation continues to persist. In cases when there is not a strong source of nutrients, the background circulation must be discerned by relatively small variations in the chlorophyll concentration. These variations are caused by weak upper-ocean vertical currents associated with the convergence and divergence of the eddy field.

SST imagery during cloud-free conditions provides synoptic views of surface thermal patterns that can be used to infer the upper-ocean general circulation. Because of sharp and strong horizontal temperature gradients, SST imagery is most useful in the eastern and central GOM for monitoring the LC and LCE separation during the months from November through May; however, during the summer months the nearly isothermal surface makes detection of the upper ocean circulation features very difficult. Even during times of strong thermal contrast, the surface thermal signal of mesoscale eddies in the western GOM often have eroded enough that the detection of the eddies is difficult using thermal imagery alone. Nevertheless, SST imagery can provide synoptic views of the ocean surface thermal patterns that are valuable for interpreting rapidly evolving circulation events, events that are usually under sampled by the satellite altimetry. In our experience, however, we find that ocean-color imagery is typically more useful than SST imagery in the western GOM. As an example of the relative utility of color over SST imagery, we show the color and SST images from 29 Nov 2004 in Figures 3.1-3

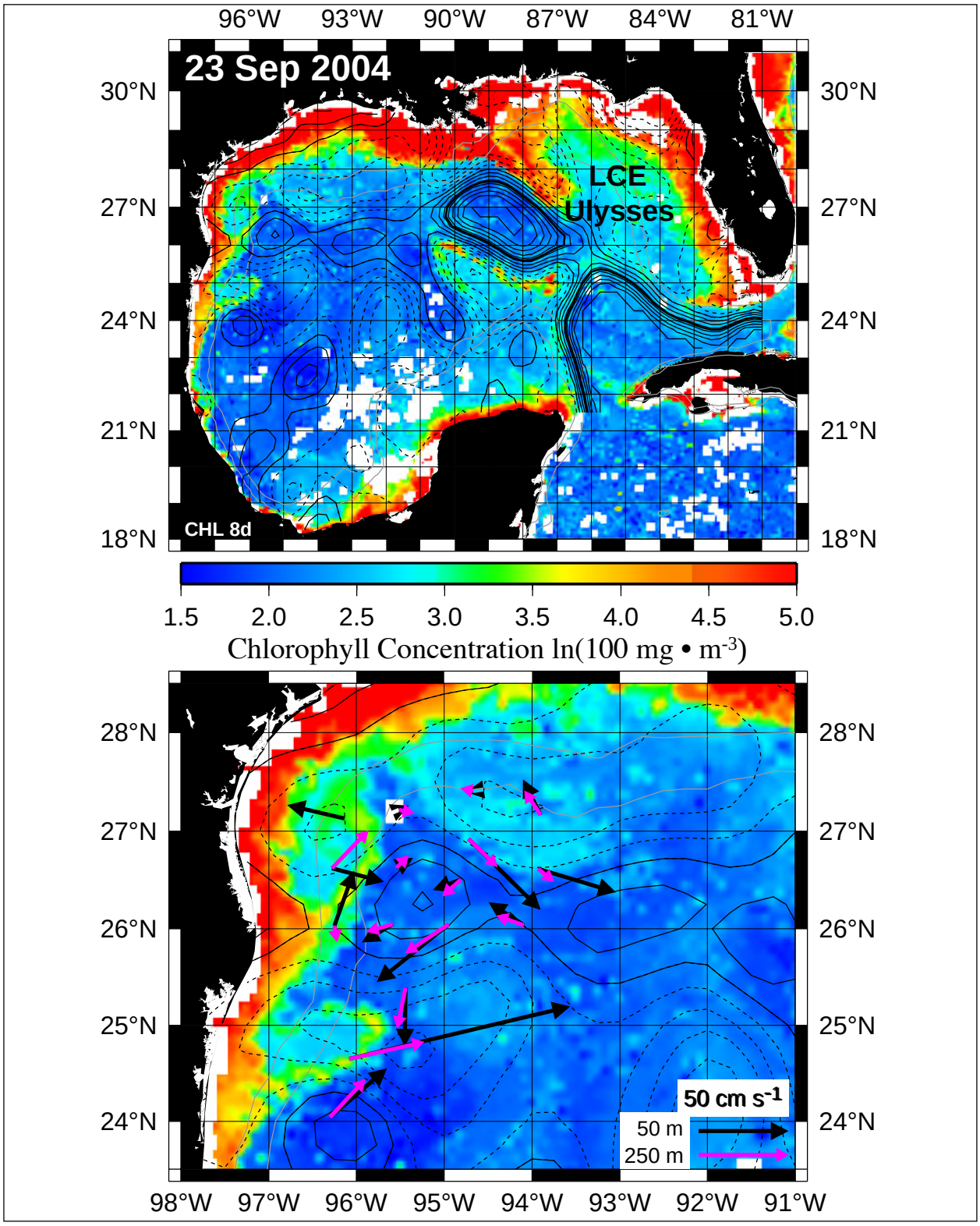

Figure 3.1-2. Chlorophyll concentration 8-day composite image from 23 Sep 2004 showing LCE Ulysses (upper panel) and a zoom of the study region overlaid with currents at 50 and 250 m depth (lower panel).

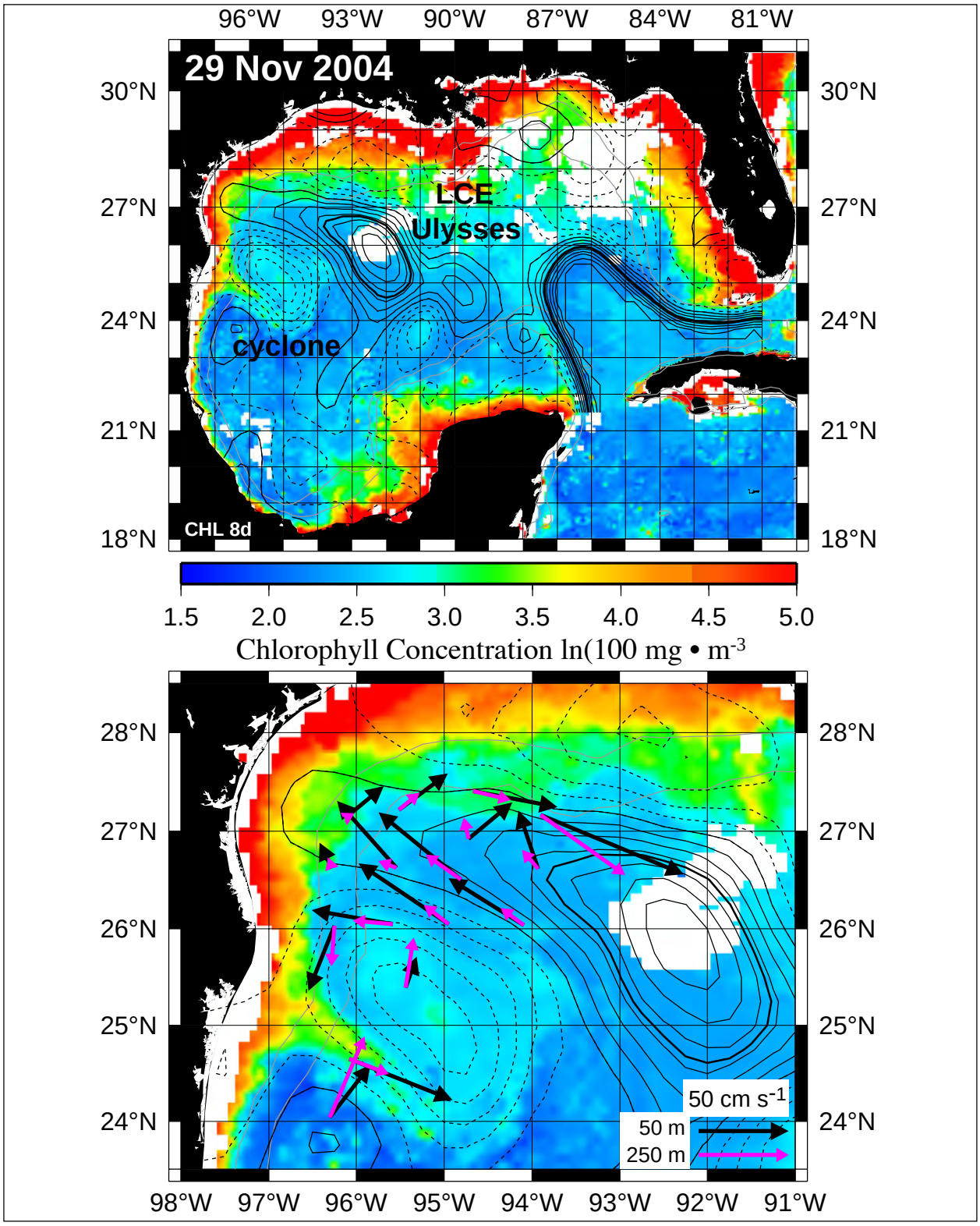

Figure 3.1-3. Chlorophyll concentration 8-day composite image from 29 Nov 2004 showing LCE Ulysses and a strong cyclone in the western GOM (upper panel) and a zoom of the study region overlaid with currents at 50 and 250 m depth (lower panel).

and 3.1-4. The warm and chlorophyll-poor waters associated with the LC and LCE Ulysses are seen, respectively, in both the 8-day composite color image and the 3-day composite SST image. Ulysses had propagated over 450 km in just over 3 months since separating from the LC, averaging 4.6 km·day^{-1}. Also seen in both images is a large cyclone centered at 25°N, 95°W. Cyclones are more difficult to detect in SST because they may have little or no surface thermal signal. The exceptions are cases such as this large cyclone where the feature had recently intensified and entrained cooler continental shelf waters on its periphery. On the other hand, deepwater cyclones are consistently difficult to identify in SST, but can often be detected in ocean color. A useful example is the small cyclone that was located to the SE of Ulysses (upper panel of Figure 3.1-5). This cyclone can be seen in the ocean color composite image as an area of chlorophyll concentration that is slightly higher than the background signal. The SST image exhibits no surface thermal signal associated with this feature (lower panel of Figure 3.1-5).

In this study, altimetric SSH contours overlaid on ocean color imagery will be a primary remote sensing visualization tool for monitoring mesoscale circulation in and around the study region.

3.1.2 LC and LCE Monitoring

The extent of LC intrusion and the timing of LCE separation and propagation through the western GOM determine, in large part, the energetic upper-ocean circulation events observed in the study region during the program measurement time period. We use an objective LC-tracking technique to monitor the time-dependent behavior of the LC using daily SSH maps based on satellite altimetry in combination with a model mean. This technique automatically tracks the 17-cm SSH contour that follows the edge of the high velocity core of the LC and calculates LC metrics such as extent, boundary length, enclosed area, volume and circulation (Leben, 2005). This allows us to identify these events objectively and place them in a Gulf-wide and historical context to better understand the influence of the LC on the NW Gulf study region.

The breaking of the 17-cm contour between the LC and a detaching LCE into separate contours causes a discrete change in LC boundary length, which can be used to identify objectively LC eddy-separation events. The day that the tracking contour breaks is identified as the time of separation; however, sometimes the detached eddy will reattach to the LC. In those cases the time associated with the ultimate detachment of the eddy is referred to as the eddy separation time. A total of 20 LC intrusions and eddy separation events have been identified in the time period from 1 Jan 1993 through 30 Jun 2006. The LC length time series and SSH maps for each of these events at the time of LCE separation are shown in Figure 3.1-6. LCEs are defined as anticyclonic eddies formed by separation events that cause a significant change in the extent of the LC, and are objectively identified by the closed 17-cm SSH contour that forms after an eddy separates from the LC. The LCE separation date, separation period, eddy name, and eddy area at the time of separation are tabulated for each of these events in Table 3.1-1. Horizon Marine Inc. names eddies in alphabetical order as anticyclones separate from the LC and/or impact offshore operations in the northern GOM. The names appear in the EddyWatch™ reports provided to the GOM offshore oil and gas industry by subscription. All LCEs identified in the altimeter record using the SSH 17-cm tracking contour to date have been monitored by the EddyWatch™ service, although a number of smaller anticyclonic eddies (seven total) were also named, which results in breaks of the alphabetical sequence. Only one marginal eddy separation event is identified by

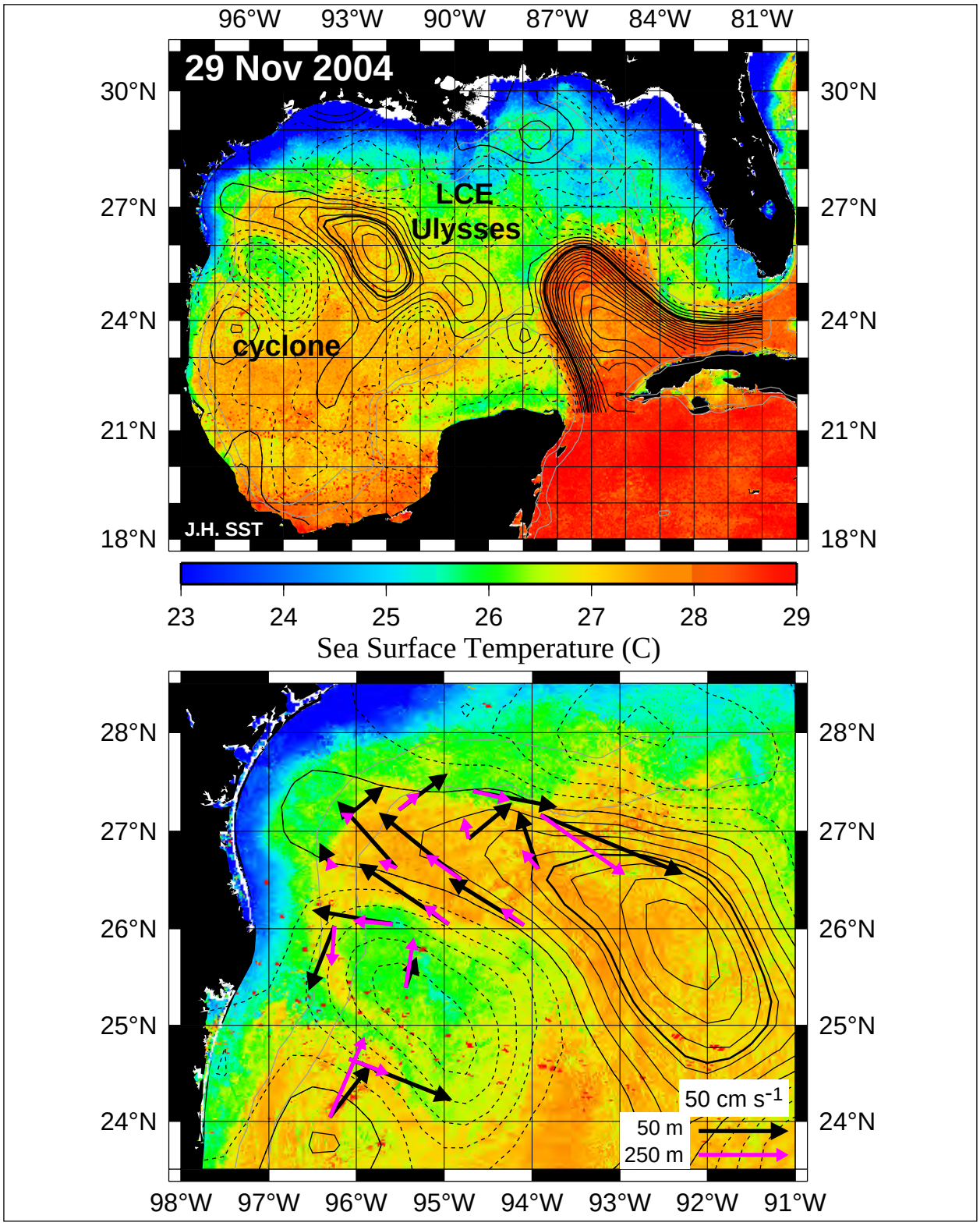

Figure 3.1-4. SST 3-day composite image from 29 Nov 2004 showing LCE Ulysses and a strong cyclone in the western GOM (upper panel) and a zoom of the study region overlaid with currents at 50 and 250 m depth (lower panel).

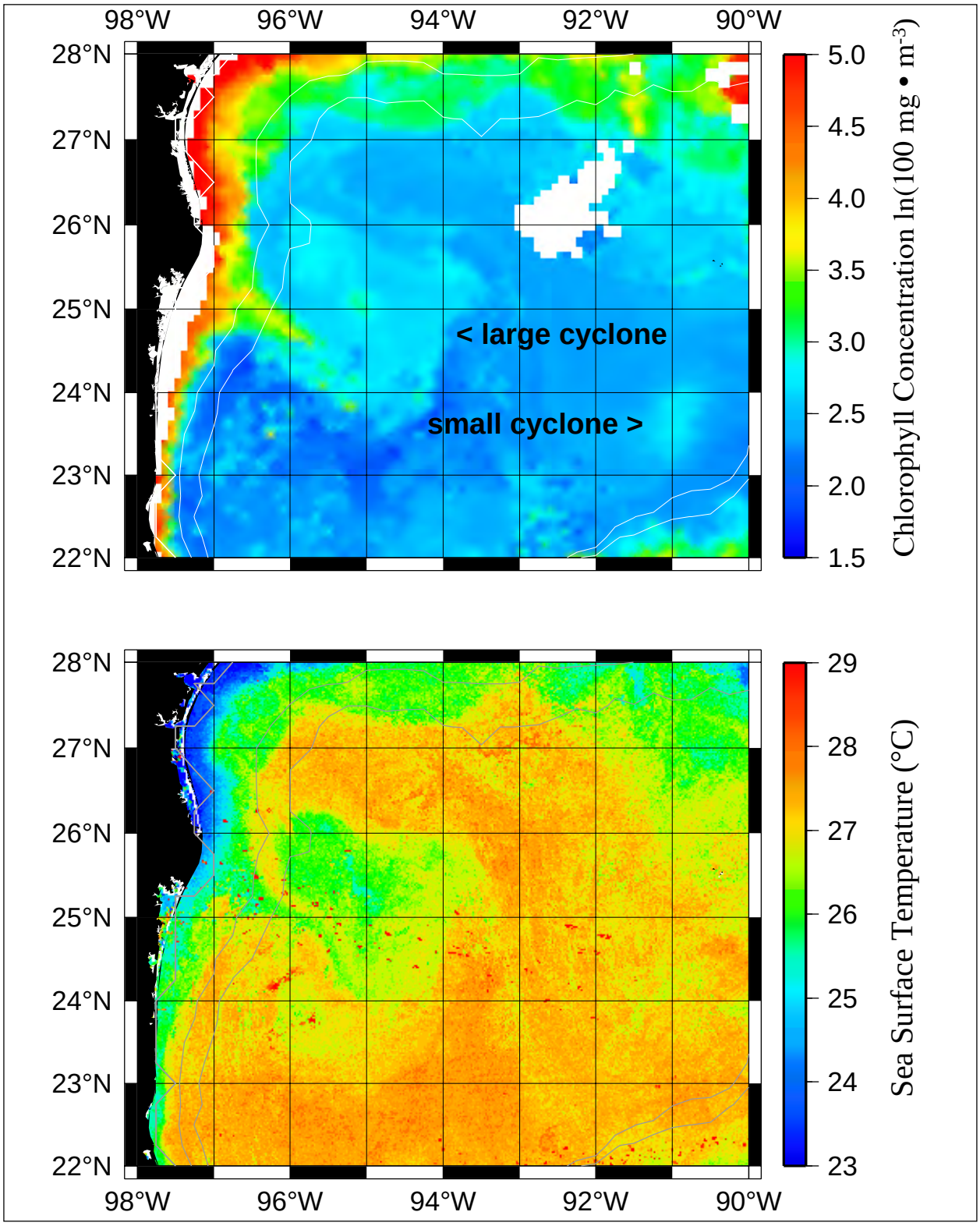

Figure 3.1-5. Zoom of western GOM showing comparison of ocean color (upper panel) and SST (lower panel) images of cyclonic eddies in the western GOM on 29 Nov 2004. Small cyclone can only be detected in the ocean color image.

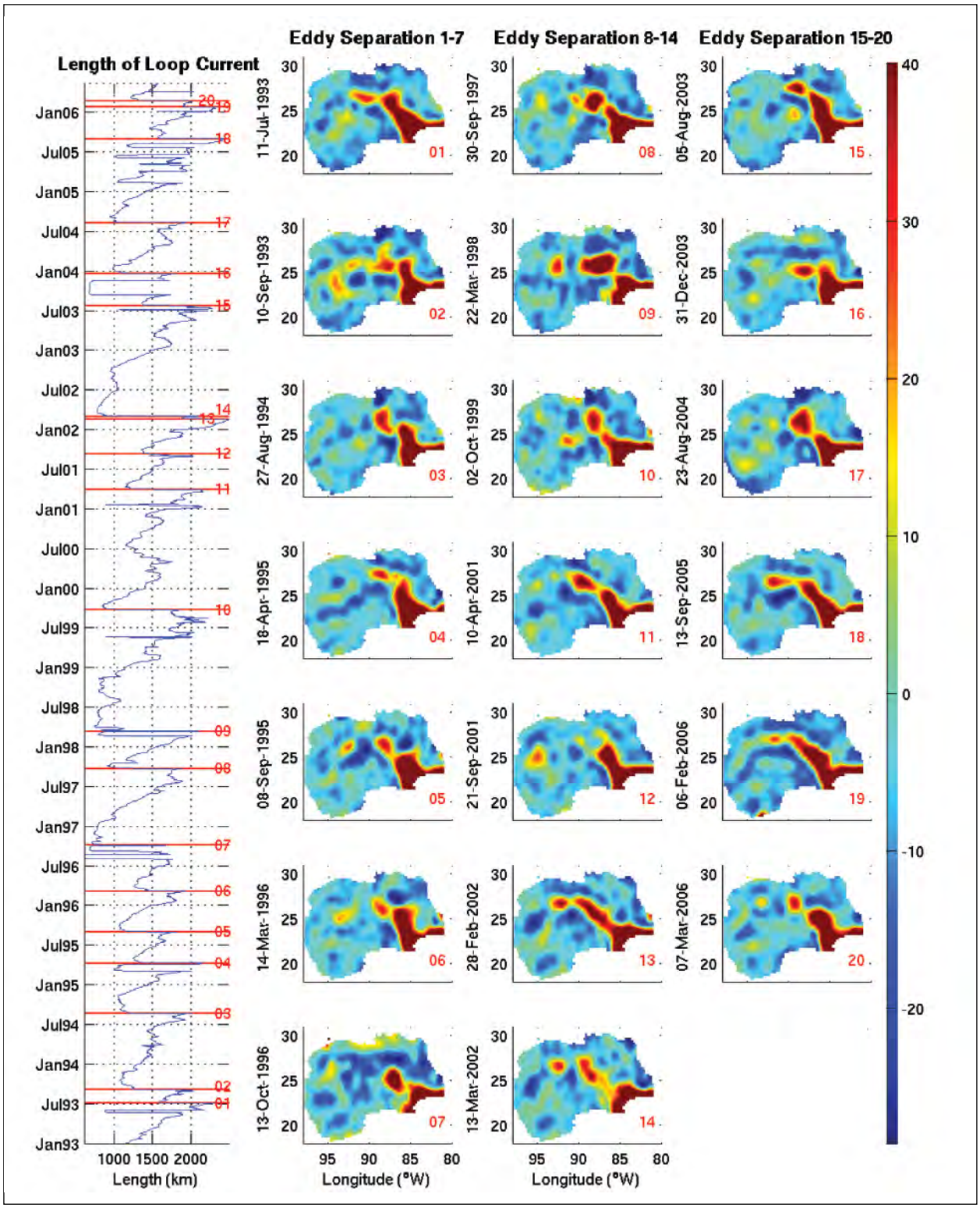

Figure 3.1-6. LCE separation events identified in the altimeter record. SSH maps on the separation dates are shown in the panels to the right (values above 40 cm and below -30 cm have been clipped). The LC length time series is overlaid with red lines corresponding to the separation dates.

the objective-tracking procedure (Eddy Odessa/Nansen, LCE #12), which dissipated so quickly that an estimate of the eddy area could not be made using the tracking contour. These smaller eddies are of LC origin, but form on the outer edge of the LC through interaction of frontal cyclones with the current. Ideally, these anticyclones should not be counted as LCEs since they are better categorized as minor, peripheral eddies. Other anticyclonic eddies are created as primary LCEs split and/or form smaller anticyclonic eddies during or after separation. A good example is the splitting of an unnamed anticyclonic eddy off of the southwestern flank of LCE Sargassum that was well observed using *in situ* and satellite observations collected during the Exploratory Study as described in Donohue et al., (2006).

Table 3.1-1

Loop Current Eddy (LCE) Separation Events from the Altimetric Record: 1 January 1993 through 30 June 2006

LCE Number	Separation Date	Separation Period (months)	Industry Eddy Name	Area (km^2)	Eddy Maximum SSH (cm)
1	11 Jul 1993	11.5	Whopper	24,183	33
2	10 Sep 1993	2.0	Xtra	38,481	39
3	27 Aug 1994	11.5	Yucatan	43,022	39
4	18 Apr 1995	7.5	Zapp	21,337	36
5	8 Sep 1995	4.5	Aggie	24,899	36
6	14 Mar 1996	6	Biloxi	24,912	32
7	13 Oct 1996	7	Creole	49,644	69
8	30 Sep 1997	11.5	El Dorado	49,229	56
9	22 Mar 1998	5.5	Fourchon	89,143	72
10	2 Oct 1999	18.5	Juggernaut	40,325	39
11	10 Apr 2001	18.5	Millennium	45,705	44
12	21 Sep 2001	5.5	Odessa/Nansen	?	12
13	28 Feb 2002	5.5	Pelagic	22,119	41
14	13 Mar 2002	0.5	Quick	49,936	41
15	5 Aug 2003	17	Sargassum	25,302	49
16	31 Dec 2003	5	Titanic	33,278	43
17	23 Aug 2004	8	Ulysses	68,633	42
18	13 Sep 2005	12.5	Vortex	29,541	38
19	6 Feb 2006	5	Walker	11,366	29
20	7 Mar 2006	1	Xtreme	22,111	37

3.1.3 Historical Perspective of LC in the Western GOM

Although the LC is usually located in the central and eastern GOM, the current has been observed west of 92°W during extreme western intrusion events. Based on the altimeter record, a total of four LC intrusion events penetrated westward of 92°W. Historically, extreme western LC intrusion events are associated with the near-simultaneous or tandem separation of two LCEs during a single intrusion event (Leben, 2005). Tandem separation differs from LCE splitting in that each eddy separates from the LC individually with one LCE separating first from the LC, followed closely by the second eddy. The formation of each eddy thus affects the LC length and can be objectively identified as a LC eddy separation event. LCE names associated with each

separation event are listed in Table 3.1-1. The first event of this type observed in the altimeter record occurred in early 2002 with the separation of Pelagic (#13) on 28 Feb 2002 followed by Quick (#13) on 13 Mar 2002 just two weeks later. The maximum westward extent during this LC intrusion was 93.1°W (based on the 17-cm SSH tracking contour) just as Pelagic was separating from the LC. This was the maximum westward LC extension observed in the altimeter record. The second tandem separation event occurred early in 2006 with the separation of two LCEs, Walker (LCE #19) on 6 Feb 2006 and Xtreme (LCE #20) on 7 Mar 2006, over an interval of about one month. The LC intrusion associated with this tandem eddy separation event reached a maximum westward extent of 92.3°W.

Two other LC intrusion events penetrated westward of 92°W in the altimeter record: Whopper (LCE #1) and Vortex (LCE #18). In 1993, the LC intrusion associated with the separation of Whopper reached 92.05°W. The other event, Vortex, occurred in the summer of 2005 near the end of the NW Gulf Program when the only remaining moorings were those in Mexican waters. The maximum westward extent during this intrusion was 92.8°W and was associated with the ultimate separation of Vortex (LCE #18). These events were not strictly speaking tandem eddy separations. In both cases, however, the next LCE separated relatively quickly following the initial separation of the first eddy from the far westward LC intrusion, with Xtra (LCE #2) separating two months after Whopper and Walker (LCE #19) separating five months after Vortex.

3.1.4 Historical Perspective of LCEs in the Western GOM

The influence of the LC on upper-ocean circulation in the western GOM is typically indirect and primarily induced through the propagation of LCEs through the western deepwater basin. LCEs are a primary source of heat, momentum, and salinity in the western GOM (Elliot, 1982) and move westward due to the westward-propagation tendency of vorticity on a rotating planet, the so-called β effect (Rhines, 1975). There is also a self-advective tendency associated with the nonlinear strength of an isolated vortex that arises as the circulation becomes asymmetric through the dispersion of Rossby waves (McWilliams and Flierl, 1979). Over flat topography, such as the abyssal GOM plain, this nonlinear effect induces a southward component of propagation for anticyclonic eddies in the northern hemisphere (Smith and O'Brien, 1983). The combined westward and southward propagation tendencies give LCEs their characteristic west-southwest trajectory when isolated from the influences of bottom topography and the ambient flowfield (Smith, 1986).

Although there is a general tendency for west-southwest propagation, LCEs frequently interact vigorously and nonlinearly with the energetic eddy field in the western GOM (Biggs et al., 1996) and arrive at the western continental margin along disparate paths (Hamilton et al., 1999; Vukovich, 2007). The location of a LCE at separation may also influence the path traversed by an eddy. Initial attempts to track LCE pathways using satellite imagery (Vukovich and Crissman, 1986) identified three characteristic paths: a northern path, a central path, and a southern path (Figure 3.1-7, upper panel). All three pathways led to a region in the northwestern corner of the GOM that has been informally referred to as the "eddy graveyard" (Biggs et al., 1996). An updated characterization of the eddy paths (Vukovich, 2007) shows three like-named paths (Figure 3.1-7, lower panel); however, the actual pathways differ remarkably from those

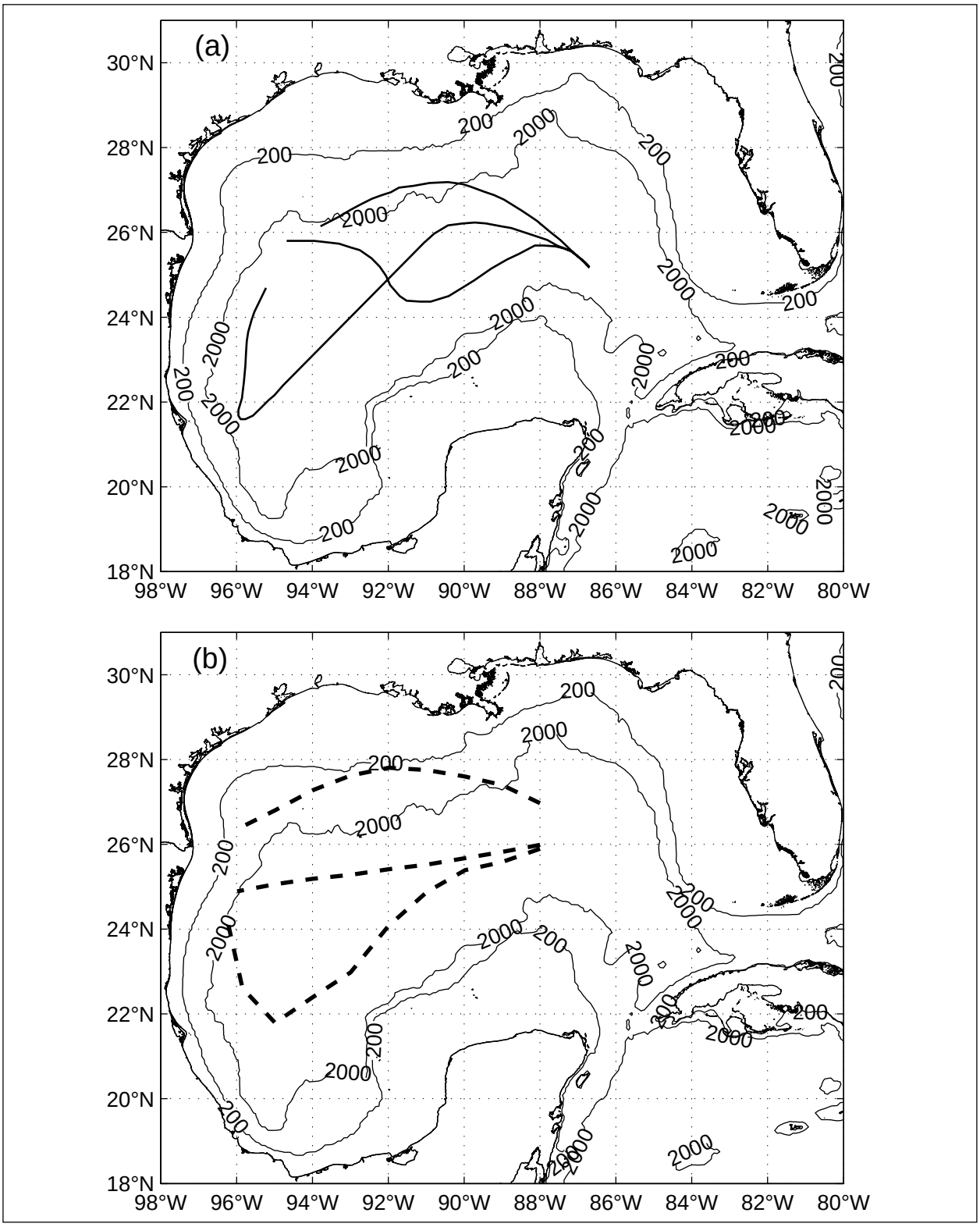

Figure 3.1-7. LCE pathways from (a) Vukovich and Crissman (1986) and (b) Vukovich (2007).

originally proposed. A composite of the eddy paths are shown to highlight the changes (Figure 3.1-8). Presumably the differences are attributable to the increase in the observational database; however, there are also significant differences in the methodology employed in the two respective studies, and it is not clear how these differences affect the results. Specifically, in the second study, the major LCEs that merged with other anticyclones or LCEs that split into two rings were excluded from the analysis. In another study of LCE propagation, Hamilton et al., (1999) conclude that there are no preferred eddy pathways through the deep basin. This result is based on the paths of eddy center positions determined using a kinematic analysis of the trajectories of satellite-tracked drifters orbiting within 10 LCEs. The eddy center paths from that study are shown in Figure 3.1-9.

3.1.5 Altimeter Record of LCEs in the Western GOM

The continuous 13.5-year altimetric record from 1 Jan 1993 through 30 June 2006 provides a unique perspective on LCE propagation through the western GOM. To be rigorous in this assessment, LCEs are defined as anticyclonic eddies arising from separation events that caused a significant change in the extent of the LC (Table 3.1-1). This objective definition allows the systematic identification of LCEs and the tracking of their trajectories through the western GOM.

Previous altimetry-based studies of LCE trajectories through the western GOM tracked eddies by tracking extrema in SSH maps (Leben and Born, 1993) or by tracking a fixed tracking contour (17 cm) encircling the eddy until the eddy decayed (Berger et al., 1996). Both of these techniques were automated, but typically failed as the LCEs reached the western continental margin. These techniques were, however, successfully used to determine the time series of LCE characteristics such as position, translation velocity, eccentricity, mean radius, swirl speed, vorticity, and circulation as the eddies transited the deep western GOM. In this study, we focus on the ultimate fate of the LCEs more than their quantitative metrics. The goal is to track LCEs throughout the duration of their existence by tracking them from their initial formation at separation from the LC, through any interaction with the ambient eddy field and western margin, until their ultimate decay or dissipation.

A review of the altimetric record found that LCEs often merge and split. Merging occurs when LCEs coalesce with nearby anticyclones or existing LCEs (Kirwan et al., 1984; Lewis and Kirwan, 1985; Berger et al., 1996). Splitting or cleaving (Biggs et al., 1996; Donohue et al., 2006) occurs when pieces of anticyclonic circulation of varying size split off from a LCE through the interaction of the eddy with peripheral cyclones. Nevertheless, in either case, the anticyclonic circulation associated with the LCE, or pieces of the LCE, could be tracked through these eddy-eddy interactions. In cases where a nearly equal splitting of the LCE occurred, both pieces of the cleaved eddy were tracked. This was preferable to arbitrarily terminating LCE tracking at merging and splitting events since the ultimate goal was to track LCEs as far as possible into the western GOM to assess their influence on the circulation in the study region. In most cases the eddy could be tracked even after reaching the western margin by carefully following the closed circulation contours around the eddy.

The eddy-tracking procedure has been automated as much as possible, but could not be made completely objective because of the rapid evolution of LCEs during merging and splitting events

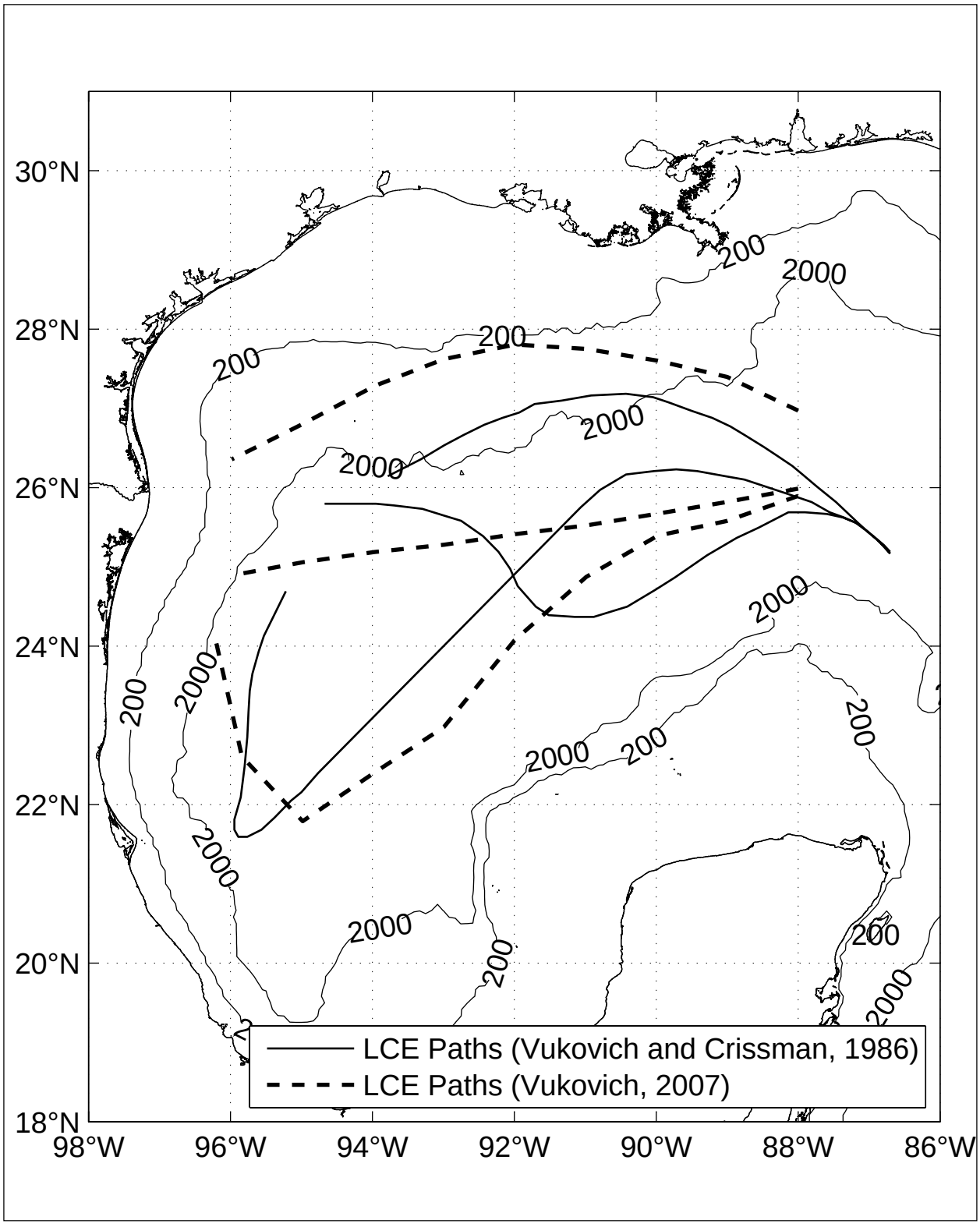

Figure 3-1-8. Composite of the LCE pathways from Vukovich and Crissman (1986) and Vukovich (2007).

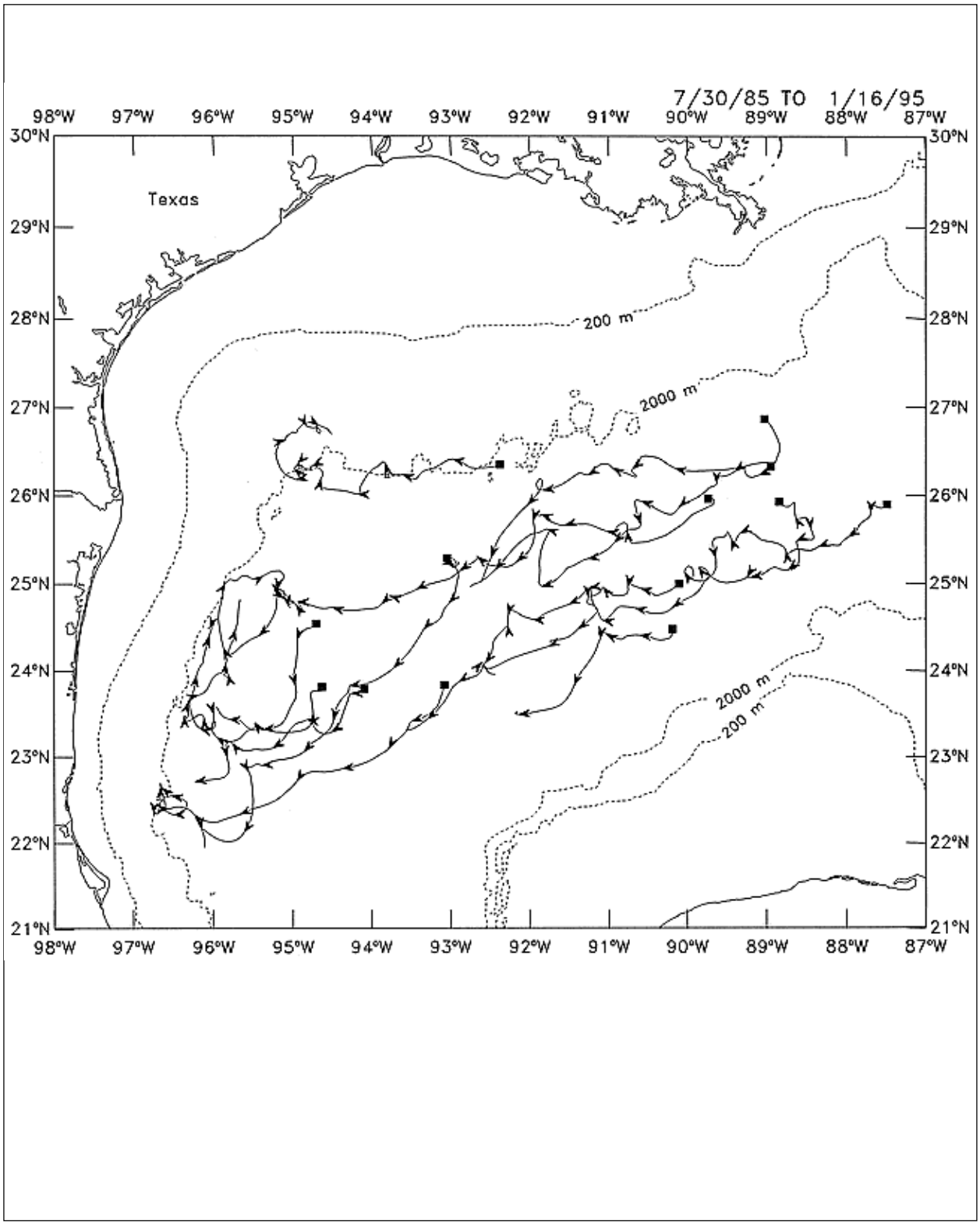

Figure 3.1-9. Paths of LCE center positions from Hamilton et al. (1999). Arrowheads are at 10-day intervals.

and during interaction with the ambient eddy field and continental slope along the western GOM margin. Some of the tracking difficulty is attributable to under sampling of the LCEs by the intermittent along-track altimetric sampling. To reduce these difficulties, tracking used the closed SSH anomaly contours that encircle the eddy, which are less affected by the along-track sampling than the maximum height within the eddy. The tracking contour values are changed from 30 cm at initial formation of the LCE in decrements of 10, 5, 3 or 2 cm until the eddy could no longer be tracked, which usually occurred at a contour level of about 8 or 5 cm. The eddy-center location is estimated using the mean latitude and longitude of points on the tracking contour. The maximum SSH values within the eddy were also logged. The SSH anomaly maps used in this analysis were calculated relative to the Goddard Spaceflight Center mean sea surface (GSFC00.1_MSS) described in Wang (2001). This mean surface has some small residual mean anomalies relative to the 13.5-year record time internal that do not significantly affect the tracking. The primary advantage of using an existing independent mean is that as additional altimeter data becomes available, LCE tracking consistent with the analysis described here can be added without redoing the entire analysis relative to a new mean.

A total of 17 LCEs were tracked in the 13.5-year altimetric record. The naming convention follows EddyWatch™ names as listed in Table 3.1-1. Three of the LCEs split in two: Xtra, Juggernaut, and Ulysses. For these splitting events, we used names consistent with EddyWatch™. The names Juggernaut and Ulysses refer to the portion of the splitting LCEs that took more southerly trajectories, which is consistent with the LCEs tracked by EddyWatch™ using satellite-tracked drifters. For Xtra, we followed the convention of retaining the LCE name for the more southerly eddy in the splitting pair. Since EddyWatch™ did not name the northerly portions that split off from LCEs Xtra and Juggernaut, we have named these eddies Xtra Split and Juggernaut Split. EddyWatch™ gave the name U2 to the northernmost piece of Ulysses. LCE #12 (Odessa/Nansen) was not included because it is considered a minor LCE. LCE #19 (Walker) and LCE #20 (Xtreme) occurred too late in the data record to be tracked over their entire lifetimes, so they were also excluded.

Figure 3.1-10 shows the individual LCE center paths through the western GOM taken by the 17 LCEs and the three "split" eddies tracked using the satellite altimetry. A total of 20 eddy paths are included in this analysis, twice the number of eddies tracked using satellite-tracked drifters in the study by Hamilton et al., (1999). The basic conclusions concerning the LCE paths in the western GOM are in agreement with that study: eddy centers seldom cross the 2000 m isobath, the paths occupy a broad band of latitude (2° to 3°) in the center of the western deep basin with a mean west-southwest trend, and there is no apparent preferred pathway either in the main basin or along the western slope. The agreement between these two analyses also suggests that LCE propagation is a relatively stationary process and is well sampled by the 13.5-year altimetric record.

In contrast to this study and Hamilton et al., (1999), Vukovich (2007) finds three preferred pathways through the western GOM, which are shown overlaid on the altimeter-tracked LCE paths in Figure 3.1-11. The pathways shown were digitized from Figure 17 in Vukovich (2007). It is not clear how these pathways were quantitatively determined; nevertheless, the partitioning of LCEs into each of pathway categories was based on objective criteria according to the description of the method in the paper. Those rings that spent at least 75% of the time north of

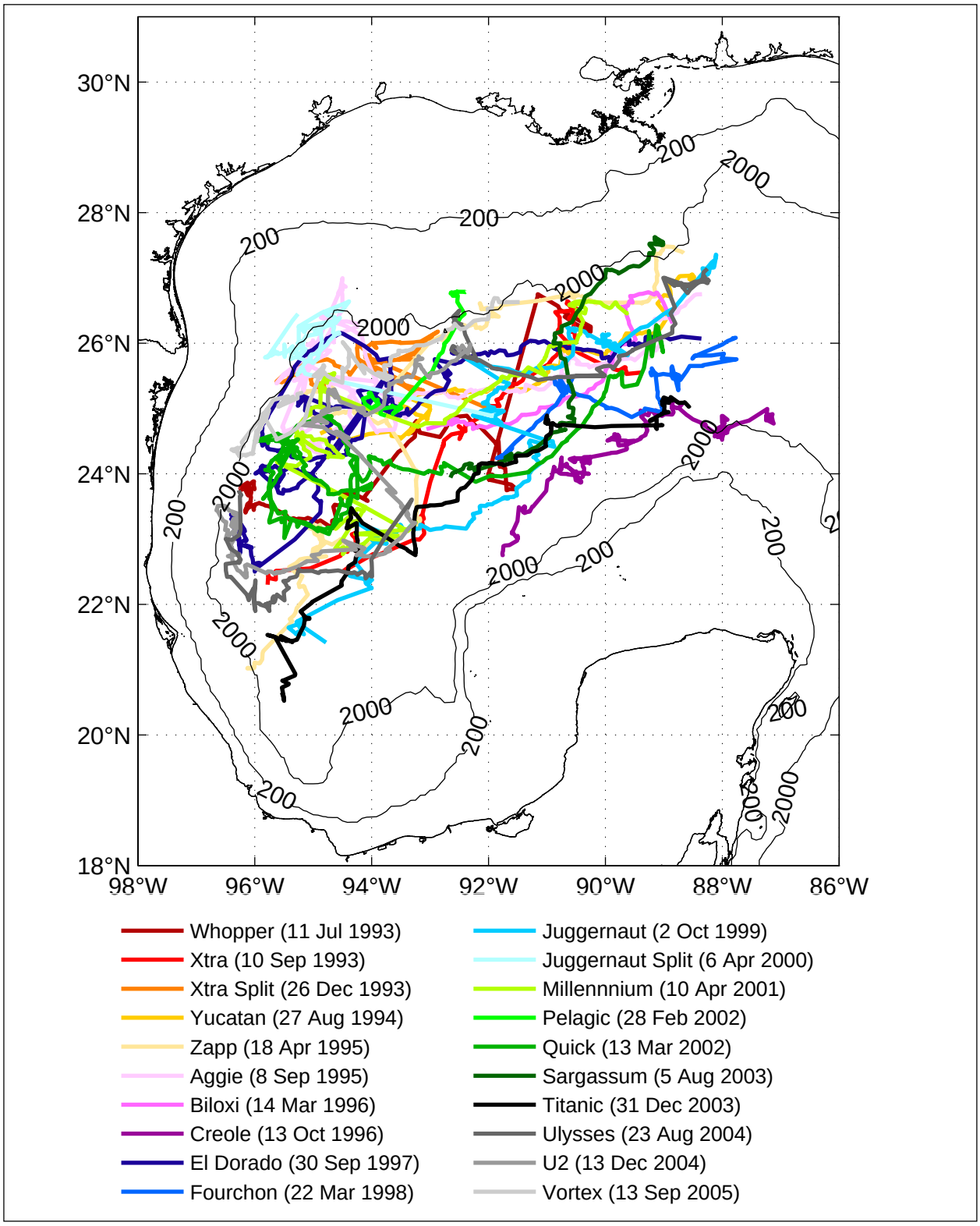

Figure 3.1-10. LCE center paths through the western GOM taken by the 17 LCEs and the three "split" eddies tracked using satellite altimetry.

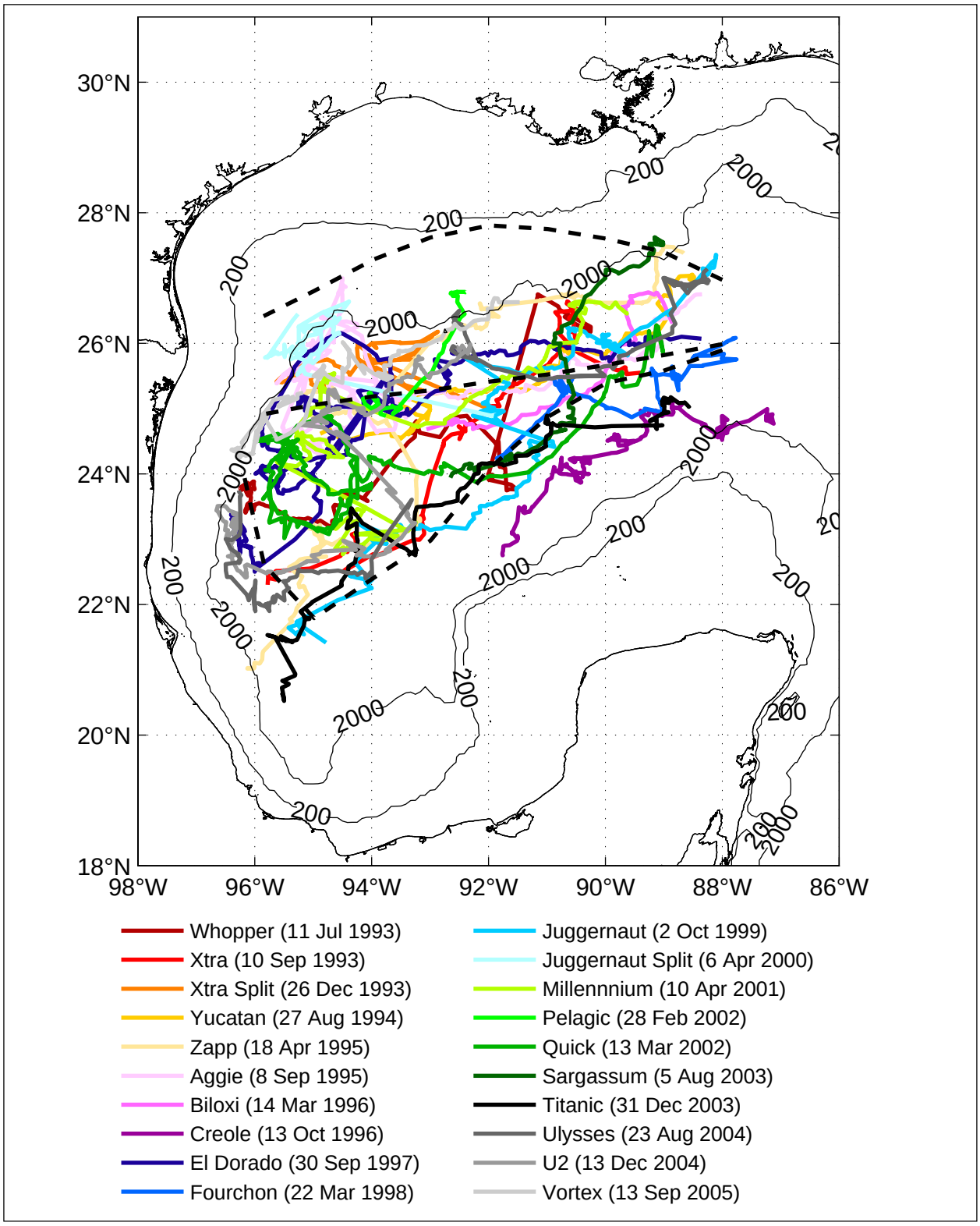

Figure 3.1-11. Altimeter-tracked LCE center paths overlaid with the three prescribed pathways from Vukovich (2007).

26°N before reaching the western wall were on the "northern path". Those that spent at least 75% of the time between 24° and 26°N were on the "central path," and those that spent at least 75% of the time below 24° were on the "southern path." The frequencies of each path were 24%, 62%, and 18% for the northern, southern and central paths respectively, summing to a total of 100%. Curiously, there did not appear to be cases where a LCE was, for example, above 26°N for 50% of the time and then below 26°N for the remainder of the time and thus not fall into either one of categories. According to the author (Fred Vukovich, personal communication), there were no cases where an eddy path did not fit into one of these three prescribed path categories. Whether or not these pathways were quantitatively determined or subjectively inferred, the northern path as depicted in Vukovich (2007) is not exhibited by any of the LCEs from the altimetric record. LCE eddy centers seldom cross the 2000-m isobath, and have never been observed on the continental slope near the 200-m isobath. Furthermore, we find the partitioning of LCE paths into prescribed pathways defined by fixed latitude bins problematic because of the tendency of LCEs to propagate west-southwestward.

A more straightforward estimate of the central tendency of the LCE paths is a "mean" path. Nevertheless, even this simple metric is difficult to calculate because LCE paths are of disparate length and duration, and LCE centers are not evenly distributed along the eddy paths because of the variation of the eddies' propagation speed. Smoothing can mitigate some of these effects, so several methods were used to estimate the mean path in order to access the robustness of the results. These techniques are based on windowing of the daily LCE positions in longitude and averaging within the window to calculate mean latitude. In the first method, individual LCE center latitude values were averaged within a centered window that was initially set to a width of ¼° of longitude and then averaged over all LCE paths. We call this the "path-averaged mean path". In the second method, all LCE center latitude values within a centered averaging window (initially ¼° of longitude) were averaged to estimate the mean path directly from all eddy center points. We call this the "point-averaged mean path". The results are calculated at each ¼° of longitude spanning the eddy path distribution independent of the width of the averaging window.

When the averaging window is set to ¼° of longitude there is no smoothing in longitude because the data in each window is independent of the neighboring windows. The ¼° path-averaged mean and point-averaged mean paths, including a one standard deviation whisker bar for each averaging window, are shown respectively in Figures 3.1-12 and 3.1-13. The paths are similar, however, the path averaged mean path is smoother than the point averaged mean path. Both paths tend to the west-southwest and are consistently south of the central path in Vukovich (2007). The mean paths are also shown in Figures 3.1-14 and 3.1-15 overlaid on all of the individual eddy center paths. The affect of the distribution of eddy-center locations and eddy paths is more pronounced in the point-averaged path in comparison to the path-averaged mean path.

Since both the LCE paths and LCE centers are not evenly distributed in longitude some smoothing is required to obtain a robust estimate of the mean path that is less affected by these variations. The degree of smoothing is increased as the width of the averaging window is increased. Two-degree windows were selected because the mean paths changed very little with further increases in window size signifying that the mean paths had converged. The 2° window path-averaged mean and 2° window point-averaged mean paths are shown in Figures 3.1-16 and

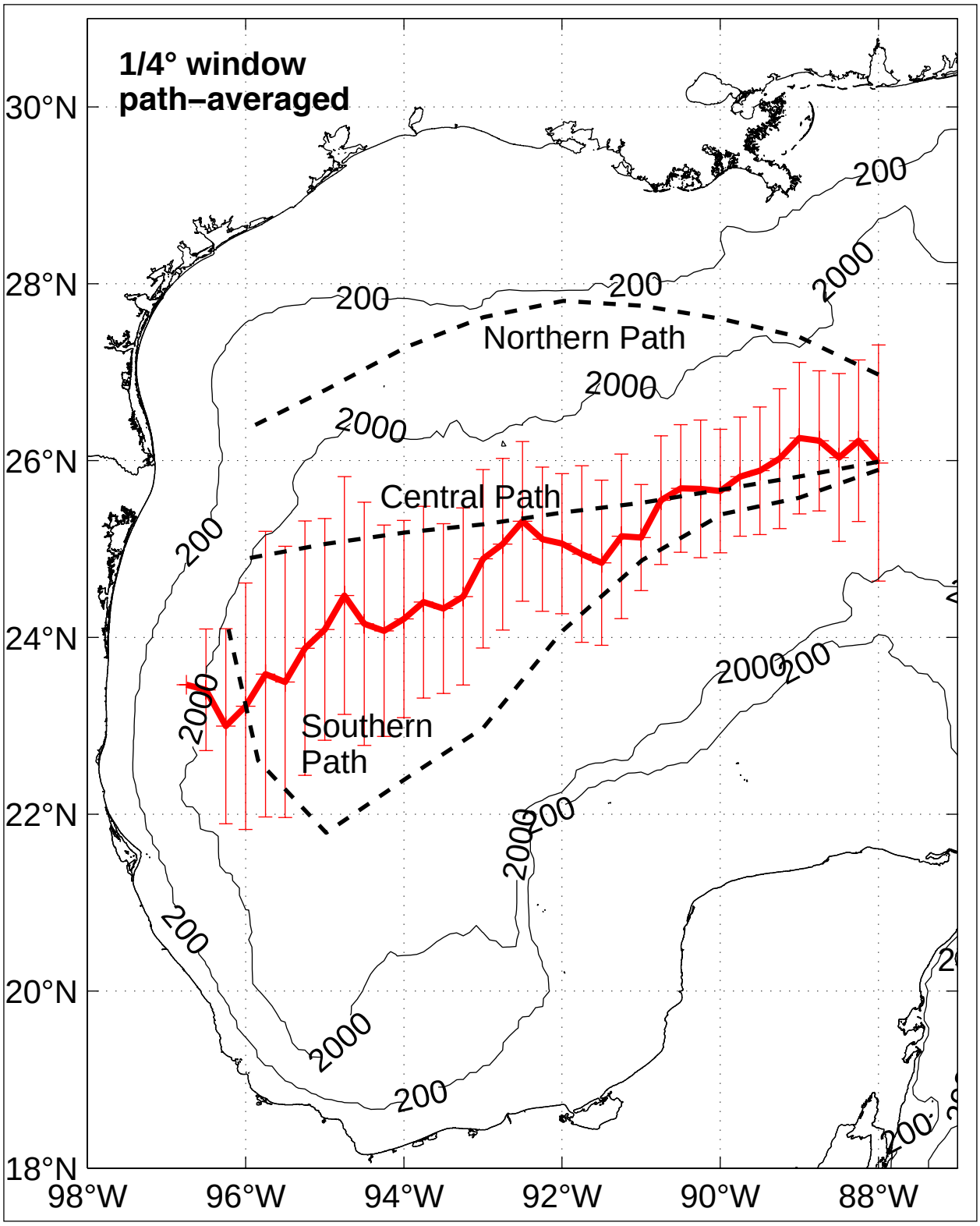

Figure 3.1-12. The ¼° path-averaged mean path overlaid with a one standard deviation whisker bar for each averaging window and the three prescribed pathways from Vukovich (2007).

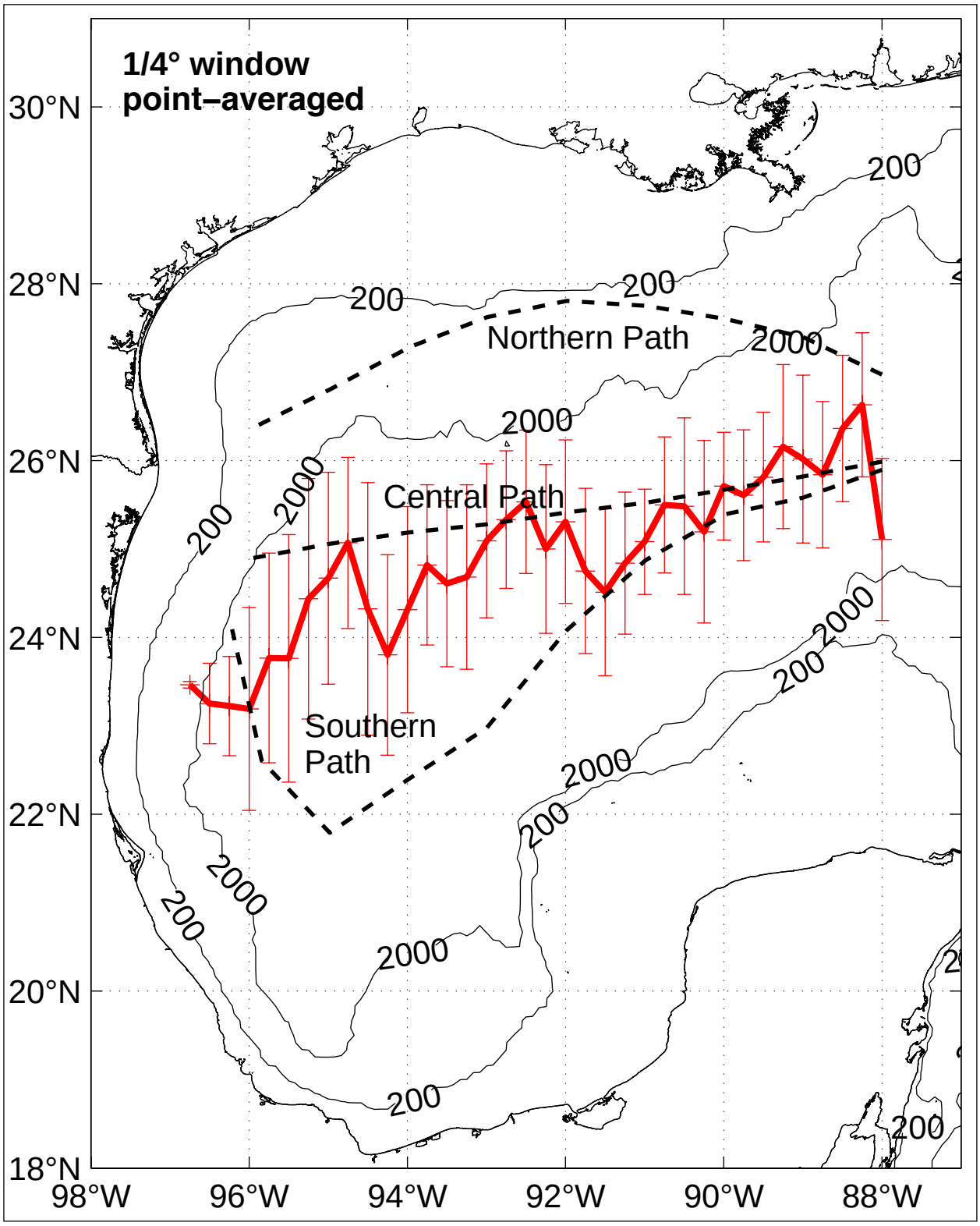

Figure 3.1-13. The ¼°point-averaged mean path overlaid with a one standard deviation whisker bar for each averaging window and the three prescribed pathways from Vukovich (2007).

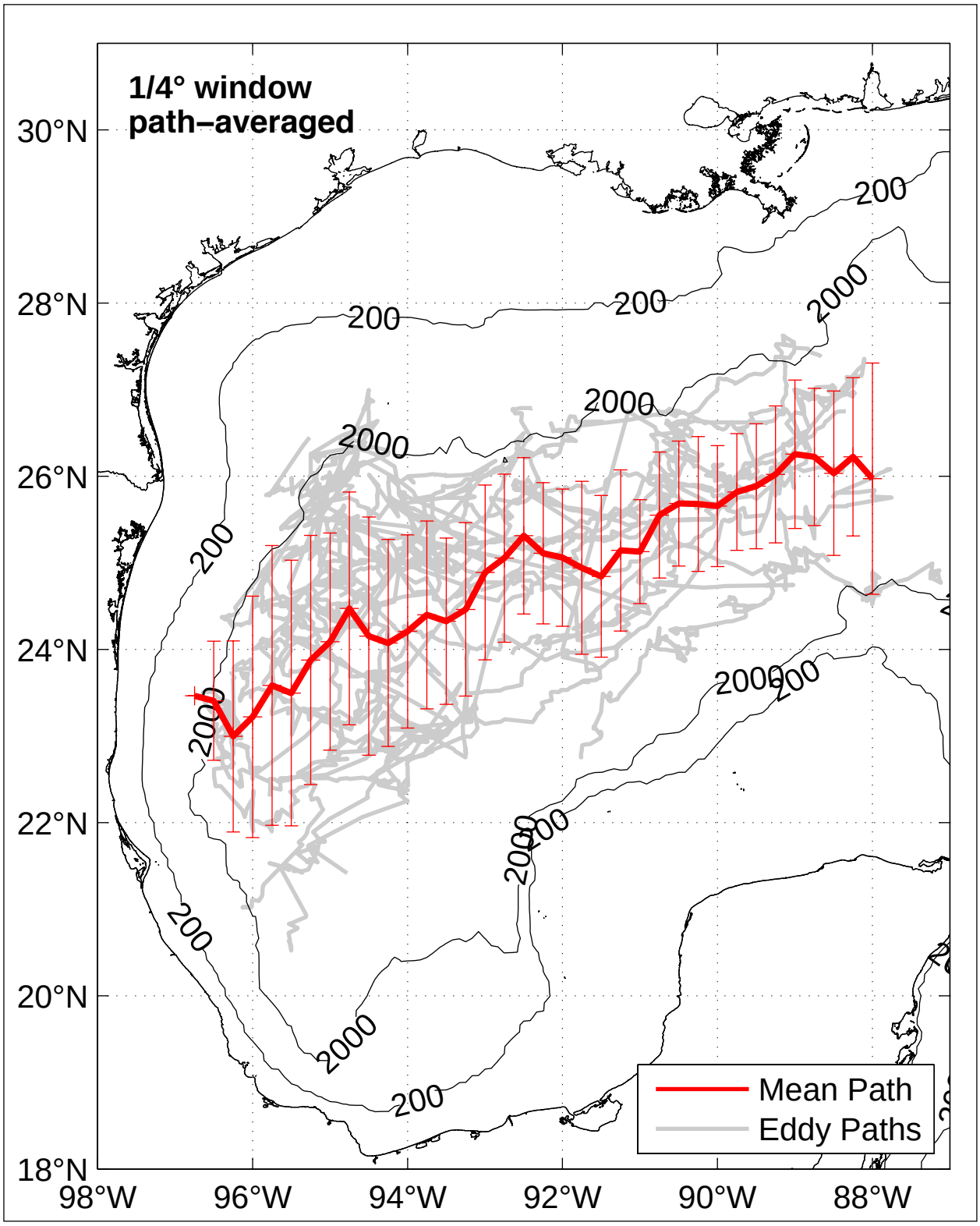

Figure 3.1-14. The ¼° path-averaged mean path overlaid on altimeter-tracked LCE center paths.

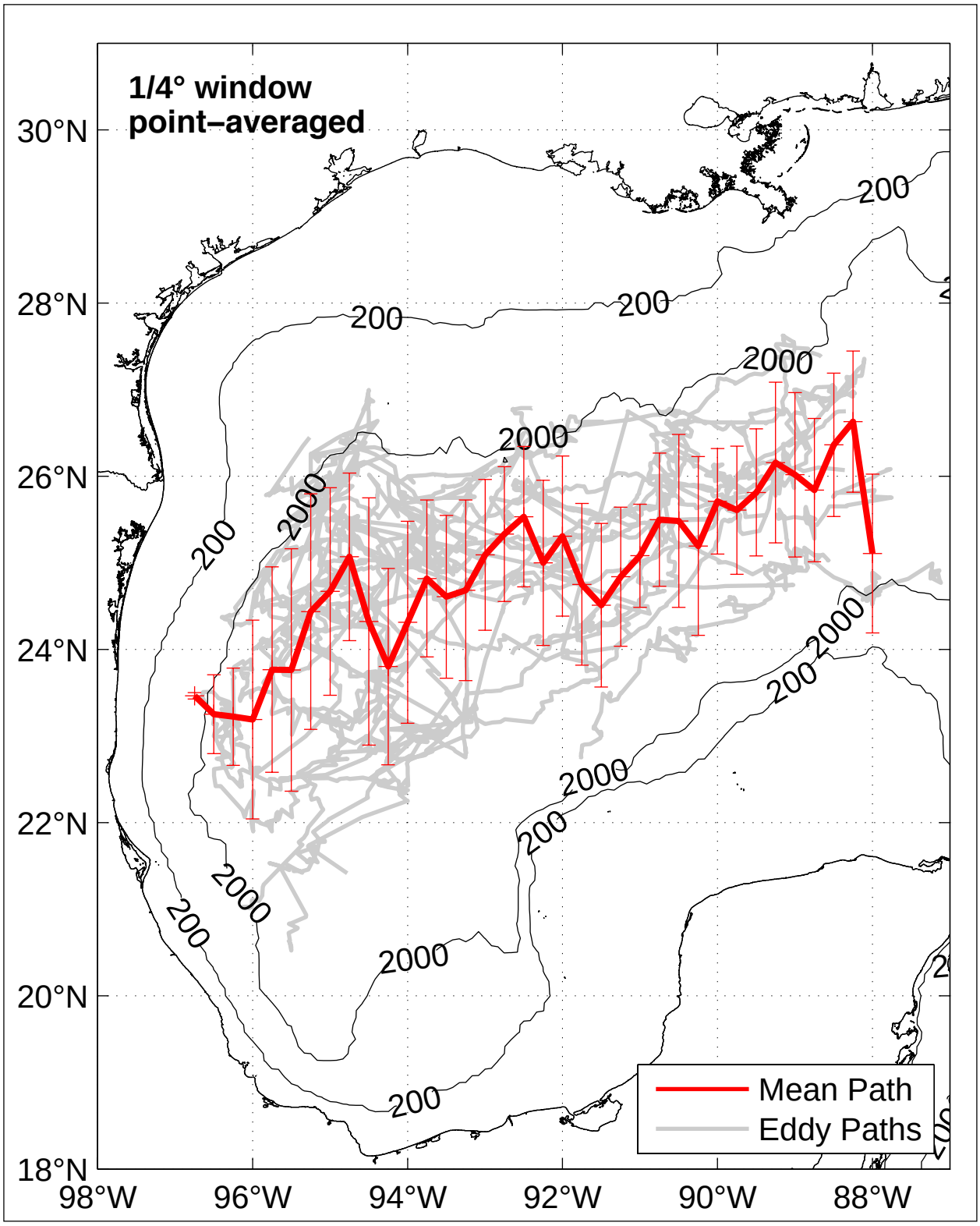

Figure 3.1-15. The ¼° point-averaged mean path overlaid on altimeter-tracked LCE center paths.

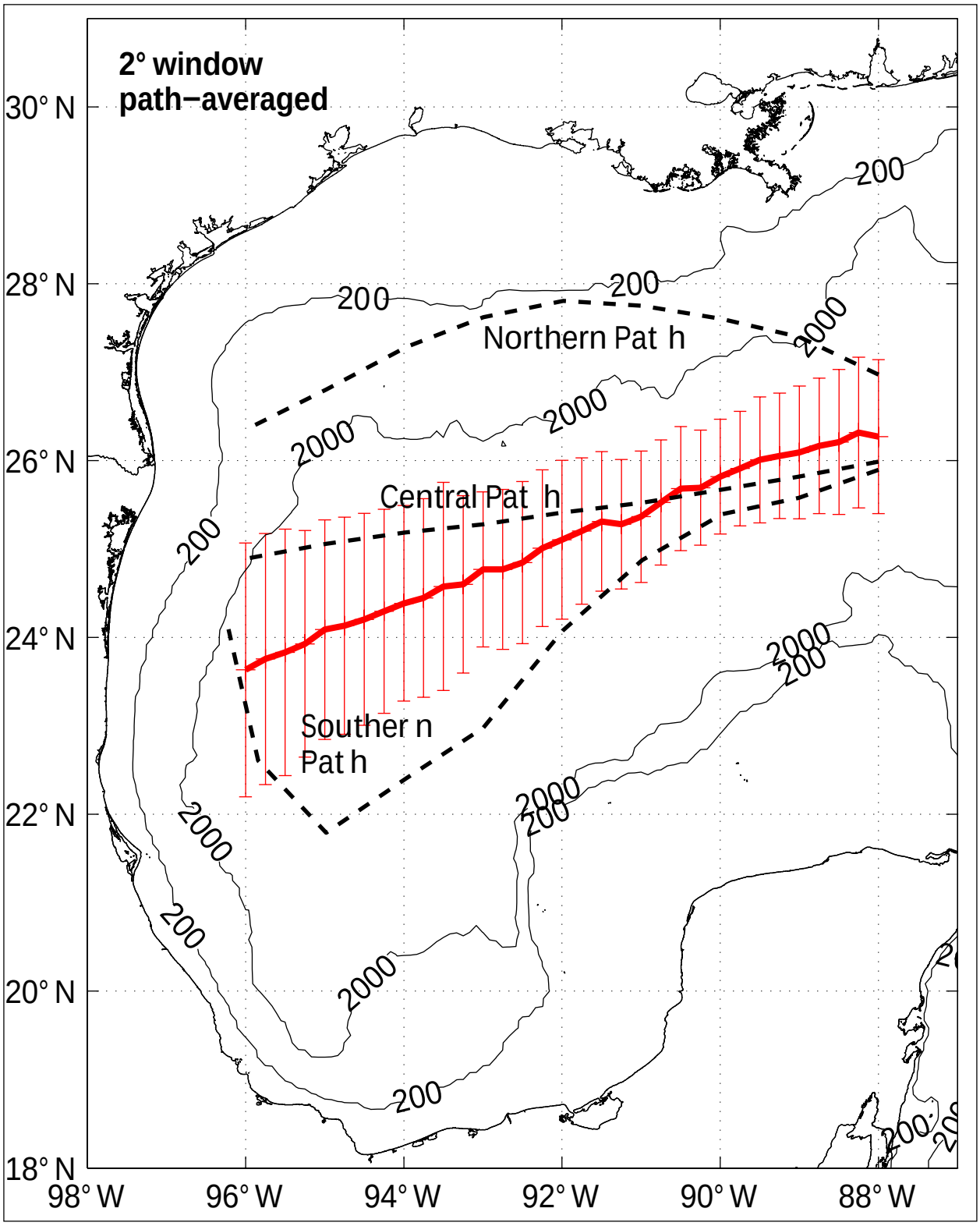

Figure 3.1-16. The 2° path-averaged mean path overlaid with a one standard deviation whisker bar for each averaging window and the three prescribed pathways from Vukovich (2007).

3.1-17, respectively, including a one standard deviation whisker bar for each averaging window. The paths are also shown in Figures 3.1-18 and 3.1-19 overlaid on all of the eddy tracks. Each of the 2° smoothed paths captures a reasonable mean path of LCEs through the western GOM. A comparison of the two mean paths is shown in Figure 3.1-20. The mean paths are both nearly linear and oriented in a west-southwest direction. The approximate directions of the path-averaged and point-averaged means are 242°T and 233°T, respectively. These directions are in very good agreement with the study by Hamilton et al., (1999) that found a direction of 235°T associated with the principal axes of the mean translation of 10 LCEs in the central GOM determined from kinematic analysis of satellite-tracked drifters. Of those 10 LCEs, only two (Whopper and Yucatan) were common to both analyses indicating that the LCE mean path or at least its direction may be a nearly stationary statistic.

The stationarity of the mean path is likely caused by the dynamical influence of planetary β on the propagation of LCEs, which is time independent. Another contributing factor to the stationarity is the restriction of LCE separation to a relatively confined geographic region in the central GOM. In contrast to the mean path, which shows almost no change in the linear trend going westward, the variance of the individual paths about the mean path increases westward. *This is consistent with an eddy field induced "random" walk of LCEs away from the mean path as eddies propagate westward.* Thus, there is a reasonable physical hypothesis for the observed LCE mean pathway and the distribution of the LCE paths around the mean. In contrast, no physical argument has been put forward as to why preferred LCE pathways might exist and why the pathways have changed so much with time (Figure 3.1-8). It should be noted, however, that some numerical model simulations have shown distinct eddy pathways [see, for example, the bimodal pattern of LCE paths shown in Figure 2 of Kantha et al., (2005)]. Nevertheless, the central pathway of Vukovich (2007), which occurs with a frequency of 62%, is better approximated by the mean pathways estimated here, which have 68% of LCE center locations within one standard deviation of the path assuming that the distribution of eddy center locations about the mean is normal.

The mean LCE path is well south of the study region (Figure 3.1-21); nevertheless, four out of the 20 tracked LCEs had eddy center positions that made it into the study region. These were LCEs Xtra Split, Aggie, El Dorado, and Juggernaut Split. The impact of LCEs on the circulation in this region will be discussed in more detail in Section 3.2, where we review the historical altimeter record of anticyclonic and cyclonic eddies that have been observed in the study region. In the next section, we will discuss the altimeter tracking results on the lifespan and ultimate fate of LCEs in the western GOM.

3.1.6 Lifespan and Dissipation of LCEs

Systematic tracking of LCEs throughout their lifespan from separation to dissipation was possible using the continuous sampling provided from satellite altimeters. Continuous tracking with satellite-tracked drifters or satellite radiometry is much more difficult. Tracking of LCEs with satellite-tracked drifters can be complicated by the tendency of drifters to be ejected from the eddy circulation as the eddy decays. This requires a concerted program to reseed drifters into the eddy being tracked, which is very difficult and expensive to accomplish throughout the lifetime of an eddy. Cloud cover and seasonally poor viewing conditions make continuous

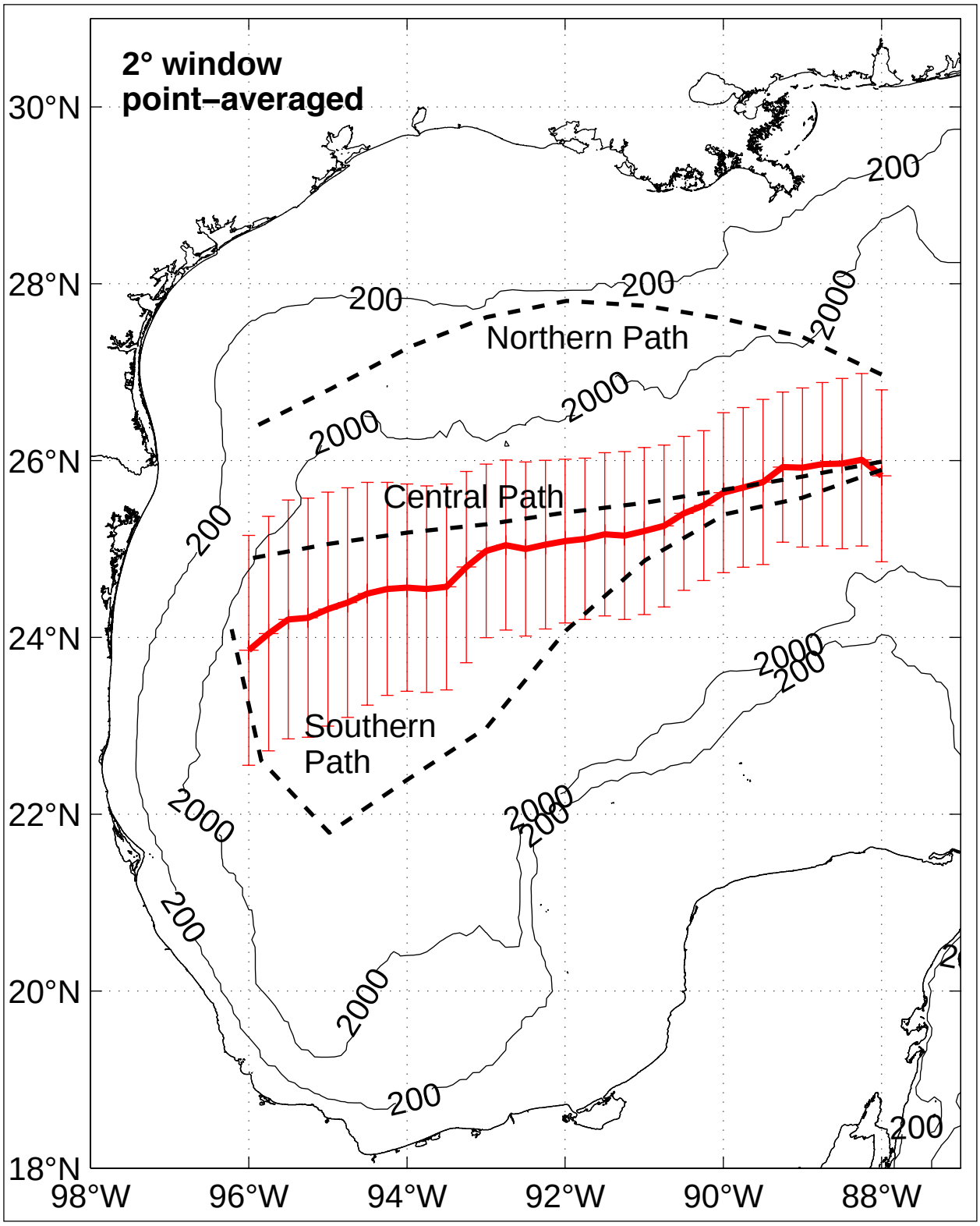

Figure 3.1-17. The 2°point-averaged mean path overlaid with a one standard deviation whisker bar for each averaging window and the three prescribed pathways from Vukovich (2007).

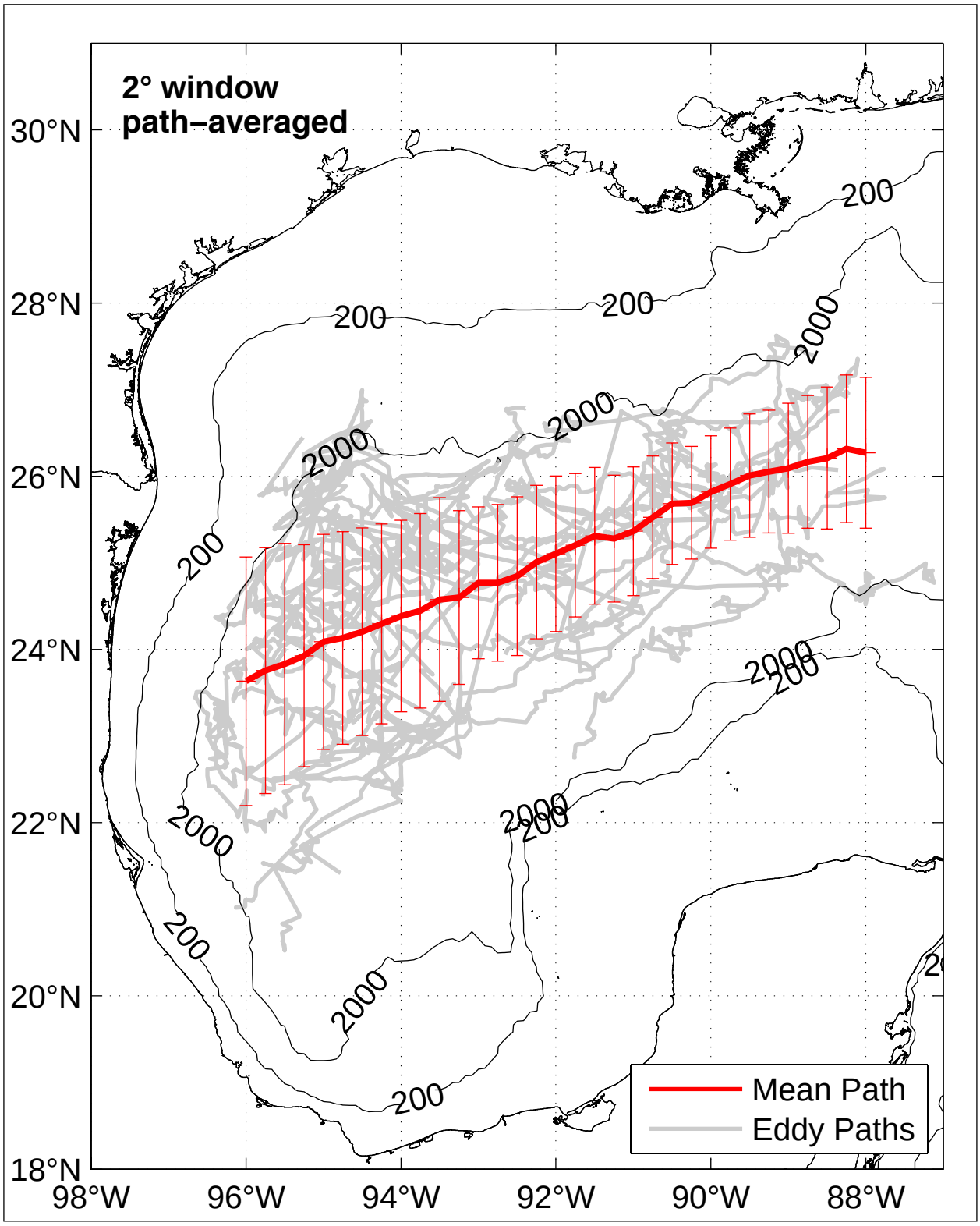

Figure 3.1-18. The 2° path-averaged mean path overlaid on altimeter-tracked LCE center paths.

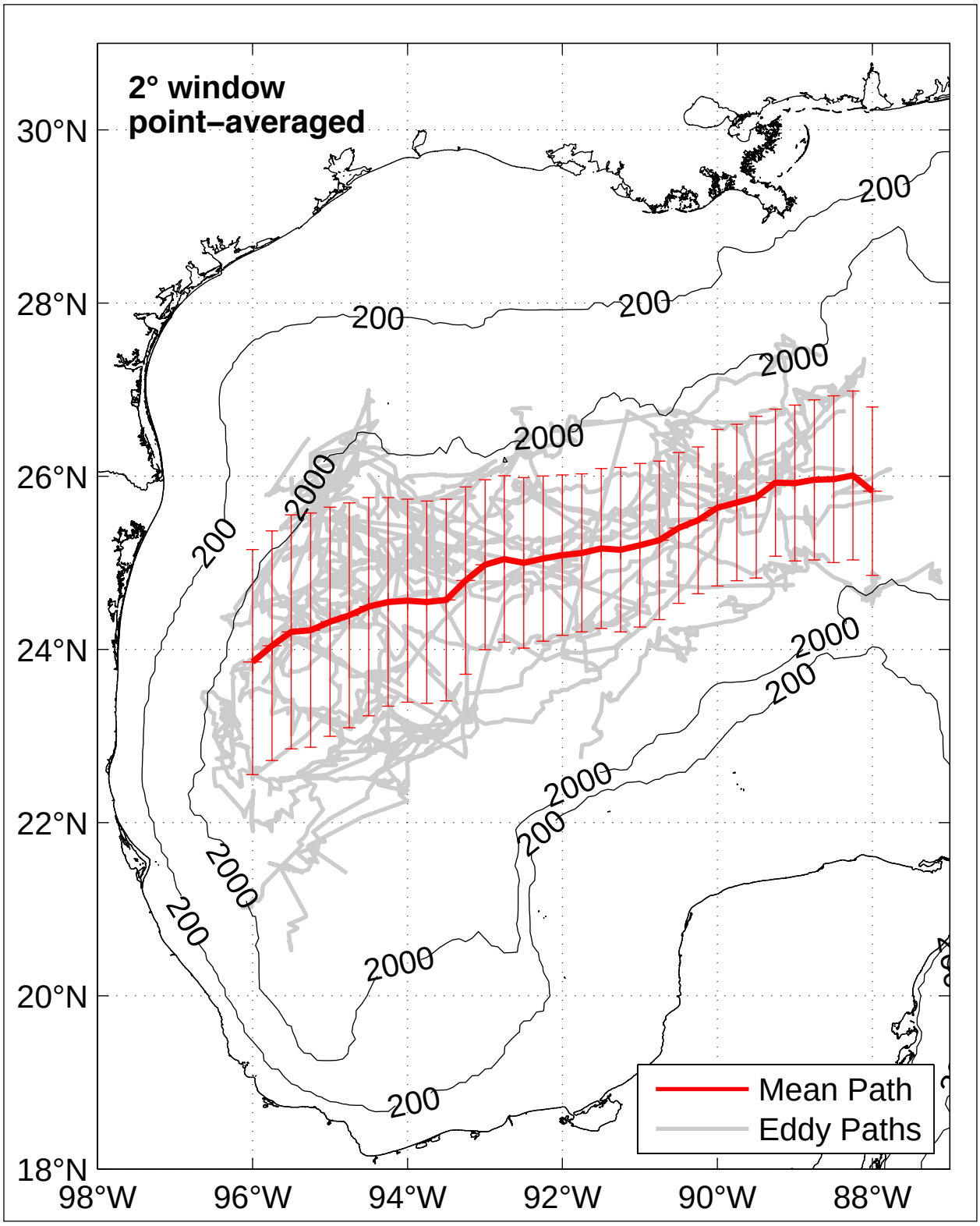

Figure 3.1-19. The 2° point-averaged mean path overlaid on altimeter-tracked LCE center paths.

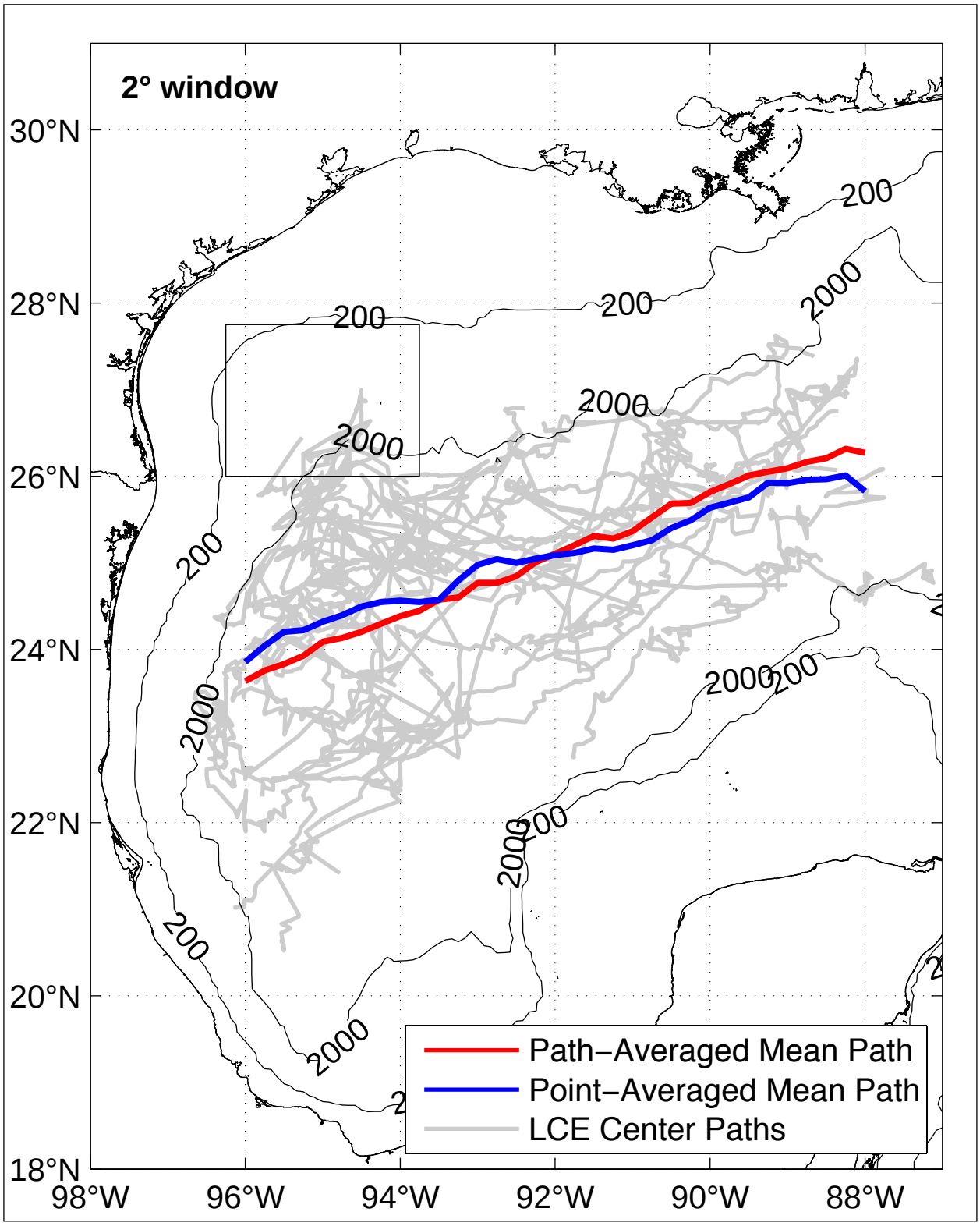

Figure 3.1-20. Path-averaged and point-averaged mean paths (2° averaging window) are shown overlaid on altimeter-tracked LCE center paths. Box identifies NW Gulf study region.

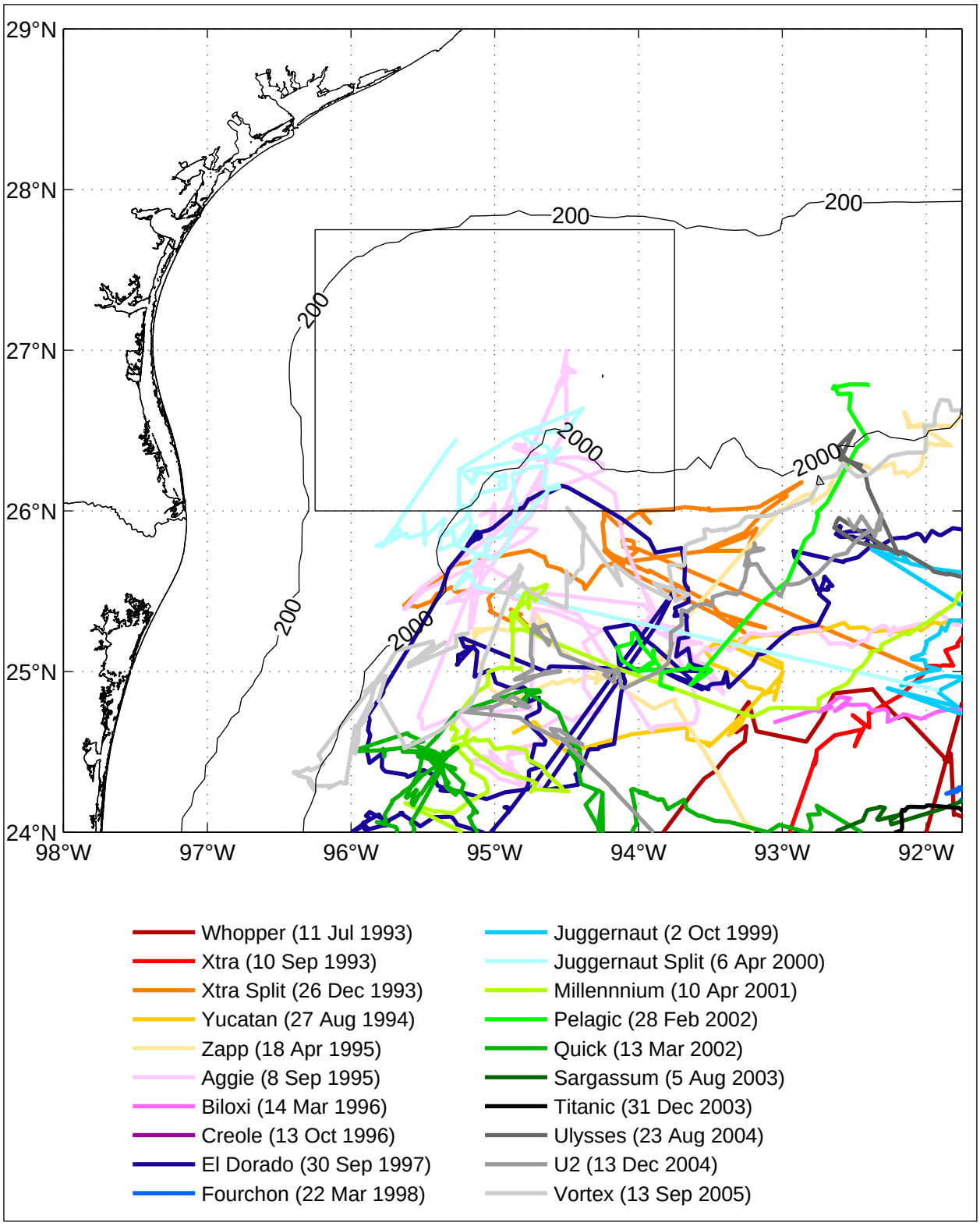

Figure 3.1-21. Altimeter-tracked LCE centers in the northwestern GOM. Box identifies NW Gulf study region. Centers of four LCEs were tracked into the study region: Xtra Split, Aggie, Juggernaut Split, and El Dorado.

tracking with satellite radiometry even more difficult. Thus, altimetric tracking gives the first comprehensive and detailed look at the lifespan and ultimate fate of LCEs in the western GOM.

The individual lifespans of the LCEs are listed in Table 3.1-2. The mean lifespan for the 17 LCE separation events was 284 days, or about 9.5 months. This mean was calculated using the average of the two lifespans quoted for each LCE that split (Xtra, Juggernaut, and Ulysses), so that each of the 17 LCE separation events was weighted equally in the overall average. The longest-lived LCE was El Dorado, which was tracked for over 600 days. The shortest was Pelagic, which merged with Quick within three months after separation. If Pelagic were classified as a minor LCE, because of its relatively short lifetime, the mean LCE lifespan would increase to 296 days.

Table 3.1-2

LCE Separation/Splitting and Lifespan (in days) Statistics from the Altimetric Record: 1 January 1993 through 30 June 2006

Industry Eddy Name	Separation Date	Split Date	Lifespan From Split	Lifespan
Whopper	11 Jul 1993			178
Xtra	10 Sep 1993	26 Dec 1993	81	188
Xtra Split		26 Dec 1993	121	228
Yucatan	27 Aug 1994			216
Zapp	18 Apr 1995			371
Aggie	8 Sep 1995			493
Biloxi	14 Mar 1996			153
Creole	13 Oct 1996			395
El Dorado	30 Sep 1997			601
Fourchon	22 Mar 1998			136
Juggernaut	2 Oct 1999	6 Apr 2000	183	370
Juggernaut Split		6 Apr 2000	200	377
Millennium	10 Apr 2001			333
Pelagic	28 Feb 2002			84
Quick	13 Mar 2002			391
Sargassum	5 Aug 2003			161
Titanic	31 Dec 2003			266
Ulysses	23 Aug 2004	13 Dec 2004	125	237
U2		13 Dec 2004	216	328
Vortex	13 Sep 2005			193
			Mean:	284*

*The overall mean LCE lifespan was calculated using the average of two lifespans quoted for each LCE that split so that each LCE separation event was weighted equally in the average.

A plot of the individual locations on the last day that the LCEs could be tracked is shown in Figure 3.1-22. LCEs were found to dissipate throughout the western GOM west of 91°W, usually with centers in ocean depths greater than 2000 m. Only one eddy (Juggernaut Split) dissipated when an eddy center was in a water depth less than 2000 m. This was also the only eddy to dissipate within the NW Gulf study region. Historically this region has been informally referred to as the "eddy graveyard" (Biggs et al., 1996) because the three characteristic pathways described by Vukovich and Crissman (1986) all led to the northwest corner of the GOM. Numerical ocean model simulations have also contributed to eddy graveyard paradigm (Hurlburt and Thompson, 1982; Sturges et al., 1993; Oey, 1995; Welsh and Inoue, 2002; Kantha et al., 2005) by exhibiting LCE pathways leading to the northwest corner. It should be noted in these

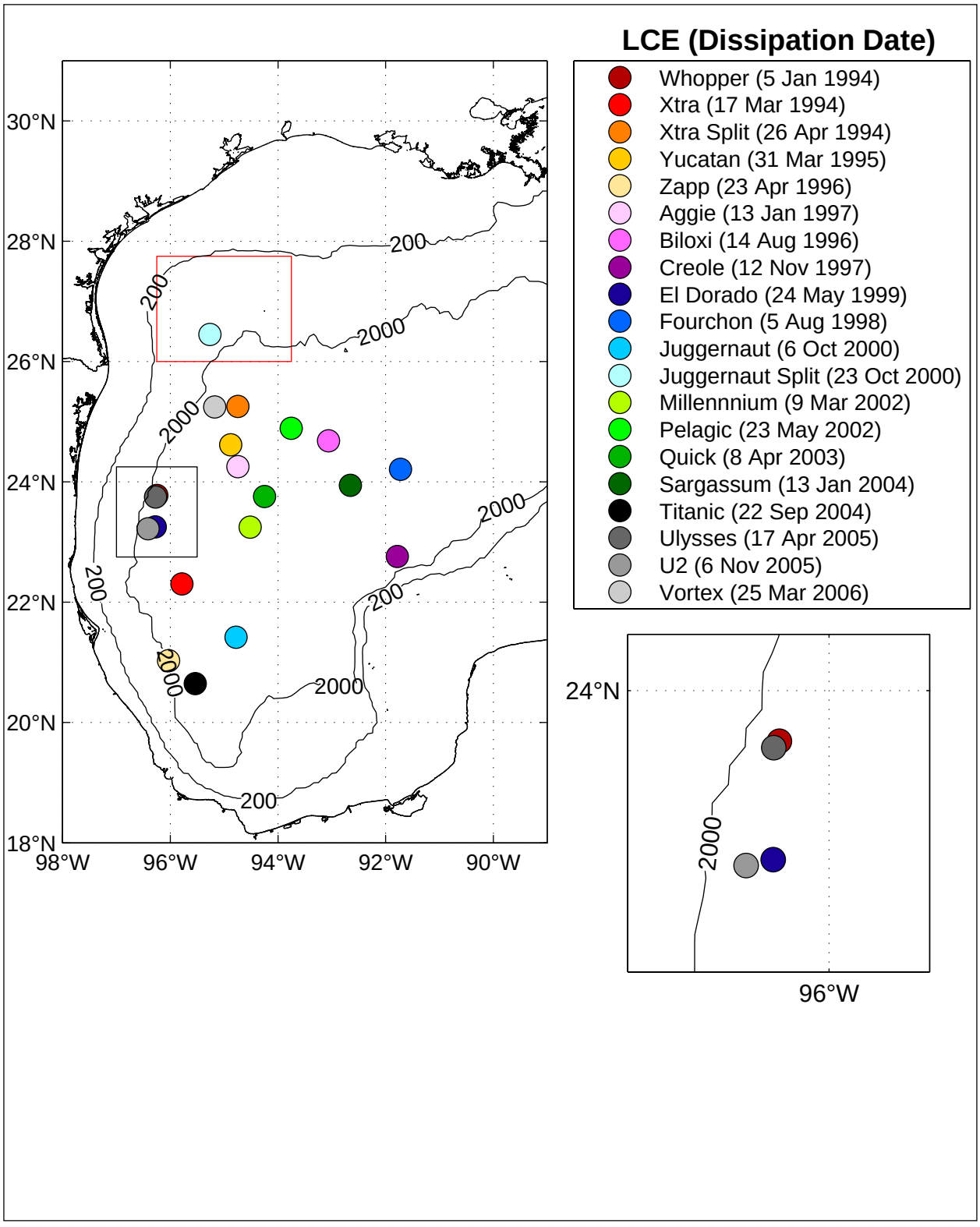

Figure 3.1-22. Plot of the individual LCE locations on the last day that each eddy could be tracked. Inset black box is close-up of final locations of Whooper, El Dorado, Ulysses, and U2. Red box identifies NW Gulf study region.

model simulations that the northward propagation along the western continental margin leading to the eddy graveyard from more southerly LCE paths is primarily caused by an image or wall effect. This effect plays a less significant role in recent numerical simulations using more realistic topography and physics where LCEs do not come into close enough contact with the boundary to feel the presence of the vertical wall (Frolov et al., 2004). In agreement with that modeling study, observational studies support the idea that the image or wall effect is not the dominant controlling mechanism on propagation because *no preferred direction has been observed in LCE trajectories along the western margin* (Hamilton et al., 1999; Vukovich, 2007). Altimeter tracking of LCE eddies from the time they first came within 100 km of the 2000 m isobath along the western margin until they ultimately dissipated also confirms these findings. North/south displacements of the 14 LCEs that reached the western wall ranged from 430 km southward to 230 km northward; however, the overall mean displacement was 75 km to the south, which is opposite to the direction that would be induced by the image or wall effect. A total of four LCEs moved north and ten moved south upon approaching the western margin.

3.1.7 Altimeter Record of Anticyclonic and Cyclonic Eddies in the Study Region

Although the NW Gulf study region is clearly not a LCE graveyard, this area of the northwestern GOM continental slope is nevertheless an eddy-rich region exhibiting strong eddy circulation down to scales smaller than the Rossby radius of deformation (Hamilton, 2007). A key question is whether this eddy variability is caused by the LC/LCEs, or is locally generated eddy variability originating on the continental slope.

To assess the most energetic events in the altimeter record, we extracted the SSH extrema within the study region defined by the bounding box from 26°N to 27.25°N and 96.25°W to 93.75°W. The time series of the maximum SSH within this region is shown in the upper panel of Figure 3.1-23. Six well-defined local maximums are identified in the time series, and the corresponding SSH maps are shown in the lower panels. Each of the local maxima in SSH in the region is associated with anticyclonic circulation that is intruding into the study region. In two cases, a center of circulation exists within the region so that the local SSH maximum is also located within the study region. In the other four cases, the SSH maximum is on the deepwater boundary of the study region and associated with anticyclonic circulation partially intruding into the region. Figure 3.1-24 shows a larger area perspective of the region for each of the six cases. In all cases, a large anticyclone produced the local maximum in SSH in the study region, and each of these anticyclones could be identified as a LCE. Each of the corresponding LCEs is labeled in Figure 3.1-24. Three of these LCEs – Aggie, El Dorado, and Juggernaut Split – had eddy centers that were tracked through the study region. The strongest maximum SSH event in the study region was associated with El Dorado, although the maximum did not occur when the eddy center was within the region. Two LCEs, Ulysses and Vortex, caused strong circulation within the study region during the program time period and will be discussed when we review those events in Section 3.2.

The time series of minimum SSH within the study region is shown in the upper panel of Figure 3.1-25. The six lowest SSH minimums are identified in the time series, and the corresponding SSH maps for those dates are shown in the lower panels. Each of the SSH local minima is associated with cyclonic circulation that is primarily contained within the study region. The

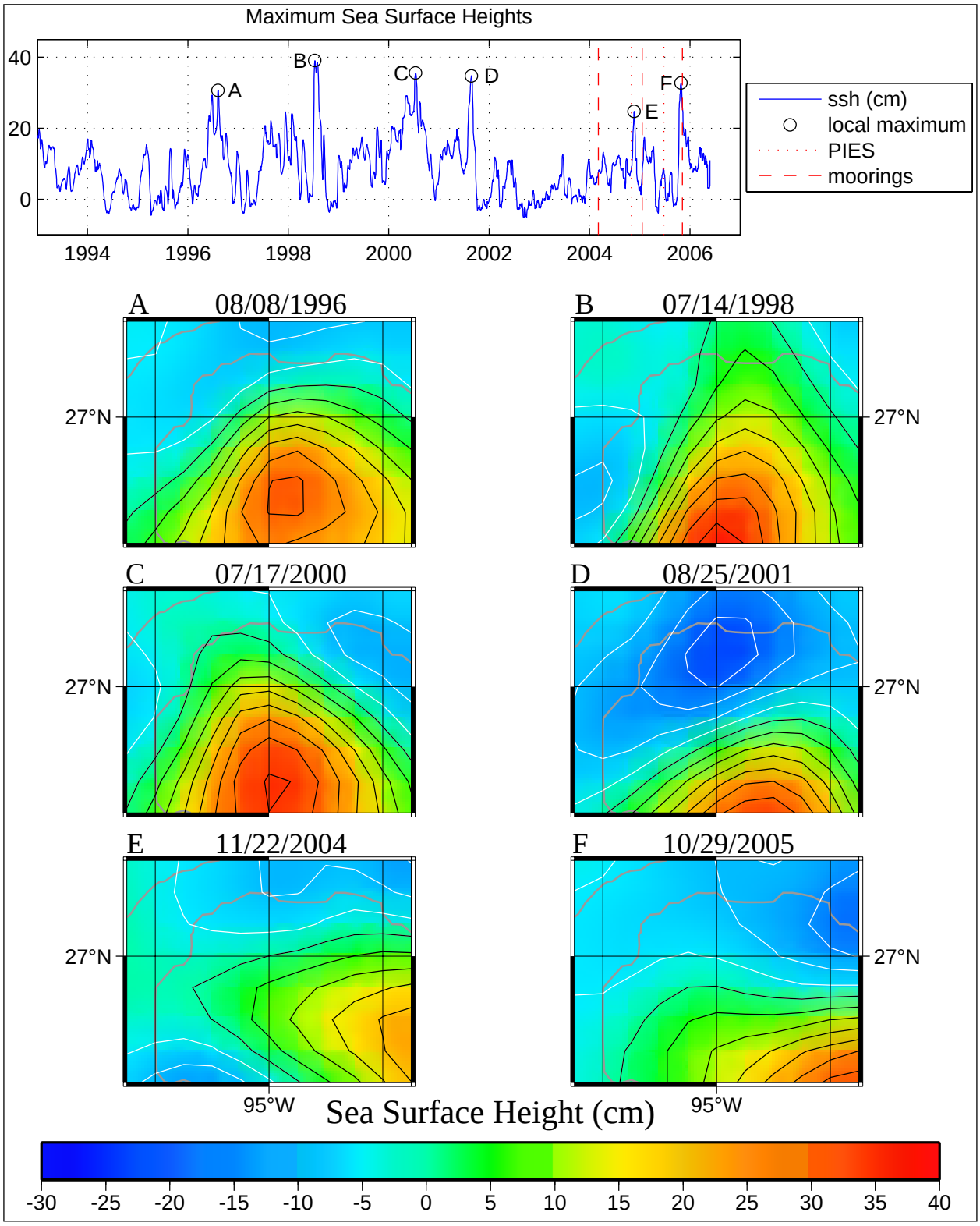

Figure 3.1-23. Time series of the maximum SSH within the NW Gulf study is shown in the upper panel. The local maximums are identified and the corresponding SSH maps are shown in the lower panels.

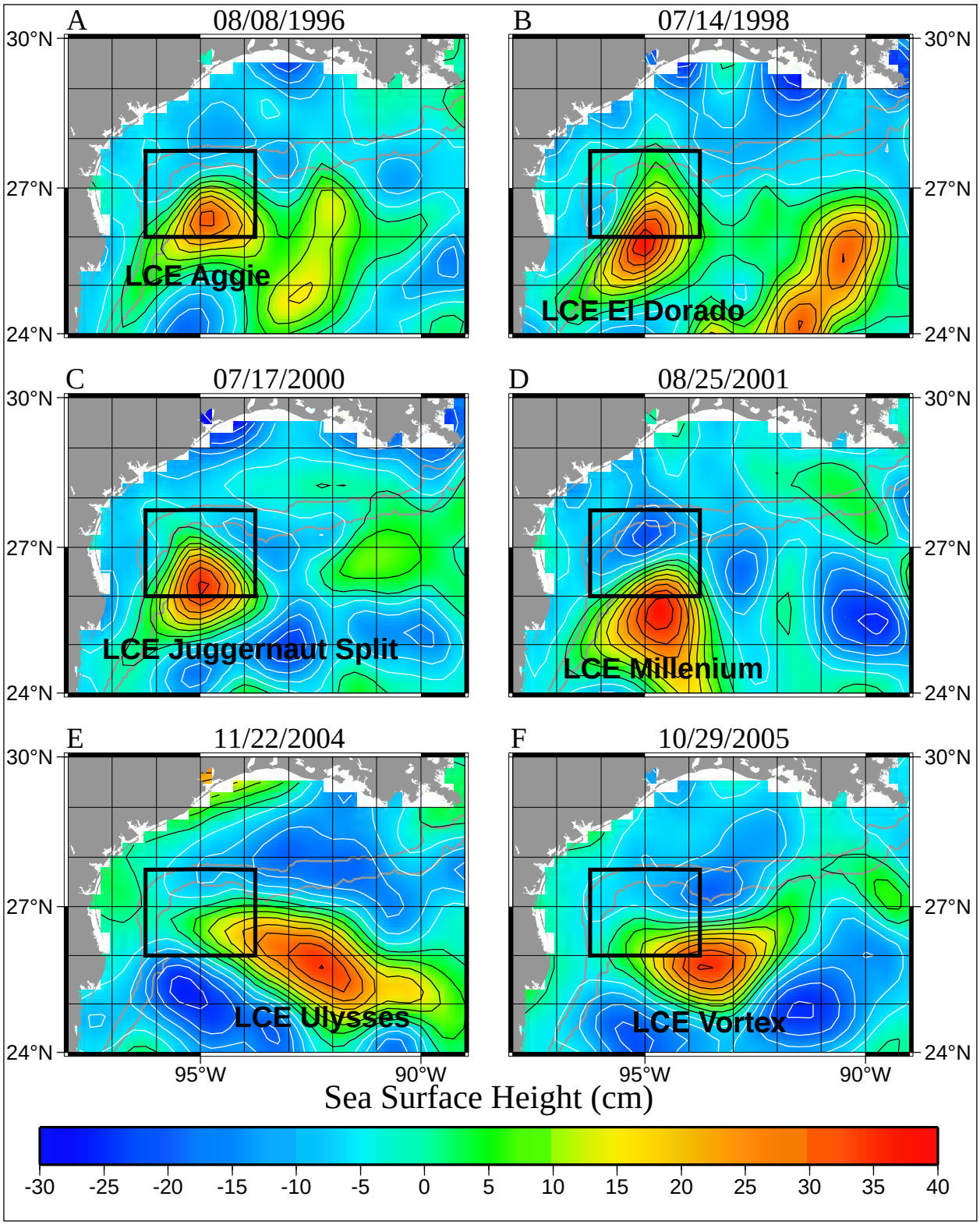

Figure 3.1-24. Larger area perspective of the six anticyclonic event maps shown in Figure 3.1-23. Each of these events is associated with an LCE, and the individual LCE is identified on each map.

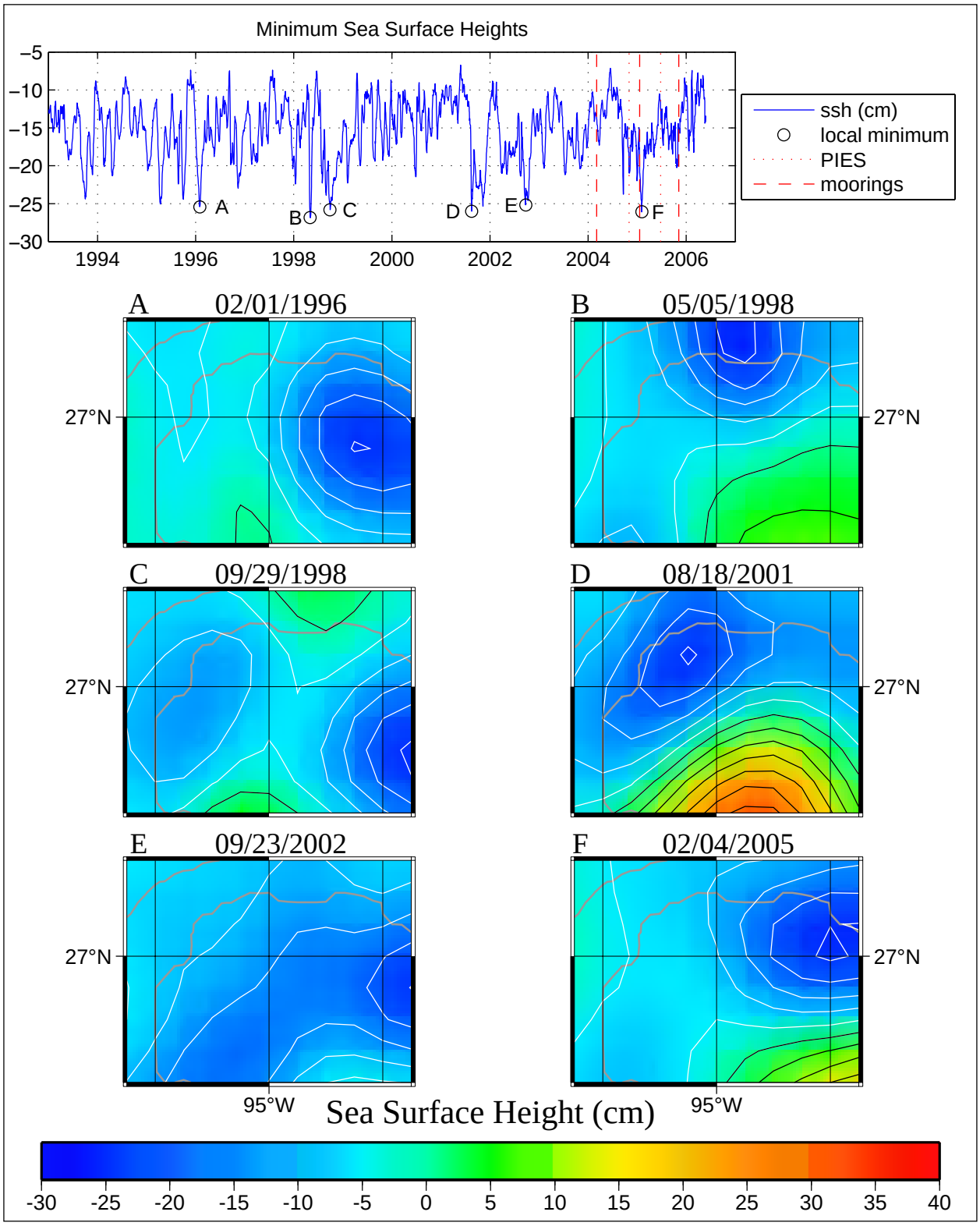

Figure 3.1-25. Time series of the minimum SSH within the NW Gulf study is shown in the upper panel. The local minimums are identified and the corresponding SSH maps are shown in the lower panels.

larger area perspective of each event (Figure 3.1-26) shows that these local minima are associated with cyclonic eddies that are companions of larger anticyclonic eddies adjacent to the study region. Each of these anticyclonic eddies can be identified as LCEs. In most cases, the cyclonic eddies moved into the study region as companions of the westward propagating LCEs. The one clear exception was event D, which was a cyclone that formed within the region as LCE Millennium arrived at and interacted with the western continental slope margin directly south of the study area. Event B also appeared to form on the northern upper slope within the study region as El Dorado reintruded into the region for a second time after first arriving in the far western GOM.

The primary conclusion of this review is that the most energetic anticyclonic and cyclonic events in the historical record are all associated with LCEs. Thus, the LC is a dominant source of eddy energy even as far away as the continental slope in the extreme northwestern corner of the GOM. The LC influence is indirect and caused by the propagation of LCEs into the western GOM, and in some cases propagation into the study region. The LC may not only influence the intensity of the eddy field, but also the number of cyclonic eddies. The kinematic analysis of Surface Current and Lagrangian-drift Program (SCULP) drifter tracks by Hamilton (2007) suggests a possible link between the LC and the number of cyclonic eddies along the northern continental slope through the influence of propagating LCEs. Thus, there is good observational evidence that eddy activity in the NW Gulf study region is related to the LC and LCE shedding cycle.

3.2 Gulf-Wide Conditions during the NW Gulf Program from a Remote Sensing Perspective

The review of the GOM altimetry record in the preceding section found that the LC has a significant impact on the intensity of anticyclonic and cyclonic mesoscale circulation in the study region through the propagation of LCEs into the western GOM. Three LCE separation events, Titanic, Ulysses, and Vortex, affected the upper ocean circulation in the western GOM during the program time period from March 2004 through October 2005. The upper-ocean heat content associated with these LC events also contributed to the very active and destructive GOM hurricane seasons in 2004 and 2005. In this section, we review these events from a Gulf-wide perspective using remote sensing data.

3.2.1 LCE Titanic

Titanic separated from the LC on 31 Dec 2003 based on the breaking of the LC tracking contour, which is defined as the 17-cm contour associated with the LC in the CCAR SSH maps. The time of separation was corroborated by coincident SST imagery (Donohue et al., 2006). The path of Titanic through the western GOM relative to all LCE paths determined from the historical altimetric record is shown in Figure 3.2-1. Titanic's path was one of the most southerly eddy center paths tracked, and the position where the eddy dissipated along the western GOM continental slope was located the furthest south.

Titanic had reached the western GOM continental slope by mid-August 2004, but was well south of the NW Gulf study region. The location of Titanic on 22 Aug 2004 is identified in the map of SSH anomaly shown in the upper panel of Figure 3.2-2. Although the eddy center location is

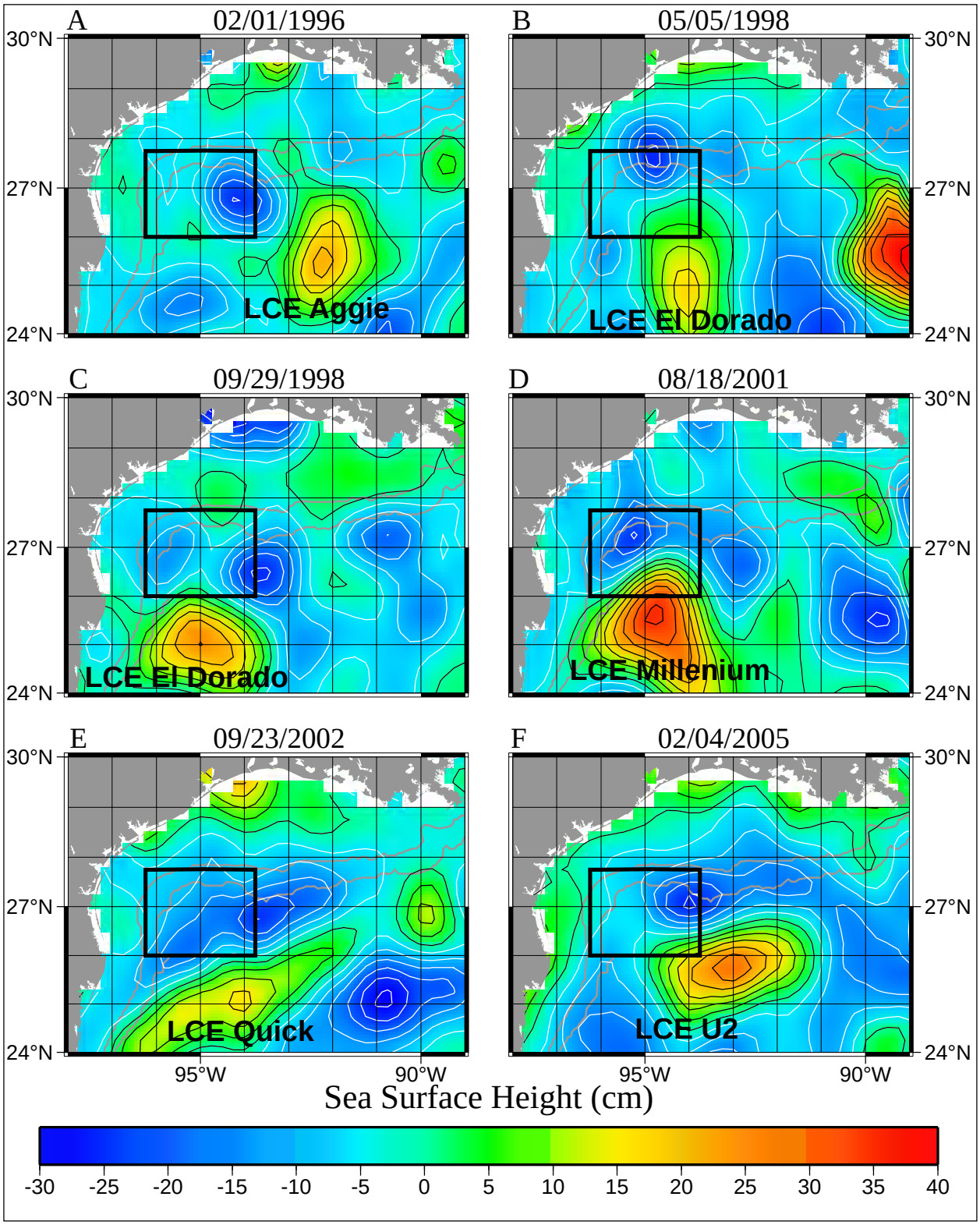

Figure 3.1-26. Larger area perspective of the six cyclonic event maps shown in Figure 3.1-25. Each of these events is associated with an LCE, and the individual LCE is identified on each map.

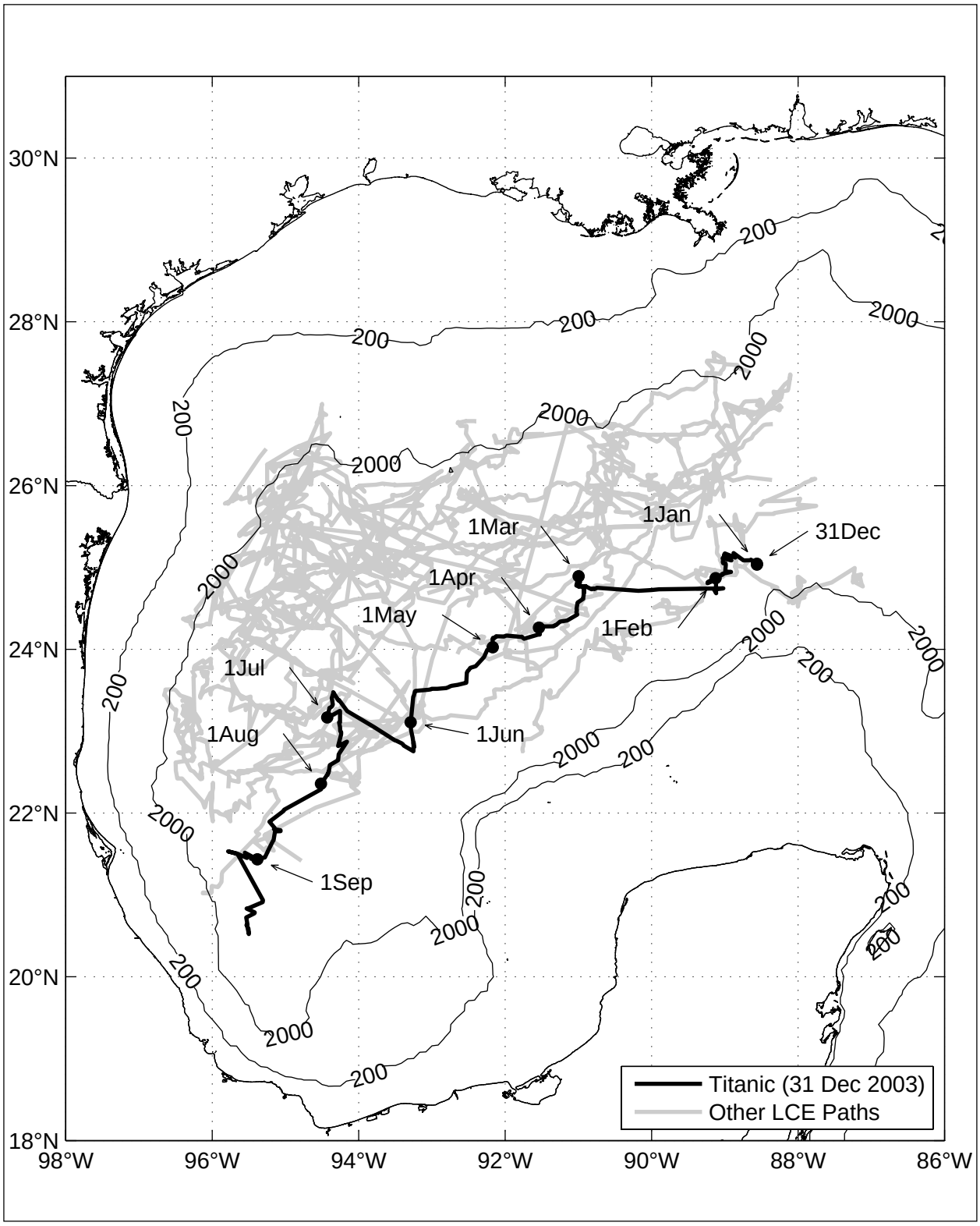

Figure 3.2-1. LCE Titanic eddy center path overlaid on all altimeter-tracked LCE paths. Titanic separated on 31 Dec 2003 and dissipated on 22 Sep 2004. Arrows show positions of the eddy centers on the first of each month.

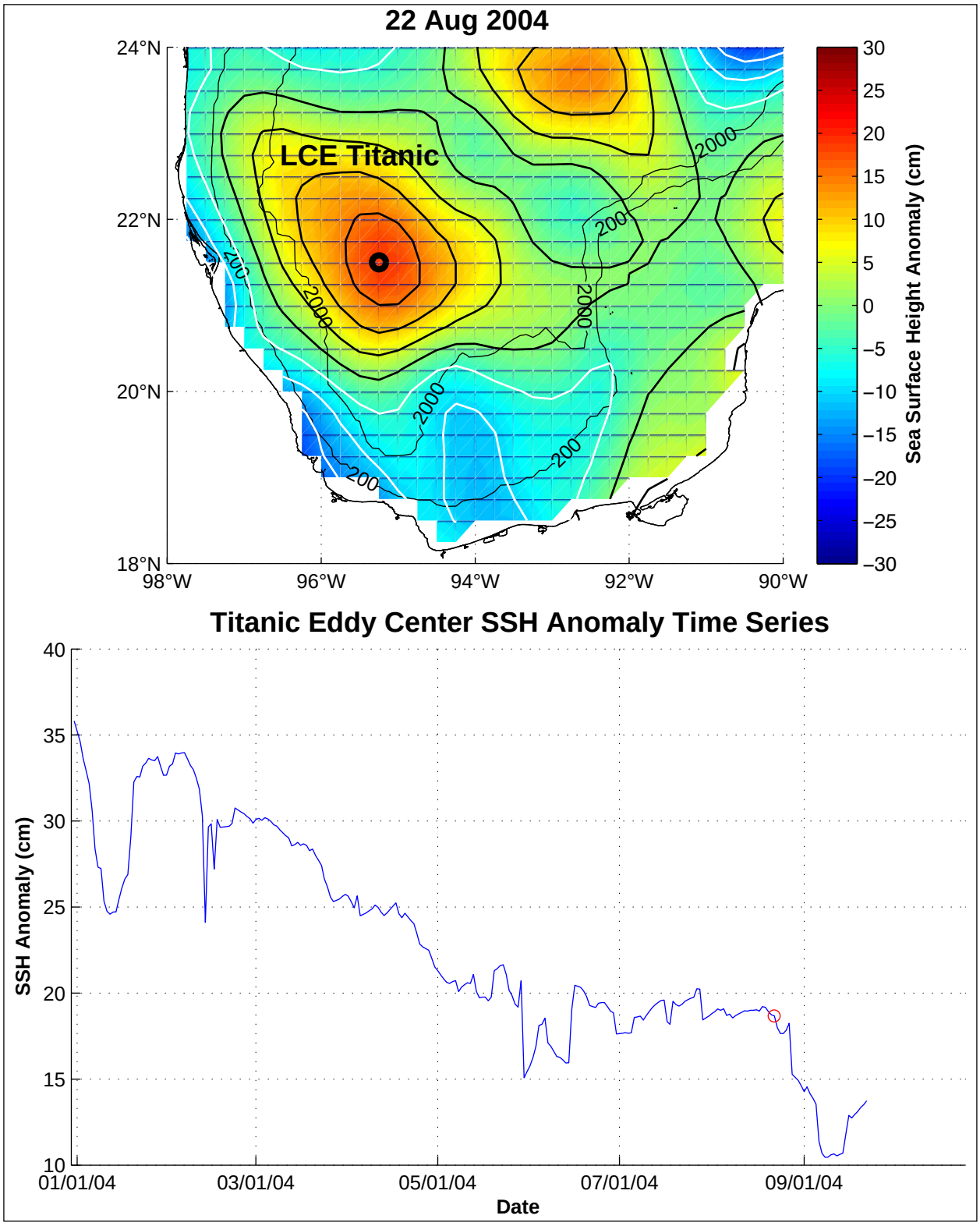

Figure 3.2-2. SSH map of LCE Titanic on 22 Aug 2004 (upper panel) and maximum eddy center SSH anomaly time series (lower panel). The position of the maximum SSH is shown by the black circle and the corresponding day by the red circle.

100 km from the base of the slope, the westernmost SSH anomaly contours associated with Titanic extended well over the continental slope. Once the eddy came into contact with the continental slope, the dissipation of the eddy was very rapid as seen in the time series of the maximum eddy center SSH anomaly shown in the lower panel of Figure 3.2-2. Titanic's decay took about one month, which is more rapid than the approximately 70-day e-folding timescale found by Sturges (1993) for eddy decay at the GOM western boundary. The quickness of Titanic's decay was probably caused by its energetic interaction with the western wall and the loss of fluid to the north along the continental slope resulting in a minor splitting event. Although tracking remnants of LCEs at the western margin is difficult, a portion of Titanic appears to have moved northward along the continental slope away from the primary piece that was tracked to the south. This circulation possibly reached the southernmost mooring in Mexican waters (see color image from 23 Sep 2004 shown in Figure 3.1-2) where it eventually dissipated. Nevertheless, there is no evidence that the induced circulation associated with LCE Titanic and its interaction with the GOM western margin impacted the NW Gulf study region.

3.2.2 LCE Ulysses

The single strongest LC event to affect the study region during the program time period was Ulysses. Ulysses separated from the LC on 23 Aug 2004 (Figure 3.2-3) and at the time of separation was the second largest LCE in terms of area covered of the 20 LCEs observed in the altimeter record. After remaining relatively stationary in the north-central GOM for just over a month, the eddy moved southward away from the continental slope and then propagated nearly westward through the northern GOM deep basin during October and November to arrive in the western GOM. The path of the altimeter-tracked eddy center is shown in Figure 3.2-4.

In mid-October as the eddy propagated westward past 90°W, Ulysses merged with an anticyclonic eddy that was located near 26°N, 93°W. The merging event was completed by mid-November. The SSH maps before and after the merging event are shown in Figure 3.2-5. Around this time, the circulation of Ulysses and/or the anticyclone that Ulysses merged with first began to directly influence the NW Gulf study region. Soon thereafter, Ulysses split in two. The SSH maps before and after the Ulysses splitting event are shown in Figure 3.2-6. The northernmost piece of Ulysses, which was named U2 by Eddywatch™ after the splitting event, continued to move into the program measurement array in the far northwestern corner of the GOM deepwater basin in late November 2004. The entire splitting process took just about two months and occurred as Ulysses collided with a strong cyclonic eddy located against the western GOM continental slope at 25°N. The sequence of SSH maps over the two-month time period centered on the nominal split date of 13 Dec 2004 is shown in Figures 3.2-7 and 3.2-8. Detailed observations of large eddy splitting events are relatively rare. Only one other splitting of a LCE by a deepwater cyclonic eddy in the western Gulf has been reported (Biggs et al., 1996).

Eddy U2 continued to influence the circulation in and around the study area until April 2005 when it merged with what remained of Ulysses. By the end of May, the reorganized anticyclonic eddy propagated east and south out of the study region as it was pinched between strong cyclonic circulation on both of its southern and eastern margins. The composite path of the northern-most piece of LCE Ulysses/U2 is shown in Figure 3.2-9. The influence of the LCE Ulysses/U2 and its interaction with the ambient eddy field significantly affected the circulation in the study region.

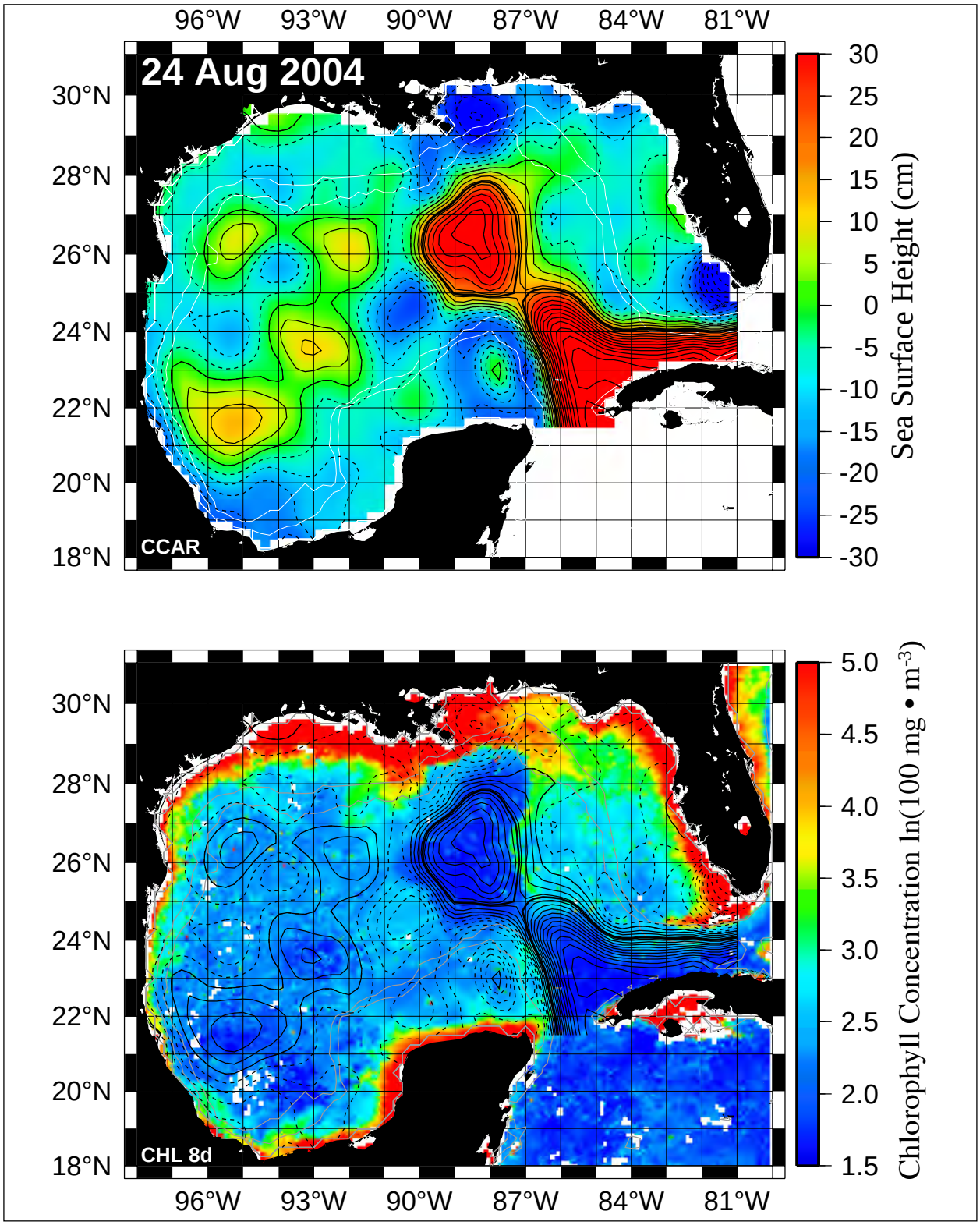

Figure 3.2-3. SSH map (upper panel) and 8-day composite color image (lower panel) show separation of LCE Ulysses on 24 Aug 2004. The 8-day composite image is from the time period from August 17th through 24th.

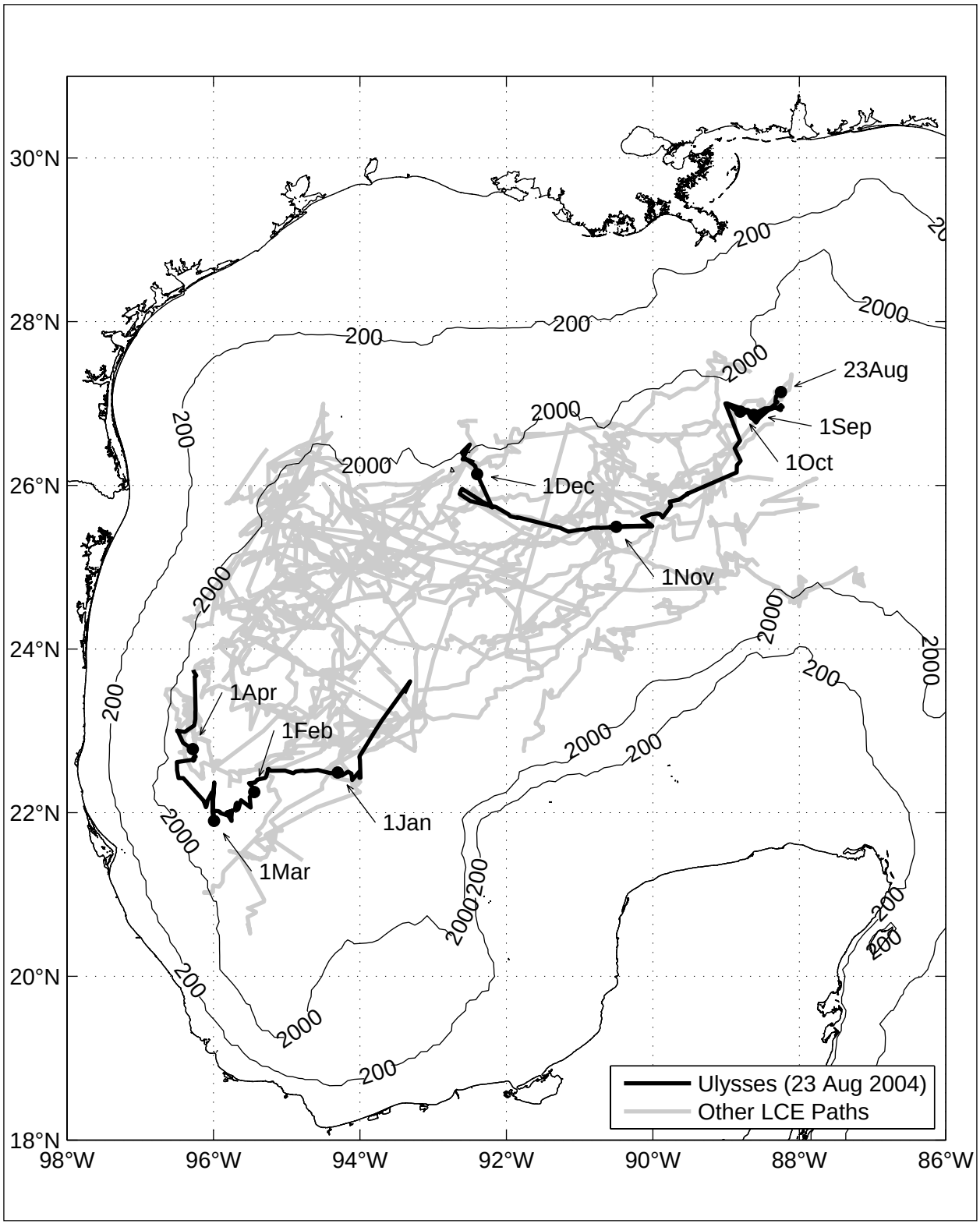

Figure 3.2-4. LCE Ulysses eddy center path overlaid on all altimeter-tracked LCE paths. Ulysses separated on 23 Aug 2004 and dissipated on 17 Apr 2005. The Ulysses/U2 splitting event caused the large displacement of the eddy center path.

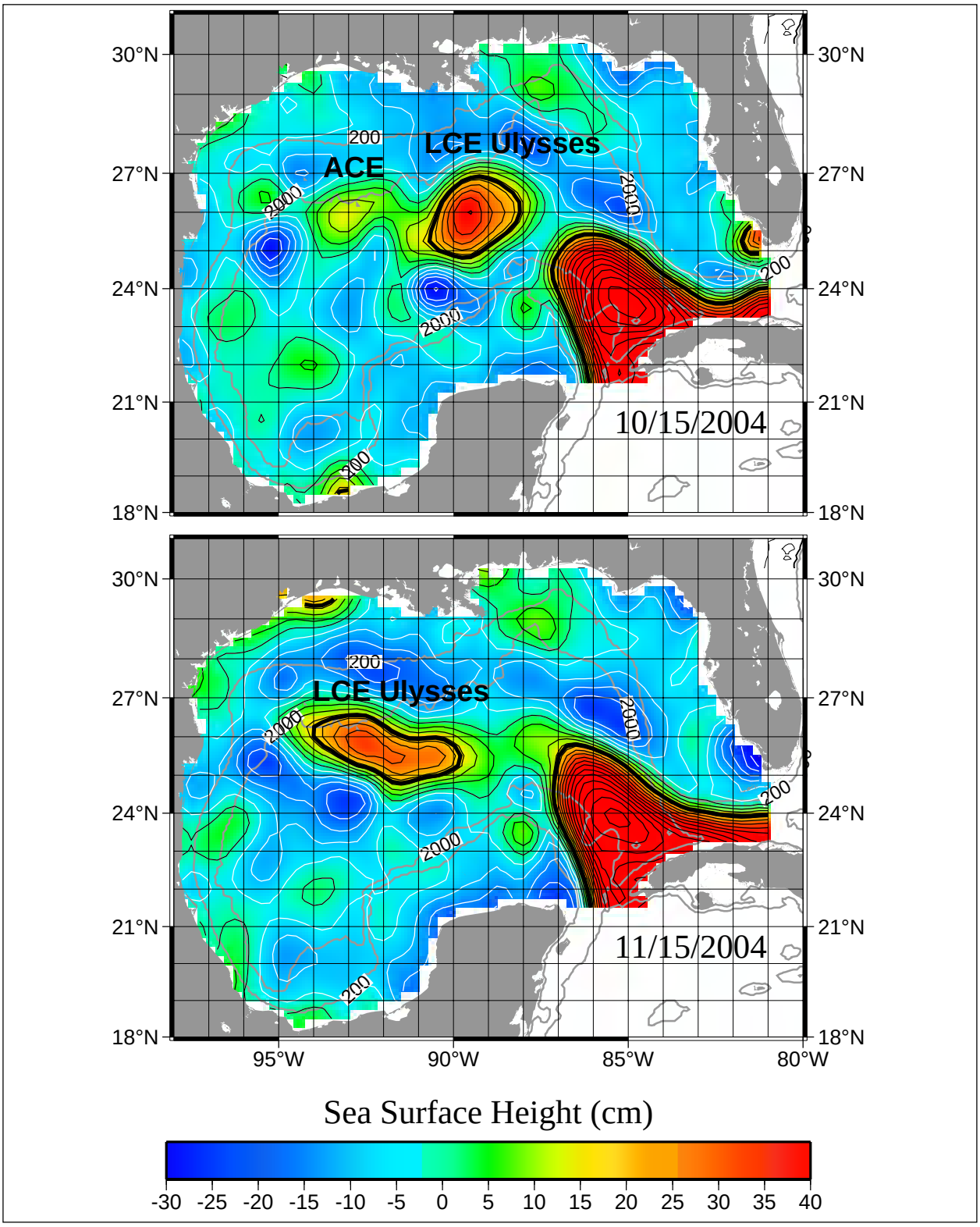

Figure 3.2-5. SSH maps of LCE Ulysses before (upper panel) and after (lower panel) merging with an anticyclonic eddy in the western GOM.

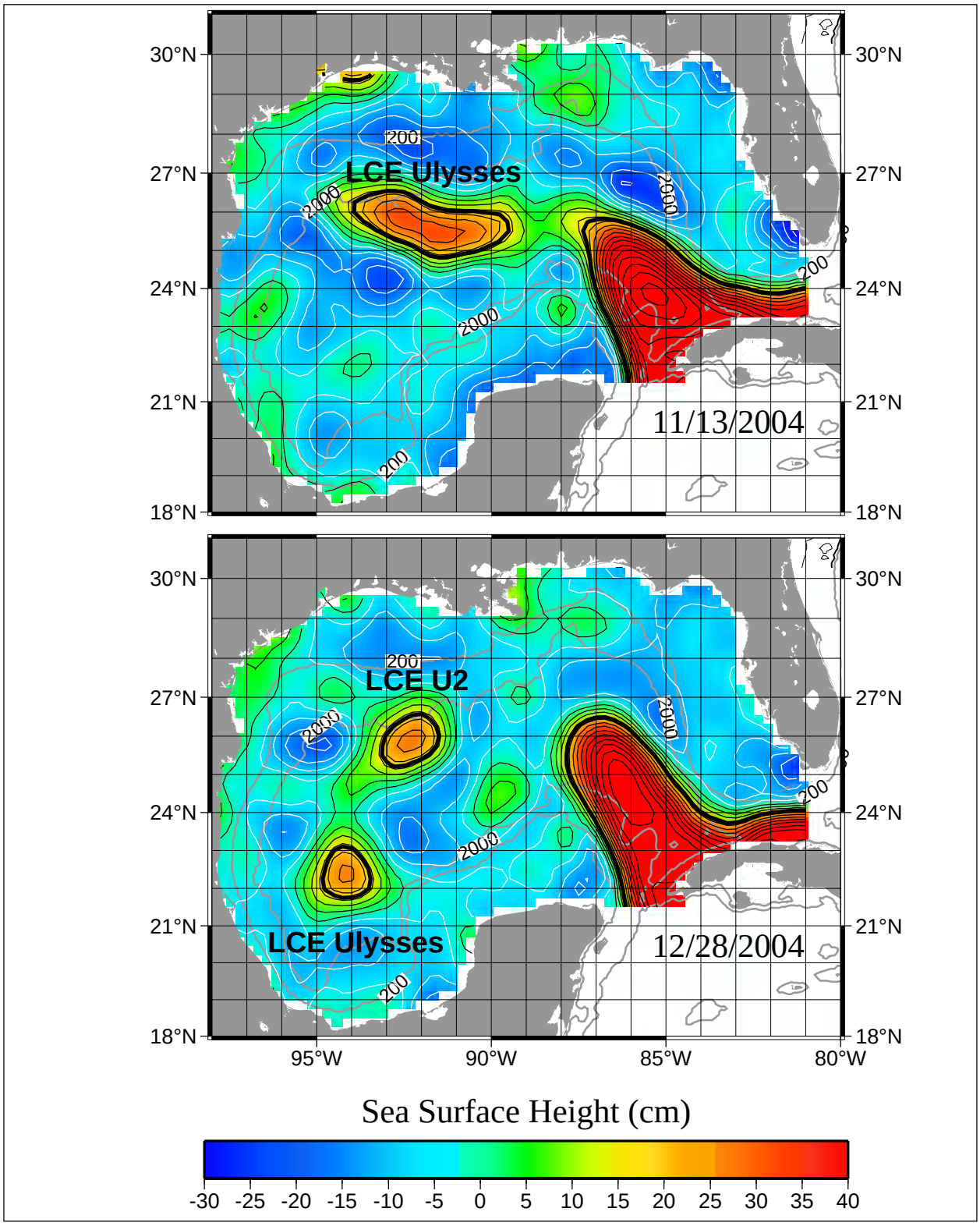

Figure 3.2-6. SSH maps of LCEs Ulysses/U2 before (upper panel) and after splitting (lower panel). EddyWatch gave the names U2 and Ulysses, respectively, to the northern and southern eddies after the splitting event.

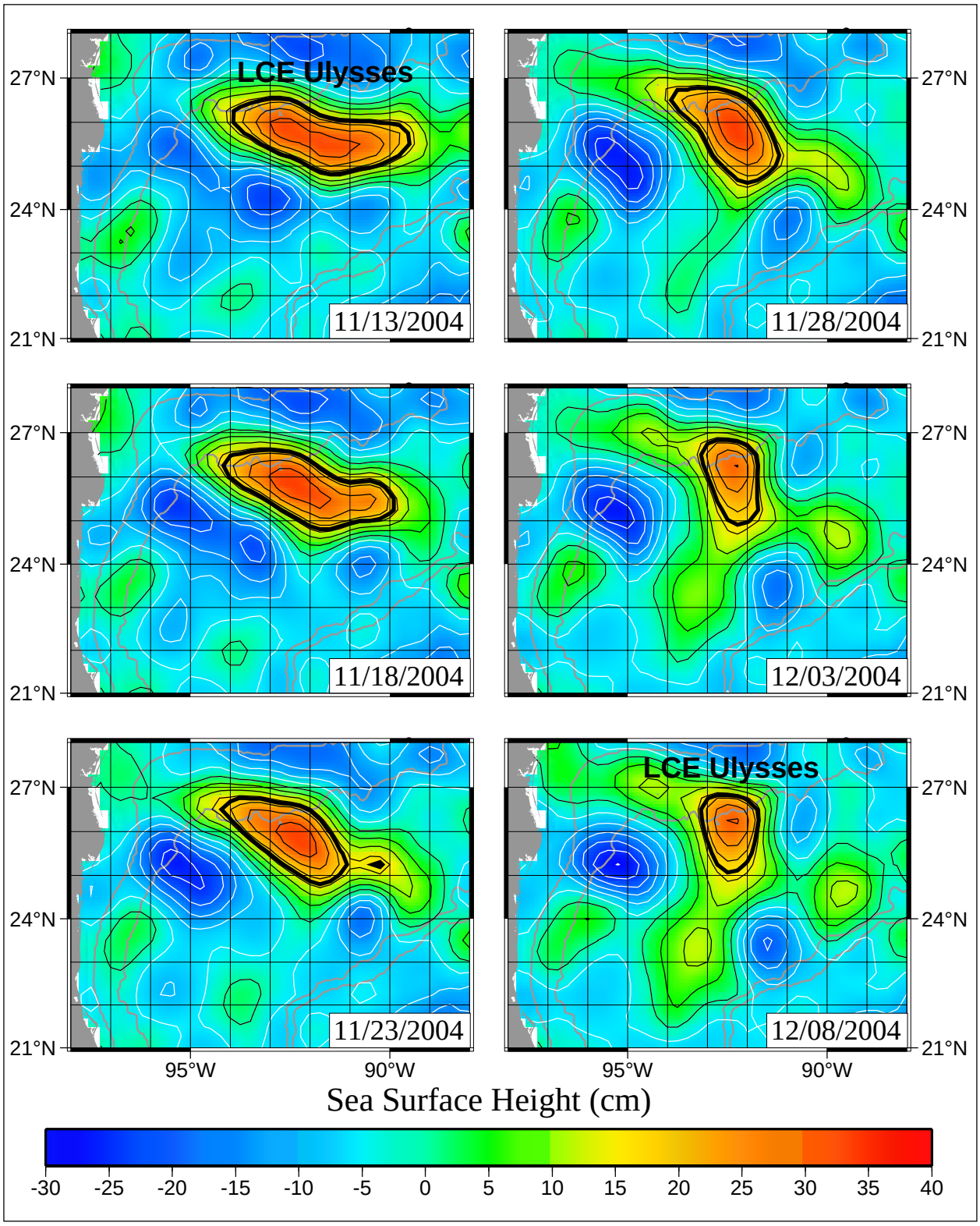

Figure 3.2-7. LCE Ulysses/U2 splitting sequence. SSH maps at 5-day intervals from 13 Nov 2004 through 8 Dec 2004 are shown.

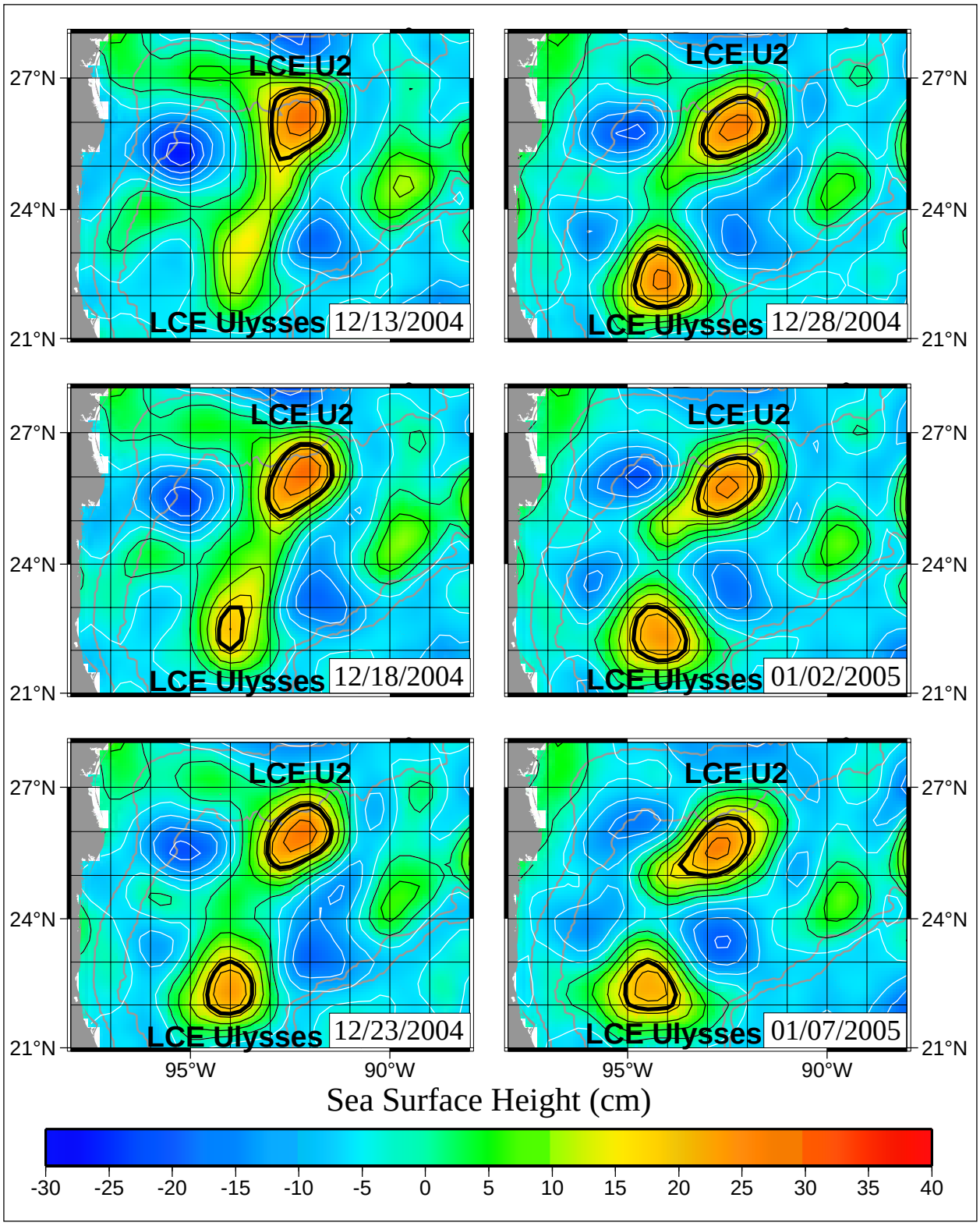

Figure 3.2-8. LCE Ulysses/U2 splitting sequence (cont.). SSH maps at 5-day intervals from 13 Dec 2004 through 7 Jan 2005 are shown. The nominal date for the splitting of the original LCE Ulysses into Ulysses and U2 was 13 Dec 2004.

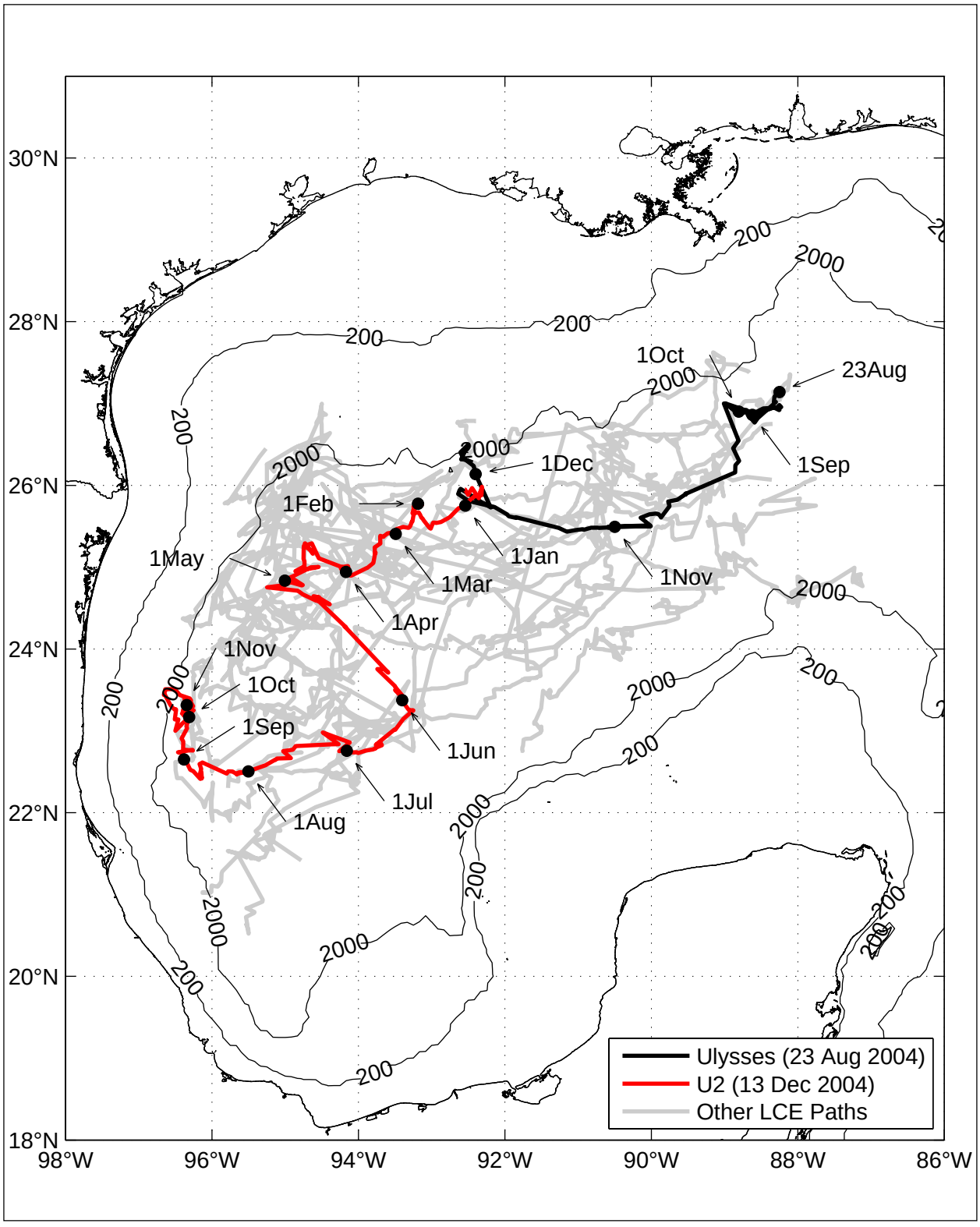

Figure 3.2-9. Composite eddy center paths of LCEs Ulysses and U2 overlaid on all altimeter-tracked LCE paths. The two LCEs split in mid-December 2004, nominally on December 13th. LCE U2 dissipated on 17 Apr 2005.

This influence and the specific events will be considered in more detail in Section 3.3 when we describe the upper-ocean events in the study area.

The large-scale discussion, derived from remote sensing of the splitting of eddy Ulysses into two parts is given above. The tongue of warm water from the northern part of the split eddy wrapped round the western slope cyclone, centered around 26°N, and intruded from the east into the central part of the U.S. sector array. This intrusion dominates the slope circulation from the beginning of November through the end of February, detaching into a separate slope anticyclone around the middle of January. One interesting question is whether this tongue of eddy Ulysses water carries the characteristic signature of LC water, namely the subtropical underwater (SUW) core at a nominal depth of 150 m. SUW is characterized by $T > 20°C$ and $S > 36.5$ psu. The array was designed to detect SUW through the placing of T/S instruments (MicroCats) on each mooring at 150 m, which is the approximate depth of maximum salinity in the LC. The 40-HLP temperatures and salinities from these instruments are shown in Figure 3.2-10. Around the middle of November, warm, salty water intrudes from the southeast and east (U4 and V4). Subsequently, the southern V line gets colder and fresher, whereas the T line becomes warm and salty. The highest salinities at V4, T3 and T4 between late November and the middle of December are ~ 36.9 psu, which is not significantly different than the maximum salinities observed in the SUW core of the LC. This implies that the core of Ulysses has not undergone much water mass modification during its migration across the western Gulf, despite the violent splitting event by the cyclone. Moreover, this intrusion of little modified SUW water onto the northwestern slope is not caused by the LC eddy per se moving up onto the slope, but by a distortion of the eddy boundary caused by its interaction with a western slope cyclone.

The T/S diagram (Figure 3.2-11), which compares T/S from the moored instruments with CTD casts made in the area, shows that the measured salinities are quite accurate. The CTD casts were taken outside the interval when Ulysses water was present, and therefore are representative of the upper layers of Gulf Common Water that is formed when SUW is mixed with the less saline waters above and below the SUW salinity maximum (Vidal et al., 1992). Above 19°C, the moored instrument salinities range between Gulf Common Water and SUW, indicating that horizontal gradients are diffuse and the SUW core in the intrusion is probably mixing vertically and with surrounding slope water. The warm eddy retreats eastward in January and then there is a small intrusion of Ulysses proper in the southeast part of the array in February (Figure 3.2-9). The anticyclone that formed from the Ulysses intrusion in November moves back onto the northwestern slope from March through May, and the 150-m salinities slightly exceed 36.5 psu when the moorings are in this eddy. This seems to indicate that SUW core water on the slope had largely dissipated during these months.

Maps of daily averaged 40-HLP temperatures and salinities at 150 m are given for the times of maximum high salinity intrusion (23 November 2004) and 14 days later (7 December 2004) when the intrusion has migrated to the northern edge of the array (Figures 3.2-12 and 3.2-13). Note that the warm, salty water has anticyclonic flow with the currents following the isolines. Therefore, the intrusion is not being passively advected by the cyclonic flow from Ulysses up onto the slope, but has its own eddy-like flow that presumably connects to the anticyclonic circulation within the core of Ulysses. The slope anticyclone eventually detaches from the deepwater part of Ulysses as it moves northeastward (Figure 3.2-13), but as a separate eddy it

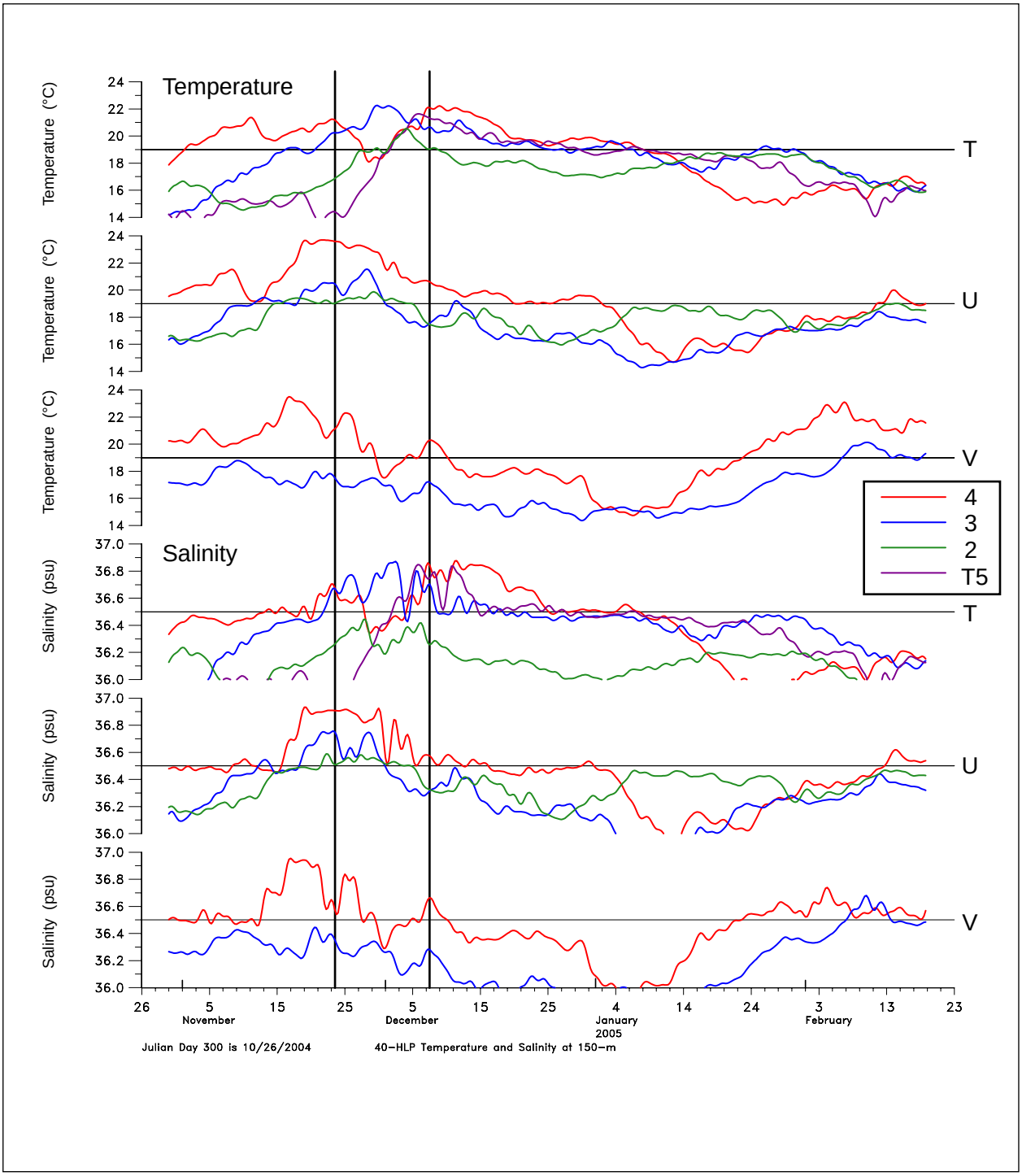

Figure 3.2-10. 40-HLP temperature and salinity from instruments at 150 m. The locations are color coded by north-south transects (e.g., T4, U4 and V4 are red) and each time series panel segregates the locations by east-west array lines (T, U and V). The vertical lines mark the dates of the T/S maps.

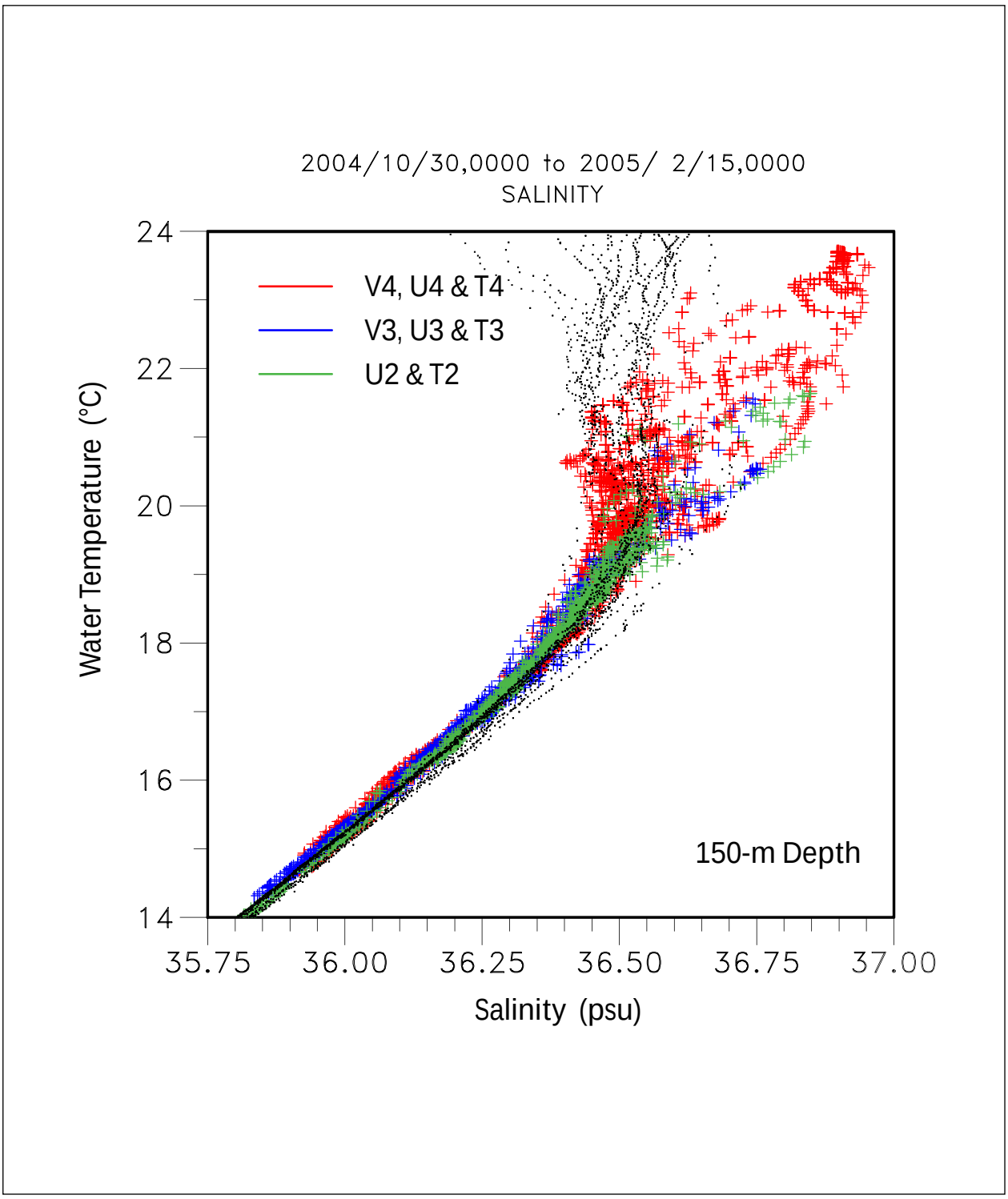

Figure 3.2-11. Temperature-salinity diagram using 40-HLP time series for the given interval from the 150-m MicroCats. The locations are color coded by north-south transects. The overlaid black dots are from CTD casts made over the northwest slope (4 from October 28-29, 2004, 9 from June 27 - July 3, 2005, and 6 from August 6-7, 2005).

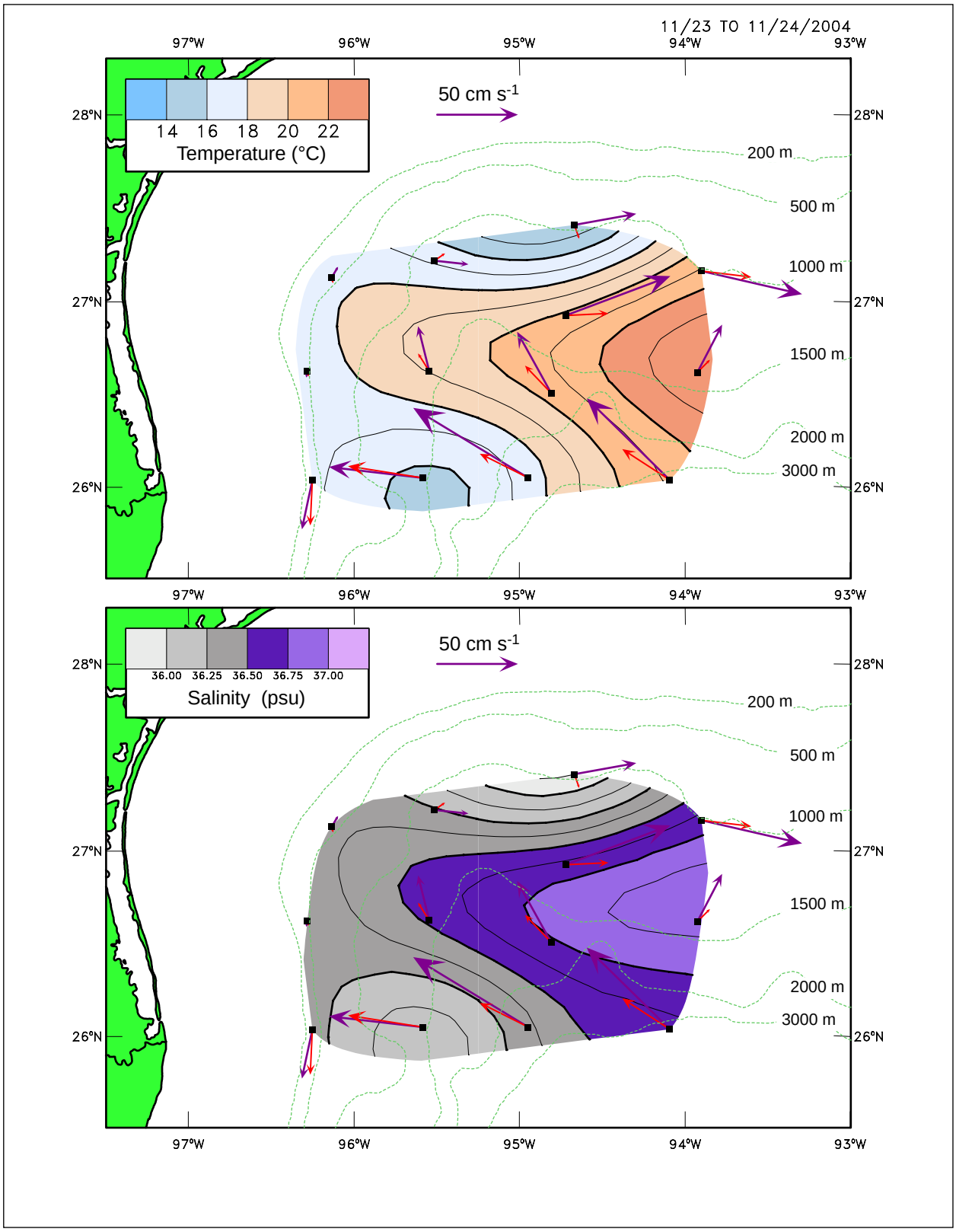

Figure 3.2-12. One-day averaged 40-HLP temperature (top panel) and salinity (bottom panel) at 150 m for 23 November 2004. The vectors are daily averaged 40-HLP currents at 50 m (purple) and 250 m (red).

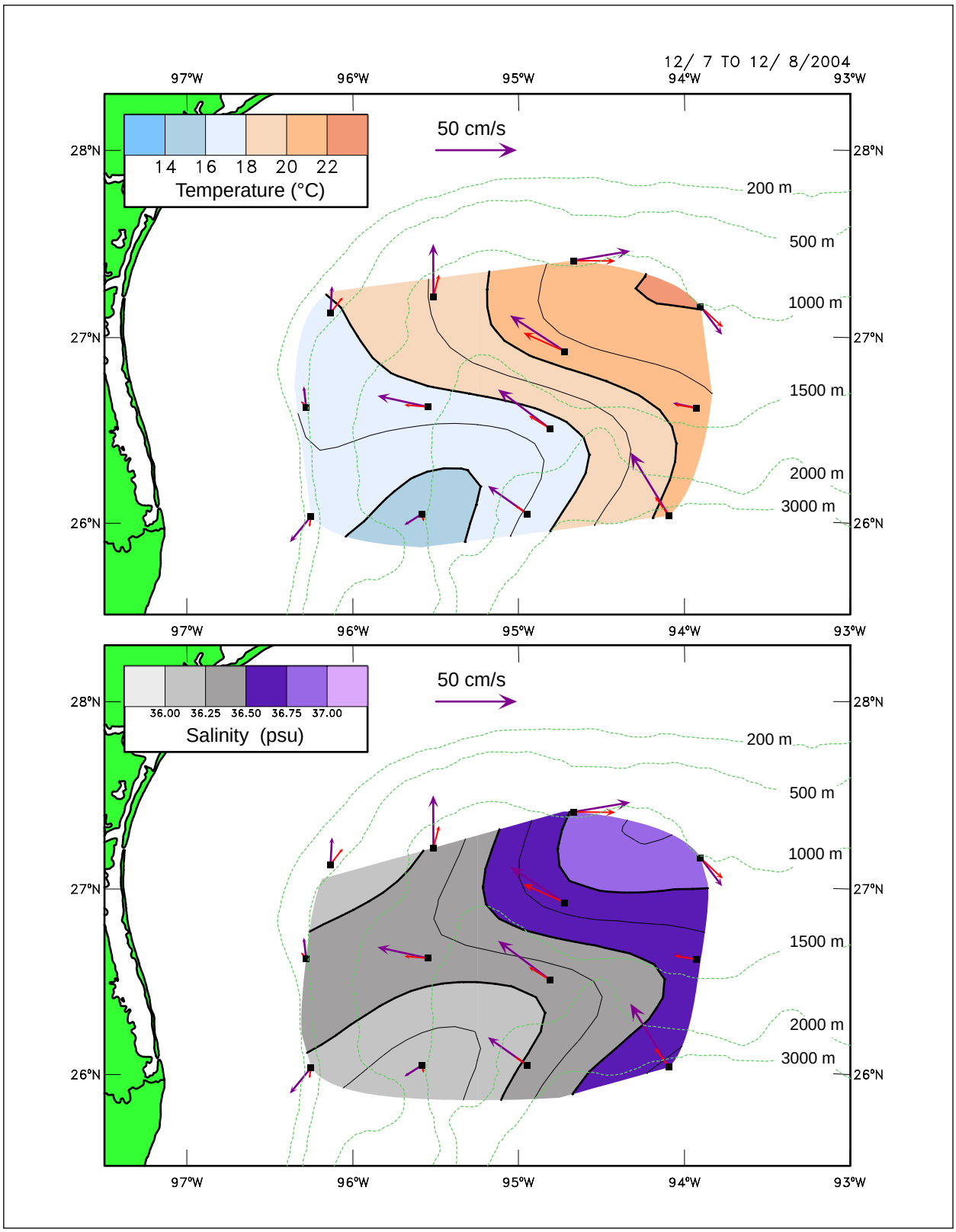

Figure 3.2-13. One-day averaged 40-HLP temperature (top panel) and salinity (bottom panel) at 150 m for 7 December 2004. The vectors are daily averaged 40-HLP currents at 50 m (purple) and 250 m (red).

still has a core of SUW. These complex interactions of a westward LC eddy with slope anticyclones result in the injection of an anticyclonic eddy onto the slope along with its mass of warm salty water more usually associated with LC eddies against the western slope (e.g., Brooks, 1984).

3.2.3 LCE Vortex

LCE Vortex detached and reattached four times from the LC based on the breaking of the 17-cm LC tracking contour before separating on 13 Sep 2005. The initial detachment was on 21 Feb 2005 after a reintrusion of the LC into the far northern GOM six months after the separation of LCE Ulysses. The detached eddy reattached to the LC on 12 Apr 2005. Three brief detachment periods of one to two weeks duration occurred beginning on 14 May 2005, 16 Jun 2005, and 2 Aug 2005. These repeated detachment and reattachment events prevented LCE Vortex from propagating westward and affecting the NW Gulf study region during the program time period. Nevertheless, the final intrusion of the LC into the western GOM to 92.8°W was one of the most westerly observed in the altimeter record. It was exceeded only by the intrusion associated with the tandem separation of LCEs Pelagic and Quick, which extended to 93.3°W (Leben, 2005). The northward and westward extension of the LC and LCE Vortex are thought to have contributed to the intensification of Hurricanes Katrina and Rita in late summer 2004.

The positions of the LC and LCE Vortex at the time of separation are shown in Figure 3.2-14. After separation from the LC, LCE Vortex propagated along a west-southwest path through the western GOM slowly moving away from the 2000 m isobath on the northern GOM continental slope. The eddy-center trajectory became more erratic after the outer edges of the eddy first reached the western GOM continental slope in late October 2005, however, the eddy still followed the general path to the west-southwest (Figure 3.2-15). Some of the erratic motion about the general west-southwest path was caused by interactions of the LCE with a cyclonic eddy that formed within the Mexican array just as Vortex approached. Strong surface currents associated with Vortex reached the far northwest Mexican mooring just as the instruments were being retrieved in early November 2005. The encounter with the western margin also initiated a rapid decay of the maximum SSH anomaly within the eddy core. The eddy center maximum height decreased from nearly 40 cm to less than 20 cm over an interval of less than one month (Figure 3.2-16). This decrease in maximum SSH was not associated with a significant decrease in eddy area, which may explain the somewhat slower eddy decay rates found by Sturges (1993) in his examination of area changes inside selected isotherms within LCEs at the western boundary.

3.2.4 Remote Sensing Perspective of GOM Hurricanes during the NW Gulf Program

The 2005 hurricane season was the most costly on record with estimated damages in the U.S. totaling $132 billion (B). The four most destructive storms – Dennis ($12B), Katrina ($100B), Rita ($10B), and Wilma ($12B) – all interacted with deep warm ocean currents in the GOM contributing to the intensity of these storms and their destructive potential.

The upper ocean heat content is the primary energy source for hurricanes, and this causes the intensity of hurricanes to be very sensitive to SST. Strong mixing under storms typically causes

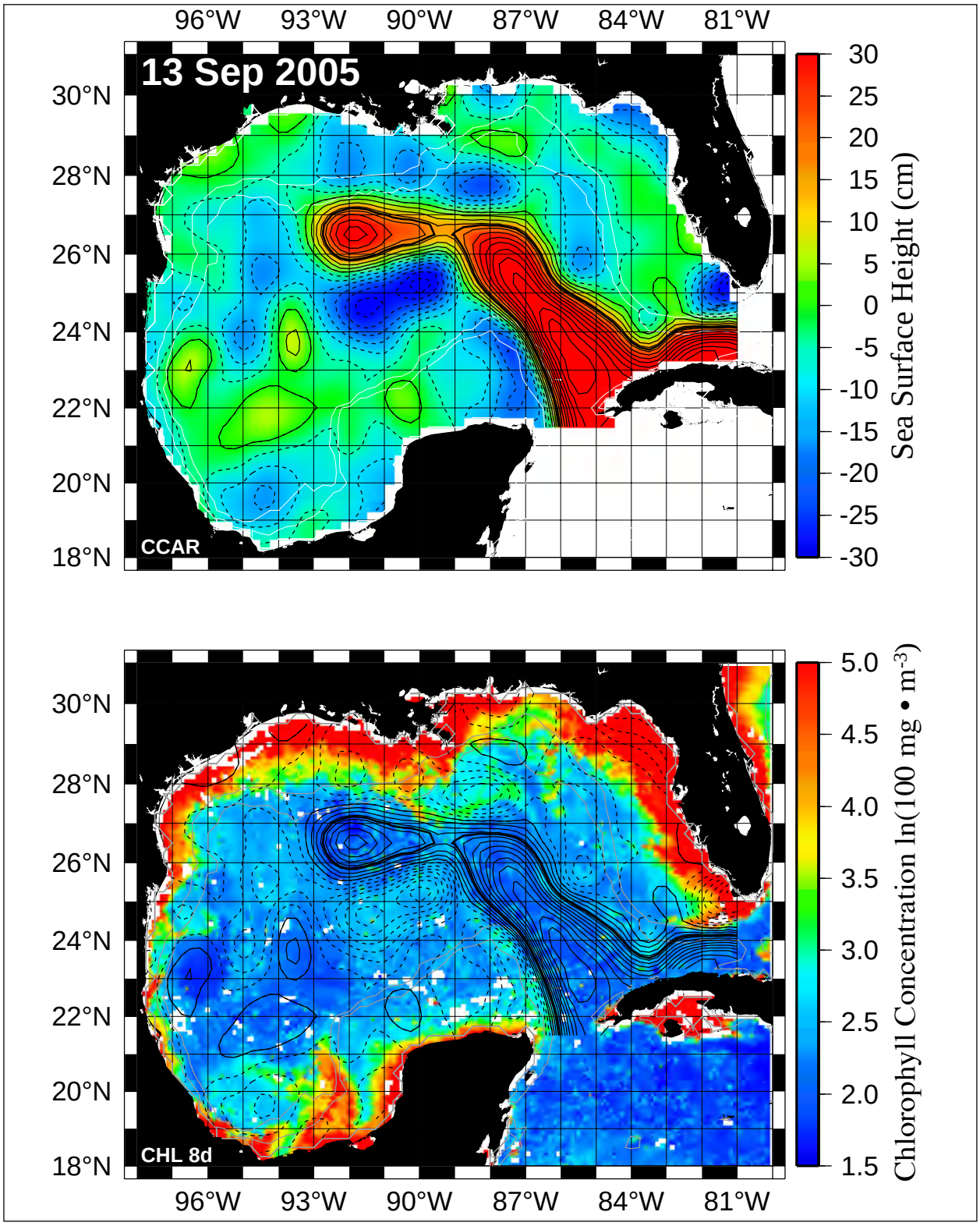

Figure 3.2-14. SSH map (upper panel) and 8-day composite color image (lower panel) of LCE Vortex separation on 13 Sep 2005. The 8-day composite image is from the time interval from 9-16 September 2005.

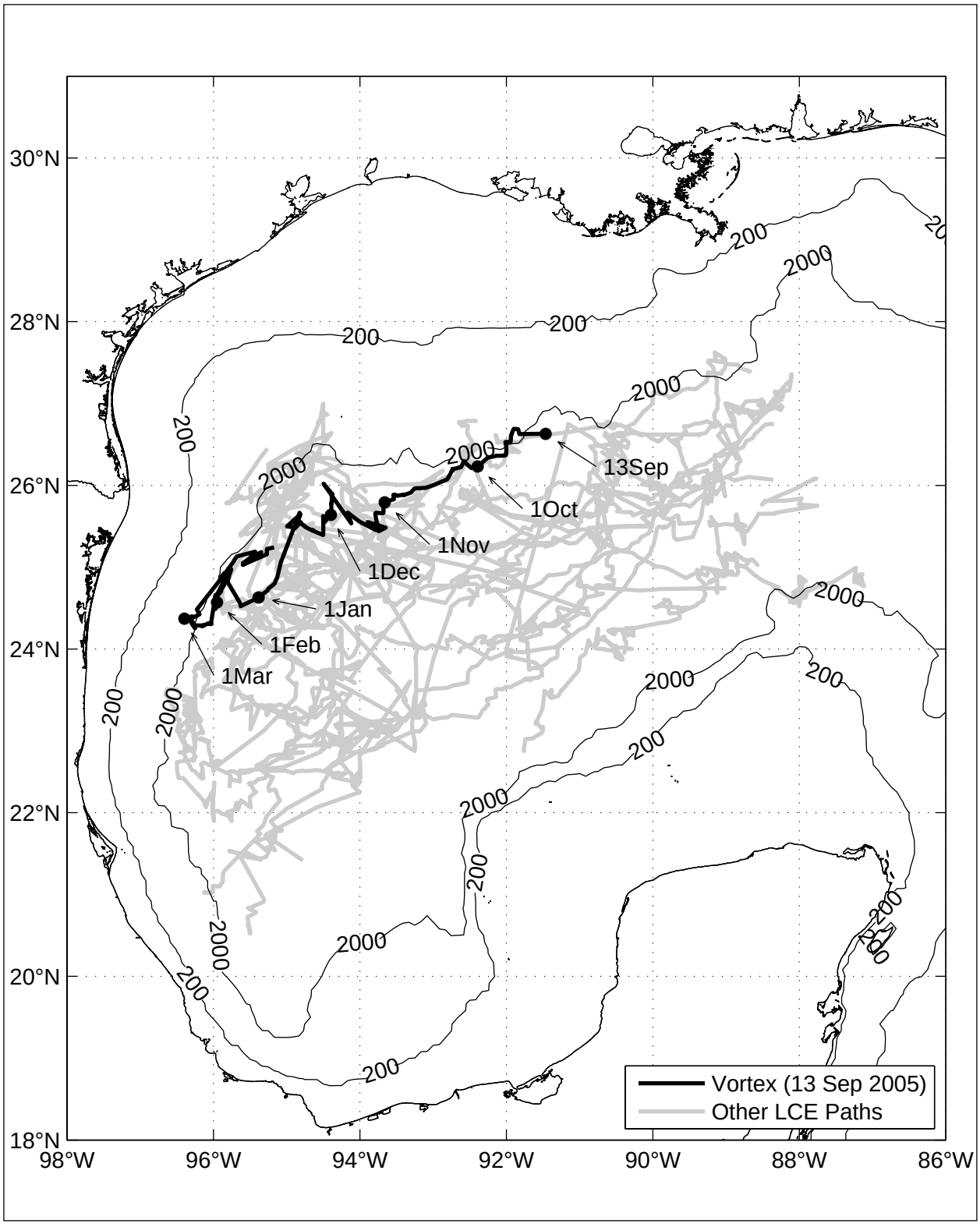

Figure 3.2-15. LCE Vortex eddy center path overlaid on all altimeter-tracked LCE paths. Vortex separated on 13 Sep 2005 and dissipated on 25 Mar 2006. Arrows show positions of the eddy centers on the first of each month.

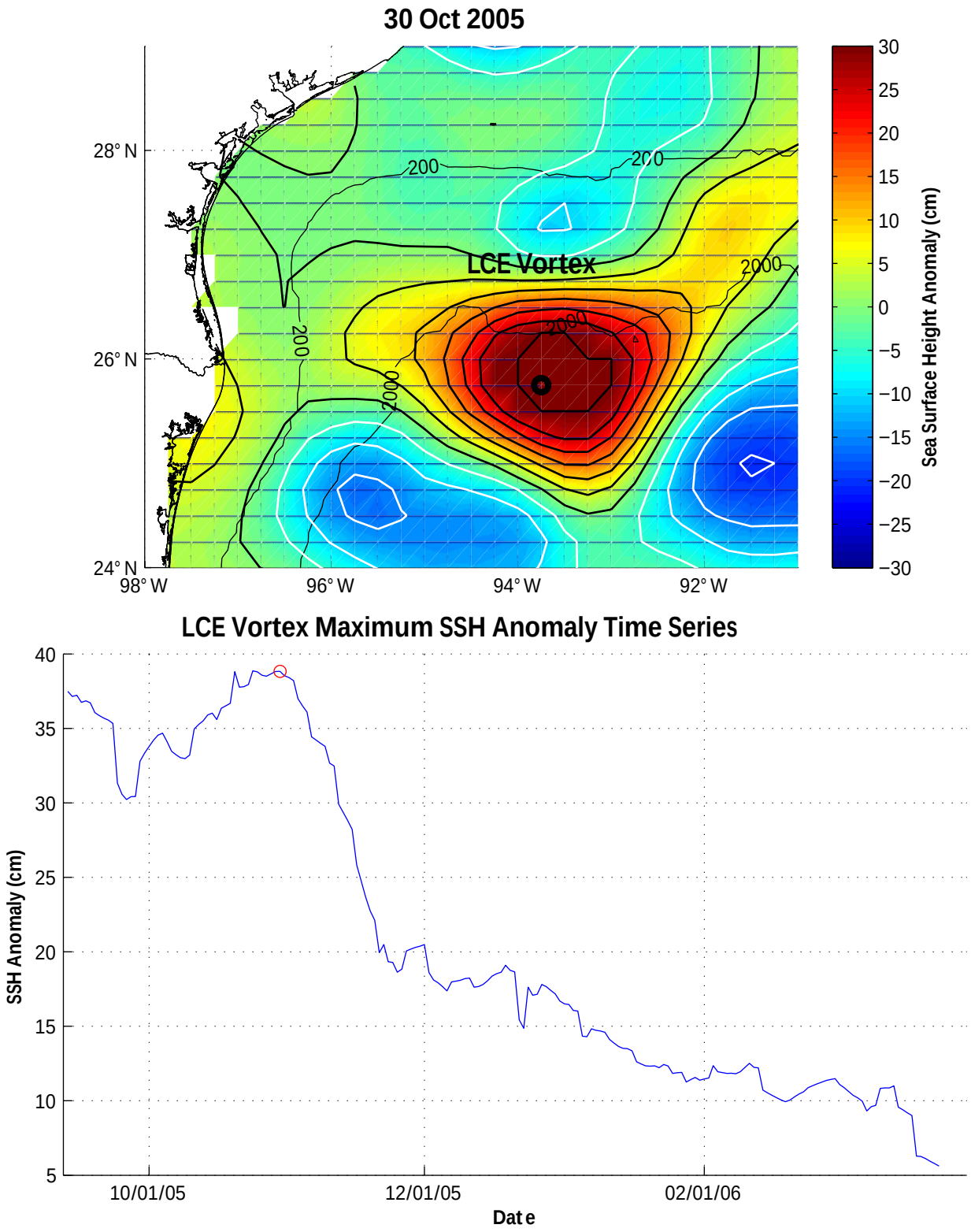

Figure 3.2-16. SSH map of LCE Vortex on 30 Oct 2005 (upper panel) and maximum eddy center SSH anomaly time series (lower panel). The position of the maximum SSH is shown by the black circle and the corresponding day by the red circle.

a significant decrease in SST by the mixing of cooler water from the thermocline into the ocean surface mixed layer. This is the major negative feedback mechanism affecting hurricane intensification. The interaction of a hurricane with a warm ocean current or warm ocean eddy, however, effectively insulates the hurricane from the negative feedback caused by entrainment of underlying colder water. Rapid storm intensification then results if atmospheric conditions are favorable. Changes in intensity from Saffir-Simpson category 1 to 4 within 24 to 36 hours have been observed (Shay et al., 2000; Goni and Trinanes, 2003). Oceanographic conditions in the GOM can support this type of rapid hurricane intensification. The warm and energetic LC and its associated eddies are a significant source of upper ocean heat content. During the 2005 hurricane season, the LC was in the process of shedding LCE Vortex. Both Katrina and Rita crossed the warm waters of the intruded LC and LCE Vortex, contributing to the marked increases in the maximum sustained wind speeds within the hurricanes as they passed over those features, as seen in Figures 3.2-17 and 3.2-18.

The effect of warm eddies on hurricane intensification has been well documented in studies of the rapid intensification of Hurricane Opal over a LCE in 1995 (Hong et al., 2000; Shay et al., 2000) and the interaction of Typhoon Maemi with a warm ocean eddy in the Northwest Pacific in 2003 (Lin et al., 2005). Cold oceanic eddies can also have an impact. The interaction of a hurricane with an underlying cold eddy enhances entrainment of colder water into the surface mixed layer thereby reducing a hurricane's intensity. This effect was observed in Hurricane Ivan where rapid negative ocean-atmosphere feedback occurred over cold ocean eddies during the hurricane's passage over the eastern deep Gulf of Mexico (Walker et al., 2005). Ivan's path and maximum sustained winds are shown in Figure 3.2-19 overlaid on the SSH map from 15 Sep 2004, the day that the hurricane passed over the recently separated LCE Ulysses. A cold eddy also affected the intensity of Hurricane Rita. This cyclonic eddy can be identified in the SSH map shown in Figure 3.2-18 by the large area of low SSH to the south-southeast of the recently detached LCE Vortex.

3.3 Timeline and Description of Upper Ocean Events

The dominant LC event affecting the upper-ocean circulation in the NW Gulf study region was the separation of LCE Ulysses and the subsequent splitting of the LCE into two eddies, Ulysses and U2, in the western GOM. As noted in the historical review, LCEs have a significant impact on the intensity of the circulation in the NW Gulf study region. In this section, we explore this connection in more detail as we describe the upper-ocean events within the study array during the program time period. In addition to the influence of LCEs Ulysses and U2 on upper-ocean circulation in the NW Gulf, several persistent and energetic anticyclonic eddies (ACEs) and cyclonic eddies (CEs) were observed within the study region.

These upper ocean events are categorized by type and will be described in individual sections for each category. The key events are tabulated in a sequence of four tables that summarize, respectively, the LC and LCE upper-ocean events, LCEs Ulysses/U2 and their associated ACEs and CEs, significant ACEs in the study region, and significant CEs in the study region that were observed during the NW Gulf program time period. Naming conventions for LCEs are consistent with the names used by Horizon Marine, Inc. in EddyWatch™ reports. ACEs and CEs associated

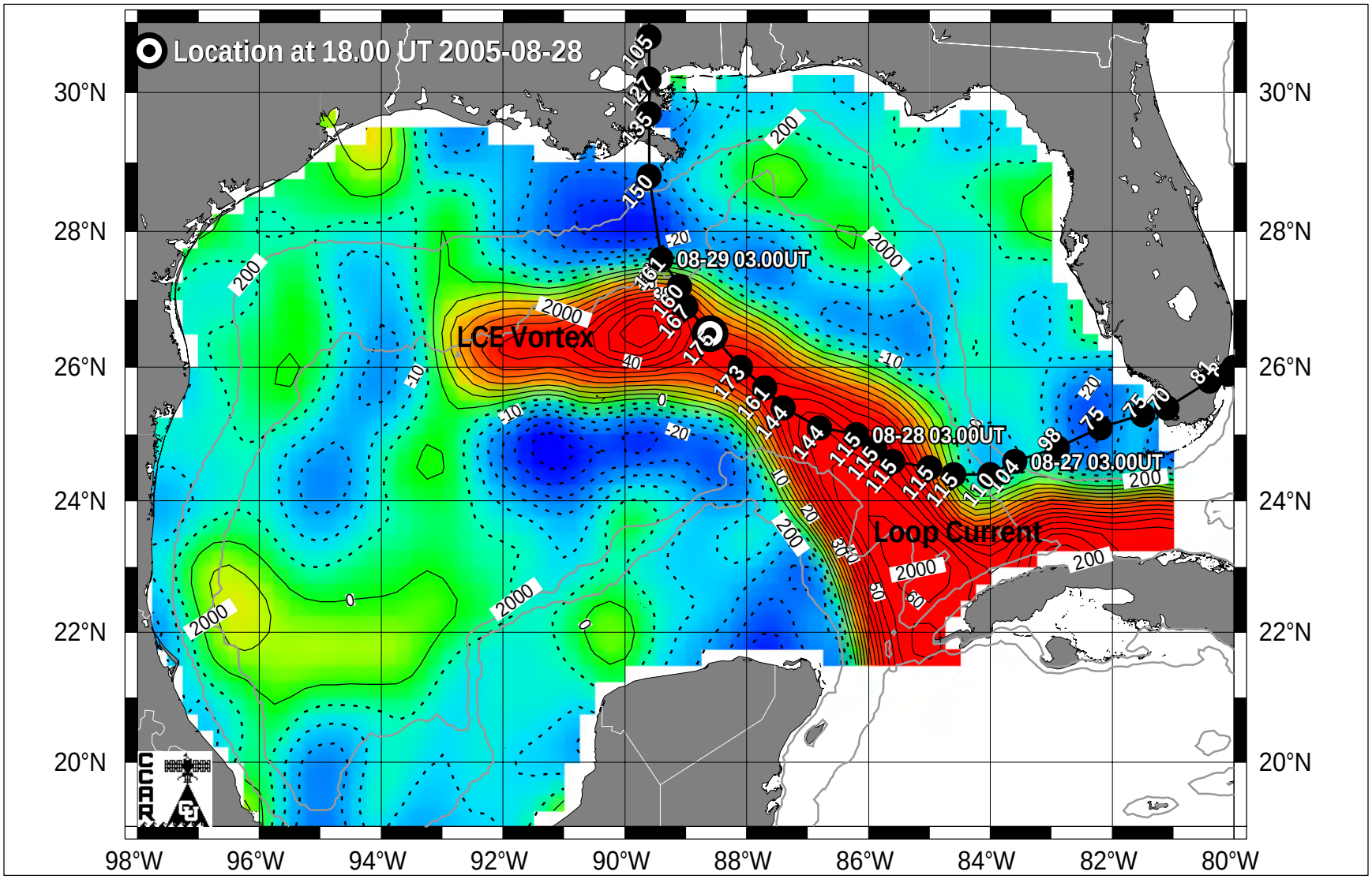

Figure 3.2-17. Overlay of Hurricane Katrina track and maximum sustained wind speeds (mph) on the 28 Aug 2005 SSH map.

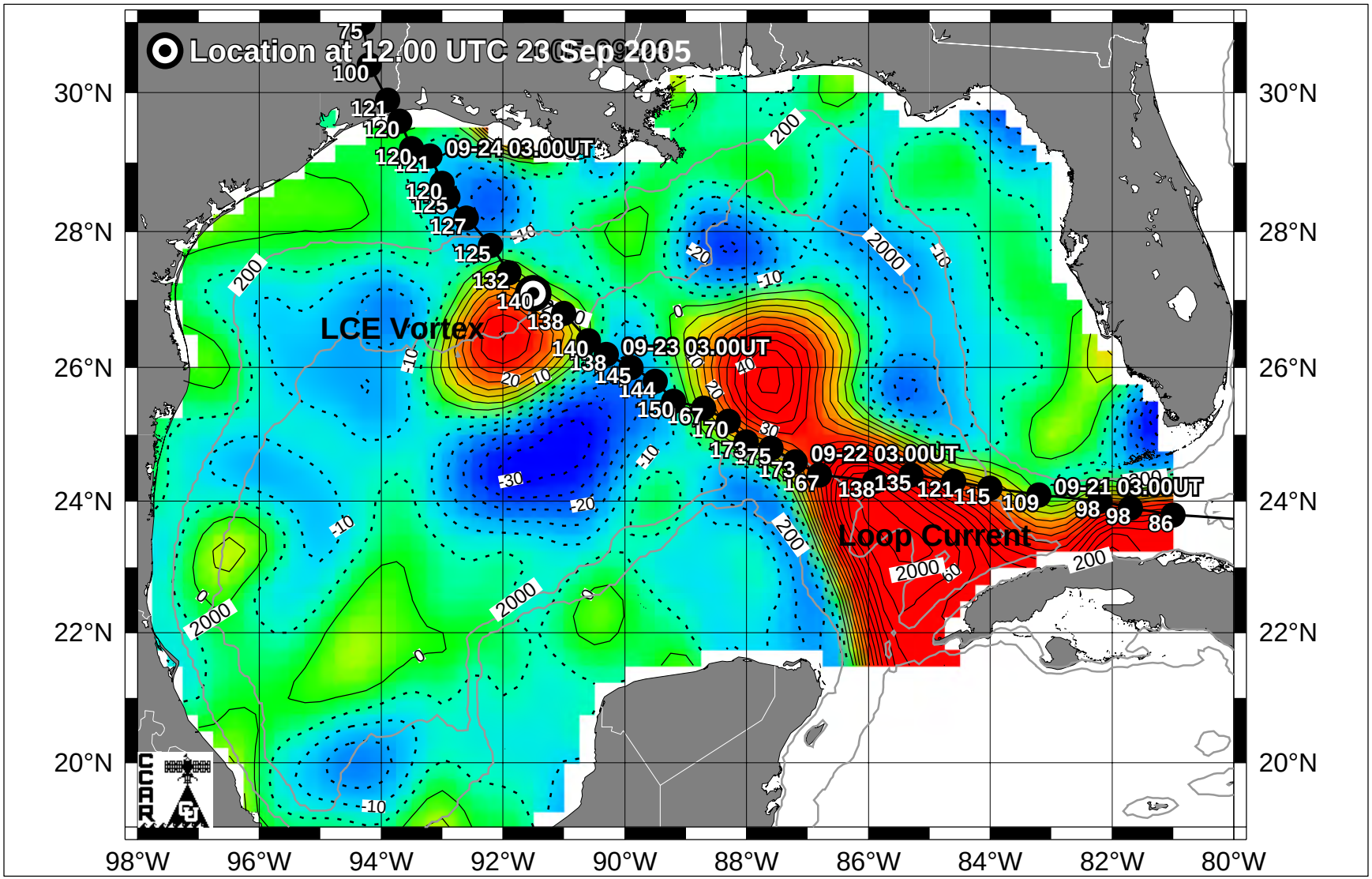

Figure 3.2-18. Overlay of Hurricane Rita track and maximum sustained wind speeds (mph) on the 23 Sep 2005 SSH map.

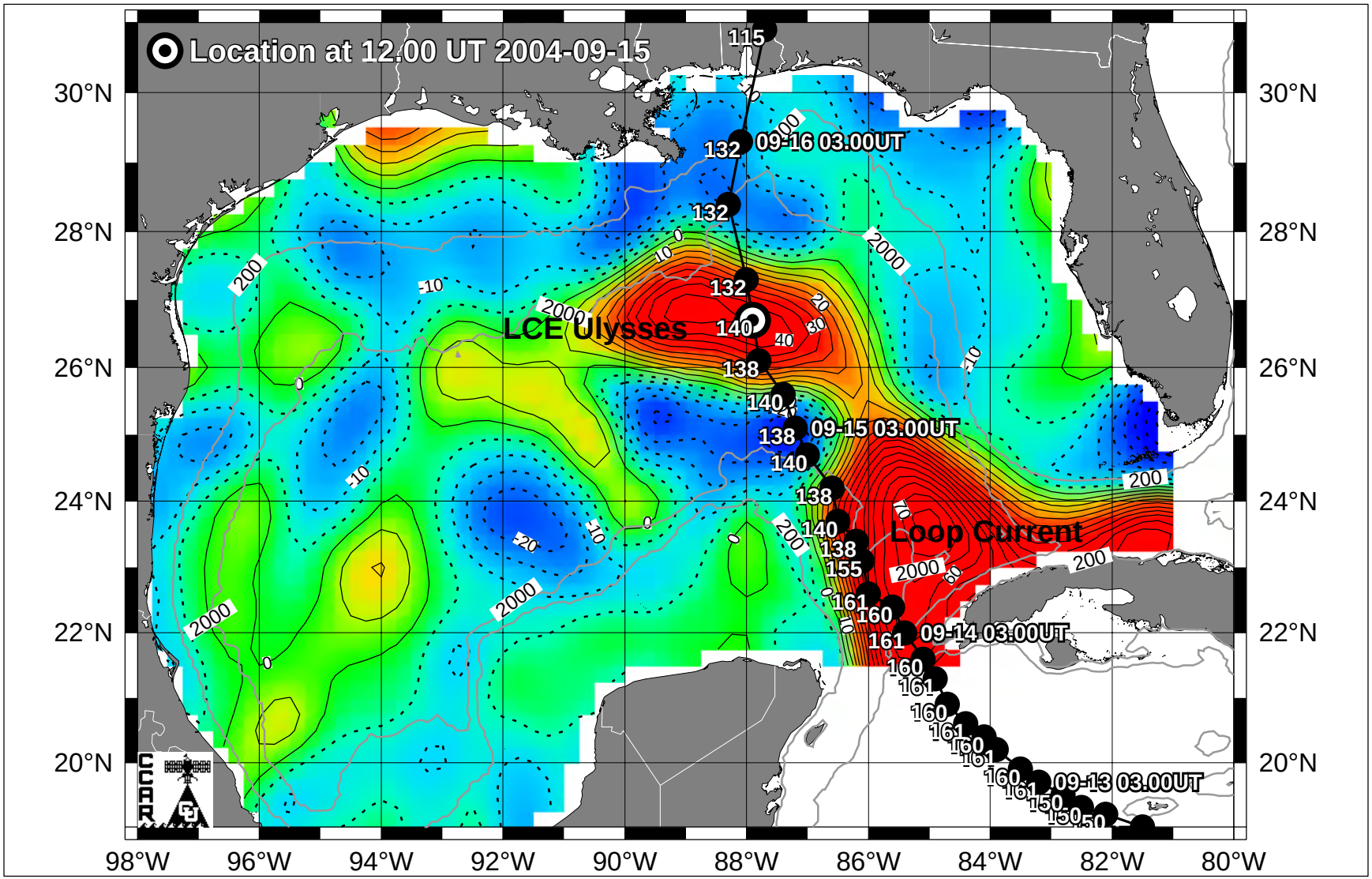

Figure 3.2-19. Overlay of Hurricane Ivan track and maximum sustained wind speeds (mph) on the 15 Sep 2004 SSH map.

with LCE Ulysses use subscripted letters, e.g., ACE_a, CE_a. ACEs and CEs in and around the study area are numbered, e.g., CE #1, CE #2.

3.3.1 LC and LCEs

The review of Gulf-wide conditions during the NW Gulf Program in Section 3.2 found that the upper-ocean circulation associated with LCEs Ulysses and U2 was the dominant LC event affecting the study region during the field observations. Ulysses separated from the LC on 23 Aug 2004. In mid-October it merged with an ACE just to the east of the U.S. array. The furthest penetration of Ulysses into the study array occurred in late November. Ulysses split in two in mid-December. After splitting, the northernmost piece, which was named U2, propagated along the SW margin of the study array and into the Mexican moorings during January through April 2005. In mid-April, the northern edge of U2 again intruded into the study array just before it merged with what remained of Ulysses, the southernmost piece of the original LCE that had propagated further to the south. In May and June 2005, a small piece of anticyclonic circulation that was ejected from the U2/Ulysses merger moved into the study array. The remaining larger portion of the U2/Ulysses merger, which we continued to track as LCE U2, propagated to the southeast away from the study region in May and then ultimately dissipated in November 2005 without further impacting the circulation in the study region. More details on the influence of Ulysses/U2 on the upper ocean circulation within the study array will be discussed in the next section.

Two other LCEs, Titanic and Vortex, also occurred during the program time period. LCE Titanic took one of the most southerly paths through the western GOM observed in the altimeter record. Titanic arrived at the western margin in August 2004 and dissipated one month later, remaining well south of the NW Gulf study region. LCE Vortex reached the study region, but not during the program time period. Vortex separated from the LC on 13 Sep 2005 after a final deep intrusion of the LC into the western GOM. The 17-cm LC tracking contour reached 92.8°W, which was the third most westerly intrusion of the LC observed in the altimetric record. By October, LCE Vortex had reached the western GOM continental slope. The maximum SSH value within the study region measured by altimetry occurred on 29 Oct 2005 and was associated with Vortex as the LCE skirted the SE corner of the NW Gulf array. Only three other events exceeded this value in our review of the 13.5-year historical altimeter record and all were associated with LCEs in or close to the study region. A summary of the LC and LCE events observed during the NW Gulf Program are listed in Table 3.3-1.

Table 3.3-1

Timeline of LC and LCE Events during NW Gulf Program

Event	Date	Comments
LCE Ulysses separation	24 Aug 2004	Defined by breaking of the 17-cm contour. See Figure 3.2-3
LCE Titanic dissipation	22 Sep 2004	See altimeter-tracked path in Figure 3.2-1.
LCE Ulysses merged with ACE #2	15 Oct - 15 Nov 2004	See Figure 3.2-5.
LCE Ulysses intrusion into array	10 – 30 Nov 2004	LC salinity signature measured in array.
LCE Ulysses/U2 split	13 Dec 2004	Nominal date of splitting based on altimeter tracking.
LCE U2 propagation along southwest margin of US array and into Mexican array	Jan – Apr 2005	Altimeter-tracked path.
LCE U2 intrusion into US array	mid-Apr 2005	Weak LC salinity signature.
U2 and Ulysses merged	Apr 2005	Altimeter-tracked paths.
Ulysses dissipation	17 Apr 2005	See altimeter-tracked path in Figure 3.2-4.
A small remnant of Ulysses/U2 moved into US array	May – Jun 2005	Weak LC salinity signature.
Maximum LC extent during NW Gulf Program	12 Sep 2005	17-cm LC contour reached 93.4°W.
LCE Vortex separation	13 Sep 2005	Defined by breaking of the 17-cm LC contour. See Figure 3.2-14.
LCE Vortex approached Mexican array	Oct 2005	Measurement array removed just as LCE arrives.
LCE U2 dissipation	6 Nov 2005	See altimeter-tracked path in Figure 3.2-9.
LCE Vortex dissipation	25 Mar 2006	See altimeter-tracked path in Figure 3.2-15.

3.3.2 LCEs Ulysses/U2 and Associated Eddies

LCEs Ulysses and U2 influenced the upper-ocean circulation in the study region both directly and indirectly. Direct influences were primarily through the intrusion of eddy circulation into the study region. The maximum altimetric SSH value within the study region occurred on 11 Nov 2004 and was associated with the intrusion of the northwestern lobe of LCE Ulysses into the moored-instrument NW Gulf array. This maximum value was the sixth largest local maximum observed in our review of the 13.5-year historical altimeter record. Maximum values were also found in the 150-m depth salinity measurements and inferred salinity values from the PIES records around this time. Salinity values in excess of 36.75 psu were measured at 150 m within the array in November and December, clearly identifying subtropical underwater (SUW) within the study region that is associated with LC waters (Wüst, 1963). Inferred 150-m salinity values from PIES measurements also showed values above 36.6 psu from mid-November through mid-

December with maximum intrusion into the study region in early December 2005. The maximum inferred salinity value was 36.65 psu on 22 Nov 2004.

Two other intrusions into the NW Gulf study region were associated with LCEs Ulysses/U2. These occurred in April and May 2005 and were associated with U2 passing across the southern margin of the American array and a small remnant of the Ulysses/U2 merger event moving into the American array. The array measured 150-m salinities on the order of 36.6 psu at V2 and V3 in both April and May and a 36.7 psu peak in mid-April at T5. These high salinity values may be patchy SUW remnants since the values are less than the salinity of 36.75 psu typical of unmixed LC water such as those previously measured in November and December. Inferred 150-m salinity values from the PIES measurements also showed values on the order of 36.6 psu in April and May 2005. The maximum inferred salinity values associated with the intrusions in April and May, were 36.64 psu on 14 Apr 2005 and 36.56 psu on 22 May 2005, respectively.

Maps of the 150-m salinity field inferred from PIES during the November, April, and May events are shown in Figure 3.3-1. The locations of the maximum values associated with each intrusion are also shown. The location of the maximum in May far to the north may indicate that some of the high salinity water from the April intrusion remained in the array through late April and May. Nevertheless, significant mixing of the LC waters on the periphery of LCE U2 had clearly occurred over this interval as U2 interacted with the continental slope and the ambient eddy field in the northwestern GOM.

The evolution and decay of LCE Ulysses/U2 near the study array is best evaluated along the composite eddy center path composed of the path taken by Ulysses before the split and U2 after the split. This composite path was previously shown in Figure 3.2-9 and is a good measure of the location of the LC-induced circulation associated with the LCEs during the study. Of course, the influence depends on the size and strength of the LCE, not just its location. To assess this influence, SSH anomaly maps on the three dates, 22 Nov 2004, 14 Apr 2005, and 22 May 2005 are shown in the upper panels of Figures 3.3-2, 3 and 4, respectively. The maps correspond to times when high 150-m depth salinity values were observed in the study array. The maximum eddy center SSH anomaly time series are shown in the lower panels of the figures. The location of the maximum SSH anomaly is shown by a black circle on each map and the corresponding date by the red circle on the corresponding plot of the SSH anomaly time series.

The SSH anomaly at the eddy center associated with the maximum intrusion of LCE Ulysses into the array in late-November 2004 was 34 cm. By mid-April 2005, the center maximum had decreased to 18 cm, only one half of the value measured four months prior. Over that same interval, the area bounded by the 10 cm contour had decreased from 89,700 to only 18,900 km^2, a reduction by a factor of five. Some of this decrease was associated with the splitting of Ulysses and, therefore, cannot be entirely attributed to the interaction of the eddy with the continental slope. The splitting off of the southern eddy (Ulysses) was complete by 1 Jan 2005. The reorganization of the remaining primary LCE circulation (U2) took a little longer because of the interaction with the cyclone to the west. This interaction split off a small piece of anticyclonic circulation from the periphery of the eddy that ended up in the study region. The signature of this small anticyclone can be seen in objectively mapped 150-m depth salinity fields shown in Figure 3.3-26. By early February 2005, the interaction with the cyclone involved in the

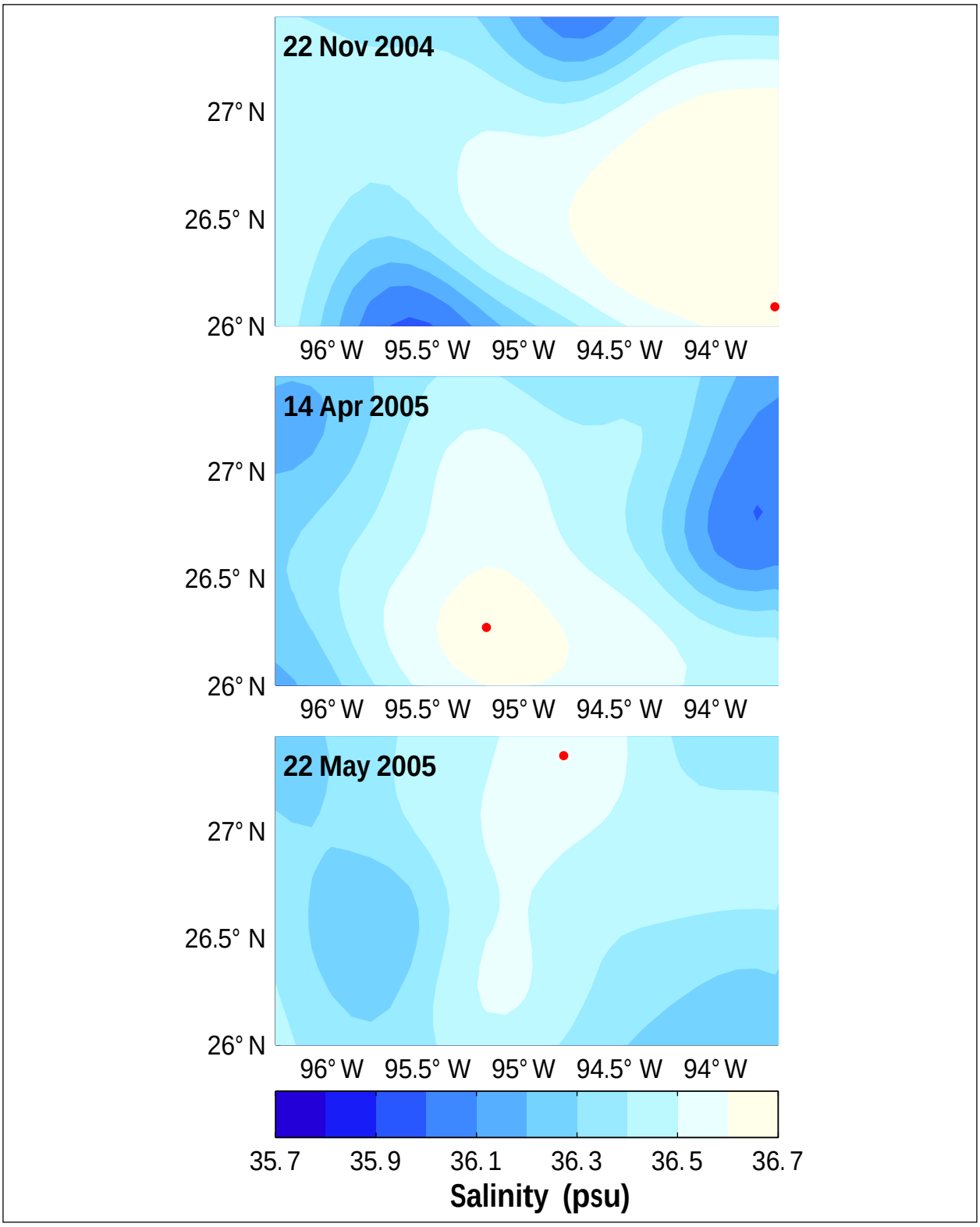

Figure 3.3-1. Optimally interpolated maps of PIES-inferred 150-m salinity on dates corresponding to intrusions of LCE Ulysses/U2 into study region. the location of the maximum salinity associated with each intrusion into the study region is identified with a red dot.

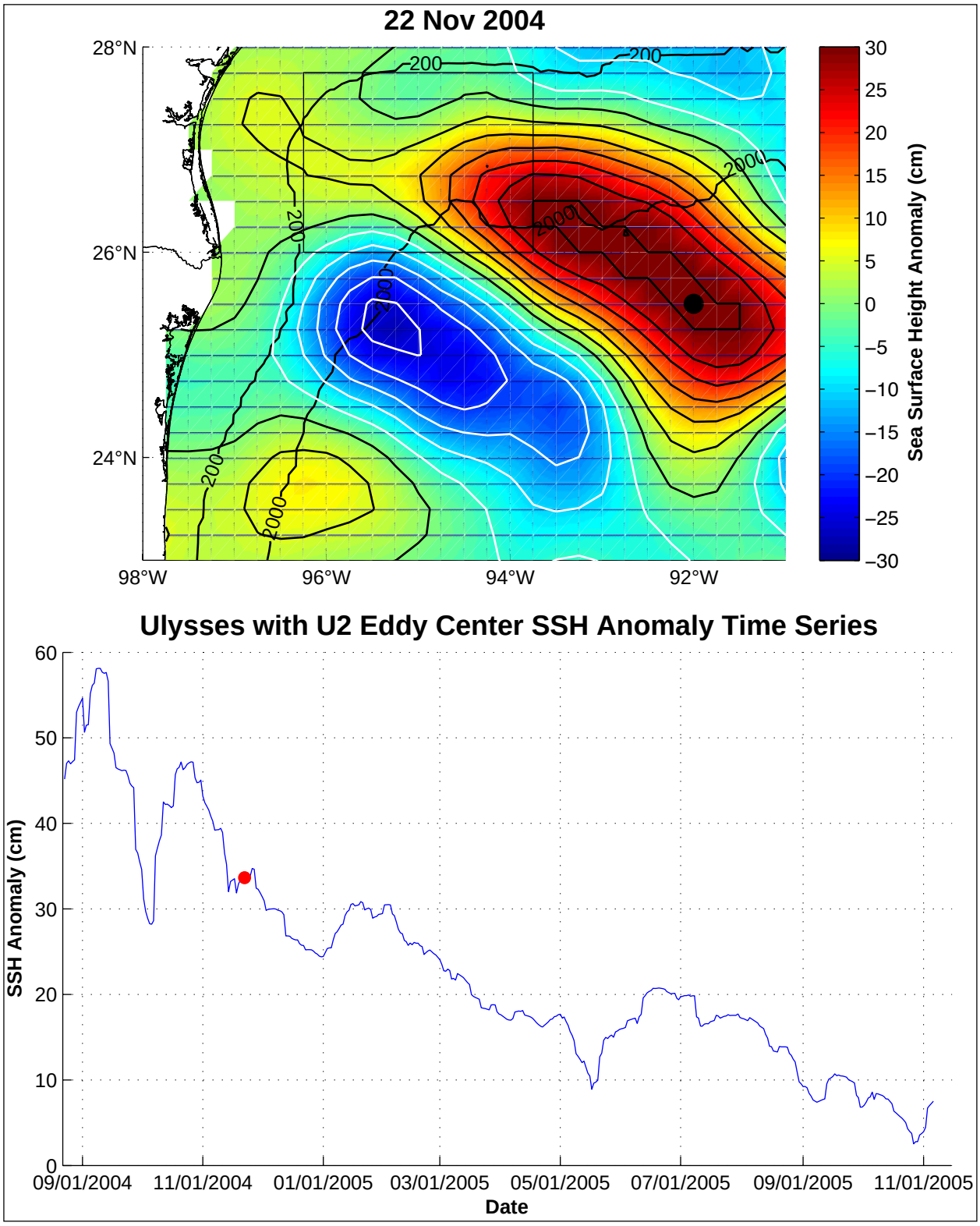

Figure 3.3-2. SSH anomaly map of LCE Ulysses on 22 Nov 2004 (upper panel) and maximum eddy center SSH anomaly time series for Ulysses/U2 (lower panel).

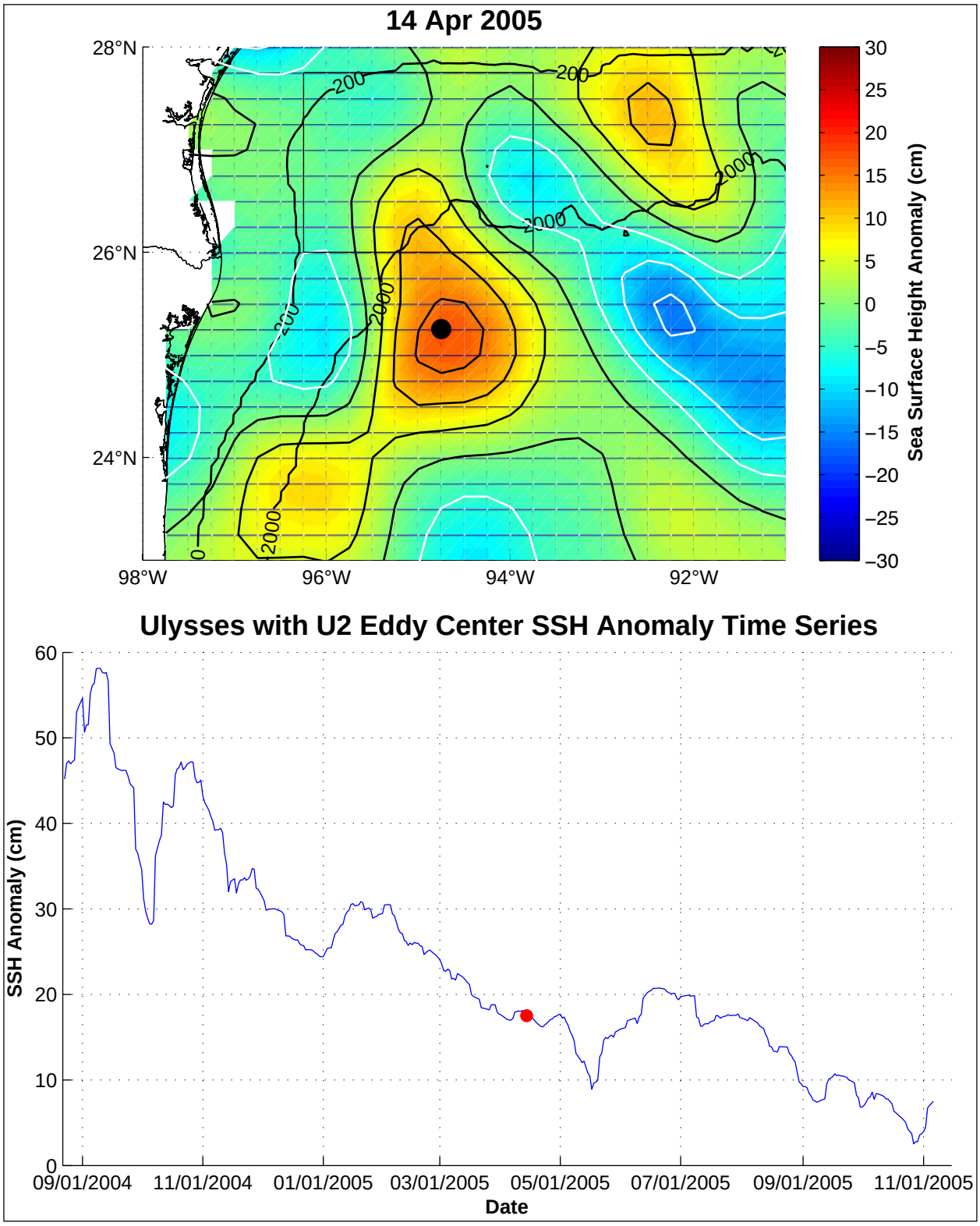

Figure 3.3-3. SSH anomaly map of LCE Ulysses on 14 Apr 2005 (upper panel) and maximum eddy center SSH anomaly time series for Ulysses/U2 (lower panel).

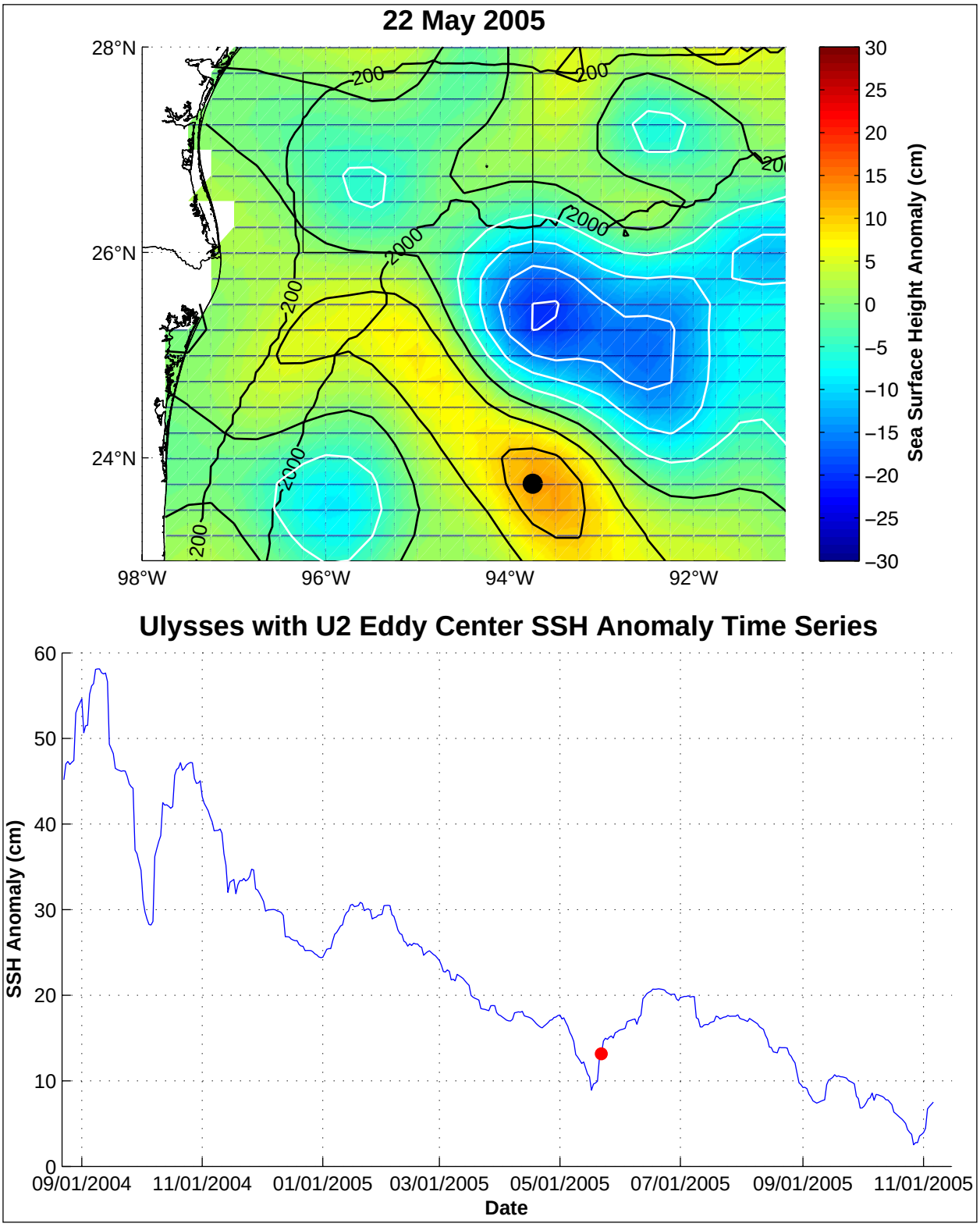

Figure 3.3-4. SSH anomaly map of LCE Ulysses on 22 May 2005 (upper panel) and maximum eddy center SSH anomaly time series for Ulysses/U2 (lower panel).

split was complete. From 1 Feb 2005 to 14 Apr 2005, the decreases in center SSH anomaly and total area within the 10-cm contour were from 30 to 18 cm and from 37,000 km^2 to 18,900 km^2, a reduction by a factor of 5/3 and a factor of 2 for the height and area, respectively.

To complete the description of Ulysses/U2, we show the maximum eddy-center SSH anomaly time series for the entire LCE Ulysses path previously shown in Figure 3.2-4. We selected dates just before and after the split, 12 Dec and 13 Dec 2004, and after Ulysses had fully reorganized on 1 Jan 2005. The SSH anomaly maps on those dates are shown in the upper panels of Figures 3.3-5, 6 and 7, respectively. The time series of the maximum eddy-center SSH anomaly is shown in the lower panels of the figures. The location of the maximum SSH anomaly is shown by a black circle on the maps and the corresponding date by the red circle on the plots of the time series. On 12 Dec 2004, LCE Ulysses had an eddy-center SSH anomaly of 29 cm and an area within the 10-cm SSH contour of 83,400 km^2. Starting nominally on 13 Dec 2004, a large lobe on the southern margin merged with a small anticyclone to the west and continued to entrain mass from the eddy to the north until it was completely split off on about 1 Jan 2005. During this interval, the maximum SSH anomaly value within Ulysses increased from a low of about 15 cm to 24 cm. It is interesting to compare the maximum SSH height and the area of the two eddies on 1 Jan 2005 after they were completely separated. LCE U2 (the northern piece) had a center height of 24 cm and an area of 42,100 km^2, and Ulysses (the southern piece) had the same center height (24 cm) and was only slightly smaller at 38,900 km^2. Thus, the splitting event was a nearly perfect cleaving in two of the original eddy. Comparison of the eddy's total area before the split to the sum of the two eddies' areas after the split show that the areal extent of the eddy coverage was nearly conserved – 83,400 km^2 before versus a sum of 81,000 km^2 after the split.

Detailed observations of large geophysical vortex splitting events are relatively rare. Only one other splitting of LCE by a deepwater cyclonic eddy in the western GOM has been reported (Biggs et al., 1996). Vortex splitting occurs frequently in fluids. Splitting, which is also called fission, has been observed in atmospheric (Charlton et al., 2005), oceanic (Biggs et al., 1996), Schouten et al., 2000), and aerodynamic flows (Freymuth et al., 1984). The process was first predicted by numerical simulations (Christiansen and Zabusky, 1973; see also the review in Saffman and Baker, 1979) well before it was observed in the laboratory or *in situ*. Splitting usually occurs when a vortex is torn in two by the strain or shear induced by a vortex of opposite sign in close proximity to the splitting vortex. Splitting, thus, typically involves a system of vortices and does not usually happen to a vortex in isolation. Ideally, we should analyze and discuss the evolving vortex system from a dynamical systems perspective using material curves to define strictly the coherent structures of the unsteady flow field (Kuznetsov et al., 2002). This rigorous analysis must be left for future work. Nevertheless, the tracking of the individual anticyclonic and cyclonic vortices (eddies) using SSH anomaly contours (streamlines) gives a reasonable qualitative representation of the evolving vortex system. Care must be exercised for unsteady flows since streamlines are not path lines, and mass transport (flux) can occur across a streamline. This would not be the case in a time-independent flow. More details concerning the splitting of Ulysses will be considered next as we discuss the indirect influences of the LC and LCEs on the study region.

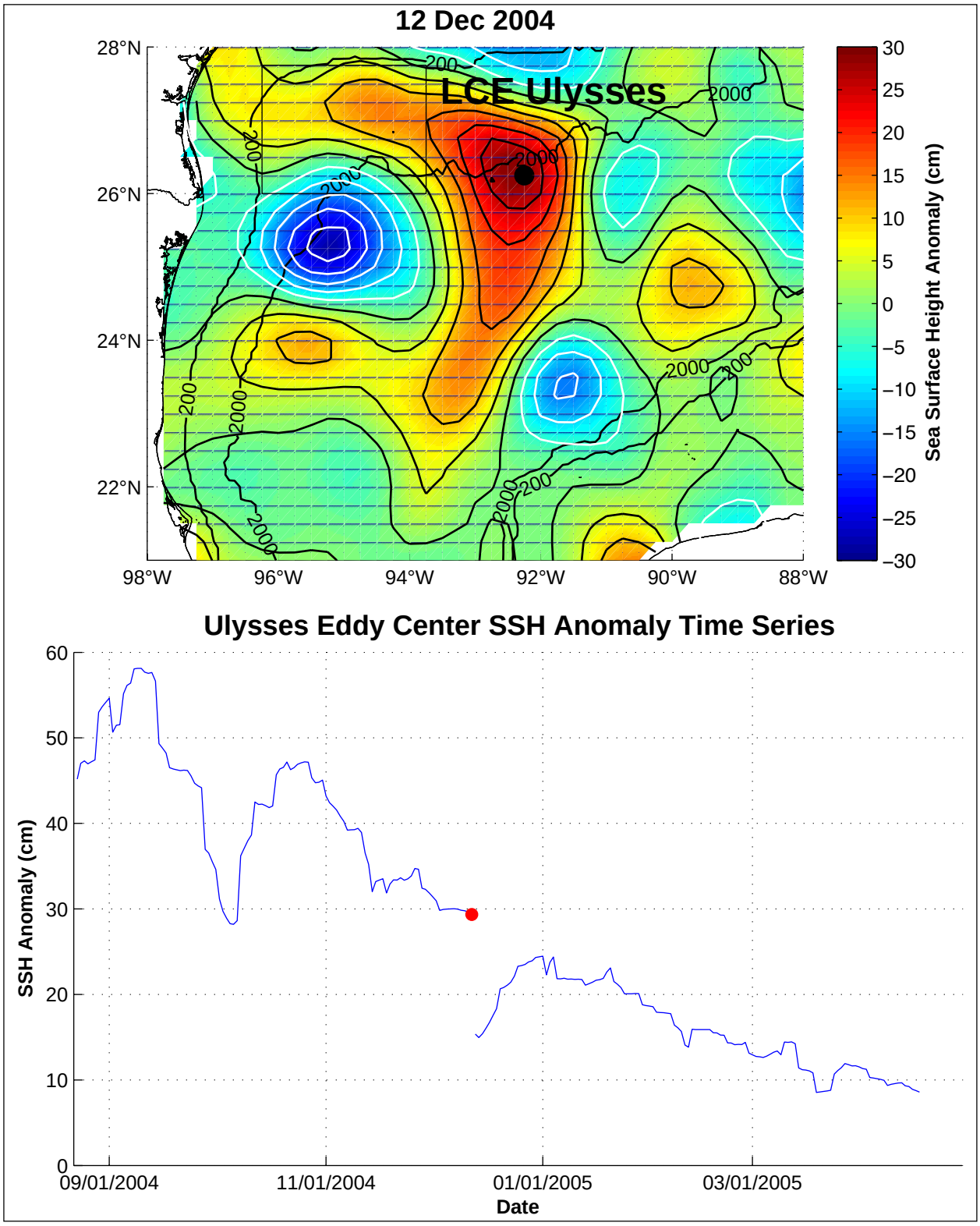

Figure 3.3-5. SSH anomaly map of LCE Ulysses on 12 Dec 2004 (upper panel) and maximum eddy center SSH anomaly time series (lower panel). This is the day before the nominal eddy splitting date based on altimetry tracking.

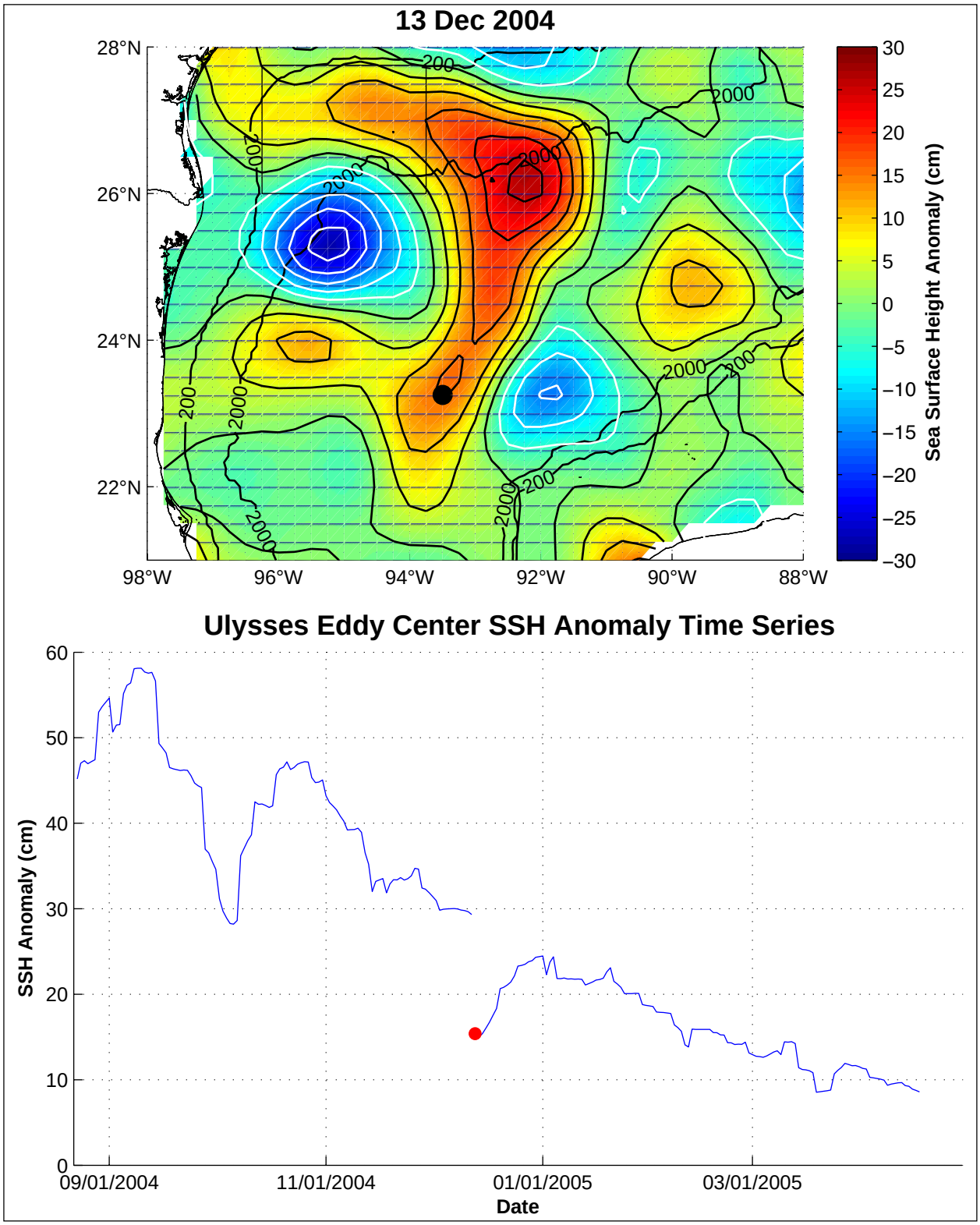

Figure 3.3-6. SSH map of LCE Ulysses on 13 Dec 2004 (upper panel) and maximum eddy center SSH anomaly time series for Ulysses/U2 (lower panel). This is the nominal eddy splitting date based on altimetry tracking.

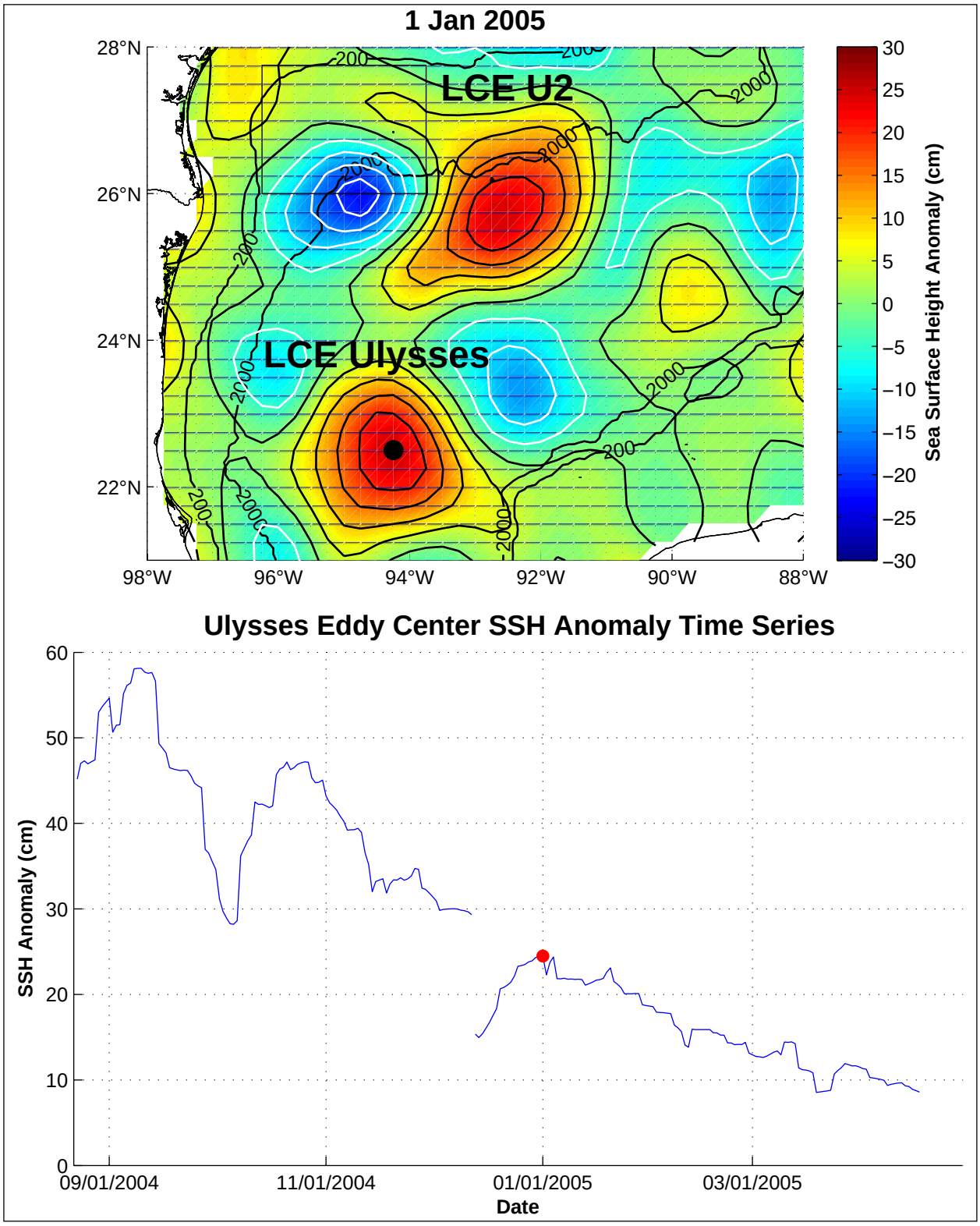

Figure 3.3-7. SSH map of LCE Ulysses on 1 Jan 2005 (upper panel) and maximum eddy center SSH anomaly time series (lower panel). Splitting of LCE Ulysses into LCEs U2 and Ulysses is complete.

Influences of LCEs on the study region were effected through a variety of complex eddy-eddy interactions that included eddy merging and splitting. These interactions produced anticyclonic and cyclonic eddies over the NW GOM continental slope that were well sampled by the study array. The most complicated eddy-eddy interaction affecting the study region during the program interval was the splitting of LCE Ulysses. This splitting event, on first inspection, appears to be an instability-driven process affecting an isolated vortex in deep water as might occur for a shielded vortex undergoing fission to a more stable supercritical state such as described by Flierl (1988). Closer inspection, however, shows that the Ulysses splitting event was not a single isolated geophysical vortex splitting in two, but instead was a complex system of vortices interacting with each other and with the surrounding slope topography. This complex interaction dramatically reconfigured the eddy field in the western GOM in less than two months.

A preliminary quantitative evaluation of the circulation in this eddy system will be discussed in Section 3.5 on eddy-eddy interactions. Here we give a brief qualitative description of the eddy field. For an overview, we show a two-month sequence of SSH anomaly maps in Figures 3.3-8 and 9 that directly correspond to the SSH maps shown in Figures 3.2-6, 7 and 8. Anomaly maps are shown to be consistent with the SSH anomaly fields that we used to track eddies in our retrospective analysis of LCE paths described in Section 3.1. As shown by the labels on the SSH anomaly maps, the Ulysses eddy system is comprised of both anticyclonic eddies (ACEs) and cyclonic eddies (CEs). Three primary CEs are implicated in the split of Ulysses. The splitting of Ulysses was not into two eddies, but four – two large (Ulysses and U2) and two small (ACE_a and ACE_b in Figure 3.3-9). The CEs surrounding Ulysses were named alphabetically, CE_a, CE_b, and CE_c, starting with the strong CE to the west of Ulysses. The correspondence between the named CEs and ACEs reflects the dynamical connection between each cyclone and the piece of anticyclonic circulation that splits off from the original LCE Ulysses. CEs were positioned on the outer edge of Ulysses in the “upstream” direction from the ACE with the same letter subscript so that, for example, CE_a is associated with the splitting of ACE_a from the original LCE Ulysses, CE_c with ACE_c. and CE_b with the post-split LCE Ulysses. Thus, cyclones were actively involved in the splitting off of each anticyclone from the primary anticyclonic circulation. Furthermore, LCE U2 was the primary remnant of LCE Ulysses left behind after the splitting off of at least three pieces of anticyclonic circulation from the LCE. All of the CEs were companions of Ulysses and were produced, in part, by the interaction of Ulysses with the continental slope. Some of the cyclonic circulation associated with CE_a and most of the circulation in CE_b formed in an interaction with the Campeche slope and propagated westward with the LCE. CE_c formed over the northern slope. The entire splitting process took just over two months. Tracking of the individual eddies are shown in Figures 3.3-10, 11, and 12. Each cyclonic eddy center path turned to the right along a clockwise-tending trajectory, consistent with the dominantly anticyclonic circulation of the entire eddy system. A summary of the LCE Ulysses splitting events and associated eddies are listed in Table 3.3-2.

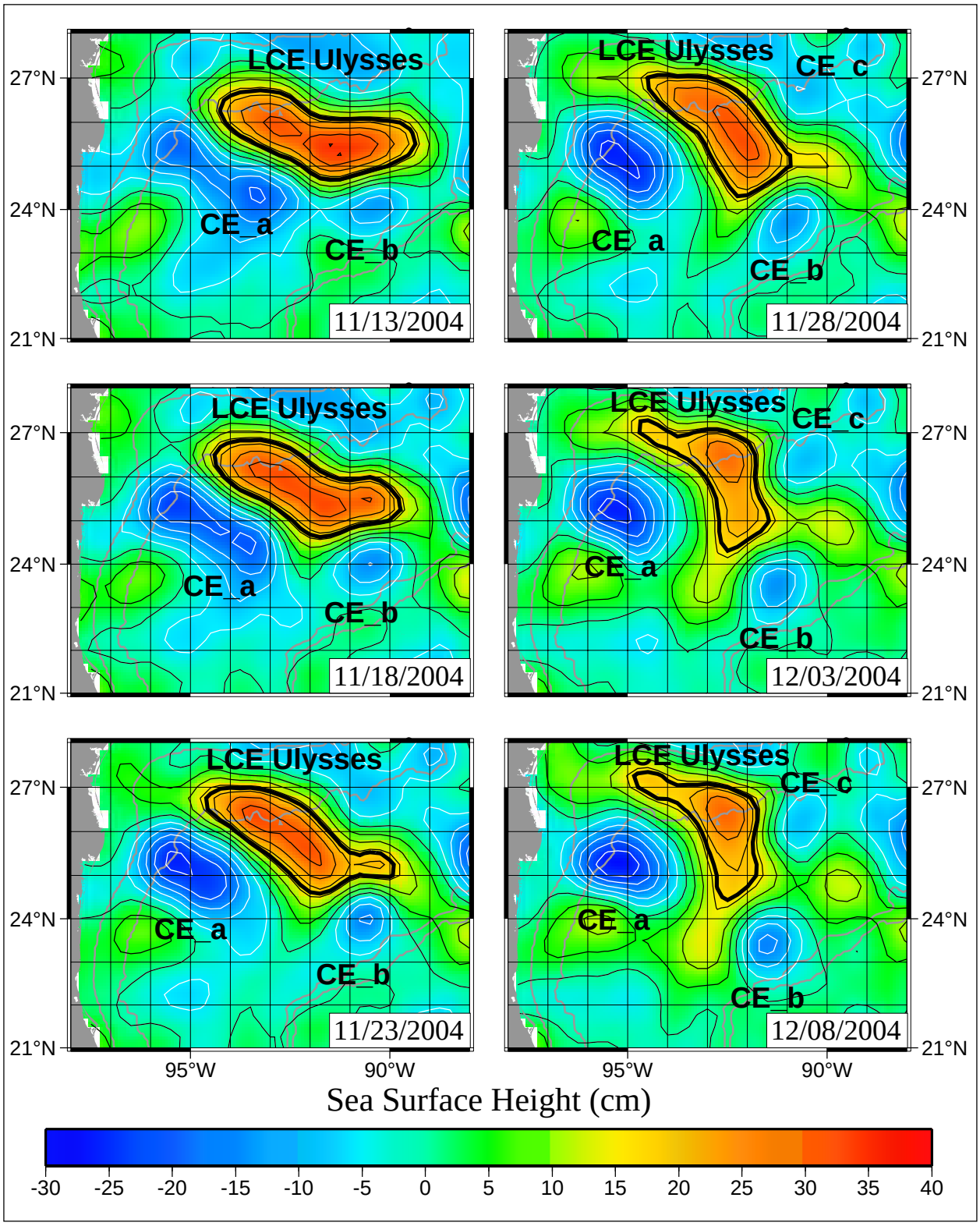

Figure 3.3-8. LCE Ulysses/U2 splitting sequence. SSH anomaly maps at 5-day intervals from 13 Nov 2004 through 8 Dec 2004 are shown. Selected companion cyclonic eddies discussed in the text are identified.

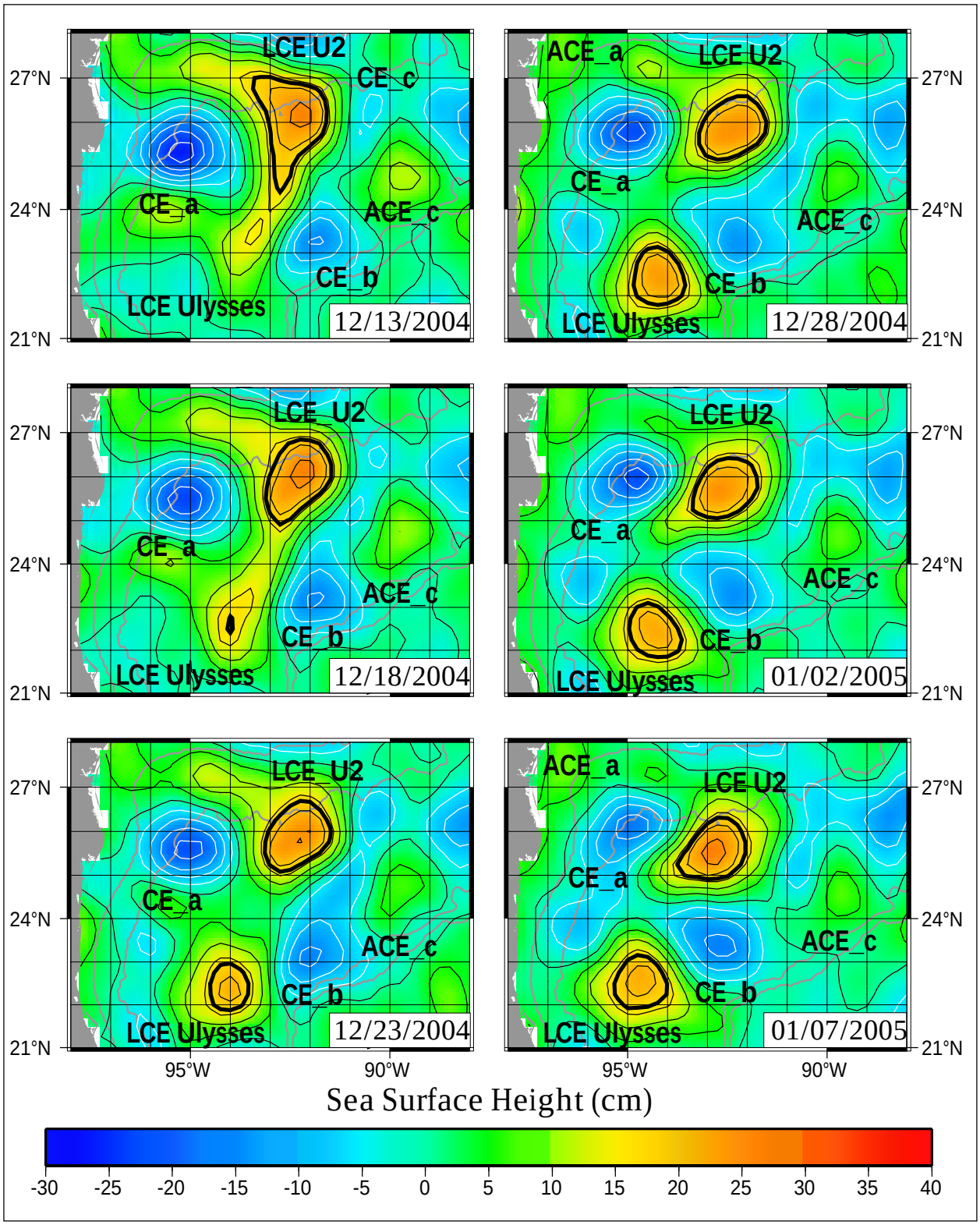

Figure 3.3-9. LCE Ulysses/U2 splitting sequence (cont.). SSH anomaly maps at 5-day intervals from 13 Dec 2004 through 7 Jan 2005 are shown. Selected companion cyclonic eddies (CEs) and anticyclonic eddies (ACEs) discussed in the text are identified.

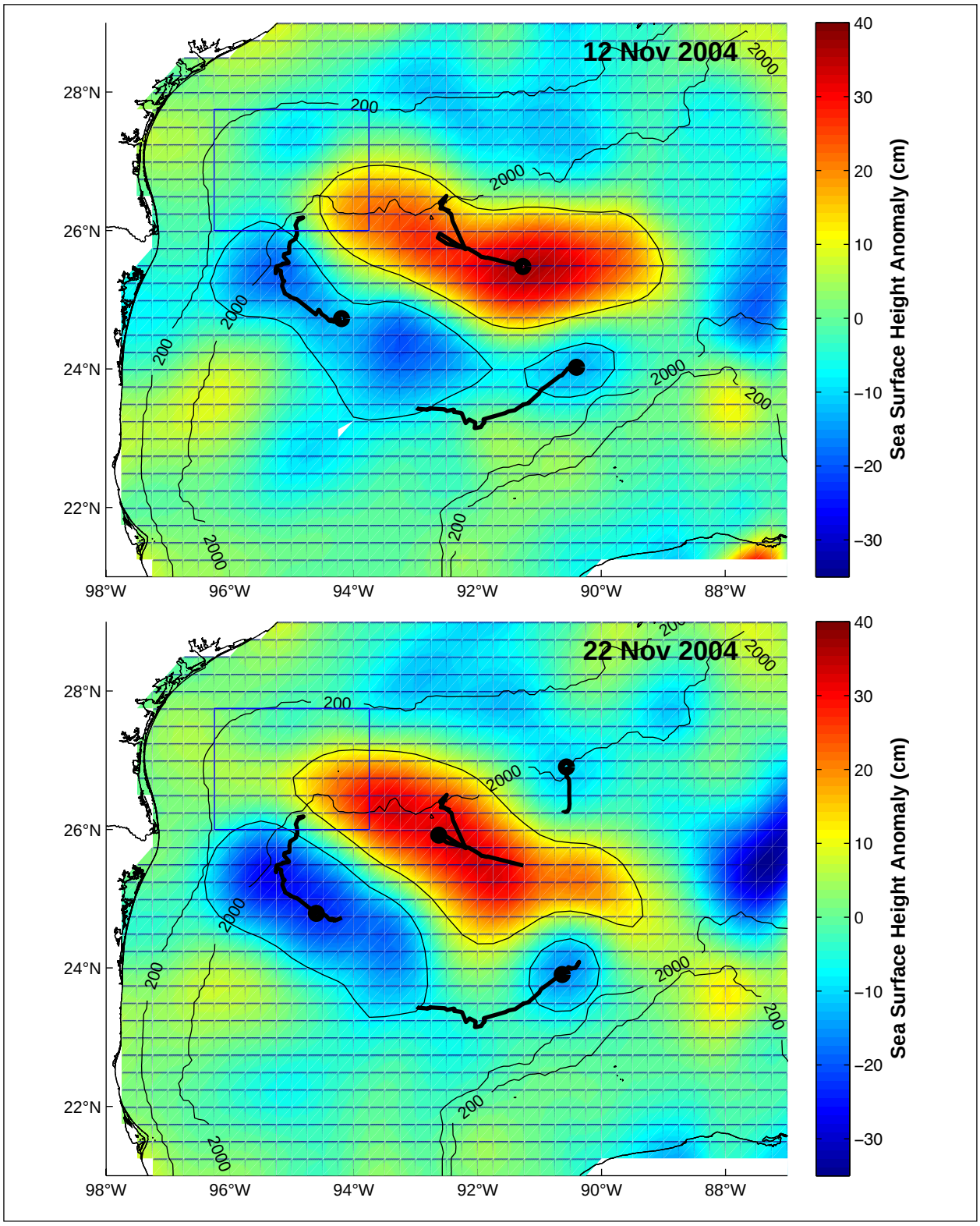

Figure 3.3-10. Eddy center paths of eddies involved in Ulysses/U2 split overlaid on 12 Nov and 22 Nov 2004 SSH anomaly maps. The eddy center is the mean of the tracking contour points. The filled circle is the center location on the given date.

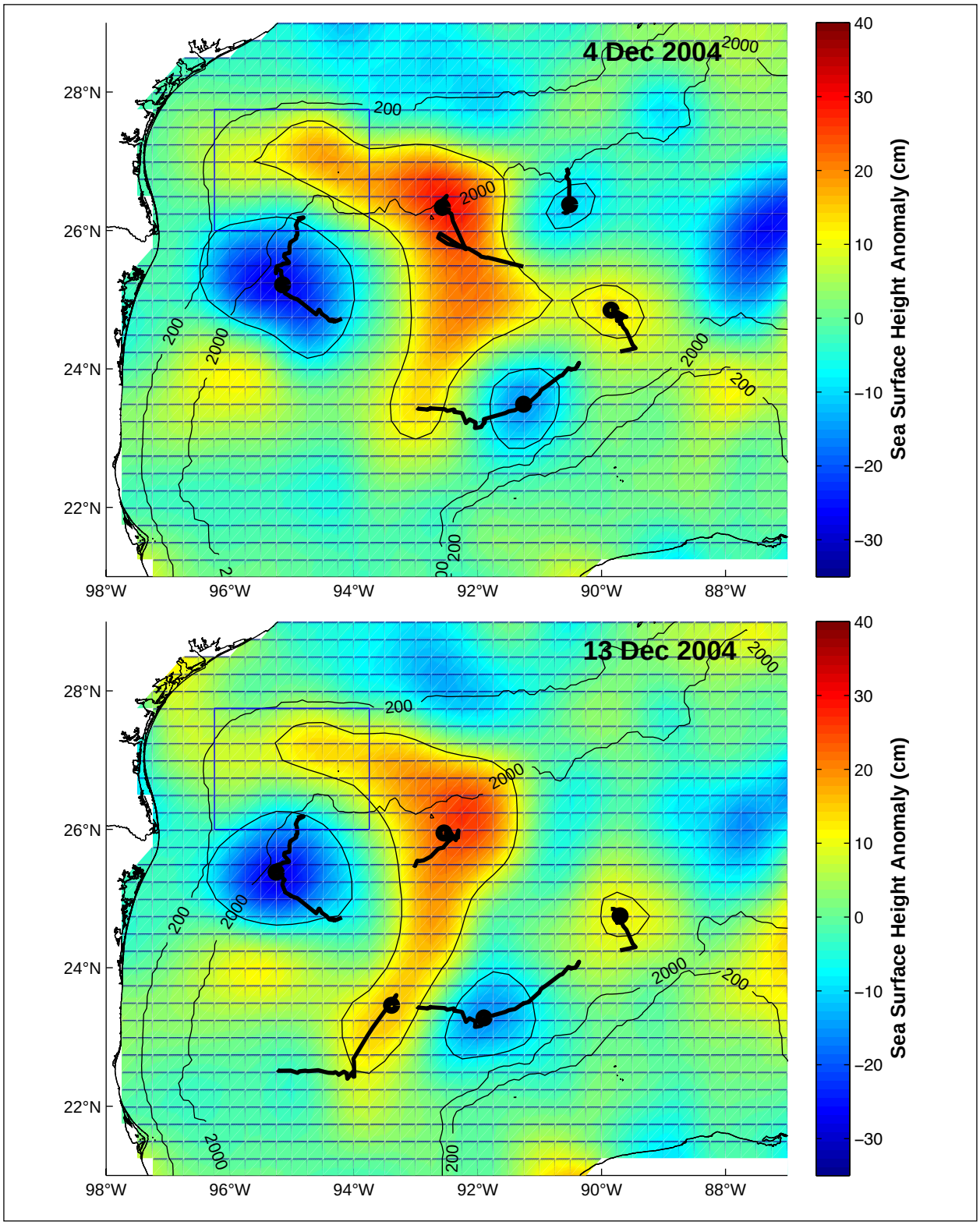

Figure 3.3-11. Eddy center paths of eddies involved in the Ulysses/U2 splitting event overlaid on 4 Dec and 13 Dec 2004 SSH anomaly maps. The eddy center is the mean of the tracking contour points. The filled circle is the center location on the given date.

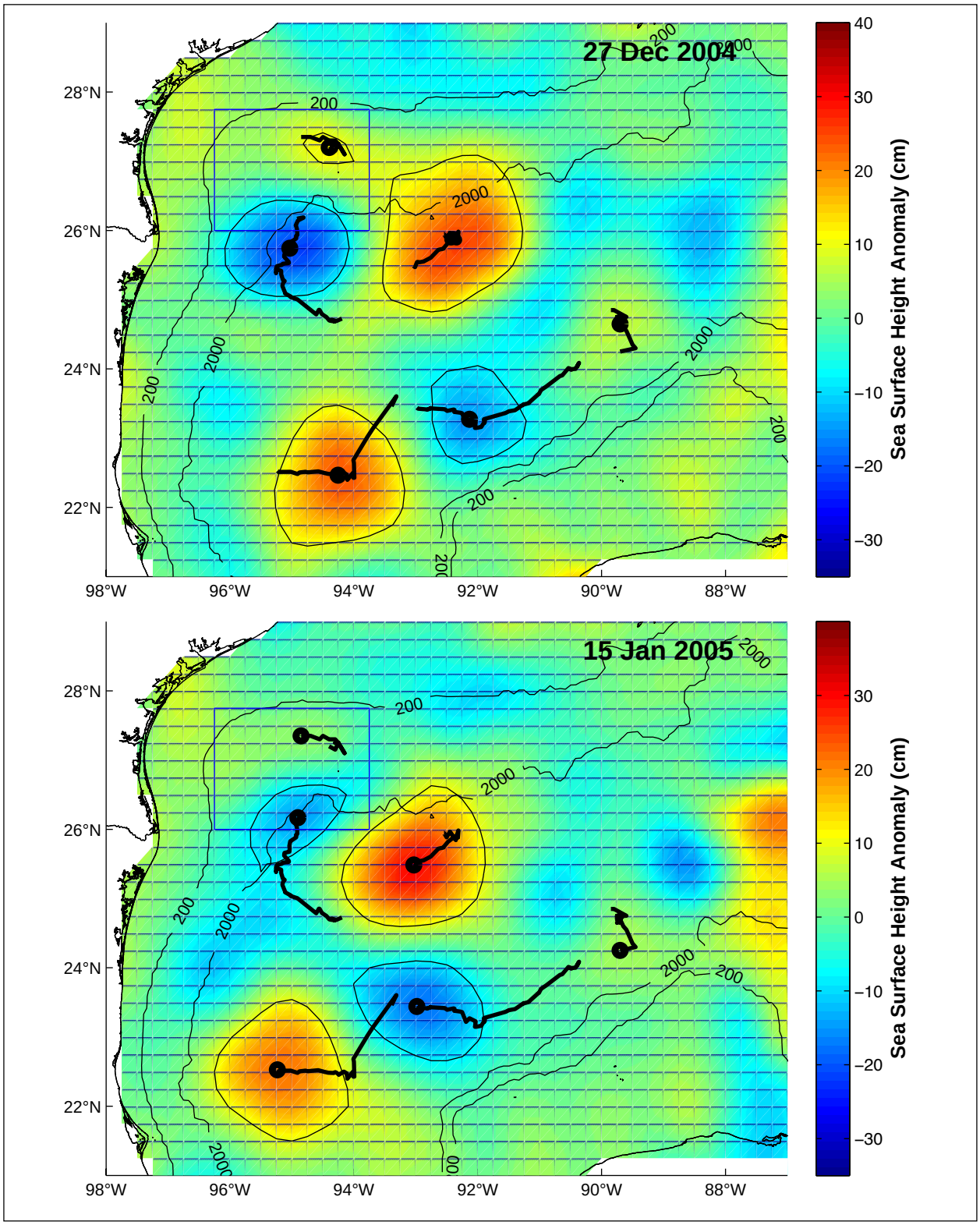

Figure 3.3-12. Eddy center paths of eddies involved in the Ulysses/U2 splitting even overlaid on 27 Dec 2004 and 15 Jan 2005 SSH anomaly maps. The eddy center is the mean of the tracking contour points. The filled circle is the center location on the given date.

Table 3.3-2

Timeline of LCE Ulysses Splitting Event and Associated Eddies

Event	Date	Comments
LCE Ulysses separation	24 Aug 2004	Defined by breaking of the 17-cm contour. See Figure 3.2-3
First Ulysses companion cyclone formed along Campeche escarpment	Oct 2004	Altimetry/ocean color. See top panel of Figure 3.2-5.
Companion cyclone merged with cyclone west of Ulysses to form CE_a.	mid Nov 2004	Altimetry/ocean color. See bottom panel of Figure 3.2-5.
Second companion cyclone, CE_b, formed along Campeche escarpment	mid Nov 2004	See the 12 Nov 2004 SSH anomaly map in the top panel of Figure 3.3-10.
CE_c formed over northern continental slope	late Nov 2004	Altimetry/ocean color.
ACE_c split off from southeastern flank of Ulysses	early Dec 2004	Altimetry/ocean color.
LCE Ulysses/U2 split	13 Dec 2004	Nominal date of splitting based on altimeter tracking.
Split and reorganization of Ulysses/U2 completed	late Dec 2004	Altimetry/ocean color.
ACE_a split off from northwest flank of LCE U2	late Dec 2004	Well observed by PIES and mooring array.
CE_a propagated clockwise around LCE U2 and crossed northeast through study array	Jan 2005	Well observed by PIES and mooring array.

The evolution of the Ulysses eddy system split an energetic cyclone off from CE_a, which passed through the study array splitting off a small anticyclonic eddy (ACE_a) from the northwest margin of LCE U2. As noted in our historical review, kinematic analysis of SCULP drifter trajectories by Hamilton (2007) suggests a possible link between the LC and the number of cyclonic eddies along the northern continental slope through the influence of propagating LCEs. Thus, there is good observational evidence that eddy activity in the NW Gulf study region is related to the LC and LCE shedding cycle. Observations during the NW Gulf program confirm this connection and also indicate that anticyclonic eddies may also be generated, although the relative number of eddies favors cyclones to anticyclones by a factor of about two (Hamilton, 2007). Thus, eddy-eddy and eddy-slope interactions are the primary indirect influence of the LC and LCEs on the study region. This connection will be explored in further detail in the following sections when we review the anticyclones and cyclones that were observed in the study region.

3.3.3 Anticyclonic Eddies (ACEs) in the NW Gulf Study Region

Strong anticyclonic eddy events unrelated to LCEs in the NW Gulf study region are rare. One of the strongest events of this type observed in the altimeter record occurred during the NW Gulf program time period. We refer to this eddy as ACE #1. During its 5-month lifespan from June through October 2004, the eddy remained within the study array. A sequence of maps of 8-day composite chlorophyll concentration images overlaid with currents and altimetry are shown in Figures 3.3-13 and 14**.** In May, the study region circulation was dominated by a cyclone, CE #1. ACE #1 formed in early June, and remained in the study array throughout the summer. Although

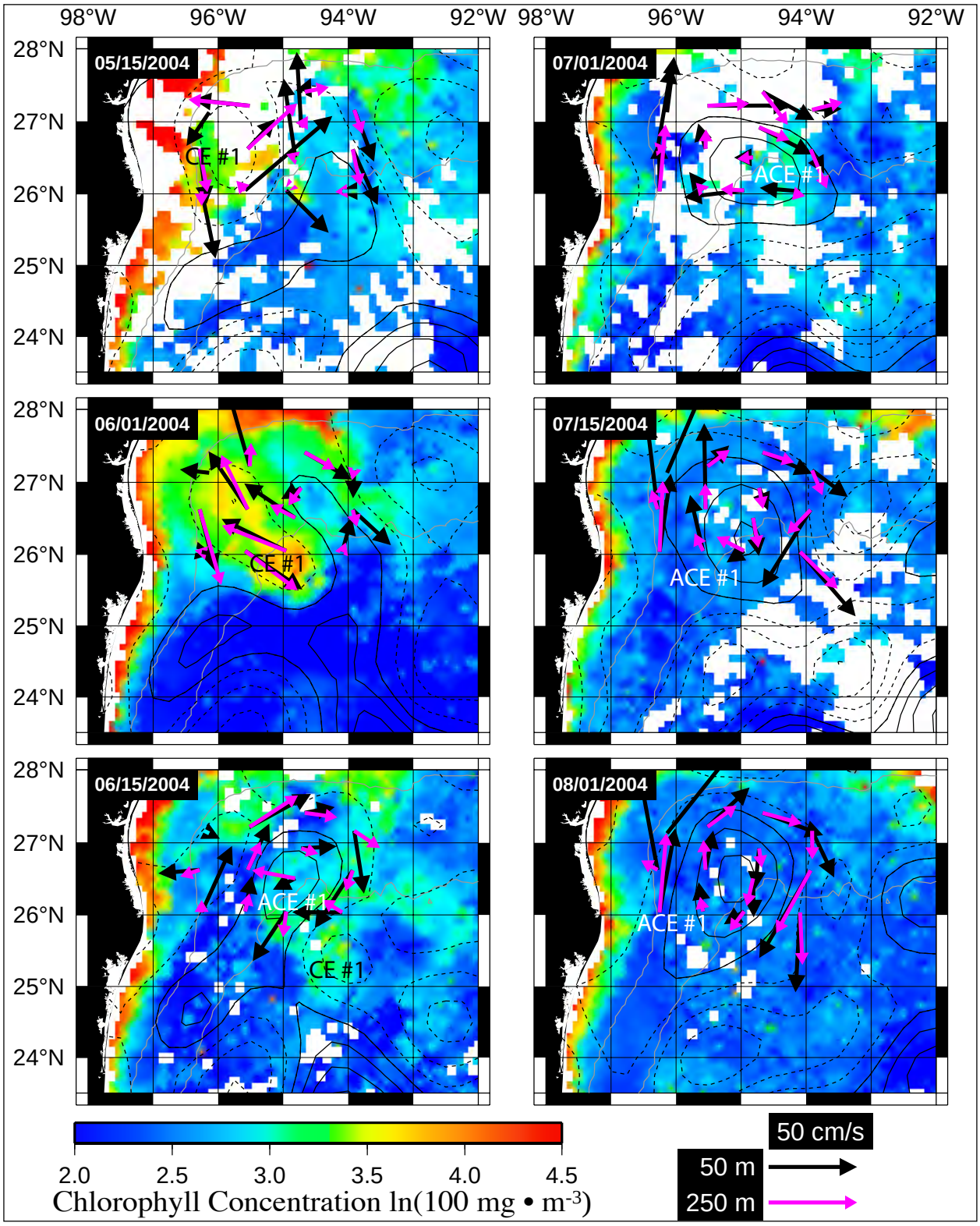

Figure 3.3-13. Chlorophyll concentration 8-day composite image sequence of NW Gulf ACE #1. Twice monthly images from 15 May through 1 Aug 2004 are overlaid with 50 and 250-m depth currents and SSH contours. ACE #1 formed in early June.

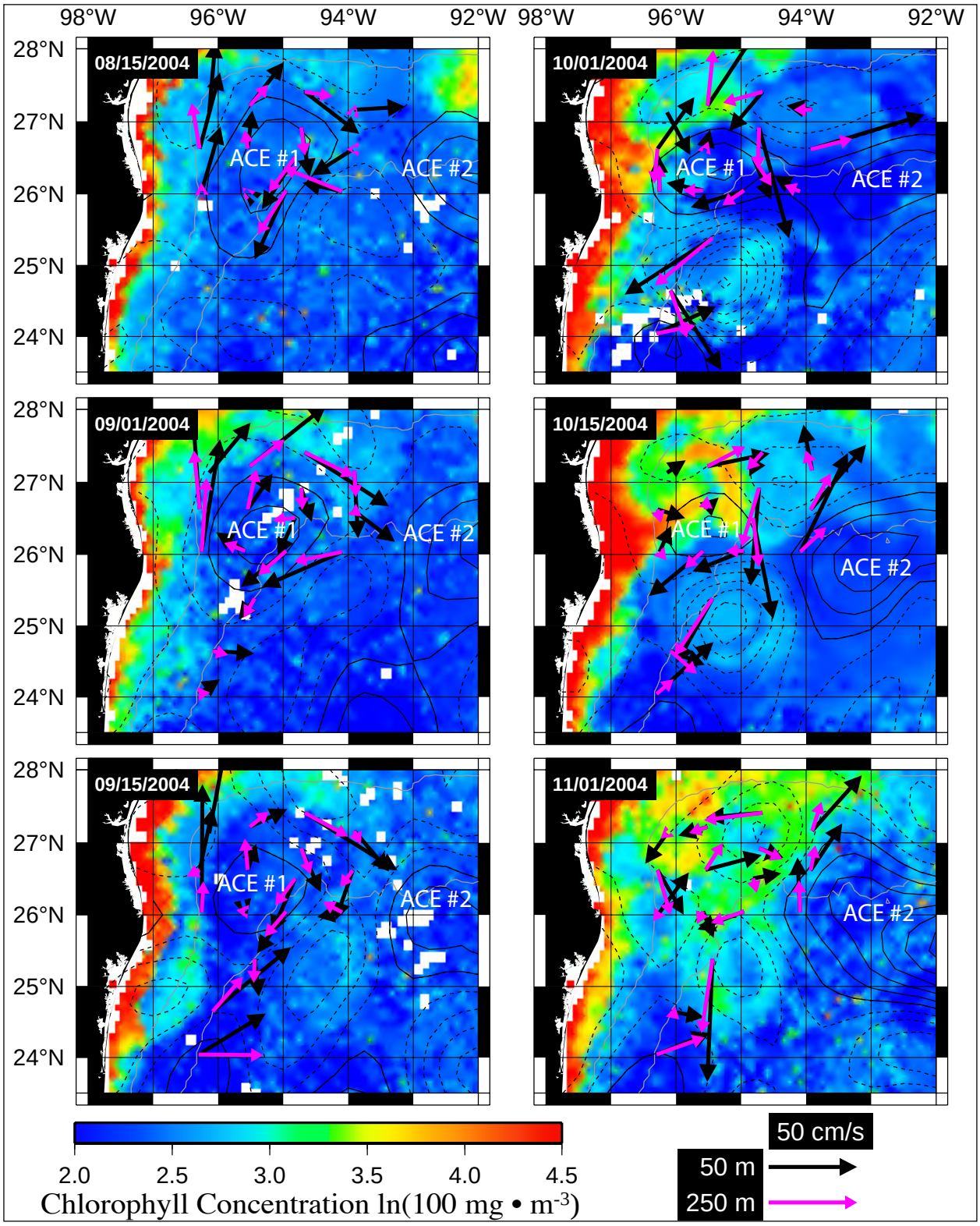

Figure 3.3-14. Chlorophyll concentration 8-day composite image sequence of NW Gulf ACE #1 (cont.). Twice monthly images from 15 Aug through 1 Nov 2004 are overlaid with 50 and 250-m depth currents and SSH contours. ACE #1 dissipated in late October.

the eddy appeared to form primarily within the study array, some surface waters may have been entrained into the eddy from south of the array. Ultimately, ACE #1 dissipated as it was squeezed between CEs #3 and #4.

Just before ACE #2 dissipated, a cyclone, CE #5, formed over the northern slope in the study array primarily through the interaction of ACE #1 and ACE #2 with the continental slope. It is likely that there was only weak cross-shelf-break flow in the confluence between ACE #1 and CE #5 since the ocean color in CE #5 was less pronounced than the signatures in CEs #3 and #4. Vigorous cross-shelf-break flows were associated with the strong color signatures in CEs #3 and #4. The presence of CE #3 may have also reduced the cross-shelf-break flow near CE #5. Nevertheless, CEs #3, #4, and #5 all formed in the NW Gulf study array coincident with the landfall of Hurricane Ivan in the eastern Gulf. These cyclones and their connection to Ivan will be discussed in more detail in the section on cyclonic eddies observed during the program time period to follow.

Another anticyclonic eddy in the study region, ACE #2, also appeared to be unrelated to the LC or LCEs. This was the anticyclone previously discussed in Section 3.2 (see Figure 3.2-5) that merged with LCE Ulysses in late October and early November 2004. The western periphery of this eddy briefly entered the NW Gulf array causing strong surface currents at the easternmost moorings. The eddy field configuration in the NW Gulf in October just before the merger with Ulysses was one of the most interesting observed during the program record. A quadrapole eddy consisting of two anticyclone/cyclone dipoles is clearly seen in the 8-day composite image of chlorophyll concentration for 15 Oct 2004 shown in Figure 3.3-15. ACE #1 and CE #5 to the north and CE #4 and ACE #2 to the south form the two dipoles. The ACEs and CEs are identified in the image, which also shows overlaid 50 and 250-m depth currents and SSH contours. The quadrapole structure is also clearly seen in the 450-m daily mean 40-hour low passed temperature measurements shown objectively mapped in Figure 3.3-16 from 15 Oct to 16 Oct 2004.

The final ACE of note in the study region, ACE #3, was the small piece of Ulysses that split off from the northwestern flank of the eddy in January 2005 near the end of the Ulysses splitting event. In our description of the Ulysses splitting event in the previous section, this ACE was referred to as ACE_a and was associated with cyclone CE_a. This cyclone will be discussed in further detail as CE #4 in the description of CEs in the study region to follow. ACE #3 was quite small, but was well observed by the PIES array. A sequence of 8-day composite images of chlorophyll concentration are shown in Figure 3.3-17 overlaid with PIES SSH and 50 and 250-m depth currents from the moorings. The ACE remained relatively stationary on the mid-slope near the center of the array after splitting off from U2 and ultimately dissipated in early February 2005. A summary of these three study region ACEs is listed in Table 3.3-3.

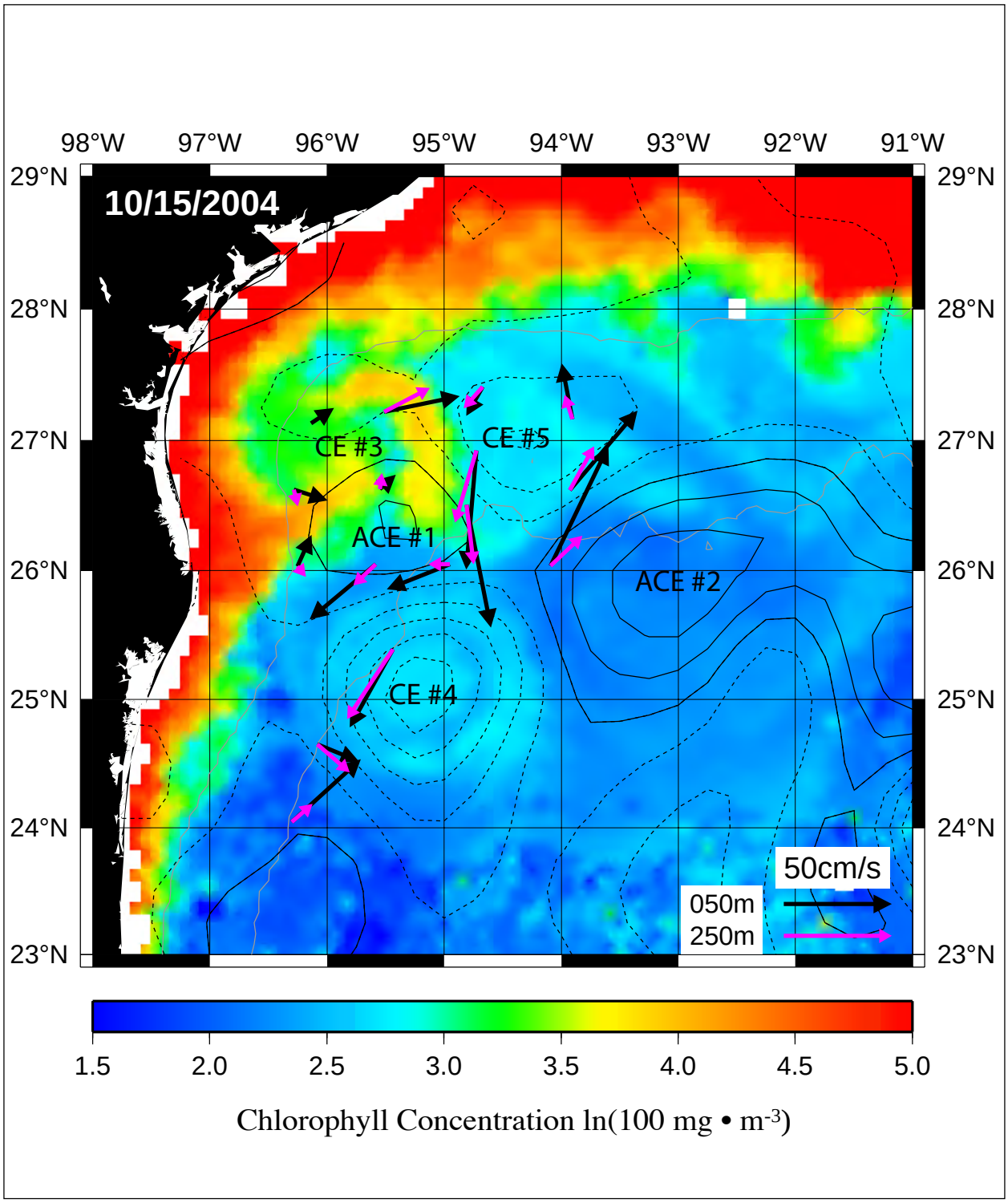

Figure 3.3-15. Quadrapole eddy in NW Gulf on 15 Oct 2004. The quadrapole eddy consists of a pair of anticyclone/cyclone dipoles that are formed by ACE #1 and CE #5 in the north and CE #4 and ACE #2 to the south. The 8-day composite images of chlorophyll concentration are overlaid with 50 and 250-m depth currents and SSH contours.

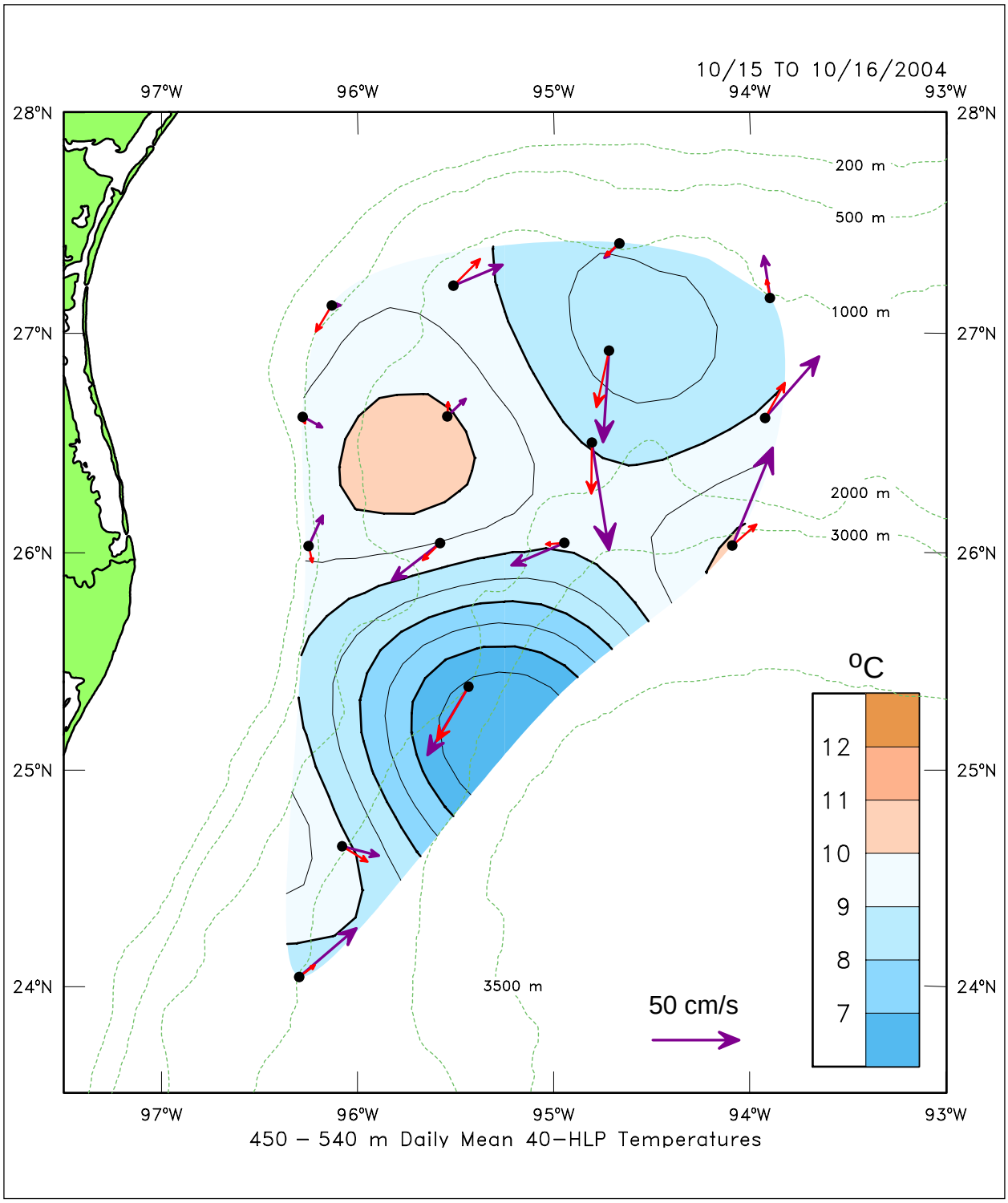

Figure 3.3-16. Quadrapole eddy thermal signature at 450-m depth measured by NW Gulf array. Objectively mapped daily mean 40-hour low passed temperature values for 15 Oct 2004 are shown. The red and purple arrows are daily mean 40-hour low passed currents at 250 and 50 m, respectively.

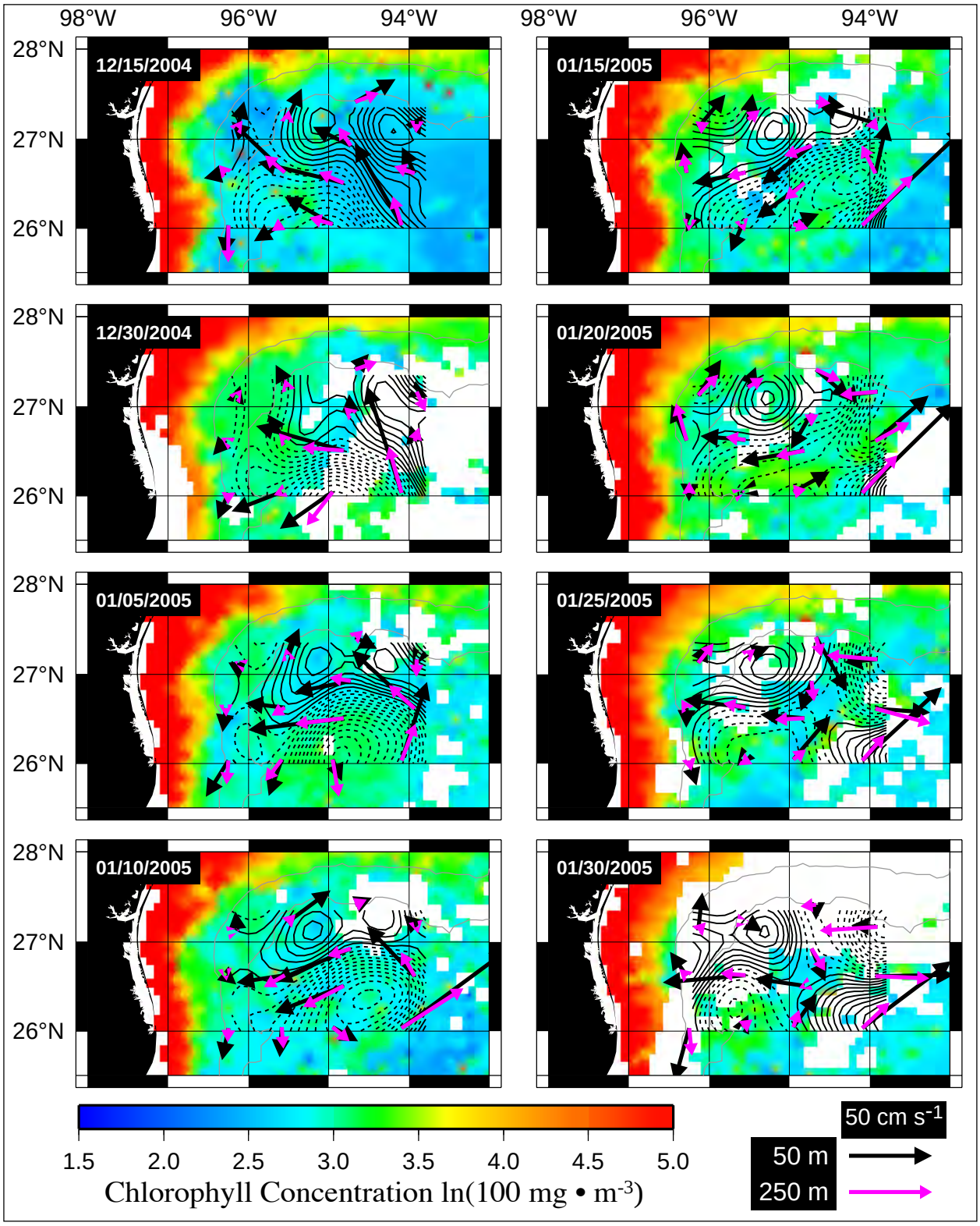

Figure 3.3-17. Sequence of 8-day composite images of chlorophyll concentration showing ACE #3 in the study array. Images are overlaid with PIES SSH and 50 and 250-m depth currents from the moorings. Contour increment is 2 cm.

Table 3.3-3

Timetable of Anticyclonic Eddies in Study Array

Event	Date	Comments
ACE #1 formed in study array	Jun 2004	Altimetry/ocean color, surface currents in array.
ACE #1 reached peak size and intensity	late Jul 2004	Altimetry/ocean color, surface currents in array.
ACE #1 dissipated in interaction with CEs #3 & #4.	Oct 2004	Altimetry/ocean color, surface currents in array.
ACE #2 currents at eastern moorings	Oct 2004	Altimetry/ocean color, surface currents in array.
ACE #2 merged with LCE Ulysses	15 Oct – 15 Nov 2004	Altimetry/ocean color.
ACE #3	late Dec 2004	PIES SSH, PIES-inferred 150-m depth salinity, and surface currents in array.

3.3.4 Cyclonic Eddies (CEs) in the NW Gulf Study Region

Cyclonic eddies in the study region occurred more frequently than anticyclones, consistent with the eddy census by Hamilton (2007) using historical drifter and *in situ* observations in the region. CEs were forced by a variety of sources during the program time period including LCEs and hurricanes and in most cases formed next to and/or over the continental slope. Animations of the mapped 450-m depth temperature measurements from the moorings and 150-m depth PIES-inferred salinity fields were ideal for detecting and tracking cyclones in the study region, complementing the ocean-color and altimetry remote sensing surface observations. Here we briefly review some of the well-observed and dynamically interesting cyclones that occurred during the study program.

The first cyclonic eddy observed during the program time period, CE #1, moved into the study region from the south in late March 2004 just before the NW Gulf mooring array was put in the water. The eddy remained relatively stationary and persisted through May 2004. The daily-averaged objectively mapped 450-m depth temperature fields clearly show the CE throughout this time period. In late May, the cyclone quickly moved to the east-southeast out of the array as ACE #1 formed in the study region. A sequence of 8-day composite images of chlorophyll concentration during this time period is shown in Figure 3.3-18 overlaid with 50 and 250-m depth currents from the moorings and altimeter-derived SSH.

CE #2 was the smallest cyclone clearly observed in the study array (Figure 3.3-19). The apparent diameter of the eddy at the time of formation was only about 35 km, approximately the Rossby radius of deformation over the NW Gulf slope. The eddy formed on the edge of ACE #1 and propagated in a clockwise direction around the periphery of the anticyclone, increasing in size

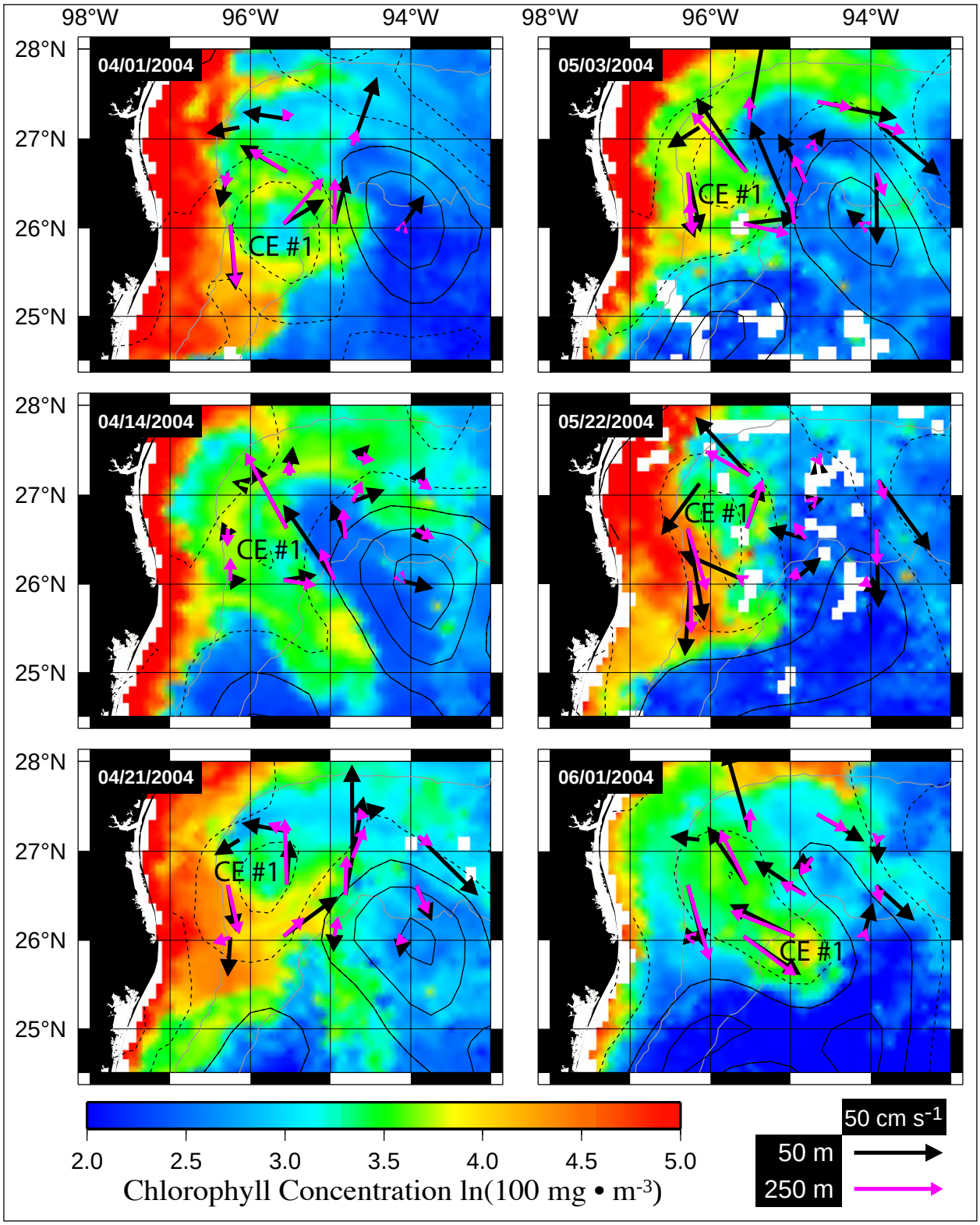

Figure 3.3-18. Sequence of 8-day composite images of chlorophyll concentration showing CE #1 in the study array. Images are overlaid with 50 and 250-m depth currents from the moorings and altimeter-derived SSH.

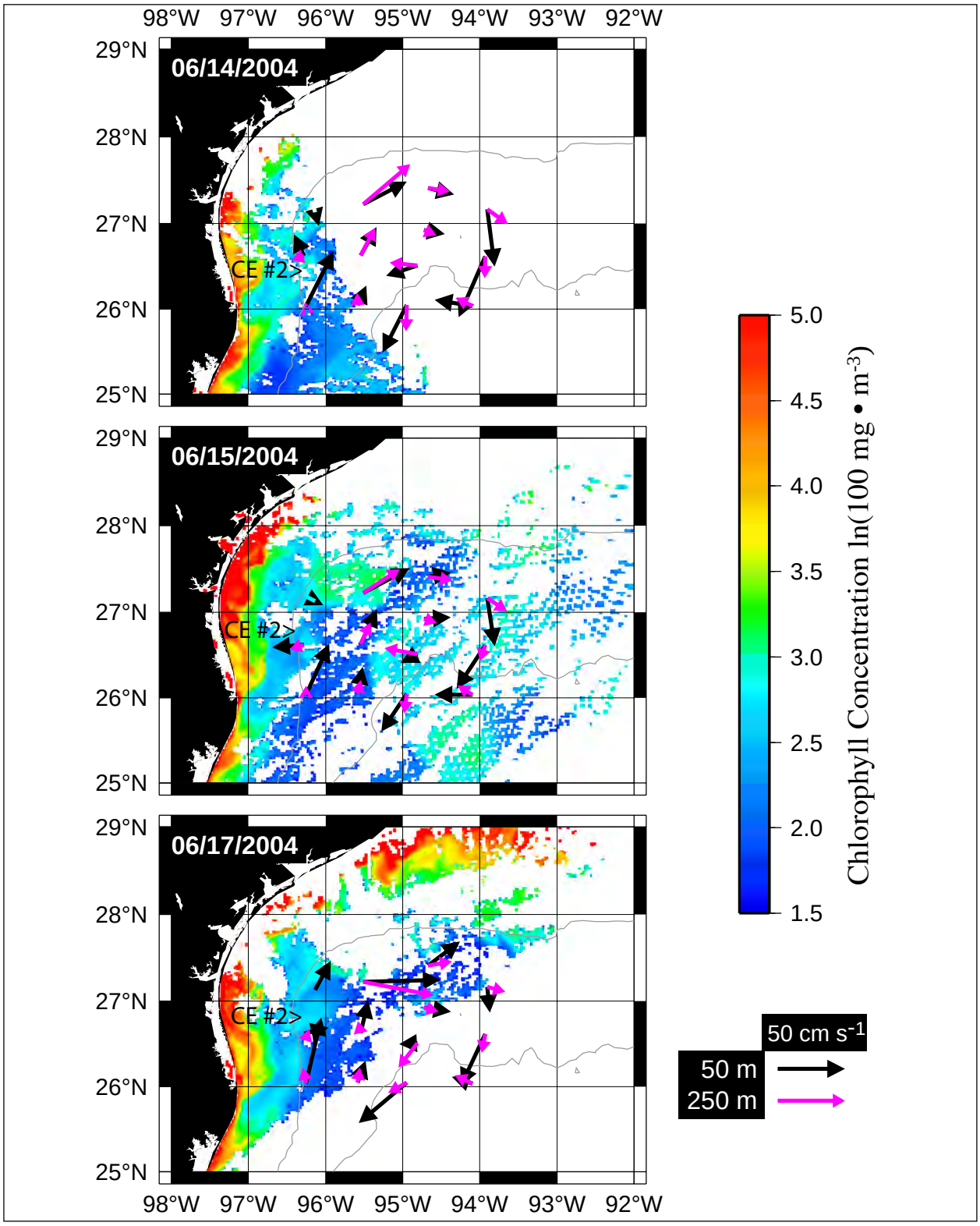

Figure 3.3-19. Sequence of daily chlorophyll concentration images for the indicated dates showing CE #2 on the western periphery of ACE #1 in the study array. Images are overlaid with 50 and 250-m depth currents from the moorings.

and intensity. Cloudy conditions prevented consistent tracking of the CE using satellite imagery alone, but a combination of ocean-color images and along-track altimetry showed that a frontal disturbance associated with the feature propagated from the western side of ACE #1 in mid-June to the northeast quadrant of the anticyclone in early July (Figure 3.3-20). The subsurface thermal signature of the cyclonic eddy also propagated around ACE #1 in the 150-m and 450-m depth temperature fields. CE #1 passed directly over mooring U1 just after forming, and currents associated with the eddy were measured at the outer moorings in the array during the translation of the eddy around ACE #1. It is not clear, however, if the propagation of the eddy or the frontal instability associated with the eddy caused the July 2004 subsurface jet event observed at mooring U4 that is discussed in Section 5.3.2. The cross-slope streamer of ocean color near 93°W in the 2 July 2004 chlorophyll image (upper panel of Figure 3.3-20) was associated with a cyclone on the eastern margin of the study array. This cyclone propagated southward between ACE#1 and ACE #2 and may have contributed to the generation of the subsurface jet.

CEs #3 and #4 were a pair of cyclonic eddies that formed over the continental slope in mid-September 2004. Initially, it looked as though these eddies might have formed by an instability process because of the regular spatial wavelength exhibited by the features. Further investigation, however, showed that the cyclones formed coincident with the landfall of Hurricane Ivan in the eastern GOM and were, in part, forced by surface currents on the shelf resulting from the storm. Teleconnection of the hurricane forcing to the NW Gulf study region was through strong hurricane-forced circulation over the northern GOM continental shelf that ultimately forced downcoast flow on the Louisiana-Texas (LATEX) shelf and cross-shelf-break flow onto the NW GOM continental slope. This circulation is similar to the response of the northern GOM shelf circulation to tropical storm Josephine described by Ohlmann and Niiler (2001) using satellite-tracked SCULP drifters. Josephine made landfall in the northeastern GOM in October 2006 and forced a strong surface current jet that extended from the west Florida shelf to the LATEX shelf and lasted for nearly a week. The current was particularly strong along the LATEX shelf break.

Since the NW Gulf program did not measure currents on the continental shelf, we obtained currents from the Texas Automated Buoy System (TABS) operated by the Geochemical and Environmental Research Group at Texas A&M University (Blaha et al., 2000). TABS 2-m depth currents were 40-hour low-pass filtered and overlaid on the 8-day composite chlorophyll images along with the 50 and 250-m depth currents from the study array. A 12-day sequence of the images is shown in Figures 3.3-21 and 22. The wind-forced circulation associated with Hurricane Ivan caused a strong downcoast flow on the LATEX shelf as far out as the shelf break. Before the hurricane-forced circulation reached the LATEX shelf, the flow inshore of the study region at TABS mooring K in 61 meters of water was northward, which was in the same direction as the northward flow associated with ACE #1 measured at the far western moorings in the study array. On 15 Sep 2004 the flow on the shelf abruptly reversed direction just before Hurricane Ivan made landfall on the Alabama coast on 16 Sep 2004. The flow reversal at K was associated with a southward flow that extended from the coast to the shelf break off South Padre Island. Both CE #3 and CE#4 formed immediately following the flow reversal.

Presumably, the narrowing of the continental shelf in the direction of downcoast currents forced a cross-shelf-break flow that led to the formation of the eddies as the current flowed southward along the southern Texas and northern Mexican coast. Anticyclonic eddies offshore of the

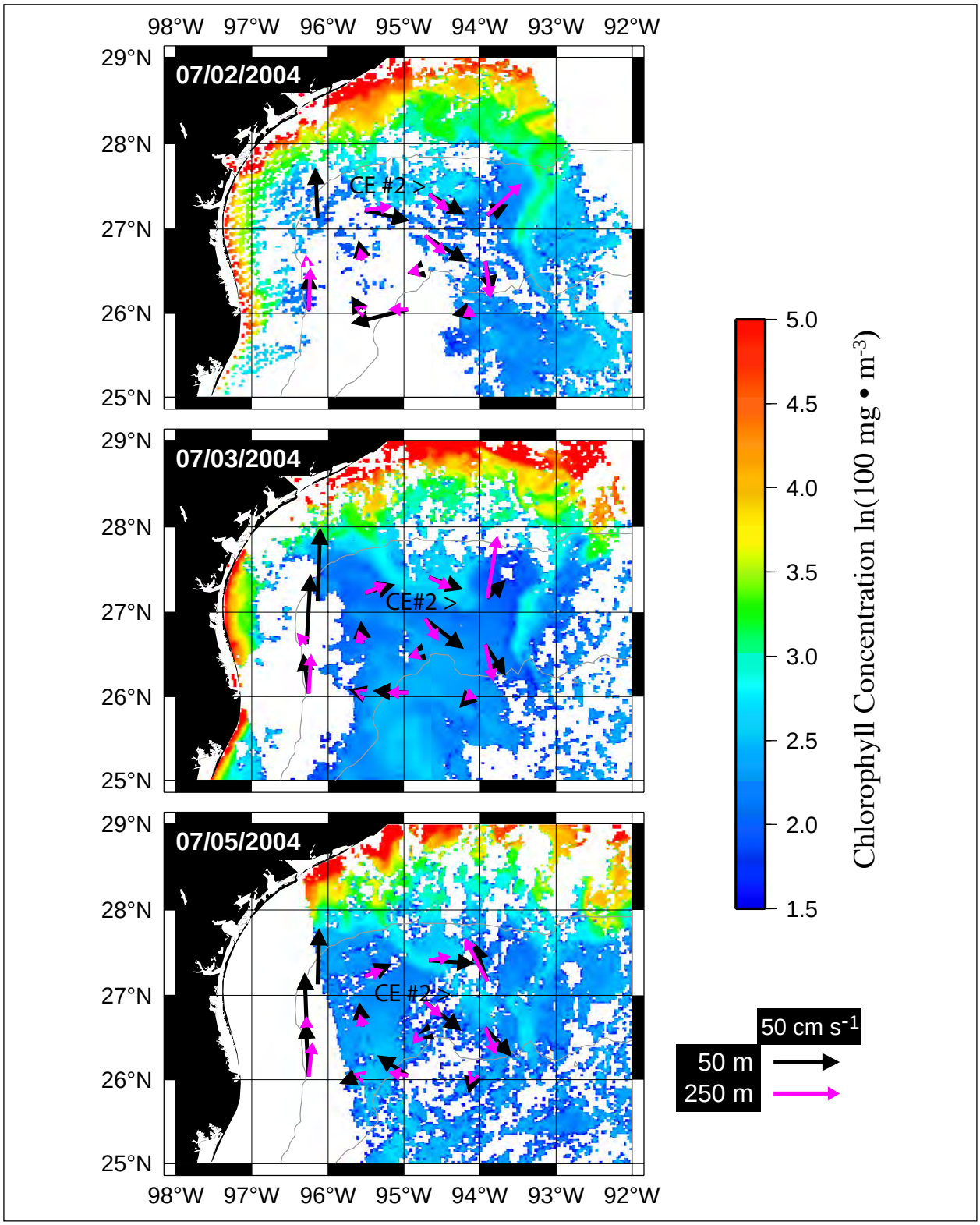

Figure 3.3-20. Sequence of daily chlorophyll concentration images for the indicated dates showing CE #2 on the northeastern periphery of ACE #1 in the study array. Images are overlaid with 50 and 250-m depth currents from the moorings.

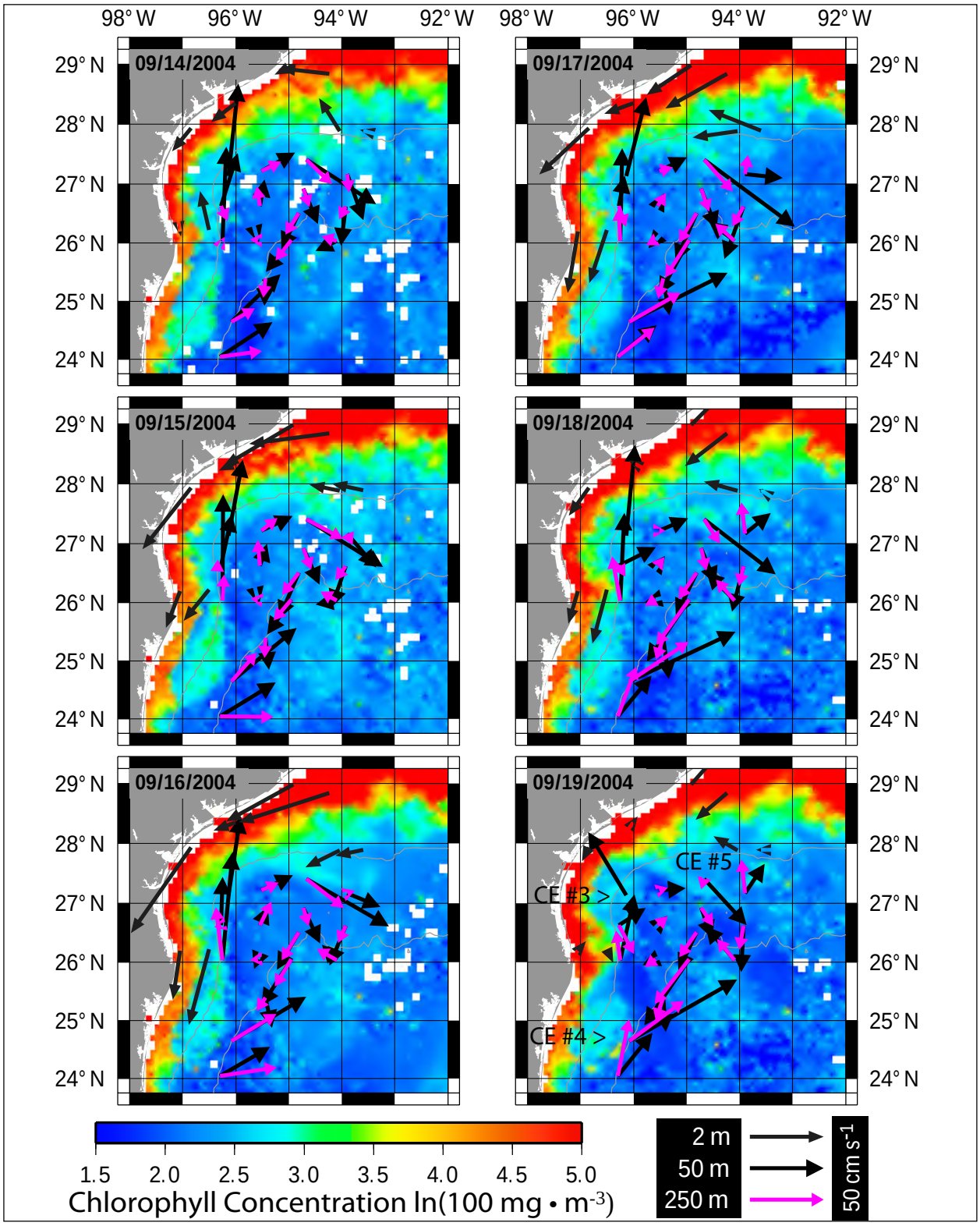

Figure 3.3-21. Daily sequence of 8-day composite chlorophyll concentration images for the indicated dates showing the formation of CE #3, #4 and #5 (14-19 Sept. 2004). Images are overlaid with TABS 2-m currents on the shelf and 50 and 250-m depth currents from the NW Gulf moorings.

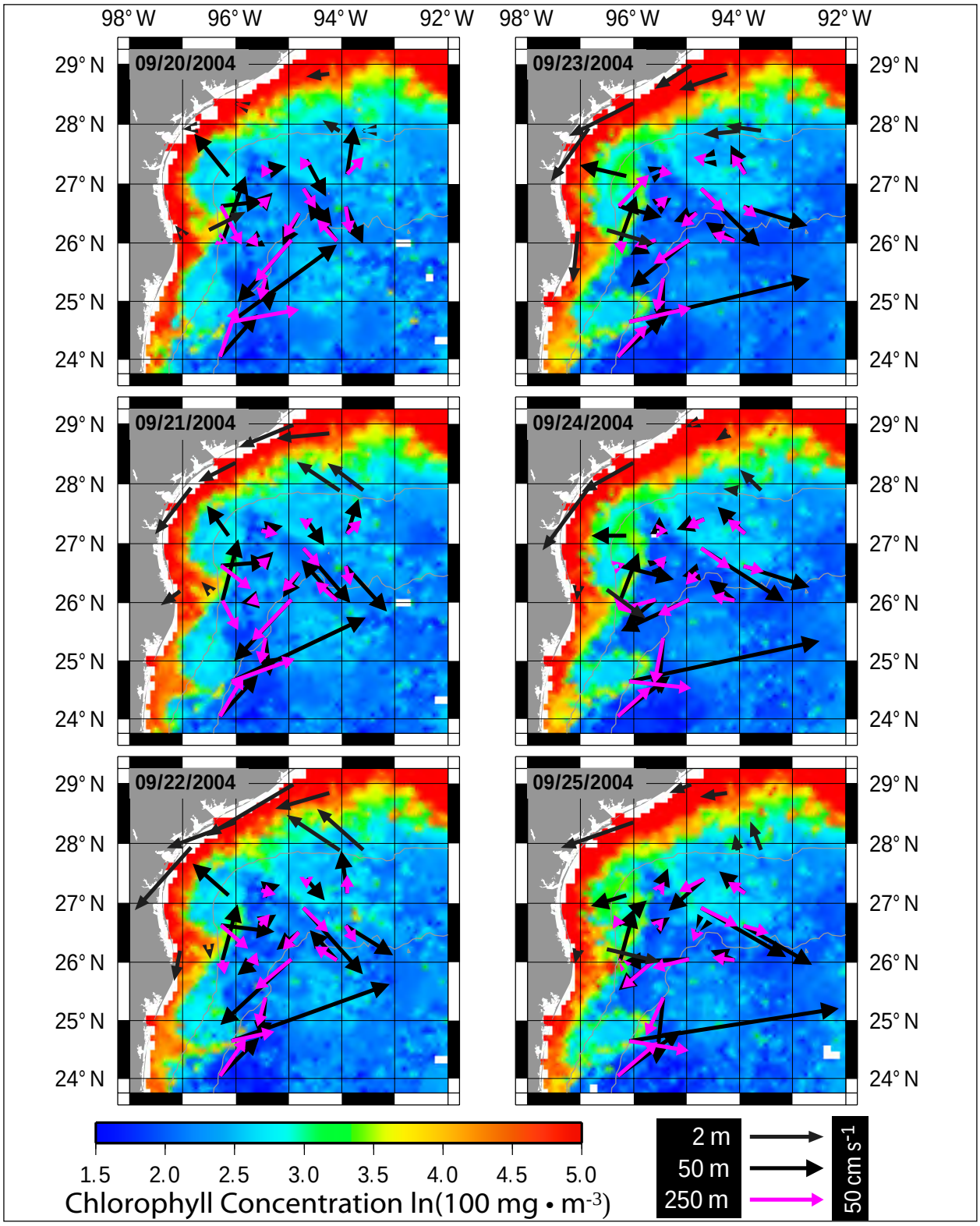

Figure 3.3-22. Daily sequence of 8-day composite chlorophyll concentration images for the indicated dates showing the continuing formation of CE #3, #4, and #5 (20-25 Sept. 2004). Images are overlaid with TABS 2-m currents on the shelf and 50 and 250-m depth currents from the NW Gulf moorings.

Mexican and Texas shelf may have also contributed to the generation of the cyclones. A remnant of LCE Titanic was located near 24°N, and ACE #1 was located just north of 26°N within the study area. CE#2 and CE#4 formed just north of these anticyclones. The circulation of each of the anticyclones briefly increased as the cross-slope flow in the confluence between the anticyclone/cyclone pairs increased in intensity in late September.

The ultimate fates of the two cyclones, which were well-observed during the study program, were remarkably different. The northern cyclone of the pair, CE #3, remained in the far northwestern corner of the study array until moving eastward in mid-November and merging with a cyclone in the eastern margin of the array, CE #5. Figure 3.3-23 shows a sequence of nearly cloud-free 8-day composites of chlorophyll concentration over the lifetime of the eddy. The cyclonic eddy resulting from the merger dissipated in late November as LCE Ulysses intruded into the study region. The lifespan of CE #3 was just over two months.

CE #4 was a longer-lived eddy because it was repeatedly energized by interactions with the surrounding field and the continental slope, existing for over five months from its formation until its ultimate dissipation by absorption into CE #6. CE #4 initially formed as the southern eddy of the hurricane-forced eddy pair discussed previously. On initial spinup, the circulation was much stronger in CE #4 than in CE #3, growing explosively as the cross-slope jet extended far offshore. The cyclone was further energized upon merging with the first Ulysses companion cyclone that propagated westward with the LCE. This merger occurred in late November and early December and can be seen in the third (15 Nov 2004) and fourth (1 Dec 2004) frames of the sequence of 8-day composite chlorophyll concentration images overlaid with currents and altimetry shown in Figure 3.3-24. The Ulysses companion cyclone formed along the Campeche escarpment and propagated westward with Ulysses. CE #4 was also energized and then split in an interaction with LCE Ulysses/U2 along the western wall. The sequence of chlorophyll images shown in Figure 3.3-25 shows the four best cloud-free 8-day composite images of this interaction. The combined contribution of energy from the hurricane, LCEs, and eddy-slope interactions produced a very strong cyclone that was the largest and longest-lived cyclone observed during the NW Gulf program. The northern margin of the eddy extended well into the NW Gulf array. Ultimately, CE #4 was split in two by U2 as the LCE propagated westward. The piece that split off to the north propagated clockwise around the periphery of U2 taking a northeast path through the array in January 2005 that was very well mapped by the 150-m salinity field inferred from the PIES data shown in Figure 3.3-26. The passage of this eddy through the array was one of the six minimum SSH extrema observed in the historical altimeter record (see Figures 3.1-25 and 26.). The cyclone was also interesting from a dynamical perspective because the upper layer circulation associated with it was one of the best examples of upper and lower layer vertical coupling found in the program's measurement record.

CE #5 formed in mid-September on the northern slope in the study array but did not have as strong a color signature as the two other cyclones (CEs #3 and #4) that formed at about the same time along the western slope (Figures 3.3-21 and 22). CE #5 formed primarily through the interaction of ACE #1 and ACE #2 with the continental slope. The cyclone strengthened in October and ultimately merged with CE #3 in late October and early November 2005 according to the altimetry and ocean color (Figure 3.3-23). Animation of the PIES data shows that the

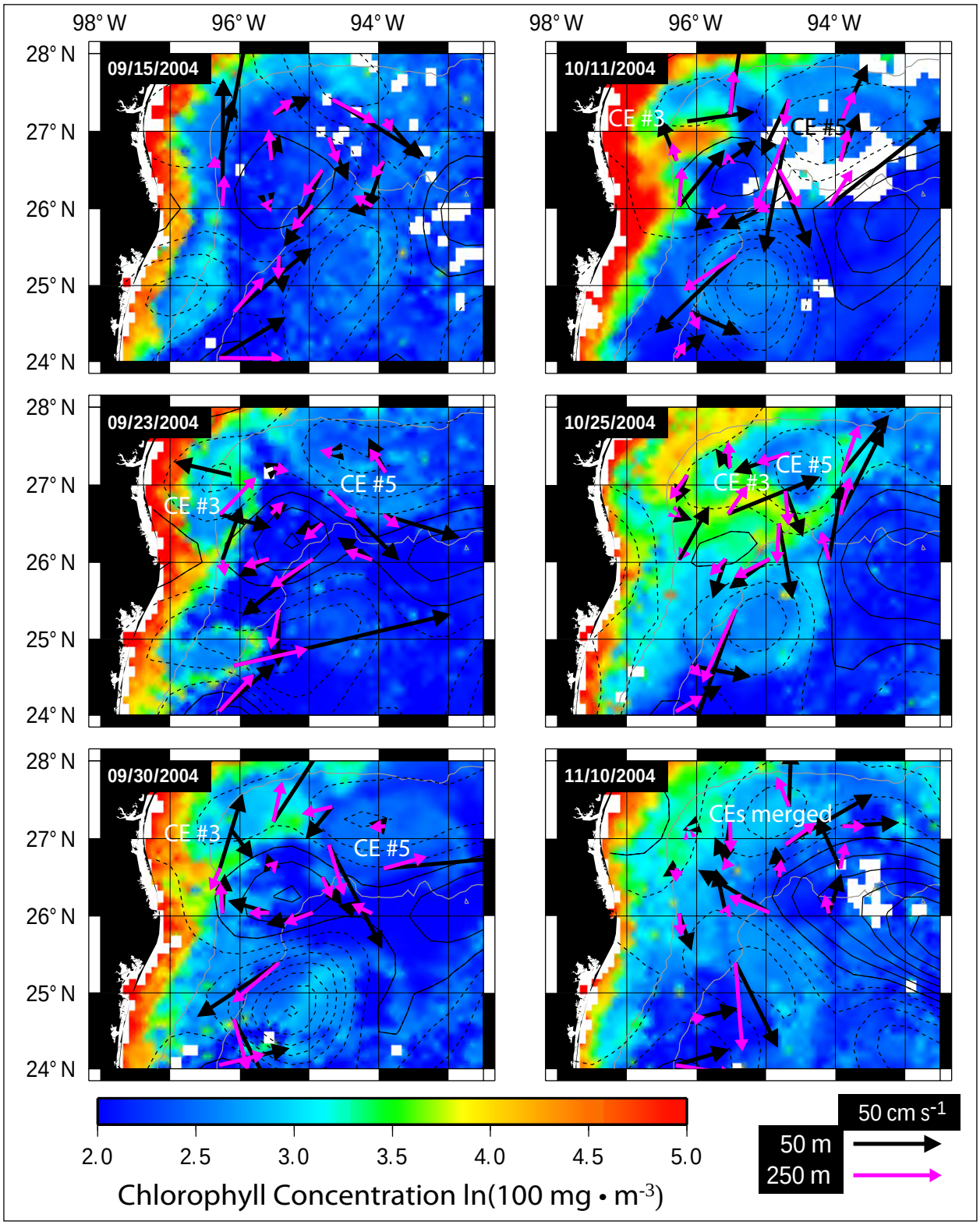

Figure 3.3-23. Chlorophyll concentration 8-day composite image sequence of NW Gulf CE #3 and merger with CE #5. Twice monthly images from 15 September through 10 November 2004 are shown. Images are overlaid with 50 and 250-m depth currents and SSH contours.

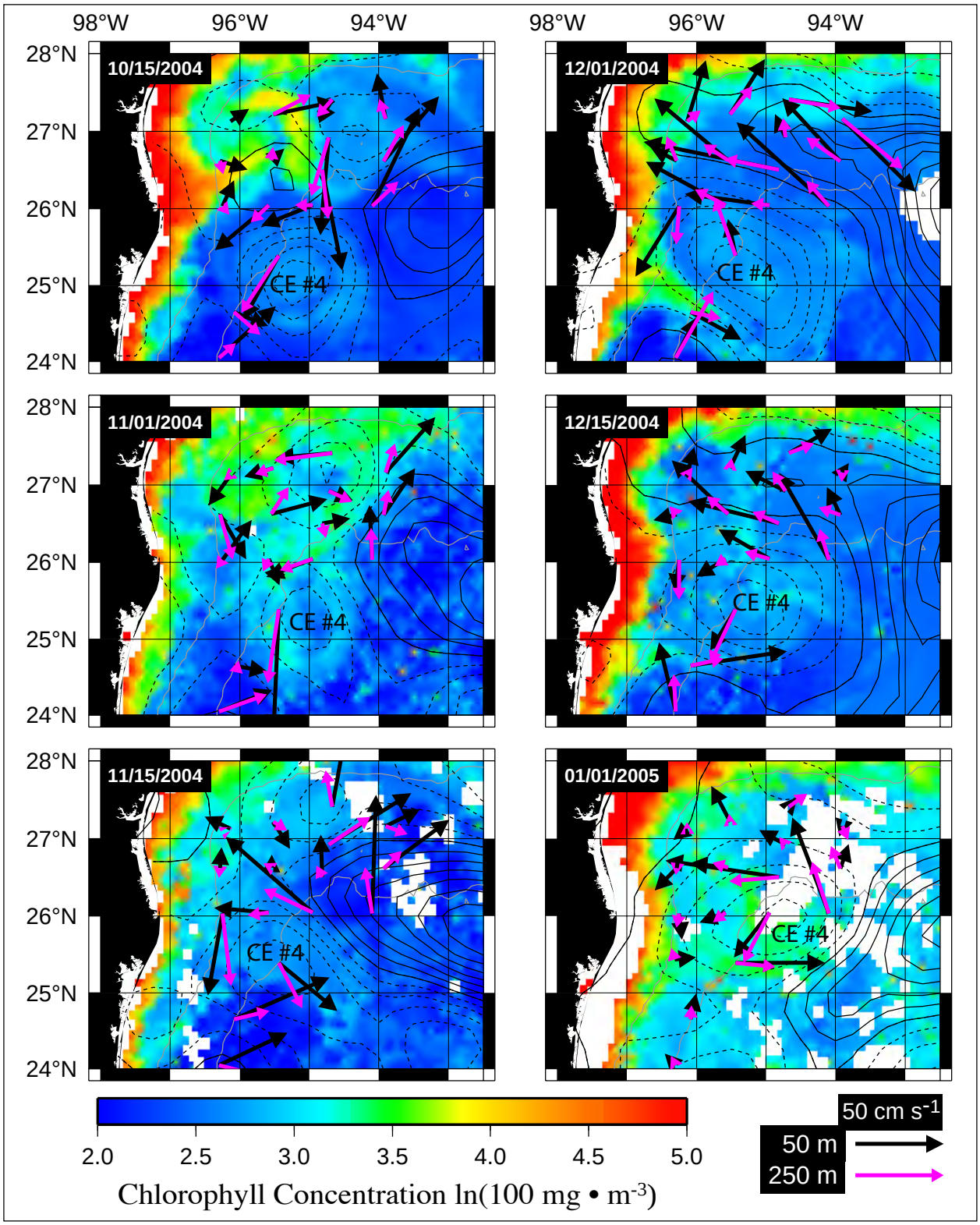

Figure 3.3-24. Chlorophyll concentration 8-day composite image sequence of NW Gulf CE #4. Twice monthly images from 15 October 2004 through 1 January 2005 are shown. Images are overlaid with 50 and 250-m depth currents and SSH contours.

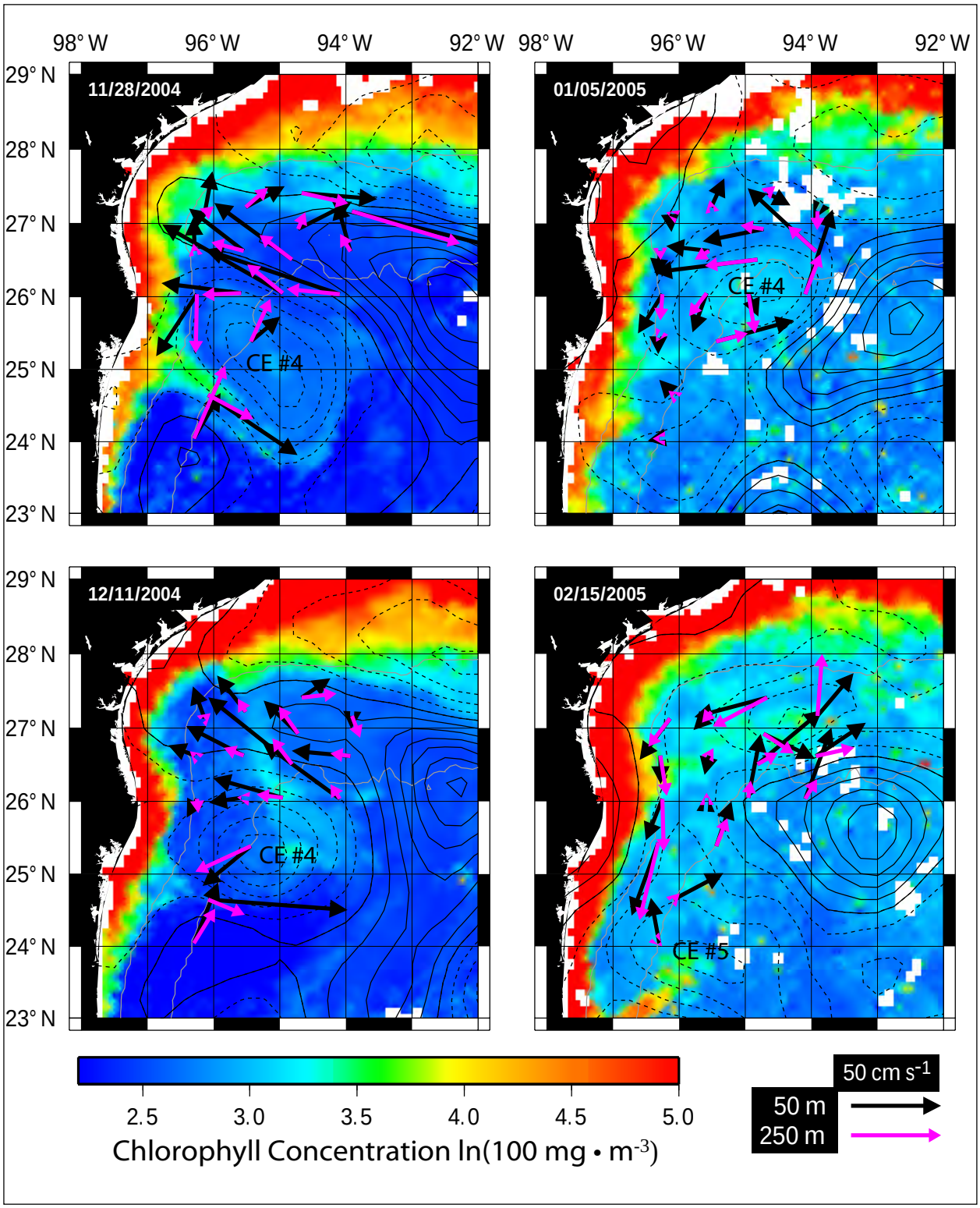

Figure 3.3-25. Chlorophyll concentration 8-day composite image sequence of NW Gulf CE #4 interacting with LCE Ulysses/U2 (28 Nov 2004 - 15 Feb 2005). Selected cloud-free images are shown of the interaction of the LCE with the CE that split the cyclone into two pieces. Images are overlaid with 50 and 250-m depth currents and SSH contours.

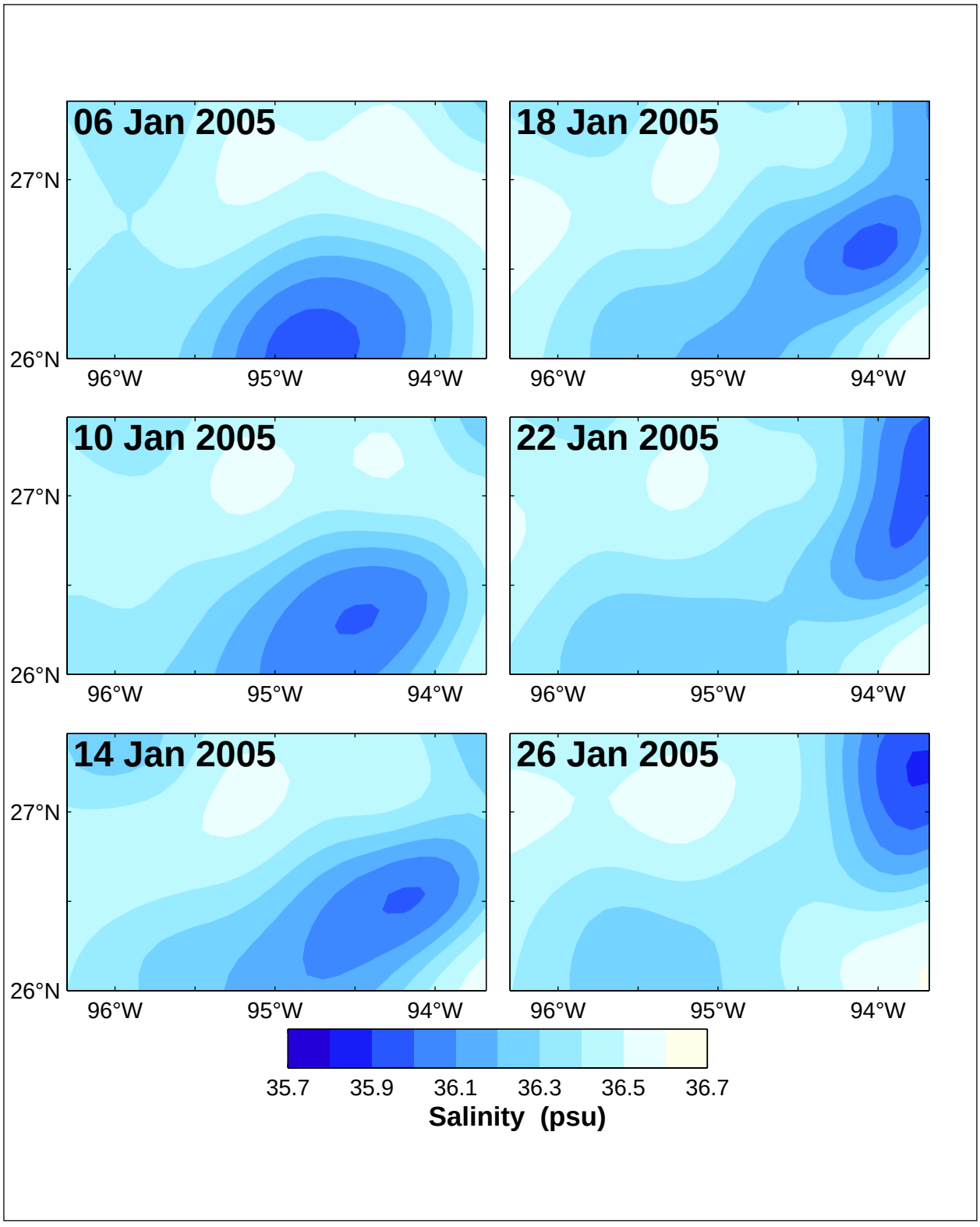

Figure 3.3-26. Propagation of CE #4 through study array in January 2005 as observed by the PIES array. Objective maps of 150-m depth salinity inferred from PIES are shown at 4-day intervals from 6 Jan 2005 through 26 Jan 2005.

merged eddy moved onto the upper-northern slope and then quickly propagated eastward around the periphery of Ulysses as the LCE intruded well into the study array in late November. The direct influence of the strong LATEX shelf circulation associated with Hurricane Ivan on CE #5 was likely minimal since there was only weak cross-shelf-break flow in the confluence between ACE #1 and CE #5. Unfortunately, there were no current measurements on the shelf to investigate further possible connections between the shelf and slope. Indirect influences of the strong shelf circulation on CE #5 through the induced changes in the ambient eddy field, however, were likely significant. This is expected because of the sensitivity of the evolution of a nonlinear turbulent geophysical flow to small changes in the flow field.

CE #6 formed in the Mexican array along the western wall to the north of LCE Ulysses and west of LCE U2 (Figures 3.3-27 and 28). Weak cyclonic circulation initially formed from the southern remnant of the splitting in two of CE #4 in January. This circulation intensified in February through the interaction with LCEs Ulysses and U2. A significant addition of cyclonic circulation occurred as CE #5 merged with the westward-propagating Ulysses companion cyclone, CE_b, in mid-February. By late April, the bulk of the cyclonic circulation associated with the eddy had been squeezed between LCEs U2 and Ulysses and forced northward into the NW Gulf array where it briefly reformed over the continental slope. CE #6 and another cyclone along the western wall acted together to split a small piece off of the merged Ulysses/U2 that was pushed northward into the study array. A small remnant of CE #6 may have remained behind in the array that later intensified within the study array as CE #7.

CE #7 formed within the US array in mid May. As noted previously, some of the initial cyclonic circulation may have been left behind by CE #6 as that cyclone rapidly advected out of the study region around the periphery of the anticyclone formed by the merger of U2 and Ulysses. Animations of the PIES SSH show a small cyclone on the upper slope (200 m – 1000 m depths) in the far northwestern corner that advected southward and downward across the slope in mid-May contributing to the formation of CE #7. Cross-slope advection in the confluence between CE #7 and an anticyclone to the south (the remnant of the Ulysses/U2 merger) also likely contributed to the formation and intensification of the cyclone. In all likelihood, it was a combination of all three processes that contributed to the formation and evolution of CE #7.

Late spring upper-ocean conditions were favorable for looking in detail at the formation and evolution of CE #7 in ocean color imagery. Figure 3.3-29 shows a sequence of 8-day composite images of chlorophyll concentration showing CE #7 in the study array. Images are overlaid with 50 and 250-m depth currents from the moorings and PIES SSH. The PIES data were referenced to the array-wide mean value over the entire observational record. Contours with values above or equal to this mean value are shown by solid contours and values below by dashed contours. The contour increment is 2 cm. Referencing of the SSH to the mean in this manner delineates the cyclonic circulation from the anticyclonic circulation. The color images and the PIES SSH clearly show that the cyclone propagated parallel to and just offshore of the 1000-m isobath in the NW corner of the array. The NW Gulf program ended with the cyclone still in the array.

The final cyclone of note, CE #8, formed in the Mexican array in September 2005. This cyclone was quite similar in character to CE #4 and also formed immediately following the landfall in the northern Gulf of two strong hurricanes, Katrina and Rita. Katrina made landfall near the

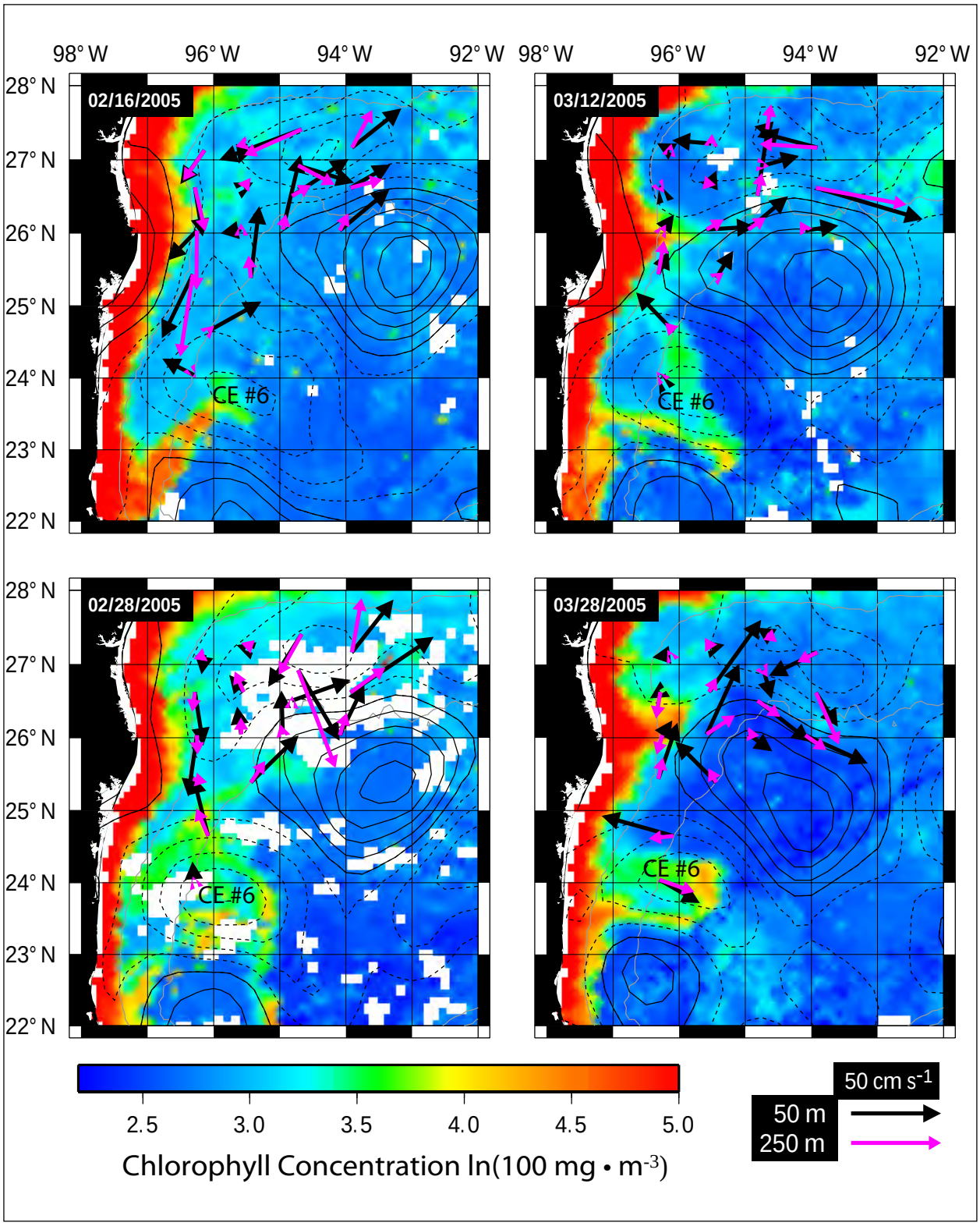

Figure 3.3-27. Chlorophyll concentration 8-day composite image sequence of CE #6 (16 Feb - 28 Mar 2005). Selected cloud-free images are shown overlaid with 50 and 250-m depth currents and SSH contours.

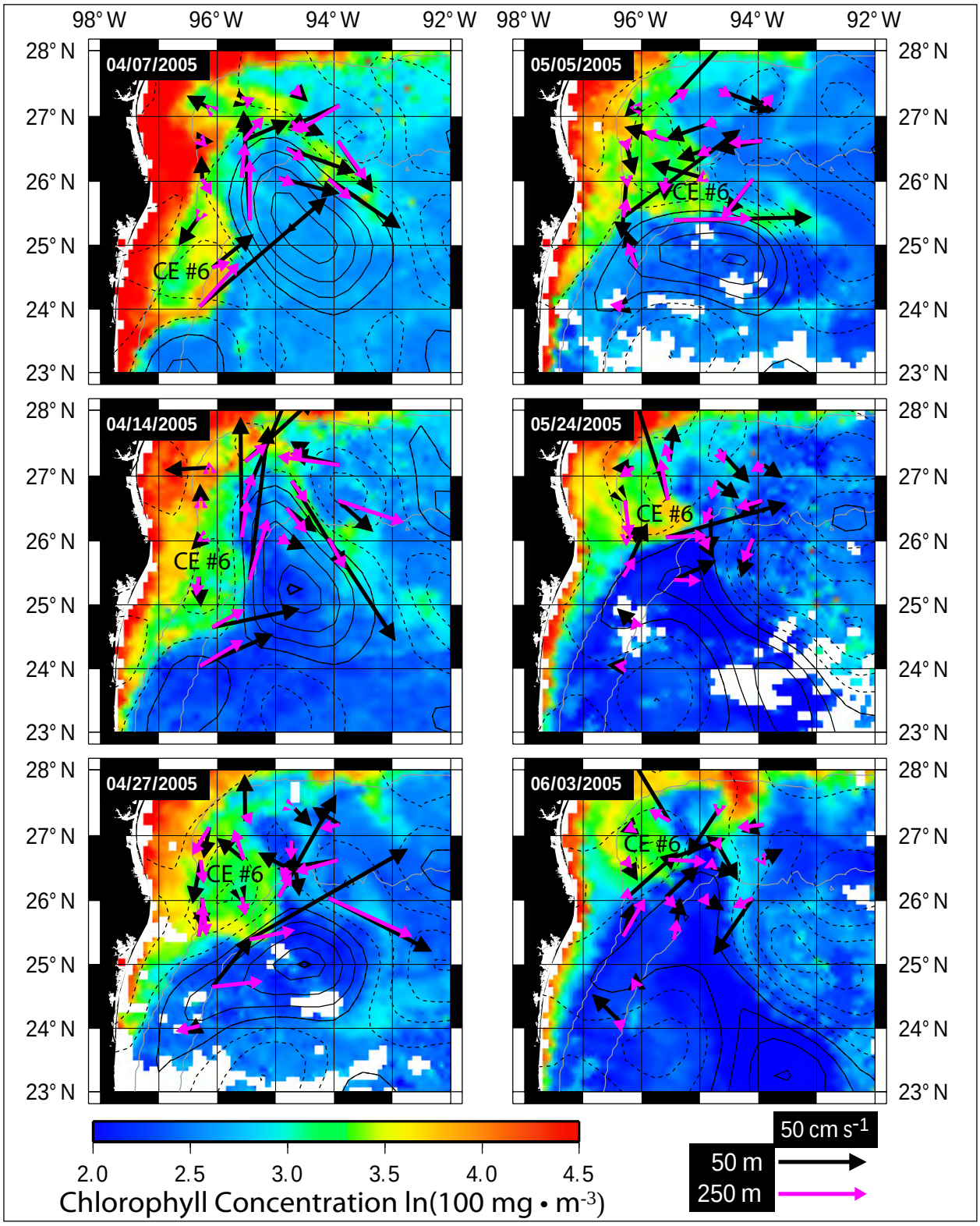

Figure 3.3-28. Chlorophyll concentration 8-day composite image sequence of CE #6 (7 Apr - 3 Jun 2005). Selected cloud-free images are shown overlaid with 50 and 250-m depth currents and SSH contours.

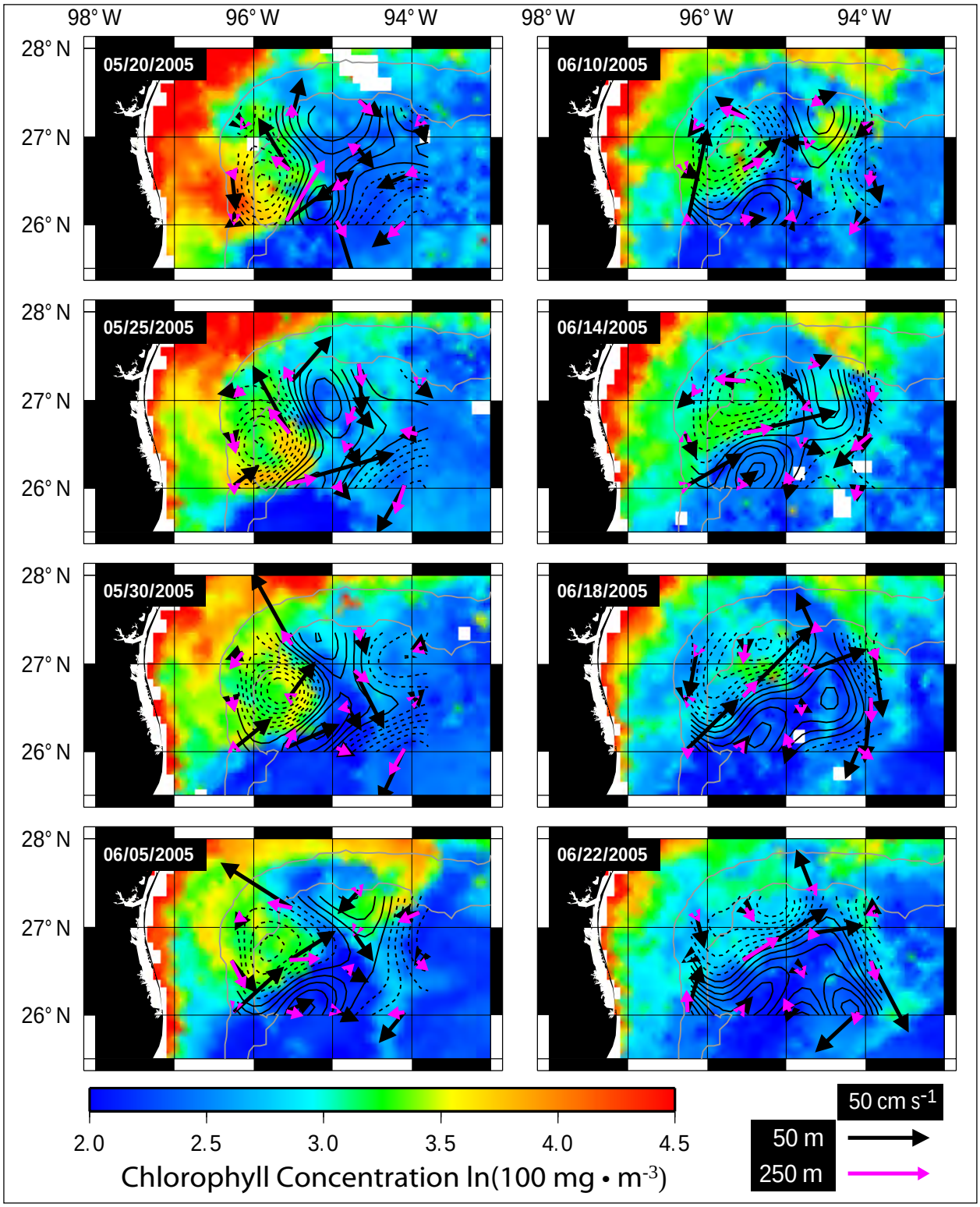

Figure 3.3-29. Nearly cloud-free sequence of 8-day composite chlorophyll concentration images of the propagation of CE #7 parallel to and just offshore of the 1000-m isobath in the study region (20 May - 22 Jun 2005). Images are overlaid with 50 and 250-m depth currents from the moorings and PIES SSH. The SSH contour increment is 2 cm.

Louisiana/Mississippi border on 29 Aug 2005. Rita made landfall later near the Texas/Louisiana border on 24 Sep 2004. Current at 2-m depth from the TABS moorings J in 20-m depth water and K in 62 m depth water off of Padre Island, TX ended abruptly on 24 Sep 2005. Strong downcoast currents approaching 80 $cm \cdot s^{-1}$ were observed at both J and K near the end of the time series. At mooring J, downcoast currents of up to 50 $cm \cdot s^{-1}$ were observed just after landfall of Katrina and then again about 10 days later. CE #8 appears to have begun forming at about the same location as CE #4, coincident with the landfall of Katrina. By 15 Sep 2005, strong currents were observed offshore in the array in the confluence of offshore flow between CE #8 and a remnant of U2 to the south. Strong currents and a significant plume of high chlorophyll concentration extended well offshore by the end of October. Figure 3.3-30 shows a sequence of 8-day composite chlorophyll concentration images that show the spin-up of CE #8 in the Mexican array. In late October, the westward propagating LCE Vortex also interacted with the cyclone possibly contributing to the intensification of the circulation. The similarities between CE #4 and CE #8 are striking. Both eddies formed from the combined contribution of energy from hurricanes, LCEs, and eddy-slope interactions. To highlight the similarity, we show a side-by-side comparison of the eddy fields in the NW Gulf in September 2004 and 2005 in Figure 3.3-31. This concludes our survey of CEs during the program time period. A summary of the study region CEs is listed in Table 3.3-4.

Table 3.3-4

Timetable of Cyclonic Eddies in Study Array

Event	Date	Comments
CE #1 – first cyclone observed in array	Apr - May 2004	Altimetry/ocean color, currents, 450m temperature
CE #2 – small cyclone on periphery of ACE #1	Jun - early July 2004	Altimetry/ocean color, currents, 150 and 450-m temperature
CE #3 & #4 – hurricane forced cyclonic eddy pair over western slope	mid Sept 2004	Altimetry/ocean color, currents
CE #5 – slope cyclone formed from interaction of ACE #1 and ACE #2 with northern continental slope	mid Sept 2004	Altimetry/ocean color ,currents
CE #3 (cont.)– moved onto northern slope	mid Sep - Oct 2004	Altimetry/ocean color, currents
CE #4 (cont.) – moved into deepwater west of Mexican moorings and intensified, interacted with LCE U2, split, and moved through US array.	mid Sep 2004 - Jan 2005	Altimetry/ocean color, currents, 450m temperature, PIES inferred 150-m depth salinity.
CE #3 and #5 (cont.) merged and propagated eastward out of array	late Oct - Nov 2005	Altimetry/ocean color, currents, 450m temperature, PIES
CE #6 – formed along the western continental margin	Feb – Mar 2005	Altimetry/ocean color, currents.
CE #6 (cont.)– moved north into US array as LCE U2 propagated westward and merged with Ulysses.	Apr – May 2005	Altimetry/ocean color, currents.
CE #7 – formed within US array	late May 2005	Altimetry/ocean color, PIES SSH, 150m and 450m temperature
CE #8 – small energetic slope cyclone possibly hurricane forced that moved eastward through Mexican array	mid Sep – Oct 2005	Altimetry/ocean color, currents.

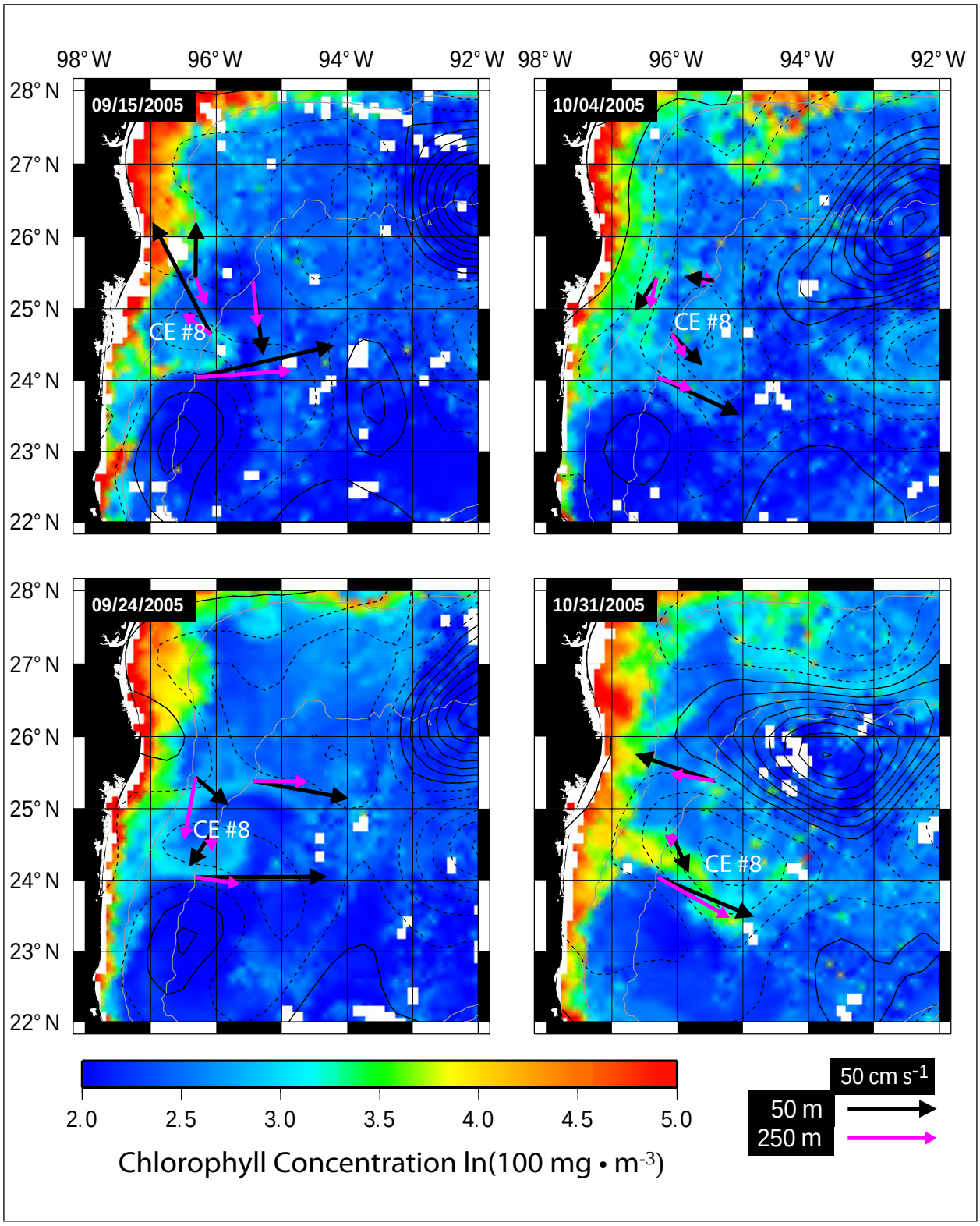

Figure 3.3-30. Sequence of 8-day composite chlorophyll concentration images showing the spin up of CE #8 over the Mexican array (15 Sep - 31 Oct. 2005). Images are overlaid with 50 and 250-m depth currents from the moorings and SSH contours.

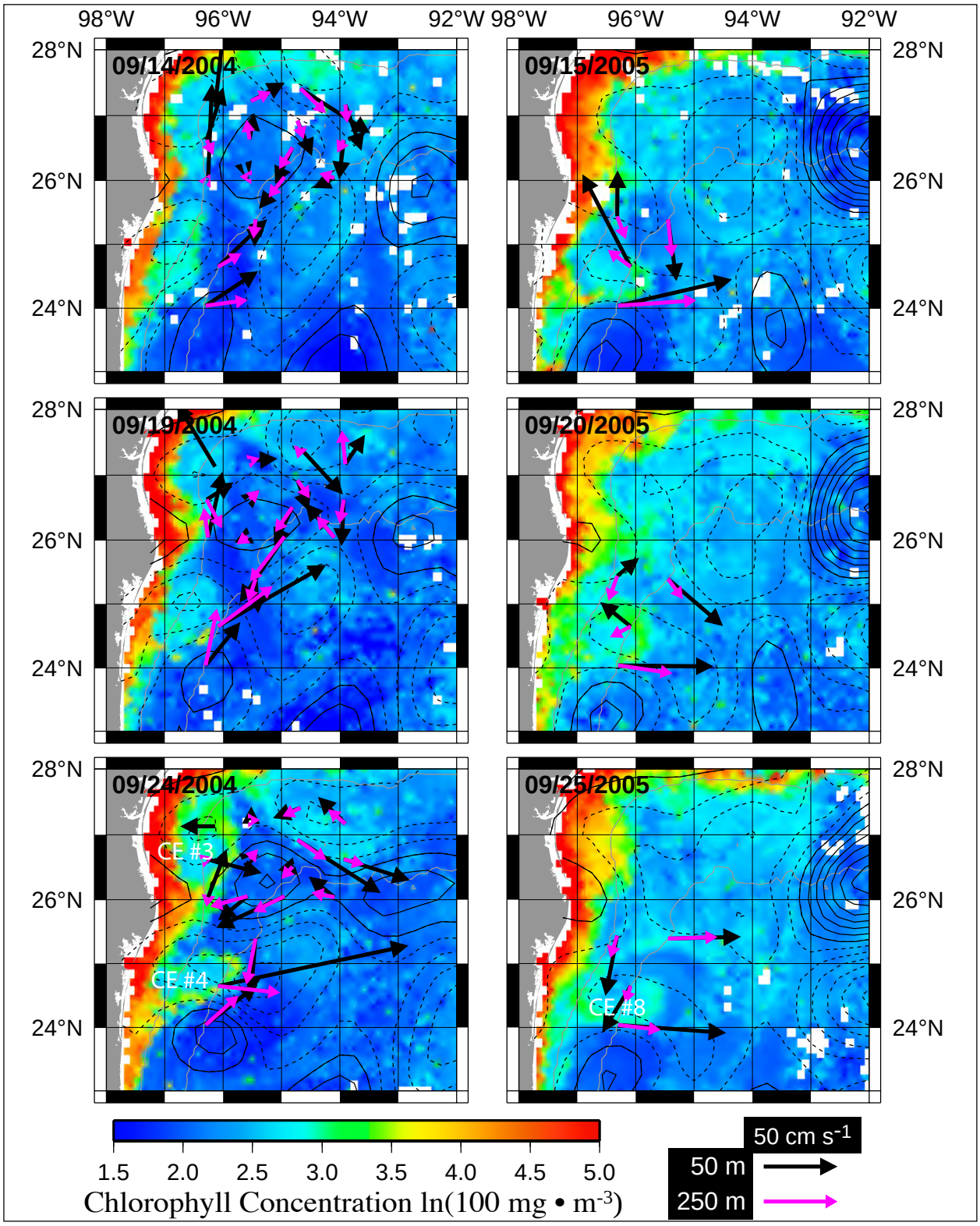

Figure 3.3-31. Side-by-side comparison of the eddy fields in the NW Gulf in September 2004 and 2005. CEs #3, #4, and #8 discussed in the text are labeled.

3.4 Basic Statistics

3.4.1 Measured Currents

Basic statistics from the upper-layer current records are given for the complete interval of the U.S. sector deployments (April 2004 to June 2005) and for the overlap interval between the U.S and Mexican sectors (September 2004 to June 2005). For the complete interval, the statistics were calculated for all the available data, which means that the averaging intervals are different for the U.S. and Mexican Sectors. However, these intervals overlap by approximately 10 months, therefore there is considerable commonality between statistics calculated for the complete and overlap intervals. As will be shown later, even the complete deployments of the both the Mexican and U.S. arrays do not resolve the lowest frequencies, however, the basic patterns of the statistics for the two intervals are qualitatively the same for the U.S array, indicating that the sequence of eddy events were sufficiently slow moving so that the two sets of overlapping statistics are sampling similar circulations. Figures 3.4-1a and b show the mean current vectors at selected depths from 40 m to 750 m overlaid on the mean temperature field at a nominal 450-m depth. (The ADCPs in the Mexican sector had deployment depths ranging from 434 m (W1) to 553 m (W5) so the temperature means will be biased low in the south compared to the U.S. moorings. The structure of this mean, however, would only be expected to be slightly modified if all the instruments were at the same depths.)

The mean temperature field shows a warm eddy over the NW slope, flanked by cold features to the northwest and northeast (Figure 3.4-1a). When the southern moorings are included, there is also a cold feature to the south. The currents are consistent with these features with anticyclonic flow over the NW slope and strong northward and offshore flow along the 2000-m isobath off the Mexican slope (Figure 3.4-1b). The northeastward flow is also evident along the 500-m isobath to the north of 25°N, but primarily at the 40-m level. Below this, at V1, U1 and T1, the mean flows are more southward, converging towards the strong offshore mean flows in the vicinity of W1, and also appear to be part of the cyclone between the slope anticyclone and the western shelf break. Otherwise the mean flows tend to be in the same direction through the upper water column, with the largest magnitudes nearest the surface. The 450 to 500 m temperature mapping in Figure 3.4-1b seems to become a little distracted in the Mexican sector because of the relatively larger spacing between the moorings. The directions of the vectors at W2, W4, and W5 are more consistent with cyclonic flow if the cold center is moved northwards between W2 and V3. Flows at W1 seem to be part of anticyclonic circulation adjacent to the slope.

The standard deviation ellipses for the moorings and intervals used in Figures 3.4-1, are given in Figures 3.4-2a and b. The highest EKE was in the southwestern part of the U.S. sector array and W2 and W4 in Mexican waters. Note that there are no data available from W3 in this plot. The EKE decreased eastward and to a lesser extent northwards. The decrease in fluctuation amplitudes with increasing depths was similar at all the moorings with little evidence of a preferred direction of the principal axes except along the 500-m isobath (W1, V1, U1 and T1), where the fluctuations were constrained by the direction of the upper slope, and at W4 and W5, where the across-isobath dominated over the along-isobath fluctuations. Thus, for most of the array along- and across-isobath fluctuations had similar magnitudes, indicating that the

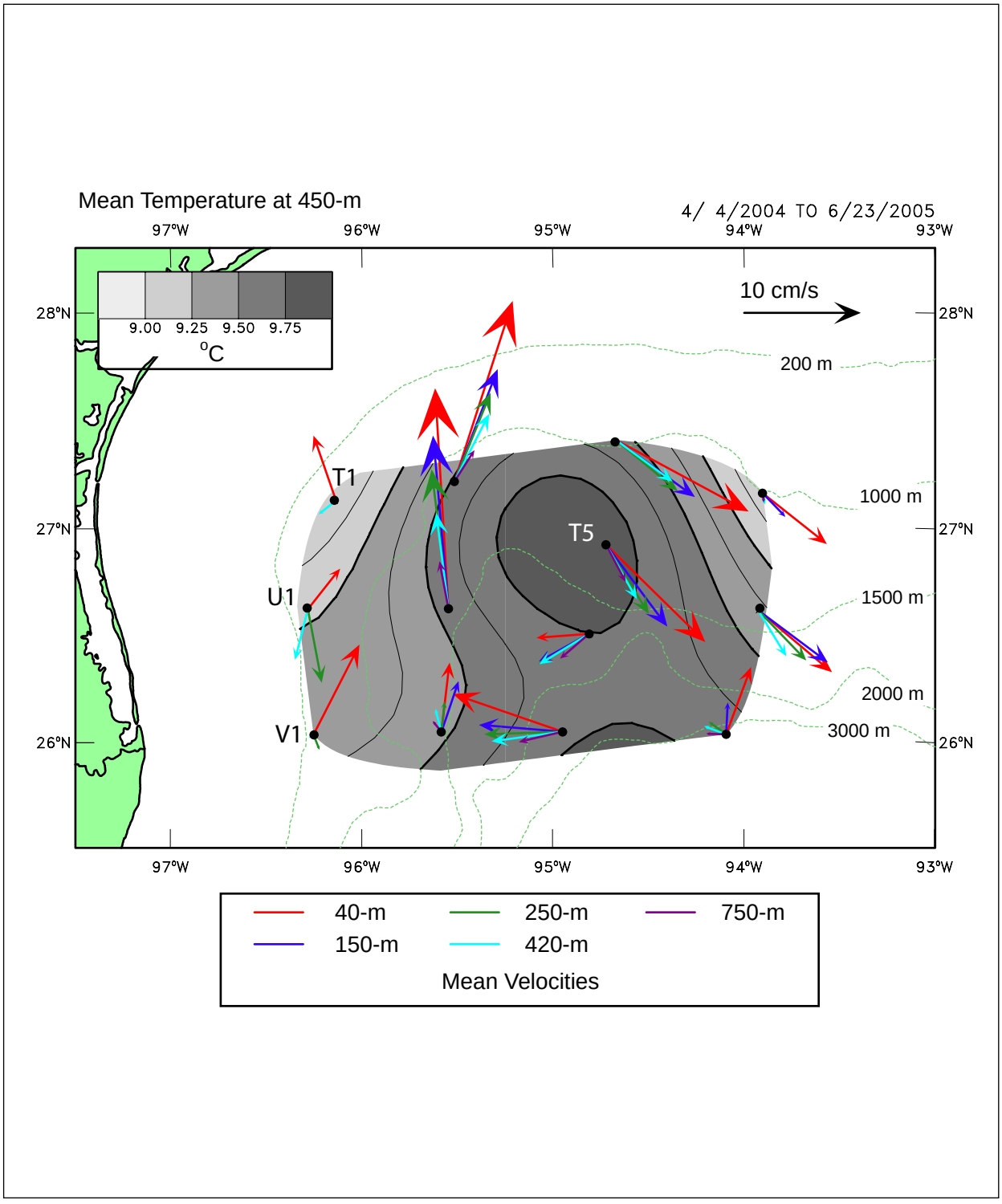

Figure 3.4-1a. Mean current vectors for the U.S. sector array, calculated from 40-HLP records, for the indicated interval and depths. The contoured mean 40-HLP temperature field at 450-m is also shown.

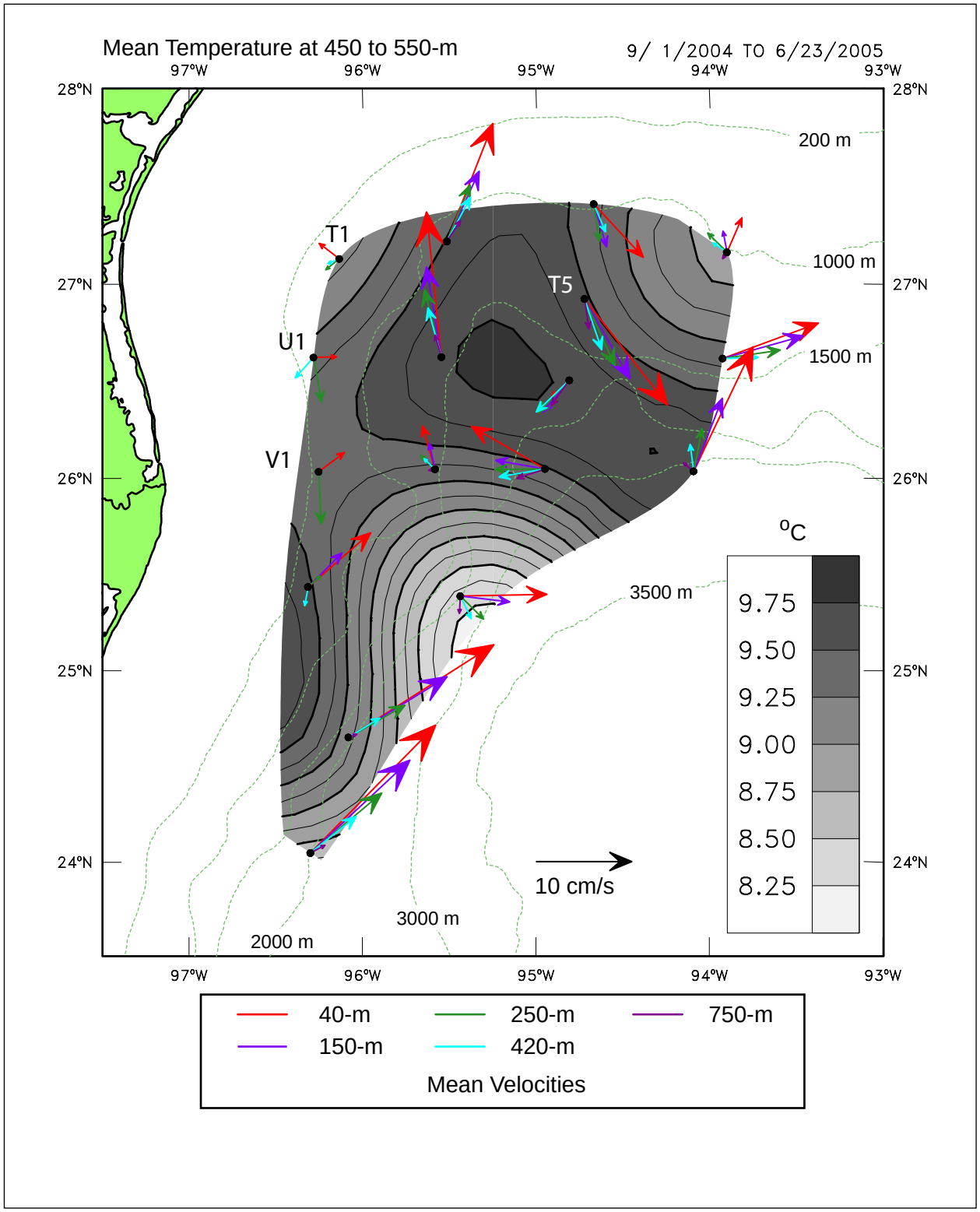

Figure 3.4-1b. Mean current vectors for the complete array, calculated from 40-HLP records, for the indicated common interval and depths. Note that the record at W1 is short relative to the common interval. The contoured mean 40-HLP temperature field at nominal depths of 450-m (in the north) to 550 m (in the south) is also shown.

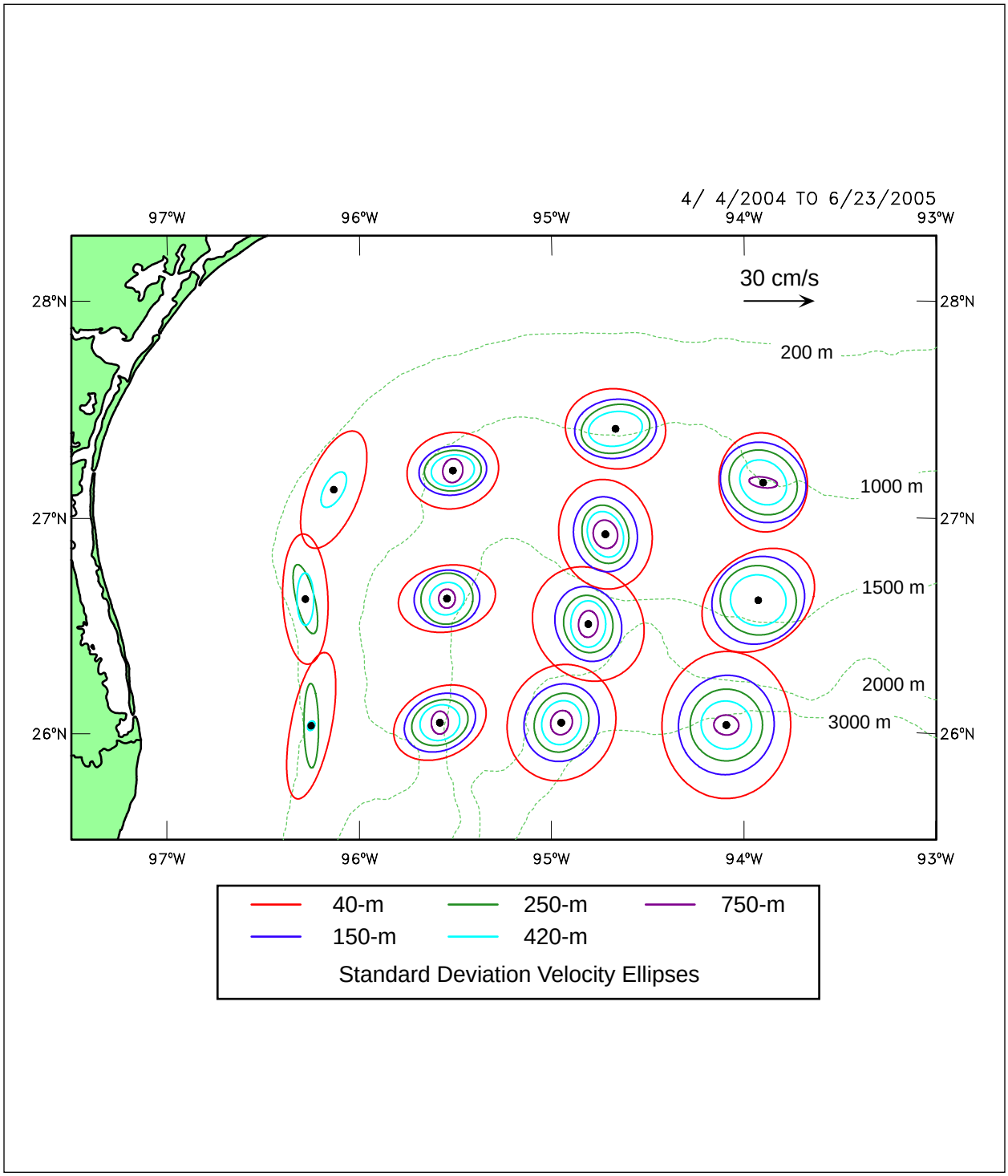

Figure 3.4-2a. Standard deviation ellipses for the U.S. sector array, calculated from 40-HLP current records, for the indicated interval and depths.

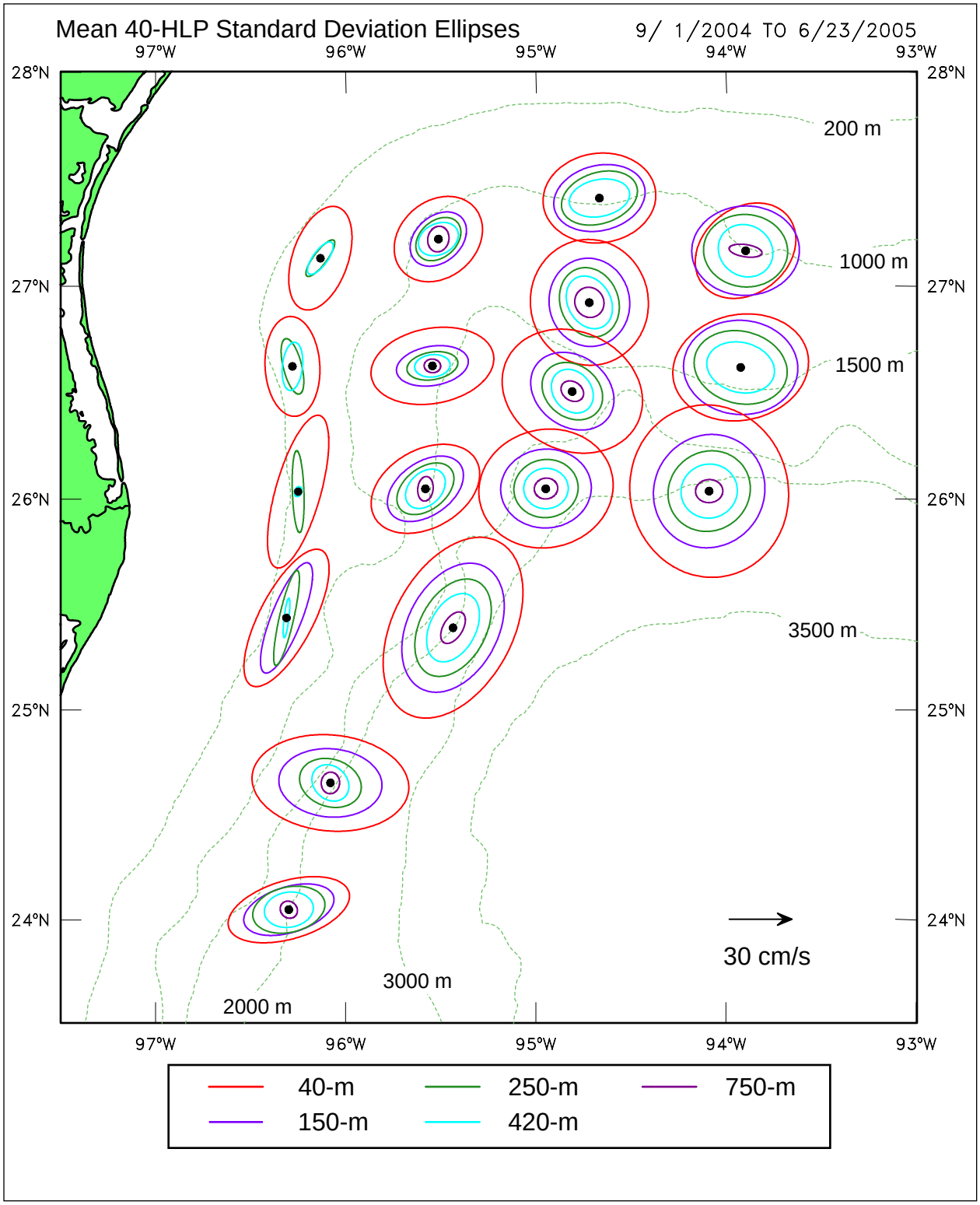

Figure 3.4-2b. Standard deviation ellipses for the complete array, calculated from 40-HLP current records, for the indicated common interval and depths. Note that the record at W1 is short relative to the common interval.

bathymetry was not constraining flow directions except along the upper slope. This is not inconsistent with the upper layer being dominated by eddies that move through the array such that instantaneous low-frequency currents could be in any direction relative to the deeper bathymetry of the slope.

ADCPs measure velocity profiles and produce a large number of records per instrument. Previous experience has shown that the volume of data can be substantially reduced by reducing the time series to a few vertical CEOF modes, which account for the majority of the variance of all the measured levels at a given mooring. CEOF analysis is used because it is more efficient at reducing vector time series to a low number of complex modes. The usual convention is followed here where the spatial CEOFs are rotated into the principal axis coordinate system of the corresponding (complex) time-dependant amplitudes of the mode (Merrifield and Winant, 1989). Therefore, at each mooring, seven equally-spaced depth levels from the 450-m ADCP, along with the 750-m current-meter measurements, were input into a CEOF analysis. For the shallow moorings, eight ADCP levels were used at W1, and five ADCP levels from the 100-m ADCPs along with the 250 and 450 current meters were used for V1, U1 and T1. The complete time series, after removing the means (see Figures 3.4-1), were used for each mooring, which corresponds to 440 days beginning on 4 April 2004, for the U.S. sector, and 430 days beginning on 1 September 2004 for the Mexican sector moorings. The CEOFs were calculated separately for each location, and the results for the first modes are given in Figure 3.4-3, where the percentages of the total variances of the input 40-HLP currents are given. Thus, a single mode can account for the majority of the variance of the depth profile at a given location. The lowest percentage (79.7%) was at W1, which was also a shorter record, while the rest were above 85%, and 11 out of the 17 locations had percentages above 90%. The principal axes of the first mode CEOFs show very little variation of direction with depth, tending to align with the isobaths on the upper slope, but showing no preferred direction elsewhere. Note that because the spatial CEOFS were multiplied by a complex amplitude time series, the instantaneous currents can have flows orthogonal to these directions as can be seen from the variance ellipses (Figures 3.4-2). All the first modes show a decrease of magnitude with depth, with the coherent response at 750-m being essentially negligible. Therefore, these are surface trapped modes and for the most part the near-surface current fluctuations were similar to those at depth, with the latter having reduced magnitudes.

The KE spectra of the first mode amplitudes were calculated and are presented in variance preserving form in Figure 3.4-4. The highest energies were at the lowest frequencies and this indicates that the 18-month measurement intervals were not long enough to resolve the full range of flow periodicities. This is perhaps unsurprising if the major source of energy was dominated by LCEs moving into the western slope region. LCE shedding ranges from about 6 to 18 months (Sturges and Leben, 2000). This result also indicates that the eddy flow patterns discussed here are not necessarily representative of long-term or “typical” conditions in the NW Gulf, and thus, motivates the case-study approach taken here.

Despite the limitation of the lengths of the experiments, it is useful to attempt to investigate flow patterns from a statistical point of view. The mode 1 amplitude time series from the 9-month interval when the U.S. and Mexican moorings were both in place are shown in Figure 3.4-5. In EOF analysis, it is usual to normalize to unit variance either the spatial or time-dependant

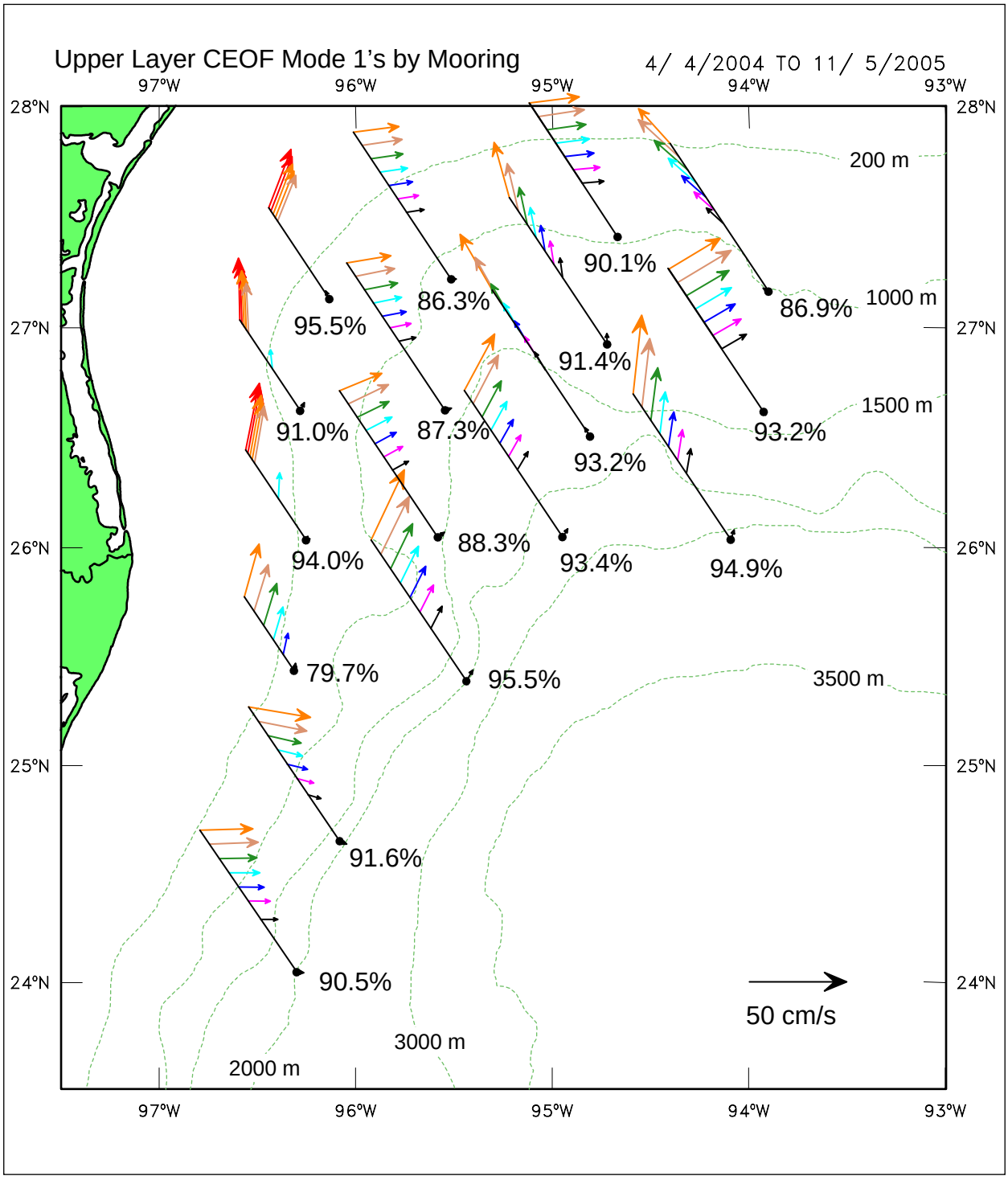

Figure 3.4-3. Upper-layer CEOF Mode 1 eigenvectors calculated for each individual mooring using the longest available 40-HLP current records. The modes are displayed as pseudo 3-D vectors (color coded by depth) where the sloping black line represents the height above 750 m or 450 m (for W1, V1, U1 & T1). The percentage of the total variance represented by each mode 1 is given at the location of each mooring (black dot).

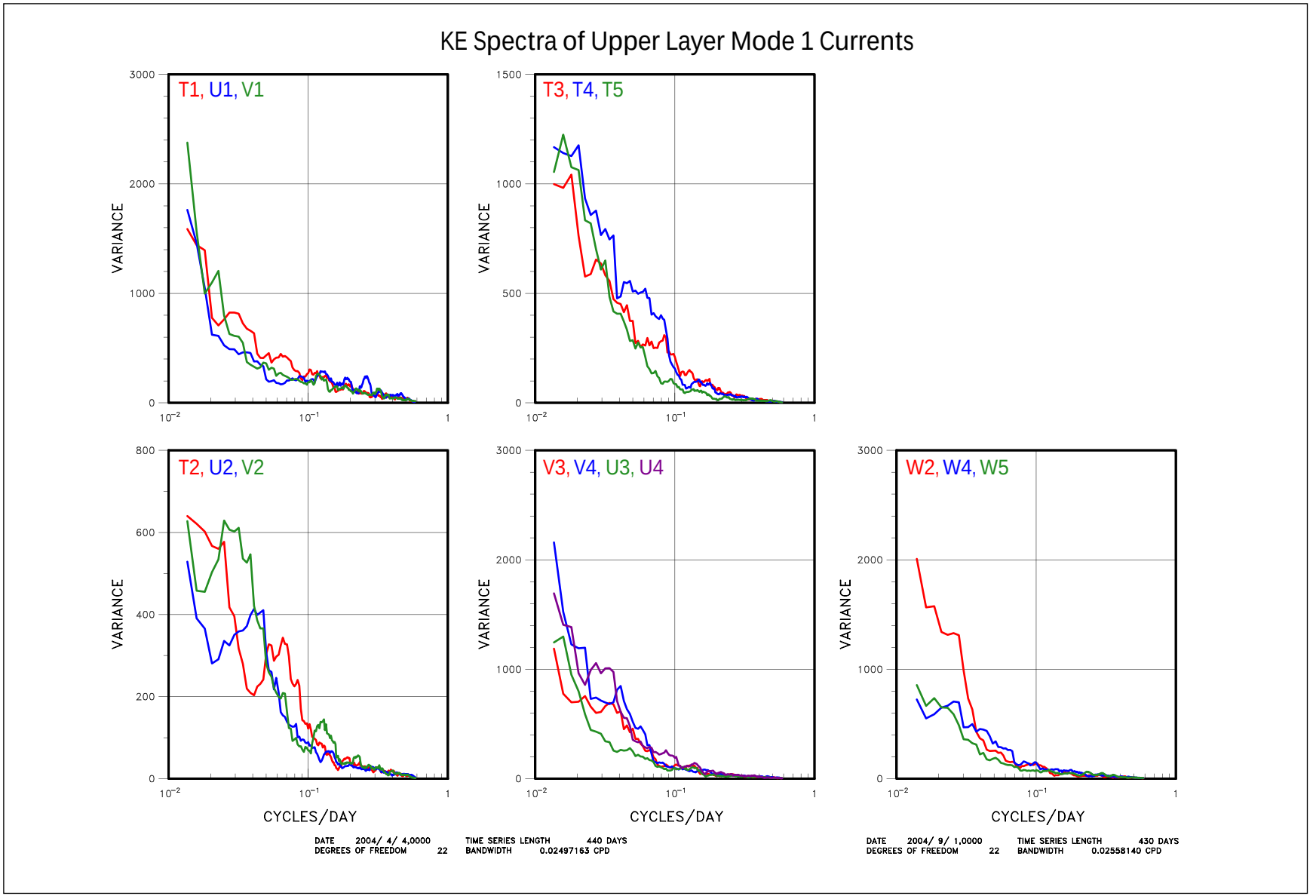

Figure 3.4-4. Kinetic energy spectra of the upper-layer CEOF mode 1 amplitudes for the individual moorings whose eigenvectors are given in Figure 3.4-3.

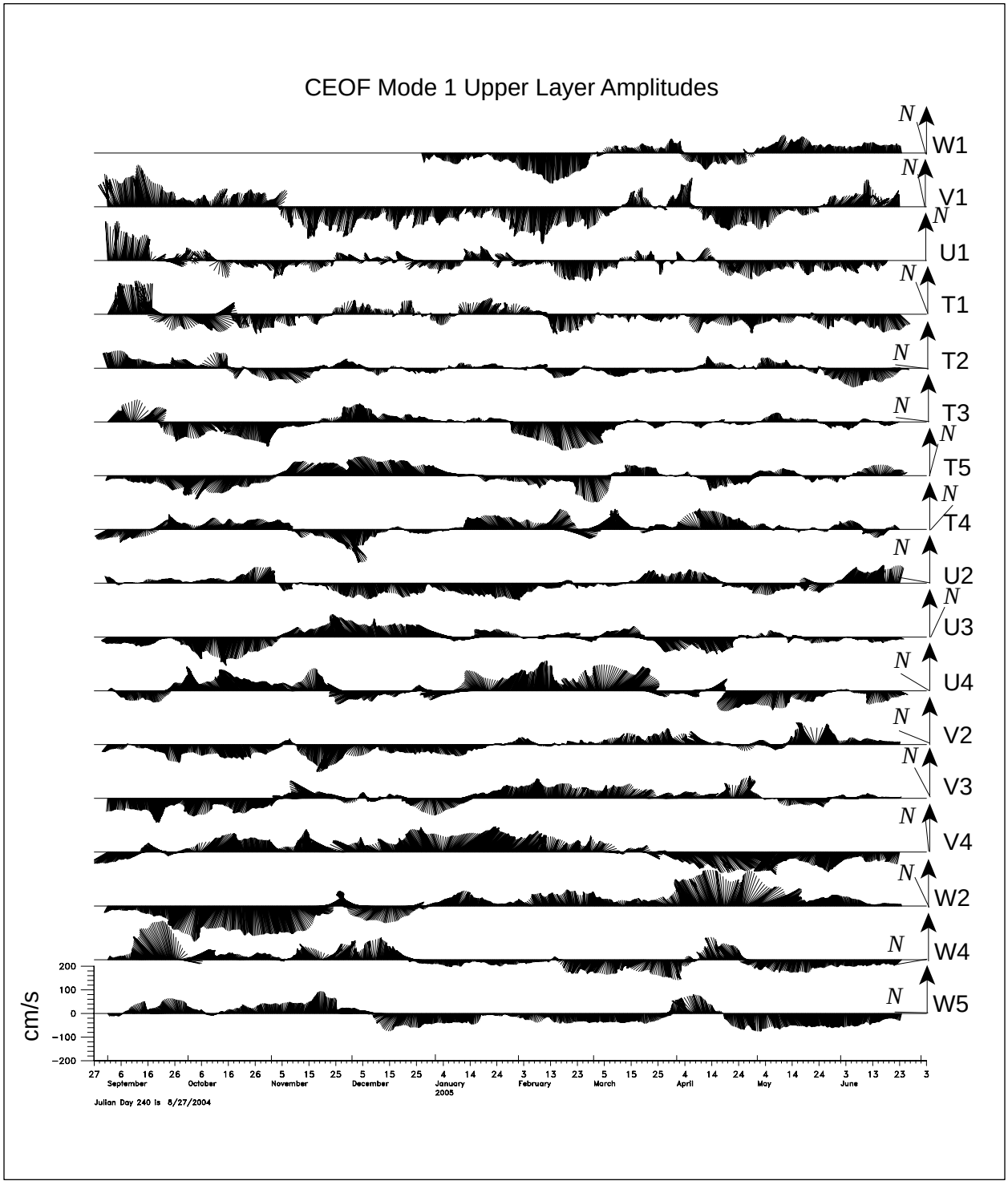

Figure 3.4-5. The amplitudes (in units of velocity) of the first mode CEOFs from each location for the interval where U.S. and Mexican sectors experiments overlap. The principal axis directions, relative to north, are shown on the RHS of each time series.

component. In this case, because the (complex) amplitude time series were input into another CEOF analysis that examines the coherent horizontal patterns, the mode 1 amplitudes have the same units of velocity as do the spatial components in Figure 3.4-3, in order to better represent the spatial variability of the variance across the array. Thus, the variances of the vector time series in Figure 3.4-5 are the same as the mode 1 percentages of the total variances reported in Figure 3.4-3. There is very little obvious visual coherence between the time series in Figure 3.4-5, and their most notable characteristic is the generally long (often several months) time scales of the fluctuations. The results of the horizontal CEOF analysis of the upper-layer mode 1 currents are given in Figure 3.4-6. The first three modes are significant and represent 59% of the total variance of the input time series. The normalized mode amplitudes are given in Figure 3.4-7.

The modes (Figure 3.4-6) indicate three eddy-like circulations that emphasize different regions of the study area. The direction of rotation depends on the directions of the corresponding amplitude time series (Figure 3.4-7) and it turns out for all 3 modes that positive (negative) amplitude vectors correspond to clockwise (anticlockwise) flow patterns. The first mode corresponds to eddies dominating the lower slope in the SE part of the arrays (W4, W2 V2, V3, U3, U4 and V4), the second to a similar eddy further west over the U.S. and Mexican slopes (W2, V1, U1, U2, U3 and V3), and the third tends to dominate over the northern part of the slope with a possible closed cell in the NE (T3, T4, U4, U3 and T5), but with an extension over to the west (U1 and T1). At any instance the circulation is a combination of the modes, and because the modes have fairly similar variances, different modes are likely to dominate at different times. It is likely that, for some of the events, mode 2 may represent a mode 1 eddy after it moves from the lower slope towards the northwest because EOF modes often break up translating features in this manner. The amplitude time series (Figure 3.4-7) show that mode 1 is cyclonic between October 2004 and January 2005, and anticyclonic between March and June 2005. Mode 2 is important in September and October 2004, with an anticyclone over the slope, and then reinforces the mode 1 cyclone through January. The large positive mode 3 event in December 2004 is a representation of the intrusion of Ullyses-2 water over the mid-slope, north of the lower slope cyclone Mode 3 becomes less important after the middle of March 2005.

As illustrations of the contributions of the modes to the eddy circulations in the study region, four snapshots of the flows are given when one or two of the modes are dominant (Figure 3.4-8). The dates of the figures are shown in the amplitude time series plot (Figure 3.4-7). It is again noted that the 3 modes account for 59% of the total variance, and therefore, the instantaneous circulations only correspond in a general sense to the dominant modes as they have contributions from the unaccounted modes, which are considered as noise in this analysis. On September 19, 2004 (Figure 3.4-8a), mode 2 is dominant and positive giving an anticyclonic circulation on the western side of the array. On November 22, 2004 (Figure 3.4-8b), modes 1 and 2 have negative amplitudes that reinforce each other, and the circulation shows a large cyclonic eddy over the SW part of the array. The influence of positive mode 3 patterns are beginning to be felt with the warm anticyclonic intrusion from the east in the middle of the slope, which is a lobe of Ullyses-2. On February 25, 2005 (Figure 3.4-8c), the strongly negative mode 3 accounts for the cyclonic circulation in the NE corner, and negative mode 2, the weak cyclonic circulation on the western side of the array. Finally, on April 16, 2005 (Figure 3.4-8d), the strongly positive mode 1 largely accounts for the anticyclonic lobe intruding over the lower slope in the central part of the array.

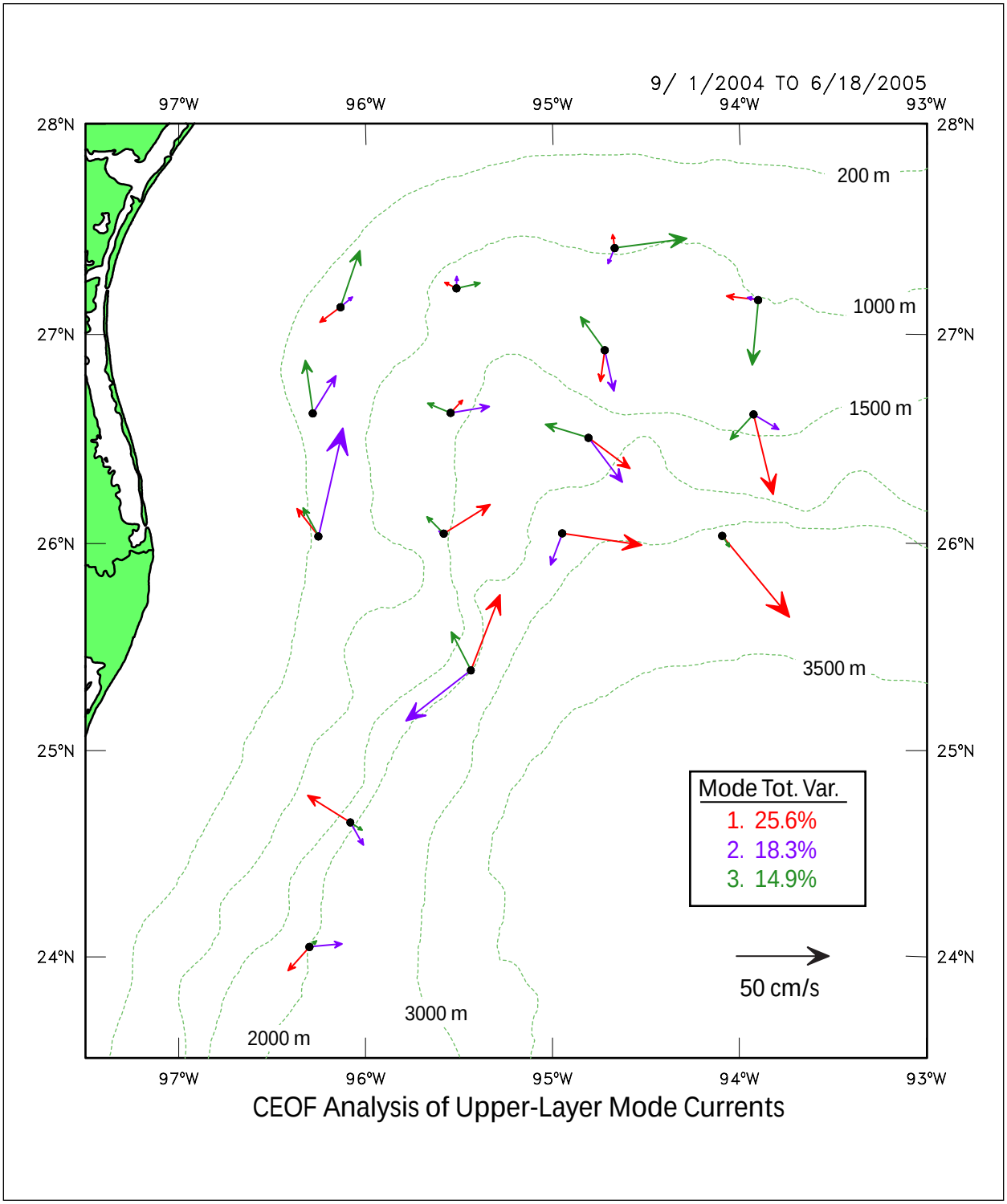

Figure 3.4-6. CEOF modes (color coded) from an analysis of the mode 1 current amplitude time series at each location. Upper layer indicates currents in the upper 1,000 m of the water column.

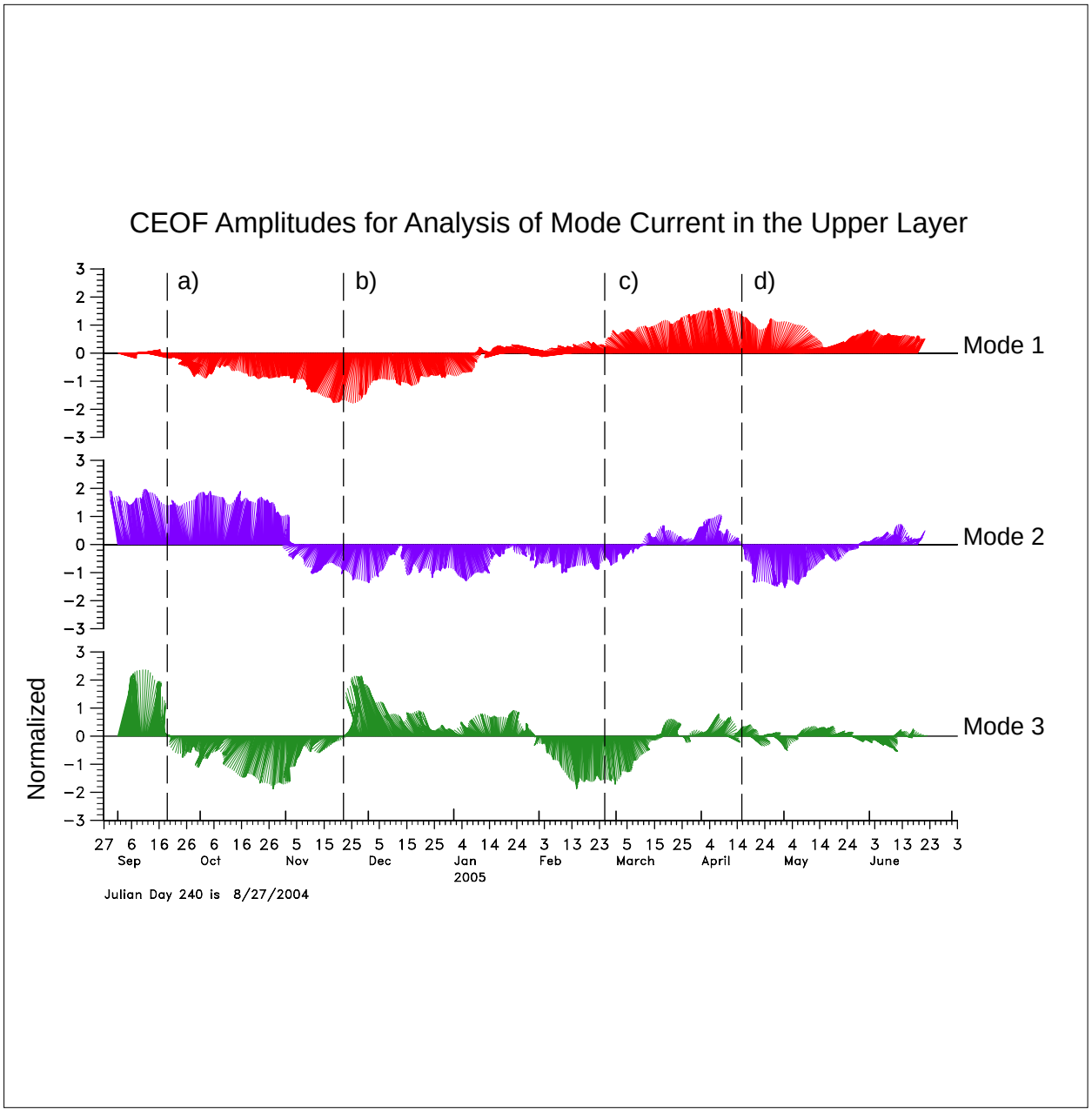

Figure 3.4-7. Mode amplitudes (normalized) from the CEOF analysis of the mode 1 current amplitude time series at each location. The colors correspond to the modes in Figure 3.4-6, and the vertical dashed lines to plots in Figure 3.4-8.

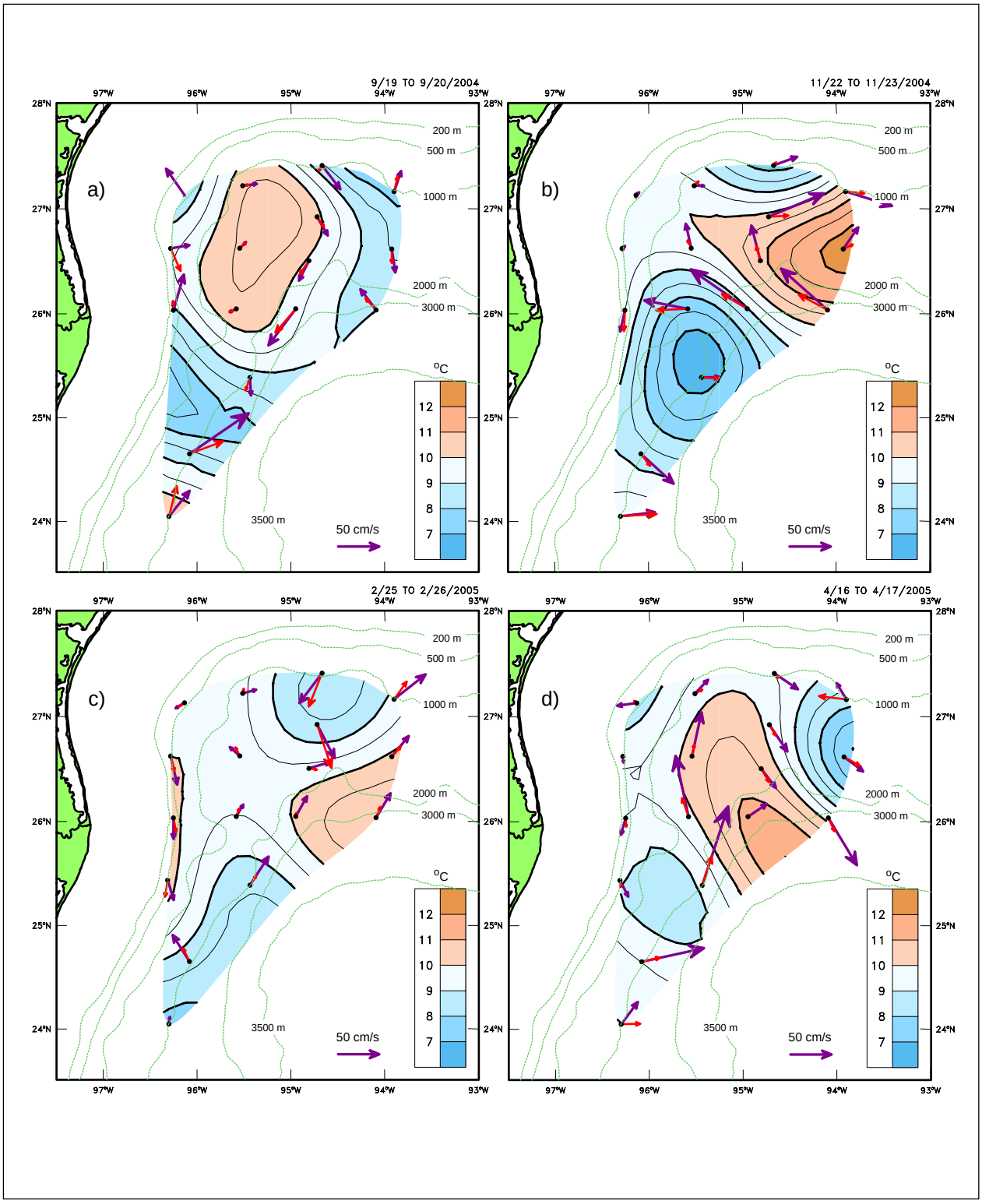

Figure 3.4-8. Illustration of the circulation on a) September 19, b) November 22, 2004, c) February 25, and d) April 16, 2005. Daily averaged 40-HLP fields are temperature at 450 to 550 m, and currents at 50 m (purple arrows) and 250 m (red arrows).

The complexity of these CEOF modes is an indication of the difficulties of characterizing a relatively slowly evolving field of eddies where the dominant structures change with time.

3.4.2 PIES Mapped Statistics in the Upper Layer

Time-averaged mapped currents for the 8-month period, 30 October 2004 through 23 June 2005, determined from the PIES and current meter mooring measurements are shown in Figures 3.4-9 and 3.4-10 for the surface and 250 m, respectively. The surface map includes SSH; the 250 m map includes streamfunction. SSH multiplied by gravity and divided by the Coriolis parameter converts to the surface streamfunction. During this 8-month period, the mean upper-ocean current was mainly anticyclonic and weak with mean speeds typically less than 20 cm s^{-1}. Two distinct anticylonic circulations existed, one in the southeast and another in the north central parts of the array. Adjacent to the western boundary mean speeds exceeded 20 cm s^{-1}, and flowed south and parallel to local isobaths. As mentioned in the previous section, currents in and above the thermocline tended to exhibit an "equivalent barotropic" structure, in which the currents decrease their speed with increasing depth but remain aligned in the same direction. Current speeds decreased by about 15% from the surface to 250 m depth, yet the pattern remained quite consistent between levels. The currents were observed to turn markedly with depth when subthermocline currents were strong, for example near U4 and V4. These mean maps (Figures 3.4-9 and 3.4-10) were consistent with those computed from the moorings alone. Recall that the absolute currents, generated by the methods described in Chapter 2, agreed well with directly measured currents. Different patterns arose between the PIES-derived mean maps and the mooring-alone mean maps in Figure 3.4-1a, for example, for two main reasons. First, the inclusion of the PIES increased the horizontal resolution and therefore revealed a richer spatial structure. Second, the averaging time periods were different. The PIES array did not sample the large anticylconic eddy that existed within the study array from June through October 2004. This highlights that the time-average currents were dominated by a few strong events: mean maps should not be interpreted as representative of the long-term mean.

The structure of the array-mean current can be clarified by looking at the major events. First, we determined current variability as expressed by mean eddy kinetic energy (EKE),

$$EKE = (1/2)\langle (u')^2 + (v')^2 \rangle$$

where < > was the mean over the 8-month interval that the PIES and current meter mooring measurements overlapped. Figure 3.4-11 shows surface EKE. The highest values occurred along the eastern edge. A second ridge of high EKE trended east-west from the western edge of the array along 26.4ºN to 95.5ºW, then slightly northeast. The time history of the spatially-averaged EKE revealed several (four to five) episodes of peak EKE lasting 10-20 days, indicative of an event-dominated time series. We mapped mean surface currents over four time periods described below in order to capture these major events (Figure 3.4-12). The four panels associate with the following circulations.

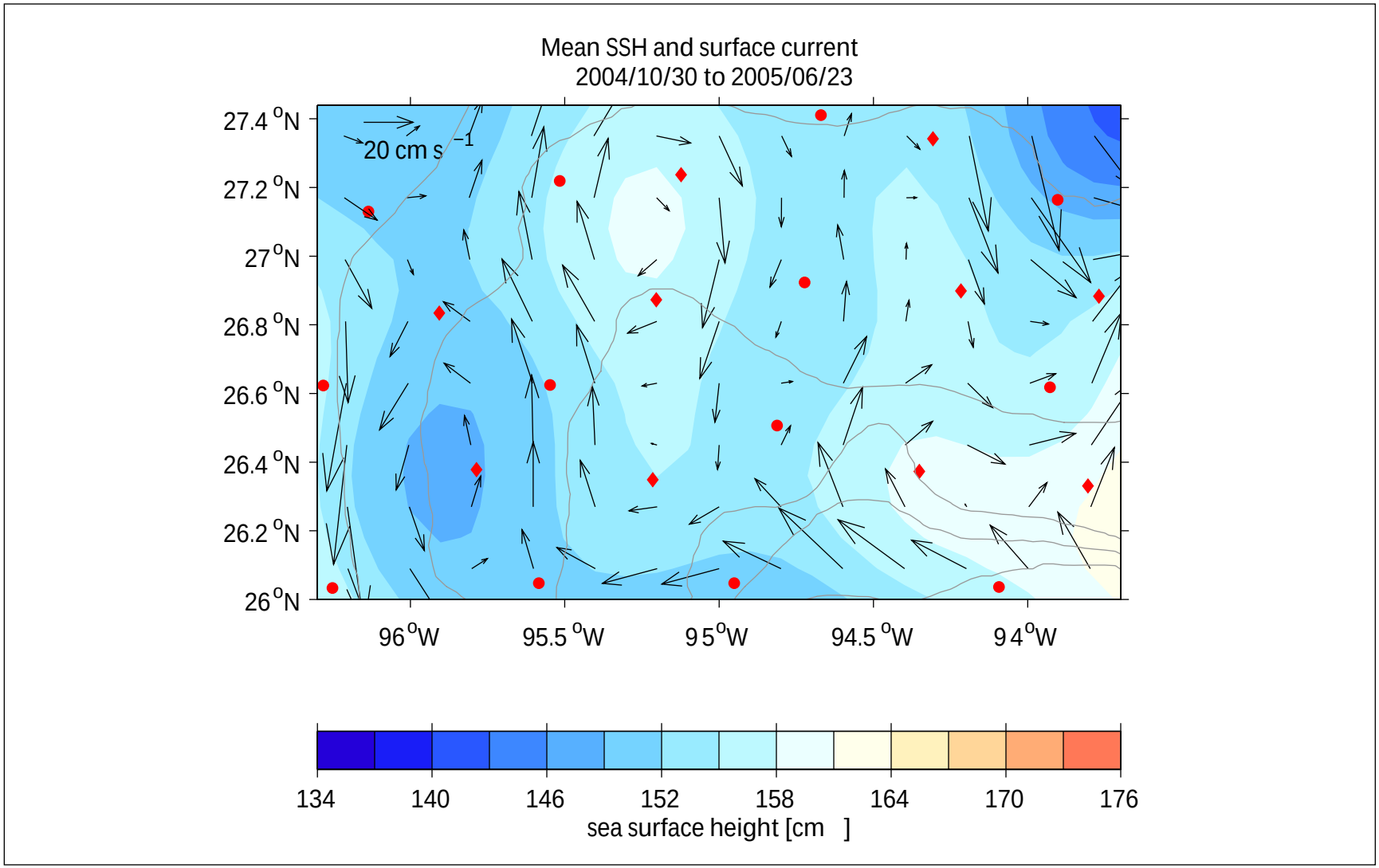

Figure 3.4-9. Time-average mean SSH (contours) and currents (black vectors) at the surface. Averaging period is from 30 October 2004 through 23 June 2005. SSH is contoured every 3.5 cm with low (high) values shown with blue (red) hues. Current vectors plotted at 20-km spacing. PIES sites indicated by diamonds, current meters denoted by circles. Vector key is shown in upper left corner. Bathymetry contoured every 500 m with gray lines.

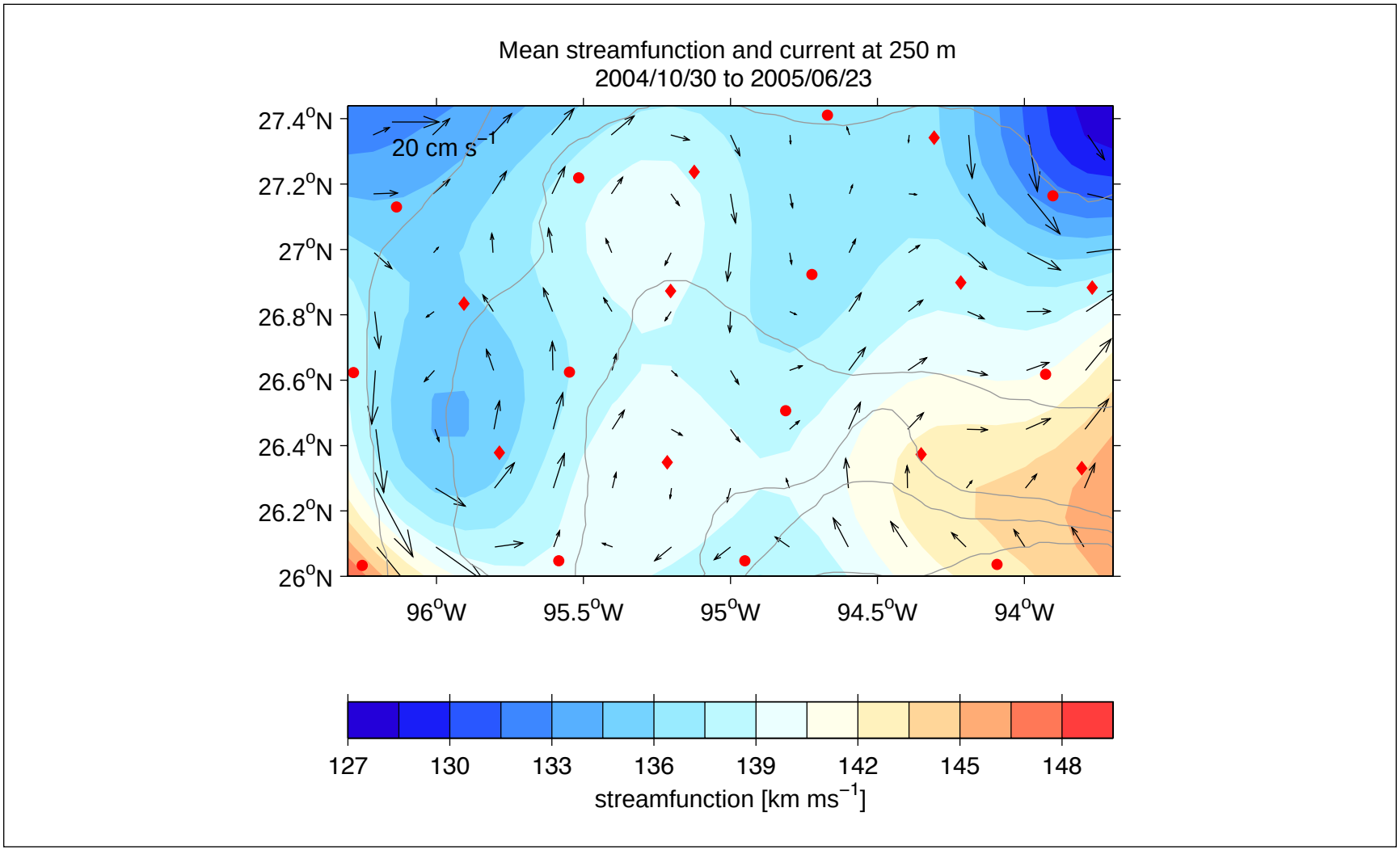

Figure 3.4-10. Time-average mean streamfunction (contours) and currents (black vectors) at the 250 m. Averaging period is from 30 October 2004 through 23 June 2005. Streamfunction is contoured every 3 km m•s^{-1} with low (high) values shown with blue (red) hues. Current vectors plotted at 20-km spacing. PIES sites indicated by diamonds, current meters denoted by circles. Vector key is shown in upper left corner. Bathymetry contoured every 500 m depth with gray lines.

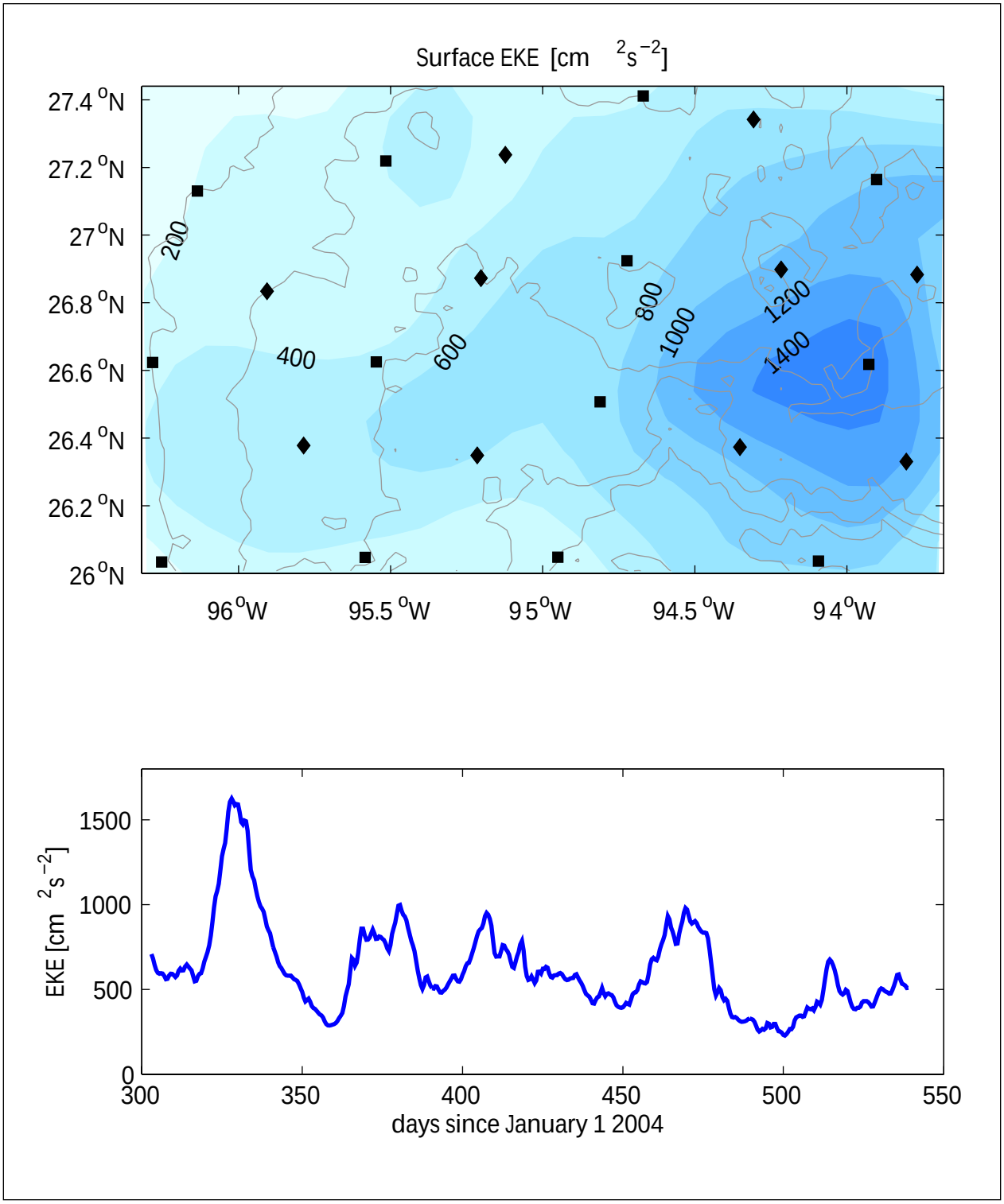

Figure 3.4-11. Upper panel: Mean surface eddy kinetic energy averaged between 30 Oct 2004 through 23 Jun 2005 contoured every 200 cm^2 s^{-2}. Bathymetry contoured every 500 m (gray lines). PIES sites indicated by diamonds, current meters denoted by circles. Bottom panel: Array-average mean surface EKE.

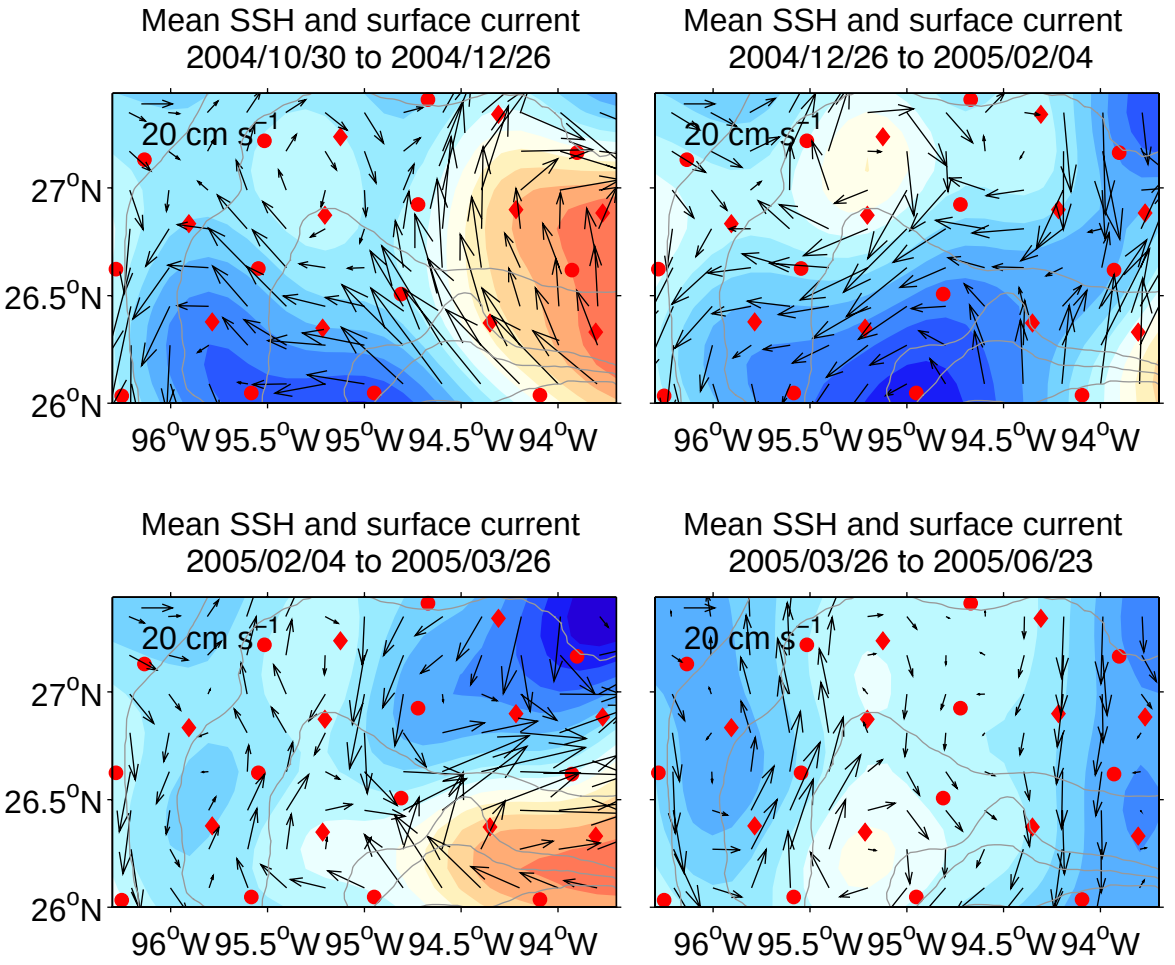

Figure 3.4-12. Event-averaged mean SSH (contours) and currents (black vectors) at the surface. Averaging period is stated in each panels' title. SSH is contoured every 3.5 cm with low (high) values shown with blue (red) hues. Current vectors plotted at 20-km spacing. PIES sites indicated by diamonds, current meters denoted by circles. Vector key is shown in upper left corner. Bathymetry contoured every 500 m (gray lines.)

- 30 October 2004 – 26 December 2004 Loop Current Eddy U2 entered the array along the eastern edge and propagated northward while Cyclone #4 persisted along the southern boundary of the array. (Compare to Figure 3.4-8(b), a one-day snapshot during this time interval.)
- 26 December 2004 – 4 February 2005 Cyclone #4 moved northeastward across the array whilst Loop Current Eddy U2 retreats eastward outside of the array.
- 4 February 2005 – 26 March 2005 Activity was concentrated in the eastern portion of the array with Loop Current Eddy in the southeastern sector and Cyclone#4 in northeastern sector. (Compare to Figure 3.4-8(c), a one-day snapshot during this time interval.)
- 26 March 2005 – 23 June 2005 A portion or remnant of the merged Loop Current eddies U2 and Ulysses moved northward into the central portion of the array and was surrounded by smaller cyclonic features. (compare to Figure 3.4-8(d), a one-day snapshot during this time interval.)

The strongest array-average EKE signal coincided with the simultaneous appearance of Cyclone #4 and the Loop Current Eddy U2 within the array in late 2004. Subsequent events have almost half the array-average EKE levels. The maximum in EKE in the central-east sector of the array resulted from the propagation of both U2 and Cyclone #4. Returning to the mean circulation map (Figure 3.4-9), the anticyclonic feature near 27.1ºN, 95.25ºW relates to a persistent feature, while the anticyclonic feature in the southeast corner resulted from the appearance of Loop Current Eddy U2 in late 2004 and again in February – March 2005. The cyclonic flow patterns in the southwest and northeast arose from the propagation of Cyclone #4. The duration of the joint PIES and current meter mooring array was not long enough to produce stable mean statistics; the circulation associated with each major event was quite distinct.

Finally, we calculated surface relative vorticity ($\zeta = \partial v/\partial x - \partial u/\partial y$) divided by the Coriolis parameter. The 8-month mean ζ /f (Figure 3.4-13) revealed positive values as high as 0.3 and negative values as low as -0.2. Note that these values reflect the combination of somewhat weak (20-30 cm s^{-1}) flow speeds over short (20-30 km) horizontal scales. The passage of both the Loop Current Eddy U2 and Cyclone #4 lead to the largest variability in ζ /f to occur, fluctuating from -0.5 to +0.5 in the eastern part of the study region. These Rossby numbers seem large compared to what one might expect in the ocean interior but not as large as those found in strong western boundary currents where the magnitude of the Rossby number can reach a value of 2 (e.g., Brooks and Niiler, 1977).

3.5 Examples of Eddy-Topography Interactions

Whenever currents have a component of flow across the isobaths, the water column is stretched or compressed and this leads to the generation of positive or negative relative vorticity anomalies, respectively, through the conservation of potential vorticity (PV). PV is defined at $(f + \zeta)/h$ where f is the Coriolis parameter, ζ is the relative vorticity and h is the larger depth. Increasing h by stretching caused by cross-isobath flows into deeper water require a compensating increase in ζ which implies that such flow will acquire a cyclonic tendency. As a cyclone forms, geostrophy will require the isotherms at the center of the vortex to rise. The situation is reversed for cross-isobath flows over shoaling topography. PV applies to layers defined by sigma-t surfaces, which are approximated by isotherms for this discussion. There are

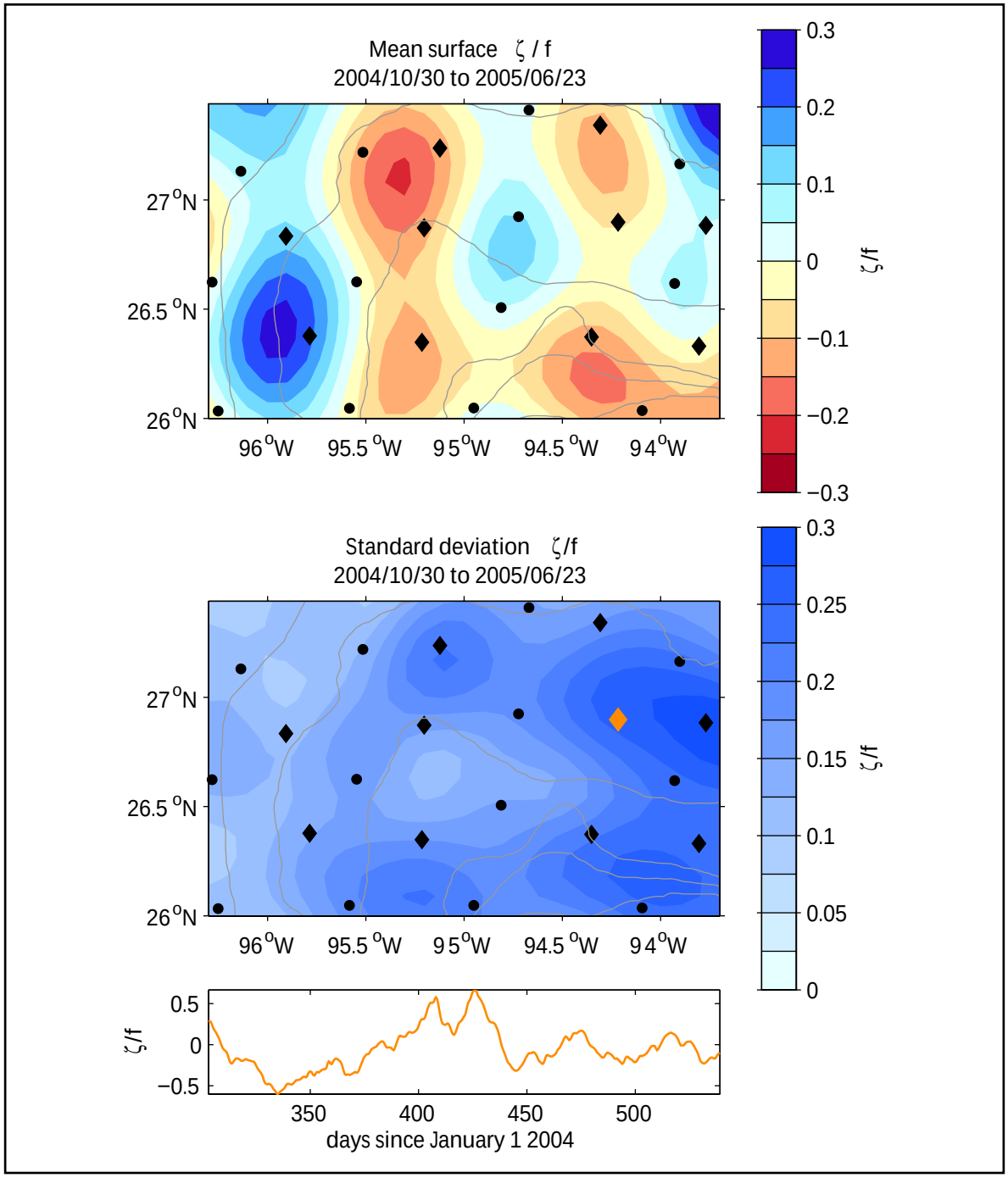

Figure 3.4-13. Upper panel: Time-average (30 Oct 2004 through 23 Jun 2005) mean relative vorticity scaled by local Coriolis parameter. Low (high) values shown with red (blue) hues. Middle panel: Standard deviation associated with the mean in the upper panel. PIES sites indicated by diamonds, current meters by circles. Bathymetry contoured every 500 m (gray lines.) Lower panel: Time series of relative vorticity scaled by the local Coriolis parameter at the PIES site denoted by the orange diamond in the middle panel.

a number of occasions in the observations when the deeper layers have different spatial structures than the near-surface layer, and in the two cases discussed below, it appears to involve separation of flows from the isobaths and the spin up of cyclones adjacent to the slope. Because upper-layer eddy flows, in general, do not have significant currents below ~ 750 to 1000 m, this type of eddy topography interaction is more likely to be observed when there are substantial flows over the upper slope in water depths < 1000 m. The two events discussed below use the moored current and temperature observations and present the large-scale dynamics. The second event occurred with the PIES deployed and thus can also be analyzed at smaller scales.

May 2004

At the beginning of the study, in April 2004, a cyclone-anticyclone pair with the cyclone to the west of the anticyclone moved northwards onto the NW slope. The cyclone weakened towards the end of April and then underwent a rapid intensification during the first part of May. This intensification involved cross-isobath flows that departed from the western slope towards deeper water. Therefore, even though the initial generation of this slope cyclone was not observed, its intensification was clearly documented.

Figure 3.5-1a shows the depths of the 18°C and 11°C isotherms, and in Figure 3.5-1b, the 18°C and 7°C isotherms, which represent the bottoms of upper, intermediate and deep layers, with mean depths of ~ 150, 350 and 650 m. Comparing the isotherm depths in the vertical section through the U moorings in Figure 3.5-1a and b, shows the intensification and uplifting of the isotherms at U2 between 29 April and 10 May (the 7°C isotherms were below 550 m on 29 April). The almost barotropic southward flow along the 500-m isobath at T1 and U1 on 29 April clearly turned offshore as V1 was essentially a null point, and offshore flow was observed at V2. The depth isopleths for the 18°C surface indicate that the anticylone was being fed by northward slope flow from south of 26°N. Otherwise the upper and lower layer density fields closely corresponded (Figure 3.5-1a). Ten days later, the 18°C surface had undergone considerable distortion as the cyclone intensified, producing a fairly complex structure along the U-mooring section (Figure 3.5-1b). The cyclone had evolved an anticyclonic cap, which was not strong enough to reduce significantly the cyclonic flows in the western side of the array. Current magnitudes were generally less than on 29 April, and the cyclone began to weaken after 10 May. Between 10 May and the end of the month, the cyclone weakened and drifted southwards, subsequently strengthening the north and northwestward flow at V3, U2 and T2 (Figure 3.5-1c). This flow encountered the shallower water of the northern part of the slope and appeared to strengthen the northern anticylonic center that formed around T5 and is seen in the 18°C surface on 10 May. Flow over shoaling topography would be expected to develop negative relative vorticity anomalies through PV conservation.

As an aside, the vertical temperature section through the U moorings in Figure 3.5-1b, shows reversing east-west thermal gradients through the water column at U1. This sort of thermal structure is associated with subsurface jets that are discussed in Chapter 5. The U1 mooring did not have the vertical resolution of the current profile that the deeper moorings had, but the southward flow was fairly depth independent at U1 for the depths shown on Figure 3.5-1, and the 250 m current on 28 May (Figure 3.5-1) is the maximum of the three. Thus, cyclonic flow along

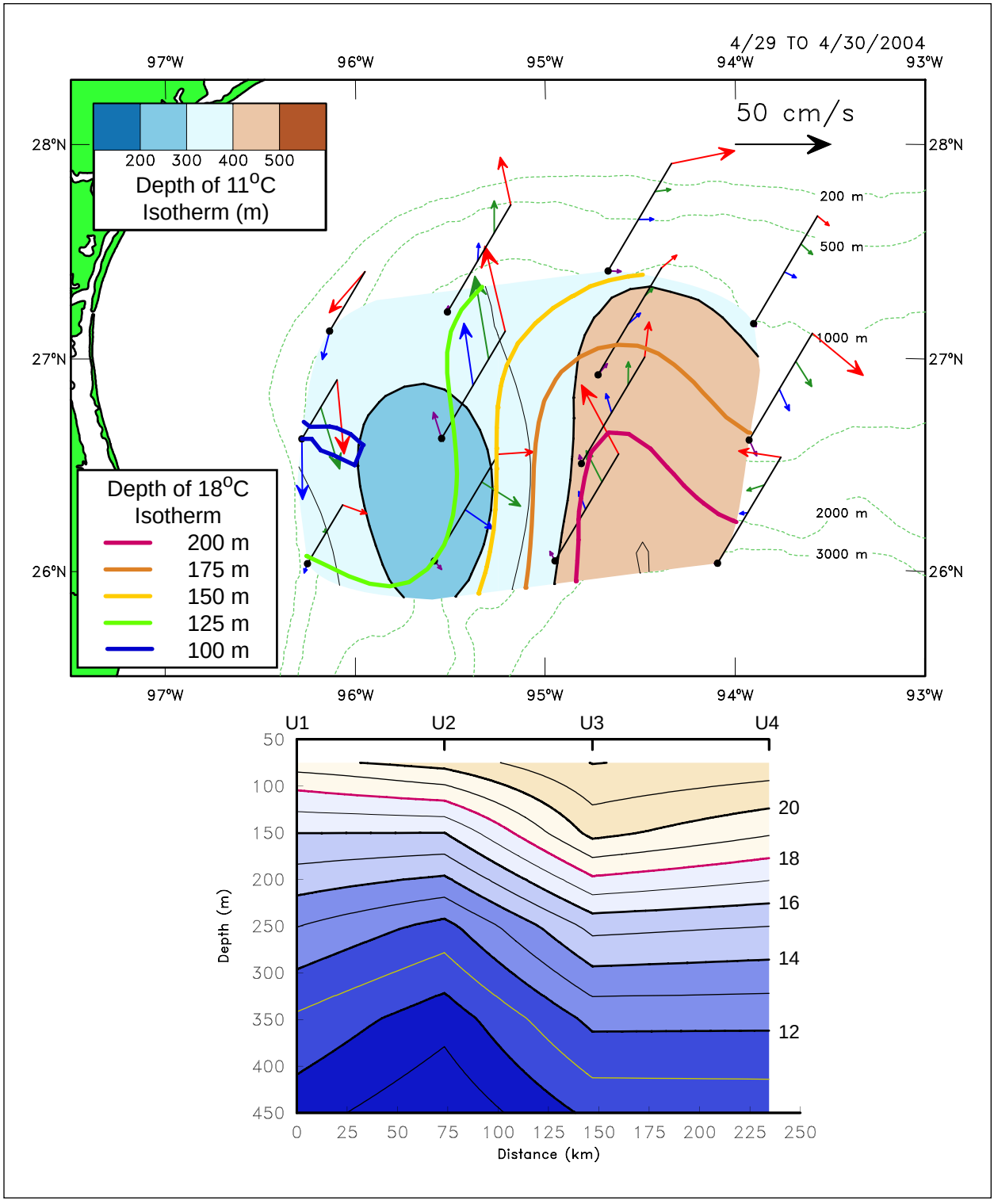

Figure 3.5-1a. Top panel: Contours of depths of the 11°C (filled) and 18°C (colored thick lines) isotherm surfaces for 28 Apr 2004. Velocity vectors, in a pseudo-3D view, are at 75 (red), 250 (green), 430 (blue), and 750 m (purple). Lower panel: East-west vertical temperature section through the indicated U moorings. All quantities are derived from 1-day averages of 40-HLP time series.

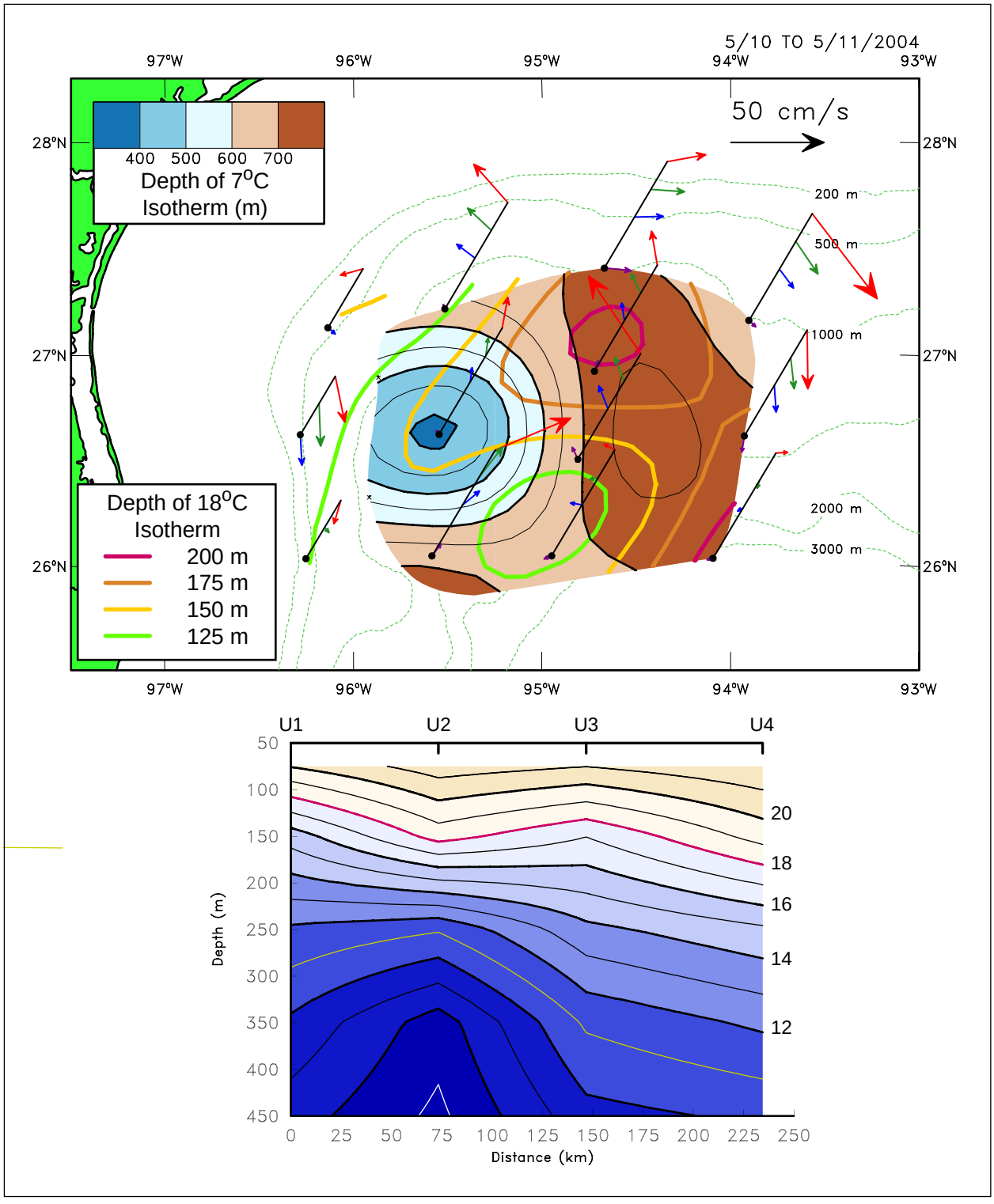

Figure 3.5-1b. Top panel: Contours of depths of the 7°C (filled) and 18°C (colored thick lines) isotherm surfaces for 10 May 2004. Velocity vectors, in a pseudo-3D view, are at 75 (red), 250 (green), 430 (blue), and 750 m (purple). Lower panel: East-west vertical temperature section through the indicated U moorings. All quantities are derived from 1-day averages of 40-HLP time series.

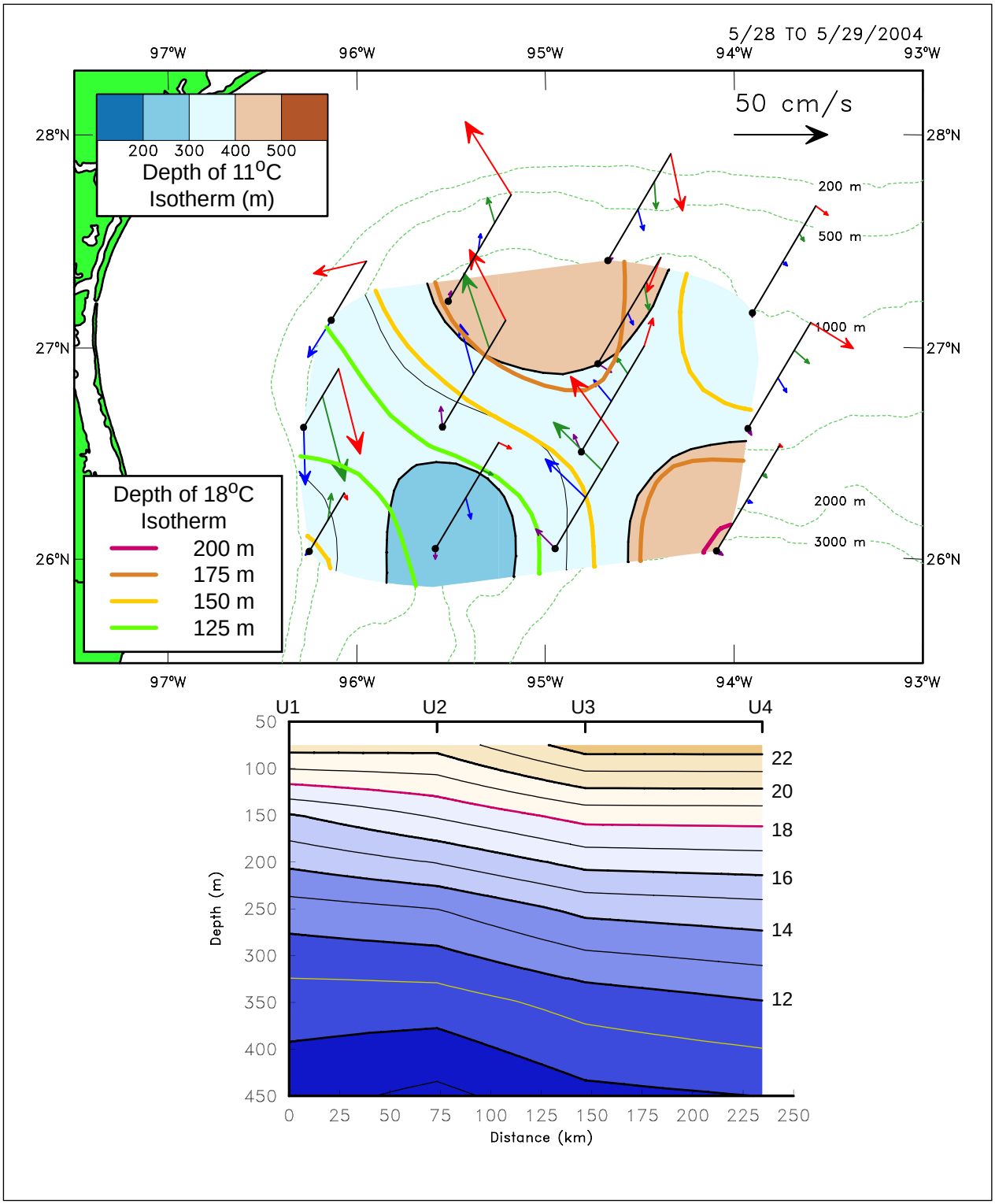

Figure 3.5-1c. Top panel: Contours of depths of the 11°C (filled) and 18°C (colored thick lines) isotherm surfaces for 28 May 2004. Velocity vectors, in a pseudo-3D view, are at 75 (red), 250 (green), 430 (blue), and 750 m (purple). Lower panel: East-west vertical temperature section through the indicated U moorings. All quantities are derived from 1-day averages of 40-HLP time series.

the upper slope appears favorable for subsurface jet events that could be similar to the observations at W1 discussed in Chapter 5.

May 2005

The previous May 2004 event was suggestive of the formation of both cyclonic and anticyclonic slope flows interacting with topography through PV conservation. Clearly eddy-eddy interaction was also occurring and complicates the picture. The May 2005 event was similar though it had the advantage that a cyclone was spun up from almost a state of rest. Figure 3.5-2a shows a cyclone beginning to intrude over the southeastern part of the array (V4) and that caused flows to be entrained from the slope south of 26°N. Thus offshore across-isobath flows were occurring at W1, W2 and V2. Most of the other moorings had weak flows corresponding to the weak thermal gradients. Fifteen days later (Figure 3.5-2b) a cyclone had spun-up in the vicinity of U2 and a surface-layer anticyclone, which was just about present on 15 May, had partly intruded from the south. As in the previous case, the maps of the 18°C and 11°C surfaces were quite different at the peaks of the cyclone's development and in this case some of the velocity depth profiles (e.g., V2 in Figure 3.5-2b) diverged from the more usual unidirectional flows. By the middle of June the cyclone had migrated northwards along the slope and was centered in the vicinity of T2 (Figure 3.5-2c). This was presumably the result of the stronger flows in the anticyclone. This migration is opposite to what happened to the May 2004 cyclone. Upper and lower temperature surfaces had similar structures in Figure 3.5-2c.

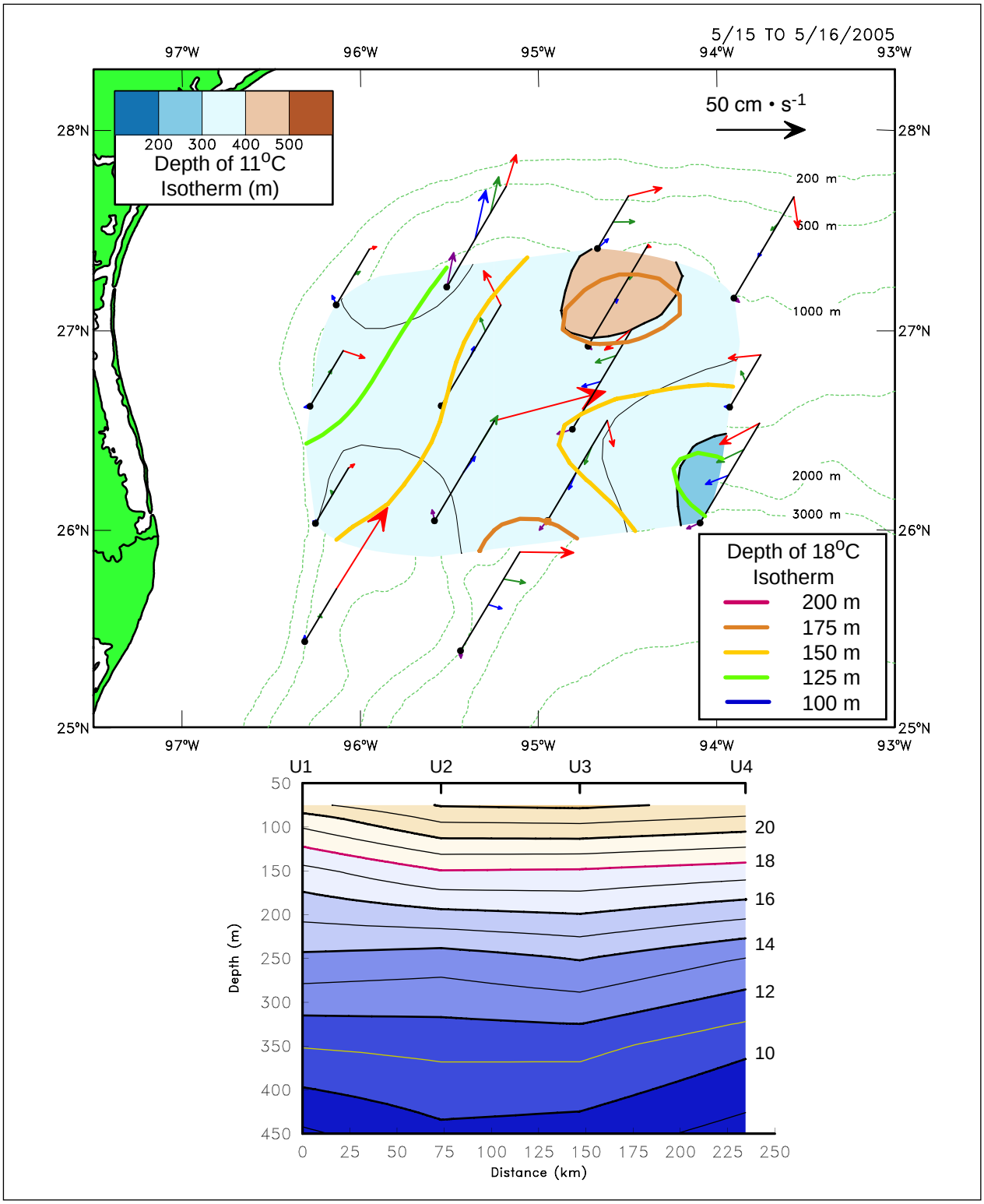

Figure 3.5-2a. Top panel: Contours of depths of the 11°C (filled) and 18°C (colored thick lines) isotherm surfaces for 15 May 2005. Velocity vectors, in a pseudo-3D view, are at 75 (red), 250 (green), 430 (blue), and 750 m (purple). Lower panel: East-west vertical temperature section through the indicated U moorings. All quantities are derived from 1-day averages of 40-HLP time series.

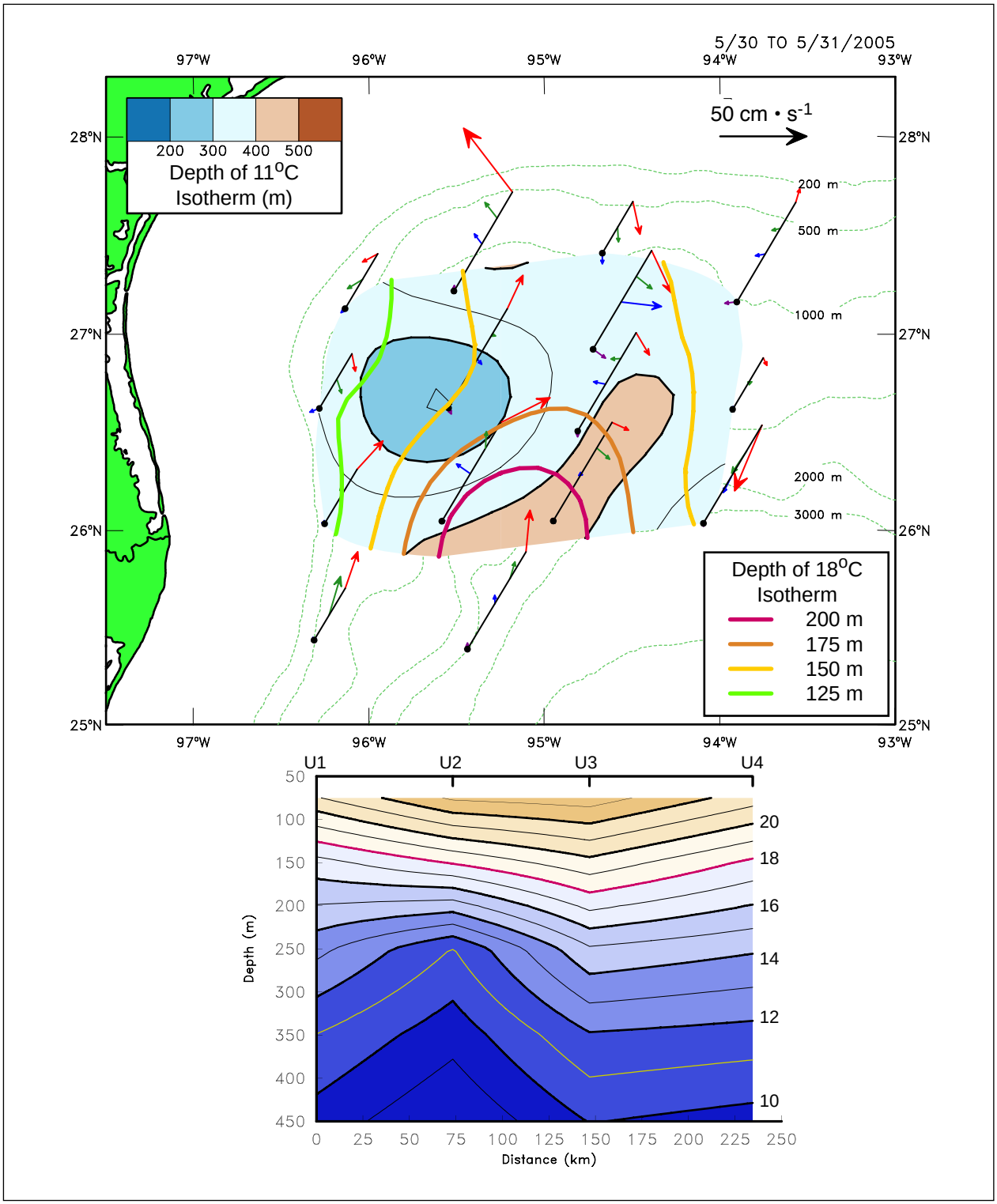

Figure 3.5-2b. Top panel: Contours of depths of the 11°C (filled) and 18°C (colored thick lines) isotherm surfaces for 30 May 2005. Velocity vectors, in a pseudo-3D view, are at 75 (red), 250 (green), 430 (blue), and 750 m (purple). Lower panel: East-west vertical temperature section through the indicated U moorings. All quantities are derived from 1-day averages of 40-HLP time series.

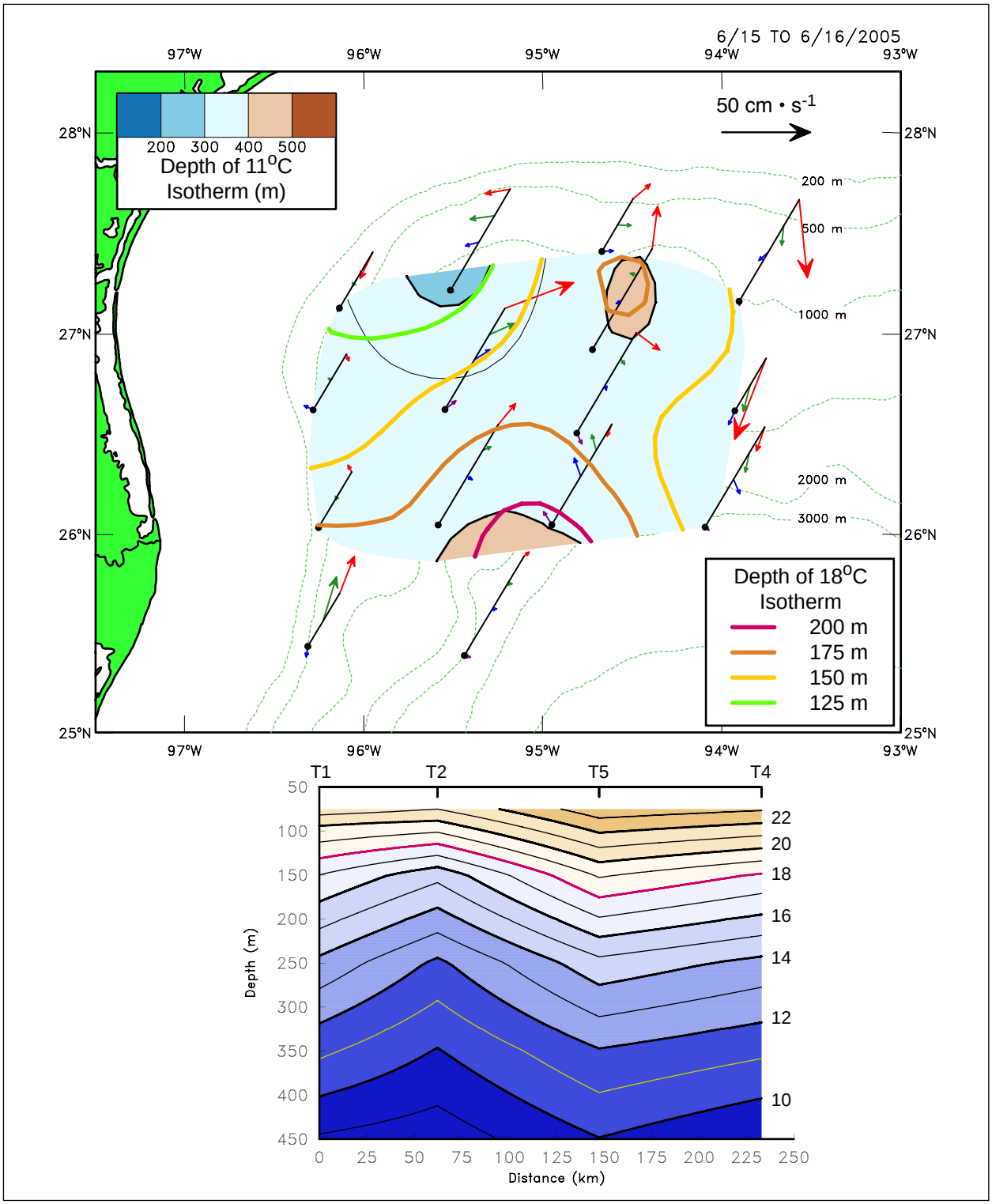

Figure 3.5-2c. Top panel: Contours of depths of the 11°C (filled) and 18°C (colored thick lines) isotherm surfaces for 15 Jun 2005. Velocity vectors, in a pseudo-3D view, are at 75 (red), 250 (green), 430 (blue), and 750 m (purple). Lower panel: East-west vertical temperature section through the indicated T moorings. All quantities are derived from 1-day averages of 40-HLP time series.

CHAPTER 4 BASIC DESCRIPTION OF DEEP CIRCULATION IN STUDY AREA

4.1 Historical Prespective

In the deep western GOM, previous deep-current measurements were made during Year 3 of the MMS-funded Gulf of Mexico Physical Oceanography Program, and reported by Hamilton (1990). In that study, five deepwater moorings were deployed in water depths greater than 2000 m within the Mexican EEZ from June 1985 to May 1986. The lower-layer subtidal fluctuations were highly coherent with depth and showed some bottom intensification particularly in water depths of 3500 m over the abyssal plain. The spectra show a prominent peak at about 25 to 30 days, similar to other deep-current observations made in the following years in the central Gulf. Hamilton (1990) interpreted the deep-current observations made in the 1980s in terms of topographic Rossby waves (TRWs), and drew an analogy with the TRWs radiated from the deep Gulf Stream in the northwestern Atlantic (Hogg, 1981). The source of TRWs was not clear at the time, though Hamilton (1990) did find moderate correlations between currents in the deepest western Gulf and a mooring under the eastern side of the LC with a lag that gave a minimum group velocity of 9 $km \cdot day^{-1}$ that is compatible with TRW theory (Rhines 1970; Thompson 1977). The basic concepts arising from these early studies were that LC extensions and retractions, the shedding of LCEs, and the translation of LCEs into the western GOM generated disturbances over the sloping bottom of the deep basin, that radiated away as TRWs (Malanotte-Rizzoli et al., 1987). The TRW-trains propagate generally westward at higher group speeds than LCE translation speeds, and so motions in the lower layer are decoupled from eddy-related currents in the upper layer. Numerical modeling studies by Oey (1996) and Oey and Lee (2002) showed that simulated deep currents could be interpreted as TRWs, and the results suggested that TRWs radiated towards the northern slope as LCEs translated across the western GOM basin. Oey and Lee (2002) also suggested that the topography and the anticlockwise deep-mean flows of the northern slope provided sufficient refraction of the TRWs that most of the energetic deep waves were confined to the deep basin.

As more deepwater moorings were deployed during the 1990s through to the present, it has become clearer that the distribution of lower-water-column kinetic energy is highly inhomogeneous. Over the Desoto Canyon slope, north of the LC, energy levels at depth were low (Berger et al., 1996), but further west at the base of the Sigsbee Escarpment, south of the Mississippi delta (90°W), energy levels were very high. Hamilton and Lugo-Fernàndez (2001) reported maximum speeds of 90 $cm \cdot s^{-1}$, 100 m above the bottom, at a site on the 2000-m isobath at the base of the steep Sigsbee Escarpment. Moreover, the wave trains were dominated by short period fluctuations of ~ 10 days. Subsequent analysis (Hamilton, 2007) of up to 2-years of current measurements at this site indicated that these highly energetic fluctuations are probably generated fairly locally and trapped by the topography in the region seaward of the escarpment. Ray tracing indicates that the west side of the LC is a likely generation region, and the wavelengths (~ 60 to 100 km) and periods (~ 7 to 20 days) could correspond to the propagation of cyclonic LC frontal eddies (LCFEs) around an extended LC front. It is known from satellite imagery and altimetry (Zavala-Hidalgo et al., 2003) that LCFEs can undergo explosive growth northeast of the Campeche Bank. The mechanism for transferring the energy from propagating LCFEs to the lower-layer TRWs may be akin to the wavenumber coupling mechanism,

originally proposed by Malanotte-Rizzoli et al. (1995). Pickart (1995) showed that this mechanism could account for the generation of 40-day TRWs that were observed at Cape Hatteras by 40-day eastward propagating meanders of the Gulf Stream. TRWs propagate westward and southwestward along the slope in the northwest Atlantic, and the coupling to eastward propagating meanders requires that the bottom slope have a direction such that a 40-day TRW wavenumber has an eastward component that matches the eastward wavenumber of the meanders. This coupling mechanism may be important for short period TRWs in the GOM; however, because waves are observed to have a wide range of periods between ~ 10 and 100 days, the generation of broadband TRW radiation by the large-scale movements of the LC and LCEs (Malanotte-Rizzoli et al., 1987) should not be discounted. Hogg (2000) indicates that energetic near-bottom currents, with TRW characteristics, observed over the tail of the Grand Banks seems to agree better with broadband radiation by the Gulf Stream and warm rings, rather than the meander coupling mechanism.

A characteristic of the deep currents south of the Mississippi delta was that 4 to 5 wave trains were observed over a 2-year interval, generally beginning with a high-energy burst (speeds >50 $cm \cdot s^{-1}$) and decaying over the next 3 to 4 months. Each wave train had slightly different characteristic wavelengths and periods, indicating different geographical source regions. Some could be associated with the presence of LCEs; however, at least one occurred when upper-layer eddy activity was weak (Hamilton, 2007). It seems to be characteristic of the eastern side of the basin, where the LC is dominant, that lower-layer current fluctuations are much more intermittent than has been observed in the central and western parts of the Gulf (Hamilton, 1990). In the central and western parts of the basin, TRW activity has a much more continuous character, and does not seem to be directly related to the passage of LCEs.

Subsequent to the studies discussed above, a major study (known as the Exploratory Study) involving one year of field measurements was conducted in 2003 and 2004 of the central northern GOM slope. This study employed an array of lower-layer moorings and PIES spanning the Sigsbee Escarpment between ~ 88.5 and 92°W, and ~ 25.5°N and the 1000-m isobath (Donohue et al., 2006) and also deployed and tracked deep (>1000 m) Lagrangian RAFOS floats. The results showed that the steep escarpment had a profound effect on the transmission and reflection of TRWs. The region above the escarpment was largely insulated from the energetic TRWs propagating westward and northwestward across the abyssal basin. Furthermore, the escarpment topography acted like a filter with short-period waves trapped near the steep slope in the east, whereas the southwestern part of the region was dominated by much longer period (~ 60 day) fluctuations. Motions with intermediate periods between 10 and 60 days appear to have been reflected back into deeper water with paths that suggest that not all these waves would reach the northwestern GOM. The variation of dominant fluctuation periods along the escarpment, from short in the northeast to long in the southwest, does not correspond to a conceptual model of deep eddies translating along the escarpment wall. If the latter governed the circulation, then similar frequency content of the motions would be observed at all sites along the escarpment. However, for short intervals of a few weeks, the spatial (2-D) current and bottom-pressure anomaly fields, derived from both current meters and PIES, can show cyclonic circulations stalling against the escarpment or moving northeastward along the escarpment, and anticyclonic circulations moving southwestward along the escarpment. Thus, there is some similarity to eddies encountering a wall. At present, these eddy-like deep flow events are

thought to be a result of combinations of packets of different frequency TRWs propagating towards and reflecting from the steep slope. The evidence, from the float trajectories, is that these motions were wave-like in that their locations oscillated in the same general area as the "eddies" moved through the study region. Therefore the evidence indicates that these deep motions should not be considered as eddies that transport both momentum and mass.

Mizuta and Hogg (2004) modeled theoretical TRWs propagating onto a shoaling slope. The shoaling slope induces a reflected wave component and a principal result is that a mean flow develops over the slope, forced by convergence of boundary-layer Reynold stresses. As part of the Exploratory Study, a closely spaced array of industry-funded bottom current meters were deployed across a steep part of the escarpment at ~ 91°W. A strong (~ 12 $cm \cdot s^{-1}$) jet-like mean flow was found centered over that slope. DeHaan and Sturges (2005) came to similar conclusions in that they attributed the observed anticlockwise (i.e., westward) deep-mean flow along the base of the northern slope to rectification of TRWs propagating towards the slope from deep water. The deep Lagrangian float tracks tend to confirm the view that the deep basin is dominated by TRWs in that, away from the escarpment, the tracks are fairly rectilinear with principal directions at small angles to the isobaths. The floats tend to stay in the same general vicinity for periods of order 6-months or more. Being propagating waves to first-order, TRWs do not transport mass. These characteristics are quite different from surface-layer drifters deployed in LCEs, which can be transported from east to west across the whole GOM in six months (Kirwan et al. 1984; Lewis et al. 1989). When the deep floats moved into the vicinity of the escarpment, they got entrained in the mean flow and could be transported long distances along the base of the northern slope towards the west. In the Exploratory Study, only one float out of 36 showed a looping path that could be the result of a translating deep lower-layer eddy. This occurred close to the western Mexican slope and will be presented later in this chapter. Welsh and Inoue (2000), using a numerical model, show that the shedding of LCEs generates a lower-layer accompanying cyclone and anticyclone pair, which translate with the surface-layer LCE as it moves westward across the GOM. The RAFOS float tracks, as discussed above, did not show evidence of such deep circulations, and so it remains an open question whether such deep eddies exist in the center of the GOM basin.

The Exploratory Study array also provided some evidence that major LCEs and the LC can spin-up vortices in the lower layer as the sloping thermocline associated with the front is displaced by meanders or rotating lobes of an upper-layer eddy. It is not clear, at present, if such lower-layer vortices, spun-up through potential vorticity (PV) conservation, remain as coherent lower-layer eddies or disperse into TRWs. There were a few examples of similar lower-layer vortices being spun up as upper-layer eddies propagated over the shoaling topography of the northwestern slope in this present program. A case study is presented in Section 4.5.

The present NW Gulf study is in some sense a "downstream" successor to the Exploratory Study. Based on previous observations, it is expected that abyssal flows will be dominated by TRWs. The northwestern Gulf, however, is dominated by LCEs moving onto the steep Mexican slope, a process that usually generates a companion cyclone (Frolov et al., 2004; Smith, 1986; Vukovich and Waddell, 1991). Such strong surface-layer eddy interactions with the slope topography are likely to produce vortices in the lower layer through PV conservation. Thus, there is a possibility that the lower Mexican slope is a secondary region of TRW generation. TRWs generated in this

region will propagate off to the south towards the Bay of Campeche. Therefore, there could be both local and remote forcing of the deep-current fluctuations. This region also has complex topography and the Sigsbee Escarpment extends into the northwest corner at depths of 2500 to 3000 m. These topics will be discussed below after the basic statistics of the lower-layer flow have been presented in Section 4.2.

4.2 Basic Statistics

The means and variances of the 40-HLP lower-layer currents have been calculated two ways: 1) using the longest possible records at each mooring, and 2) using the common overlap interval between the NW and Mexican moorings. This is similar to the upper layer statistics discussed in Section 3.4.1. The time series vector plots for selected records are given in Figure 4.2-1. The deep currents at W3, V4, V3, and W2 (Figure 4.2-1a) show characteristics of TRWs with intensification of the fluctuations towards the bottom and high vertical coherence between widely spaced instruments. Speeds are much lower than in the central Gulf, and are usually less than 20 $cm \cdot s^{-1}$. Southward mean flows are evident at V3, W2, W4 and W5, where reversals of the predominant flow directions are quite rare. Longer period fluctuations are evident at W3, when compared with the more energetic flows at V4 and V3. The two southern-most moorings, W4 and W5, have very weak current fluctuations. The near-bottom currents are somewhat weaker than those 400 m higher in the water column and clearly less vertically coherent than the other moorings. The bottom instruments at all the W moorings were 300-kHz ADCPs directed upwards. The records from the highest-level bin are about 55 to 60 m above the bottom, which is less than the 100 m from the bottom of the lowest instruments on the U.S. sector moorings. Thus, there may be bottom-boundary-layer effects in these records, and because W4 and W5 were deployed on a relatively steep slope, there may also be side boundary-layer effects on these near-bottom currents. The records from the moorings on the NW slope are given in Figure 4.2-1b. The majority of these moorings had an instrument at 1000 m and an instrument 100 m above bottom. Records at 1000 m are often in a transition depth zone where some of the time the currents are at the bottom of upper-layer eddy circulations, and some of the time, at the top of the lower-layer flows. Speed at all these slope moorings are < 20 $cm \cdot s^{-1}$ and most of the time < 10 $cm \cdot s^{-1}$, and in some cases the near-bottom flows are much weaker than flows at 1000 m (e.g., V2 and U2).

The lower-layer mean flows using both total records and the common interval are given in Figure 4.2-2, which also shows the near-bottom eddy kinetic energy ($EKE = 1/2(\langle u'^2 \rangle + \langle v'^2 \rangle)$). It can be seen that there is little difference in the results between the two cases, which indicates that the statistics derived from the 10-month common interval are fairly robust. Mean flows were quite depth-independent, particularly below 2000 m, with the largest bottom intensification in the mean flow occurring at V3. The mean flows were strongest along the base of the slope and had the same anticlockwise sense (west and south) that was observed in the central Gulf (Donohue et al., 2006). The EKE was greatest at V4 and decayed from the deep water towards the Mexican slope and up onto the NW slope. The only region of the NW slope that had somewhat higher EKE is U4 that may indicate some upslope penetration of EKE from the deep basin. Another view of near-bottom current statistics is given in Figure 4.2-3, where the means and variances in the form of standard deviation ellipses are shown. The reduction of the variances along the 2000 m isobath from the corner at V3 towards the south at W4 and W5,

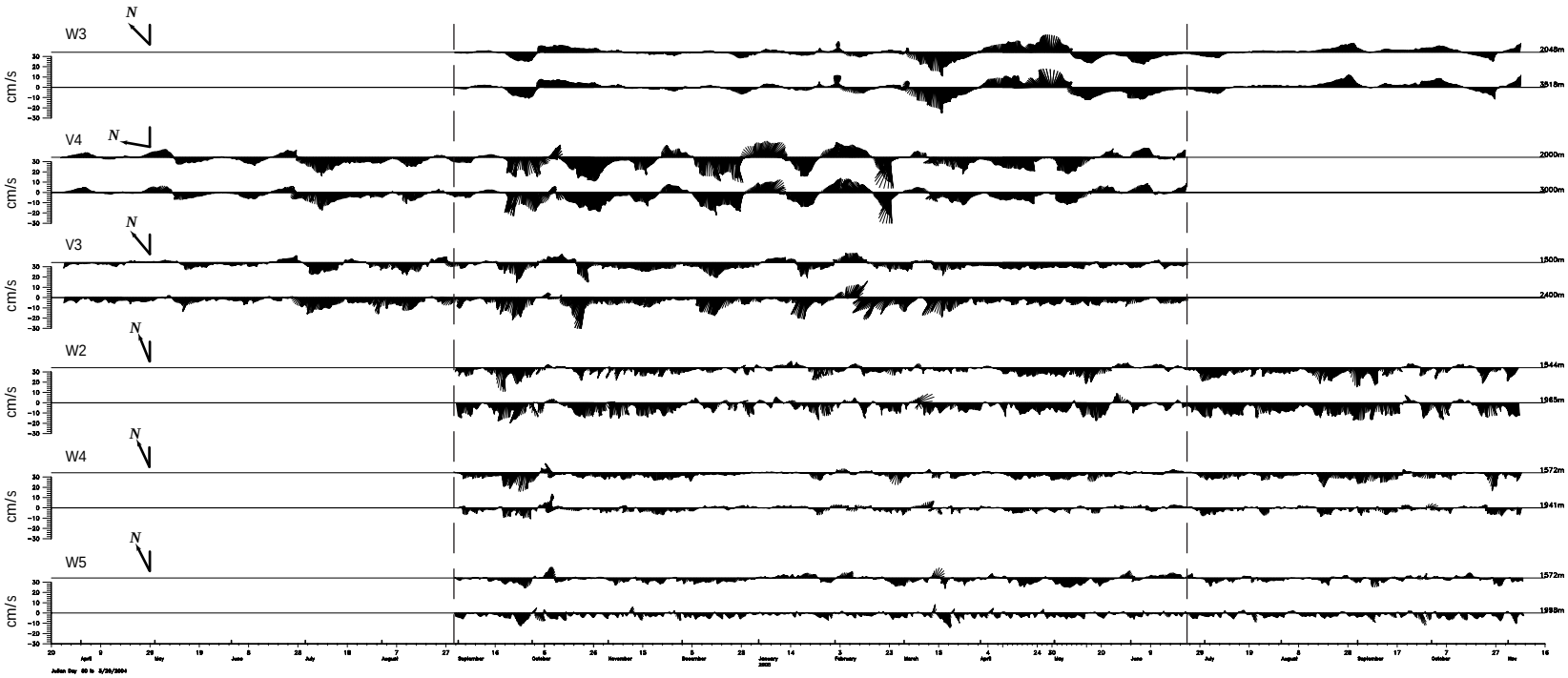

Figure 4.2-1a. Near-bottom 40-HLP current records from the lower slope of the Mexican (W2 through W5) and U.S. (V3 and V4) sectors. Dashed lines denote the common interval.

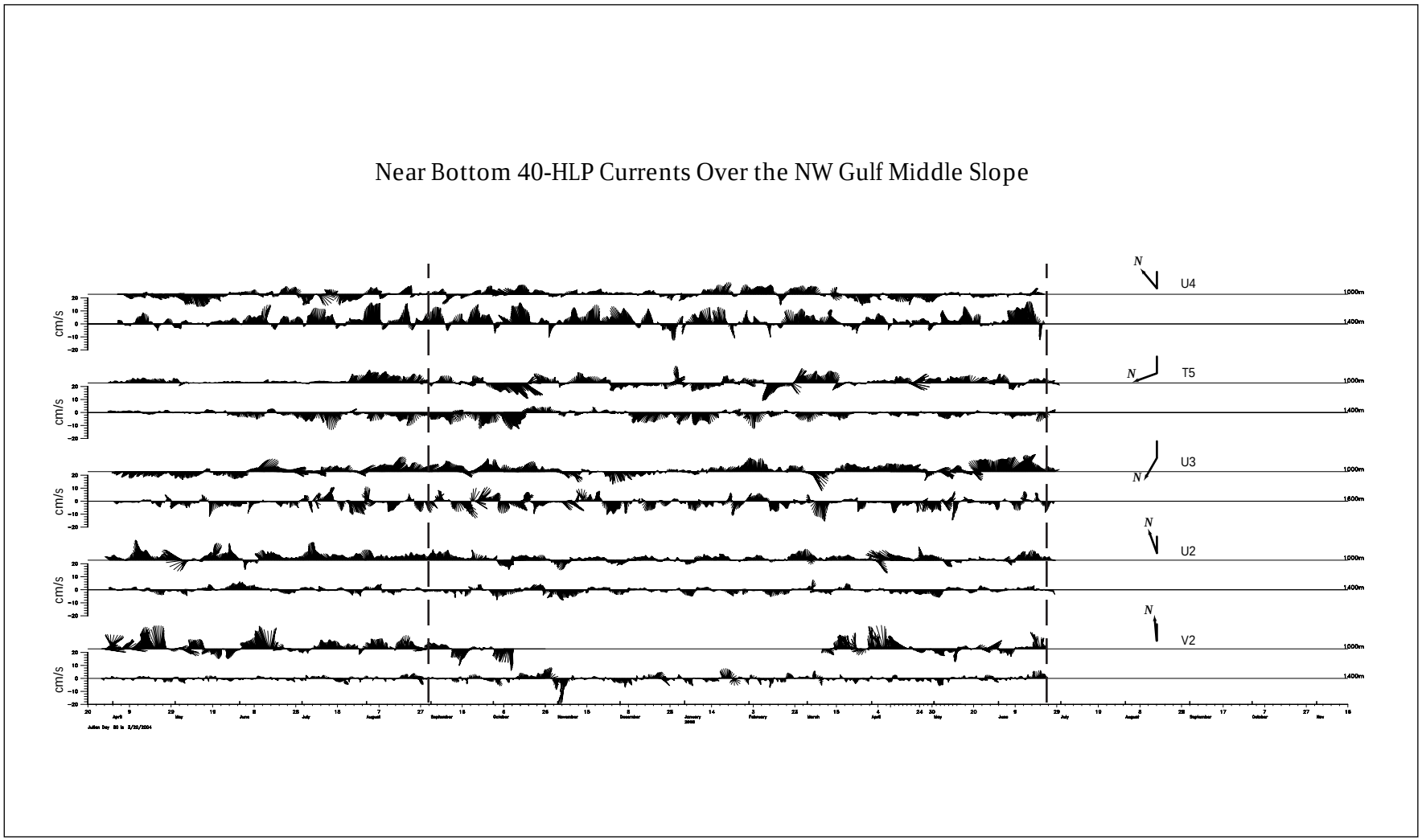

Figure 4.2-1b. Near-bottom 40-HLP current records from the middle slope of the U.S. (T5 through V2) sector. Dashed lines mark the common period.

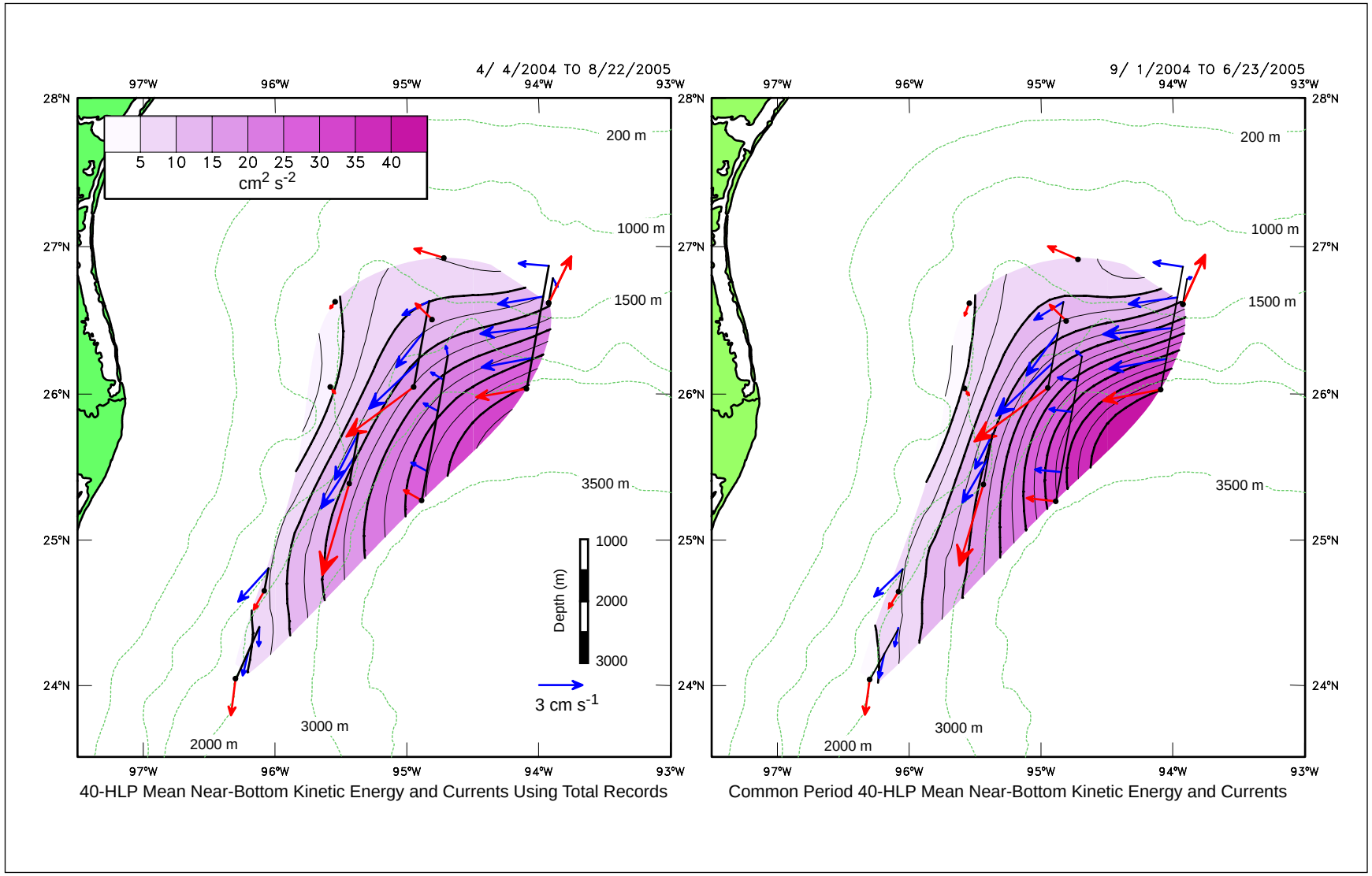

Figure 4.2-2. Mean 40-HLP currents plotted as pseudo 3-D profiles where the red arrow is the deepest meausurement (~ 60 - 100 mab) and contoured eddy kinetic energy at 100 mab. Left panel using complete records at each mooring, and right panel using the common interval.

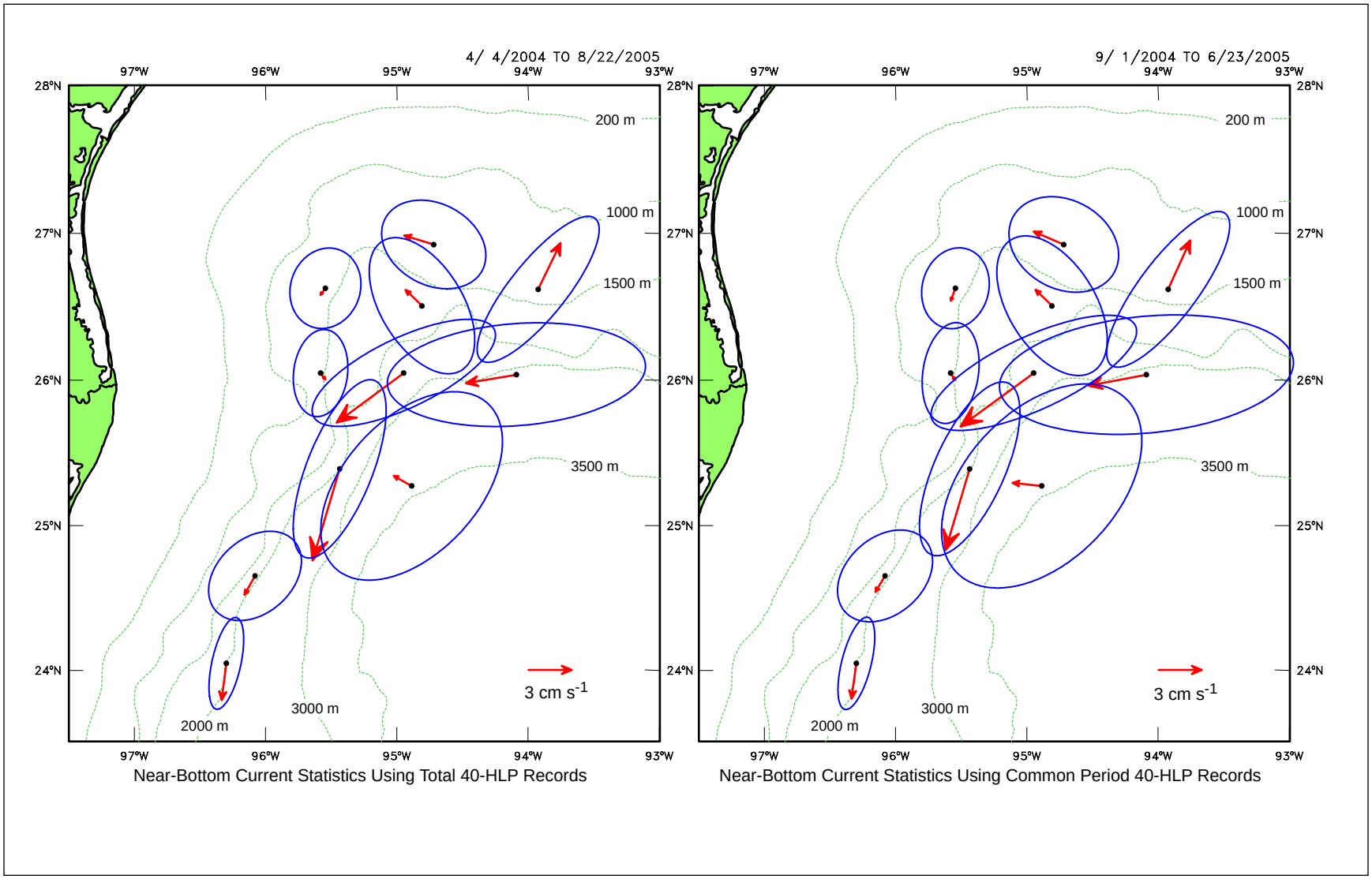

Figure 4.2-3. 40-HLP mean currents and standard deviation ellipses for measurements ~ 60 - 100 mab. Left panel using complete records, and right panel using the common interval.

where the fluctuation standard deviations were as small as on the middle NW slope. The major axes of the ellipses generally aligned with trends of the local isobaths. This was the case at U4 also as the near-bottom currents are influenced by a northeastward trending ridge just west of the measurement site.

4.2.1 Spectra

The kinetic-energy spectra, in variance preserving form where equal areas under the curve represent equal contributions to the total variance of lower-layer currents from U.S. sector instruments are given in Figure 4.2-4. The two moorings at the base of the slope (V3 and V4), which had large variances relative to the middle slope, had distinct peaks ~ 30-day periods, with most of the energy concentrated between ~ 60 and 20 days. V3 shows increasing KE from 1000 m to 2400 m, consistent with bottom intensified TRWs, however, V4 measured a KE increase from 1000 m to 2000 m. Below this depth, the variances at 30-day periods were less than at 2000-m with essentially no variation down to 3000 m. Therefore, at V4 there was intensification with depth to around the top of the escarpment, with some reduction below this. This may have been caused by some topographic blocking by the steep slope at depths below 2000 m. In the Exploratory Study, lower-layer flows became nearly depth independent below 2000 m, though reductions of variance below this depth were not observed. The middle slope KE was much smaller than for the two moorings below the escarpment, and also the dominant fluctuations had shifted to shorter periods of ~ 15 to 25 days. KE on the eastern side (U4 and U3) was higher than the western and northern sides (T5, U2 and V2). At V2, U4 and U3, short-period motions of ~ 5 to 10 days were also present. Therefore, fluctuations above the escarpment were much less energetic and had spectral peaks at different frequencies when compared to sites below the escarpment.

The KE spectra calculations for the Mexican sector used the complete 431-day interval, which is very similar to the 445 days used for the U.S. sector currents, though the overlap in time is only 10-months. In the Mexican sector (Figure 4.2-5), only W3 on the abyssal plain had KE spectra unambiguously characteristic of TRWs with energy being bottom intensified with energy in distinct frequency bands. The 30-day motions at W3 were prominent and similar in magnitude to those at V3, although at V3 there were more energetic motions at longer periods of 50 to 60 days. These latter period motions were only barely present at the other sites in both sectors. The other moorings (W2, W4 and W5) were along the base of the steep lower part of the Mexican slope and have much more complex spectra, both in the distribution of energy with frequency and with depth. All these spectra had peaks at ~ 20 to 25 days, but the lowest depth level on all three moorings had energy at higher frequencies that was not present 400 m higher in the water column. This implies that there were some highly bottom-trapped, high-frequency modes along the base of the slope. However, the overall energy levels at W4 and W5 are comparable to U2 and V2 on the 1500-m isobath of the middle slope.

4.3 Eddies and Waves

This section addresses the fact that in the GOM and elsewhere, two or more terminologies are used to describe the same phenomena and processes, as observed by different measured variables. The spatio-temporal variability is conventionally interpreted sometimes as eddies and

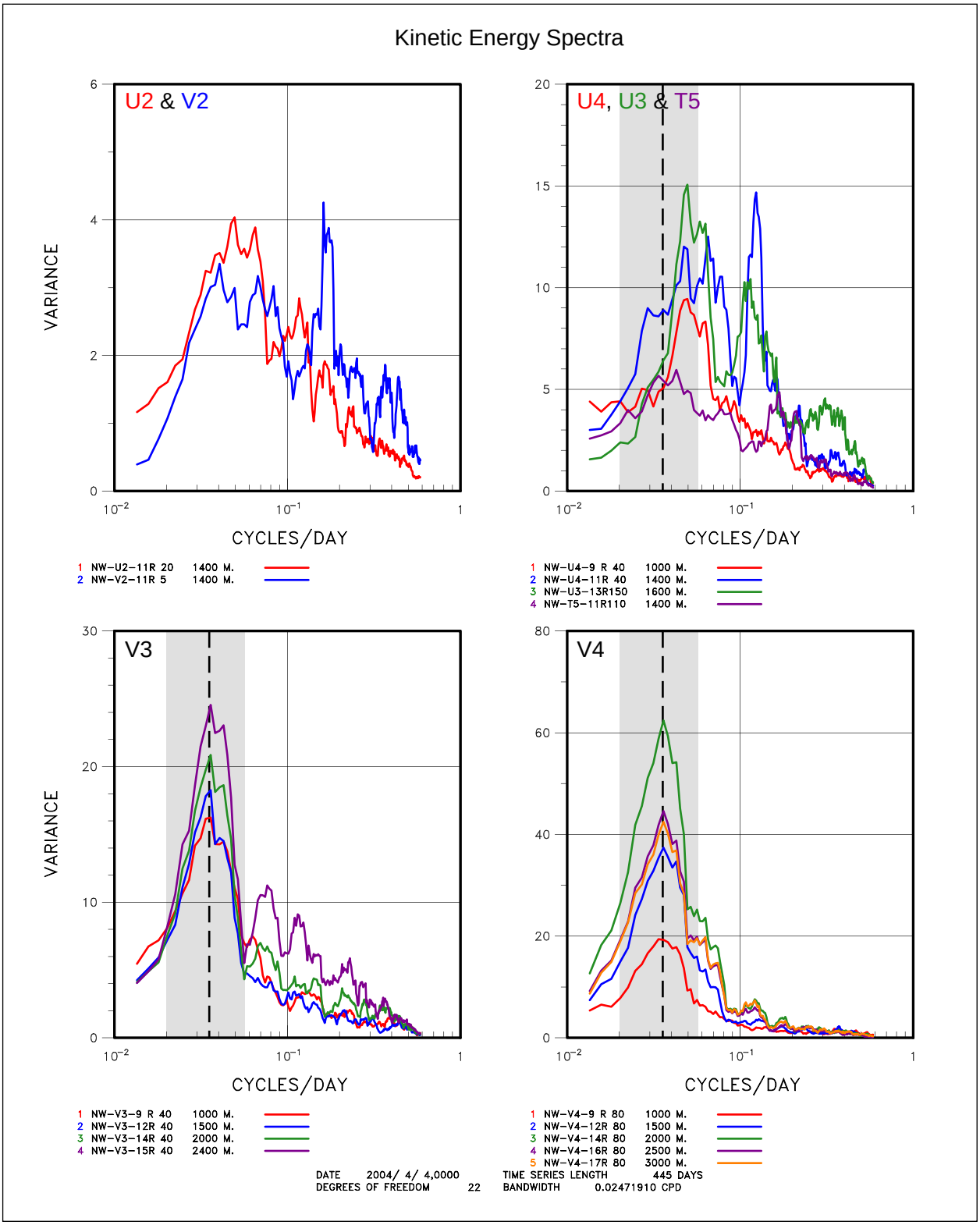

Figure 4.2-4. Kinetic energy spectra from the indicated 40-HLP records from lower-layer instruments in the U.S. sector. The dashed line and shading show the peak frequency and band of high energy at V3 and V4.

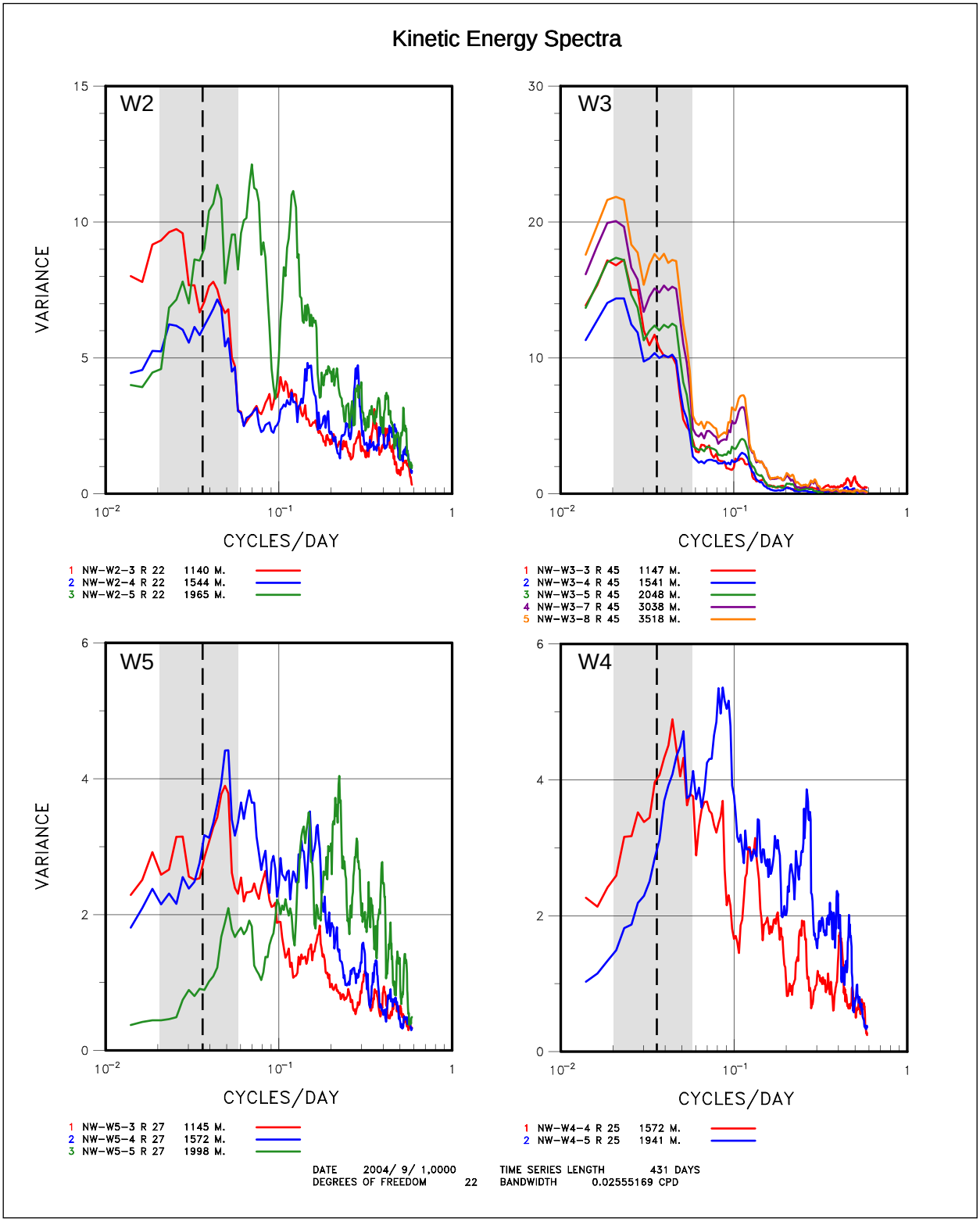

Figure 4.2-5. Kinetic energy spectra from the indicated 40-HLP records from lower-layer instruments in the Mexican sector. The dashed line and shading show the peak frequency and band of high energy at V3 and V4.

sometimes as waves. For example, in the surface waters the "Loop Current Eddies" enclose and carry cores of distinct water properties (as would be called "rings" in other locations), and alternatively many weaker "eddies" are observed in other surface features, that travel without transporting a core of water that is distinct from its surroundings. Another example from deep waters in the GOM can be cited from the current-meter analyses, which have projected the observations onto TRWs, while their stream function maps from PIES bottom pressure observations exhibit a field of high and low-pressure centers that are described as "eddies".

The terminology in the literature can be confusing. The term "eddy variability" has been applied in some literature to any fluctuation from the time-mean. At the other extreme, the term "eddy" has been applied in some literature only to a ring that transports a core. We will now present and discuss a consistent terminology to mesoscale variability in the upper and deep portion of the water column of the GOM.

Let the word "fluctuation" denote any departure from a mean current or mean-scalar variable, irrespective of what process or sum of processes might cause it. Waves, eddies, and turbulence may all contribute to observed fluctuations. The present focus is on mesoscale processes, organized coherently over time scales from days to months and length scales from tens to hundreds of kilometers. Smaller-scale, uncorrelated processes are not treated in the following discussion other than recognizing that they contribute to the fluctuation variance.

The ocean responds to small amplitude perturbations on these scales, according to geophysical fluid dynamics, by a sum of wave processes. The wave processes are governed by the local stratification and topography on the rotating spherical earth. Data analyses commonly seek to determine the observed frequencies and wavelengths, and we often find that a great proportion of the observed variance can be interpreted as waves. Moreover, often the variance can be projected onto a limited bandwidth spectrum of plane waves and interpreted in relation to planetary wave / topographic wave theory.

Mathematically, plane waves have long crests and troughs aligned perpendicular to their direction of propagation. However, when our observations span two horizontal dimensions, the mapped features contain fields of high and low pressure centers. These features rarely "look like" pure plane waves with long crests and troughs, but rather they look more approximately elliptical with similar scales in both horizontal dimensions. A field of high and low pressure centers can be generated by summing plane waves with wavenumber vectors crossing each other at an angle (e.g., Figure 4.3-1). Correspondingly, the observations indicate a sum of components having different, crossed wavenumbers. Components with crossing wavenumbers may originate from different locations, and/ or the waves may have reflected off a boundary.

Snapshots of the observed high and low-pressure centers include features with closed contours, but they do not necessarily carry a closed core of fluid mass and water properties with them. The features may instead simply propagate through the fluid. The field in Figure 4.3-1 of closed highs and lows, generated by the linear sum of plane waves with crossed wavenumbers, propagates through the fluid medium in the x direction. One can show mathematically that the factor determining whether or not an eddy carries a core is its strength or amplitude. If a high or low-pressure center is strong enough that the swirl velocity (U) around it exceeds its translation

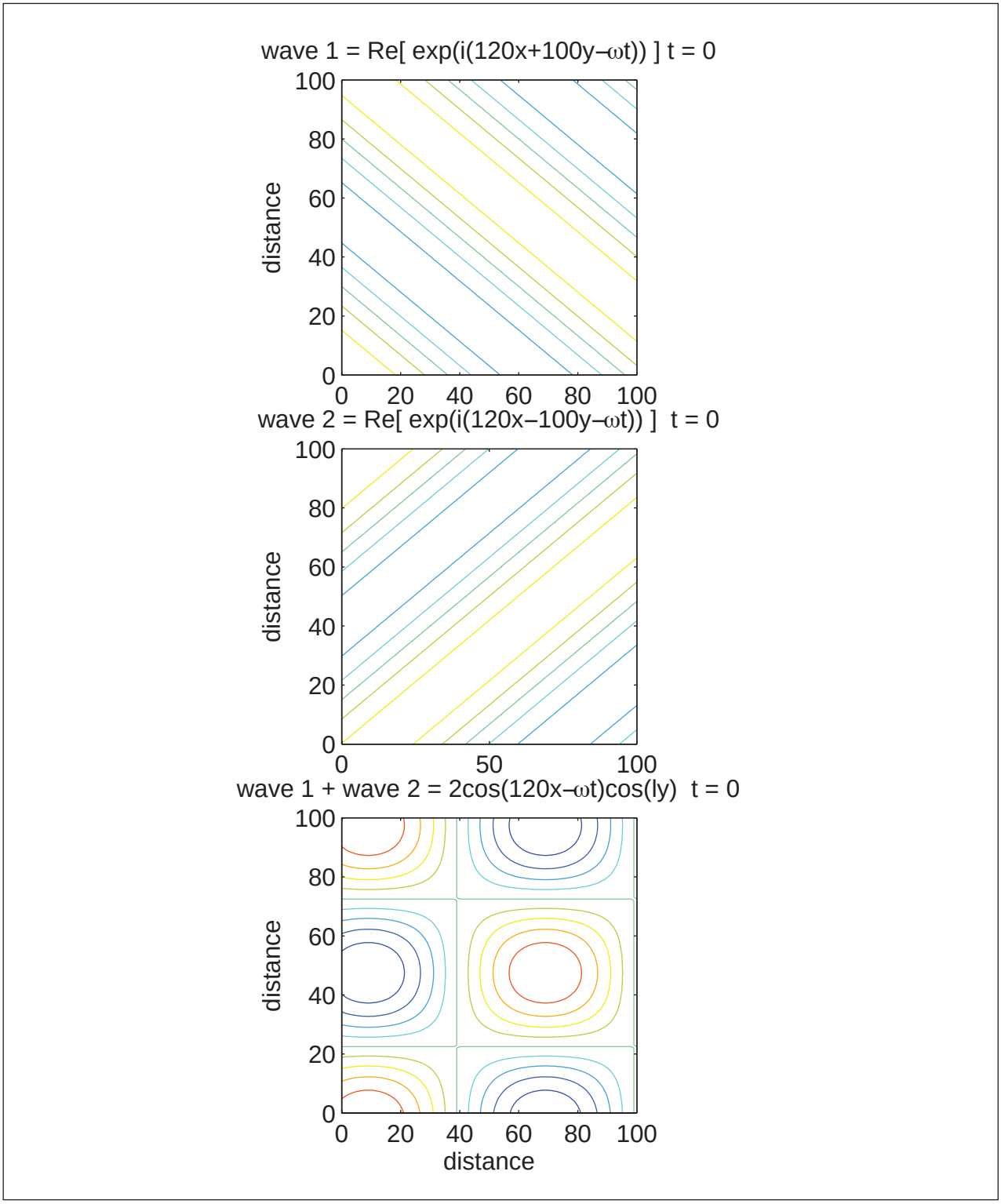

Figure 4.3-1. This idealized case is drawn from the sum of two waves, Re[exp(i(kx+ly-wt)) + exp(i(kx-ly-wt))] = 2 cos(kx-wt) cos(ly), which is a field of high and low pressure centers, modulated in two dimensions, propagating in the x direction. In this example, k=2 pi/100, and l=2 pi/120, and we view a snapshot at t=0. A localized wave group would comprise a bandwidth of k wavenumbers and l wavenumbers.

velocity (C), such that U/C > 1, then its streamlines enclose a core, whose mass and properties are carried with it.

In a LCE the upper velocities are of order U~100 cm·s^{-1}, and a typical translation speed is C~10 cm·s^{-1}, so U/C>1 and they carry a core. In contrast, for a typical deep eddy U~10 cm·s^{-1} and C~20 cm·s^{-1}, giving U/C<1, and they move thru the medium rather than carry a core. Deep eddies can momentarily "appear in place" by constructive adding of various waves – and may subsequently "disappear" as the phases of the constituent waves change. The translation speed, C, is simply how fast a high or low-pressure feature actually moves, not the theoretical wave propagation speed. Momentary bursts of speed C can "lose" (tear apart) those outer portions of a strong eddy core beyond a boundary defined by U/C=1. Hence, for an eddy to carry a core persistently of anomalous water properties, it must have maintained a high enough U and low enough C so that U/C>1 surrounding its core since it was formed.

As discussed previously and below in Section 4.4, the current velocities measured on the moorings exhibit kinematics remarkably conformant to TRWs – variance ellipse orientation relative to topography, their frequency and time scales, some examples of bottom-intensification, and their lateral phase relations which determine their wavenumbers. The PIES deep pressure maps exhibit many closed-contour features, with currents that agree well with the directly measured currents. It is important to reiterate that the current meters and the PIES are observing the same processes, with consistent currents and streamfunctions. They are TRWs, and they include components with crossed wavenumbers from different locations or wave reflections. This sum of waves with crossed wavenumbers produces closed eddy streamlines. So it is also proper to call them eddies. Eddies in the deepwater column or in the upper-water column can be either small amplitude and carry no core, or large amplitude and non-linear enough (U/C>1) to carry a core.

Lastly, it is noted that even a feature that propagates through the medium without carrying a core can produce a loop in a float's trajectory -- and a propagating wave train can correspondingly produce a sequence of loops. Hence loops observed in float trajectories are not unequivocal evidence that an eddy carries a core.

4.4 Topographic Rossby Waves

Fluctuations of lower-layer currents were analyzed using frequency domain EOFs in a similar manner to Hamilton (1990) and Donohue et al. (2006) for the Exploratory Study. For the moorings with large variances and more than two instrumented levels below 1000 m, frequency domain EOFs are appropriate because they take into account spatial phase differences. W3, V3 and V4, the depth variability at each mooring was analyzed separately for the dominant spectral peaks using the longest possible records. Thus, the analysis interval for W3 was not the same as for V3 and V4. Furthermore, W3 had two distinct peaks, whereas V3 and V4 have one (see Figures 4.2-4 and 4.2–5). The results are given in the form of elliptical velocity hodographs for each depth level in Figure 4.4-1. The strongest fluctuations in the frequency band corresponding to the 25 – 30-day peak were at V4. The first modes at V3 and V4 accounted for > 90% of the total variance at each mooring for the depth levels indicated. The fluctuations were fairly rectilinear with the major axis either parallel, or at slight angle to, the general trend of the

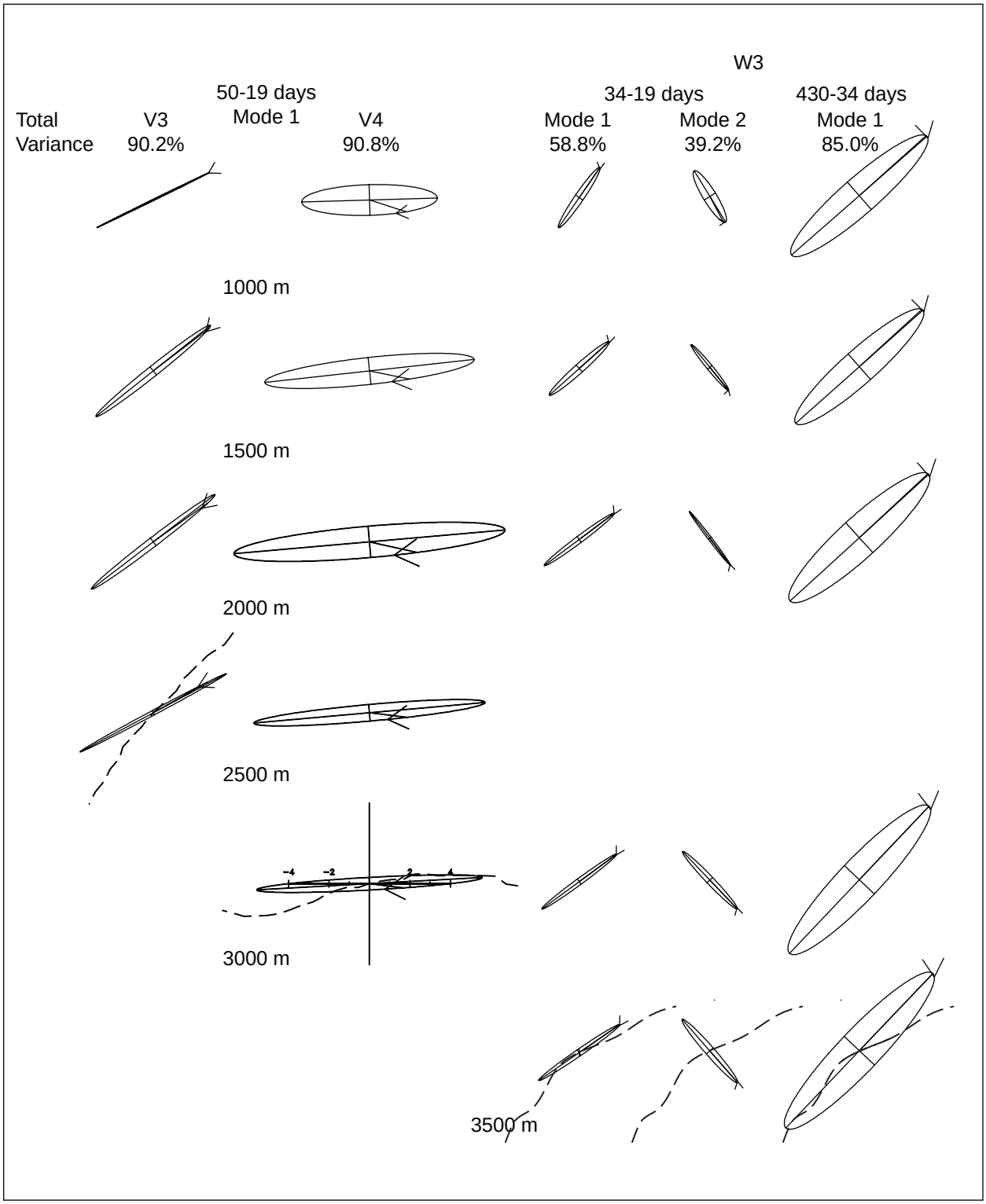

Figure 4.4-1. Vertical distribution of mode amplitudes (cm s^{-1}) from frequency domain EOF analyses of lower layer currents at V3, V4 and W3 (from left to right). Frequency bands and percent of total variances accounted for by the modes are indicated above each column of hodographs. The dashed line represents the local isobath at each site.

isobaths. Motions were in-phase through the lower water column with almost no change in direction of the major axis with depth. At V3 there was a slight bottom intensification, but at V4, there was significant intensification with depth between 1000 and 2000 m, followed by a reduction to depth-independent amplitudes at 2500 m. This latter depth distribution was commented upon in Section 4.2, otherwise these coherent fluctuations through the lower water column are entirely characteristic of TRWs and very similar to those previously analyzed in other regions of the Gulf (Hamilton 1990, Hamilton 2007; Donohue et al. 2006). Particularly noteworthy is the result that one mode can account for the majority of the total variance of the lower layer at each site.

At W3 (Figure 4.4-1), however, the 25 – 30-day fluctuations required two modes to account for > 90% of the total variance in this frequency band. The major axes of the two modes were approximately parallel and perpendicular to the isobaths. Apart from this unusual occurrence, the two modes had similar characteristics to the modes at V3 and V4, being rectilinear, in phase with depth and having amplitudes that were nearly depth independent. For short period TRWs, the group velocity is parallel to the major axis and directed such that shallower depths are to the right of the direction of propagation. This suggests that modes 1 and 2 at W3 represented up- and down-slope propagating waves, respectively. A separation into two uncorrelated waves with the same period at a single site has not previously been observed in the deep waters of the Gulf. The lowest frequency band at W3, with periods of 50 to 60 days, had larger amplitudes than the shorter period fluctuations, and again one mode accounted for the majority (85%) of the total variance. The fluctuations showed little depth variation through the lower 2500 m of the water column. If the shorter and longer period mode 1 major axes are compared then there was a small, but significant, anticlockwise rotation of this axis between the 30- and 60-day fluctuations, such that the longer period motions were more parallel to the mean direction of the isobaths at W3. This axis rotation with frequency is predicted by TRW theory (Rhines, 1970) and has been previously observed in the northwestern Atlantic (Thompson, 1977) and the northern Gulf (Hamilton, 1990). Therefore, in general, the depth variations of the hodographs in Figure 4.4-1 agree with previous observations of TRWs in the Gulf.

EOFs were calculated similarly for the moorings on the 2000-m isobath (W2, W4 and W5) except that W4 and W5 were used together so that a mode represents coherent motions of the lower-layer currents at both sites (Figure 4.4-2). The two frequency bands that correspond to the energetic TRWs at W3 were used, centered on 50 – 60 days and 25 – 30 days, respectively. The EOF amplitudes have similar characteristics to those in deeper water except for the low amplitudes, which decreased with increasing depth at all three sites for the longer periods, and at W5 for the shorter periods. There was a small amount of clockwise turning of the major axes between 1500 and 2000 m, which could be consistent with Ekman turning in a bottom-boundary layer. However, the bottom most measurement is ~ 60-m above the bed, so it is more likely that this was caused by topographic steering. The phase differences between W4 and W5 were very small with some indication that W4 leads W5. This could be consistent with TRWs in that the alongslope wavenumber is likely to be small with the direction of phase propagation being across the slope (Thompson, 1977; Hamilton, 1990). Therefore, along the base of the Mexican slope, the vertical EOFs were consistent with weak TRWs except for the decreases of amplitude with depth.

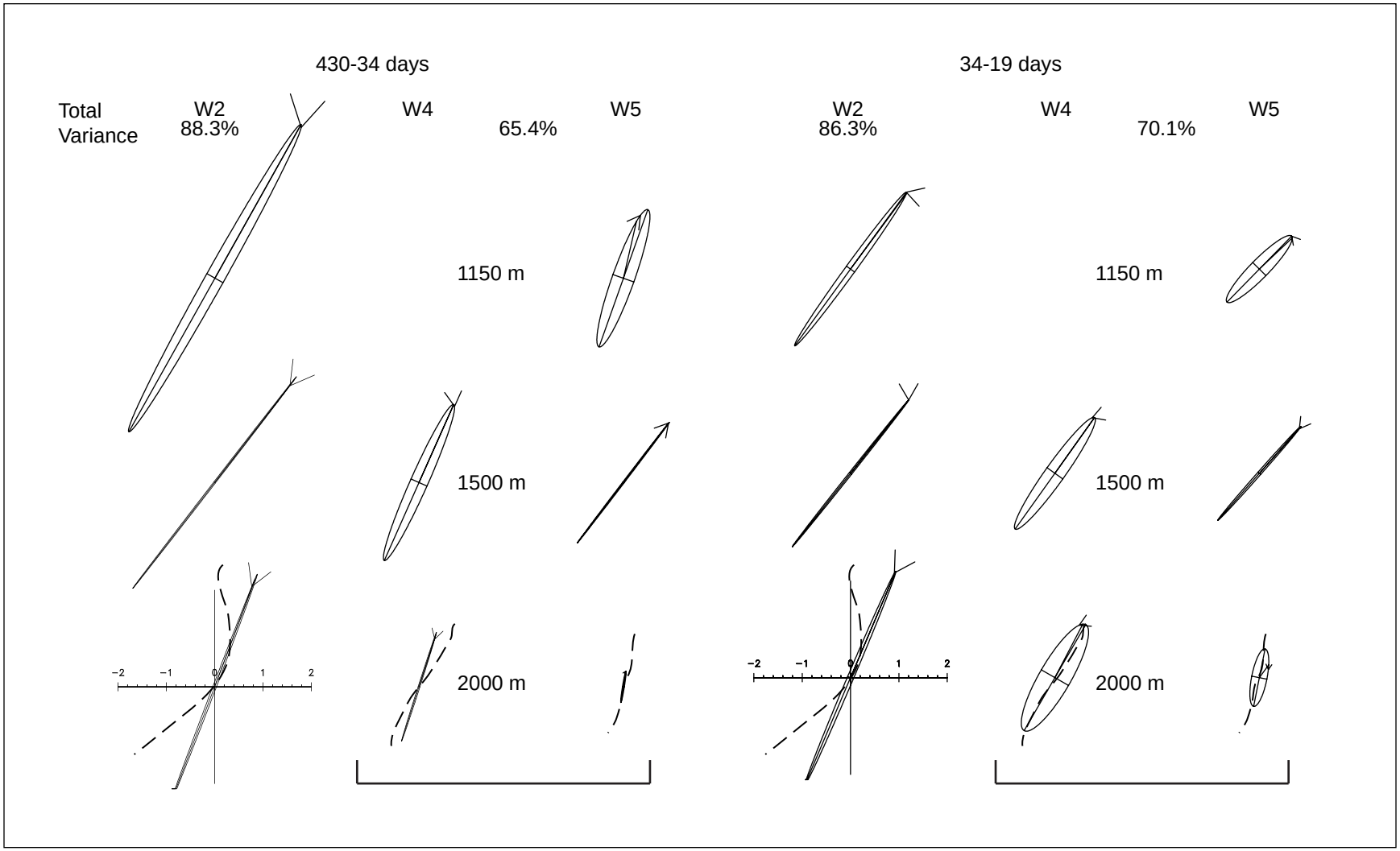

Figure 4.4-2. Vertical distribution of mode 1 amplitudes (cm s^{-1}) from frequency domain EOF analyses of lower layer currents along the 2,000-m isobath in the Mexican sector for W2, W4, and W5 (from left to right). Frequency bands and percent of total variances accounted for by the modes are indicated above each column of hodographs. The records from both W4 and W5 were combined for the EOFs. The dashed line represents the local isobath at each site.

Horizontal EOFs were calculated using the near-bottom currents (~ 60 meters above bottom (mab) in the Mexican sector, and 100 mab in the U.S. sector) at all the moorings. Spectra for the common overlap interval of nine months were used as they resolve the fluctuations of interest almost as well as the complete spectra given in Section 4.2. The results for the shorter period fluctuations (19 to 34 days) are given in Figure 4.4-3. There were two significant modes accounting for 68.7% of the total variance of all the bottom records in this frequency band. The mode phase differences of the U and V components at V3, V4 and W3 were used in a least-square fit of the wavenumbers (Hamilton, 1990) to estimate a characteristic wavelength for the TRWs in the vicinity of the bottom of the escarpment. In some of these estimations, there were 2π ambiguities in the phase differences between W3 and the bottom of the slope because of the relatively large spacing of ~ 80 to 100 km between the moorings. With some 2π adjustment, the wavelength was calculated to be a reasonable 90 km for both modes and thus similar to estimates in other regions of the Gulf (Hamilton 1990, Hamilton 2007; Donohue et al. 2006). The period and wavelengths were input into a ray-tracing algorithm that uses the complete TRW dispersion relation. The details are given in Hamilton (2007) and Donohue et al. (2006). Rays were traced backwards and forwards from the position at the center of the V3-V4-W3 triangle. Initialization of the rays included cases with up- and down-slope wavenumber components, which correspond to waves with down- and up-slope components of group velocity, respectively. In interpreting the hodographs in Figure 4.4-3 with respect to the rays, it is useful to note that the local group velocity was approximately parallel to the major axis of the ellipses such that the shallower water was to the right of the direction of propagation. The phase velocity vector was perpendicular to the major axis and was directed such that it was either in the 2^{nd} or 3^{rd} quadrant of a coordinate system where the x-and y-axes are directed along the isobath and upslope, respectively.

Mode 1 shows energy propagating into the corner (around V3) from the east and decaying towards the south. Some energy was also penetrating onto the northwest slope at U3 and U4. The mean bottom flows were largest at W2 and V3 (Figure 4.2-3). Therefore, the results were similar in character, though with weaker magnitudes, to the Sigsbee escarpment in the central Gulf (Donohue et al., 2006), where the mean flow was being forced by TRWs propagating towards the slope and reflecting from the shoaling topography. In Figure 4.4-3, the direction of the major axes at the W sites, are compatible with both weak up-slope transmission (W2, W4 and W5) and stronger reflection (W3). It is fairly clear that the shoaling topography was generating an anticlockwise mean flow along the base of the slope through the rectifying of TRWs (Mizuta and Hogg, 2004; DeHann and Sturges, 2005). Mode 2 only had significant fluctuations at W3, and to a lesser extent V4 and U4. It is noteworthy that the mode 2 and mode 1 ellipses at W3 were approximately perpendicular, as was found for vertical EOF analyses at W3 for this frequency band (Figure 4.4-1). Thus, motions represented by mode 2 were apparently propagating towards the slope at W3, but were subsequently almost completely damped out by the time they reach W2. Because modes were uncorrelated, motions represented by mode 2 were probably unrelated to the waves represented by mode 1.

The two EOF modes for the lowest frequency band, centered on a 66-day period, are given in Figure 4.4-4. The TRW wavelength estimates from phases of modes were calculated as above and the ray paths for up- and down-slope propagating waves shown. The mode 1 wavelength estimate was larger than for the 23-day period waves and had a very similar distribution of energy with large amplitudes at V3, V4 and W3 that decay southwards along the slope. The

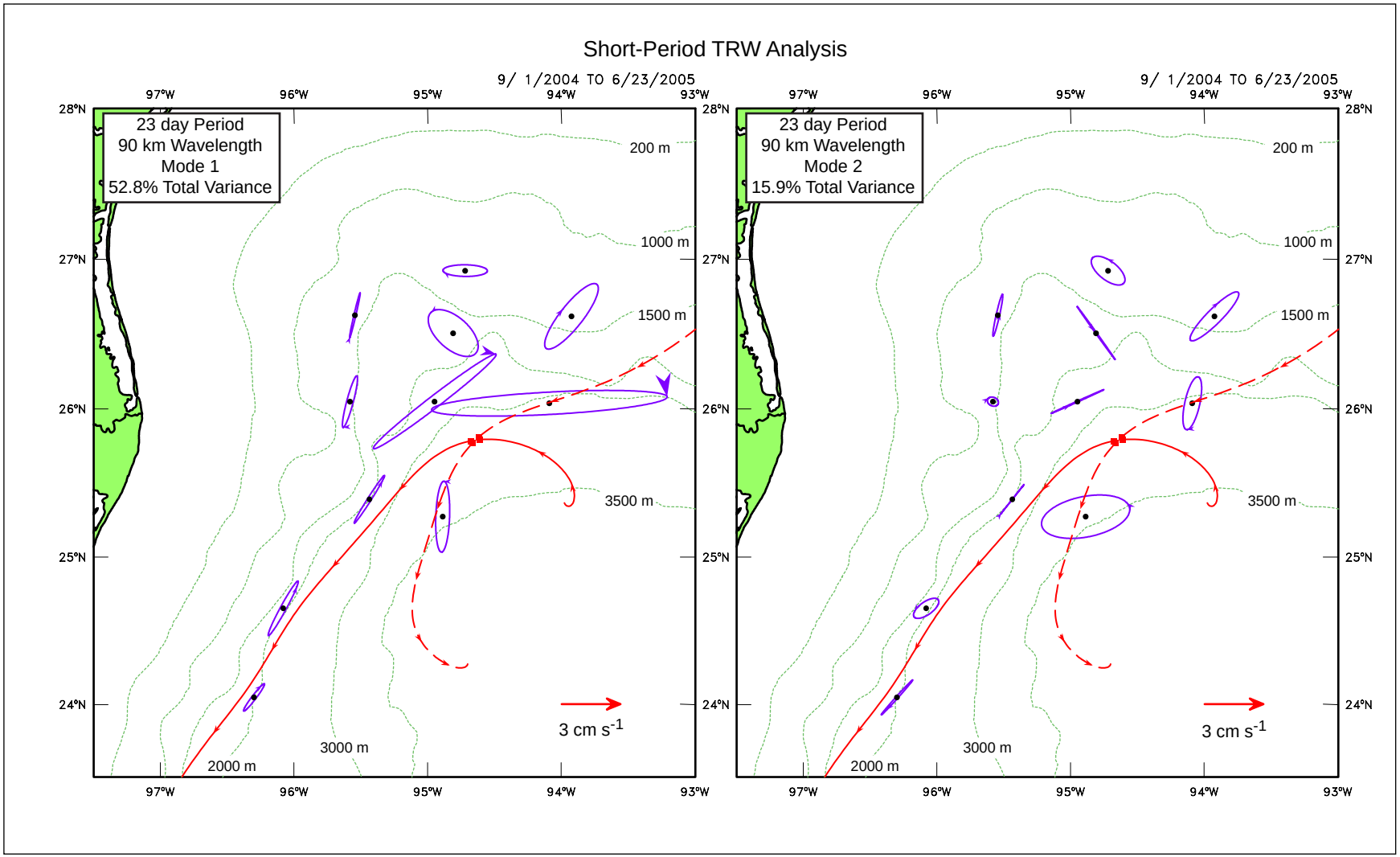

Figure 4.4-3. Short-period EOF mode amplitudes of near-bottom currents for the common interval using all moorings (left panel: Mode 1; right panel: Mode 2). Red lines represent ray traces of TRW paths for the indicated periods and wavelengths. Arrowheads are at 5-day intervals and solid and dashed lines represent onshore and offshore propagating waves, respectively.

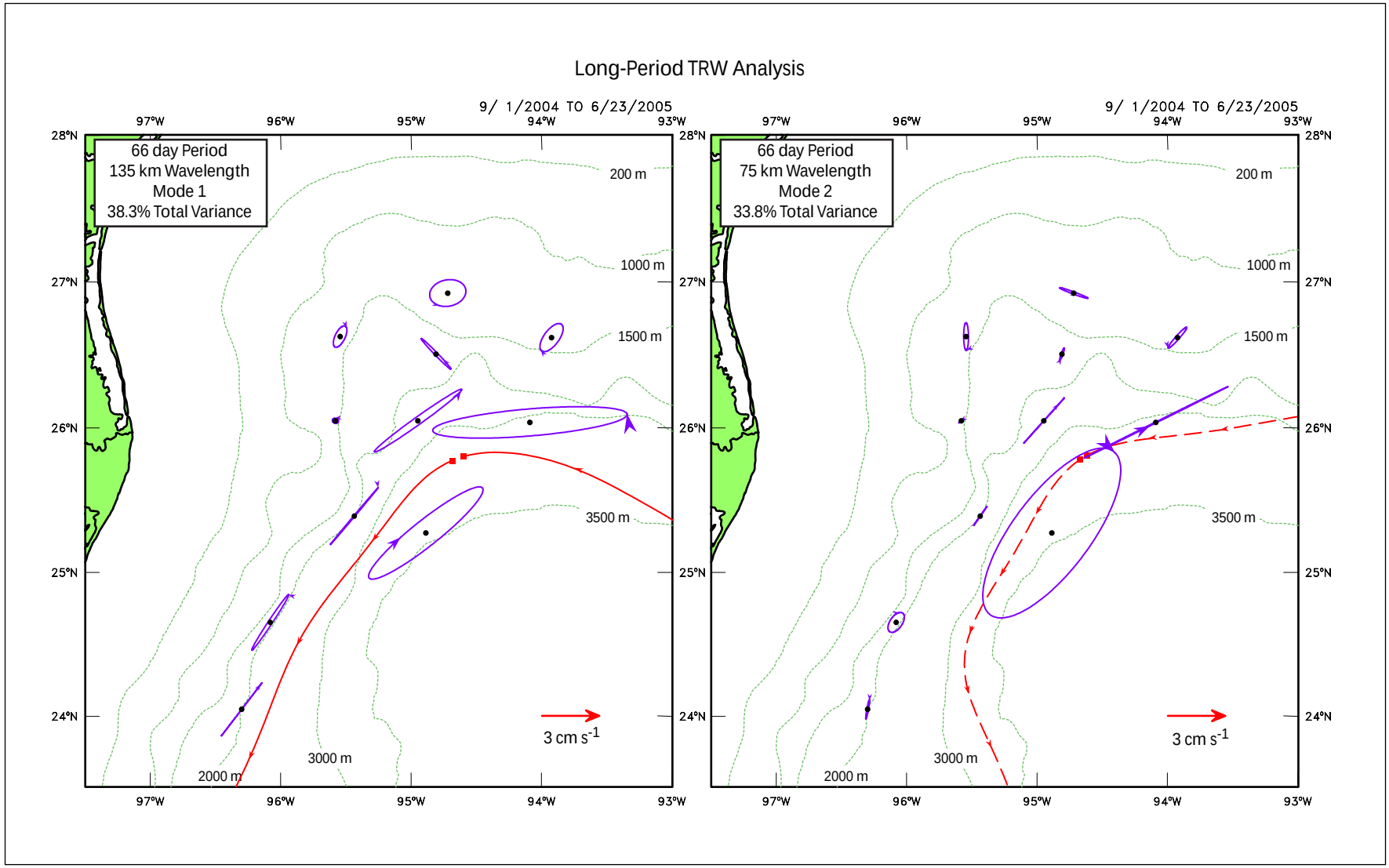

Figure 4.4-4. Long-period EOF mode amplitudes of near bottom currents for the common interval using all moorings (left panel: Mode 1; right panel: Mode 2). Red lines represent ray traces of TRW paths for the indicated periods and wavelengths. Arrowheads are at 5-day intervals and solid and dashed lines represent onshore and offshore propagating waves, respectively.

directions of the ellipse axes were more compatible with an upslope propagating wave originating from deep water to the east that was refracted by the topography towards the south. Comparing the phase angle (given by the arrow heads on the ellipses) at V4 and W3, it can be seen that W3 lagged V4, which indicates off-slope phase propagation. Mode 2 was primarily observed at V4 and W3, and the wavelength was about half that of mode 1. The major axis directions of the ellipses indicate offshore propagation and this is confirmed by the phase lead of W3 over V4. In terms of amplitude, this mode 2 wave dominated over mode 1 at W3 and implies that source may have been the lower slope region of the central Gulf.

A wider view of possible TRW ray paths for the periods and wavelengths diagnosed above is given in Figure 4.4-5. The 66-day period waves, with both short and long wavelengths, could have originated in the deep basin of the central Gulf, however the only reasonable path that connects to the eastern Gulf is the down-slope 66-day period wave. The currents at W3 increased in amplitude around the beginning of March 2005 (Figure 4.2-1a), and on February 15, 2005 eddy Ulysses was centered at 25.5°N, 93°W, which puts the center over the 66-day upslope path and the northern part of the eddy over the down-slope path with about the correct time lag for a wavetrain to arrive at the corner. The modes (Figure 4.4-4) seem to indicate that TRW amplitudes decreased rapidly to the south along the Mexican slope, so it is unlikely that TRWs from this source would have propagated along the slope into the Bay of Campeche as indicated by the ray tracing. The 66-day down-slope forward path does, however, indicate that TRWs reflected from the corner region may have propagated back into deepwater. The shorter 23-day period ray paths indicate that these period motions were probably generated fairly locally and remained trapped in the corner region, producing relatively large amplitudes at V3 and V4, along with relatively large mean flows along the base of the steep slope. This is similar to the Sigsbee Escarpment in the central Gulf, apart from the fluctuations and means having much smaller amplitudes. Local sources may have been a result of surface eddies interacting with the lower slope topography such as the case study given in the next section.

4.5 Vertical Coupling

In this section, the nature of upper and lower-layer interaction in the Northwestern Gulf is discussed. At first glance, the layers appear decoupled. Animations of upper and lower-layer circulation revealed few patterns that appear to be linked. Moreover, the character of even a simple metric like the array-averaged EKE differs between upper and deep layers (Figure 4.5-1). Upper EKE reflects the propagation of Loop Current eddies and cyclones into and out of the array. These strong low-frequency episodic pulses in the upper ocean did not correlate with the more frequent strong lower-layer events. Deep EKE peaks were associated primarily with events along the northern and northwestern array boundary. Yet one could argue that in the deep layer, a mix of locally and remotely generated variability, each with similar magnitudes, could obscure the upper and lower-layer interactions. Therefore, we have explored aspects of the lower-layer PV to help elucidate vertical coupling and have stopped just shy of a potential-vorticity budget analysis. One ‘case study’ of vertical coupling is shown where the change in lower-layer potential vorticity was achieved primarily through the balance of stretching and the production of relative vorticity. It is speculated that along the steep mean-potential-vorticity gradients in the deep layer (which are caused by topographic gradients), advection plays an important role in potential vorticity conservation.

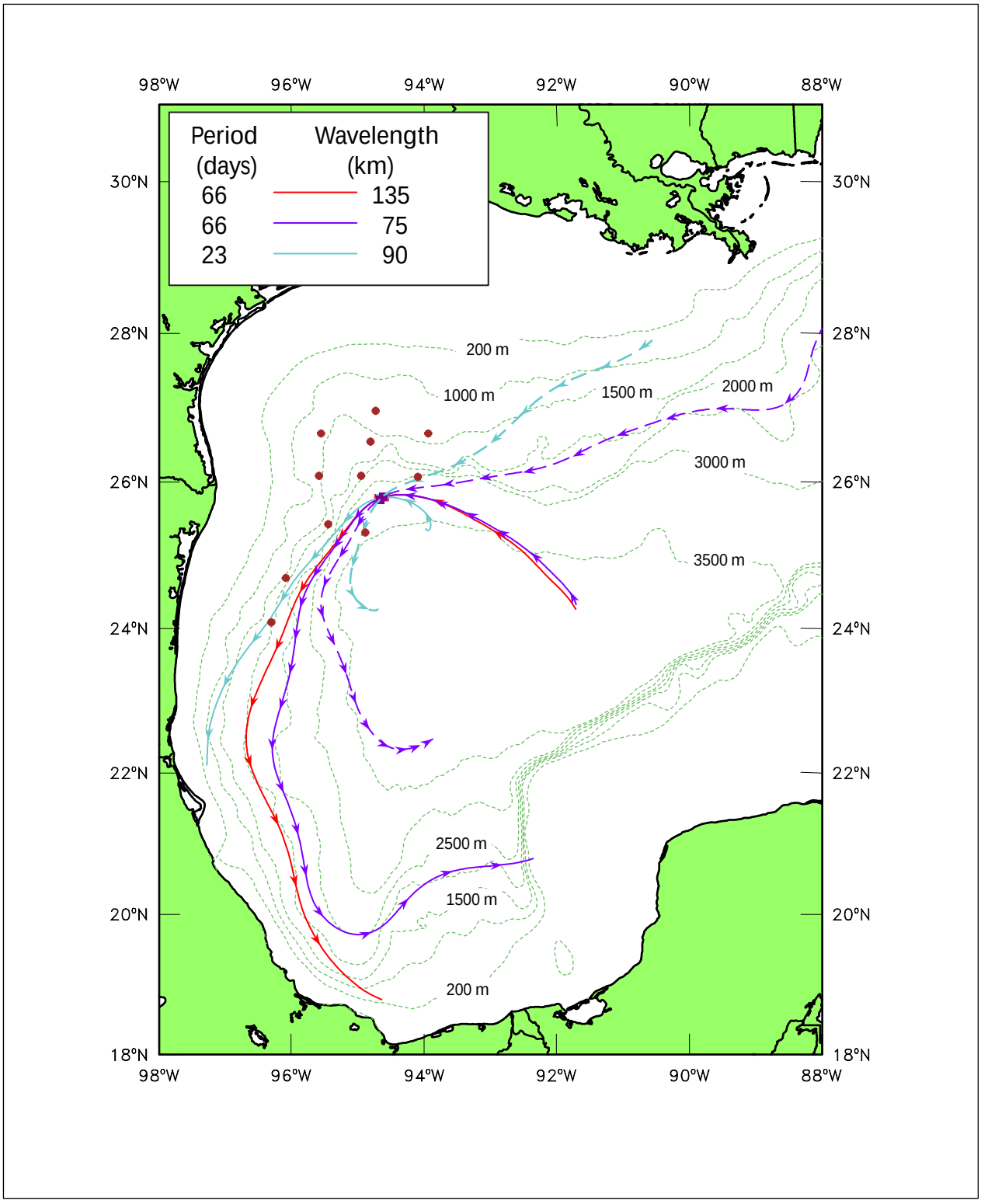

Figure 4.4-5. TRW ray traces for given periods and wavelengths. Arrow heads are at 5-day intervals, and solid and dashed paths are on- and off-slope propagating waves, respectively. Small solid circles are mooring locations.

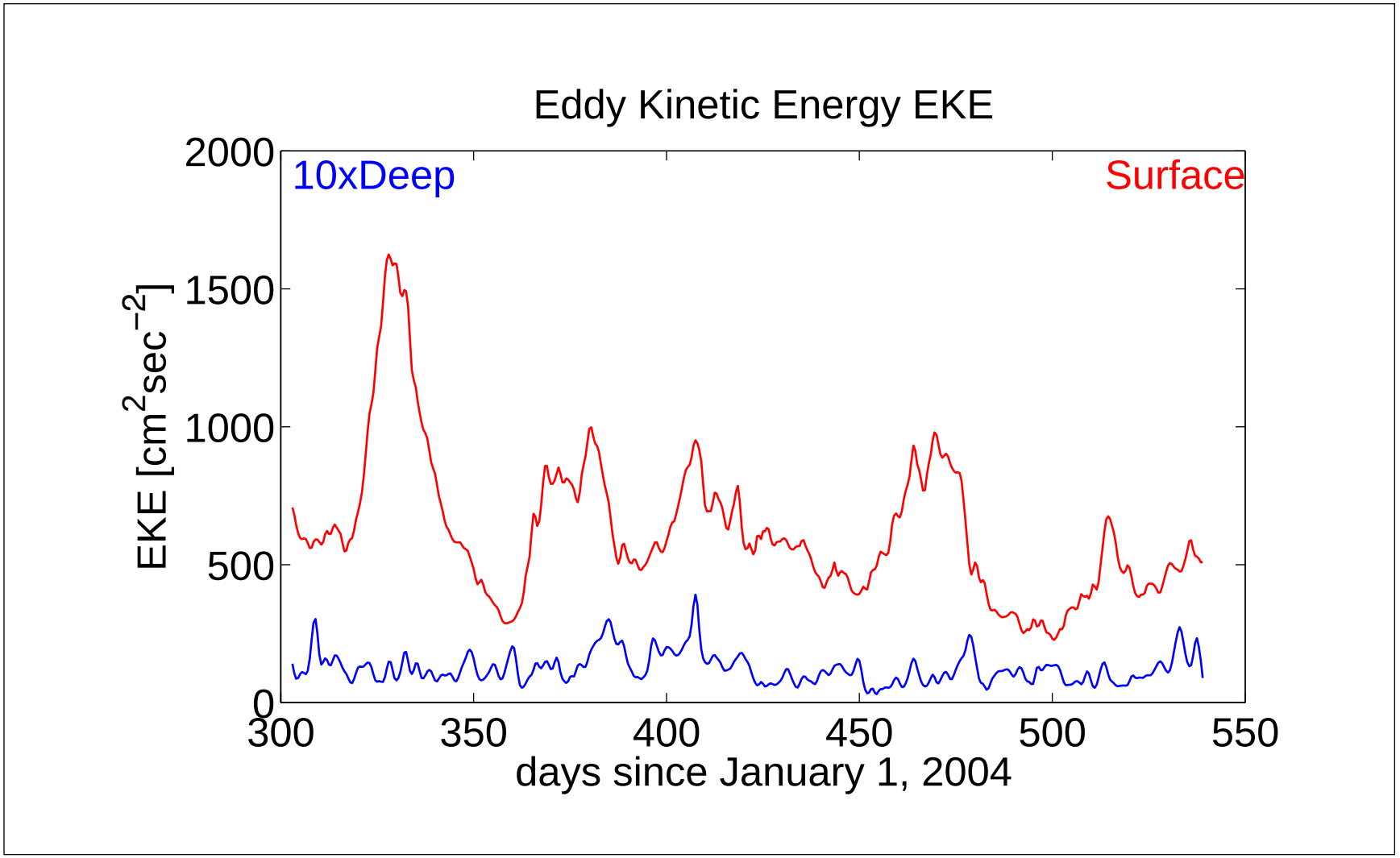

Figure 4.5-1. Array-mean eddy kinetic energy (EKE) at the surface (red) and at 1,500 m (blue).

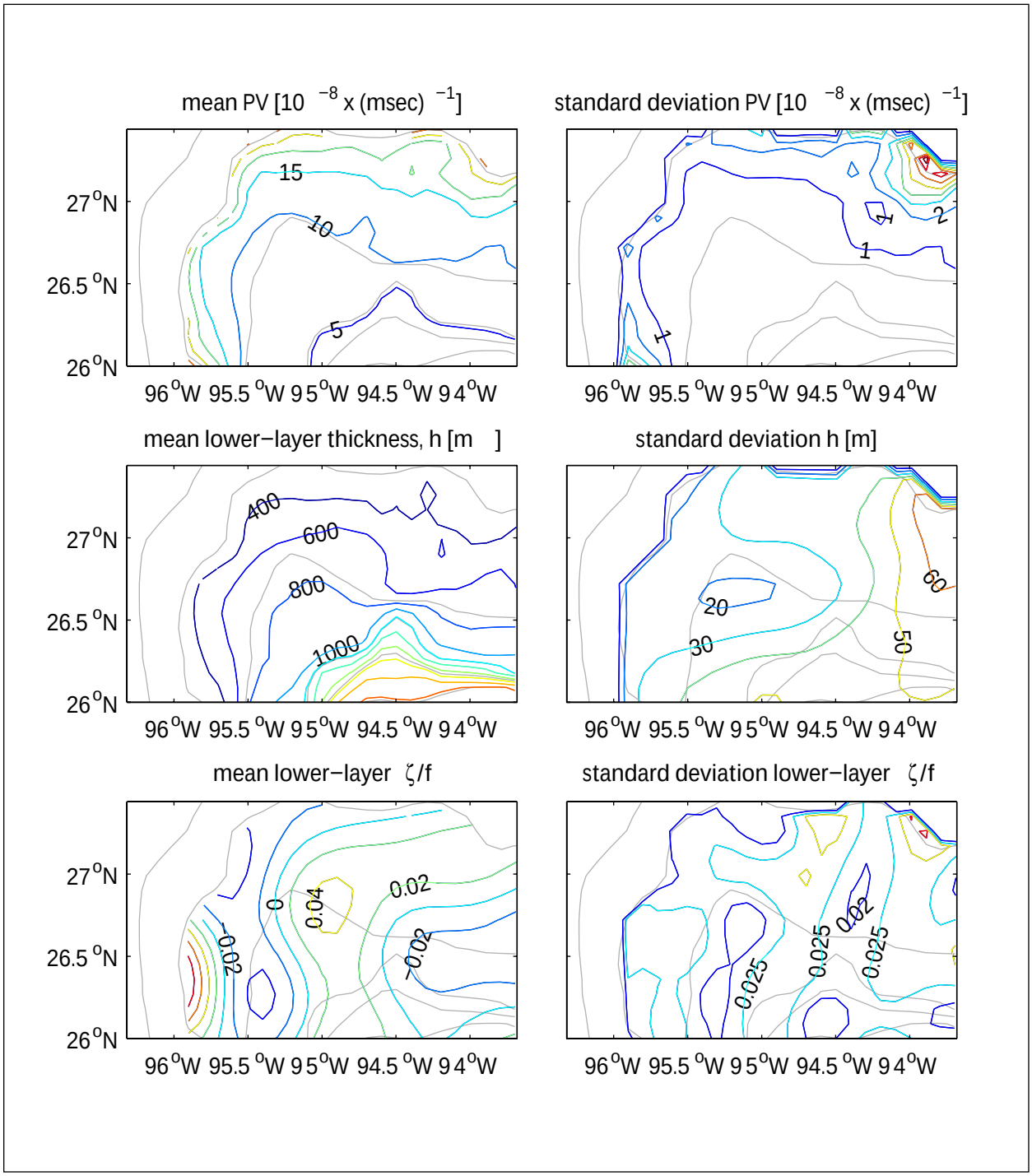

Figure 4.5-2. Left panels: Mean lower-layer potential vorticity (top), thickness (middle); and relative vorticity divided by the Coriolis parameter (bottom). Right panels: Standard deviation of lower layer potential vorticity (top), thickness (middle), and relative vorticity divided by the Coriolis parameter (bottom). Topography contoured every 500 m as denoted by gray lines in each panel.

Lower-layer potential vorticity, *q*, is defined as the sum of the Coriolis parameter, *f*, and relative vorticity, $\zeta=\partial v/\partial x-\partial u/\partial y$, divided by lower layer thickness, *h*,

$$q=\frac{f+\zeta}{h}.$$

The distance between the ocean bottom, *H*, and the 6°C isotherm depth, *h6*, defines lower-layer thickness. In the absence of external torques, lower-layer potential vorticity will be conserved,

$$\frac{Dq}{Dt}=\frac{\partial q}{\partial t}+u\frac{\partial q}{\partial x}+v\frac{\partial q}{\partial y}+w\frac{\partial q}{\partial z}=0.$$

The advective terms present a challenge because they require a highly-resolved array of measurements to determine the spatial gradients of a second-order term, *q*. One can easily anticipate that the advective terms might play an important role in regions of strong PV gradients.

Topography greatly influenced the mean potential vorticity (Figure 4.5-2). The largest contribution to mean lower-layer thickness was derived from *H* rather than *h6*. Mean relative vorticity was weak. Scaled by the Coriolis parameter, (ζ/f) expresses the Rossby number and ranged from near 0.04 in the interior to 0.12 in the southwest corner.

Away from the relatively flat topography, lower-layer PV exhibited the largest fluctuations in the northeast array corner coincident with large fluctuations in lower-layer thickness and relative vorticity (Figure 4.5-3). Additionally, there was a north-south ridge of elevated relative vorticity variability that trended slightly to the southwest in the interior of the array (near 94.5°W to 95°W).

Our goal is to evaluate local vertical coupling in which deep relative vorticities were generated to balance vertical stretching. In other words, where did $\partial q/\partial t = 0$. Therefore, regions for study were selected where the standard deviation of q scaled by mean q was less than 0.05, *i.e.*, where $\partial q/\partial t$ is close to zero. We find that ζ and h are highly correlated near 94.7°W, along the ridge of elevated deep relative vorticity variability. Confidence intervals have not been determined for the correlation between ζ and h; here the statistic was used as a guide to identify a case-study of local vertical coupling. Two negative correlations appeared, both along the array periphery, one near 94.2°W and another near 95.2°W which was near a minimum in both lower-layer thickness and relative vorticity. In these regions, while $\partial q/\partial t$ may have been small, advection played an important role in the vorticity budget.

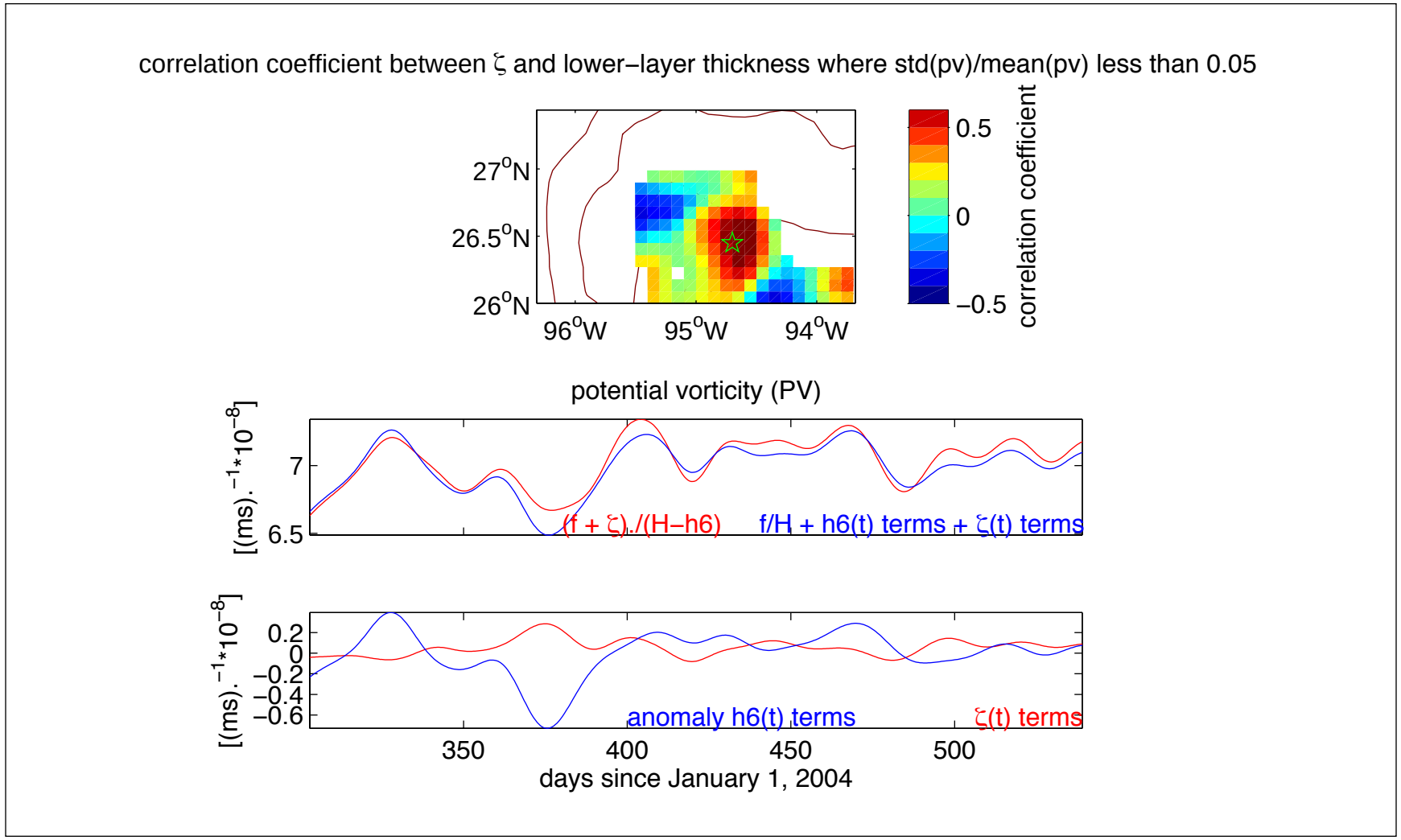

Figure 4.5-3. Top panel: Correlation coefficient between lower-layer relative vorticity and thickness contoured where the standard deviation of lower-layer potential vorticity divided by its mean is less than 0.05. Topography contoured every 500 m depth. Middle panel: Lower-layer potential vorticity (red) from the black star in top panel and an approximation of lower-layer potential vorticity (blue) that does include contributions from mixed ζ-h6 terms. Bottom panel: Contribution to lower-layer potential vorticity anomaly from changes in h6 (blue) and changes in ζ (red).

To separate the contributions of lower-layer stretching and vorticity, q was expanded using a binomial series,

$$q = \frac{f + \zeta}{H - h6}$$

$$q = \frac{f(1 + \frac{\zeta}{f})}{H - h6}$$

$$q = f(1 + \frac{\zeta}{f})(\frac{1}{H} + \frac{h6}{H^2} + \frac{h6^2}{H^3} + \ldots)$$

$$q = \frac{f}{H} + \frac{\zeta}{H} + \frac{h6\,f}{H^2} + \frac{\zeta\,h6}{H^2} + \frac{h6^2\,f}{H^3} + \frac{\zeta\,h6^2}{H^3} + \ldots$$

$$\tilde{q} = \frac{f}{H} + \frac{\zeta}{H} + h6terms$$

$$h6terms = \frac{h6\,f}{H^2} + \frac{h6^2\,f}{H^3} + \ldots + \frac{h6^{10}\,f}{H^{11}}.$$

In the bottom two lines a modified lower-layer PV, $\tilde{q}$, is defined that approximates q and does not contain any joint *h6* and ζ terms. Interestingly, while these terms were found to be small, they were not insignificant; see for example the difference between q and $\tilde{q}$ shown the middle panel of Figure 4.5-3. We found it necessary to include higher order *h6* terms. Potential vorticity time series from the region of high *h*-ζ correlation illustrate an event centered near day 360 where a decrease in *h*6 (increase in lower-layer thickness) decreases potential vorticity while cyclonic (positive) relative vorticity increases potential vorticity. A case-study from this time interval shows that an upper-layer cyclone enters the array from the south and propagates north and westward (Figure 4.5-4). As the upper-layer cyclone advances, the lower layer stretches and a deep cyclone develops.

4.6 A Deep Eddy

As discussed in the introduction to this chapter, regions that are over the abyssal depths and not close to steep slopes had RAFOS float tracks that tended to oscillate over a limited region with no preferred direction of rotation (Donohue et al., 2006). This has been interpreted as indicating that TRWs dominated the lower-layer dynamics in the deep basins. However, of the 36 deep RAFOS floats deployed in the Exploratory Program, there was one, and only one, that had a track that had translation and consistent rotation similar to that seen by surface-layer drifters in LCEs. This occurred close to the northwestern slope just before the moorings were deployed in the U.S. sector. The float was at a nominal depth of 2000 m and so was well below the direct influence of the upper-layer eddy field. Initially, the float was traveling westward along the escarpment at around 6 – 8 cm·s^{-1} until it reversed course at approximately 95°W and moved off into deeper water where it made a sequence of three cyclonic loops as it resumed its westward path towards the slope (Figure 4.6-1). The record ends as the float surfaced on 13 April 2004

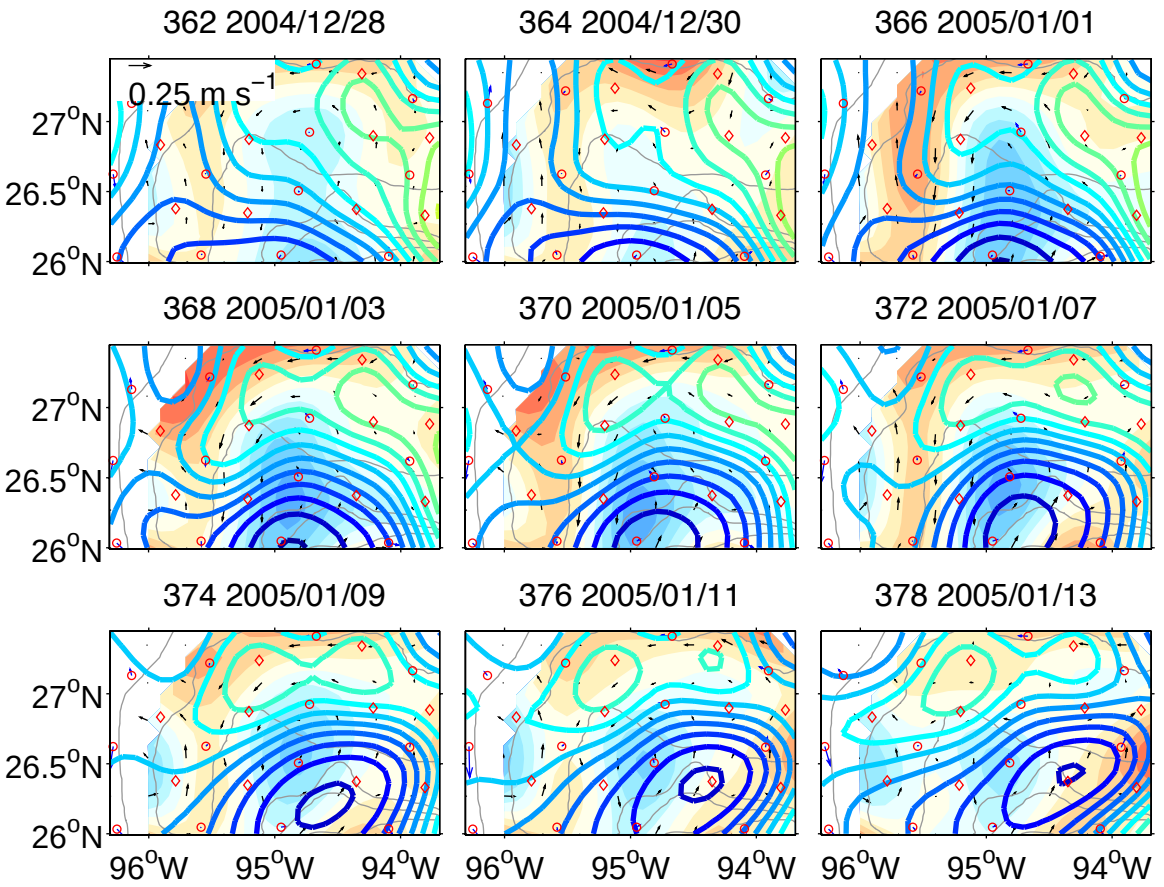

Figure 4.5-4. Case study of local upper and lower layer interaction. A lower-layer cyclone leads an upper-layer cyclone as they translate northeastward [12 Dec 2004 – 13 Jan 2005]. Maps of surface streamfunction (bold contour lines) superimposed upon shaded contours of 1500 m depth pressure. The sequence begins with the top left panel and progresses left to right. Topography in grey contoured every 500 m depth. PIES sites indicated by diamonds; current meters by circles.

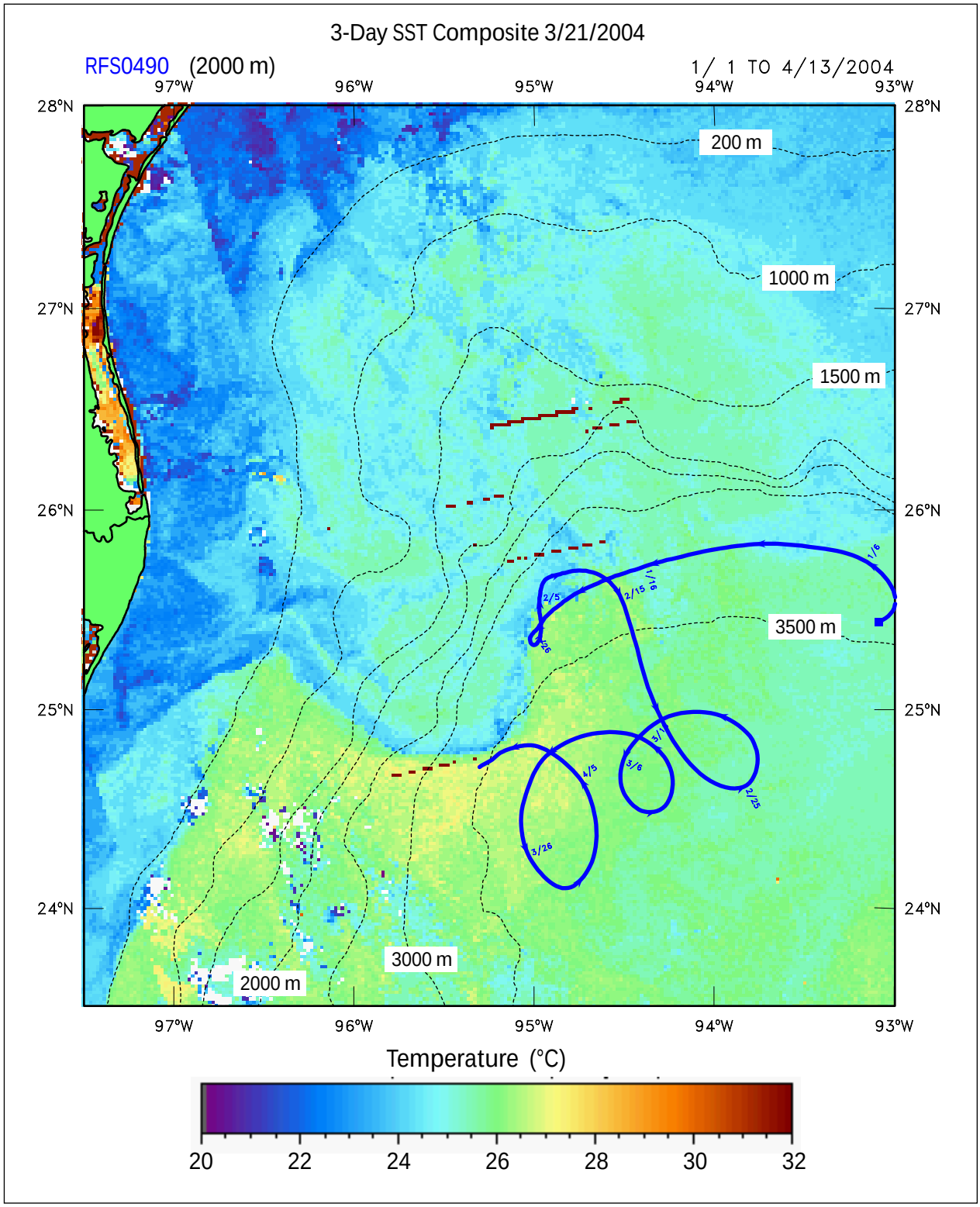

Figure 4.6-1. The smoothed track of RAFOS float RFS0490 at 2,000 m for the indicated time interval. Arrow heads are at 5-day intervals and dates (mm/dd) are the positions at 0000 GMT. The overlaid satellite image (courtesy JHU-APL) of SST is a 3-day composite center around 21 March 2004.

over the 3500-m isobath near the Mexican slope. The SST from 21 March 2004 (Figure 4.6-1) clearly shows a cyclone centered at ~ 25.3°N, 95.5°W against the western slope pulling cold water off the shelf. There does not appear to have been an obvious relationship between this fairly stationary upper layer cyclone and the translating deep eddy shown by the drifter.

A kinematic analysis, using the translating ellipse model devised by Glenn and Ebbesmeyer (1993) for LCEs, and subsequently used by Hamilton et al. (1999) to characterize statistically LCEs in the western Gulf, was used to obtain rotational parameters of the three loops of the RAFOS float track. The rotational periods and geometric-mean radii from the analysis are given in Table 4.6-1, and the individual loops overlaid on the SSH maps are given in Figure 4.6-2.

Table 4.6-1

Kinematic Analysis of Drifter Track in Deep Cyclone

Date	Rotational Period (days)	Geometric Mean Radius (km)
2004/02/26	12.0	21
2004/03/12	13.4	21
2004/03/31	17.8	27

The deep eddy was between 40 and 50 km in diameter and the rotation period lengthened as the eddy approached the western slope. The upper-layer circulation consisted of the cyclone against the western slope that was ahead of the deep eddy. This upper-layer cyclone appeared to weaken and move northwards as the deep eddy translated westward. Another surface-layer cyclone, which was peripheral to LCE Titanic, moved in behind the deep eddy, and this latter cyclone and eddy Titanic continued to translate westward at a similar speed to the deep eddy ($1 - 3$ cm·s^{-1}). This cyclone on the eastern side of the deep eddy may have produced enough lower-layer stretching to form a deep cyclone ahead of its direction of propagation (see discussion in Section 6.7 of Donohue et al. (2006)). However, because of the complexity of the upper-layer eddy flow, it was difficult to determine if this was a valid process in this case. It is noted that the loops of the RAFOS float had diameters that were similar to the spacing of the current meter moorings that were subsequently deployed (Figure 4.6-2). This implies that such deep motions, as represented by this Lagrangian drifter, would be barely resolved by the moored array as deployed. This is an intriguing result and is the only observational evidence obtained so far that shows that translating cyclones may exist in the lower layer of the GOM.

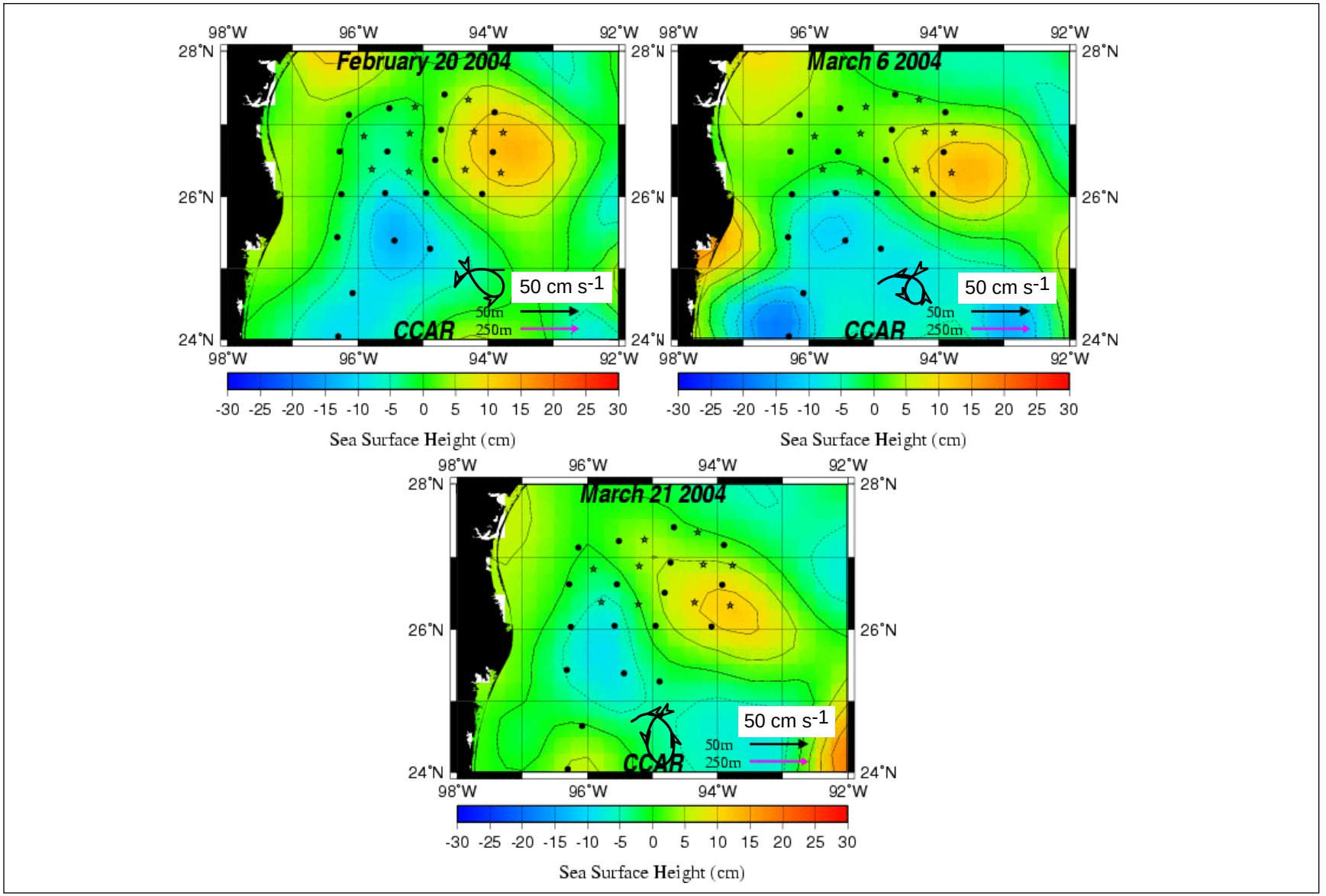

Figure 4.6-2. The cyclonic loops of RAFOS float RFS0490 beginning on the date of each of the SSH maps. Arrow heads are at five-day intervals.

CHAPTER 5 HIGH-FREQUENCY CURRENTS

5.1 Introduction

Inertial currents usually dominate the high-frequency motions in the upper layer of the slope and deep basin waters of the GOM. Inertial currents are characterized by clockwise (when viewed from above) rotary motions of the current vectors that have periods close to $2\pi/f$, where f is the Coriolis parameter. In the northern GOM, this period (~ 26 hours) is close to that of the diurnal tide. However, barotropic diurnal tidal currents are expected to be very small (a few $mm \cdot s^{-1}$) in water depths > 200 m, therefore no attempt has been made to "detide" the current records. Inertial oscillations will propagate as inertial-internal waves when the frequency ω is greater than an effective f_e, where the relative vorticity, ζ, modifies the lower limit for propagating internal waves through (Mooers, 1975):

$$f_e^2 = f\,(f + \zeta) \tag{5.1}$$

The background relative vorticity has both horizontal and vertical gradients caused by the meso-scale eddy field, and the resulting variations in f_e can allow rapid propagation or trapping of inertial waves. Anticyclonic eddies, with negative ζ fields, are known to trap inertial oscillations and a peak in the inertial kinetic energy is often found just above the thermocline in the center of such eddies (Kunze, 1986). Propagating inertial-internal waves are characterized by upward propagating phase and downward propagating kinetic energy. The group velocity vector is at a small downward angle to the horizontal, thus observed inertial oscillations at a given mooring can be the result of generation events at different horizontal distances from the site. Generation events are usually associated with storm or strong wind shifts, such as caused by the passage of a cold front. The rotational sense of the initiating "impulse" can influence the strength of the inertial response. For example the wind on the right hand side of a hurricane track, are more effective at generating clockwise inertial currents. The inertial response on the right side of a rapidly moving hurricane is usually much greater than on the left side where the effective winds, relative to a stationary observer, turn anticlockwise.

Inertial oscillations in the deep GOM have been previously analyzed using moored current (velocity) and temperature data from the DeSoto Canyon (Hamilton et al., 2000), DeSoto Extension (Hamilton et al., 2003), and Exploratory (Donahue et al., 2006) programs. Results from the DeSoto Canyon study showed that the eddy field over the northeast slope could trap some inertial events, and that inertial currents in this region were more energetic and prevalent than on the outer shelf and upper slope of Louisiana (Chen et al., 1996). This study measured continuous profiles of currents, using ADCPs, only in the upper 100 m of the water column. However, it did produce some of the best data on the slope response to two hurricanes, Earl in early September 1998, and Georges, a month later. The other two studies employed upper-layer ADCPs that observed the upper 450-m of the water column, however, these moorings (one in DeSoto Extension, and five in the Exploratory Study) were fairly isolated so spatial variability of high frequency currents was not explored. The strongest inertial currents are in the upper 500 m of the water column, however, weaker (amplitudes < ~ 5 $cm \cdot s^{-1}$) were found to depths of about 1200 m over the central slope. Data from the Exploratory Study documented the trapping of strong inertial currents at depths of 100 to 300 m, with frequencies lower than the local f, in the

interior of Eddy Sargassum. The present study employs 450 m depth ADCPs deployed on all moorings except those on the 500-m isobath (T1, U1 and V1). This allows a more comprehensive analysis of both the horizontal and vertical spatial variability over the slope, both for individual events and the winter storm season. No major hurricanes affected the NW Gulf during the deployment of the American sector arrays during summer 2004.

DiMarco et al. (2004) discussed the possibility that high-speed subsurface currents can occur between 150 and 350 m depth, while surface currents were weak. Drilling operators had reported cases of shutdowns caused by such high-speed subsurface flows, which have become known as jets. Oey and Zhang (2004) give an example from industry observations of the so-called "Boutus" event, which caused the shutdown of operations on this platform. The most likely explanation is that this subsurface jet event on the northern slope, southwest of the Mississippi delta was associated with a rapidly growing translating, cyclonic frontal eddy on the northern edge of LCE "Millennium". However, the available database was plagued with instrumentation problems and results were inconclusive on whether such phenomena could occur in deep water. It was recognized that vertically propagating near-inertial internal waves could produce higher speeds at depth than at the surface, and DiMarco et al. (2004) cite the case of Hurricane Georges where deep inertial energy occurred over the DeSoto slope several days after the passage of the storm. There are also a number of examples in these NW Gulf data that show subsurface speed maxima caused by near-inertial internal waves. However, the available database, after excluding inertial events, suggested that if such jets occurred, then they seemed to be associated with the edges of anticyclones that were possibly interacting with an adjacent cyclone or frontal eddy. Only moorings that had continuous current profiles from ADCPs in the upper 400 to 500 m of the water column might have a chance of capturing such a subsurface jet. For such moorings in the central Gulf (five from the Exploratory and one from the DeSoto Extension – a total of ~ 7 years of measurements), no significant jet-like events were found. However, in these NW Gulf upper-layer ADCP records, a number of subsurface jets were observed that fit the criteria of maximum speeds > 50 $cm \cdot s^{-1}$, occurring between 150 and 350 m depth with lesser speeds above and below these depths. These are distinct from inertial events in which downward propgating near-inertial internal waves generate a subsurface maximum velocities a number of days after the originating storm event because at this time the near surface oscillations have changed. Therefore, subsurface velocity maxima in this data set appear to be caused by two distinct mechanisms: 1) down propagating inertial events, and 2) eddy-eddy or eddy-topography interactions. The latter are the subject of the analysis in Section 5.3. Of the 17 subsurface jet events identified in the 450-m ADCP records (excluding the Mexican sector), 10 are considered to be primarily inertial events, and 7 are non-inertial. Other than having more 450-m ADCP months in the western Gulf than in the central Gulf, it is not yet clear why the NW part of the slope may have more subsurface jet events than the central or eastern parts of the slope.

5.2 Inertial Oscillations

Upper-layer inertial currents are intermittent and highly spatially variable. Complex demodulation using a period of 26 hours was performed on the east (U) component of the currents at depths of 50, 150 and 250 m. A running 26-hour mean was removed and the resulting amplitudes and phases filtered with a 4-day low pass (DLP) Lanzcos kernel. The time series of

inertial-oscillation amplitudes for all the moorings with 450-m ADCPs are given in Figures 5.2-1. Generally, the amplitudes at 50 m were larger than seen deeper in the water column; however, there were numerous events when the amplitudes at 150 m exceeded those at the upper level (e.g., V4 at the beginning of December, U2 in the middle of February, and T3 in May). The May event at T3 was caused by a propagating atmospheric cold front and was a particularly clean example of upper-layer inertial response to a rapid shift in the wind direction. This event will be examined in detail below. December and January storms produced a particularly strong inertial response at a number of the moorings (e.g., V2, U2 and V3), and this interval was also investigated in more detail as characteristic of winter (Figures 5.2-1a-c).

5.2.1 May 2005 Event

The current speeds from the upper-layer at T3 along with the wind from 42019 are given in Figure 5.2-2. In a pure inertial oscillation, U and V components have the same amplitude and there is a phase shift such that V leads U by 90°. This would result in a constant speed over the period of the inertial oscillation. However, when the inertial currents are propagating as internal waves, the U and V amplitudes are no longer equal ($=\sqrt{(U^2 + V^2)}^1$, and with the addition of background currents, the speed time plots will show variation of the inertial period in almost all field measurement of near-surface currents. High-speed (> 60 $cm \cdot s^{-1}$) approximately daily pulses propagated down through the upper 200 – 250 m of the water column over an interval of 12-15 days. The origin can be extrapolated up to the surface and corresponds to an abrupt wind shift on 30 April, followed by strong ~ 15 $m \cdot s^{-1}$ northerlies that lasted about a day. The slope of the speed maxima with depth shows upward propagation of phase that is consistent with an inertial-internal wave with a downward group velocity component, which was the direction of the vertical component of kinetic energy flux. The temperature record at 350 m, which was below the region of energetic current fluctuations, showed large-amplitude, approximately-daily fluctuations from 6 to 11 May. This implies the presence of large inertial-vertical-velocity components at this level. The velocity components at selected depths from the ADCP observations are given in Figure 5.2-3. The north (V) component led the east (U) component by about a quarter of a period (90°) which is characteristic of current vectors rotating clockwise at the inertial period. The wave trains seemed to amplify and become longer around 100 to 150-m depth. At 60 m, there were approximately two oscillations beginning 1 May, but at 130 m, there were > 8 oscillations beginning four days later. The horizontal inertial-period current fluctuations had completely decayed at 350 m, but as noted above, there seems to have been vertical pumping of the isotherms at this depth, which was reasonably consistent in timing with the downward propagation of inertial energy from above. The isotherm plot given in Figure 5.2-4 is constructed by linear interpolation from five fixed-level temperature records. Despite this fairly coarse vertical resolution it is clear that the diurnal period isotherm displacements were not observed above 250 m, which was the region of strong inertial-period horizontal currents, but had large amplitude oscillations from 7 to 11 May at 350 m and a little bit later (8-10 May) with less amplitude at 450 m. It is noted that there were negligible inertial horizontal currents at these depths and times, which implies the isotherm displacements were the result of vertical velocity oscillations.

The May event took place while mooring T3 was on the northern side of a slope anticyclone (Figure 5.2-5) and thus $\zeta < 0$. The calculation of ζ, by least squares plane fits to current records,

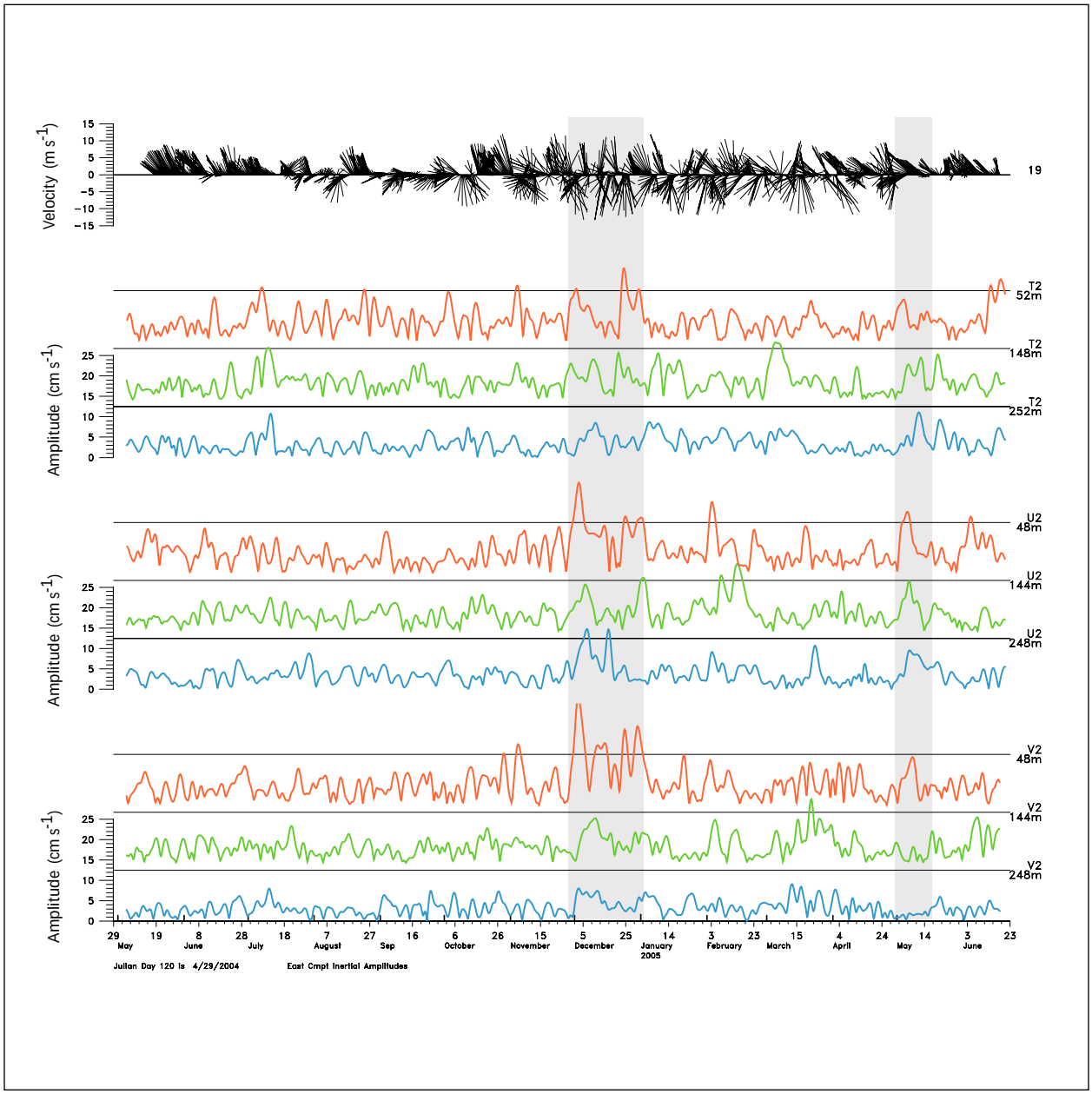

Figure 5.2-1a. Amplitudes of inertial oscillations from the complex demodulation at 26 hours of the indicated east-components of the currents. Amplitudes from V2, U2 and T2 are shown. The top panel shows the 40-HLP wind record from NDBC buoy 42019. The intervals discussed in the text are indicated by the shading. The black horizontal lines indicate the zero level for the trace immediately above that line.

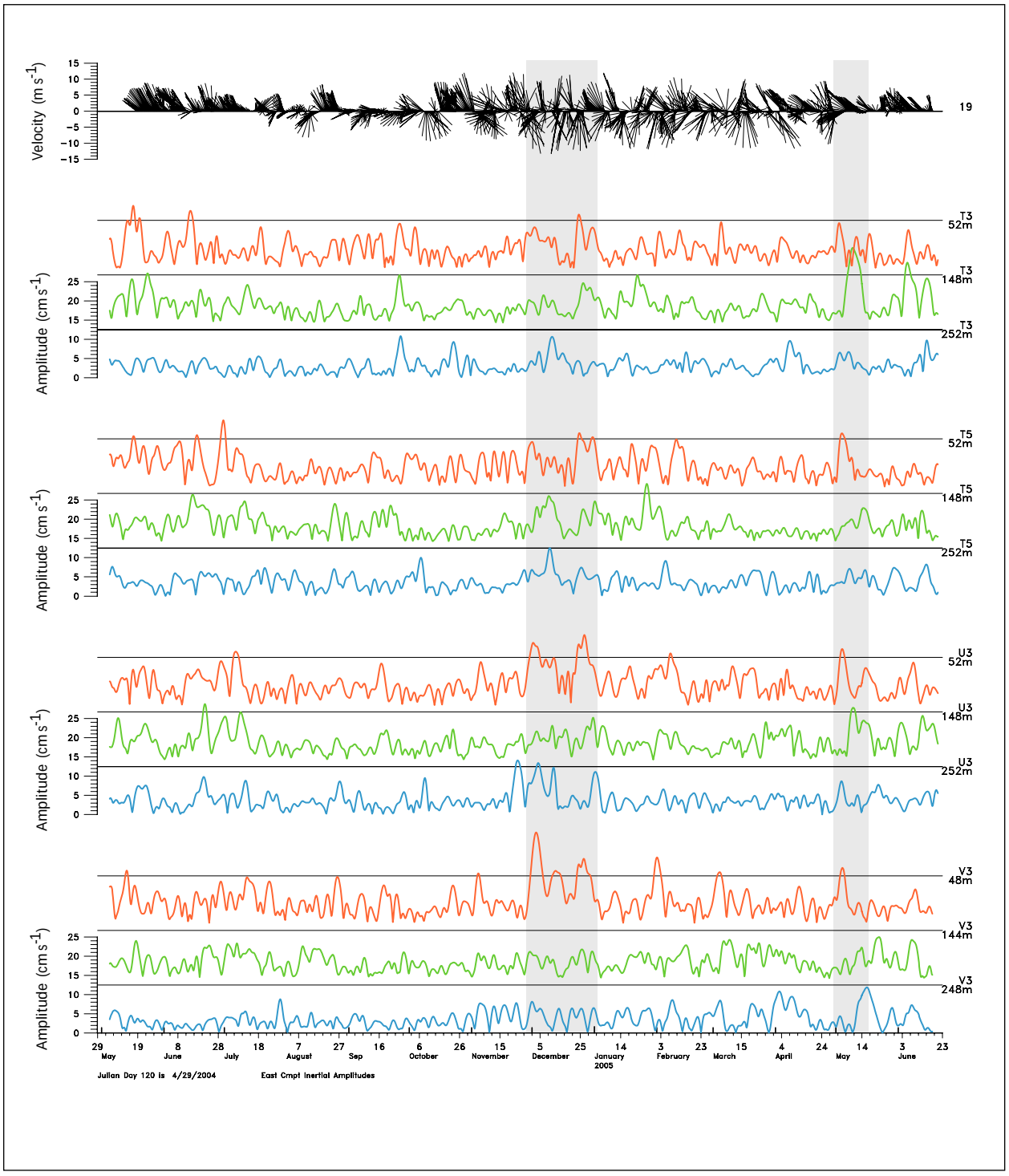

Figure 5.2-1b. Amplitudes of inertial oscillations from the complex demodulation at 26 hours of the indicated east-components of the currents. Amplitudes from V3, U3, T5 and T3 are shown. The top panel shows the 40-HLP wind record from NDBC buoy 42019. The intervals discussed in the text are indicated by the shading. The black horizontal lines indicate the zero level for the trace immediately above that line.

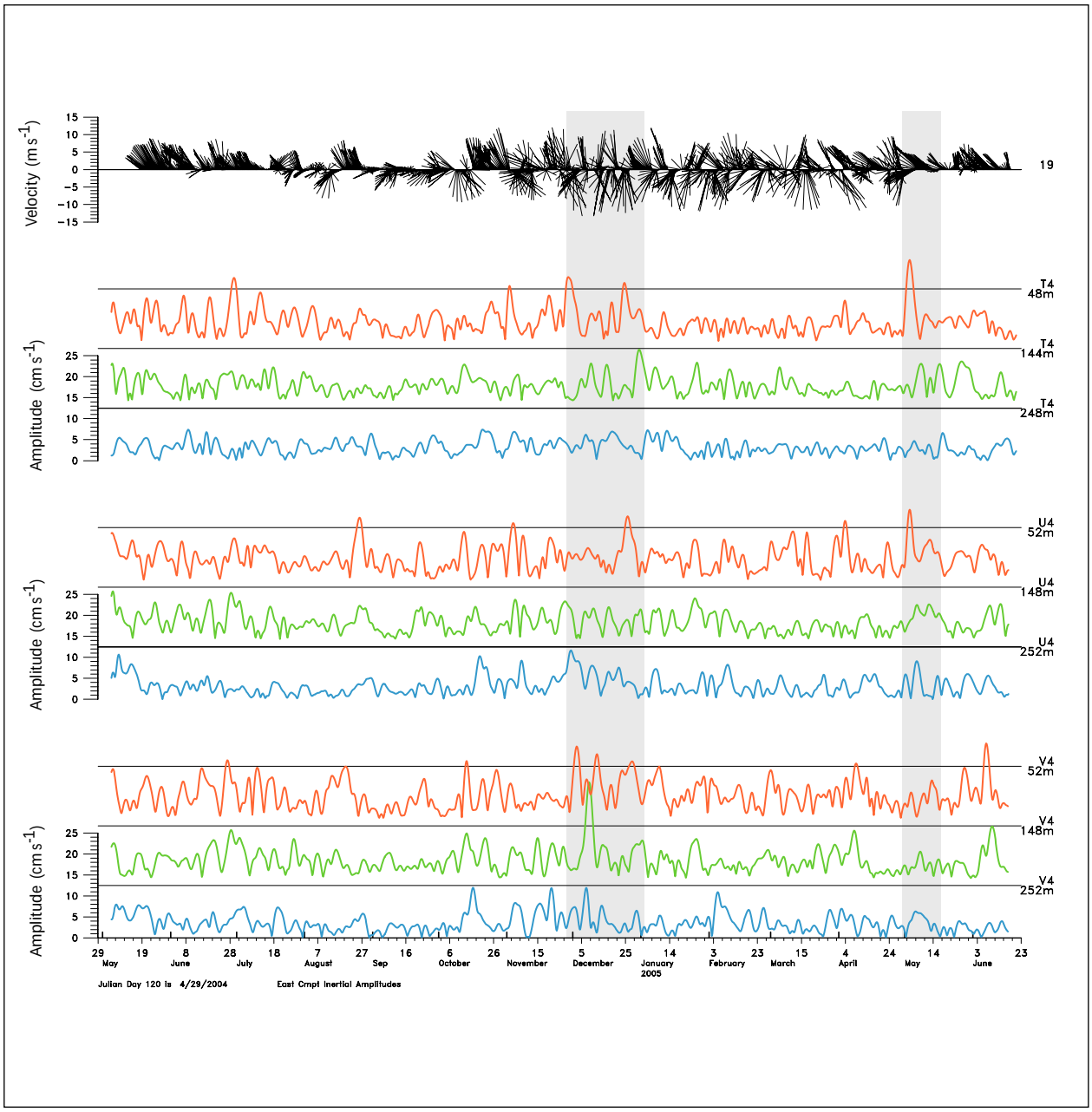

Figure 5.2-1c. Amplitudes of inertial oscillations from the complex demodulation at 26 hours of the indicated east-components of the currents. Amplitudes from V4, U4 and T4 are shown. The top panel shows the 40-HLP wind record from NDBC buoy 42019. The intervals discussed in the text are indicated by the shading. The black horizontal lines indicate the zero level for the trace immediately above that line.

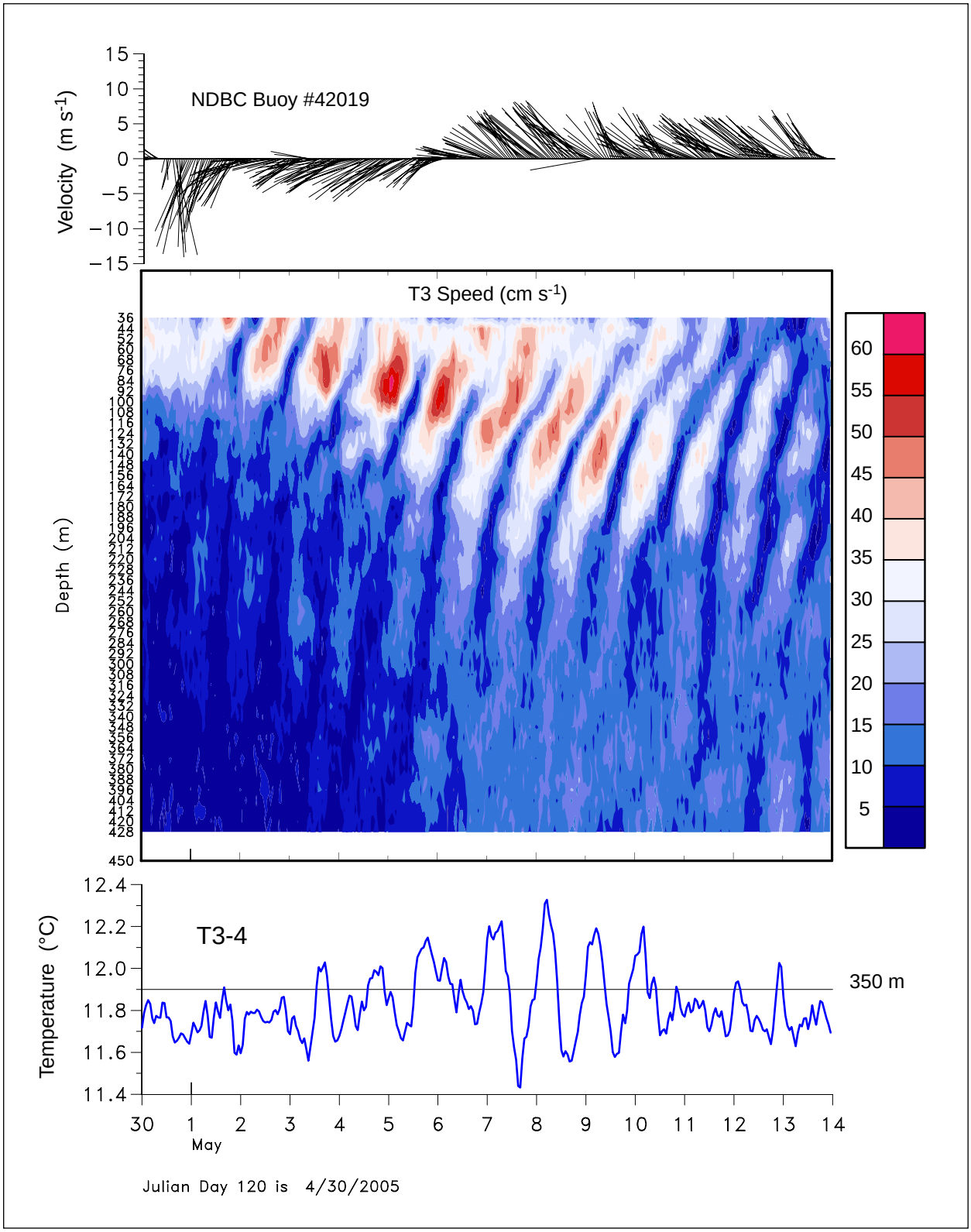

Figure 5.2-2. Unfiltered speed/depth observations from the upper-layer ADCP at T3. Bottom panel shows the temperature record at 350 m, and the top panel the hourly wind vectors (up = North) from NDBC buoy 42019.

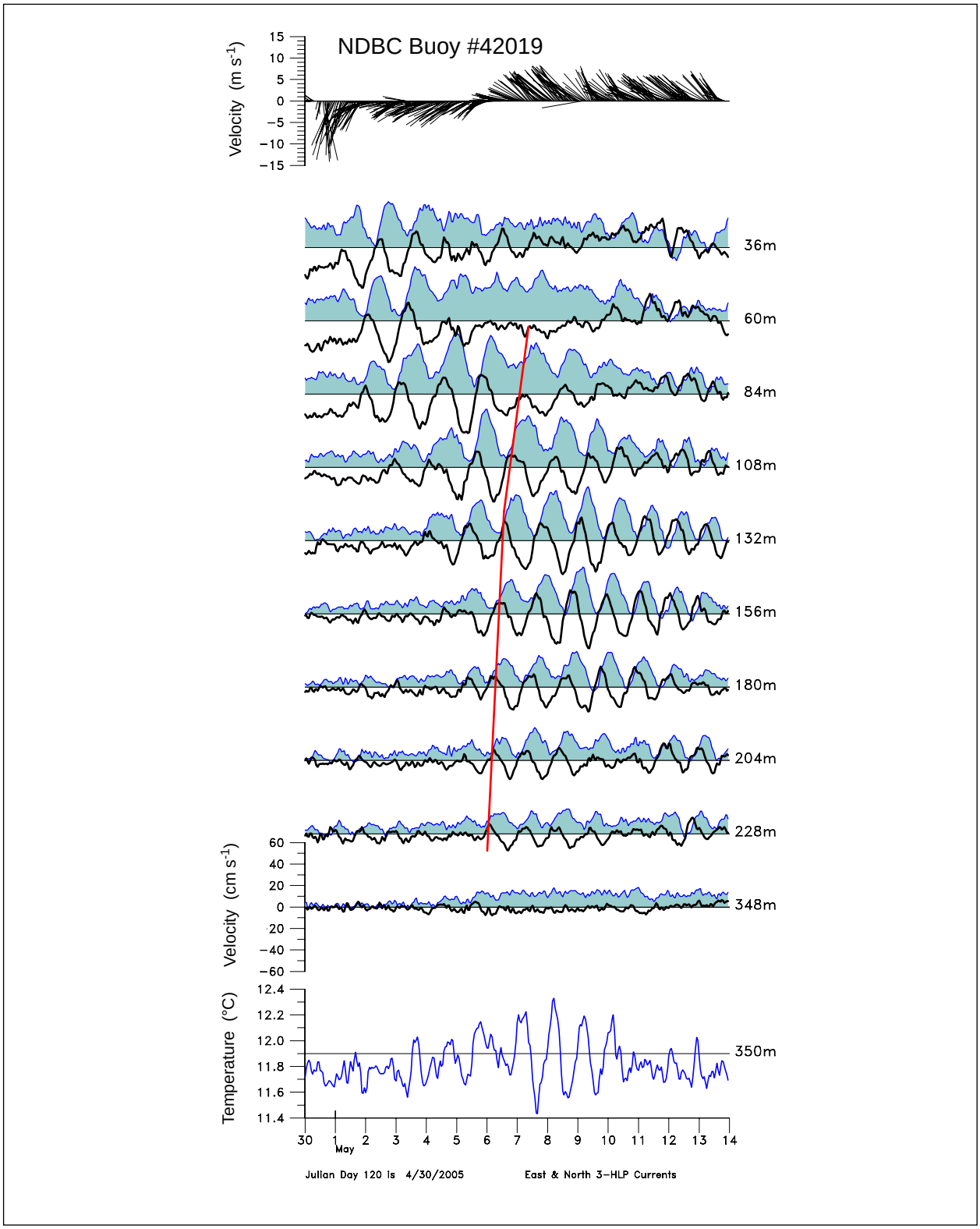

Figure 5.2-3. East (blue shaded) and north (black line) velocity components at T3 for the indicated depths. Bottom panel shows the temperature record at 350 m, and the top panel the hourly wind vectors (up = North) from NDBC buoy 42019.

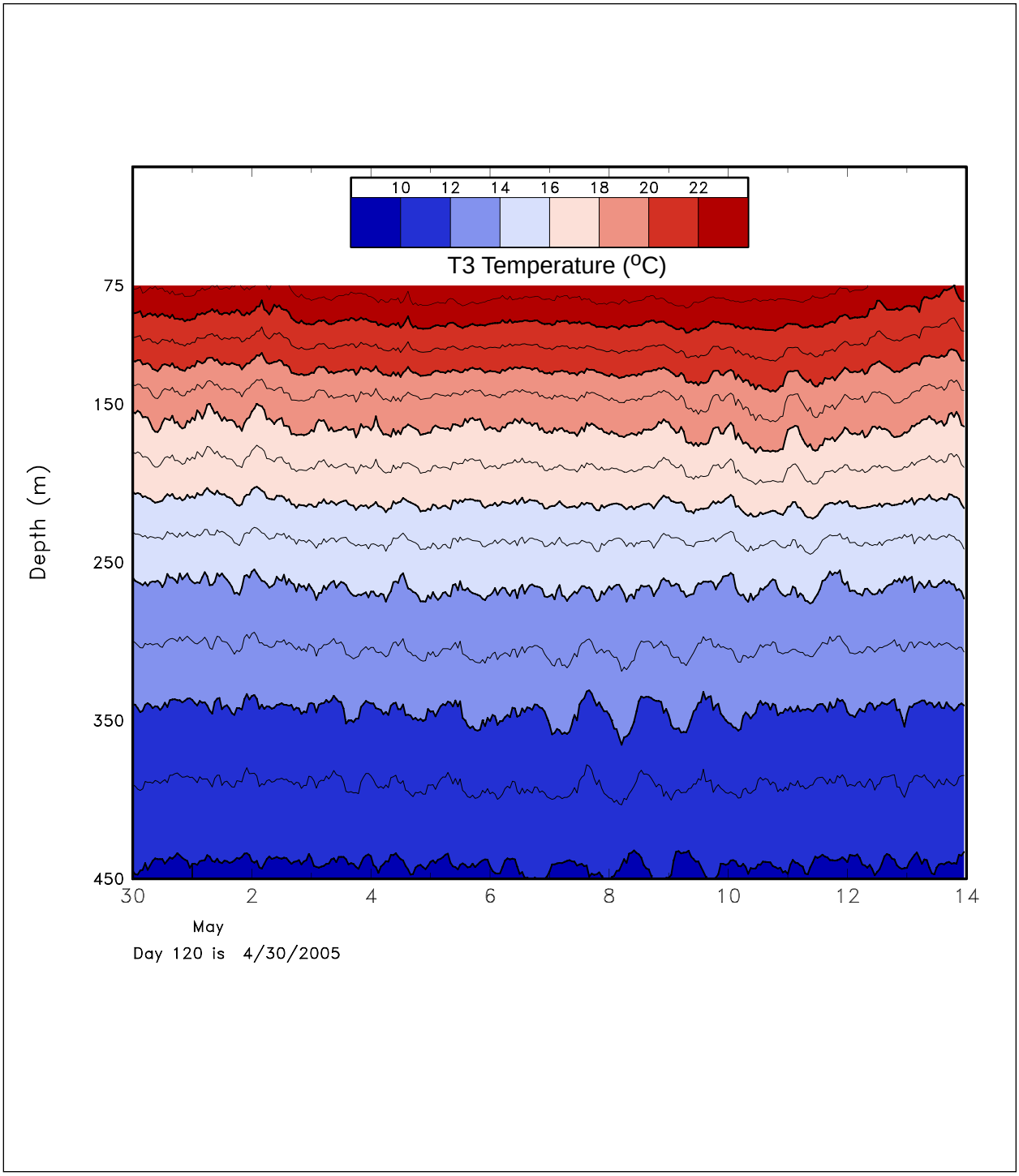

Figure 5.2-4. Unfiltered temperature - depth plot at T3 for the May event.

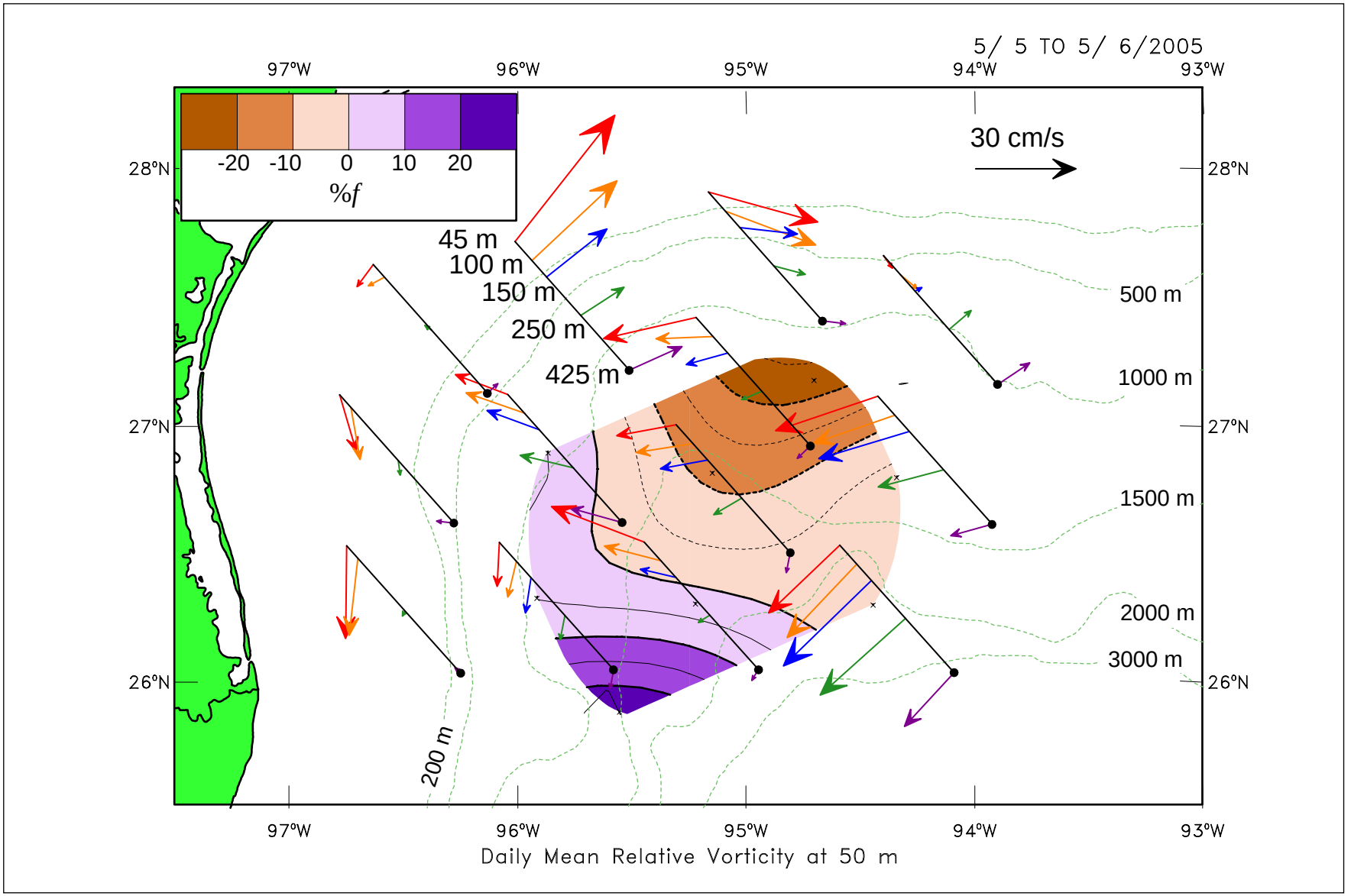

Figure 5.2-5. Daily mean currents for May 5 (0-24h GMT) at indicated depths along with the relative vorticity (percent of f) field at 50 m. Currents are shown as a pseudo-3D perspective where the dot at the base of the line is the mooring site, and arrow directions are true in geographic coordinates.

was discussed in Chapter 3. The relative-vorticity map indicates that ζ was between –3 to –5% of f at T3 and this would allow near-inertial internal waves of frequency f to propagate down to depths of ~ 250 m where the relative vorticity became small (~ 0%f). This is illustrated in Figure 5.2-6, where the clockwise rotary spectra of the 3 to 45-hour band passed (HBP) currents are shown for a number of depths. A time series length of 21 days, centered on the May event, was used to give reasonable spectral resolution, and the results suggest that the centers of the spectral peaks are slightly above f_e. The energy at 150 m exceeded that at 45 m and 250 m, and the fluctuations had lost most of their energy by 350 m. Vertical velocities were estimated from isotherm displacements using:

$$w = - \partial\eta/\partial t \qquad (5.2)$$

where η is the depth of a given isotherm calculated by linear interpolation between the 3-HLP temperature records. The 12°C and 18°C surfaces have nominal depths of ~ 350 and 150 m, respectively (see Figure 5.2-4), during this May interval, and the vertical velocity power spectra (Figure 5.2-6) show that the inertial peak was at a frequency greater than f, and was also about an order of magnitude greater at the deeper depth. Thus, horizontal inertial motions were being converted into predominantly vertical motions at depths below ~ 300 m.

The vertical structure of the inertial currents at T3 was examined using frequency domain EOFs (Figure 5.2-7). Only the clockwise rotary spectra were used, however, the results are almost identical to analyses using the U and V velocity components, because U and V amplitudes for the principal modes are almost identical with V leading U by ~ 90°. Two modes were significant, indicating that the near surface was somewhat decoupled from the stronger subsurface response. It is not clear whether this mode separation, which has been observed in previous inertial band EOFs (Donohue et al., 2006) was caused by the slow vertical phase propagation in the surface layer or whether there were different signals with different sources. The surface and subsurface modes (2 and 1, respectively) had vertical wavelengths (360° phase change) of ~ 150 and 200 m, respectively. Mode 1 amplitudes peak at ~ 150 m and both modes were negligible below ~ 300 m. Phase propagation was upward (positive phases lead) as was indicated by the velocity component plots, and the relative reduction of vertical phase velocity in the surface layer compared with deeper was indicated by the change of slope of the phase lines in Figure 5.2-3.

The variability of the inertial amplitudes across the array and with depth is indicated in Figures 5.2-1a-c for this May 2005 event. Relatively weak amplitudes were observed at T2, V2, and V4, and large amplitudes at 50-m at T4 and U4, for example. The vertical EOF modes for T5 clockwise inertial period currents are given in Figure 5.2-7. The rms amplitudes were less than half the peak amplitude at T3; however, the oscillations penetrated to greater than 400 m depth, and the vertical wave length was much greater (~ 600 m) than at T3. T5 was on the south side of the anticyclonic circulation and also closer to the center (Figure 5.2-5) and therefore, the thermocline was deeper even though the 50 m relative vorticity is about the same as at T3. Thus, the difference in response at T5 versus T3 could have been attributed to different wind forcing, the deeper thermocline that allows the energy to propagate more rapidly to deeper depths, or there was also the possibility that wave trains propagating southward interfere to produce inhomogeneities. Wind forcing was similar over the array as will be shown below.

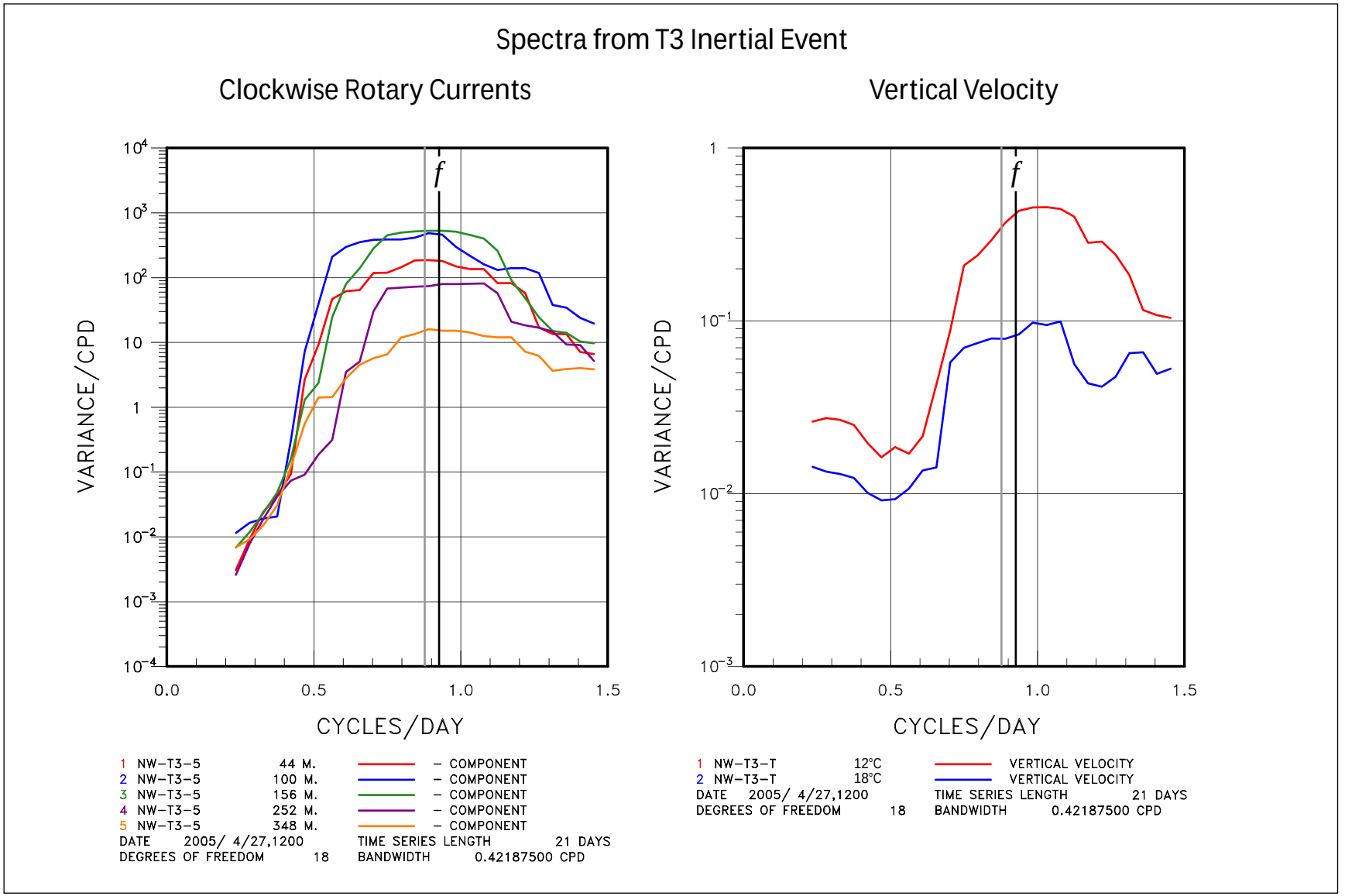

Figure 5.2-6. Clockwise rotary spectra of 3-to 45-hour, band-passed currents from the indicated depths at T3 (left panel). Local f is marked and the vertical gray line is 95% of the Coriolis parameter, f. The right panel shows the spectra of vertical velocities calculated from the 12 and 18^{o}C isotherm displacements.

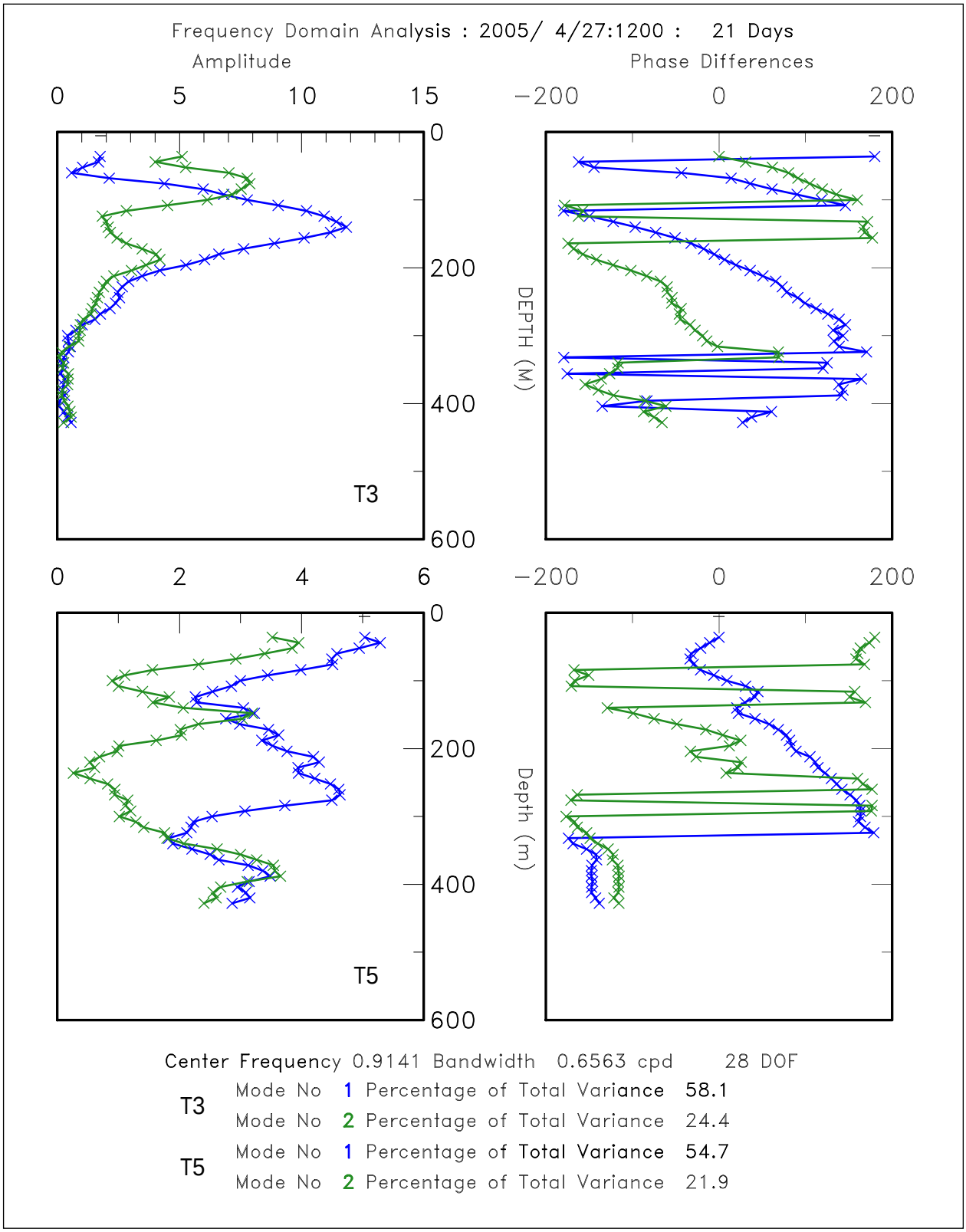

Figure 5.2-7. Frequency domain EOF analysis of inertial-band currents for T3 (upper panel) and T5 (lower panel) for the May interval events. Amplitudes are in $cm \cdot s^{-1}$.

The winds from the available NDBC buoys are given in Figure 5.2-8, and it is clear that a cold front moved from the northwest (42019 and 42020) to the southeast (42038 and 42002) in about 12 hours, resulting in a rapid switch to strong (~ 15 $m \cdot s^{-1}$) northerly winds and therefore similar forcing for the inertial currents observed over the whole of the array. The clockwise inertial spectra for the 450-m ADCP current records are given in Figure 5.2-9, and show considerable variability in both the magnitude of the spectral peaks and their distribution through the upper water column. The highest 50 m energy was in the NE corner of the array (T4, T5, U3 and U4), and the lowest energy was on the southern boundary (V2, V3 and V4). T3 and U3 had subsurface maxima that were greater than the near surface, while T2, U2, and T5 had much more uniform depth variations. The centers of the spectral peaks tended to be slightly above local *f* on the southern boundary (V2, V3 and V4), and also at T2, whereas at T3, T4 and U4, most of the peaks fell slightly below local *f*. These frequency shifts are reasonably consistent with the distribution of relative vorticity (Figure 5.2-5) with an anticyclone in the NE and cyclones on the southern edge and NW parts of the array.

In an attempt to quantify the inertial variability resulting from this cold-front passage, frequency domain EOFs were calculated for the clockwise rotating currents from the 450-m ADCP at each mooring location. Results for T3 and T5 are given in Figure 5.2-7 and discussed above. The eigenvalues give the variance explained by each mode, and the first 2 modes accounted for between 70% and 90% of the total variance of all the inertial currents in the upper 450 m at each location. Therefore, the first two eigenvalues were summed to represent the variance through the upper 450 m of clockwise inertial currents. The map of this mode variance is given in Figure 5.2-10, and shows alternating bands of higher and lower energy regions that were directed east-west. This can be compared with the 16°C surface generated from both PIES-derived temperature profiles and 40-HLP temperature observations from the moorings (Figure 5.2-10), which had better horizontal resolution than using moorings alone. The 16°C isotherm was in the lower thermocline and the results from T3 (Figure 5.2-7) suggest that the inertial energy was trapped above this depth at least for anticyclones. The implications are that the north and south sides of the anticyclone had relatively high inertial energy, while the center of the anticyclone and the cyclones on the southern edge of the array had relatively low energy.

The east-west banded structure of the energy may also have been a result of complex interfering, southward-propagating near-inertial internal waves. The horizontal group velocity was difficult to estimate because it depended on the small difference of (ω - *f*), where ω ($> f$) is the inertial wave frequency. Typical values are about 50 $cm \cdot s^{-1}$ and thus inertial-internal waves forced by the cold front could have propagated between T3 and T5 in 1 to 2 days (Hamilton, 1984). This suggests that even with a single-impulse wind event, inertial currents at a given location were not likely to be entirely related to the local winds. The complexities were further compounded by the trapping and suppression of the waves by the 3-dimensional background relative-vorticity field (Kunze, 1986).

5.2.2 Winter Storms

In winter, storms are more frequent and upper-layer inertial currents are more frequently excited. The month of December 2004 was particularly energetic as can be seen from the inertial amplitudes in Figures 5.2-1. Even with more continuous wind forcing the inertial amplitudes

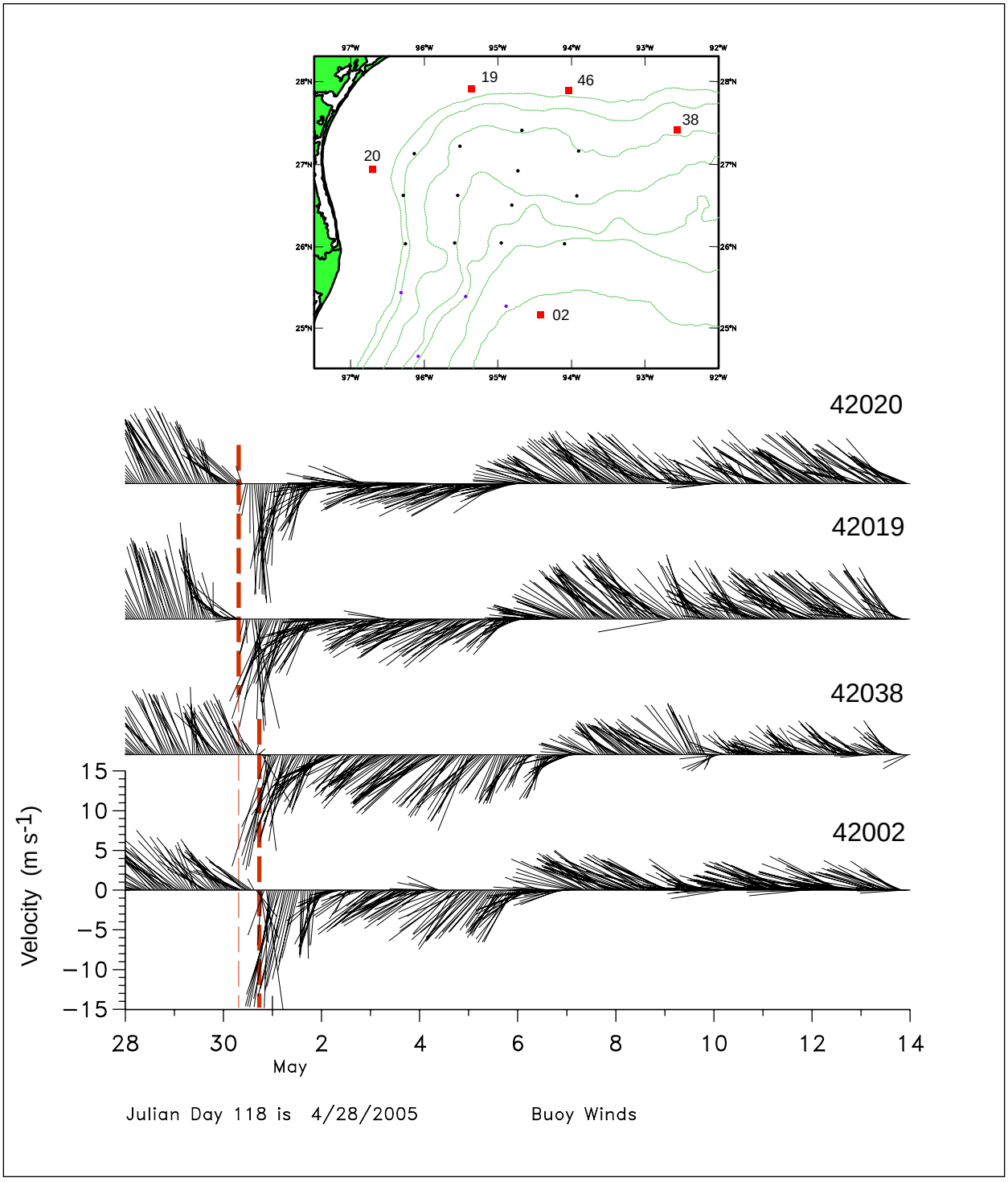

Figure 5.2-8. Hourly wind vectors from the buoys indicated on the map (red squares) for the May cold front event.

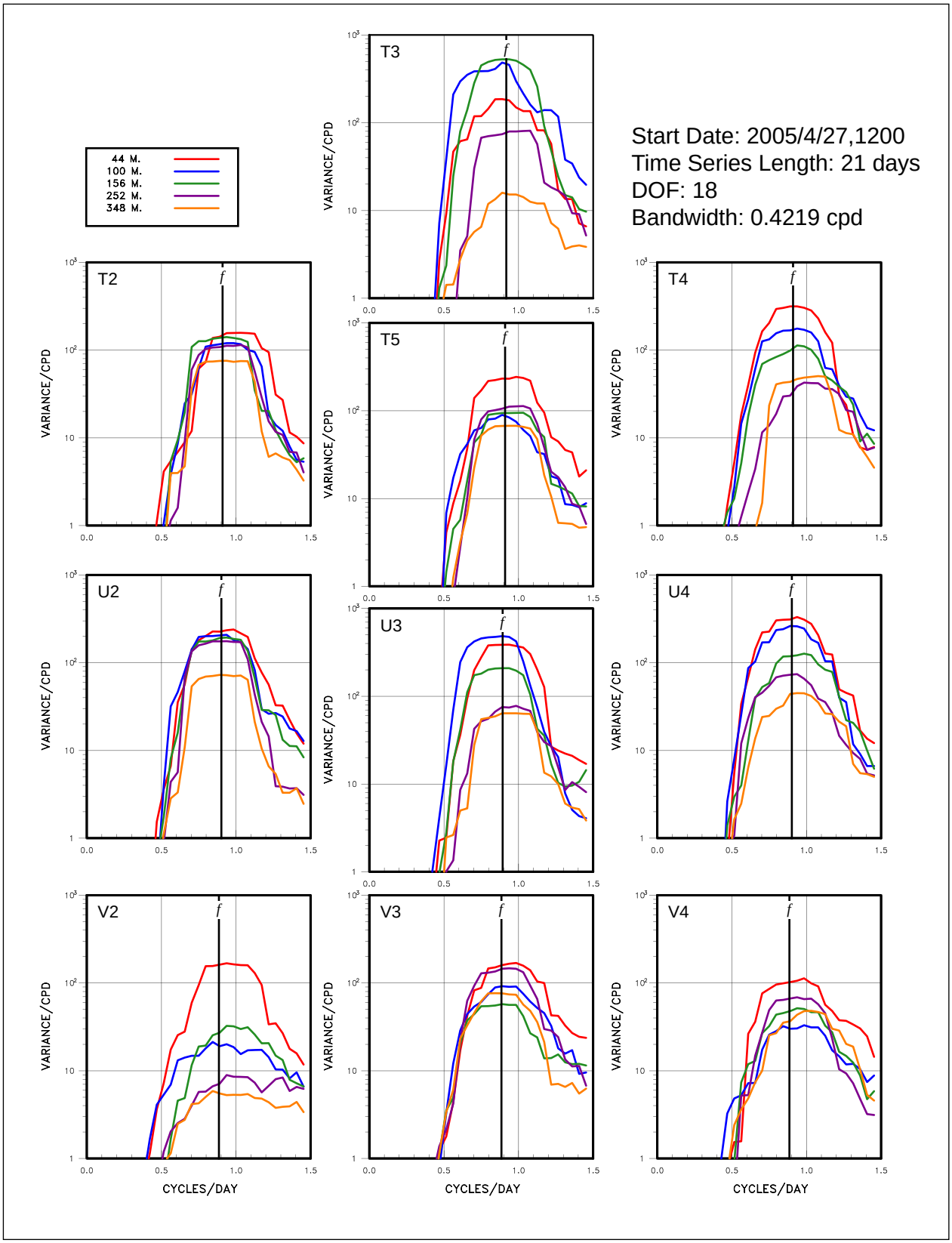

Figure 5.2-9. Clockwise inertial band spectra for the indicated moorings and depths for the May event. Local *f* is given by the vertical line.

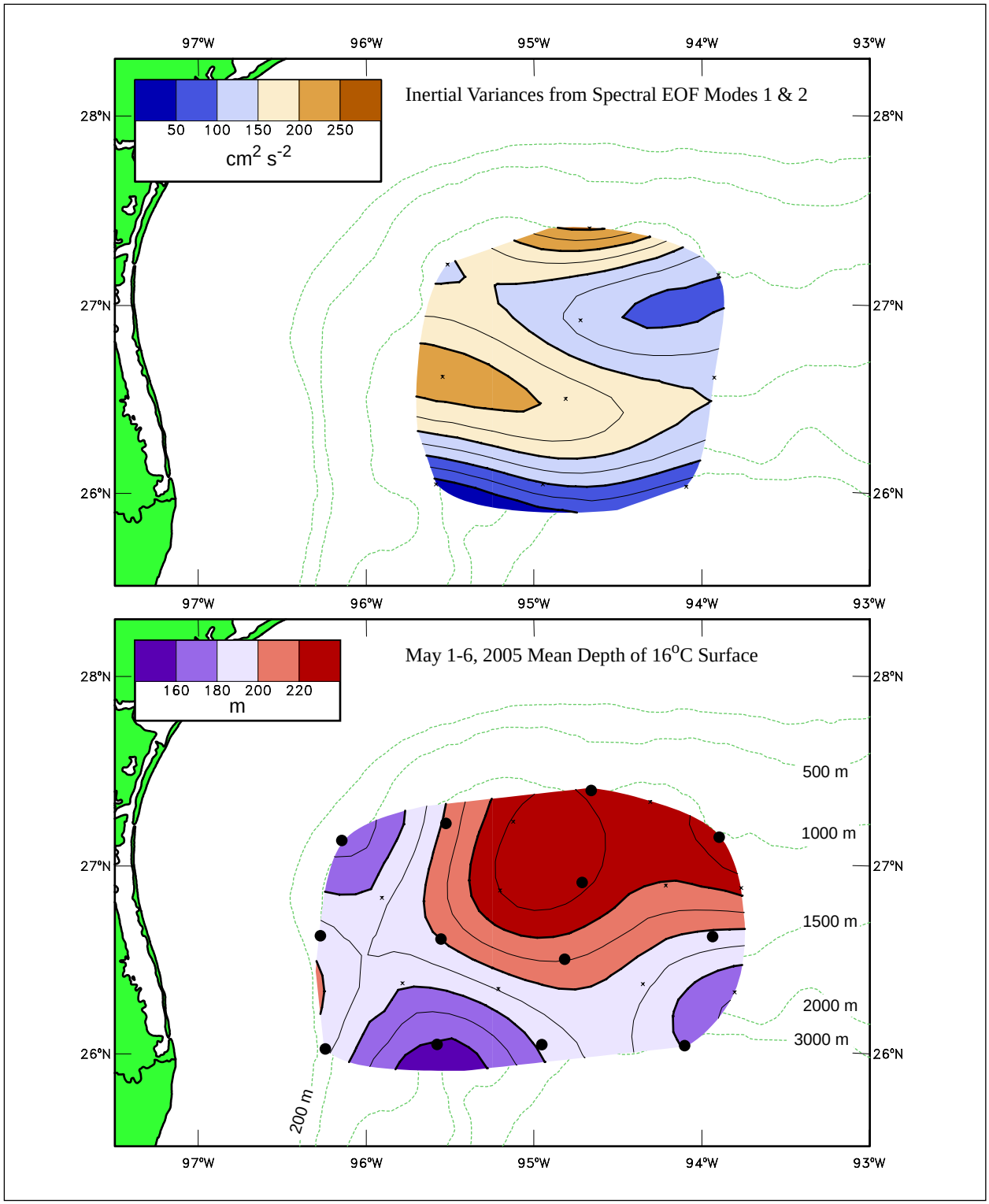

Figure 5.2-10. Top panel: Inertial variances from the spectral EOF analyses of vertical modes of the clockwise inertial motions at each ADCP for the May event. Eigenvalues for modes 1 and 2 are summed. Bottom panel: 5-day mean depth of the 16°C surface obtained from 40-HLP temperature records on moorings (dots) and temperature profiles derived from PIES (crosses).

were still highly variable both with location and depth. As an illustration of this, Figures 5.2-11 and 5.2-12 show the upper-layer current speeds at V4 and V2. The events at V4 generally penetrated to deeper depths, and this was particularly noteworthy for the 3-11 December wave train. The currents speeds at V4 had larger background speeds than at V2 (e.g., the high speed event at V4 at the end of November is not primarily inertial), and at both sites the strongest response was at 50 m and decayed with depth. The temperature records at 450 m were also different with V2 being more than 1°C cooler than V4, and V4 having larger fluctuations including some daily periodicities, particularly in the first half of December when the near-inertial internal waves penetrated to greater depths. The cooler temperatures at V2 were confirmed in Figure 5.2-13, where the whole of the upper water column from 75 to 450 m was much cooler than at V4. Figure 5.2-14 shows the background temperature and current fields at the end of November and 10 days later. There was a prominent cyclone slowly moving westward at about 25.5°N, with a warm anticyclone over the northwest slope. The latter was part of U2 and is discussed elsewhere. However, it is clear that V4 was primarily in the anticyclonic circulation, with the deepest depression of the upper level isotherms, and the greatest depth penetration of the inertial currents both occurring on 7-9 December. Similarly, V2 was clearly within the cyclone. Therefore, strength and depth penetration of the inertial oscillations seem to have been influenced by the background low-frequency relative vorticity fields.

Similar to the May event, clockwise rotary spectra were calculated for a 35-day interval, beginning 27 November 2004 for all the 450-m ADCP band-passed current records. At each location, the EOFs were found for the depth profile and the first two eigenvalues summed to represent a depth-integrated measure of the clockwise inertial kinetic energy. The map of this energy measure is given in Figure 5.2-15, along with the depth of the 16°C temperature surface. There are similarities with the results for May (Figure 5.2-10) in that there were anticyclonic and cyclonic flows in the northeast and southern parts of the array, respectively, with the transition between them being further north in the winter. The inertial-energy contours were also similar with a band of increased energy roughly corresponding to the region between the eddies with a maximum on the west side (at U2 in both cases) and a marked reduction towards the southern cyclonic flow region. It is noted that upper-layer flows and the interaction between the warm and cold eddies was much stronger in winter than in May. The 35-day winter interval contained multiple inertial-internal wave events with winds being from several storms and similar over the array region (not shown). Clockwise rotations of the wind vectors were prevalent along the upper slope (42019, 42020, 42046, and 42038), but not as persistent on the southern boundary at 42002 (see Figure 5.2-8 for locations, and Figure 5.2-11 for the hourly vectors), even though the latter's wind speeds were similar. This may have contributed to the lesser magnitude of the inertial response in the south. The results suggest that the horizontal scales of inertial variability were on the order of the mooring spacing (40 km) in the north-south direction and greater than the mooring spacing in the east-west direction. Both scales were much less than the scales of the wind field, and the consistency of the inertial energy distributions for different wind forcings suggest internal-wave propagation processes with similar characteristic scales were in effect in both intervals.

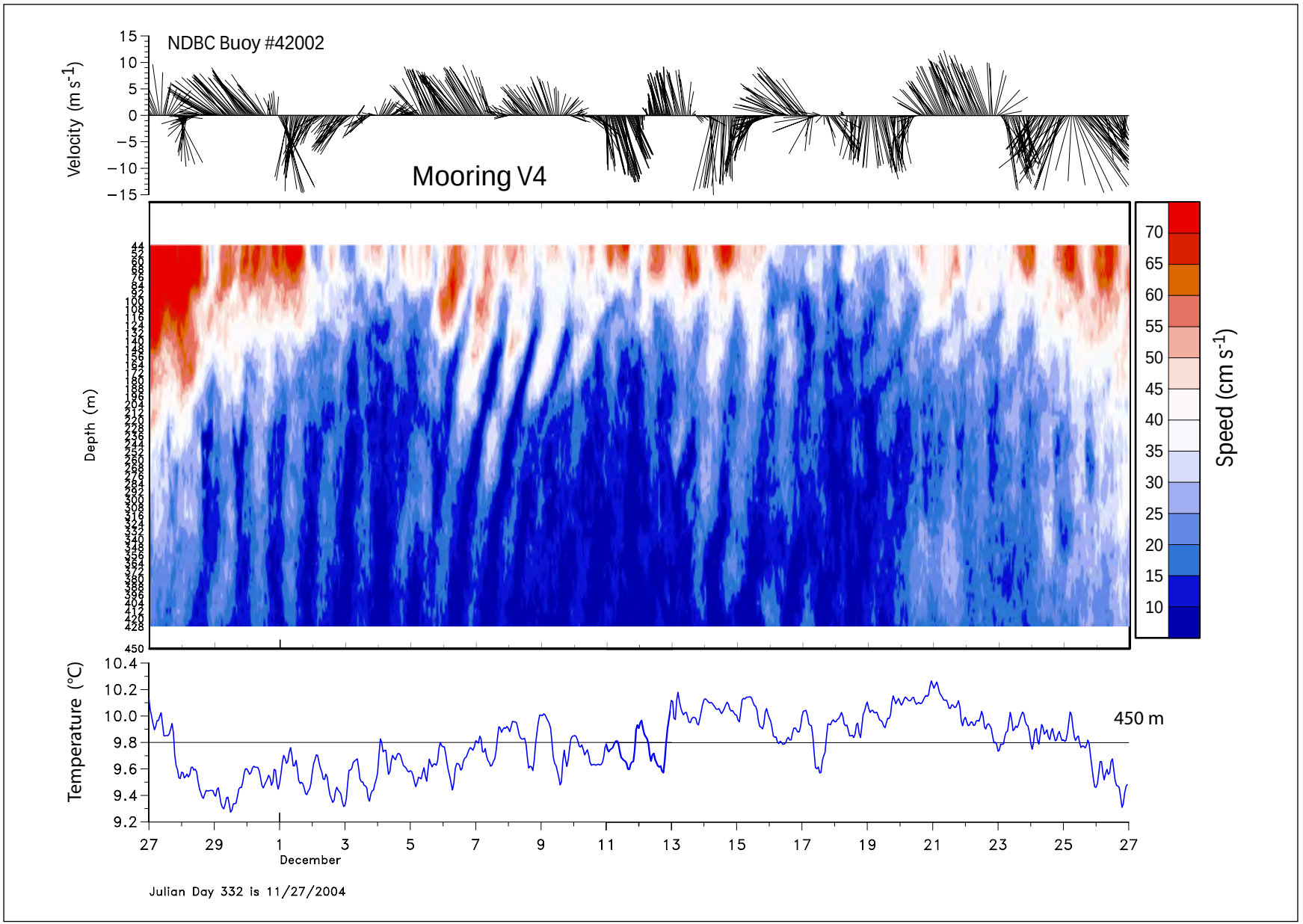

Figure 5.2-11. Unfiltered speeds from the 450-m ADCP at V4, along with hourly wind vectors from NDBC buoy 42002 and the temperature record at 450 m.

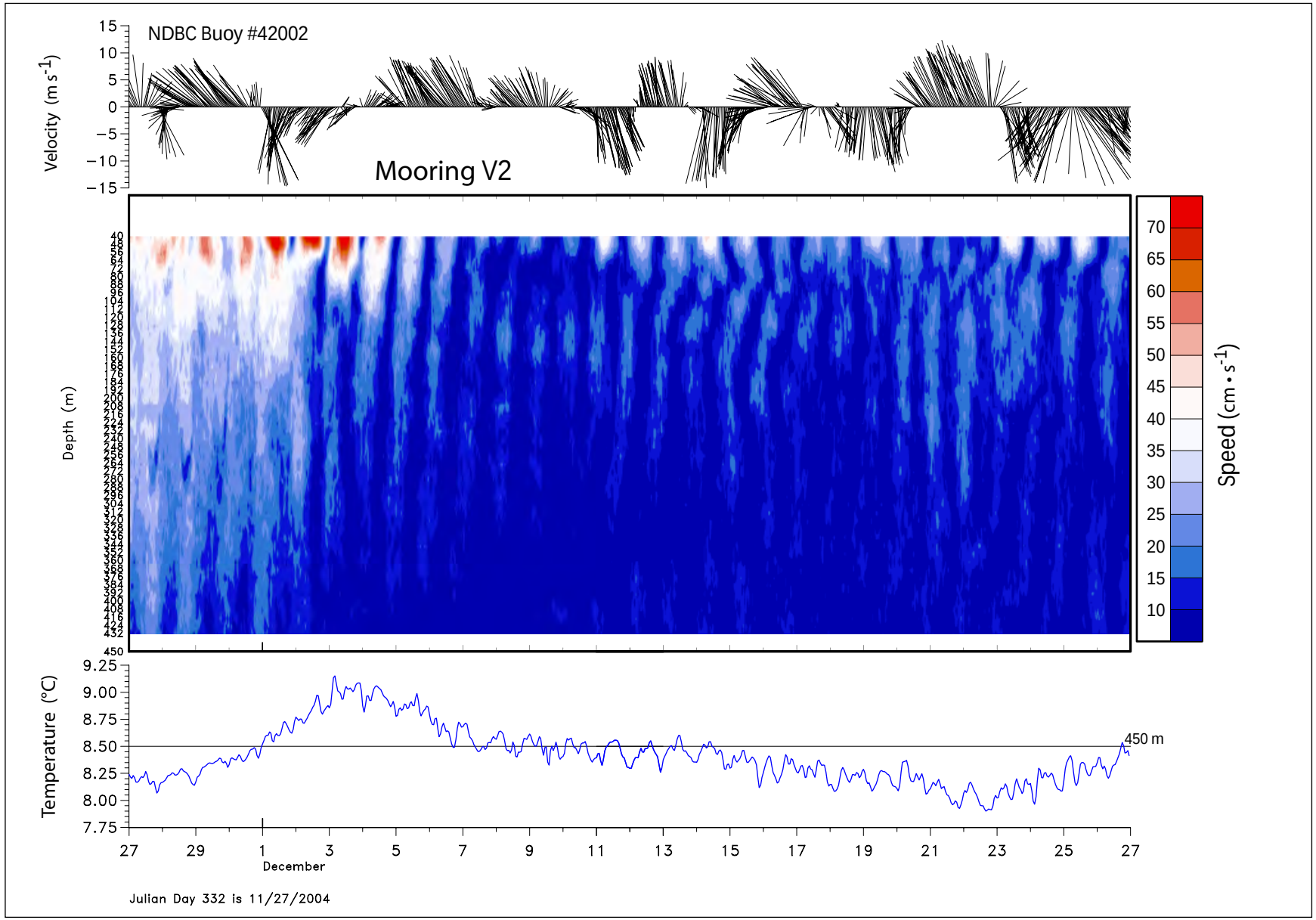

Figure 5.2-12. Unfiltered speeds from the 450-m ADCP at V2, along with hourly wind vectors from NDBC buoy 42002 and the temperature record at 450 m.

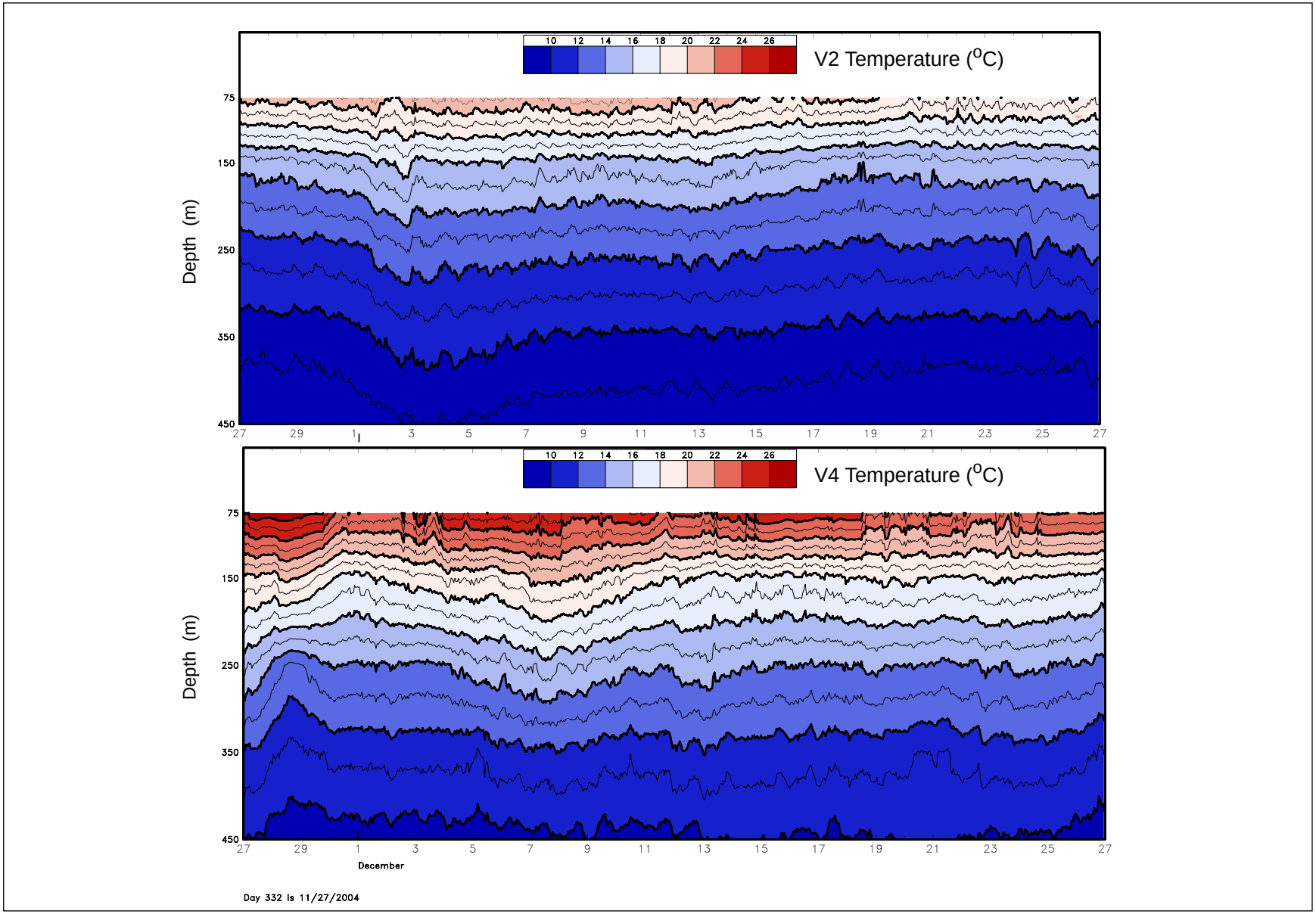

Figure 5.2-13. Unfiltered temeprature-depth plots from instruments in the upper 450 m at V2 (top panel) and V4 (bottom panel).

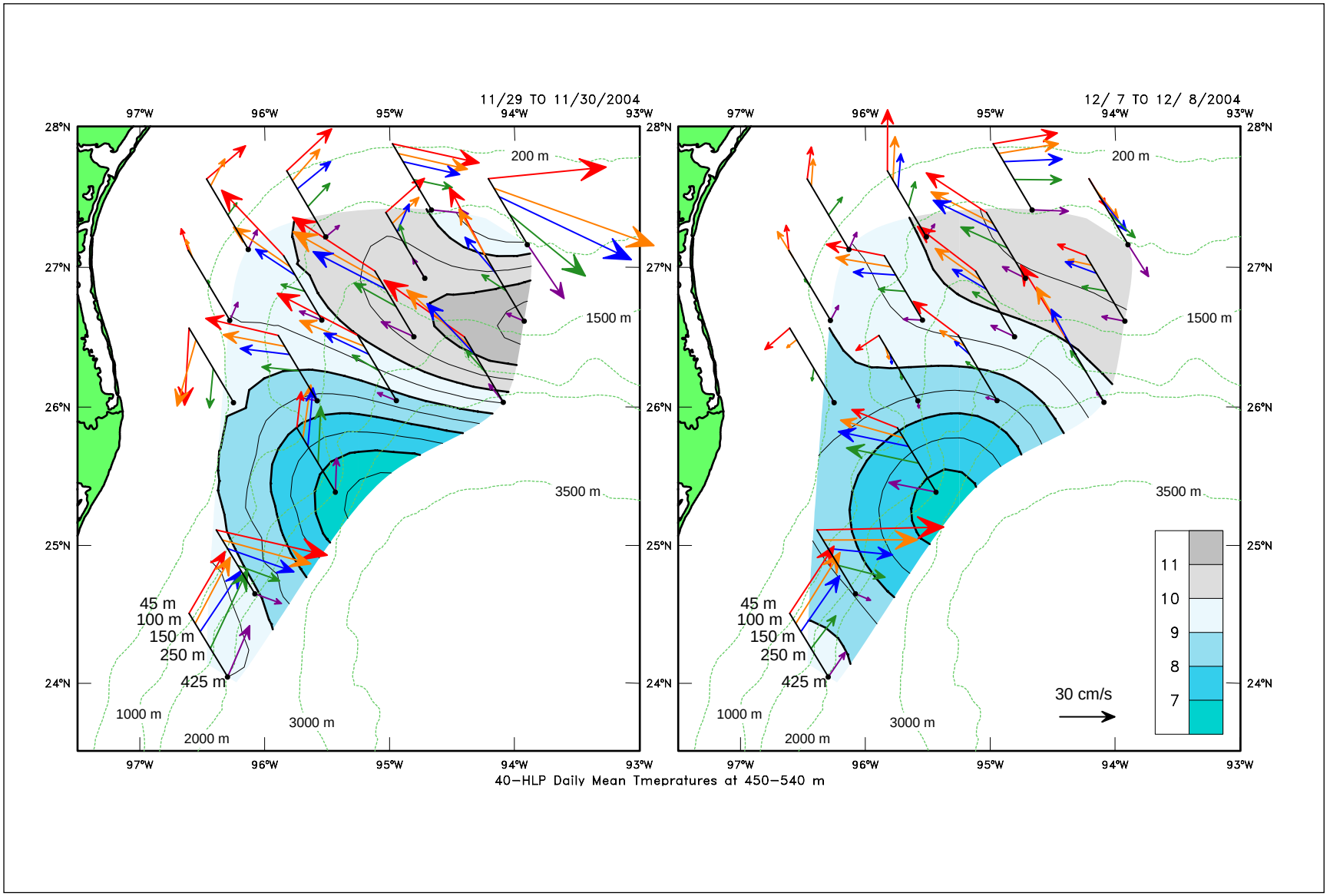

Figure 5.2-14. Daily mean 40-HLP temperaure at 450 m and currents (displayed as pseudo-3D profiles) at the indicated depths for November 30 (left panel) and December 7, 2004 (right panel).

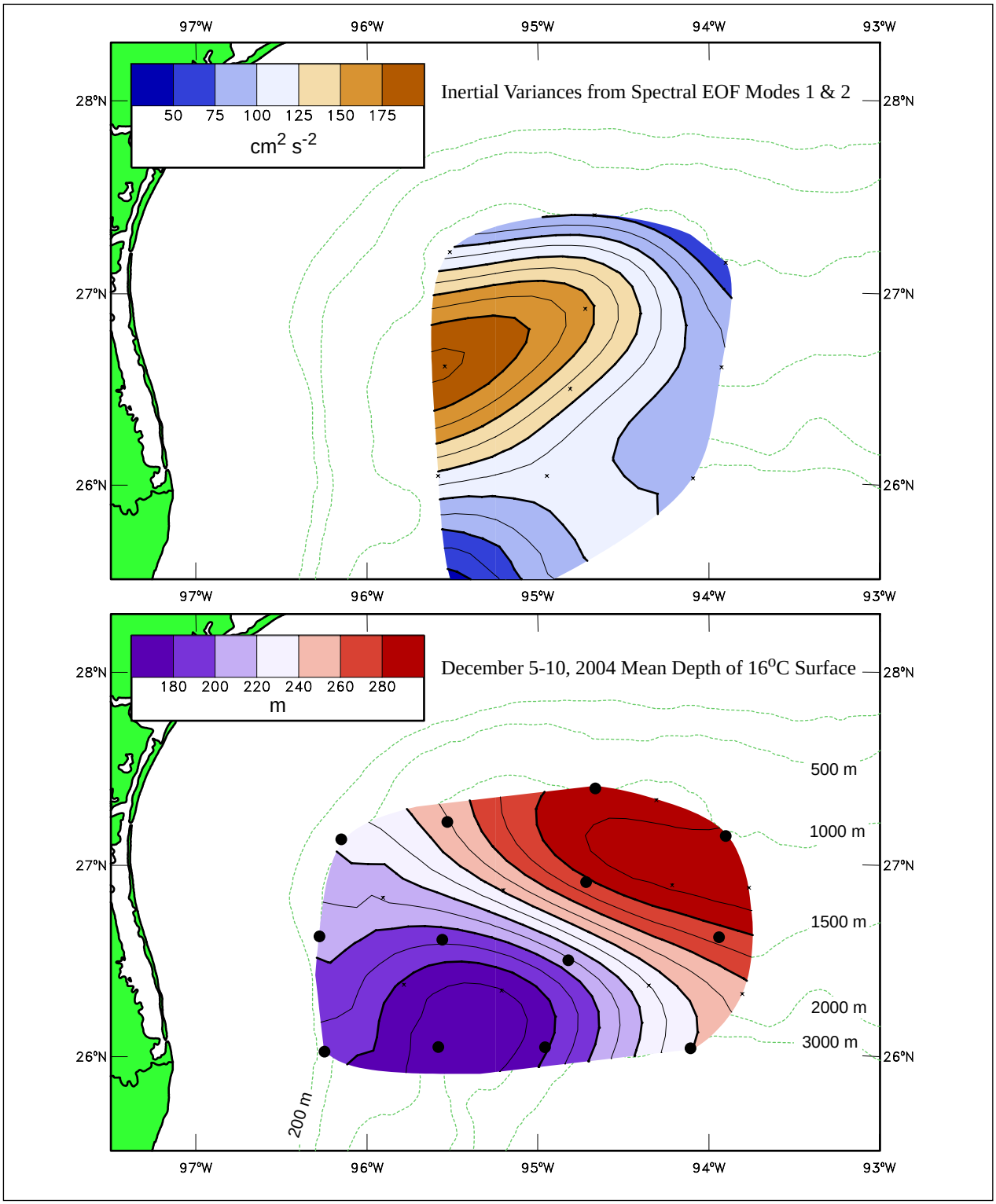

Figure 5.2-15. Top panel: Inertial variances from the spectral EOF analyses of vertical modes of the clockwise inertial motions at each ADCP for the winter interval. Eigenvalues for modes 1 and 2 are summed. Bottom panel: 5-day mean depth of the 16°C surface obtained from 40-HLP temperature records on moorings (dots) and temperature profiles derived from PIES (crosses).

5.2.3 Low-Mode Inertial Oscillations from PIES

As indicated and shown above in Section 5.2.2 for near-inertial waves generated at the sea surface, phase propagation is nearly vertical (with wave vector upwards) but their group velocity and energy propagates nearly horizontally slanting downward into the ocean interior. Their velocities (perpendicular to the wavenumber vector) are also slightly inclined from level and produce small vertical displacements of the thermocline (LeBlond and Mysak 1978). The hourly τ measurements allow us to investigate the lowest internal mode near-inertial signal because τ variability signifies internal waves that displace the thermocline. Here we follow the methodology of Park and Watts (2005). Their study utilized τ records from an array of PIES in the Japan/East Sea. Similar to Park and Watts (2005), we find that low-mode near-inertial energy tends to be trapped in anticyclonic features.

To isolate the near-inertial signal in the hourly τ measurements, the following steps were taken. First, the contribution to τ from mass loading was removed. We converted the hourly dedrifted pressure record variations, p', to round-trip travel time, $\tau_{\text{mass loading}} = (2p')/(\rho gc)$ where c is the speed of sound, g is gravity, ρ is density, and subtracted $\tau_{\text{mass loading}}$ from τ. Note that removing this mass-loading component also removed the barotropic tide. Second, each τ time series was band-passed filtered with a 4^{th} order Butterworth filter with cutoff at ±1.75 hours from its local inertial period. The filter was run forward and then backward to eliminate phase shift. PIES 2 had noisy hourly τ records and was not included in the near-inertial analysis.

The low-mode near-inertial signal, τ_I, (Figure 5.2-16) shows bursts of energy in pulses that last 15-30 days. Similar to the results from the current-meter analysis in the previous section, the horizontal scales of the inertial variability were on the order of the station spacing. Inertial events sometimes appeared coherently between neighboring pairs of records but are rarely coherent among several records. The low-mode inertial signal lacked a clear seasonal signal although there was a tendency for the strongest events in each record to occur in winter. Additionally, τ_I -event strength, frequency and duration are comparable between records. The strongest event occurs at PIES 6 in December 2004.

Maps of the low-mode, near-inertial variance interpreted in the context of the mesoscale circulation reveal a consistent pattern of enhanced τ_I in anticyclonic features. The previous section highlighted two inertial events, a winter storm in December 2004 and a cold-front passage in May 2005. Here we present the corresponding low-mode case studies for these two events. The variance in the low-mode, near-inertial signal is averaged over the time intervals of these events (grey bars in Figure 5.2-16) and mapped in the left panel of Figures 5.2-17 and 5.2-18. These figures also show the upper-ocean relative vorticity scaled by the local Coriolis parameter and the SSH field.

During the December winter storm, high initial variance (energy) in the low-mode inertial signal coincided with the negative vorticity associated with the anticyclone (U2) in the northeast corner of the array. The signal was largest at PIES6 with elevated signal at PIES 3, 7, and 9 and small amplitudes elsewhere. Note that this was a different spatial structure than resulted from the EOF analysis in the previous section. In particular, the largest signal in the ADCP records was found near mooring U2, not near T3 the closest mooring to PIES 6. The May 2005 event had elevated

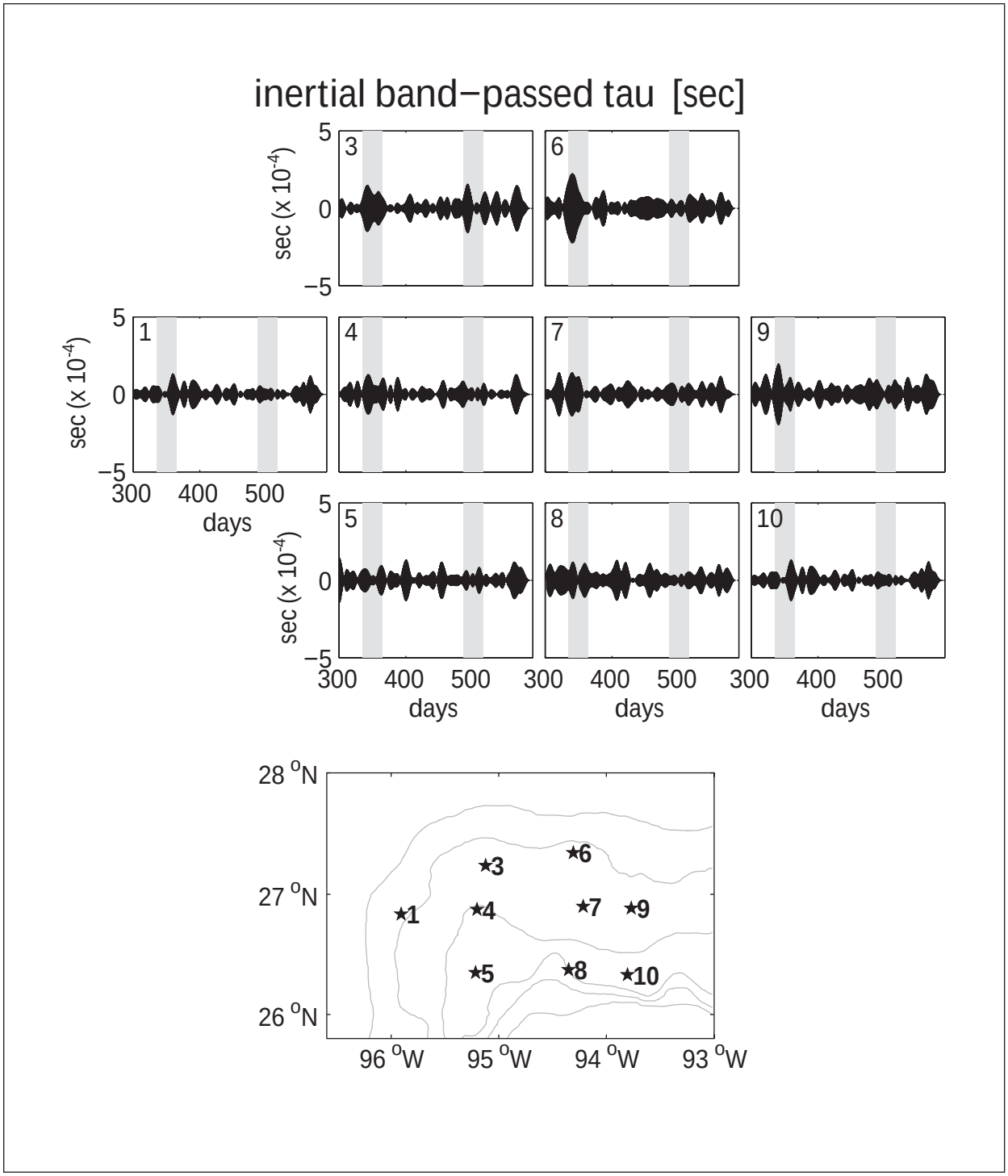

Figure 5.2-16. Time series of near-inertial band-passed τ in seconds plotted according to approximate geographic location. Instrument number noted in the upper left corner of each subplot. Shaded gray regions correspond to the averaging period for two case studies. Bottom panel: Bathymetry contoured every 500 m depth. PIES are denoted as stars. Above, Day 300 corresponds to the beginning of the PIES observations.

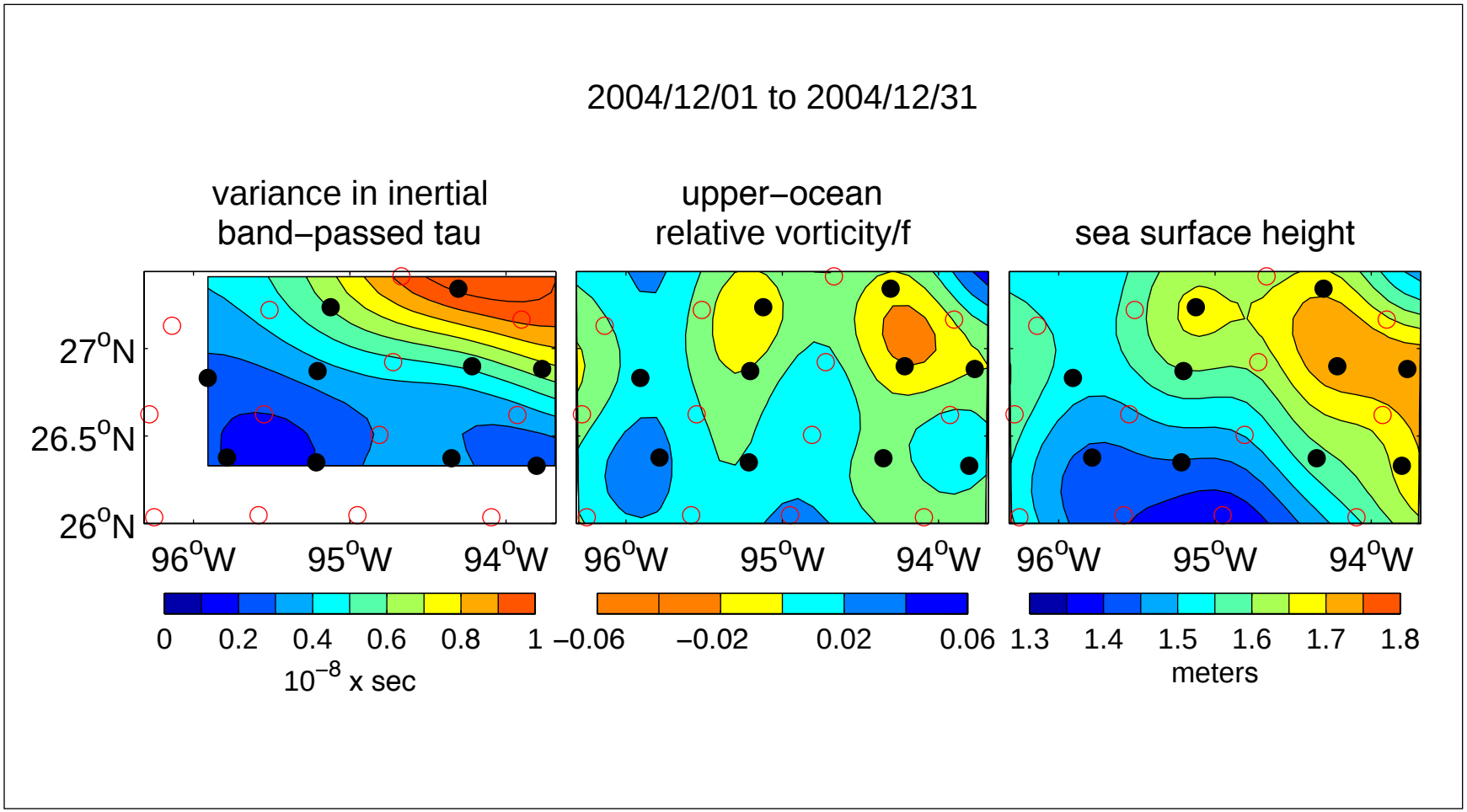

Figure 5.2-17. Case study of the low-mode near-inertial response December 2004. All maps represent an average from December 1, 2004 to December 31, 2004. Left panel: Variance in the low-mode near-inertial signal averaged from Middle panel: Upper-ocean relative vorticity scaled by the local Coriolis parameter. Right panel: Sea surface height field. The PIES denoted by filled black circles; current meter moorings denoted by red circles.

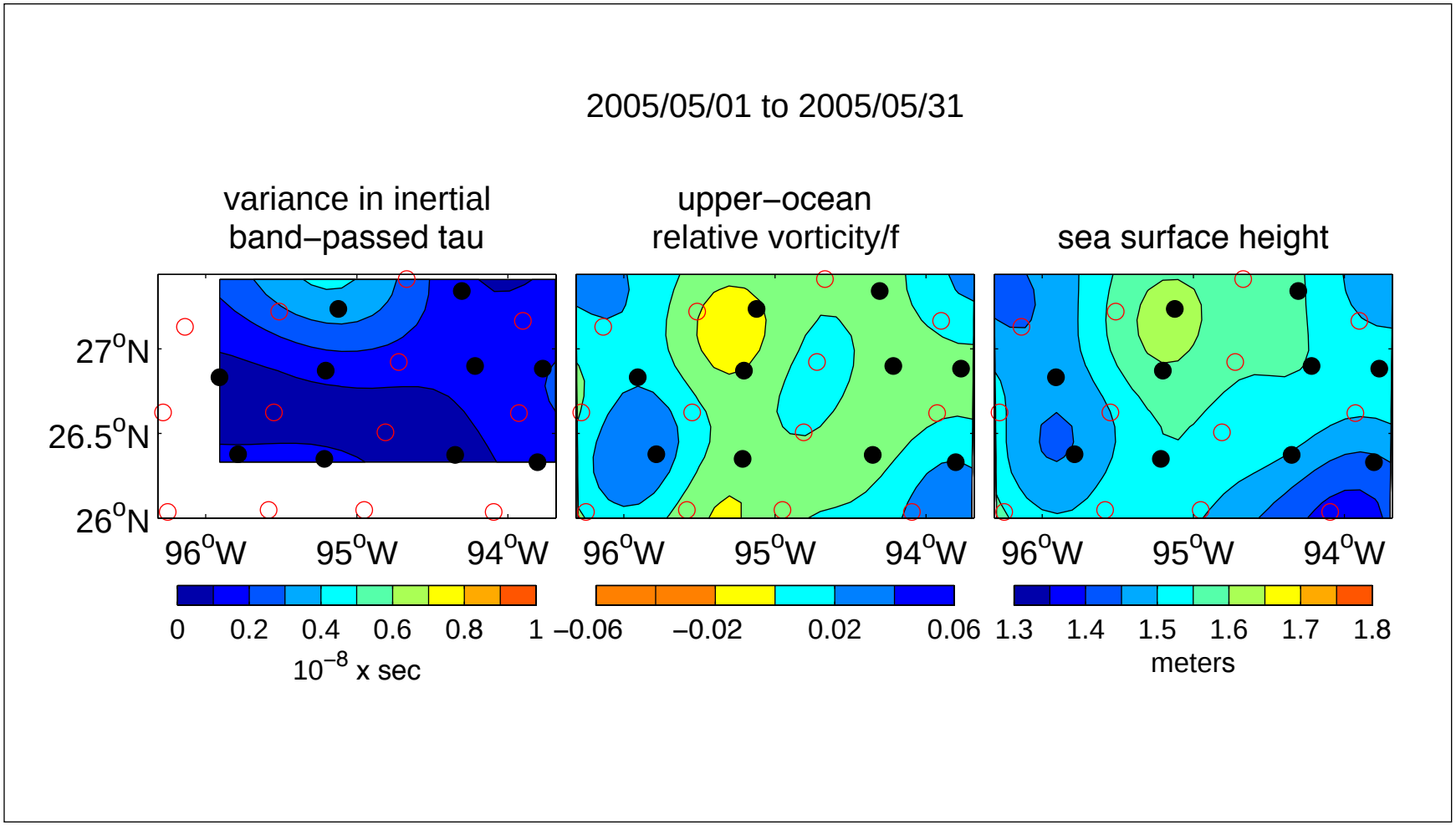

Figure 5.2-18. Case study of the low-mode near-inertial response May 2005. All maps represent an average from May 1, 2004 to May 31, 2004. Left panel: Variance in the low-mode near-inertial signal. Middle panel: Upper-ocean relative vorticity scaled by the local Coriolis parameter. Right panel: Sea surface height field. The PIES denoted by filled black circles; current meter moorings denoted by red circles.

low-mode inertial variance near PIES 3 coincident with a region of anticyclonic vorticity. Variance was weak elsewhere. This event also reveals differences between the low-mode and ADCP inertial variance. The ADCP signal was strongest at T3 and U2.

In both cases, the ADCP currents were concentrated between the surface and 150 to 200 m and typically exhibited current reversals within that range, which would project most of their variance onto higher internal modes. Nevertheless, D'Asaro (1991) argues that the relatively smaller amount of inertial current variance that projects onto a low-internal mode has least dissipation and can travel farthest, horizontally toward regions of lower f_e (planetary and relative vorticity). Because the τ_I measurements respond to just the lowest internal mode, which must have propagated a long distance horizontally (possibly hundreds of km), it is not surprising that the ADCP and PIES observations find different locations of near-inertial energy concentration.

Additional support for the tendency for the low-mode near-inertial signal to be elevated in anticyclonic features derives from the negative correlation between 15-day averages of relative vorticity and 15-day averages of τ_I (Figure 5.2-19). We performed this analysis at PIES 4, 5, 7 and 8, because they were array interior sites and therefore the relative vorticity calculation was well resolved at these sites. The correlation coefficient is -0.45 and statistically significant at the 95% confidence level when the 15-day averages are assumed to be independent of each other.

Further study would be required to account for the observed different locations of upper-ocean, inertial-current events and mid-thermocline near-inertial vertical displacement events. Bursts of inertial energy should arise from a combination of inertial-mode vertical and horizontal propagation and the steering and focusing by the larger-scale currents and shear in mesoscale eddies (Kunze, 1985; D'Asaro, 1991).

5.3 Subsurface Jets

This section discusses in detail the characteristics of three non-inertial subsurface jets. They occurred at T5 at the end of February 2005, at U4 at the beginning of July 2004, and at W1 in July 2005. The first two are similar in character and are the longest lasting with some of the highest speeds (> 70 $cm \cdot s^{-1}$) of the events found in the ADCP records. The last one at W1 occurred just after the end of the American sector deployments, but may represent a different process in that it occupied the lower half of the water column on the 500 m isobath. Thus, for this latter case, slope topography probably was important to the jet generation, which was not the case for other jets that were all in much deeper water.

5.3.1 T5, February 2005

The current speeds from the 450-m ADCP at T5 are given in Figure 5.3-1. The jet was clearly subsurface with little evidence of daily (inertial) oscillations and vertically propagating near-inertial internal waves. The event lasts ~ 6 days with speed maxima > 65 to 70 $cm \cdot s^{-1}$ occurring 3 times at different depths. The first was at ~ 250 m on 25 February, the second between ~ 100 and 250 m on 26-27 February, and the last ~ 300 m on 28 February – 1 March. The time evolution of the temperature profile at T5 gives an indication that the structure of the jet was approximately geostrophic with the vertical shears being balanced by the horizontal temperature

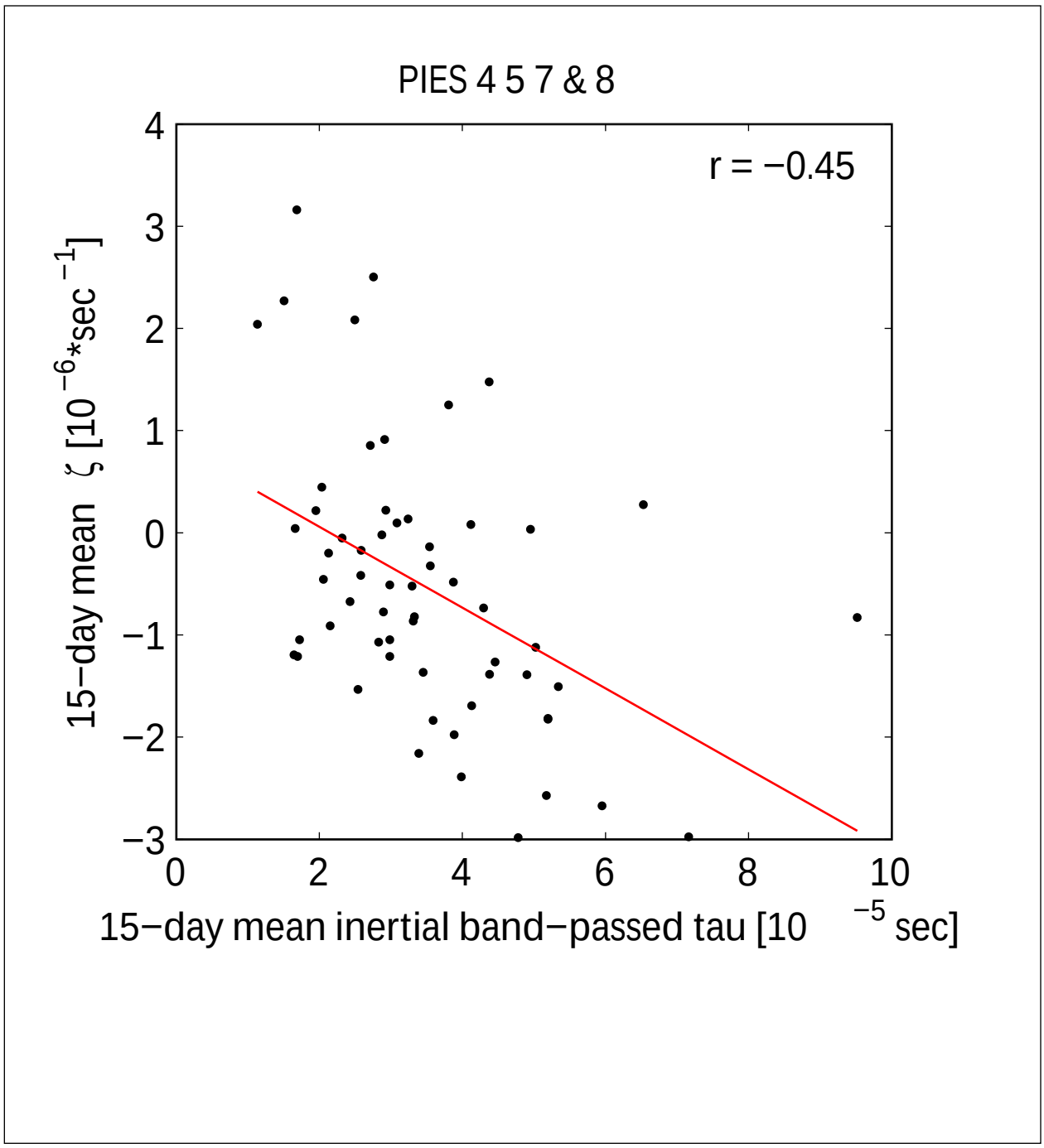

Figure 5.2-19. 15-day relative vorticity at PIES sites 4, 5, 7 and 8 versus 15-day inertial band-passed τ_I . The red line is a least-squares fit. The correlation coefficient is -0.45 and noted in the upper right corner.

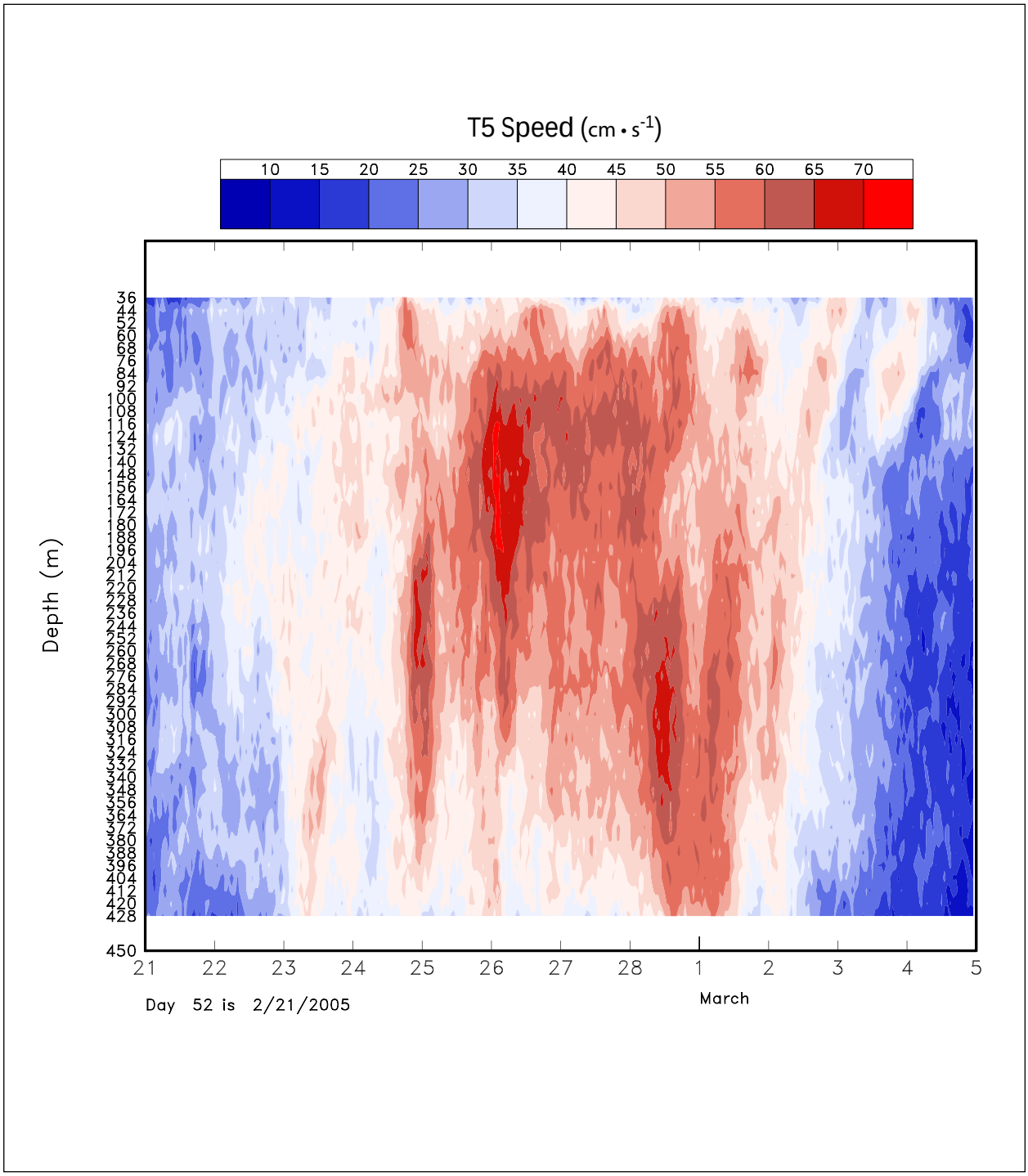

Figure 5.3-1. Unfiltered speed from the 450-m ADCP at T5 for the indicated interval.

gradients (Figure 5.3-2). The cores of the three highest speed events occurred where temperatures were cooling and warming above and below the jets, respectively. This produced regions of the water column where the distance between the isotherms increased with time, and these locations approximate the speed maxima. Normally in the GOM, isotherm displacements are in-phase as warm and cold eddies pass by a given location. Indeed this characteristic is why the gravest empirical mode approximation to the density structure is so successful in producing density profiles from PIES measurements. However, in this case, the displacements became a little out-of-phase at different depths indicating that the horizontal gradients of temperature changed sign with depth through the jet maxima. The direction of the current was towards the south and southeast and fairly steady over the duration of the event (Figure 5.3-2), with little or no inertial oscillations superimposed on the flow.

The sequence of warm and cold events through the water column at T5 (Figure 5.3-2) indicates a cold eddy was moving over the site. The water column below ~ 300 m began to warm steadily after 24 February, however, at 75-m the coldest water did not arrive until 26 February and warming does not commence until 1 March. This suggests a cold cyclone was interacting with a warm anticyclone, and this can be seen in Figure 5.3-3 where the cyclone was to the north and the anticyclone was in the southeast corner of the array. On 26 February, T5 was in the cyclone and it is notable that T3 and U4 also had relative daily average subsurface speed maxima at ~ 150 m, though they are not as large as that at T5 (Figure 5.3-3). The speed-depth plots for T3 and U4 are given in Figure 5.3-4. The subsurface jet at T3 occurred about two days before the jet at T5 and the high speeds at U4 were generally in the upper 100 m and occurred after 26 February. The latter jet was more characteristic of the edge of an anticyclone and therefore the anomalous subsurface speed maxima seems to have been propagated anticlockwise around the cyclone and merged with the outer edge of the anticyclone at U4 in early March. The temperatures at T3 (not shown) also showed diverging isotherms between 21 and 26 February with warming at depth and cooling near the surface. At U4, the whole of the upper 450 m showed a slow cooling through early March as the cyclone began to displace the anticyclone. A spatial perspective of the eddies is given by maps of the temperature field at two different depths. On 26 February (Figure 5.3-5), the center of the cyclone was displaced southward at 150 m compared to 250 m, and the cross section through the eddies confirms this with the deeper waters having had continuously up-sloping isotherms to the north, and the surface layers having had a temperature minimum around T5. If allowances are made for the relatively coarse horizontal resolution, then the implication is that the axis of rotation of the cyclone was tilted towards the anticyclone as the surface was approached. Figure 5.3-3 shows that the cyclonic flow at T3, T4 and T5 extended down through the 450-m surface layer. Two days later (Figure 5.3-6), the surface waters of the cyclone had moved slightly towards the southeast as the anticyclone begins to bulge out towards the northwest, apparently responding to the anticlockwise flows of the other cyclone in the southwest part of the array. At this time, the cross-section shows the 12°C isotherm was beginning to form a shallow minimum depth around T5, while the 10°C surface remained sloping upward. The 350-m temperature surface (Figure 5.3-6) implies that the deep center of the cyclone was beginning to move off to the east, while the surface layers remained fairly stationary. Therefore, the cyclone center axis remains tilted towards the anticyclone, but on this date the region of diverging density surfaces had moved deeper as did the jet (Figure 5.3-1 and 5.3-2).

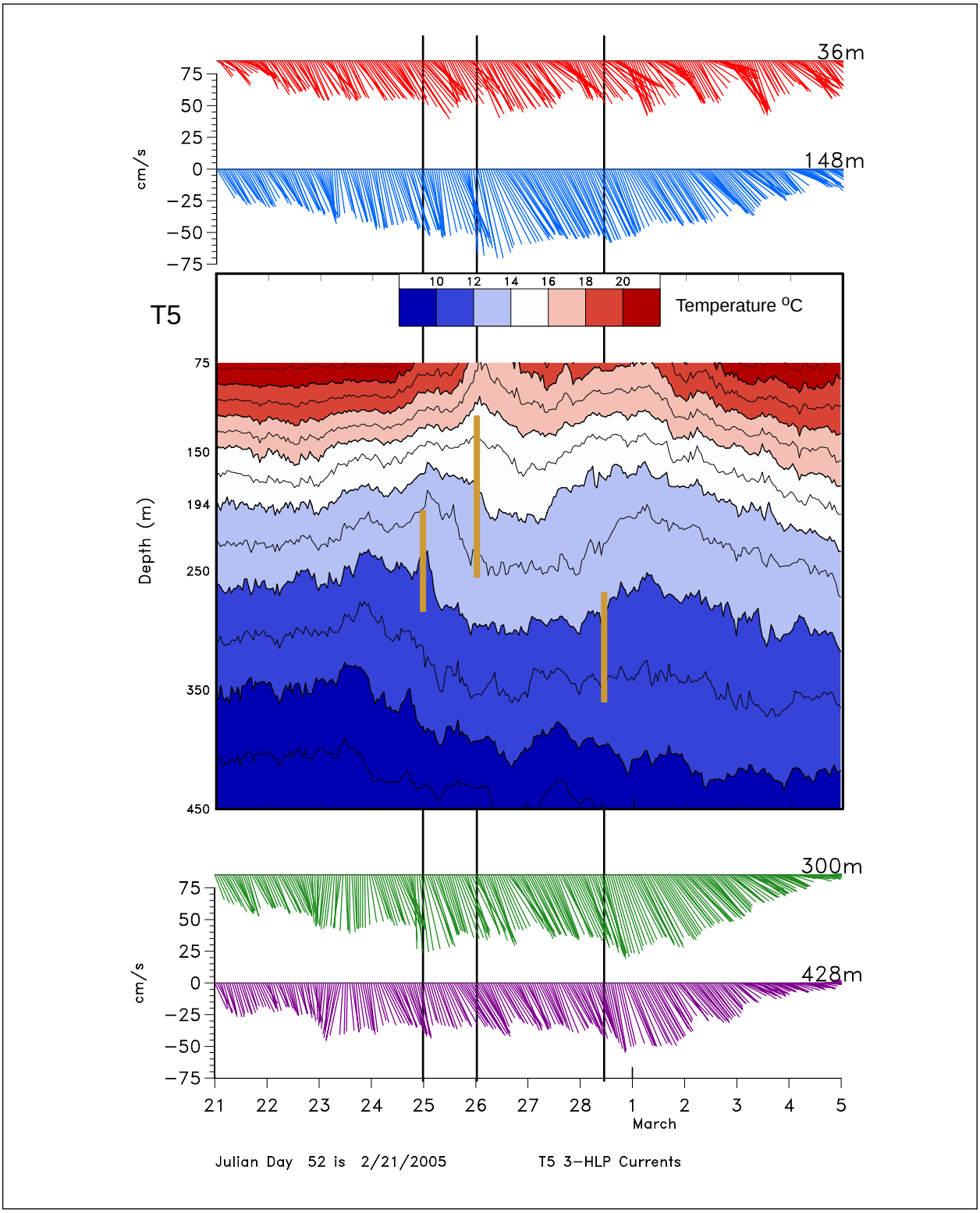

Figure 5.3-2. Unfiltered temperature-depth plot with 3-HLP hourly current vectors at selected depths at T5 for the indicated interval. The vertical lines mark the centers of the highest speed events discussed in the text. The gold vertical lines on the temperature plots mark the approximate verical extents of the cores of these jets.

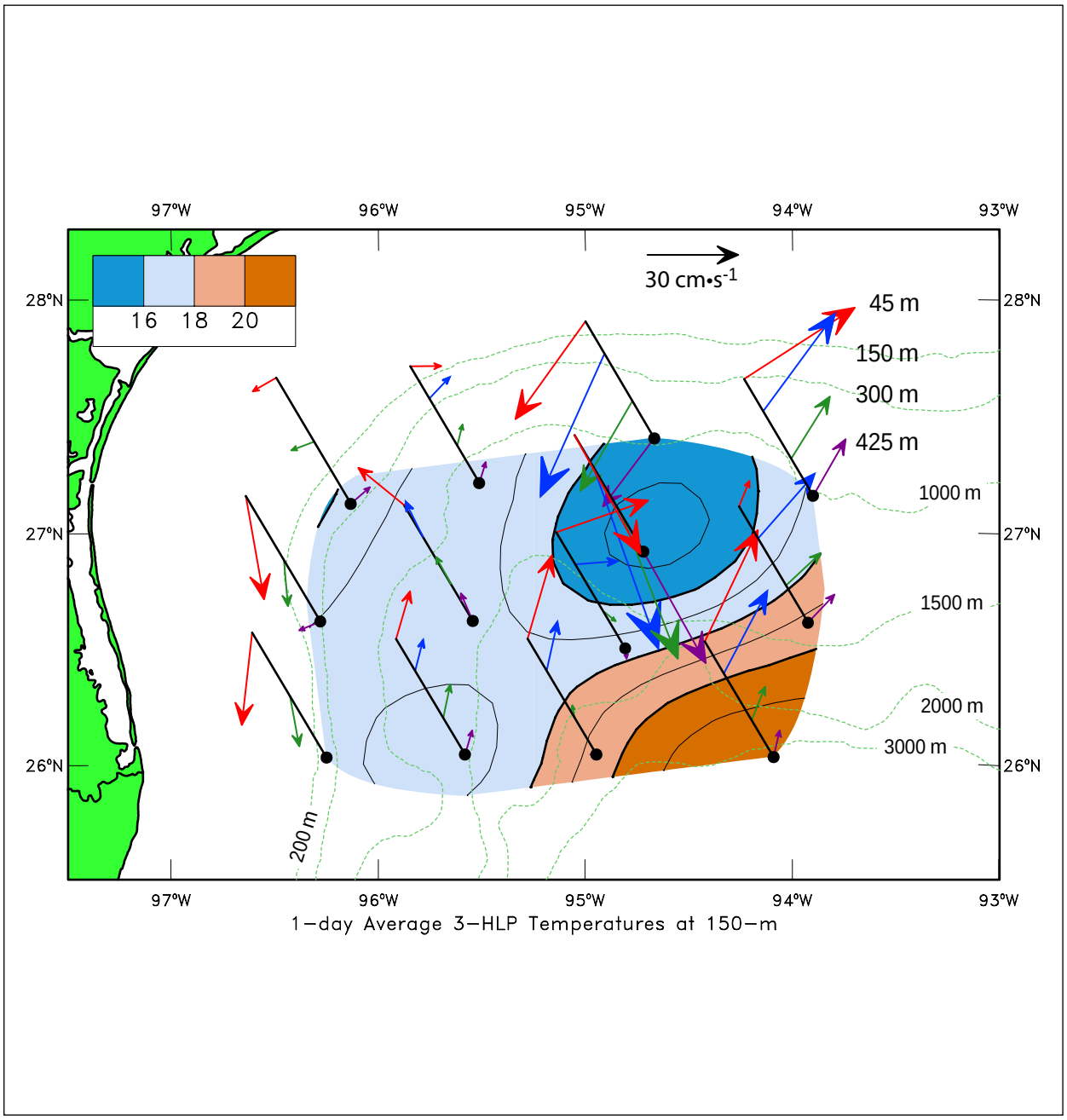

Figure 5.3-3. 1-day mean 3-HLP temperature at 150 m and currents at selected depths for February 26, 2005, 0000 GMT. The currents are plotted as pseudo- 3D profiles.

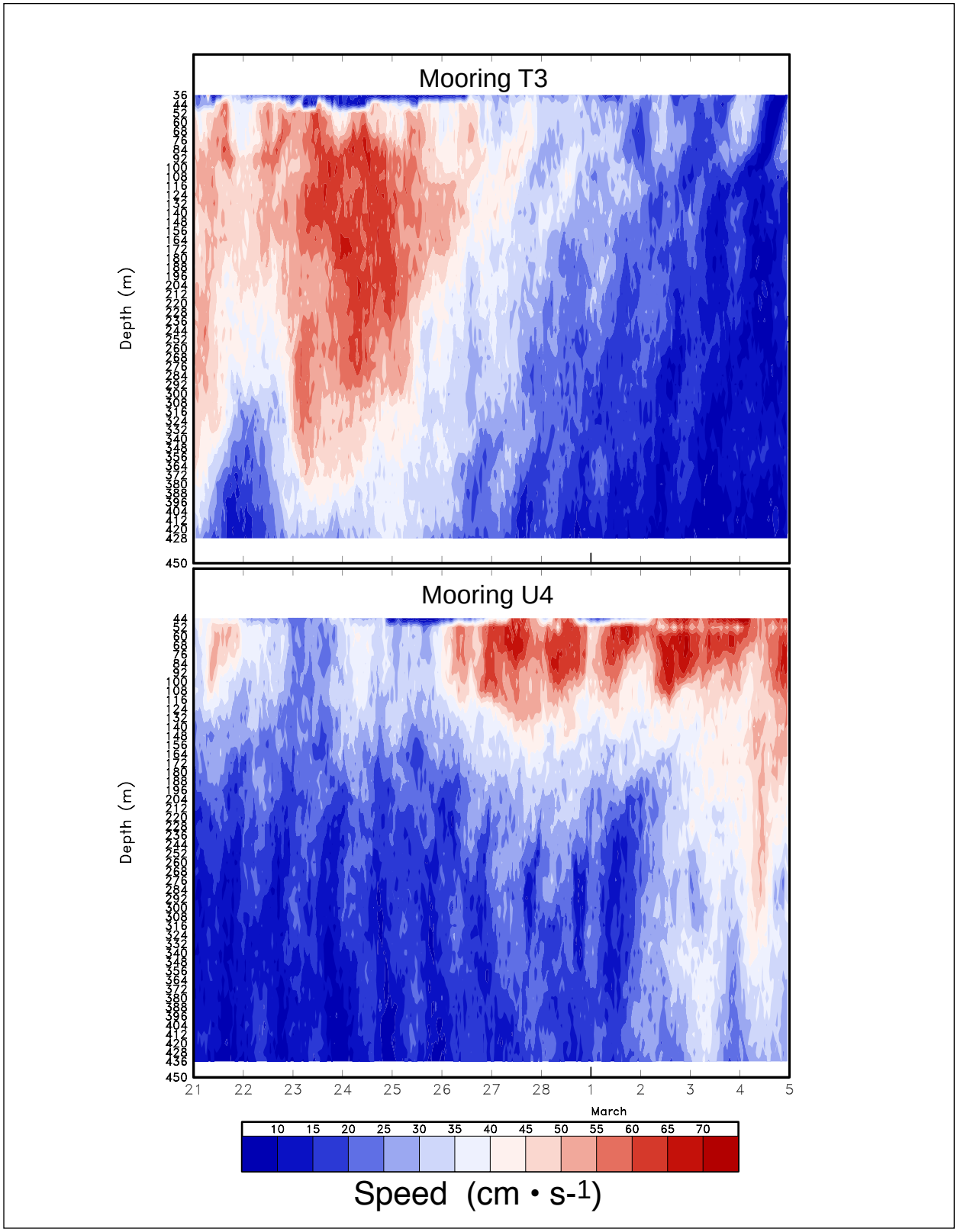

Figure 5.3-4. Unfiltered speed from the 450-m ADCP's at T3 (upper panel) and U4 (lower panel) for the February 2006 event.

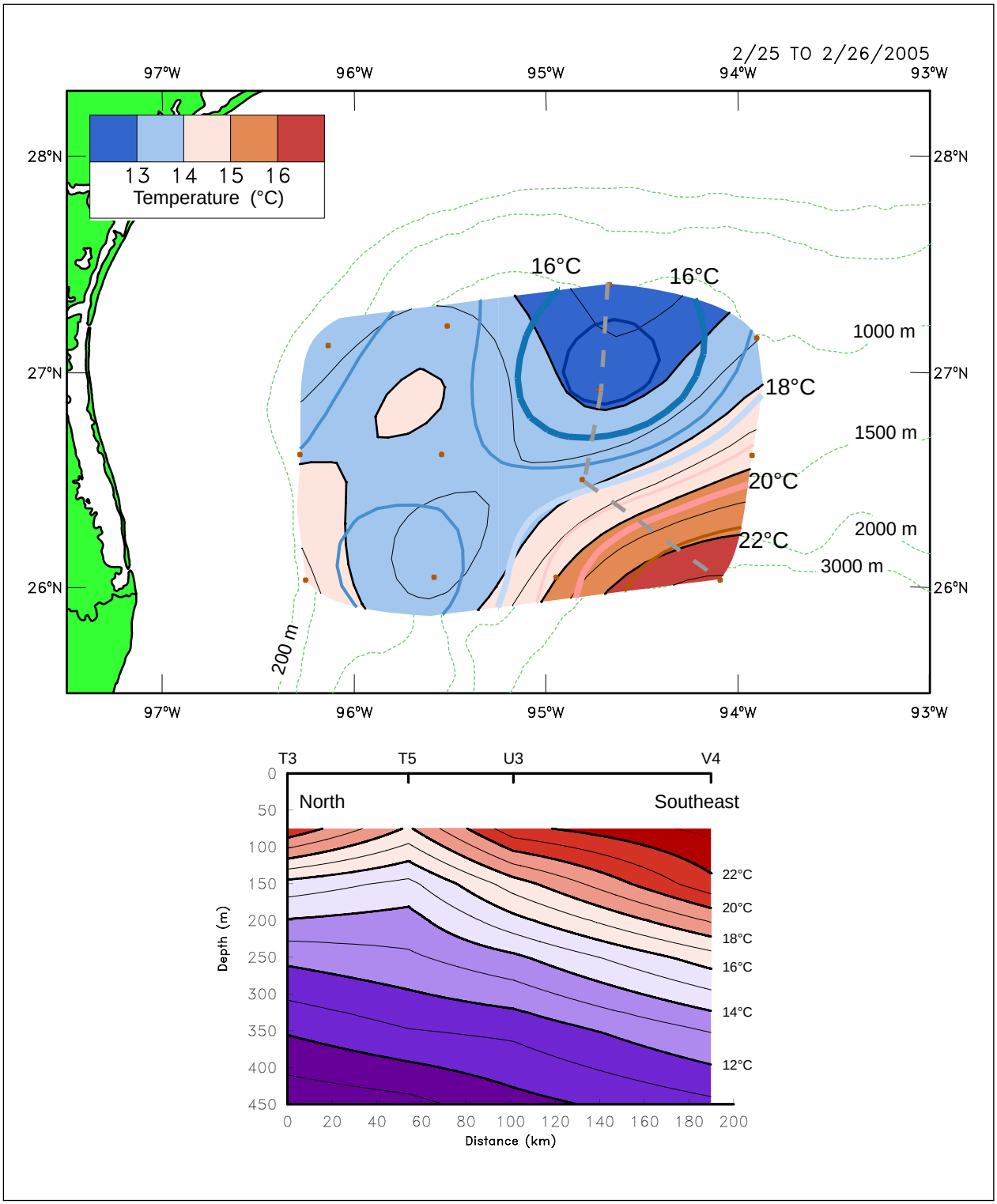

Figure 5.3-5. Top panel: 1-day mean 3-HLP temperature fields centered on February 26, 2005, 0000 GMT. The black filled contours and scale are temperatures at 250 m, and overlaid open colored contours are temperatures at 150 m. Bottom panel: 1-day 3-HLP temperature-depth section corresponding to the dashed gray line on the map.

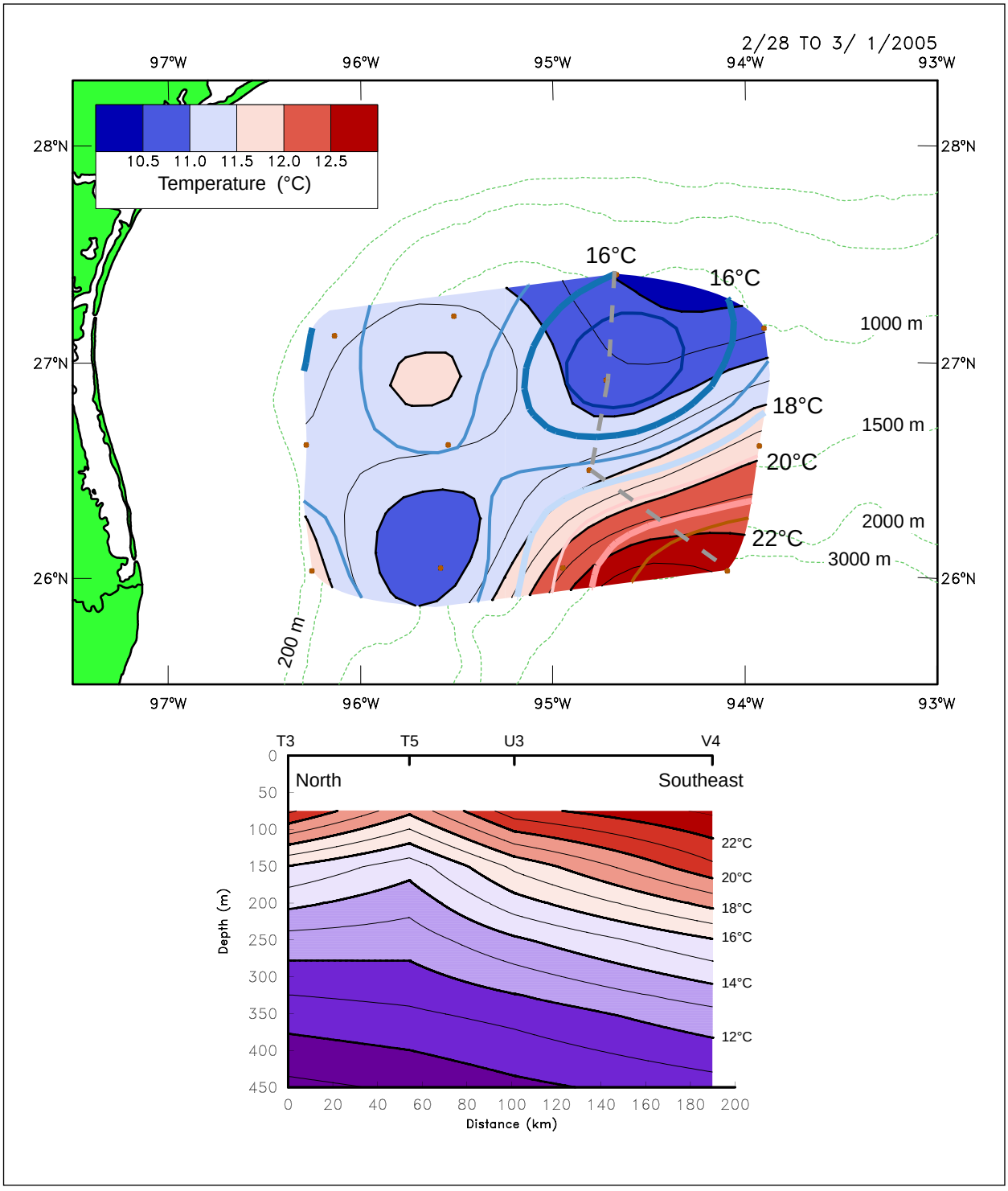

Figure 5.3-6. Top panel: 1-day mean 3-HLP temperature fields centered on February 28, 2005, 1200 GMT. The black filled contours and scale are temperatures at 350 m, and overlaid open colored contours are temperatures at 150 m. Bottom panel: 1-day 3-HLP temperature-depth section corresponding to the dashed gray line on the map.

The tilting of the rotation axis of a cyclone interacting with a larger anticyclone has been previously observed in hydrographic surveys of eddies. For example in the LATEX-C program, eddy Y's interaction with a slope cyclone (Hamilton et al., 2002), and eddy W_N's with another lower-slope cyclone (Berger et al., 1996), showed horizontal displacements of the cyclone centers with depth. Because velocity profile measurements were not made in these earlier studies, the resulting complex temperature fields could not be associated with subsurface jets.

5.3.2 U4, July 2004

The speed profile from U4 at the beginning of July 2004 is given in Figure 5.3-7. The subsurface jet persisted for about two days over the depth range 120 to 350 m. Speeds briefly exceed 70 $cm \cdot s^{-1}$ on 10 and 11 July. Thus, this U4 jet did not affect this site for as long an interval, and was generally deeper than the T5 jet discussed above. The hourly current vectors in Figure 5.3-8 again show flows with fairly constant directions towards the southeast, with a little more inertial activity in the upper 100 to 150 m than at T5 in February 2005. However, the subsurface flows were more similar to the T5 jet than being from a vertically propagating near-inertial internal wave.

The temperature evolution at U4 (Figure 5.3-8) shows the colder water of a cyclone moved over the site, and again there was a difference in the arrival times of the coldest water with depth. In this case the coldest water at 150 m, (i.e., at the top of the jet) arrived two to three days before the minimum temperatures at 450 m (i.e., at the bottom of the jet). Sequences of temperature and current maps show a cyclone moved into the array from east or northeast and interacted with an anticyclone in the center of the study area. Figure 5.3-9 shows the 250-m temperature field and daily averaged currents for the time interval of maximum subsurface speeds. Subsequent to 13 July, the cyclone moved off southwards in the direction of the clockwise flows of the anticyclone, towards deeper water. Between 8 and 12 July, U4 was clearly within the cyclone, similar to T5 in February 2005, and this seems to have been the interval when the cyclone was most strongly interacting with its neighbor to the west. The 150-m and 350-m temperature fields for 10 July are given in Figure 5.3-10 and show larger displacements of the center of the anticyclone with depth than the cyclone. However, movies of the temperature fields show that the upper layers of the cyclone moved into the eastern part of the array, perhaps influenced by the surface flows of the anticyclone, before the deeper parts, consistent with Figure 5.3-8. The result of tilting of the vertical central axis of both eddies was that east-west temperature gradients in the vicinity of U4 and U5 (Figure 5.3-10) were weakened in the surface layer and strengthened with depth because of the strong westward cold intrusion below 350 m. It is noted that flows around the anticyclone (Figure 5.3-9) were fairly depth independent in the upper 450 m, presumably because of the merging of same direction cyclonic and anticyclonic flows. Isolated warm eddies usually have strongly vertically sheared flows on their outer edges, but cyclones have fairly depth-independent flows in the upper layer (Hamilton et al., 2002). Thus, the currents at T3, T5 and V4 seem to be a mixture of both types of flow. Enhanced 250-m jet flows at U4 seem to have resulted from larger thermal gradients and had some consistency with geostrophy.

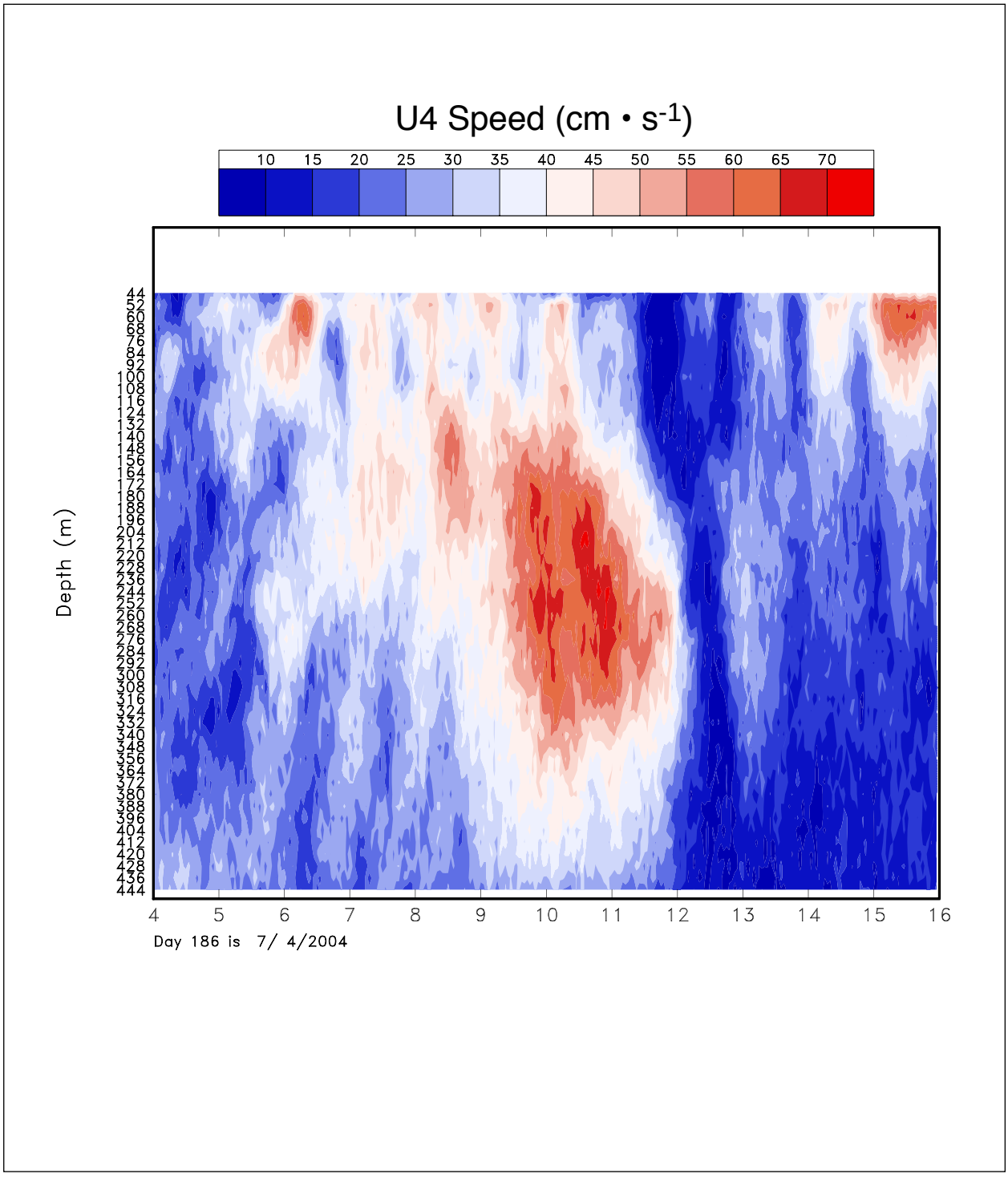

Figure 5.3-7. Unfiltered speed from the 450-m ADCP at U4 for the indicated interval.

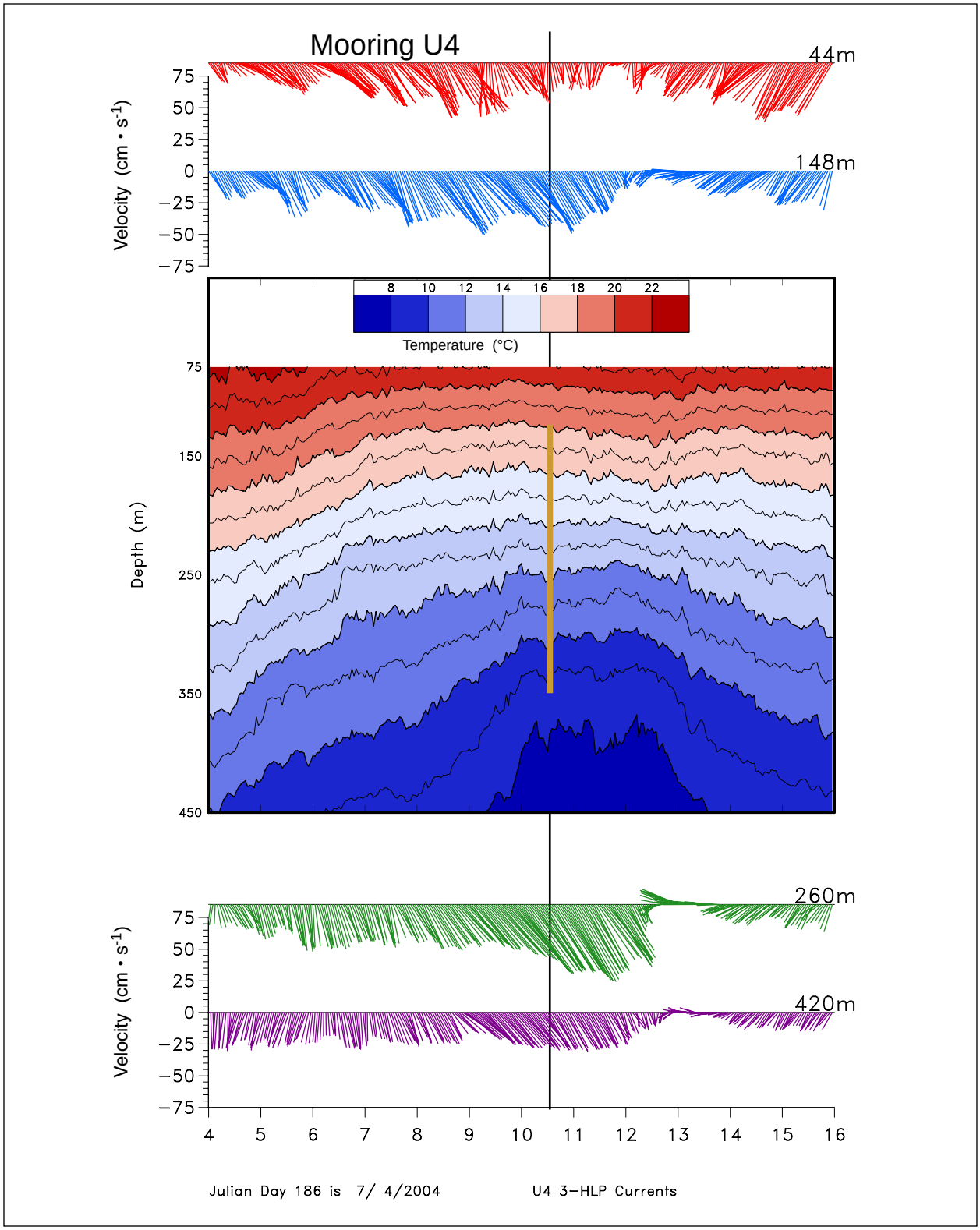

Figure 5.3-8. Unfiltered temperature-depth plot with 3-HLP hourly current vectors at selected depths at U4 for the indicated interval. The vertical line marks the center of the highest speed event discussed in the text. The gold vertical line on the temperature plots mark the approximate verical extent of the core of this jet.

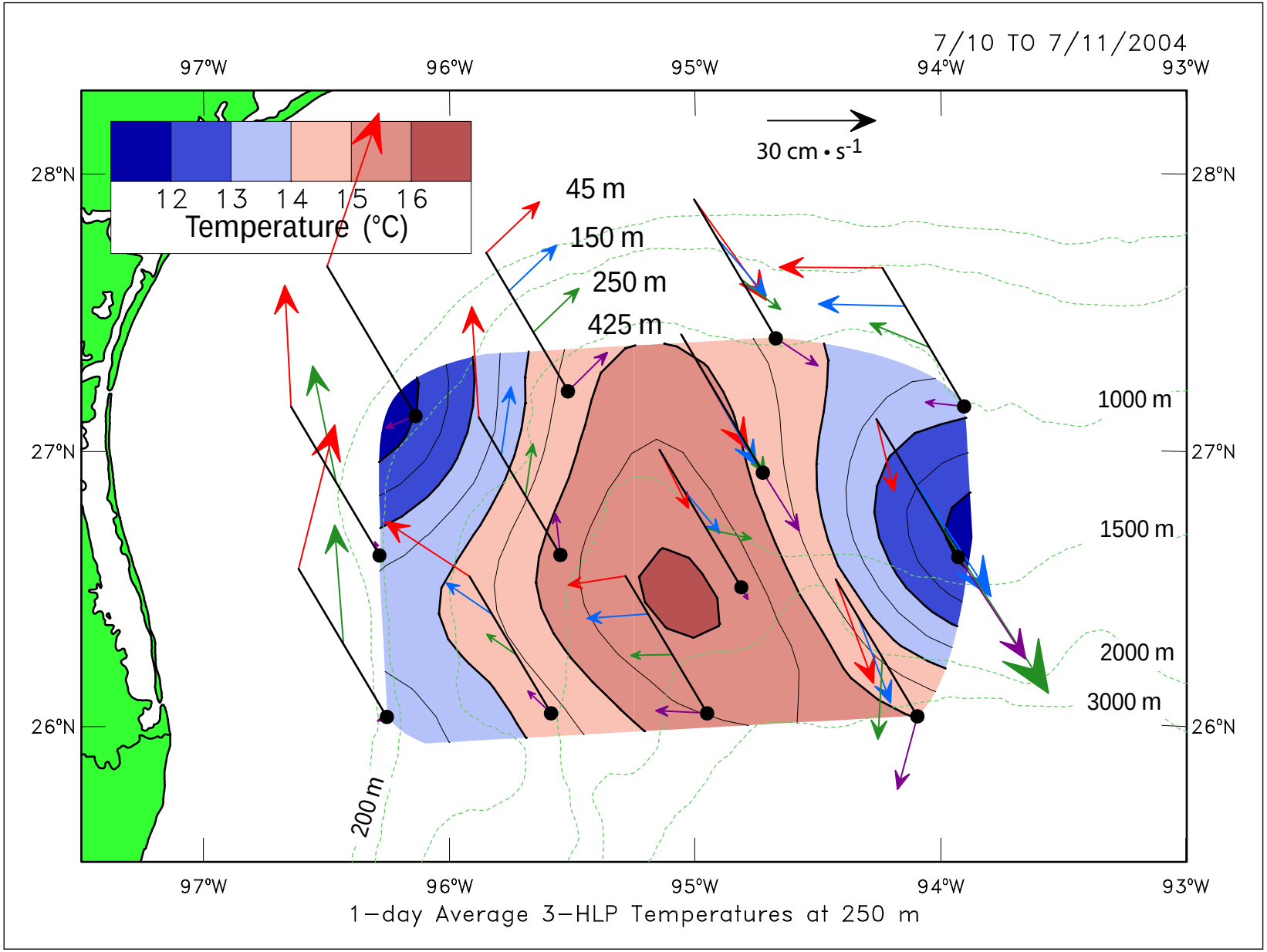

Figure 5.3-9. 1-day mean 3-HLP temperature at 250 m and currents at selected depths for July 10, 2004, 1200 GMT. The currents are plotted as pseudo-3D profiles.

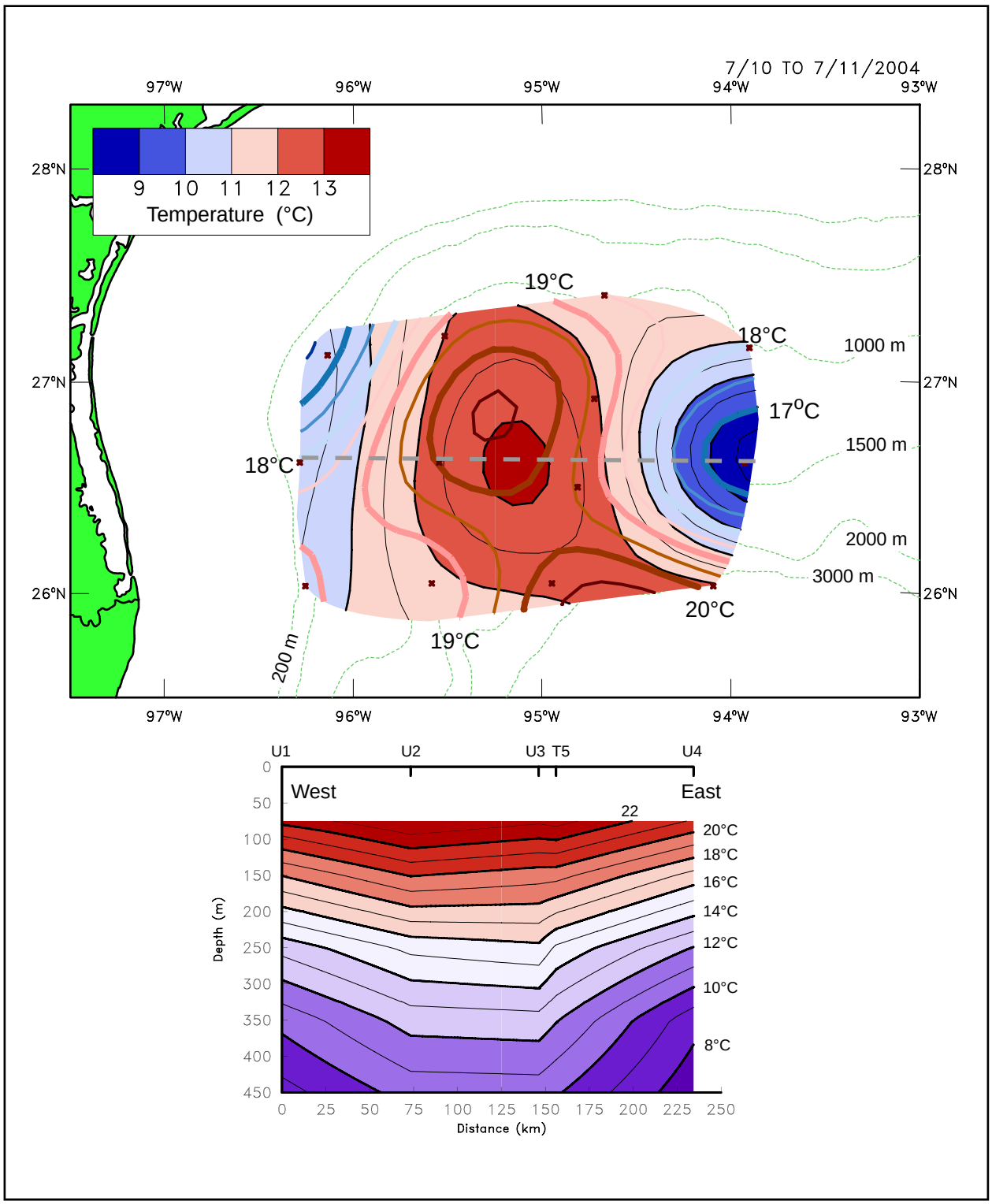

Figure 5.3-10. Top panel: 1-day mean 3-HLP temperature fields centered on July 10, 2004, 1200 GMT. The black filled contours and scale are temperatures at 350 m, and overlaid open colored contours are temperatures at 150 m. Bottom panel: 1-day 3-HLP temperature-depth section corresponding to the dashed gray line on the map.

5.3.3 W1, July 2005

The subsurface jet at W1 during July 2005 occurred in the lower half of the water column (Figure 5.3-11). Maximum speeds of ~ 60 $cm \cdot s^{-1}$ were at about 300-m depth in a 450-m water column. This is different from the two cases discussed above, which were in water depths of 1000 m or greater. Temperature measurements were only available at the depths of the ADCP's for the moorings in the Mexican sector, and this event took place just after the American sector moorings were retrieved. However, temperature records at W2, W4 and W5, though at slightly different depths, had little temporal variability during this interval, while temperatures at W1 were mostly colder than W2 and W4, even though the instrument was at a shallower depth (434 m versus 500 m or greater - Figure 5.3-12). Remotely sensed images indicate that W1 was on the southwest edge of a warm eddy that was impinging on the Mexican slope ~ 26°N. There is some suggestion that there may have been a small cyclone between this anticyclone and the slope. Even if there was not a cyclone between W1 and the shelf break, the cold temperatures are consistent with uplifted isotherms around the periphery of a warm eddy. Thus, the subsurface jet was probably between the up-sloping thermocline of the eddy and the sloping bottom. Flow direction at W1 during this event was to the north (Figure 5.3-12), and the highest currents at 300 m occurred when temperatures near the bottom were at a minimum of ~ 7.5°C on 10 July. This temperature would be typically at ~ 700 m in the center of a western basin anticyclone, and such a large upward displacement may indicate the presence of a small cyclone or frontal eddy moving northwards through W1. The daily mean 3-HLP currents for all the active ADCPs, on 10 July 2005, is given in Figure 5.3-13. W1 had the strongest currents and the flow directions at W1 and W2 were consistent with being in a warm eddy with W2 being closer to the center. Flows at W4 and W5 were also northwards but were quite weak with almost no depth structure.

Oey and Zhang (2004) proposed a model of an anticyclone impinging against a steep slope that would generate a subsurface cyclonic flow to the south of the anticyclone (for a western slope). This model would predict a southward subsurface jet against the slope, which is opposite to the observations at W1.

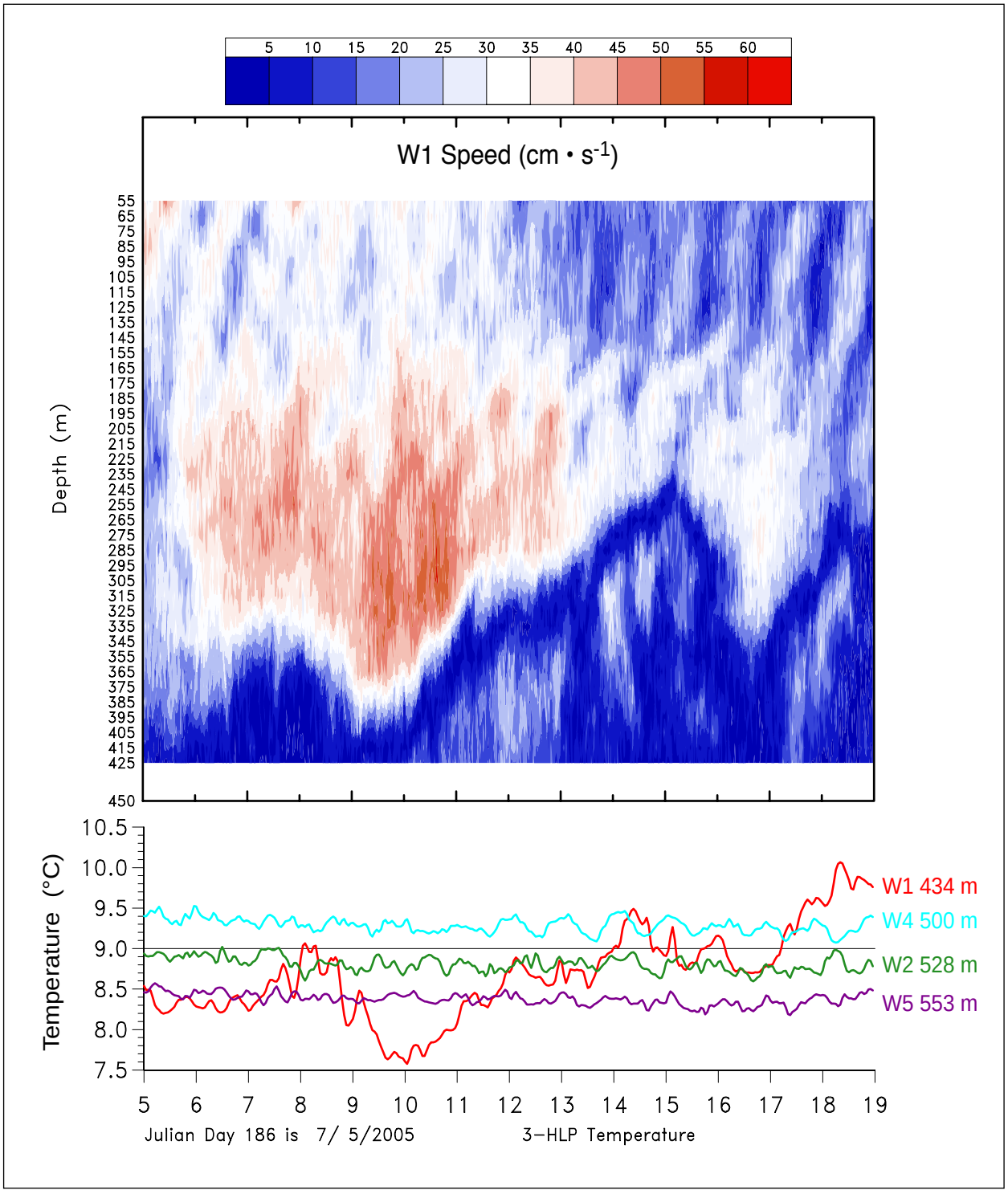

Figure 5.3-11. Unfiltered speed from the 450-m ADCP at W1 for the indicated interval, along with 3-HLP temperature records at the indicated depths and locations.

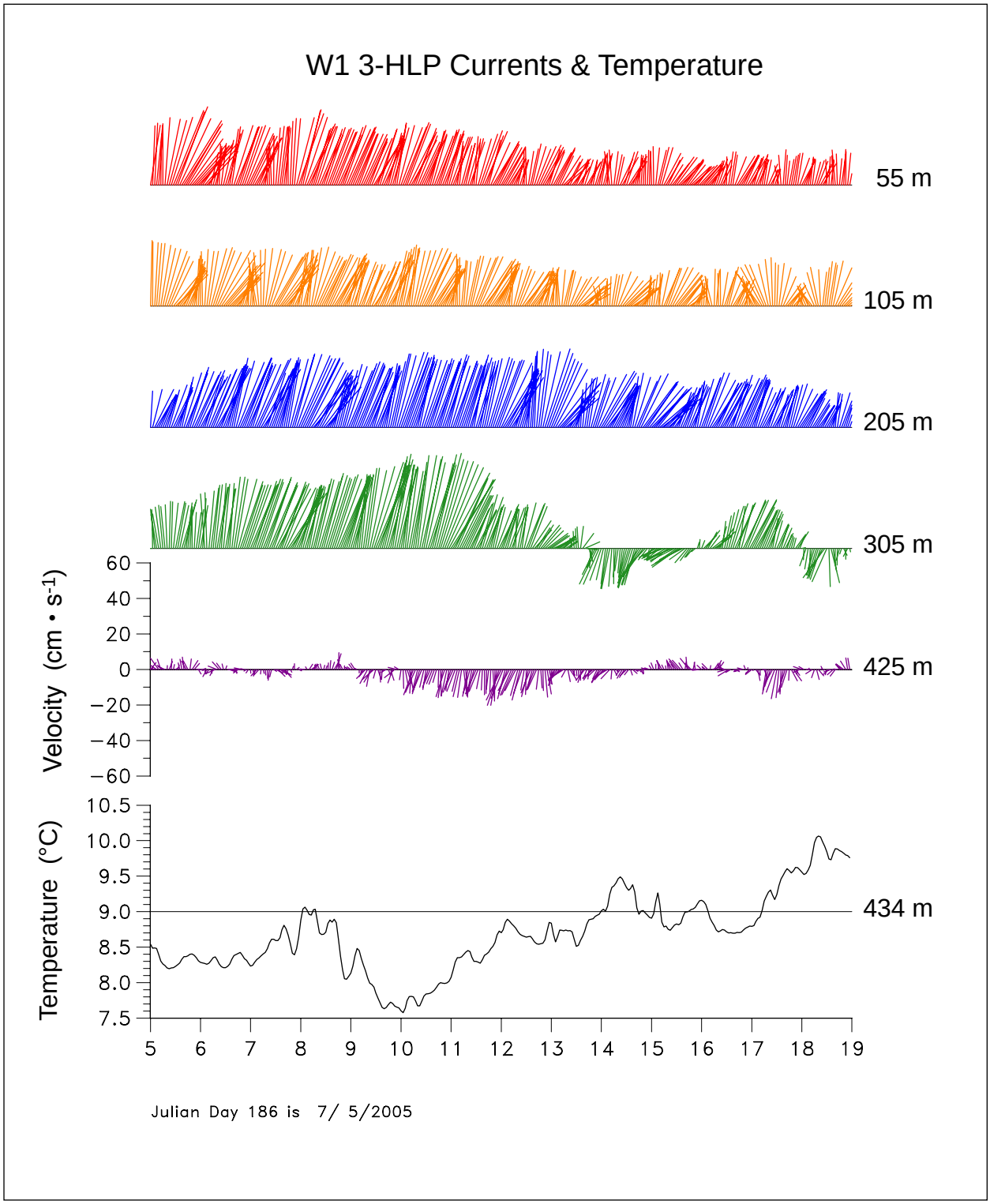

Figure 5.3-12. Hourly current vectors and temepratures from 3-HLP ADCP records at seleted depths at W1 for July 2005.

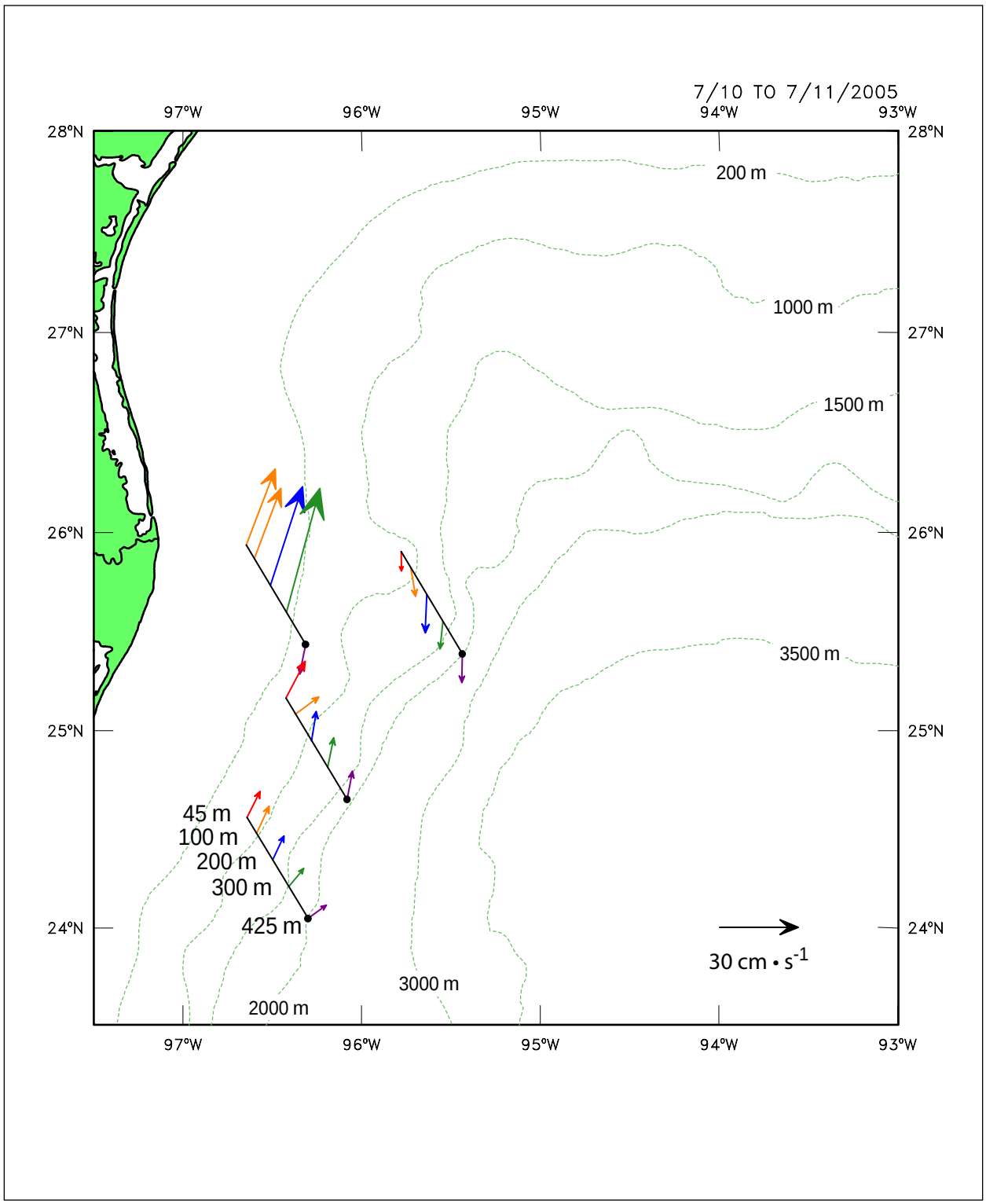

Figure 5.3-13. 1-day average 3-HLP velocity vectors at selected depths for July 10, 2005, 1200 GMT. The vectors are displayed as pseudo-3D profiles.

CHAPTER 6 SUMMARY AND CONCLUSIONS

6.1 Introduction

This chapter provides a general overview of conditions and processes identified as occurring in the Northwestern GOM during the field measurement effort described in the earlier chapters of this report. What is not included below is a presentation of details. For such a comprehensive description, the reader is referred to the prior report material.

Also provided is a brief list of recommendations for additional GOM field measurements that are based on the present study and other recent observations that will lead to a substantial expansion of our understanding of key ocean processes and features. In turn, this will support a process-based characterization of physical oceanographic conditions of importance to development of deepwater oil and gas resources. This expanded knowledge should also substantially enhance numerical modeling of circulation and transport, which will provide a basis for improved oil spill analyses that more accurately reflect and incorporate our increasing understanding of the varied and complex ocean conditions in the GOM.

6.2 Upper-Layer Circulation Patterns

The LC and associated mesoscale-eddy fields dominate the upper-ocean circulation in much of the deepwater of the GOM. Aperiodically, the LC extends northward into the GOM basin. At times during such an extension, a portion of the northwest LC is "pinched off" by processes that are not fully understood, and a closed clockwise rotating (anticyclonic) circulation feature is formed, a LCE. Over time, these LCEs generally translate westward into the western GOM basin (Figure 1.2-1). In migrating westward, LCEs follow a variety of paths and undergo changes that are key factors affecting western GOM circulation patterns and water mass characteristics. LCEs also spawn features as they move to the west and encounter the western GOM continental slope. Second and lower-order eddies (both cyclonic and anticyclonic) result from the complex pattern of LCE interaction with the continental slope and with other eddies. The result of these patterns is a western GOM that can be rich with eddies with differing rotation senses, spatial scales and ages. These eddies can have a significant influence on exhange between the shelf and slope, in particular along the western GOM margin.

A variety of satellite remotely-sensed images has been available to support the present program. These include SSH, sea-surface temperature and ocean color. These can be used both individually and jointly to help identify key ocean features and associated circulation and transport. Each sensing variable has particular strengths which, in composite, can provide substantial insights to surface-layer conditions in the western GOM.

Using altimetry in conjunction with a 17-cm SSH criteron, the time-dependent location of the LC boundary was documented. Establishing this nominal LC boundary allowed the computation of a number of associated metrics such as LC area, length, and northern, eastern and western extent. Use of the elevation based boundary criterion also allows determination of LCE separation. The criterion defining when separation occurs is a substantial change in the LC area contained within the 17-cm surface contour that enters the GOM through the Yucatan Strait. LCEs can also be

quantitatively defined by appropriate surface-height values, that typically decrease as the eddy translates westward. Defining the evolving SSH boundary of LCEs provides a quantitative basis for evaluating such things as the time-dependent, eddy-center location and hence the eddy migration path. Locations of LCE boundaries help identify when eddy-eddy interaction may be occurring, as well as when eddy-bathymetry interaction might be a consideration in eddy behavior and dynamics.

Since 1993, satellite-based SSH has been used to identify 20 eddy-shedding episodes (Table 3.1-1). It is of note that, based on analyses of altimetry records, only twice in 14 years did the LC extend westward past 92°W and at no time did it extend past 93°W. Thus, in the western GOM, upper-layer, LC influence is transmitted to the area via LCEs and related features.

Using historical paths of LCEs determined from satellite altimetry, westward movement of eddy centers passed over much of the area of the western GOM. Some LCEs have even exhibited short intervals of retrograde motion. Using two different averaging schemes, similar smoothed mean paths of eddy centers were defined that are directed slightly south of west with much of the related circulation in the western GOM being south of the EEZ of the US. Over the available 14-year record, on three occasions, altimetry was able to document the splitting of LCEs into two separate anticyclones as they moved westward. Using altimetry, the life span of all altimetry defined LCEs was determined and ranged from 84 to 601 days with a mean life span of 284 days (~ 9.5 months). With altimetry, eddy tracking ended when the central SSH of mature LCEs could not reasonably be differentiated from the background SSH. Hence, the life span of a LCE was not a function of circulation patterns, but rather a function of the ability of the processed altimetry to resolve central elevations as they decreased with eddy decay.

Although not an endpoint for most LCEs, nor even a portion of the trajectory of many LCE centers, the NW GOM study area has been observed to be a region rich in eddies (both anticyclonic and cyclonic) over a broad range of spatial scales (Berger, 1996). An evaluation of SSH minima showed that many cyclones were associated (paired?) with anticyclones. The conclusion from the historical record is that the most energetic cyclones and anticyclones over a range of scales were associated with or derived from LCEs. Thus, through an energy cascade, the LC is a dominant source of eddy energy in the extreme northwestern portion of the GOM.

During this study, between March 2004 through October 2005, three LCEs affected the upper-ocean circulation in the western GOM. These were, in chronological order, Titanic, Ulysses and Vortex. Eddy Titanic followed a more southerly path across the GOM, staying well south of the study area. Once in the western GOM and interacting with the western continental slope, Titanic rapidly dissipated and became indistinguishable from background SSH after one month. While this LCE appeared to undergo a splitting event with each portion eventually moving separately, there was no evidence that the induced circulation associated with Titanic impacted the American sector of the NW GOM.

Ulysses (life span of 237 days with 125 being after splitting) had an initial area of 68,633 km^2 with a maximum SSH of 42 cm. In terms of area, Ulysses was the second largest eddy documented in the 14-year altimetry record. In its life span, Ulysses both merged with another anticyclone in the western GOM and later split into two definable anticyclones. Whether or not

the subsequent splitting was associated with the prior merger is not known. U2, as the more northern of the divided anticyclone is called, moved into portions of the present program field measurement array. The splitting process took about two months and coincided with Ulysses colliding with a strong cyclonic eddy located against the continental slope centered at 25°N (Figure 6.2.a). This history of eddy-eddy interaction and eddy-bathymetry interaction was a nonlinear process that substantially reconfigured the eddy field in the NW GOM. A comparison of altimetry with measured temperatures and salinities, which can identify the presence of SUW, supported the presence of U2 within the study area. U2 was the dominant upper-ocean event affecting the study region during these field observations. This influence was intermittent in the sense that as the eddy and possible daughter eddies migrated in the dissipation process, they moved into and out of the fixed instrumented study area.

Eddy Vortex had four partial separation events prior to parting from the LC and traveling west southwest. On reaching the western continental slope, it interacted with a slope cyclone resident in the area south of the Mexican Sector moorings. As a result of interacting with both bathymetry and the cyclone, Vortex's central elevation diminished by 50% in the one month after this interaction began.

Averaging of upper-layer temperature and velocities over the study interval (Figure 3.4-1a,b), showed a pattern consistent with a LCE over the NW slope flanked by cold features to the northwest and northeast. The mean currents were generally consistent with patterns one might expect from the presence of an anticyclone over the NW slope. At each measurement site, the vertically-sheared mean current profiles tended to be in the same direction through the upper water column. Current magnitudes decreased with increasing depth as did the velocity variance. Results of CEOF analyses show that the first mode generally accounted for 85% or more of the total variance of the depth profile at a given location. The CEOFs show little variation in direction with depth and tend to align with the isobaths on the upper slope, but have no preferred direction elsewhere – generally in deeper water. Using the above CEOF first modes, kinetic energy spectra were computed to partition the associated first mode variance according to the frequency at which it occurred. These computations show that the greatest fluctuating energy (largest variances) were at lowest frequencies, which indicates that 18-month records may not have been of sufficient duration to resolve confidently the full range of velocity periodicities occurring at the sites. This might be expected since the primary energy source is LCEs, which are shed at intervals ranging from 6 to 18 months.

Using PIES-based SSH, gravity and the Coriolis parameter, the surface stream function was computed. This showed that for the 8-month PIES deployment, the mean upper-ocean currents were mainly anticylonic and weak (< 20 cm·s^{-1}). There was a general agreement between PIES-based mean current patterns and means from directly measured currents. Some differences between these two types of measurements can be attributed to differing spatial resolution and to measurements not being over coincident intervals. Since they were not yet deployed, PIES-based means did not include the effects of the large, vigorous LCE that was in and adjacent to the study area from June-October 2004.

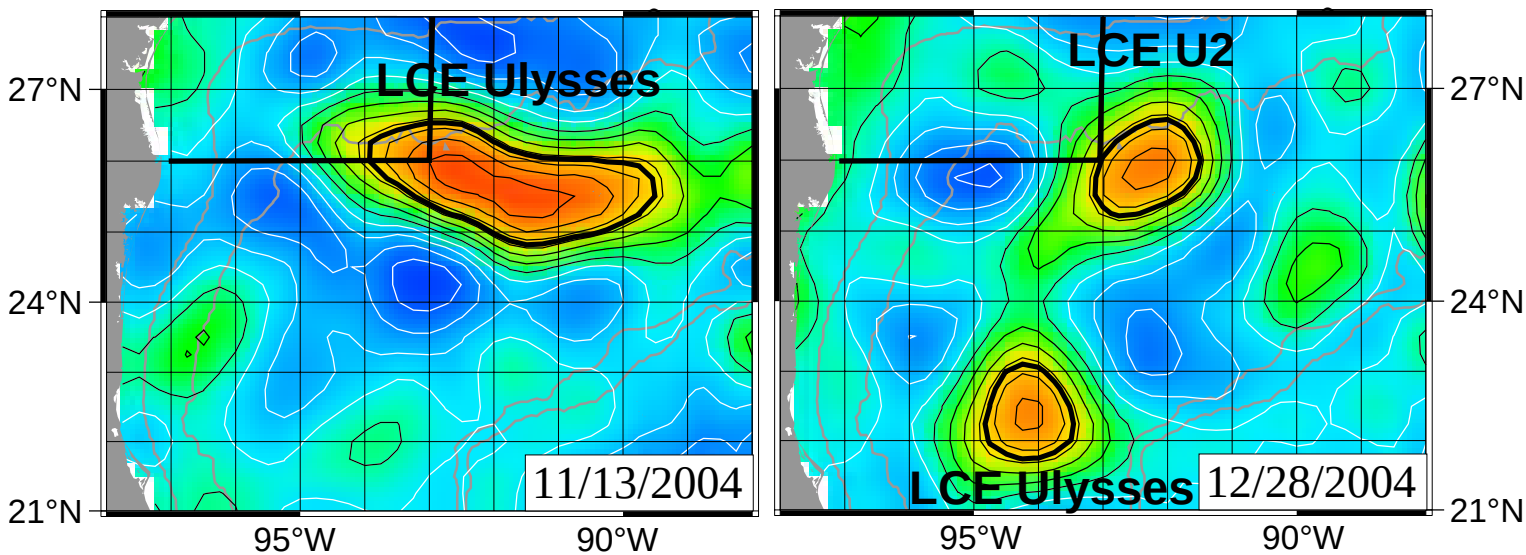

Figure 6.2-1. Configuration of LCE Ulysses pre- and post splitting. Note that the splitting was completed over approximately 1.5 months. Prior to splitting LCE Ulysses circulation patterns were affecting the SE corner of the study area. Following the split, altimetry indicates that U2 circulation is only marginally within the study area.

Using spatially averaged surface kinetic energy from both PIES and moored instruments, four "events" lasting 10 to 20 days were identified and associated with individual eddy features or combinations of eddy features, in particular U2 and a cyclonic eddy in February – March 2005.

Using only moored instruments in one instance, and both PIES and moored instruments in another, eddy-bathymetric interaction was examined and characterized. Because substantial eddies (e.g., LCEs) did not generally extend below a nominal depth of 1,000 m, the eddy-bathymetric interaction discussed was a process confined to the upper layer of the water column. Two case studies document (Figure 3.5-1) conditions occurring when eddies (cyclonic and anticyclonic) were interacting with the adjacent slope. In May 2005, evolution of a cyclone-anticyclone pair was documented and described. In this same time frame, a similar cyclone-anticyclone pair was within the measurement array. These two instances provide a data set appropriate to describe the apparent evolution of the features, however, information for defining the explicit dynamics of the situation could not be developed.

6.3 Deep-Layer Circulation Patterns

Previous studies provided insights of how lower-layer currents are linked to TRWs (e.g., Hamilton, 2007). These studies point to variations in the character of the TRWs depending on the location, in particular, the E-W location and position relative to the Sigsbee Escarpment. Some of the character of upper-layer features such as LCEs and LCFEs may be linked to the initial vertical transfer of energy from the upper to lower layers. More specifically, the shortest period TRWs seem to originate in the eastern GOM. Observations to date seem to indicate that bottom bathymetry is such that these short-period TRWs are present only in the area near the base of the Sigsbee Escarpment in the central GOM in the vicinity of 90°W (the Green Knoll area). East and west of this central area, TRWs have been documented but have considerably less vigorous currents and longer periods. Numerical ray tracing along a TRW-sustainable path suggests limited connection between the NW GOM study area and the eastern basin of the GOM. Ray tracing did suggest that some of the velocities in the study area may have been due to locally generated, shorter-period TRWs. In the NW GOM study area, near-bottom currents were consistently stronger at sites in greater water depths at the base of the Sigsbee Escarpment. At these same sites, near-bottom current fluctuations were more energetic than those measured at moorings located in shallower depths above the Escarpment.

In this study, use is made of terms "eddy" and "wave." Depending on the character of a "wave", it may appear to have a closed or an open core of circulation. As an initial approximation, the difference in appearance is a function of the ratio of the swirl velocity (U) to the translation velocity (C), i.e., U/C. If the swirl velocity is greater than the translation velocity of the wave, $U/C>1$, then the streamlines of the associated flow field close and contain a core whose mass and properties are largely carried with the wave. If $U/C<1$, then the wave moves through the ocean without a net transport of mass - just momentum. If more than one train of TRWs occurs at a site, then the sum of the waves in an area can produce closed streamlines as might be used to describe what is often referred to as a deepwater "eddy."

As found in prior studies, for TRWs, the lower-layer velocities were weakly sheared below a water depth of approximately 1,000 m such that velocity increases with depth (bottom intensification). Although observations in this study exhibited some variation from this canonical deep-velocity structure expected with TRWs, the general pattern was found. There was speculation that interaction of the waves with the steep bathymetry of the Sigsbee and Perdido Escarpments (Figure 1.2-1) may have affected or altered some aspects of the TRW-based velocity fields.

On first examination, the upper and lower-layer currents in the study area appear to have been uncoupled. However, it is possible that locally and remotely generated processes may obscure vertical linkage between layers. A vorticity conservation argument was developed in which deep relative vorticities were generated to balance vertical stretching. Such an approach showed an upper-layer cyclone entering and moving through the measurement array. This cyclonic motion stretches the lower layer creating a deep cyclone.

A RAFOS (Lagrangian) drifter deployed at 2,000-m depth during the earlier MMS-funded Exploratory Study moved into the present study area and executed three looping trajectories. Assuming that the drifter path was the result of a deep eddy, kinematic analysis was applied to each of the loops. This showed that the eddy had a nominal diameter of 40-50 km and had a rotation period that increased from 12 to 18 days as the eddy moved westward closer to the western slope. The scale of this eddy when compared to the spacing/separation of moorings in the NW Gulf Study suggests that instruments on the deployed moorings would not have been able to make a coherent characterization of the feature - the eddy could fit between moorings and hence the motion at the separate moorings would not have been correlated as might be expected if both were simultaneously being affected by some portion of the same eddy.

6.4 High-Frequency Currents and Jets

6.4.1 Inertial Currents

Possible sources that initiate inertial waves include impulses at the water surface - this can be either application of, or change in direction of applied wind stress. The variability of the timing and location of the application of a surface-water impulse means upper-layer inertial currents can be highly spatially variable. Winds associated with the passage of winter cold fronts can impart momentum to surface water and initiate a clockwise-rotating current that propagates vertically downward through the water column.

The inertial wave energy propagates vertically downward from the surface, although the phase propagates upward (see Figure 5.2-2). In this example (Figure 5.2-2), inertial currents produced by passage of a front had the rotary current pattern propagating 200-250 m in 12 to 15 days. At the same site, at 350-m depth, no substantial inertial currents were measured, however, there appears to have been vertical motion causing isotherm depth variations.

Variations in the magnitude of wind forcing occurred for winter frontal passages such that sites further south had reduced forcing (magnitude and duration) and, as might be expected, a lower inertial response in the southern portion of the study area. Results suggest that the horizontal

scales of inertial variability were on the order of the mooring spacing in the east-west direction and much less than the spatial scale of wind forcing that initiated the inertial motions.
Hourly time series of PIES observations of acoustic travel time were also used to identify near-inertial signals. In this approach, the inertial signal is contained in fluctuations of isotherms, more specifically the thermocline. These analyses show bursts of energy in pulses that last 15-30 days (see Figure 5.2-16). These analyses did not reveal a strong seasonal dependence, however, there was a tendency for the strongest events in each record (derived from data on each PIES) to occur in winter. When evaluated in terms of the position relative to mesoscale circulation features (e.g., LCEs), a consistent pattern of enhanced motions is revealed. This low-mode inertial variance differs in magnitude and horizontal structure from that estimated from EOF evaluation of velocity records made by sensors on the moored arrays. The PIES-based and velocity-based observations of inertial waves are both affected by their location within mesoscale features such as LCEs.

Background relative vorticity has both vertical and horizontal gradients caused by the mesoscale eddy field, which results in variations in the effective Coriolis parameter, f_e. These variations in f_e allow rapid propagation or trapping of inertial waves. An examination of inertial response indicated that locations on the north and south sides of an anticyclone had relatively large amplitude inertial waves/high inertial wave energy, while the eddy center and the cyclone on the southern edge of the anticyclone had relatively low inertial wave energy.

6.4.2 Subsurface Jets

For this discussion, jets are defined as local or vertically isolated horizontal flows with maximum velocities of greater than 50 $cm \cdot s^{-1}$ (nominally one knot). Typically, these jets are identified as occurring at depths of 100 m to 300 m below the water surface as described by DiMarco et al. (2004). Internal waves that may satisfy these general criteria are not the focus; rather interest is in relatively isolated features. During the NW Gulf Study, jets satisfying these criteria were documented three times with two of the three instances occurring in deep water (>1,000 m). The third event was at a mooring in only 450 m of water depth.

One jet episode occurred at mooring T5 (Figure 1.2-1) located on the 1,500 m isobath. The currents were measured with an upward-directed ADCP positioned at 450 m below the surface. A contour plot of the current speed (magnitude of the current vector) in the upper 428 m is shown in Figure 5.3-1. At three different times over a nominal six-day interval, speeds exceeded 70 $cm \cdot s^{-1}$ within the depth interval of 100 - 350 m. During this multi-day interval, these maximum speeds were localized in that lower speeds occurred both above and below the jets.

A possible explanation for this feature is suggested based on the evolving temperature structure at mooring T5. It appears that a cold cyclone and warm anticyclone were interacting at T5. Typically, jets occurred when isotherms at the depth of the jet episode were diverging, often as the result of the cyclone moving into the area and causing local cooling at the level of the jet.

6.5 Recommendations

The field and remotely-sensed observations acquired in this program provide a complete and well-designed database with which to develop characterizations of current patterns and processes in the NW GOM. Evolving upper-layer circulation patterns and processes that were largely related to the migration and dissipation of LCEs were fairly well resolved. The resulting description and discussion help to resolve some of the dynamic patterns associated with LCEs as they move across the GOM, interact with and sometimes generate other eddies, and interact with the adjacent continental slope. The combination of fixed moorings and PIES provides compatible observations, that when taken as an integrated database, allow characterization of the sequence of many flow patterns that were occurring, as eddies moved into the NW GOM. It is of note that most of the PIES and moorings were above the Sigsbee Escarpment, and hence may have been somewhat insulated from such features as TRWs that moved westward along the base of the Escarpment. With this increased knowledge of current patterns, consistent and recurring kinematic features may be more confidently resolved and described.

The documentation of high-speed jets during this study establishes increased validity of their existence – which is a significant step. Based on prior reports from the oil and gas industry, these features can have an important impact on deepwater operations. Now that they have been more confidently documented and described, they may reasonably be part of a future experimental measurement design.

As described in the Introduction to this report, the NW GOM study is one of several non-concurrent, MMS-funded measurement programs that are helping define a rationale basis for the measurement locations and the spatial and temporal scales that need to be resolved. Knowledge of these scales will support design of a comprehensive study of upper and lower-layer flow patterns that are linked directly or indirectly to the LC and LCEs.

A key recommendation is for a field measurement program that includes sufficient spatial coverge to provide well-resolved characteristics of the LC and related LCEs, and larger boundary eddies that move along the edge of the LC and LCEs. Such a study of the "source region" for many of the dynamic features that transport mass and momentum across the GOM and into western GOM, will provide information on a key upstream condition. In conjunction with this upstream condition, additional observations need to be made along the trajectories of eddies as they move westward and are modified as they interact with other eddies and the shoaling bathymetry of the bounding continental slope. Because the time interval of LCE shedding is 6-18 months, these coordinated measurement programs should be of sufficient duration that at least two eddy shedding cycles and subsequent translation to the western GOM are completed. This duration, should at a minimum, be 36 months. The prior Exploratory Study in conjunction with the present study helps emphasize the significant role that the Sigsbee Escarpment has in affecting paths of eddies and TRWs (in particular the latter). Thus, there should be coordination of a LC study with observations further west along this important bathymetric feature.

The combined use of moored arrays supporting current measurements as well as C/T observations has proved to work effectively with PIES. In turn, the PIES and satellite altimetry are proving to be mutually consistent and hence supportive of an integrated characterization.

Certainly, to date, PIES are providing important observations that are helping to establish an appropriate method of referencing altimetric anomalies in order to define actual SSH not dependent on incorporation of long-term mean surfaces based on numerical model results. Additionally, deep Lagrangian drifters can provide unique information on total transport patterns in the deeper portions of the Gulf. Although not part of the present NW GOM study, they have provided valuable information for locating, tracking and characterizing coherent deep-current patterns in the northern GOM.

CHAPTER 7 REFERENCES

Berger, T., P. Hamilton, J.J. Singer, R.R. Leben, G.H. Born, and C.A. Fox. 1996. Louisiana/Texas shelf physical oceanography program: Eddy circulation study, final synthesis report. Volume 1: Technical report. U.S. Dept. of the Interior, Minerals Management Service, Gulf of Mexico OCS Region, New Orleans, LA. OCS Study MMS 96-0051. 324 pp.

Biggs, D.C., A.E. Jochens, M.K. Howard, S.F. DiMarco, K.D. Mullin, R.R. Leben, F.E. Muller-Karger, and C. Hu. 2005. Eddy forced variations in on- andoff-margin summertime circulation along the 1000-m isobath of the northern Gulf of Mexico, 2000-2003, and links with sperm whale distributions along the middle slope. In: Sturges, W. and A. Lugo-Fernàndez, eds. Circulation in the Gulf of Mexico: Observations and models. American Geophysical Union, Washington, DC. Geophysical Monograph 161:71-85.

Biggs, D.C., G.S. Fargion, P. Hamilton, and R.R. Leben. 1996. Cleavage of a Gulf of Mexico Loop Current eddy by a deep water cyclone. J. Geophys. Res. 101(20):20629-20641.

Blaha, J.P., G.H. Born, N.L. Guinasso, Jr., H.J. Herring, G.A. Jacobs, F.J. Kelly, R.R. Leben, R.D. Martin, Jr., G.L. Mellor, P.P. Niiler, M.E. Parke, R.C. Patchen, K. Schaudt, W. Scheffner, C.K. Shum, C. Ohlmann, W. Sturges, III, G.L. Weatherly, D. Webb, and H.J. White. 2000. Gulf of Mexico ocean monitoring system. Oceanography 13(2):10-17.

Bretherton, F.P., R.E. Davis, and C.B. Fandry. 1976. A technique for objective analysis and design of oceanographic experiments applied to MODE-73. Deep Sea Res. 23:559-582.

Briggs, W.L. 1987. A multigrid tutorial. Philadelphia, PA: Soc. for Ind. and Appl. Math. 88 pp.

Brooks, D.A. 1984. Current and hydrographic variability in the northwestern Gulf of Mexico. J. Geophys. Res. 89(C5):8022-8032.

Brooks, I.H. and P.P. Niiler. 1977. Energetics of the Florida Current. J. Mar. Res. 35(1):163-191.

Charlton, A.J., A. O'Neill, W.A. Lahoz, and P. Berrisford. 2005. The splitting of the stratospheric polar vortex in the southern hemisphere, September 2002: Dynamical evolution. J. Atmos. Sci. 62(3):590-602.

Chen, C., R.O. Reid, and W.D. Nowlin. 1996. Near-inertial oscillations over the Texas-Louisiana shelf. J. Geophys. Res. 101(C2):3509-3524. doi: 10.1029/95JC03395.

Christiansen, J.P. and N.J. Zabusky. 1973. Instability, coalescence and fission of finite-area vortex structure. J. Fluid Mech. 61(2):219-243.

Cressman, G.P. 1959. An operational objective analysis system. Mon. Weather Rev. 87:367-374.

Cunningham, S.A., G.G. Alderson, B.A. King, and M.A. Brandon, 2003. Transport and variability of the Antarctic Circumpolar Current in Drake Passage. J. Geophys. Res. 108(C5):8084. doi: 10.1029/2001JC001147.

D'Asaro, E.A. 1991. A strategy for investigating and modeling internal wave sources and sinks. In: Muller, P. and D. Henderson, eds. Dynamics of oceanic internal gravity waves: proceedings of the 'Aha Huliko'a Hawaiian winter workshop. Hawaii inst. of Geophysics, Honolulu, HI. pp. 451-466.

DeHaan, C.J. and W. Sturges. 2005. Deep cyclonic circulation in the Gulf of Mexico. J. Phys. Oceanogr. 35(10):1801-1812.

DiMarco, S.F., M.K. Howard, W.D. Nowlin, Jr., and R.O. Reid. 2004. Subsurface, high-speed current jets in the deepwater region of the Gulf of Mexico: Final report. U.S. Dept. of the Interior, Minerals Management Service, Gulf of Mexico OCS Region, New Orleans, LA. OCS Study MMS 2004-022. 98 pp.

Donohue, K., P. Hamilton, K. Leaman, R. Leben, M. Prater, D.R. Watts, and E. Waddell. 2006. Exploratory study of deepwater currents in the Gulf of Mexico. Volume II: Technical report. U.S. Dept. of the Interior, Minerals Management Service, Gulf of Mexico OCS Region, New Orleans, LA. OCS Study MMS 2006-074. 430 pp.

Elliott, B.A. 1982. Anticyclonic rings in the Gulf of Mexico. J. Phys. Oceanogr. 12(11):1292-1309.

Flierl, G.R. 1988. On the instability of geostrophic vortices. J. Fluid Mech. 197:349-388.

Fofonoff, N.P. and R.M. Hendry. 1985. Current variability near the southeast Newfoundland Ridge. J. Phys. Oceanogr. 15(7):963-984.

Freymuth, P., W. Bank, and M. Palmer. 1984. First experimental evidence of vortex splitting. Physics of Fluids 27(5):1045-1046.

Frolov, S.A., G.G. Sutyrin, G.D. Rowe, and L.M. Rothstein. 2004. Loop Current eddy interaction with the western boundary in the Gulf of Mexico. J. Phys. Oceanogr. 34(10):2223-2237.

Fu, L.-L., D. Stammer, R.R. Leben, and D.B. Chelton. 2003. Improved spatial resolution of ocean surface topography from the T/P– Jason-1 altimeter mission. EOS, Trans. Amer. Geophys. Un. 84(26):241-247. doi: 10.1029/2003EO260002.

Gille, S.T. and C.W. Hughes. 2001. Aliasing of high-frequency variability by altimetry: evaluation from bottom pressure records. Geophys. Res. Lett. 28:1755-1758.

Glenn, S.M. and C.C. Ebbesmeyer. 1993. Drifting buoy observations of a Loop Current anticyclonic eddy. J. Geophys. Res. 98(C11):20105-20119.

Goni, G. and J. Trianannes. 2003. Ocean thermal structure monitoring could aid in the intensity forecast of tropical cyclones. EOS, Trans. Amer. Geophys. Un. 84:573-580.

Greenslade, D.J.M., D.B. Chelton, and M.G. Schlax. 1997. The midlatitude resolution capability of sea level fields constructed from single and multiple altimeter datasets. J. Atmos. Oceanic Technol. 14:849-870.

Hamilton, P. 1984. Topographic and inertial waves on the continental rise of the Mid-Atlantic bight. J. Geophys. Res. 89(C1):695-710.

Hamilton, P. 1990. Deep currents in the Gulf of Mexico. J. Phys. Oceanogr. 20(7):1087-1104.

Hamilton, P. 1992. Lower continental slope cyclonic eddies in the central Gulf of Mexico. J. Geophys. Res. 97(C2):2185-2200.

Hamilton, P. 2007. Deep-current variability near the Sigsbee Escarpment in the Gulf of Mexico. J. Phys. Oceanogr. 37:708-726.

Hamilton, P., T.J. Berger, and W. Johnson. 2002. On the structure and motions of cyclones in the northern Gulf of Mexico. J. Geophys. Res. 107(C12):3208. doi:10.1029/1999JC000270.

Hamilton, P., T.J. Berger, J.J. Singer, E. Waddell, J.H. Churchill, R.R. Leben, T.N. Lee, and W. Sturges. 2000. DeSoto Canyon eddy intrusion study: Final report. Volume II: Technical report. U.S. Dept. of the Interior, Minerals Management Service, Gulf of Mexico OCS Region, New Orleans, LA. OCS Study MMS 2000-080. 275 pp.

Hamilton, P., G.S. Fargion, and D.C. Biggs. 1999. Loop Current eddy paths in the western Gulf of Mexico. J. Phys. Oceanogr. 29(6):1180-1207.

Hamilton, P. and A. Lugo-Fernandez. 2001. Observations of high speed deep currents in the northern Gulf of Mexico. Geophys. Res. Lett. 28:2867-2870.

Hamilton, P., J.J. Singer, E. Waddell, and K. Donohue. 2003. Deepwater observations in the northern Gulf of Mexico from in-situ current meters and PIES: Final report, Volume II: Technical report. U.S. Dept. of the Interior, Minerals Management Service, Gulf of Mexico OCS Region, New Orleans, LA. OCS Study MMS 2003-049. 95 pp.

Hendricks, J.R., R.R. Leben, G.H. Born, and C.J. Koblinsky. 1996. Empirical orthogonal function analysis of global TOPEX/POSEIDON altimeter data and implications for detection of global sea level rise. J. Geophys. Res. 101(C6):14131-14146. doi:10.1029/96JC00922.

Hendry, R.M., D.R. Watts, and C.S. Meinen. 2002. Newfoundland Basin sea-level variability from TOPEX/POSEIDON altimetry and inverted echo sounder-bottom pressure measurements. Can. J. Remote Sensing 28:544-555.

Hogg, NG. and D.E. Frye. 2007. Performance of a new generation of acoustic current meters. J. Phys. Oceanogr. 37(2):148-161.

Hogg, N.G. 1981. Topographic waves along 70W on the continental rise. J. Mar. Res. 39:627-649.

Hogg, N.G. 2000. Low-frequency variability on the western flanks of the Grand Banks. J. Mar. Res. 58:523-545.

Hong, X., S.W. Chang, S. Raman, L.K. Shay, and R. Hodur. 2000. The interaction between Hurricane Opal (1995) and a warm core ring in the Gulf of Mexico. Mon. Weather Rev. 128(5):1347-1365.

Hooker, S.B., E.R. Firestone, J.G. Acker, J.W. Campbell, J.M. Blaisdell, and M. Darzi. 1995. Level-3 SeaWiFS data products: Spatial and temporal binning algorithms. In: SeaWiFS Technical Report Series. Vol. 32. NASA Tech. Memorandom 104566. NASA Goddard Space Flight Center, Greenbelt, MD.

Hurlburt, H.E. and J.D. Thompson. 1982. The dynamics of the Loop Current and shed eddies in a numerical model of the Gulf of Mexico. In: Nihoul, J.C.J., ed. Hydrodynamics of semi-enclosed seas, Vol. 34, Elsevier Oceanography Series. Elsevier Scientific Publ. Co., New York. Pp. 243-298.

Kantha, L., J.-K. Choi, K.J. Schaudt, and C.K. Cooper. 2005. A regional data-assimilative model for operational use in the Gulf of Mexico. In: Sturges, W. and A. Lugo-Fernandez, eds. Circulation in the Gulf of Mexico: Observations and models. American Geophysical Union, Washington, DC. Geophysical Monograph 161:165-180.

Kirwan, A.D., Jr., W.J. Merrell, Jr., J.K. Lewis, and R.E. Whitaker. 1984. Lagrangian observations of an anticyclonic ring in the western Gulf of Mexico. J. Geophys. Res. 89(C3):3417-3424.

Koblinsky, C.J., B.D. Beckley, R.D. Ray, Y.-M. Wang, and A. Brenner. 1999. NASA Ocean altimeter pathfinder project. Report 1: Data processing handbook. NASA/TM-1998-208605.

Kunze, E. 1985. Near-inertial wave propagation in geostrophic shear. J. Phys. Oceanogr. 15(5):544-565.

Kunze, E. 1986. The mean and near-inertial velocity fields in a warm-core ring. J. Phys. Oceanogr. 16(8):1444-1461.

Kuznetsov, L., M. Toner, A.D. Kirwan, Jr., C.K.R.T. Jones, L.H. Kantha, and J. Choi. 2002. The Loop Current and adjacent rings delineated by Lagrangian analysis of the near-surface flow. J. Mar. Res. 60(3):405-429.

Leben, R.R. 2005. Altimeter-derived Loop Current metrics. In: Sturges, W. and A. Lugo-Fernàndez, eds. Circulation in the Gulf of Mexico: Observations and models. American Geophysical Union, Washington, DC. Geophysical Monograph 161:181-201.

Leben, R.R. and G.H. Born. 1993. Tracking Loop Current eddies with satellite altimetry. Adv. Space Res. 13(11):325-333.

Leben, R.R., G.H. Born, and B.R. Engebreth. 2002. Operational altimeter data processing for mesoscale monitoring. Mar. Geodesy 25(1-2):3-18. doi: 10.1080/014904102753516697.

LeBlond, P.H. and L.A. Mysack. 1978. Waves in the ocean. New York: Elsevier. 602 pp.

Lewis, J.K. and A.D. Kirwan, Jr. 1985. Some observations of ring topography and ring-ring interactions in the Gulf of Mexico. J. Geophys. Res. 90(C5):9017-9028.

Lewis, J.K., A.D. Kirwan, Jr., and G.Z. Forristall. 1989. Evolution of a warm-core ring in the Gulf of Mexico: Lagrangian observations. J. Geophys. Res. 94(C6):8163-8178.

Lin, I.-I., C.-C. Wu, K.A. Emanuel, I.-H. Lee, C.-R. Wu, and I.-F. Pun. 2005. The interaction of Supertyphoon Maemi (2003) with a warm ocean eddy. Mon. Weather Rev. 133(9):2635-2649.

Malanotte-Rizzoli, P., D.B. Haidvogel, and R.E. Young. 1987. Numerical simulation of transient boundary-forced radiation, Part I: The linear regime. J. Phys. Oceanogr. 17(9):1439-1457.

Malanotte-Rizzoli, P., N.G. Hogg, and R.E. Young. 1995. Stochastic wave radiation by the Gulf Stream: numerical experiments. Deep Sea Res. 42:389-423.

McWilliams, J.C. and G.R. Flierl. 1979. On the evolution of isolated, nonlinear vortices. J. Phys. Oceanogr. 9(6):1155-1182.

Meinen, C.S. and D.R. Watts. 2000. Vertical structure and transport on a transect across the North Atlantic Current near 42N: Time series and mean. J. Geophys. Res. 105(C9):21869-21891.

Meinen, C.S., and D.R. Watts. 1998. Calibrating inverted echo sounders equipped with pressure sensors. J. Atmos. Oceanic Technol. 15(6):1339-1345.

Merrell, W.J. and A.M. Vazquez. 1983. Observations of changing mesoscale circulation patterns in the western Gulf of Mexico. J. Geophys. Res. 88(C12):7721-7723.

Merrifield, M.A. and C.D. Winaut. 1989. Shelf circulation in the Gulf of California: A description of the variability. J. Geophys. Res. 94:18133-18160.

Mizuta, G. and N.G. Hogg. 2004. Structure of the circulation induced by a shoaling topographic wave. J. Phys. Oceanogr. 34(8):1793-1810.

Mooers, C.N.K. 1975. Several effects of a baroclinic current on the cross-stream propagation of inertial-internal waves. Geophys. Fluid Dyn. 6:245-275.

Munk, W.H. and D.E. Cartwright. 1966. Tidal spectroscopy and prediction. Phil. Trans. Roy. Soc. Lon. 259(A):533-581.

Niiler, P.P., N.A. Maximenko, and J. C. McWilliams. 2003. Dynamically balanced absolute sea level of the global ocean derived from near-surface velocity observations. Geophys. Res. Lett. 30(22):2164. doi: 10.1029/2003GL018628.

Nowlin, W.D., Jr., A.E. Jochens, S.F. DiMarco, R.O. Reid, and M.K. Howard. 2001. Deepwater physical oceanography reanalysis and synthesis of historical data: Synthesis report. U.S. Dept. of the Interior, Minerals Management Service, Gulf of Mexico OCS Region, New Orleans, LA. OCS Study MMS 2001-064. 530 pp.

Oey, L.-Y. 1995. Eddy- and wind-forced shelf circulation. J. Geophys. Res. 100(C5):8621-8637.

Oey, L.-Y. 1996. Simulation of mesoscale variability in the Gulf of Mexico: sensitivity studies, comparison with observations, and trapped wave propagation. J. Phys. Oceanogr. 26(2):145-175.

Oey, L.-Y. and H.-C. Lee. 2002. Deep eddy energy and topographic Rossby waves in the Gulf of Mexico. J. Phys. Oceanogr. 32(12):3499-3527.

Oey, L.-Y. and H.-C. Zhang. 2004. The generation of subsurface cyclones and jets through eddy-slope interaction. Cont. Shelf Res. 24(18):2109-2131.

Ohlmann, J.C. and P.P. Niiler. 2001. A two-dimensional response to a tropical storm on the Gulf of Mexico shelf. J. Mar. Sys. 29(1-4):87-99.

Ohlmann, J.C., P.P. Niiler, C.A. Fox, and R.R. Leben. 2001. Eddy energy and shelf interactions in the Gulf of Mexico. J. Geophys. Res. 106(C2):2605-2620.

O'Reilly, J.E., S. Maritorena, B.G. Mitchell, D. Siegel, K. Carder, S. Garver, M. Kahru, and C. McClain. 1998. Ocean color chlorophyll algorithms for SeaWiFS. J. Geophys. Res. 103:24937-24953.

Park, J.-H. and D.R. Watts. 2005. Near-inertial oscillations interacting with mesoscale circulation in the southwestern Japan/East Sea. Geophys. Res. Lett. 32:L10611. doi: 10.1029/2005GL022936.

Park, J.-H. and D.R. Watts. 2006. Near 5-day nonisostatic response of the Atlantic Ocean to atmospheric surface pressure deduced from sub-surface and bottom pressure measurements. Geophys. Res. Lett. 33:L12610. doi:10.1029/2006GL026304.

Parke, M.E., G. Born, R. Leben, C. McLauglin, and C. Tierney. 1998. Altimeter sampling characteristics using a single satellite. J. Geophys. Res. 103:10513-10526.

Parke, M.E., R.H. Stewart, D.L. Farless, and D.E. Cartwright. 1987. On the choice of orbits for an altimetric satellite to study ocean circulation and tides. J. Geophys. Res. 92:11693-11707.

Pickart, R.S. 1995. Gulf Stream-generated topographic Rossby waves. J. Phys. Oceanogr. 25(4):574-586.

Press, W.H., S.A. Tuekolsky, W.T. Vetterling, and B.P. Flannery. 1992. Numerical recipes in FORTRAN, the art of scientific computing. 2nd ed. New York: Cambridge University Press. 963 pp.

Rhines, P.B. 1970. Edge-, bottom-, and Rossby waves in a rotating stratified fluid. Geophys. Fluid Dyn. 1:273-302.

Rhines, P.B. 1975. Waves and turbulence on a beta-plane. J. Fluid Mech. 69:417-443.

Saffman, P.G. and G.R. Baker. 1979. Vortex interactions. Ann. Rev. Fluid Mech. 11:95-122. doi: 10.1146/annurev.fl.11.010179.000523.

Schlax, M.G. and D.B. Chelton. 1994. Detecting aliased tidal errors in altimeter height measurements. J. Geophys. Res. 99:12603-12612.

Schmitz, W.J., Jr., D.C. Biggs, A. Lugo-Fernández, L.-Y. Oey, and W. Sturges. 2005. A synopsis of the circulation in the Gulf of Mexico and on its continental margins. In: Sturges, W. and A. Lugo-Fernández, eds. Circulation in the Gulf of Mexico: Observations and models. American Geophysical Union, Washington, DC. Geophysical Monograph 161:11-29.

Schouten, M.W., W.P.M. de Ruijter, P.J. van Leeuen, and J.R.E. Lutjeharms. 2000. Translation, decay and splitting of Agulhas rings in the southeastern Atlantic Ocean. J. Geophys. Res. 105(C9):21913-21925.

Science Applications International Corporation (SAIC). 1988. Gulf of Mexico physical oceanography program. Final report: Year 3. Volume II: Technical report. U.S. Dept. of the Interior, Minerals Management Service, Gulf of Mexico OCS Region, New Orleans, LA. OCS Study MMS 88-0046. 241 pp.

Shay, L.K., G.J. Goni, and P.G. Black. 2000. Effects of a warm oceanic feature on Hurricane Opal. Mon. Weather Rev. 128(5):1366-1383.

Smith, D.C., IV. 1986. A numerical study of Loop Current eddy interaction with topography in the western Gulf of Mexico. J. Phys. Oceanogr. 16(7):1260-1272.

Smith, D.C., IV and J.J. O'Brien. 1983. The interaction of a two-layer isolated mesoscale eddy with bottom topography. J. Phys. Oceanogr. 13(9):1681-1697.

Sturges, W. 1993. The annual cycle of the western boundary current in the Gulf of Mexico. J. Geophys. Res. 98(C10):18053-18068.

Sturges, W., J.C. Evans, S. Welsh, and W. Holland. 1993. Separation of warm-core rings in the Gulf of Mexico. J. Phys. Oceanogr. 23(2):250-268.

Sturges, W. and R. Leben. 2000. Frequency of ring separations from the Loop Current in the Gulf of Mexico: A revised estimate. J. Phys. Oceanogr. 30(7):1814-1819.

Thompson, R.O.R.Y. 1977. Observations of Rossby waves near site D. Progr. Oceanogr. 7:135-162.

Tierney, C.C., M.E. Parke, and G.H. Born. 1998. An investigation of ocean tides derived from along-track altimetry. J. Geophys. Res. 103:10273-10287.

Vidal, V.M.V., F.V. Vidal, A.F. Hernandez, E. Meza, and J.M. Pérez-Molero. 1994. Baroclinic flows, transports, and kinematic properties of a cyclonic - anticyclonic - cyclonic ring triad in the Gulf of Mexico. J. Geophys. Res. 99(C4):7571-7598.

Vidal, V.M.V., F.V. Vidal, and J.M. Pérez-Molero. 1992. Collision of a Loop Current anticyclonic ring against the continental slope of the western Gulf of Mexico. J. Geophys. Res. 97(C2):2155-2172.

Vukovich, F.M. 2007. Climatology of ocean features in the Gulf of Mexico using satellite remote sensing data. J. Phys. Oceanogr. 37(3):689-707. doi: 10.1175/JPO2989.1.

Vukovich, F.M. and B.W. Crissman. 1986. Aspects of warm rings in the Gulf of Mexico. J. Geophys. Res. 91(C2):2645-2660.

Vukovich, F.M. and E. Waddell. 1991. Interaction of a warm ring with the western slope in the Gulf of Mexico. J. Phys. Oceanogr. 21(7):1062-1074.

Walker, N.D., R.R. Leben, and S. Balasubramanian. 2005. Hurricane-forced upwelling and chlorphyll a enhancement within cold-core cyclones in the Gulf of Mexico. Geophys. Res. Lett. 32(L18610):1-5.

Wang, Y.M. 2001. GSFC00 mean sea surface, gravity anomaly and vertical gravity gradient from satellite altimeter data. J. Geophys. Res. 106:31167-31174.

Watts, D.R. and H. Kontoyiannis. 1990. Deep-ocean bottom pressure measurement: drift removal and performance. J. Atmos. Oceanic Technol. 7:296-306.

Watts, D.R., X. Qian, and K.L. Tracey. 2001. Mapping abyssal current and pressure fields under the meandering Gulf Stream. J. Atmos. Oceanic Technol. 18:1052-1067.

Watts, D.R., K.L. Tracey, and A.I. Friedlander. 1989. Producing accurate maps of the Gulf Stream thermal front using objective analysis. J. Geophys. Res. 94(C6):8040-8052.

Welsh, S. and M. Inoue. 2002. Lagrangian study of circulation, transport, and vertical exchange in the Gulf of Mexico. U.S. Dept. of the Interior, Minerals Management Service, Gulf of Mexico OCS Region, New Orleans, LA. OCS Study MMS 2002-064. 51 pp.

Welsh, S.E. and M. Inoue. 2000. Loop Current rings and deep circulation in the Gulf of Mexico. J. Geophys. Res. 105(C7):16951-16959.

Whitworth, T., III. 1983. Monitoring the transport of the Antarctic Circumpolar Current at Drake Passage. J. Phys. Oceanogr. 13(11):2045-2057.

Wüst, G. 1963. On the stratification and circulation in the cold water sphere of the Antillean-Caribbean basins. Deep Sea Res. 10:165-187.

Zavala-Hidalgo, J., S.L. Morey, and J.J. O'Brien. 2003. Cyclonic eddies northeast of the Campeche Bank from altimetry data. J. Phys. Oceanogr. 33(3):623-629.

APPENDIX A

Statistics for Mooring T1

	Mean			Standard Deviation (3-HLP)			Maximum (3-HLP)			Minimum (3-HLP)			Standard Deviation (40-HLP)			Ratio 40-HLP: 3-HLP	Principal Axis Direction
Depth (m)	U	V	Speed	U	V	Speed	U	V	Speed	U	V	% of Time with Records	U	V	Speed	Kinetic Energy (%)	(Degrees True)
T1	Time Period: 3/24/2004 – 6/30/2005			Coordinate Rotation 30°						Water Depth: 506 m							
8	-3.72	7.17	29.30	15.98	31.47	21.35	66.3	111.4	115.3	-62.7	-67.5	100	13.26	30.10	20.06	87	20
52	-3.85	2.31	23.31	11.89	24.57	15.02	48.7	75.7	77.7	-56.7	-56.1	100	10.86	24.10	14.25	94	22
80	-3.39	1.53	21.57	11.53	23.12	14.86	39.8	79.4	79.9	-60.5	-61.6	100	10.71	22.77	14.28	95	21
250	-0.59	-1.83	8.51	4.67	9.35	6.29	28.1	23.1	42.2	-24.9	-40.6	56	2.75	8.61	5.49	75	37
450	-0.65	-1.84	8.09	4.75	8.68	6.04	20.8	32.0	35.4	-21.8	-33.5	100	3.99	8.27	5.49	86	30

Statistics for Mooring T2

	Mean			Standard Deviation (3-HLP)			Maximum (3-HLP)			Minimum (3-HLP)			Standard Deviation (40-HLP)			Ratio 40-HLP: 3-HLP	Principal Axis Direction
Depth (m)	U	V	Speed	U	V	Speed	U	V	Speed	U	V	% of Time with Records	U	V	Speed	Kinetic Energy (%)	(Degrees True)
T2	Time Period: 3/25/2004 – 7/1/2005			Coordinate Rotation 40°						Water Depth: 1214 m							
36	-7.16	11.76	23.94	16.12	15.65	11.05	60.9	82.0	83.5	-59.0	-40.9	100	15.14	14.73	9.96	88	95
52	-5.80	14.51	27.38	18.44	19.44	14.62	55.9	80.8	85.1	-79.7	-51.6	100	17.72	18.77	13.83	93	76
100	-4.35	12.08	23.16	15.72	16.59	12.22	51.3	69.6	70.5	-61.5	-37.3	100	15.02	16.05	11.57	93	76
148	-3.37	9.80	19.08	13.44	13.74	10.52	52.8	49.8	65.6	-48.4	-33.2	100	12.66	13.10	9.81	90	82
196	-2.70	8.34	16.54	12.12	12.03	9.63	59.4	46.4	67.7	-48.4	-30.9	100	11.41	11.44	9.02	90	85
252	-2.30	7.54	14.89	11.05	10.86	8.89	54.1	50.8	58.8	-45.8	-26.3	100	10.42	10.32	8.36	90	86
300	-1.85	6.93	13.73	10.22	10.04	8.22	51.9	46.5	55.2	-44.5	-28.0	100	9.57	9.46	7.63	88	86
348	-1.70	6.70	12.95	9.44	9.45	7.60	41.0	43.0	47.7	-36.1	-26.4	100	8.83	8.93	7.05	88	84
396	-1.52	6.42	12.39	8.85	9.03	7.07	38.6	41.1	43.9	-32.9	-27.1	100	8.28	8.54	6.54	88	82
436	-1.25	5.75	11.15	7.84	8.18	6.18	33.4	40.3	41.1	-27.8	-28.2	100	7.25	7.66	5.62	87	80
750	-0.39	3.03	6.98	5.27	5.79	4.71	21.8	36.4	37.5	-27.4	-13.4	100	4.43	4.97	3.88	72	12
1100	-1.07	-0.92	4.55	2.93	4.08	2.57	8.9	15.3	15.7	-11.9	-13.7	100	2.37	3.71	2.11	77	33

Statistics for Mooring T3

	Mean			Standard Deviation (3-HLP)			Maximum (3-HLP)			Minimum (3-HLP)			Standard Deviation (40-HLP)			Ratio 40-HLP: 3-HLP	Principal Axis Direction
Depth (m)	U	V	Speed	U	V	Speed	U	V	Speed	U	V	% of Time with Records	U	V	Speed	Kinetic Energy (%)	(Degrees True)
T3	Time Period: 3/28/2004 – 7/2/2005			Coordinate Rotation 90°						Water Depth: 999 m							
36	3.95	9.63	23.95	16.28	18.45	11.87	59.0	78.5	83.1	-53.6	-41.8	100	15.37	17.68	10.76	91	113
52	5.94	11.09	27.67	17.91	22.36	14.69	64.0	71.2	83.1	-54.3	-66.2	100	17.16	21.83	13.90	94	94
100	5.19	8.89	24.26	15.61	20.59	13.66	59.3	67.0	71.5	-45.7	-53.1	100	14.78	20.06	12.91	93	89
148	4.72	7.02	20.98	13.78	18.18	12.39	62.2	68.4	69.4	-42.4	-48.7	100	12.90	17.63	11.74	92	85
196	4.47	5.91	18.40	12.07	16.19	11.22	67.1	59.4	74.9	-43.8	-51.7	100	11.41	15.76	10.64	93	82
252	4.22	5.23	16.58	10.82	14.53	10.01	54.8	49.2	62.2	-38.4	-42.7	100	10.27	14.18	9.49	93	78
300	3.95	4.71	15.30	9.75	13.47	9.02	48.9	46.5	58.4	-33.7	-42.1	100	9.21	13.09	8.46	93	76
348	3.79	4.79	14.81	9.07	12.89	8.24	44.4	36.1	52.9	-31.1	-37.5	100	8.53	12.55	7.71	93	79
396	3.63	4.96	14.28	8.43	12.25	7.50	43.9	33.6	45.4	-25.8	-37.5	100	7.91	11.95	6.99	93	82
428	3.23	4.68	13.00	7.63	11.08	6.73	39.5	32.7	39.6	-25.5	-33.6	100	7.05	10.74	6.15	91	83
750	1.78	3.82	8.50	4.95	8.22	6.17	34.5	28.7	34.6	-13.8	-32.6	58	4.18	7.78	5.60	85	97
900	-0.36	0.60	4.42	3.03	4.31	2.97	13.1	19.4	19.5	-11.7	-17.5	100	2.31	3.90	2.52	74	98

Statistics for Mooring T4

	Mean			Standard Deviation (3-HLP)			Maximum (3-HLP)			Minimum (3-HLP)			Standard Deviation (40-HLP)			Ratio 40-HLP: 3-HLP	Principal Axis Direction
Depth (m)	U	V	Speed	U	V	Speed	U	V	Speed	U	V	% of Time with Records	U	V	Speed	Kinetic Energy (%)	(Degrees True)
T4	Time Period: 3/30/2004 – 7/2/2005			Coordinate Rotation 110°						Water Depth: 1012 m							
40	2.30	6.63	26.66	20.98	20.24	13.83	53.5	84.5	84.9	-60.7	-55.7	100	20.36	19.44	13.00	93	167
48	3.20	7.84	28.62	21.93	22.11	15.05	58.6	109.9	112.9	-64.1	-52.7	100	21.47	21.56	14.42	96	154
96	2.19	5.31	26.44	20.66	21.92	15.69	49.3	103.1	103.3	-58.2	-50.0	100	20.35	21.57	15.24	97	121
152	1.31	2.46	21.66	16.88	18.91	13.58	43.6	91.3	91.7	-54.8	-51.3	100	16.51	18.55	13.14	96	118
200	0.94	1.08	18.85	14.72	16.69	12.00	35.0	76.5	76.9	-52.4	-48.4	100	14.32	16.32	11.56	95	119
248	0.84	0.42	17.01	13.27	15.01	10.72	28.8	66.9	67.2	-52.7	-48.6	100	12.88	14.63	10.26	95	125
296	0.73	0.33	15.18	11.92	13.31	9.54	26.2	57.0	57.2	-46.4	-43.0	100	11.54	12.95	9.03	94	128
352	0.68	0.28	13.72	10.62	12.03	8.42	28.2	50.2	51.0	-38.1	-38.5	100	10.20	11.64	7.91	93	129
400	0.85	0.43	12.87	9.83	11.21	7.63	28.5	48.5	49.5	-33.8	-38.1	100	9.39	10.80	7.06	92	129
432	0.86	0.46	11.47	8.59	9.99	6.61	27.6	42.6	44.4	-30.6	-36.2	100	8.15	9.59	6.04	91	127
750	0.70	0.34	5.81	3.33	6.49	4.49	23.2	24.4	29.0	-15.2	-25.4	99	2.55	5.95	3.78	79	98
900	-0.12	-1.03	5.93	2.75	6.64	4.21	12.2	17.5	27.2	-11.0	-26.3	100	2.12	6.33	3.76	87	99

Statistics for Mooring T5

	Mean			Standard Deviation (3-HLP)			Maximum (3-HLP)			Minimum (3-HLP)			Standard Deviation (40-HLP)			Ratio 40-HLP: 3-HLP	Principal Axis Direction
Depth (m)	U	V	Speed	U	V	Speed	U	V	Speed	U	V	% of Time with Records	U	V	Speed	Kinetic Energy (%)	(Degrees True)
T5	Time Period: 3/25/2004 – 7/1/2005			Coordinate Rotation 110°						Water Depth: 1486 m							
36	3.26	7.47	25.25	20.33	18.23	13.19	75.5	80.9	90.2	-65.3	-50.6	100	19.56	17.24	11.96	91	169
52	4.37	10.85	30.06	23.41	21.57	15.77	75.4	83.4	91.4	-63.9	-55.5	100	22.87	20.93	14.98	95	171
100	4.40	9.67	26.01	20.07	18.35	13.44	78.6	75.5	78.8	-52.9	-52.6	100	19.62	17.86	12.78	95	172
148	4.31	7.53	21.07	16.55	15.05	11.65	76.6	56.6	76.9	-45.9	-51.1	100	16.00	14.50	10.93	93	171
196	4.29	6.13	17.55	13.75	12.94	10.35	68.2	51.3	70.6	-33.9	-49.2	100	13.20	12.39	9.68	92	164
252	3.97	5.21	15.07	12.04	11.08	9.24	60.4	49.7	66.8	-34.2	-38.1	100	11.45	10.46	8.56	90	165
300	3.64	4.56	13.46	10.95	10.11	8.73	56.6	47.8	67.6	-27.4	-36.9	100	10.34	9.47	8.03	89	164
348	3.48	4.30	12.70	10.20	9.58	8.16	56.3	48.2	65.9	-25.5	-31.4	100	9.69	9.05	7.51	90	162
396	3.48	4.18	12.58	9.95	9.35	7.70	51.6	45.7	60.7	-23.3	-28.0	100	9.44	8.82	7.08	90	162
428	3.15	3.79	11.44	8.97	8.54	6.94	48.1	41.4	55.8	-21.6	-23.5	100	8.52	8.06	6.35	90	161
750	2.38	2.59	8.06	6.30	5.99	4.84	32.8	24.1	33.3	-19.9	-27.1	100	5.74	5.42	4.08	83	165
1000	1.02	1.07	5.28	4.28	4.68	3.80	19.1	20.1	21.4	-16.6	-19.6	100	3.32	3.77	3.13	63	121
1400	0.13	-2.06	4.09	2.78	3.40	2.65	10.9	7.0	16.1	-12.1	-15.8	100	2.29	3.07	2.33	76	119

Statistics for Mooring U1

	Mean			Standard Deviation (3-HLP)			Maximum (3-HLP)			Minimum (3-HLP)			Standard Deviation (40-HLP)			Ratio 40-HLP: 3-HLP	Principal Axis Direction
Depth (m)	U	V	Speed	U	V	Speed	U	V	Speed	U	V	% of Time with Records	U	V	Speed	Kinetic Energy (%)	(Degrees True)
U1	Time Period: 3/26/2004 – 6/28/2005			Coordinate Rotation 355°						Water Depth: 500 m							
8	3.86	6.93	29.87	15.48	31.95	20.94	59.7	109.7	110.5	-63.3	-76.5	100	12.18	30.52	19.35	86	2
52	2.29	1.45	24.25	10.07	26.57	15.21	49.3	84.9	86.9	-40.1	-60.2	100	8.79	26.17	14.52	94	177
80	1.96	-0.48	21.80	9.23	24.68	15.06	61.9	81.1	83.1	-31.3	-61.6	100	8.24	24.40	14.55	96	175
250	0.60	-6.41	13.47	5.38	15.06	10.79	27.8	48.4	57.7	-32.4	-57.4	98	4.51	14.81	10.44	94	166
450	-1.45	-4.28	10.30	4.37	11.23	7.74	13.1	27.8	41.5	-15.4	-41.5	100	3.65	10.99	7.38	92	180

Statistics for Mooring U2

	Mean			Standard Deviation (3-HLP)			Maximum (3-HLP)			Minimum (3-HLP)			Standard Deviation (40-HLP)			Ratio 40-HLP: 3-HLP	Principal Axis Direction
Depth (m)	U	V	Speed	U	V	Speed	U	V	Speed	U	V	% of Time with Records	U	V	Speed	Kinetic Energy (%)	(Degrees True)
U2	Time Period: 3/26/2004 – 7/1/2005			Coordinate Rotation 20°						Water Depth: 1506 m							
32	-7.77	14.06	25.29	17.40	14.40	11.09	48.7	77.5	91.3	-57.9	-43.1	100	16.32	13.19	9.84	86	83
48	-7.28	17.37	29.36	20.41	17.12	14.00	58.6	79.7	90.2	-72.1	-44.3	100	19.53	16.25	13.07	91	79
96	-7.05	15.62	26.06	17.27	14.95	11.38	48.0	65.5	66.5	-52.4	-28.5	100	16.53	14.38	10.71	92	78
152	-6.41	13.38	21.84	14.58	13.14	11.18	38.9	66.3	67.1	-54.7	-21.5	100	13.87	12.47	10.55	90	84
200	-5.92	11.75	19.14	12.82	12.15	10.78	33.3	58.8	62.1	-55.8	-25.4	100	12.23	11.57	10.26	91	80
248	-5.46	10.41	17.05	11.49	11.33	10.30	28.7	57.0	59.7	-52.7	-27.6	100	10.83	10.68	9.69	89	73
296	-4.83	9.16	15.20	10.50	10.30	9.56	25.8	52.6	56.3	-49.8	-21.0	100	9.80	9.64	8.91	87	77
352	-4.59	8.40	13.97	9.41	9.21	8.30	25.5	44.9	48.9	-43.1	-21.5	100	8.74	8.57	7.67	86	74
400	-4.27	7.85	13.06	8.55	8.42	7.26	20.8	40.2	42.8	-36.6	-19.8	100	7.88	7.78	6.61	85	67
416	-3.91	7.29	12.11	7.96	7.72	6.65	19.6	37.5	39.1	-32.9	-18.9	100	7.31	7.09	6.00	84	73
750	-2.11	3.49	6.58	4.60	4.85	4.21	13.1	24.8	26.1	-23.0	-13.0	100	3.62	3.99	3.36	65	1
1000	-1.29	2.38	5.13	3.82	4.24	3.66	12.5	18.1	22.6	-21.7	-15.8	100	3.02	3.46	2.86	65	174
1400	-0.17	-0.53	3.26	2.57	2.70	1.92	10.7	9.4	11.4	-9.6	-11.4	100	1.94	2.28	1.42	64	18

Statistics for Mooring U3

	Mean			Standard Deviation (3-HLP)			Maximum (3-HLP)			Minimum (3-HLP)			Standard Deviation (40-HLP)			Ratio 40-HLP: 3-HLP	Principal Axis Direction
Depth (m)	U	V	Speed	U	V	Speed	U	V	Speed	U	V	% of Time with Records	U	V	Speed	Kinetic Energy (%)	(Degrees True)
U3	Time Period: 3/29/2004 – 7/1/2005			Coordinate Rotation 150°						Water Depth: 1716 m							
36	3.26	-3.27	27.45	20.83	22.25	13.93	64.5	60.9	76.5	-66.3	-74.7	100	19.91	21.33	12.63	92	149
52	3.92	-2.10	31.17	23.09	26.09	16.05	81.1	75.3	96.4	-67.2	-78.0	100	22.41	25.34	15.03	94	144
100	4.25	-0.70	26.89	19.13	22.45	12.81	61.5	71.8	71.9	-48.5	-63.0	100	18.45	21.86	11.97	94	147
148	4.70	-0.28	21.10	14.97	17.41	10.27	47.8	63.4	63.4	-36.2	-47.3	100	14.33	16.83	9.36	93	156
196	4.91	-0.20	17.78	12.68	14.42	8.82	45.9	55.2	55.2	-31.0	-50.2	100	12.07	13.90	8.05	92	163
252	4.93	0.00	15.59	10.99	12.42	7.55	41.3	42.0	49.0	-22.9	-41.8	100	10.32	11.81	6.61	89	169
300	4.79	-0.07	14.02	9.94	11.15	7.06	37.0	38.4	41.9	-20.7	-36.5	100	9.26	10.55	6.14	88	172
348	4.83	-0.08	13.31	9.39	10.42	6.59	39.6	34.2	43.9	-22.0	-30.0	100	8.76	9.85	5.70	88	176
396	5.00	0.05	13.02	8.98	10.11	6.20	40.7	32.7	46.0	-24.8	-31.2	100	8.40	9.57	5.40	89	179
436	4.61	0.12	11.95	8.16	9.25	5.55	38.4	29.7	42.7	-22.9	-25.3	100	7.59	8.74	4.76	88	180
750	3.17	0.63	7.68	5.40	5.83	3.88	24.7	19.7	26.7	-17.7	-19.6	100	4.70	5.20	3.16	78	5
1000	2.69	1.58	7.04	5.15	5.42	4.03	20.3	19.3	21.6	-15.8	-17.7	100	4.09	4.28	3.17	63	177
1600	0.42	-1.55	4.49	2.81	4.60	3.38	14.0	14.7	19.3	-10.0	-17.3	100	2.30	4.23	2.92	80	149

Statistics for Mooring U4

	Mean			Standard Deviation (3-HLP)			Maximum (3-HLP)			Minimum (3-HLP)			Standard Deviation (40-HLP)			Ratio 40-HLP: 3-HLP	Principal Axis Direction
Depth (m)	U	V	Speed	U	V	Speed	U	V	Speed	U	V	% of Time with Records	U	V	Speed	Kinetic Energy (%)	(Degrees True)
U4	Time Period: 3/30/2004 – 6/27/2005			Coordinate Rotation 40°						Water Depth: 1517 m							
52	10.10	-0.11	35.13	22.55	29.38	15.66	78.2	88.6	99.7	-66.6	-69.2	100	21.94	28.98	14.87	96	42
100	9.66	1.03	32.37	21.45	26.69	15.06	72.3	77.9	80.6	-60.4	-76.8	100	21.03	26.38	14.44	97	44
148	7.86	0.43	26.79	19.13	21.03	12.60	62.0	55.1	68.4	-48.2	-55.0	100	18.69	20.64	11.93	96	56
196	6.75	-0.37	23.16	17.43	17.67	11.41	64.9	43.7	67.3	-48.4	-53.9	100	17.07	17.29	10.81	96	81
252	5.94	-0.80	20.04	15.74	15.16	10.76	66.8	42.2	69.7	-47.1	-45.5	100	15.40	14.76	10.15	95	98
300	5.29	-0.97	17.92	14.37	13.66	10.22	65.0	40.7	67.2	-40.7	-41.5	100	13.98	13.24	9.55	94	99
348	4.90	-1.13	16.68	13.34	12.75	9.50	53.2	39.4	55.0	-37.0	-37.9	100	13.02	12.41	8.99	95	98
396	4.59	-1.39	15.65	12.49	11.89	8.83	53.2	34.4	55.0	-31.3	-37.7	100	12.14	11.50	8.32	94	101
444	3.98	-1.48	13.60	10.83	10.39	7.77	47.5	32.8	49.4	-28.4	-33.7	100	10.48	9.99	7.26	93	103
750	2.45	-3.59	6.62	4.41	4.44	3.71	22.4	13.8	22.7	-9.1	-18.1	41	3.82	3.74	3.12	73	91
1000	0.63	-0.23	4.91	4.01	4.23	3.18	16.9	14.5	18.4	-16.5	-17.7	100	3.13	3.48	2.34	65	56
1400	-0.87	3.46	5.37	1.96	5.25	3.95	9.4	19.4	19.5	-10.2	-15.0	100	1.58	5.08	3.71	90	39

Statistics for Mooring V1

	Mean			Standard Deviation (3-HLP)			Maximum (3-HLP)			Minimum (3-HLP)			Standard Deviation (40-HLP)			Ratio 40-HLP: 3-HLP	Principal Axis Direction
Depth (m)	U	V	Speed	U	V	Speed	U	V	Speed	U	V	% of Time with Records	U	V	Speed	Kinetic Energy (%)	(Degrees True)
V1	Time Period: 3/22/2004 – 6/28/2005			Coordinate Rotation 355°						Water Depth: 495 m							
8	7.04	9.89	35.22	17.50	34.35	19.91	83.3	118.4	118.6	-69.5	-78.3	100	14.69	33.19	18.26	89	12
52	4.04	5.38	29.04	12.10	29.60	14.86	53.2	92.8	93.1	-33.9	-69.7	100	11.11	29.05	13.95	95	11
80	3.17	4.96	27.19	10.33	28.77	15.00	42.7	86.0	87.8	-32.4	-63.2	100	9.41	28.26	14.19	95	9
250	0.37	-2.02	15.17	4.35	18.45	11.49	24.5	52.0	52.0	-19.5	-51.7	100	3.39	18.19	11.13	95	179
450	-0.40	-0.26	3.30	2.28	2.75	2.21	10.4	10.8	22.9	-18.1	-22.8	100	1.66	1.98	1.43	43	26

Statistics for Mooring V2

	Mean			Standard Deviation (3-HLP)			Maximum (3-HLP)			Minimum (3-HLP)			Standard Deviation (40-HLP)			Ratio 40-HLP: 3-HLP	Principal Axis Direction
Depth (m)	U	V	Speed	U	V	Speed	U	V	Speed	U	V	% of Time with Records	U	V	Speed	Kinetic Energy (%)	(Degrees True)
V2	Time Period: 3/22/2004 – 6/28/2005			Coordinate Rotation 5°						Water Depth: 1510 m							
48	1.97	7.39	25.17	22.22	18.32	16.10	72.7	97.0	101.8	-73.0	-47.9	100	21.61	17.64	15.36	94	66
96	2.47	6.79	22.00	18.78	16.25	13.73	72.8	79.2	79.5	-65.7	-34.7	100	18.31	15.75	13.14	95	63
152	1.51	4.73	18.13	15.47	13.35	10.75	51.4	62.6	65.5	-63.3	-37.0	100	14.95	12.81	10.11	93	66
200	0.96	3.48	15.62	13.60	11.76	9.67	50.4	57.3	59.6	-57.6	-34.1	100	13.07	11.22	9.05	92	65
248	0.47	2.92	13.74	12.17	10.44	8.84	45.6	55.3	57.2	-53.7	-31.8	100	11.69	9.93	8.26	92	66
296	0.11	2.45	12.33	10.83	9.47	7.85	41.2	44.1	51.4	-50.6	-33.0	100	10.31	8.94	7.20	90	66
352	-0.27	2.30	11.42	9.95	8.86	7.26	32.9	43.1	45.4	-45.4	-32.9	100	9.44	8.33	6.64	89	66
400	-0.39	2.25	10.96	9.36	8.49	6.70	33.1	41.1	41.2	-36.8	-25.4	100	8.84	7.97	6.12	89	65
432	-0.43	1.97	9.86	8.34	7.77	6.09	36.5	38.9	39.4	-33.9	-24.4	100	7.85	7.27	5.52	88	63
750	-0.68	0.91	6.30	4.57	5.45	3.50	18.3	23.6	25.6	-16.8	-19.2	100	3.76	4.83	2.74	74	3
1000	-0.69	1.86	6.48	4.25	6.22	4.34	20.2	26.4	27.2	-13.9	-20.2	69	3.76	5.81	3.88	84	1
1400	0.38	-0.38	2.80	2.04	3.01	2.38	14.4	12.6	29.2	-13.2	-29.0	100	1.51	2.45	1.95	63	7

Statistics for Mooring V3

	Mean			Standard Deviation (3-HLP)			Maximum (3-HLP)			Minimum (3-HLP)			Standard Deviation (40-HLP)			Ratio 40-HLP: 3-HLP	Principal Axis Direction
Depth (m)	U	V	Speed	U	V	Speed	U	V	Speed	U	V	% of Time with Records	U	V	Speed	Kinetic Energy (%)	(Degrees True)
V3	Time Period: 3/21/2004 – 6/27/2005			Coordinate Rotation 40°						Water Depth: 2507 m							
48	-9.63	-2.84	32.58	23.67	26.06	16.75	62.9	80.4	98.5	-98.3	-72.9	100	22.97	25.43	15.73	95	22
96	-7.63	-2.90	28.24	20.11	22.55	13.58	46.8	62.2	79.8	-78.4	-58.4	100	19.63	22.14	12.88	96	26
152	-6.13	-3.50	22.32	16.03	17.68	11.03	41.1	42.2	71.5	-69.6	-51.8	100	15.52	17.18	10.30	94	28
200	-5.38	-3.81	18.47	12.98	14.80	9.45	32.3	36.9	63.1	-61.1	-48.0	100	12.47	14.29	8.78	93	25
248	-5.13	-3.85	16.46	11.58	13.45	9.14	33.6	35.0	60.5	-60.2	-44.9	100	10.97	12.84	8.41	91	25
296	-4.78	-3.80	14.77	10.64	12.17	8.87	33.1	34.3	54.3	-54.1	-44.4	100	10.05	11.55	8.14	90	22
352	-4.73	-4.00	13.90	9.84	11.47	8.46	30.3	32.2	54.8	-54.7	-44.6	100	9.34	10.92	7.91	90	21
400	-4.46	-4.09	13.26	9.20	10.78	7.76	28.7	31.5	46.0	-45.1	-39.9	100	8.67	10.23	7.23	90	21
424	-4.16	-3.89	12.21	8.44	9.88	7.16	29.0	24.2	47.6	-47.3	-35.5	100	7.93	9.37	6.64	89	23
750	-2.38	-2.82	7.75	5.33	6.04	4.27	19.2	15.9	28.8	-27.0	-21.5	100	4.58	5.38	3.59	77	23
1000	-0.85	-1.80	5.03	3.83	4.88	4.15	16.2	15.7	22.6	-18.6	-22.5	100	3.07	4.30	3.59	73	56
1500	0.09	-3.08	4.96	2.04	4.53	3.13	7.7	12.7	23.6	-8.2	-23.5	100	1.84	4.41	2.93	93	51
2000	-0.53	-4.56	5.87	2.18	5.00	4.07	9.1	19.6	33.5	-11.7	-33.0	100	1.90	4.91	3.95	93	52
2400	-1.33	-5.57	6.74	3.14	5.23	4.97	14.9	17.8	37.7	-18.3	-36.8	100	2.91	5.14	4.88	94	64

Statistics for Mooring V4

	Mean			Standard Deviation (3-HLP)			Maximum (3-HLP)			Minimum (3-HLP)			Standard Deviation (40-HLP)			Ratio 40-HLP: 3-HLP	Principal Axis Direction
Depth (m)	U	V	Speed	U	V	Speed	U	V	Speed	U	V	% of Time with Records	U	V	Speed	Kinetic Energy (%)	(Degrees True)
V4	Time Period: 3/20/2004 – 6/26/2005			Coordinate Rotation 80°						Water Depth: 3098 m							
52	-5.23	3.16	37.19	31.35	27.80	20.50	83.7	93.1	102.8	-87.7	-74.1	100	30.93	27.32	19.84	97	3
100	-4.50	2.56	33.25	27.10	25.18	17.20	59.4	78.6	89.8	-70.8	-78.3	100	26.75	24.84	16.66	97	10
148	-3.14	0.99	27.55	21.93	21.25	13.79	54.9	71.9	76.7	-61.2	-61.7	100	21.54	20.88	13.17	97	17
196	-1.94	-0.58	22.06	18.02	17.57	12.46	53.8	57.5	63.0	-48.0	-51.5	100	17.65	17.22	11.95	96	15
252	-1.35	-1.31	18.64	15.27	15.28	11.18	48.6	56.5	60.6	-42.4	-52.7	100	14.72	14.83	10.54	94	94
300	-1.35	-1.36	16.64	13.60	13.82	13.29	44.2	47.6	52.2	-43.6	-45.5	100	13.08	13.36	9.65	93	103
348	-1.25	-1.56	15.30	12.50	12.70	9.48	41.1	44.1	48.3	-36.0	-41.9	100	12.06	12.31	8.97	94	112
396	-1.05	-1.71	14.19	11.41	11.64	8.41	33.4	41.6	44.5	-35.2	-39.7	100	11.01	11.26	7.90	93	112
428	-0.92	-1.64	12.67	10.06	10.38	7.34	32.0	39.8	43.3	-32.5	-33.9	100	9.66	10.00	6.83	93	109
750	-0.30	-1.63	6.75	5.01	5.78	3.98	14.7	21.3	30.8	-21.2	-27.0	100	4.29	5.22	3.39	78	94
1000	-0.54	-1.93	4.75	3.16	5.09	4.18	12.5	17.7	22.0	-14.1	-21.1	100	2.67	4.67	3.58	81	91
1500	-0.03	-3.00	6.75	3.00	6.63	4.05	10.8	13.1	27.9	-13.9	-27.9	100	2.78	6.53	3.91	95	82
2000	-0.23	-3.80	7.98	3.64	8.41	5.90	14.7	18.5	33.6	-19.0	-32.7	100	3.52	8.37	5.84	98	83
2500	0.04	-3.39	7.04	3.07	7.32	4.98	14.0	15.0	34.5	-16.6	-34.3	100	2.91	7.28	4.93	98	83
3000	0.00	-3.36	6.98	3.12	7.28	5.02	14.3	16.4	34.5	-15.6	-34.5	100	2.91	7.21	4.93	97	86

APPENDIX B

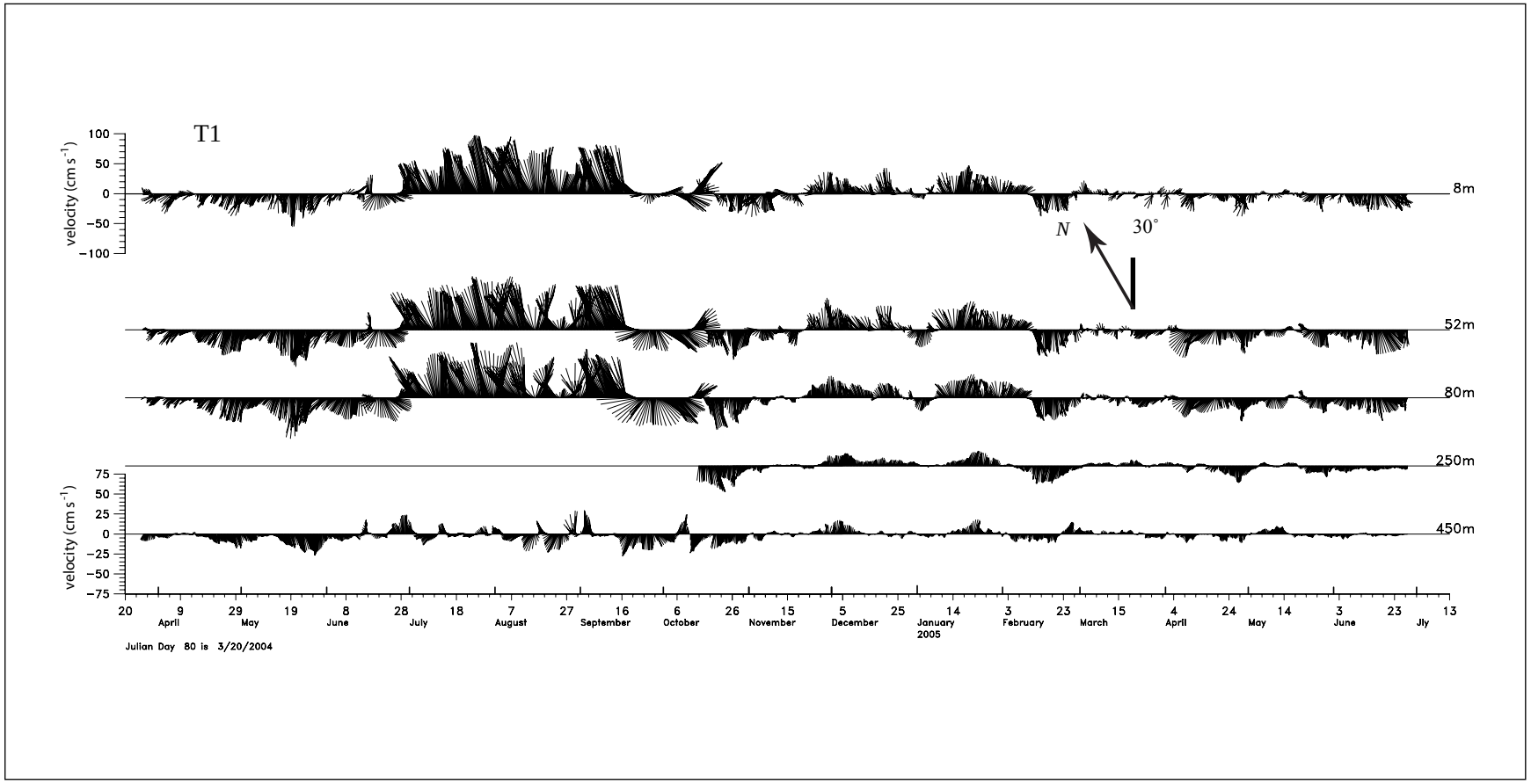

Figure B-1. 40-HLP vector plots of currents at selected depths on Mooring T1. These vectors have been rotated to the local direction of the isobaths. The direction of rotation and its relation to North is shown by the arrow in the figure..

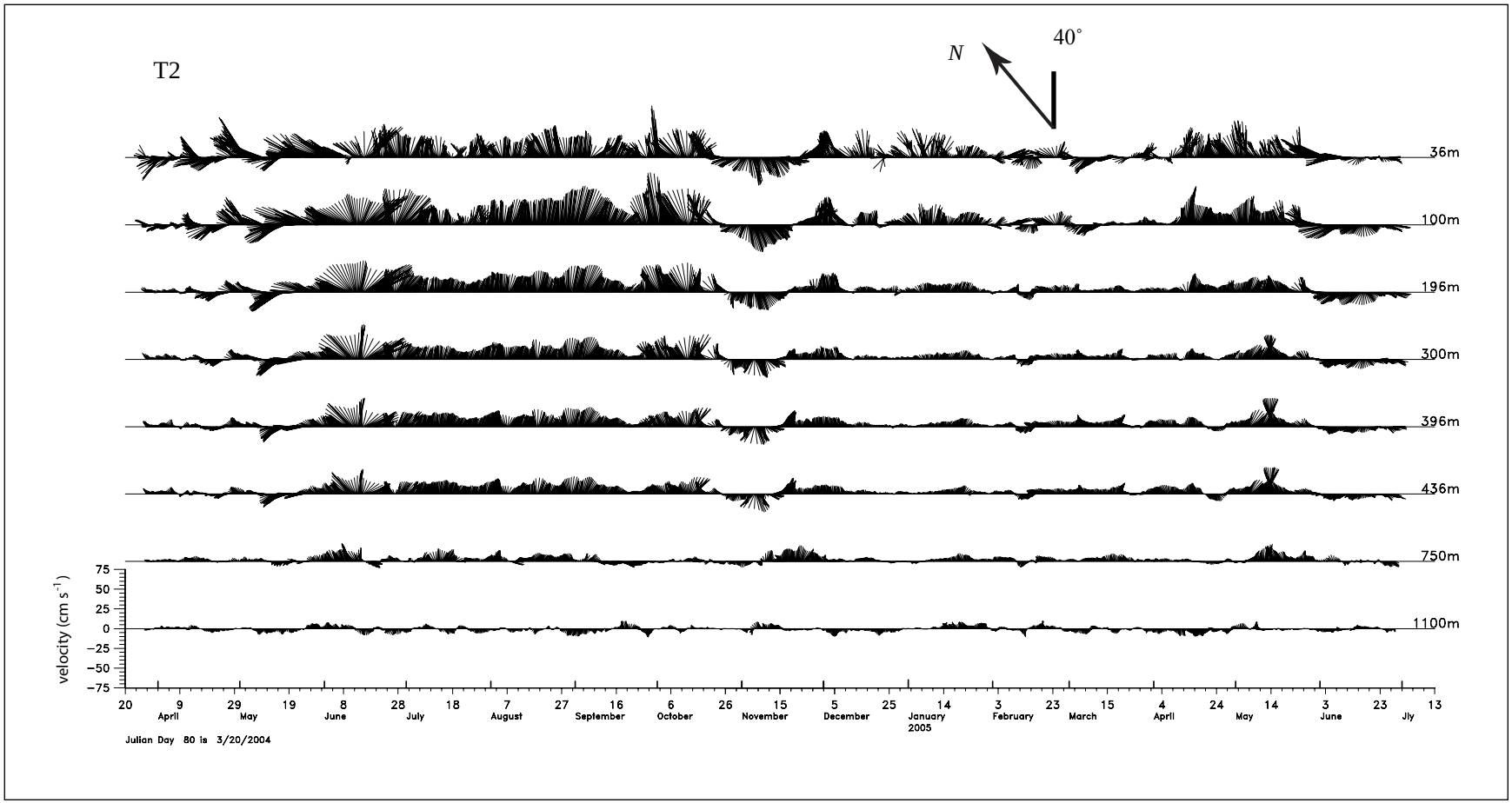

Figure B-2. 40-HLP vector plots of currents at selected depths on Mooring T2. These vectors have been rotated to the local direction of the isobaths. The direction of rotation and its relation to North is shown by the arrow in the figure..

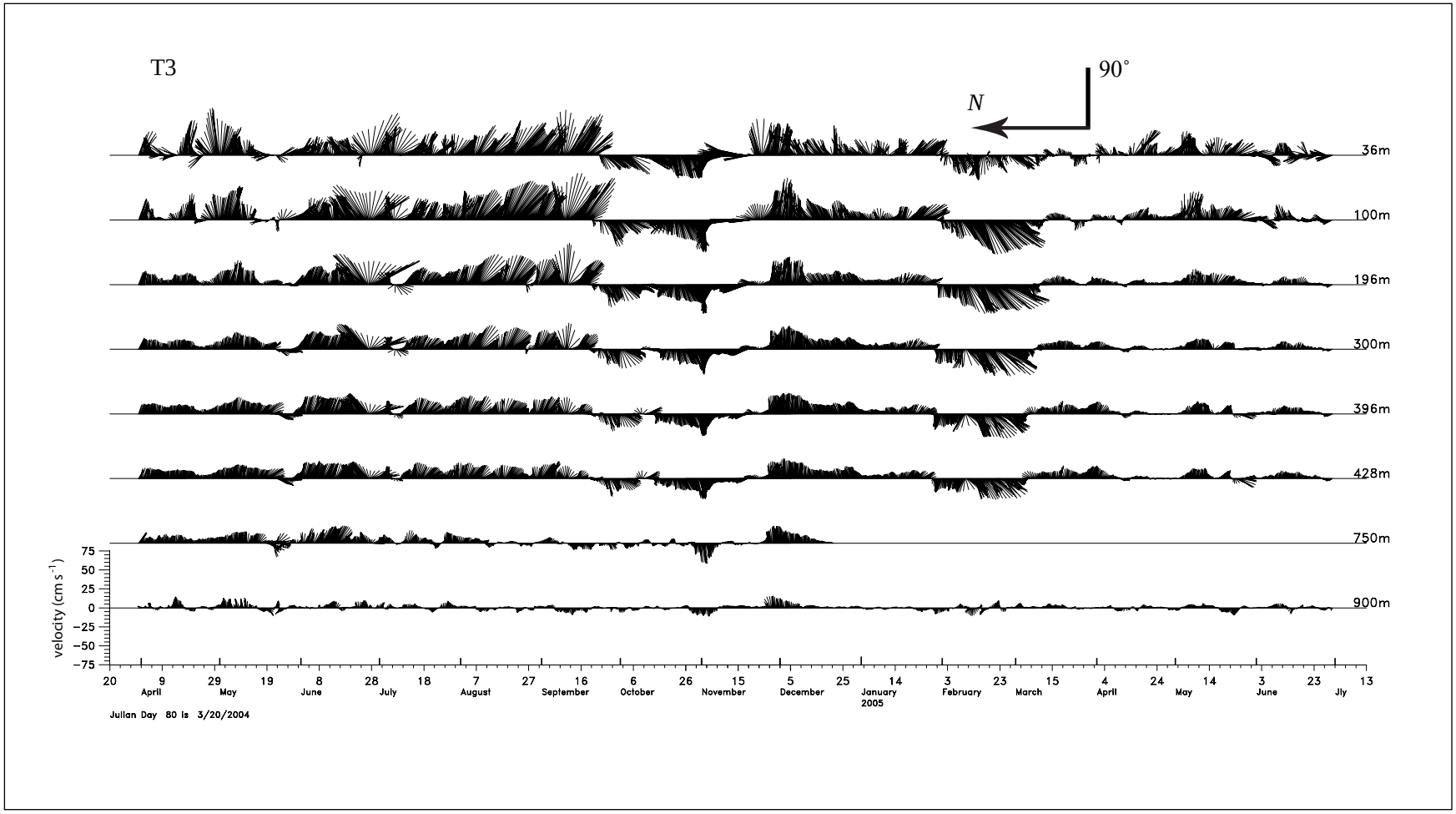

Figure B-3. 40-HLP vector plots of currents at selected depths on Mooring T3. These vectors have been rotated to the local direction of the isobaths. The direction of rotation and its relation to North is shown by the arrow in the figure..

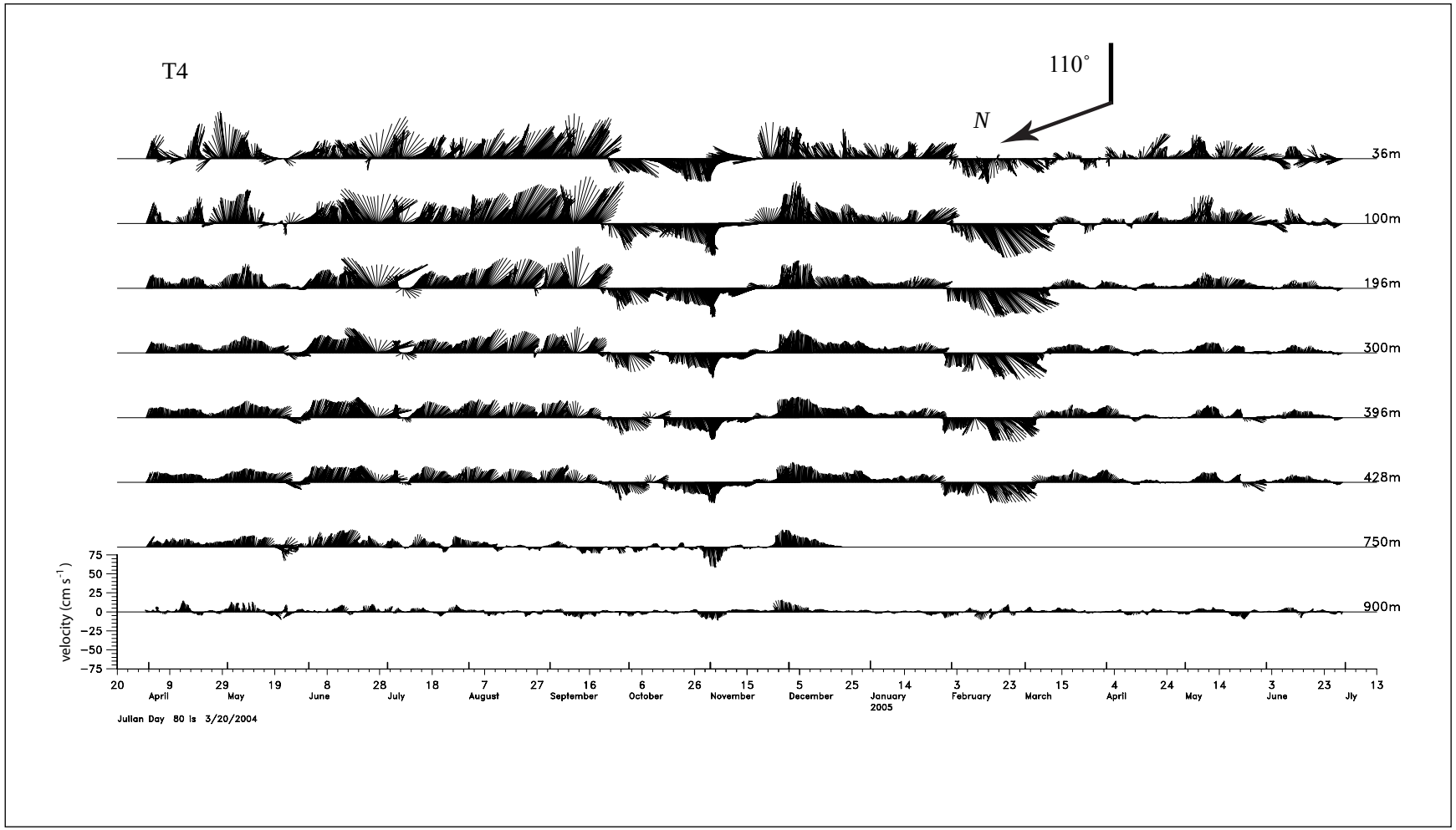

Figure B-4. 40-HLP vector plots of currents at selected depths on Mooring T4. These vectors have been rotated to the local direction of the isobaths. The direction of rotation and its relation to North is shown by the arrow in the figure..

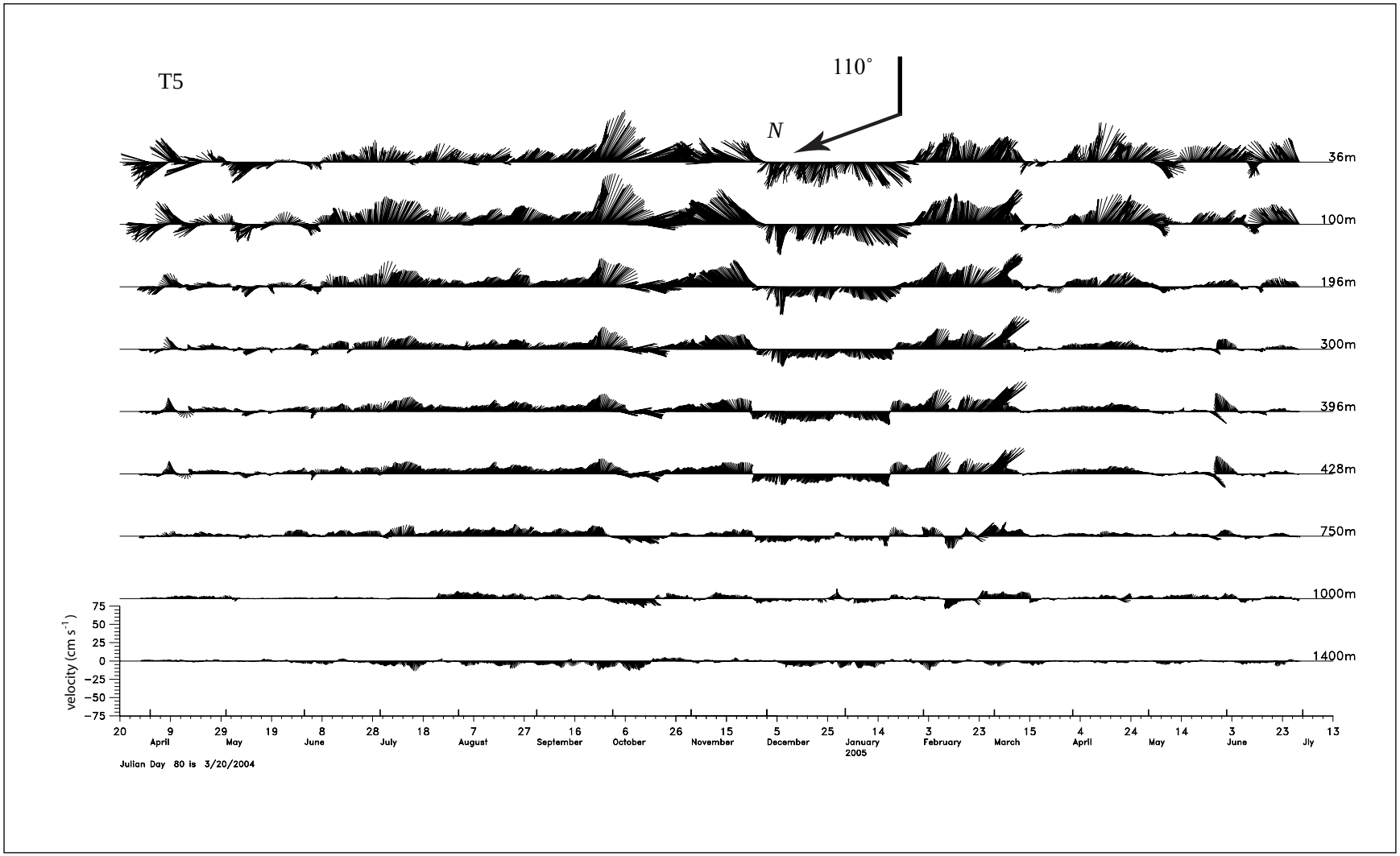

Figure B-5. 40-HLP vector plots of currents at selected depths on Mooring T5. These vectors have been rotated to the local direction of the isobaths. The direction of rotation and its relation to North is shown by the arrow in the figure..

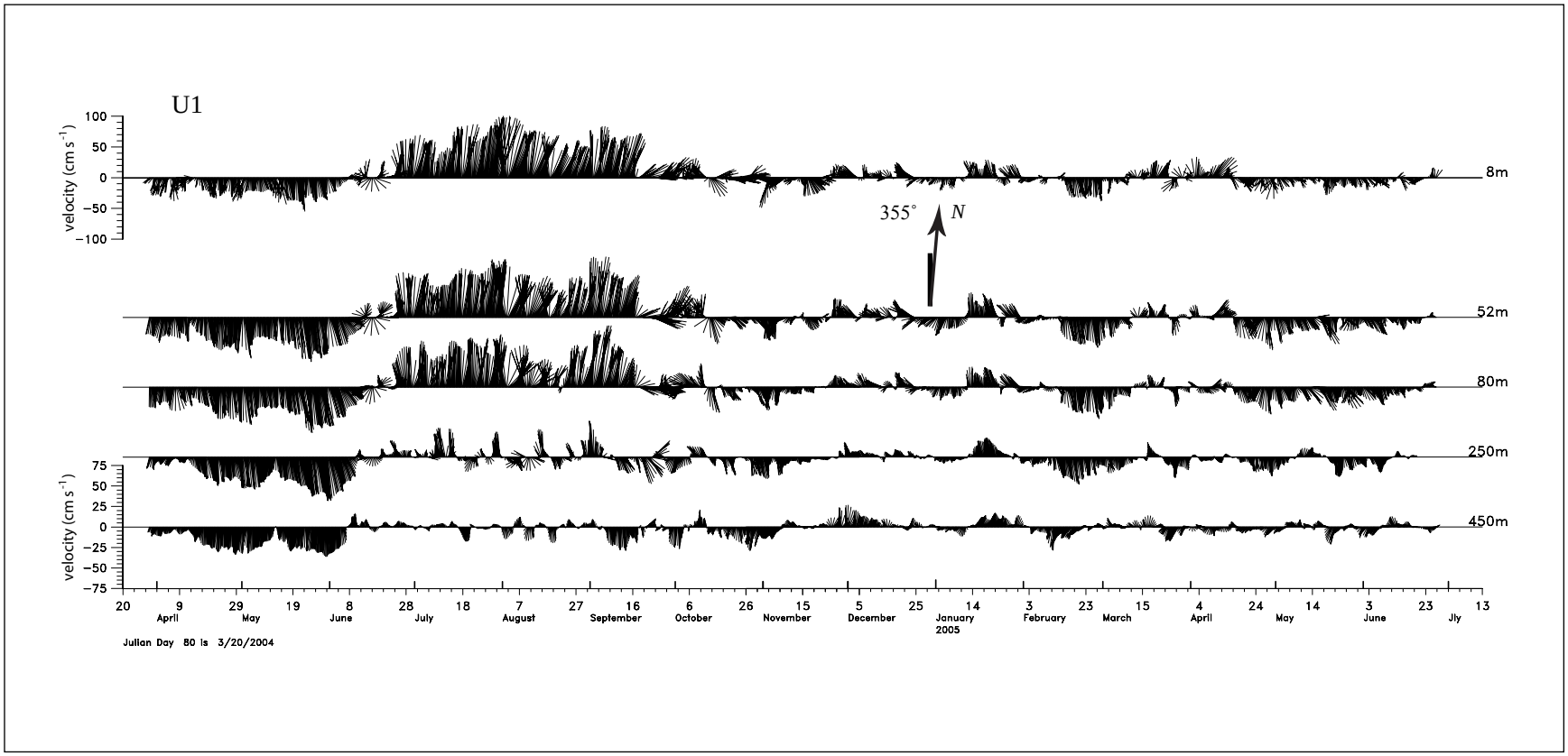

Figure B-6. 40-HLP vector plots of currents at selected depths on Mooring U1. These vectors have been rotated to the local direction of the isobaths. The direction of rotation and its relation to North is shown by the arrow in the figure..

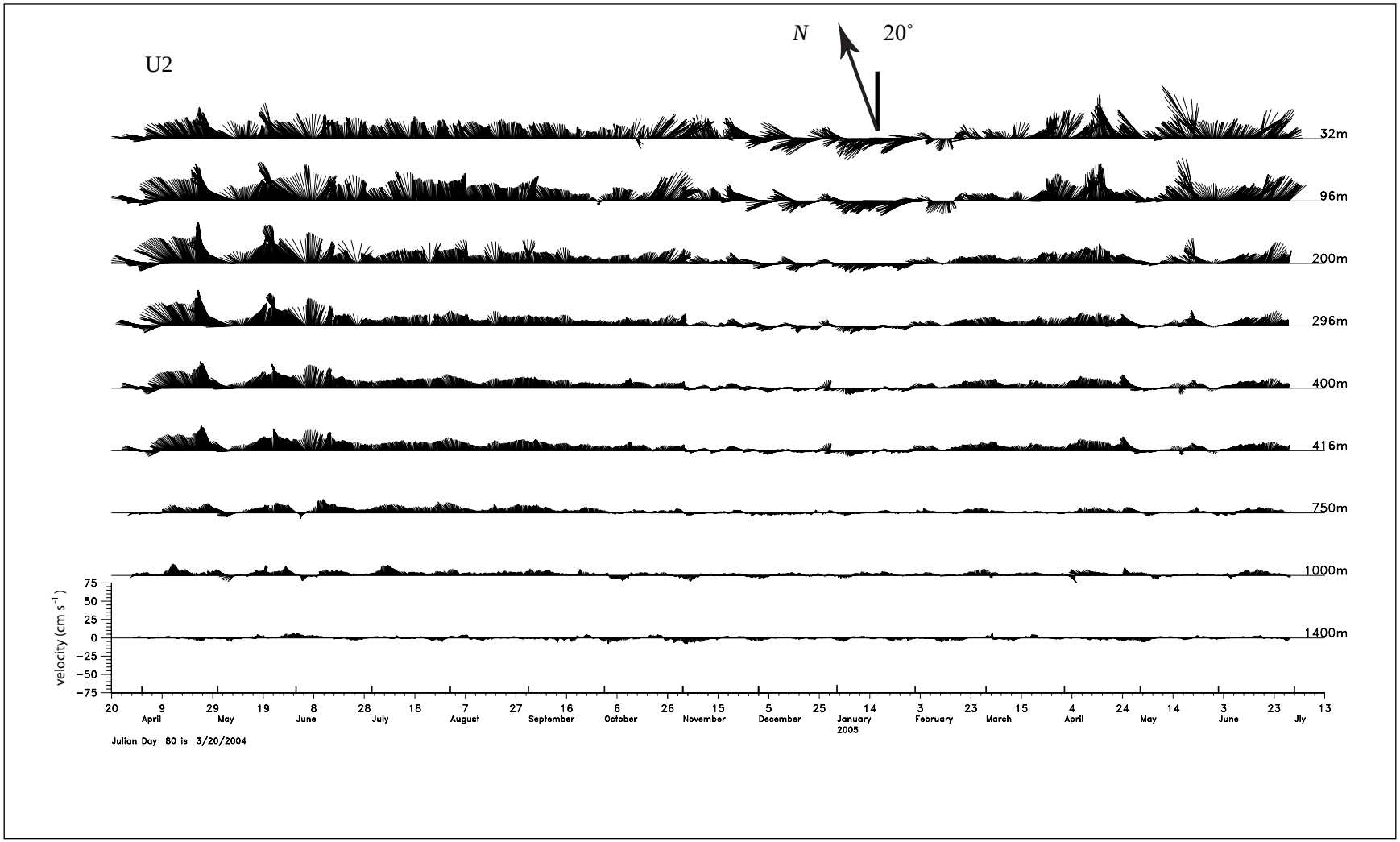

Figure B-7. 40-HLP vector plots of currents at selected depths on Mooring U2. These vectors have been rotated to the local direction of the isobaths. The direction of rotation and its relation to North is shown by the arrow in the figure..

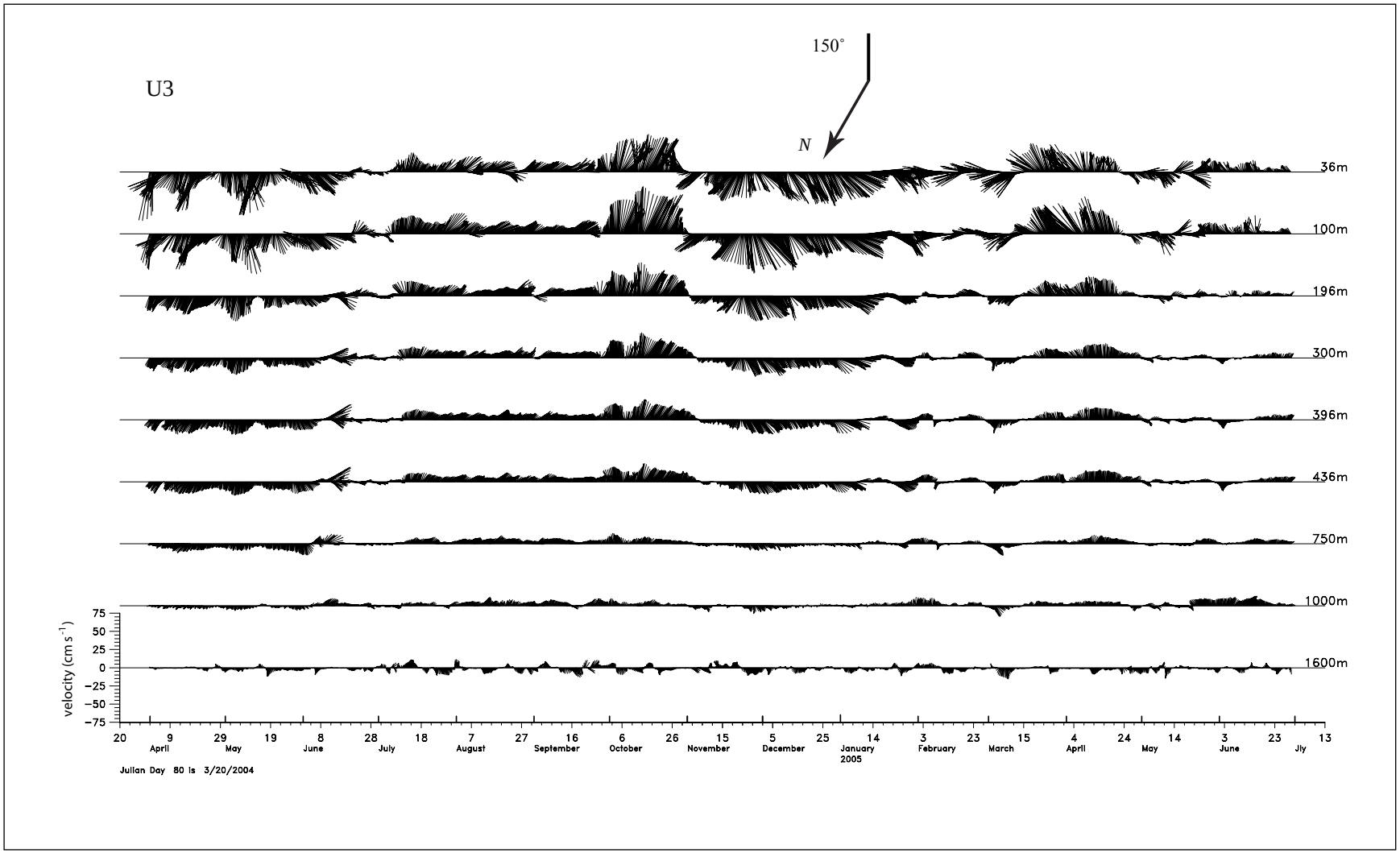

Figure B-8. 40-HLP vector plots of currents at selected depths on Mooring U3. These vectors have been rotated to the local direction of the isobaths. The direction of rotation and its relation to North is shown by the arrow in the figure..

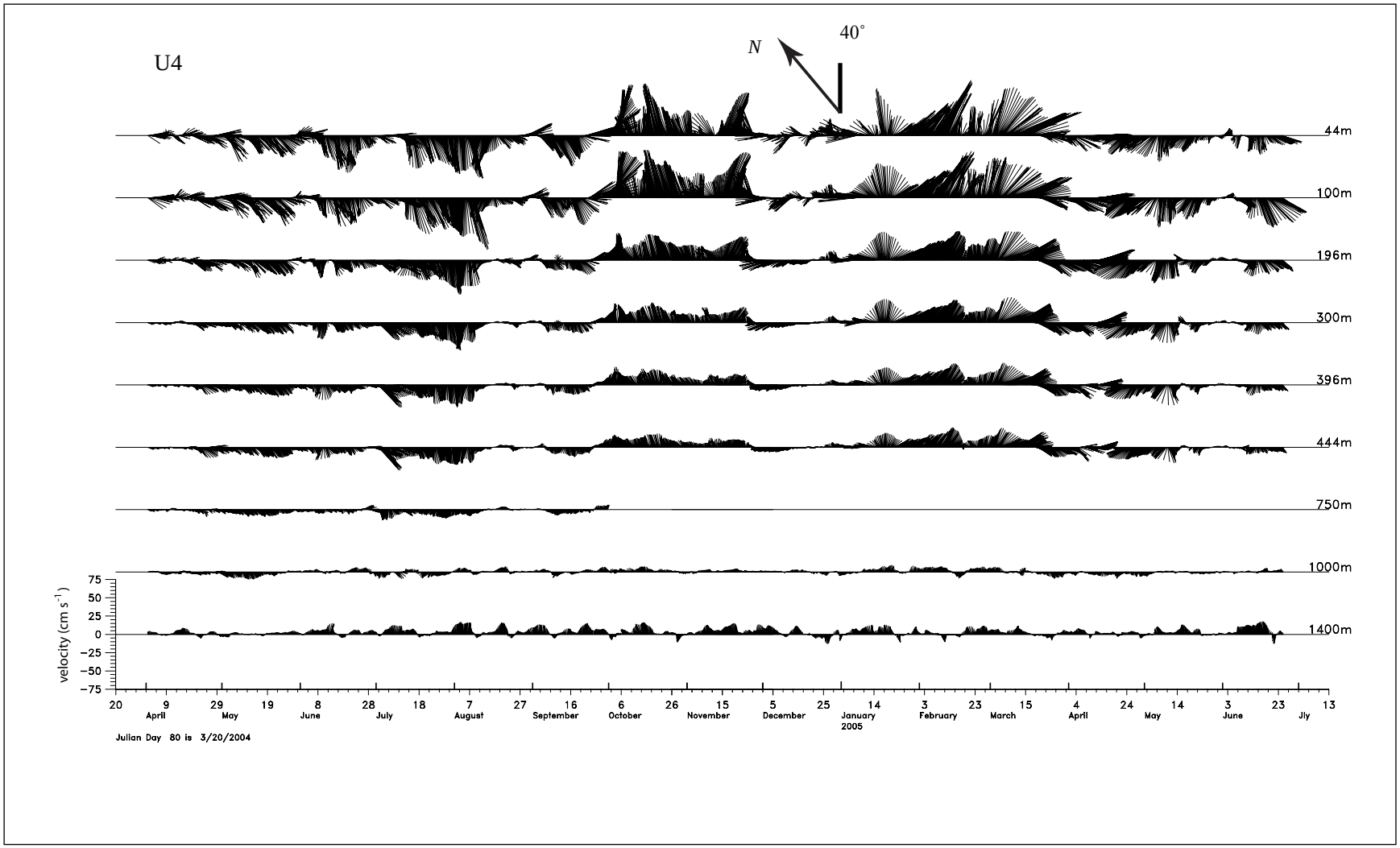

Figure B-9. 40-HLP vector plots of currents at selected depths on Mooring U4. These vectors have been rotated to the local direction of the isobaths. The direction of rotation and its relation to North is shown by the arrow in the figure..

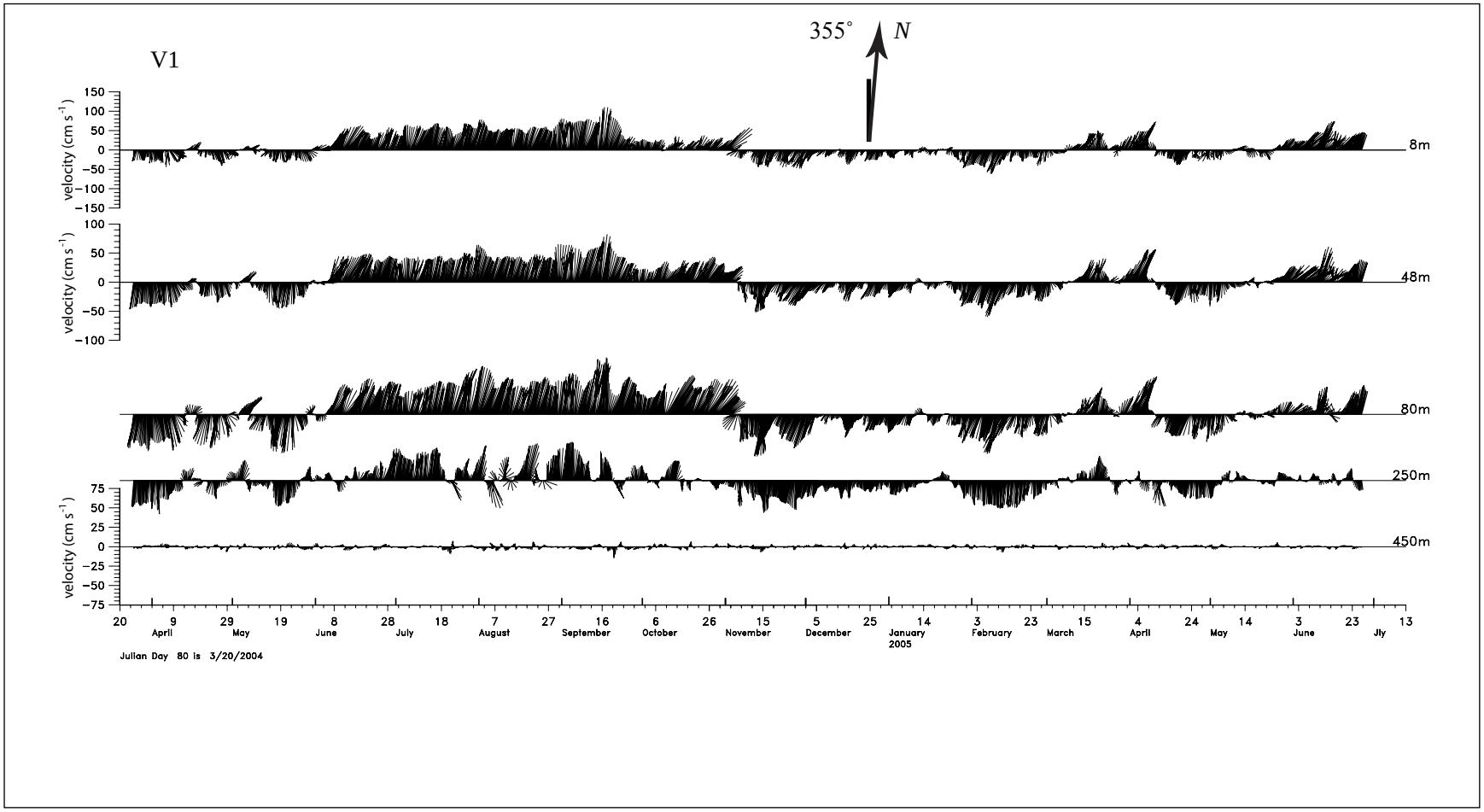

Figure B-10. 40-HLP vector plots of currents at selected depths on Mooring V1. These vectors have been rotated to the local direction of the isobaths. The direction of rotation and its relation to North is shown by the arrow in the figure..

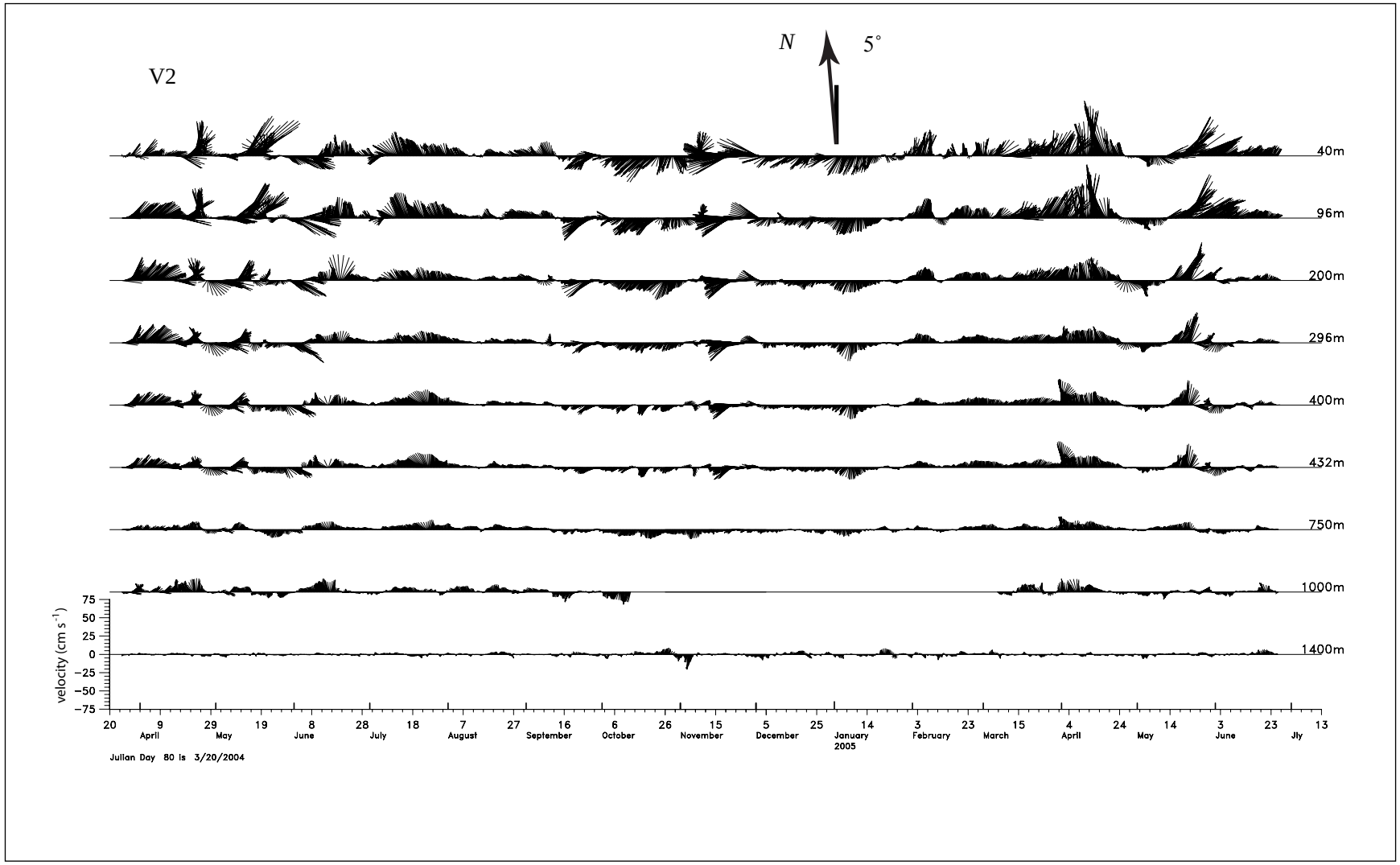

Figure B-11. 40-HLP vector plots of currents at selected depths on Mooring V2. These vectors have been rotated to the local direction of the isobaths. The direction of rotation and its relation to North is shown by the arrow in the figure..

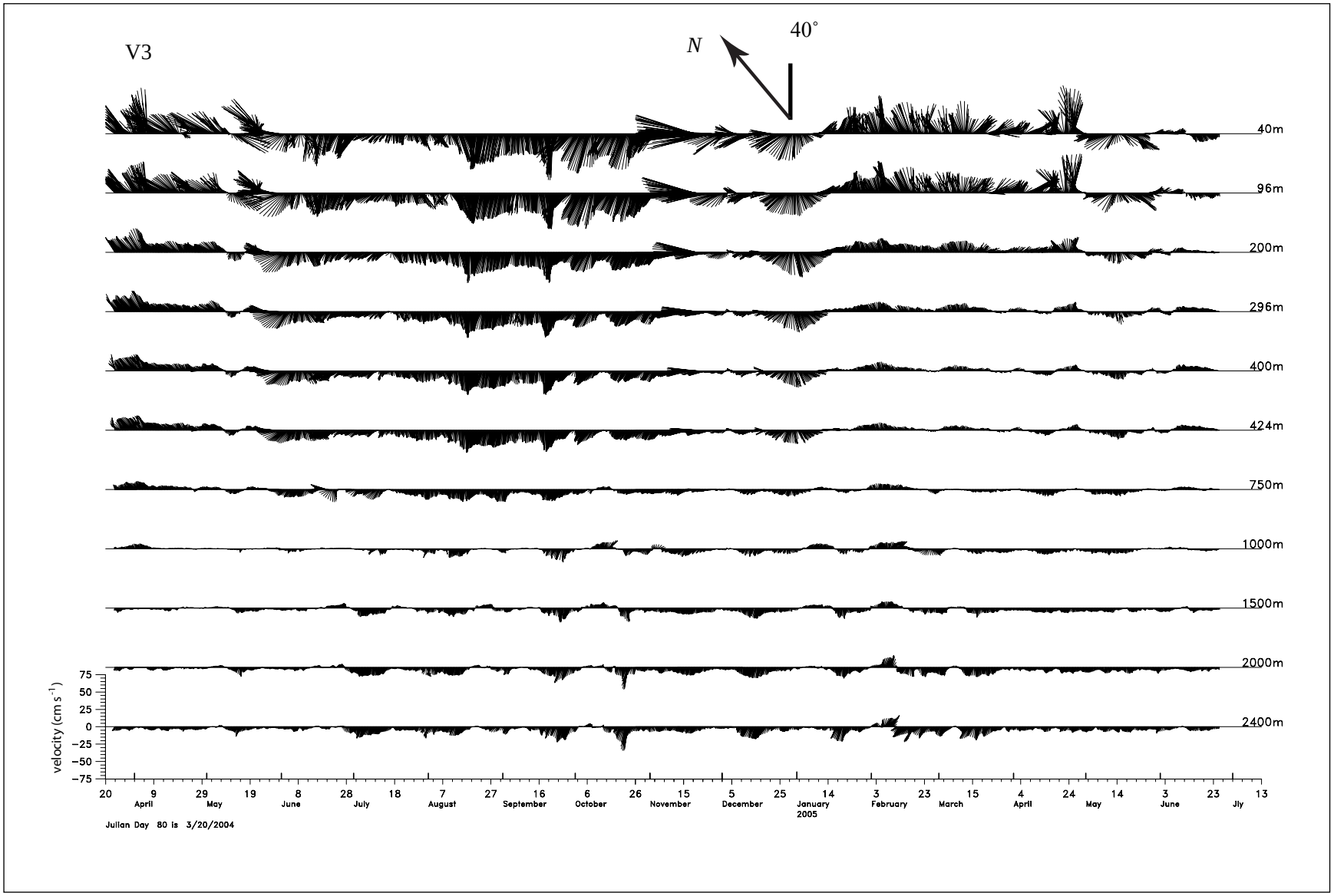

Figure B-12. 40-HLP vector plots of currents at selected depths on Mooring V3. These vectors have been rotated to the local direction of the isobaths. The direction of rotation and its relation to North is shown by the arrow in the figure..

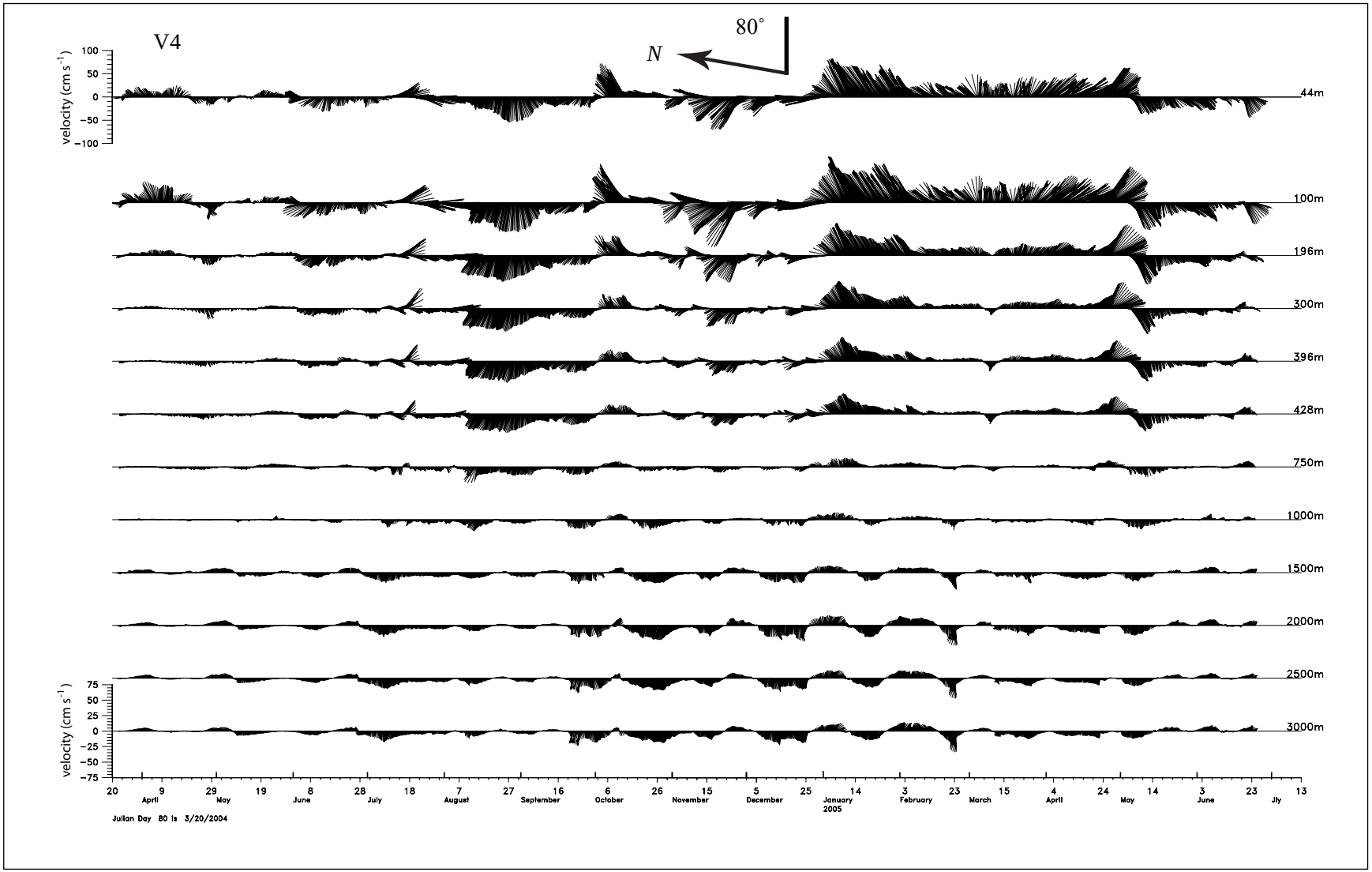

Figure B-13. 40-HLP vector plots of currents at selected depths on Mooring V4. These vectors have been rotated to the local direction of the isobaths. The direction of rotation and its relation to North is shown by the arrow in the figure..

The Department of the Interior Mission

As the Nation's principal conservation agency, the Department of the Interior has responsibility for most of our nationally owned public lands and natural resources. This includes fostering sound use of our land and water resources; protecting our fish, wildlife, and biological diversity; preserving the environmental and cultural values of our national parks and historical places; and providing for the enjoyment of life through outdoor recreation. The Department assesses our energy and mineral resources and works to ensure that their development is in the best interests of all our people by encouraging stewardship and citizen participation in their care. The Department also has a major responsibility for American Indian reservation communities and for people who live in island territories under U.S. administration.

The Minerals Management Service Mission

As a bureau of the Department of the Interior, the Minerals Management Service's (MMS) primary responsibilities are to manage the mineral resources located on the Nation's Outer Continental Shelf (OCS), collect revenue from the Federal OCS and onshore Federal and Indian lands, and distribute those revenues.

Moreover, in working to meet its responsibilities, the **Offshore Minerals Management Program** administers the OCS competitive leasing program and oversees the safe and environmentally sound exploration and production of our Nation's offshore natural gas, oil and other mineral resources. The MMS **Minerals Revenue Management** meets its responsibilities by ensuring the efficient, timely and accurate collection and disbursement of revenue from mineral leasing and production due to Indian tribes and allottees, States and the U.S. Treasury.

The MMS strives to fulfill its responsibilities through the general guiding principles of: (1) being responsive to the public's concerns and interests by maintaining a dialogue with all potentially affected parties and (2) carrying out its programs with an emphasis on working to enhance the quality of life for all Americans by lending MMS assistance and expertise to economic development and environmental protection.